Transactions of the ASME®

Technical Editor
H. L. JULIEN (1998)

Associate Technical Editors
Advanced Energy Systems
M. J. MORAN (1996)
Gas Turbine
R. KIELB (1996)
S. SAMUELSEN (1996)
J. N. SHINN (1996)
L. RIEKERT (1997)
Internal Combustion Engine
W. CHENG (1996)
Nuclear Engineering
H. H. CHUNG (1996)
Power
D. LOU (1998)

BOARD ON COMMUNICATIONS
Chairman and Vice President
R. MATES

Members-at-Large
T. BARLOW, N. H. CHAO, A. ERDMAN, G. JOHNSON, L. KEER, E. M. PATTON, S. PATULSKI, S. ROHDE, R. SHAH, F. WHITE, J. WHITEHEAD, K. T. YANG

OFFICERS OF THE ASME
President, D. T. KOENIG
Exec. Director
D. L. BELDEN
Treasurer
R. A. BENNETT

PUBLISHING STAFF
Managing Director, Engineering
CHARLES W. BEARDSLEY
Director, Technical Publishing
JANET M. WEINRIB
Managing Editor, Technical Publishing
CYNTHIA B. CLARK
Managing Editor, Transactions
CORNELIA MONAHAN
Senior Production Editor,
VALERIE WINTERS
Production Assistant,
MARISOL ANDINO

Transactions of the ASME, Journal of Engineering for Gas Turbines and Power (ISSN 0742-4795) is published quarterly (Jan., April, July, Oct.) for $175.00 per year by The American Society of Mechanical Engineers, 345 East 47th Street, New York, NY 10017. Second class postage paid at New York, NY and additional mailing offices. POSTMASTER: Send address changes to Transactions of the ASME, Journal of Engineering for Gas Turbines and Power, c/o THE AMERICAN SOCIETY OF MECHANICAL ENGINEERS, 22 Law Drive, Box 2300, Fairfield, NJ 07007-2300.

CHANGES OF ADDRESS must be received at Society headquarters seven weeks before they are to be effective. Please send old label and new address.

PRICES: To members, $40.00, annually: to nonmembers, $175.00. Add $30.00 for postage to countries outside the United States and Canada.

STATEMENT from By-Laws. The Society shall not be responsible for statements or opinions advanced in papers or . . . printed in its publications (B7.1, par. 3).

COPYRIGHT © 1996 by The American Society of Mechanical Engineers. Authorization to photocopy material for internal or personal use under circumstances not falling within the fair use provisions of the Copyright Act is granted by ASME to libraries and other users registered with the Copyright Clearance Center (CCC) Transactional Reporting Service provided that the base fee of $3.00 per article is paid directly to CCC, Inc., 222 Rosewood Dr., Danvers, MA 01923. Request for special permission or bulk copying should be addressed to Reprints/Permission Department.

INDEXED by Applied Mechanics Reviews and Engineering Information, Inc. Canadian Goods & Services Tax Registration #126148048

Journal of Engineering for Gas Turbines and Power

Published Quarterly by The American Society of Mechanical Engineers

VOLUME 118 • NUMBER 2 • APRIL 1996

TECHNICAL PAPERS

Gas Turbines: Aircraft

229 **A Method to Reduce the Rejection Rate for Low Performance at the Acceptance Test of PWC PT6T-6 Overhauled Power Sections** (95-GT-173)
S. Colantuoni, G. Mainiero, and A. Esposito

236 **Affordable Nacelle Technologies for Future Turbofans** (95-GT-402)
C. J. Smith

Gas Turbines: Ceramics

240 **Subcritical Crack Growth Life Prediction for Ceramic Components of Advanced Heat Engines** (95-GT-236)
D. C. Wu, A. D. Peralta, M. N. Menon, and J. C. Cuccio

246 **Thermal Shock Analysis and Testing of Simulated Ceramic Components for Gas Turbine Applications** (95-GT-308)
H. Rajiyah, L. P. Inzinna, G. G. Trantina, R. M. Orenstein, and M. B. Cutrone

251 **Effect of Cyclic Loading on the Creep Performance of Silicon Nitride** (95-GT-309)
A. A. Wereszczak, M. K. Ferber, T. P. Kirkland, and C.-K. J. Lin

Gas Turbines: Closed Cycles

257 **Combined Helium and Combustion Gas Turbine Plant Exploiting Liquid Hydrogen (LH_2) Physical Exergy** (95-GT-298)
G. Bisio, A. Massardo, and A. Agazzani

Gas Turbines: Combustion and Fuels

265 **Mechanisms of Coke Formation in Gas Turbine Combustion Chambers** (95-GT-49)
M. Brandauer, A. Schulz, and S. Wittig

271 **Jet Fuel Deposition and Oxidation: Dilution, Materials, Oxygen, and Temperature Effects** (95-GT-50)
S. Zabarnick, P. Zelesnik, and R. R. Grinstead

278 **Surface Effects on Deposits From Jet Fuels** (95-GT-103)
J. S. Ervin, S. P. Heneghan, C. R. Martel, and T. F. Williams

286 **Surface Fouling in Aviation Fuels: An Isothermal Chemical Study** (95-GT-45)
E. G. Jones, W. J. Balster, and J. M. Pickard

292 **Modeling of Local Extinction in Turbulent Flames** (95-GT-433)
D. G. Sloan and G. J. Sturgess

308 **Study of Flame Stability in a Step Swirl Combustor** (95-GT-111)
M. D. Durbin, M. D. Vangsness, D. R. Ballal, and V. R. Katta

Gas Turbines: Electric Utilities

316 **Evolution of Westinghouse Heavy-Duty Power Generation and Industrial Combustion Turbines** (94-GT-488)
A. J. Scalzo, R. L. Bannister, M. DeCorso, and G. S. Howard

331 **Benefits of MS 6001B Gas Turbine in Cogeneration: The UEM Power Plant Case** (94-GT-421)
P. M. Remy, Y. M. Boissenin, and M. M. Molière

Gas Turbines: Industrial and Cogeneration

337 **Advances in Steam Path Technology** (95-CTP-2)
J. I. Cofer, IV

353 **Modeling of (Cogeneration) Power Plants on Time-Dependent Power Demands of the Consumer** (95-CTP-48)
M. Witzani and P. Pechtl

359 **Air Bottoming Cycle: Use of Gas Turbine Waste Heat for Power Generation** (95-CTP-50)
O. Bolland, M. Førde, and B. Hånde

(Contents continued on page 264)

Downloaded 03 Jun 2010 to 171.66.16.159. Redistribution subject to ASME license or copyright; see http://www.asme.org/terms/Terms_Use.cfm

(Contents continued)

Gas Turbines: Marine

369 Component and Procedural Improvements for the T-62T-40-7 Gas Turbine in the LCAC Fleet (94-GT-168)
J. P. Ehrhardt and S. K. Spring

375 The Installation, Testing, and Lessons Learned of the TF40B Gas Turbine Test Facility (95-GT-310)
J. S. Patterson and H. Harris

Gas Turbines: Propulsion Systems

380 Aero Engine Test Experience With CMSX-4® Alloy Single-Crystal Turbine Blades (94-GT-169)
K. P. L. Fullagar, R. W. Broomfield, M. Hulands, K. Harris, G. L. Erickson, and S. L. Sikkenga

Gas Turbines: Structures and Dynamics

389 Experimental Leakage and Rotordynamic Results for Helically Grooved Annular Gas Seals (95-GT-179)
D. W. Childs and A. J. Gansle

394 Application of Advanced Probabilistic Fracture Mechanics to Life Evaluation of Turbine Rotor Blade Attachments (95-GT-214)
H. R. Millwater, Y.-T. Wu, J. W. Cardinal, and G. G. Chell

399 Fatigue Crack Growth Behavior of PWA 1484 Single Crystal Superalloy at Elevated Temperatures (95-GT-452)
J. Telesman and L. J. Ghosn

406 Surface Integral and Finite Element Hybrid Method for Three-Dimensional Analysis of Arbitrarily Shaped Surface Cracks (95-GT-456)
W. D. Keat, D. M. Maybury, and B. S. Annigeri

411 A Probabilistic Method for the Fatigue Life Assessment of Powder Metallurgy Parts of Aircraft Engines (95-GT-218)
R. Krafft and S. Mosset

416 Fatigue Cracking in Fiber-Reinforced Metal Matrix Composites Under Mechanical and Thermal Loads (95-GT-315)
G. Bao and R. M. McMeeking

424 Determination of Blade Stresses Under Constant Speed and Transient Conditions With Nonlinear Damping
J. S. Rao and N. S. Vyas

Gas Turbines: Vehicular

434 F117-PW-100 Hybrid Ball Bearing Ceramic Technology Insertion (95-GT-390)
J. R. Miner, J. Dell, A. T. Galbato, and M. A. Ragen

443 Predicting Steady-State Temperature, Life, Skid, and Film Thickness in a Greased Preloaded Hybrid Ball Bearing (95-GT-392)
J. V. Poplawski, D. R. Atwell, M. J. Lubas, and V. Odessky

449 Hybrid Ceramic Bearings for Difficult Applications (95-GT-391)
M. M. Dezzani and P. K. Pearson

Power

453 Thermodynamic Analysis of New Combination of Supercharged Boiler Cycle and Heat Recovery Cycle for Power Generation
M. Akiba and E. A. Thani

ANNOUNCEMENTS

250 Change of address form for subscribers

Inside back cover Information for authors

Downloaded 03 Jun 2010 to 171.66.16.159. Redistribution subject to ASME license or copyright; see http://www.asme.org/terms/Terms_Use.cfm

A Method to Reduce the Rejection Rate for Low Performance at the Acceptance Test of PWC PT6T-6 Overhauled Power Sections

S. Colantuoni

G. Mainiero

A. Esposito

ALFA ROMEO AVIO—Societa' Aeromotoristica per Azioni, R&D—Design Technologies—Propulsion & Aerothermodynamics, 80038 Pomigliano d'Arco (Napoli)—Italy

Alfa Romeo Avio is involved in the overhaul process of the Pratt & Whitney of Canada PT6T-6 for the helicopter fleet of the Italian Army and civil services. The overhauled power sections suffered from a high rejection rate (about 40 percent) for low performance at the acceptance test. Alfa Romeo Avio R&D investigated the causes and developed a method to reduce the rejection rate. A first contribution to the decision support method for the selection of the optimal engine configuration can be obtained from engine thermodynamic cycle simulation, which gives indications on the behavior of the average overhauled power section. In this paper the authors also describe a statistical model based on a cause/effect correlation between power section assembly variables and performance parameters. A simulation procedure, based on the statistical model, estimates the influence of the configuration assembly data on the power section performance parameters. A careful application of both statistical and thermodynamic models gives predictions on the optimum matching of turbine nozzle size to reach the target performance at the engine acceptance test. The method has been tested on the field during the last two years and a reduction in the rejection rate at the acceptance test to 18 percent has been obtained.

Introduction

Since 1977 Alfa Romeo Avio has assembled more than two hundred kits of the Pratt & Whitney of Canada PT6T-6 twin turboshaft for the helicopter fleet of the Italian Army, Navy, Air Force, and several civil services.

The PT6T-6 engine has two power sections (*PS*), parallel to and independent of each other, connected to a common gearbox, by which the global power is transmitted to the helicopter gearbox.

Each *PS*, a turboshaft with free power (*PW*) turbine, has a gas generator group composed of an axicentrifugal compressor (three stages axial and one stage centrifugal), a reverse annular combustor, and a single-stage gas generator (*GG*) turbine. The *PW* turbine is a single-stage shrouded turbine. Figure 1 shows the *PS* cross section.

As for the new engines, the problem of rejection at the acceptance test for low performance was easy to manage, thanks to the guidelines for trouble-shooting by PWC.

In fact, when new engines were assembled, the rejection rate for low performance was within the normal levels. Since 1986 the company has also been involved in the overhaul of the PT6T-6 and the number of engines to be overhauled rapidly increased year by year.

The engine overhaul must be done typically after 2000 flight operating hours and is relative to each module, i.e., the single *PS* and the gear box. The engine is completely disassembled, and each item is inspected to verify its integrity, status, and degree of functionality. Accordingly a series of inspective controls, repairing process applications (if possible and convenient), substitutions of components either damaged or at the end of useful life are performed.

At the end of this phase of the overhaul process, a list of all items of the engine to be assembled is defined: They are mostly items coming from the same engine, but eventually some parts are replaced with new or used ones.

In the beginning, the overhauled power sections experienced a high rejection rate at the final acceptance test for low performance.

It is well known that the operation of engine rebuilding does affect the performance. In fact, simply disassembling and reassembling a turbine engine may result in a random shift in its performance, due to small changes of the internal geometric tolerances in the flow path of the component (Macleod and Orbanski, 1992). Similarly, the compressor can change its efficiency, even by small variations between the design and the production compressor. In particular, used blading can adversely affect the performance of the compressor (Marson, 1992). This results in a rematch of the turbine with the compressor, which shows up shifts in the component and overall engine performance.

The sum of these effects can affect the engine performance up to 1 percent of the various engine parameters.

Furthermore, in case of small size engine, there is a greater sensitivity to clearance, dirt, and FOD (Badger et al., 1994).

As a matter of fact the behavior of the overhauled engines, with new and used components sometimes assembled together, very often is different when compared to that of completely new engines. Such difference is hard to quantify, due to the deteriorated aerodynamic performance of the compressor and turbine static and rotating blade rows, caused by the erosion effects produced during the operative life.

The high rejection rate for the PT6T-6 *PS* in the past has been considered acceptable by the overhaul division, because of both the initial phase of the overhaul process and the small

Contributed by the International Gas Turbine Institute and presented at the 40th International Gas Turbine and Aeroengine Congress and Exhibition, Houston, Texas, June 5–8, 1995. Manuscript received by the International Gas Turbine Institute February 16, 1995. Paper No. 95-GT-173. Associate Technical Editor: C. J. Russo.

Copyright © 1996 by ASME

Downloaded 02 Jun 2010 to 171.66.16.104. Redistribution subject to ASME license or copyright; see http://www.asme.org/terms/Terms_Use.cfm

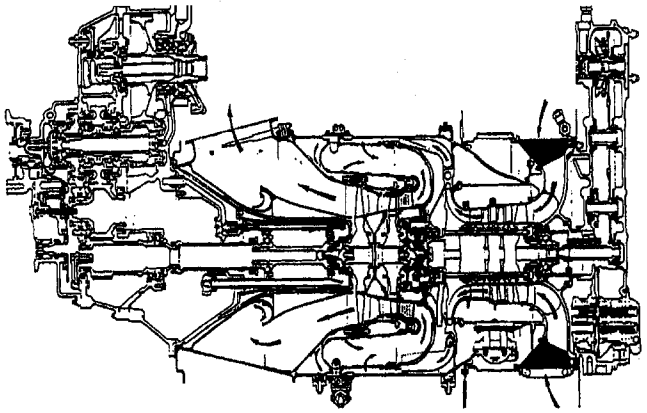

Fig. 1 Pratt & Whitney of Canada PT6T-6 engine cross section

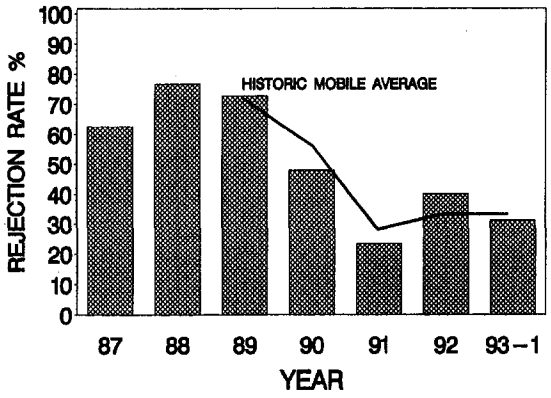

Fig. 2 Rejection rate at first acceptance test of *O/H PS* (historical trend)

number of *PS* involved. As the number of overhauled engines grew, the company experienced increasing costs of the overhaul process for high rejection rate at the final acceptance test.

Therefore Alfa Romeo Avio R&D developed a method to predict the performance of the overhauled engines in order to improve the effectiveness of the overhaul process. The goal was to define the optimum configuration of the *PS* that maximizes the possibility of passing the acceptance test.

Problem Statement

After the overhaul process, the engine must pass the acceptance test, to assure achievement of performance and mechanical requirements. The acceptance test consists of a series of readings at various power settings; then the measured performance data in terms of gas generator rotative speed (*NG*), exhaust gas temperature (EGT), specific fuel consumption (SFC) are reduced at reference conditions. The final acceptance test of the PT6T-6 requires that the engine must guarantee (with a single *PS*) a power of 970 SHP, with *NG* between NG_{MIN} and NG_{MAX}, SFC below SFC_{MAX} and EGT below EGT_{MAX}.

In 1986–87, when the overhaul process started, more than 60 percent of the total *PS* tested were rejected for "low performance" at the first acceptance test; as the experience increased with time the rejection rate decreased, but the historic average was still around 40 percent (see Fig. 2).

The rejections for low performance at the first acceptance test of overhauled *PS* were essentially due to $NG > NG_{MAX}$ (more than 71 percent of all the rejections), sometimes to EGT $>$ EGT_{MAX} (about 7 percent) or combination of EGT $>$ EGT_{MAX} and $NG < NG_{MIN}$ (about 6 percent). This high rejection rate was essentially due to a mismatch between the *GG* turbine nozzle guide vane (NGV_{GG}) throat area and the *PW* turbine nozzle (NGV_{PW}) throat area.

The problem was historically approached by correcting the NGV_{PW} area. In fact the rejected *PS* were sent back to the line, where they were partially disassembled in order to modify the NGV_{PW} and reach the target performance; sometimes a rematch between the NGV_{GG} and the NGV_{PW} was done. The main difficulty of this approach was due to effectiveness of the decisions

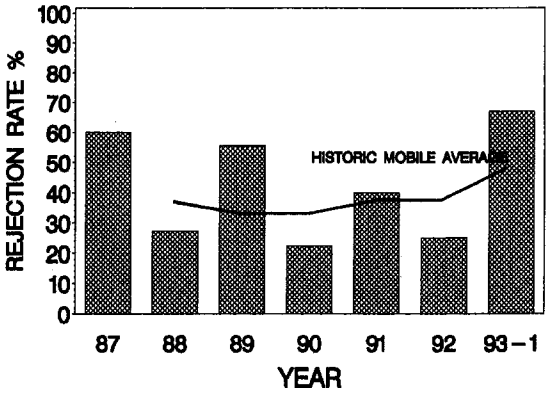

Fig. 3 Rejection rate at second acceptance test for *O/H PS* (historical trend)

regarding the overhaul to achieve the required target performance.

The criterion used to select the NGV matching, based upon the experience done at the acceptance test of new *PS*, was inefficient when applied to the overhauled *PS*. Another complication was due to the procedure to modify the NGV_{PW} throat area by imposing an effective mechanical deformation on the trailing edge of the blade in order to obtain the target flow capacity (measured with a cold air flow rig by comparison with a master nozzle of known area). An additional difficulty was due to the inhomogeneous behavior of the overhauled *PS*: The same corrective action could have different effects on the performance.

Another problem was the high rejection rate at the second acceptance test (about 45 percent). In this case, the main difficulties were on the *PS* rejected at the first acceptance test for EGT $>$ EGT_{MAX} or a combination of EGT $>$ EGT_{MAX} and $NG < NG_{MIN}$: The past experience of the overhaul division produced inefficient corrective actions because of the anomalous behavior of such critical *PS*.

Nomenclature

C = turbine nozzle capacity
EGT = exhaust gas temperature
NG = gas generator speed
NGV = turbine nozzle guide vane
O/H = overhaul
PS = power section
Q = qualitative variable
SFC = specific fuel consumption
SM = surge margin
$\mathcal{P}$ = probability
Δ = increment

Subscripts

GG = gas generator
l = lower
MAX = maximum
MIN = minimum
PW = power
u = upper

Downloaded 02 Jun 2010 to 171.66.16.104. Redistribution subject to ASME license or copyright; see http://www.asme.org/terms/Terms_Use.cfm

Technical Approach

The Alfa Romeo Avio R&D approach has been to start with an engine cycle analysis, performed to acquire a first knowledge of the problem. This has been done using a simulation code, developed "in-house" and calibrated upon the mean values of performance parameters obtained from those overhauled *PS* that passed the acceptance test.

The use of this code enabled the evaluation of the impact of turbomachine efficiency, of the turbine NGV areas, and of some air system typical failures on the performance of the "average" *PS*. On the other hand, the simulation code could not predict the performance of the single *PS*, i.e., taking into account the status of the turbomachinery components and/or the modification standard.

A possible approach to get such information was to develop an experimental campaign performing a series of tests on a single engine using the Taguchi analysis (Wheless et al., 1990). This approach could not be followed because it was time consuming and cost effective.

Therefore an alternative approach has been defined, based on the application of statistical methodologies on the *PS* information available.

In the preliminary phase of development, data for each overhauled *PS* regarding both the acceptance test performance and any significant information on the configuration assembly were collected. At the end a database has been built, where each observation is relevant to a *PS* test with assembly and performance data.

Then statistical methodologies have been applied, in order to identify existing correlations between assembly variables and performance data, and to define a statistical model for the overhauled *PS*.

Thermodynamic Model

The thermodynamic cycle simulation has been performed by means of a computer code, developed by Alfa Romeo Avio. This code is based on the state vector technique, which is to say the matching of the components with the use of their estimated characteristics map.

The matching of components is based on the assumption that the mass flow rate exiting from a component must be processed by the following component. Moreover there must not be a torque imbalance on the shaft linking the compressor and the turbine.

The reference performance level on which the computer code has been calibrated is based upon the mean of the performance of the *PS* that successfully passed the acceptance test during a period of five years.

The use of the simulation code highlighted the fact that the throat areas of both the NGV_{GG} and the NGV_{PW} turbines are influencing variables on *PS* performance.

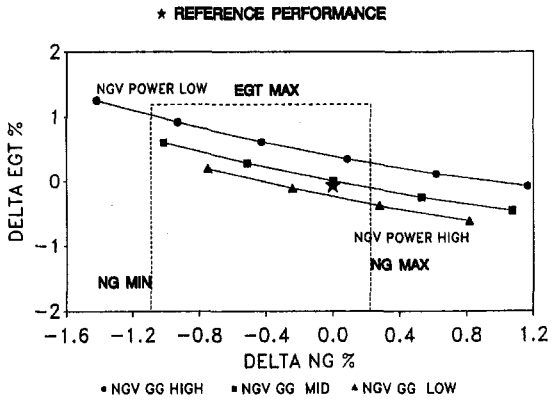

Fig. 4 Effect on performances of turbine stator areas

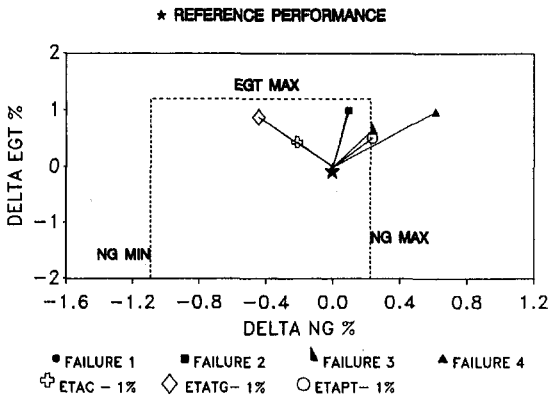

Fig. 5 Engine cycle sensitivity analysis at maximum power

As a matter of fact, as shown in Fig. 4, the *PS* performance at reference power level, expressed in terms of *NG* and EGT, are strictly dependent on the matching between the *GG* and *PW* turbine's NGV: A rise in the *PW* turbine NGV capacity (C_{PW}) increases the *NG*, lowering the EGT, whereas a rise in *GG* turbine capacity (C_{GG}) produces an increase of both *NG* and EGT.

Furthermore, the simulation code made possible the evaluation of either the effects of turbomachine inefficiency and air-system failures on the cycle or the sensitivity of the cycle to the variation of flow passages (i.e., variation of mass flow used for the cooling of turbine and disks).

Figure 5 shows the effects on EGT and *NG* of various efficiency drops and failures of air system at reference power level for a given NGV capacity matching. In this figure empty symbols indicate the effects of 1 percent component inefficiency (i.e., ETAC, ETATG, and ETATP are the effects of the compressor, the *GG* turbine, and the *PW* turbine, respectively) while dark symbols indicate the effect of air system failures (i.e., 1 for a bleed valve leakage, 2 for a cooling flow leakage, 3 for a bleed overboard at compressor exit, and 4 for a bypass of *PW* turbine).

A systematic numerical investigation has been developed in order to find the limits for the "average" *PS* upon the possible matching of turbine capacity in terms of the acceptance limits: EGT_{MAX}, SFC_{MAX}, NG_{MAX}, and NG_{MIN}. These limits for the baseline "average" *PS* are shown in Fig. 6, where the shaded area represents the NGV matchings for which the engine respects the acceptance limits.

The limit indicated with *SM* (surge margin) is a conservative rule upon the equilibrium point on the compressor map that gives an adequate surge margin during transients.

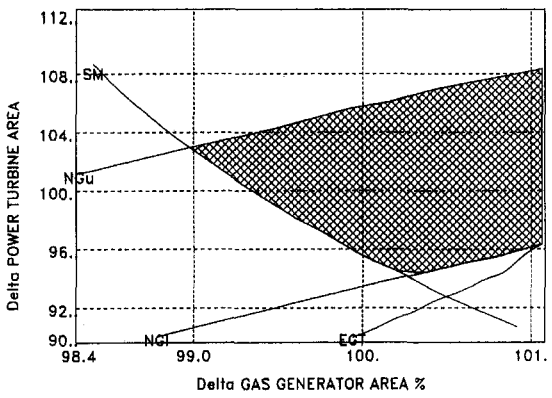

Fig. 6 Average overhauled *PS* predicted performance boundary

Downloaded 02 Jun 2010 to 171.66.16.104. Redistribution subject to ASME license or copyright; see http://www.asme.org/terms/Terms_Use.cfm

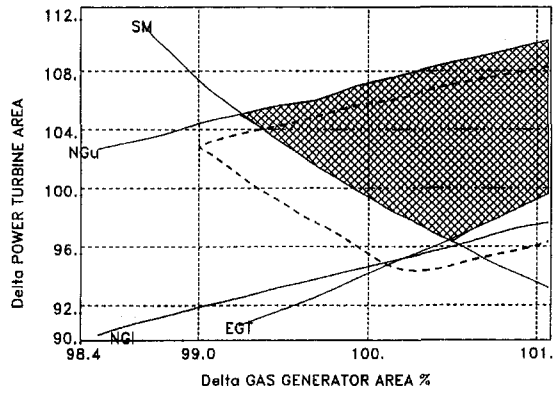

Fig. 7 Effect of compressor efficiency (−1 percent) on performance boundary

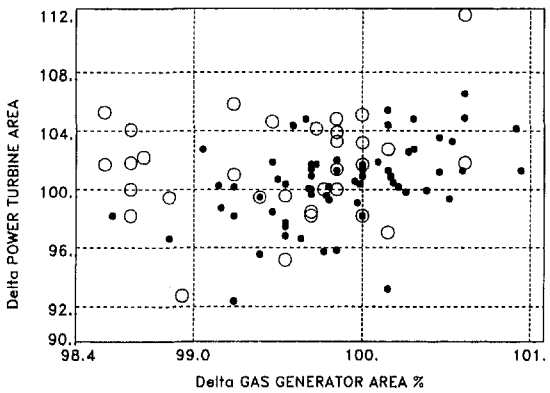

Fig. 9 Turbine capacity data base (up to 1992)

To obtain these results, it was necessary to make some hypothesis about the behavior of the *PW* turbine (i.e., the *PW* turbine efficiency is independent from the nozzle capacity).

In Figs. 7 and 8, it is very interesting to observe the simulation of the effects of a compressor and power turbine efficiency drop (1 percent) on optimum matching area of NGV turbines.

In both cases a reduction of the shaded area representative of the NGV matching is observed, which guarantees, at the prescribed power level, the satisfaction of boundary limits on *NG*, EGT, and SFC.

Furthermore, in the case of deteriorated turbomachinery components, the shaded area moves on the turbine capacity plane, which means that possible optimal matchings predicted for the "average" overhauled *PS* are not valid in case of engines having an acceptable level of deterioration that penalizes the turbomachine efficiency.

In conclusion, the thermodynamic model, calibrated on the "average" overhauled *PS* performance, which successfully passed the acceptance test, can give the following useful information:

1 Define the optimum matching of NGV turbine capacities for *PS* having typical overhauled performance behavior.
2 Perform a diagnostic of *PS* having unusual performance behavior (rejected at the first acceptance test) so that a corrective action can be defined for the specific problem identified.

In any case it is important to remark that the thermodynamic model cannot distinguish a priori the different behavior of overhauled *PS* compared with the "average" good one, and therefore a method "ad-hoc" must be developed for this problem.

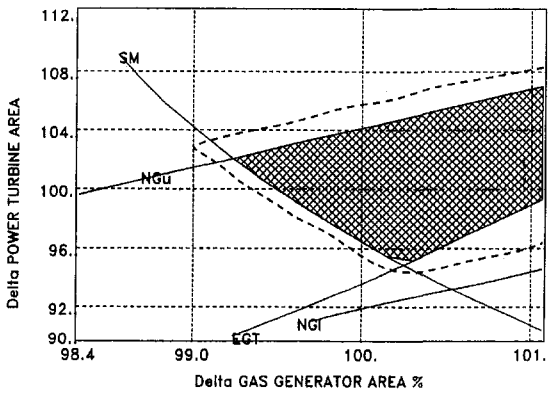

Fig. 8 Effect of *PW* turbine efficiency (−1 percent) on performance boundary

Statistical Model

The first step in the creation of a statistical model was the collection of the data relative to the configuration of the engine and the performance measured at acceptance test.

The assembly data collected were essentially the engine serial number, the turbine stator capacities, some radial clearances, and some axial clearances between rotating and static parts. Furthermore, the observations collected were classified into groups, depending on the status (new or used) of the turbines and compressor components and on *PS* modification standards. The intention was to evaluate the possible influence of the assembly of new or used components on the measured performance of the *PS*.

A descriptive analysis was performed on the data collected and classified in the database, in order to get a first screening of those assembly parameters that more strongly affect the performance.

An example of graphic representation of the data collected is shown in Fig. 9, where, using the turbine capacity plane, the empty symbols report the *PS* rejected at the acceptance test for low performance, while the dark symbols report those that passed the test.

On one hand, the figure shows some regions with prevalence of rejected *PS* while, on the other hand, it is not possible to identify clearly any area with prevalence of *PS* that passed the test.

Then, with the help of regression analysis, it has been possible to identify the clearances and the qualitative variables that could likely affect the performance. The variables that seemed to have a greater impact on the performance were: the *PW* turbine NGV and the *GG* turbine NGV capacity, the radial tip clearance of *PW* turbine rotor, the axial clearance of the *GG* turbine, and some critical clearances of the air system.

Nevertheless, the status (new or used) of the hot section turbine components seemed to be rather important.

At the beginning of the study only linear models were considered to build the statistical model due to the relatively small size of sample.

The model relates the critical performance measures (*NG* and EGT) with those variables found to have significant impact on them, and can represented generically by:

$$NG = f(C, X_I, Y_J, Q_K)$$

$$\text{EGT} = g(C, X_I, Y_J, Q_K)$$

where the independent variables represent:

C = quantitative variables, relative to the throat areas of the turbine NGVs and defined at the pre-assembly phase (C_{GG}, C_{PW});
X_i = quantitative variables, measuring some build

Downloaded 02 Jun 2010 to 171.66.16.104. Redistribution subject to ASME license or copyright; see http://www.asme.org/terms/Terms_Use.cfm

clearances, whose values are set at the pre-assembly phase and limited to prescribed tolerance ranges;

Y_j = quantitative variables, measuring some clearances, whose values are defined at the final assembly phase and are limited to prescribed tolerance ranges;

Q_k = qualitative variables, relative to the status (new/used) of turbomachinery subcomponents and modification standards.

The variables listed above were selected on the basis of the following criteria:

- an engineering judgment of all those variables having a potential strong influence on the performance measures,
- a statistical criterion for selecting a subset of these variables, that, given the sampled data, could exhibit significant effects on *NG* and EGT, and yield most precise and least biased prediction.

Afterward, it was possible to develop a procedure, based on a series of statistical models, aimed at facilitating the decision-making process about the most effective overhaul actions.

Out of the four classes of predictor variables described above, those denoted by Y_j were treated as noise, since their values could not be controlled during the pre-assembly phase. In order to assess their impact on predicting the performance, their values were randomly generated over the prescribed tolerance ranges. Thus, the procedure developed consisted of the following steps:

0 Set Q_K indicative of the *PS* status;
1 Set the range of the values of the variables C_{GG}, C_{PW} to be explored;
2 Select different levels of X_i variables;
3 Generate random Y_j variables;
4 Evaluate the predictions of *NG* and EGT, at each combination of values of predictor variables (C_{GG}, C_{PW}, and X_i).
5 Estimate the expected probabilities of both performance measures falling within the specification limits, and mean predicted *NG* and EGT, for each combination of assembly variables.

This procedure gives for each setting of C_{GG} and C_{PW} the predicted probabilities of success (both performance within limits) $\hat{P}$, and prediction interval limits, $\hat{P}_l$ and $\hat{P}_u$, showing the precision of this estimate. The width of the prediction interval ($\hat{P}_l$, $\hat{P}_u$) depends on how precisely *NG* and EGT can be predicted, for given values of C_{GG} and C_{PW}, and how far from the specification limits these predictions are.

A success is defined as an outcome when both predicted performance measures fall within the prescribed specification limits, i.e., a target area identified in the plane *NG*/EGT by the following limits:

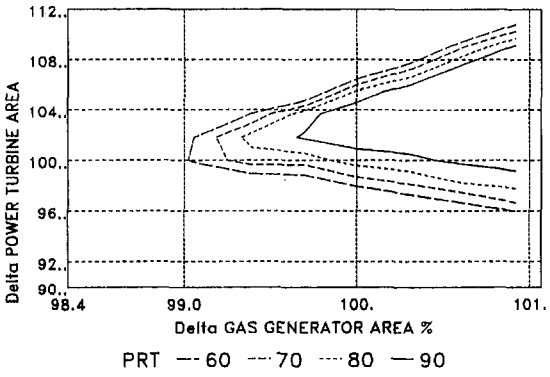

Fig. 10 Distribution of probability to pass the test (baseline configuration)

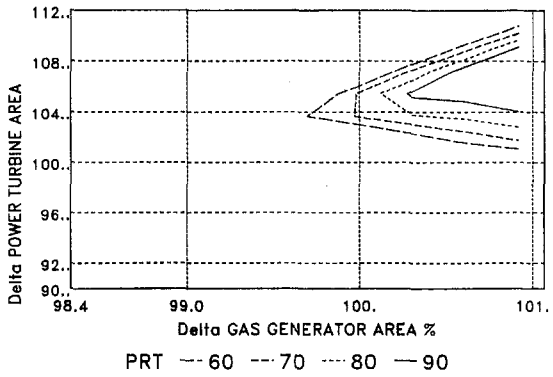

Fig. 11 Distribution of probability to pass the test (large turbine tip clearance)

$$NG_{\text{min target}} = NG_{\text{min}} + \Delta NG$$

$$NG_{\text{max target}} = NG_{\text{max}} - \Delta NG$$

$$\text{EGT}_{\text{max target}} = \text{EGT}_{\text{max}} - \Delta\text{EGT}$$

where ΔNG and ΔEGT are used in the first period to take into account, as a conservative rule, the possible differences between the reality and the statistical model adopted and NG_{min}, NG_{max}, and EGT_{max} are the limits for the acceptance test of the engine; as the application of this procedure will go on it should be possible to be more confident in the results and this Δ could be reduced.

The output of the numerical procedure can be represented graphically by plotting the results on the turbine nozzle capacity plane. The distribution of probability to pass the acceptance in the case of baseline configuration (i.e., all used components and clearances at their midvalue) is given in Fig. 10.

If the engine assembly is done with higher value of *PW* turbine rotor tip clearance, the simulation procedure predicts an optimal matching in a different region (Fig. 11). The selection of NGV matchings is limited to a more restricted area.

In the case of a *PS* assembly with a new NGV_{GG}, the simulation procedure predicts a wider range of optimum matching (see Fig. 12).

On this basis it is possible to see how the "optimum" matching of the turbine stators can change with the configuration in terms of new or used components and in terms of low or high clearances.

Application of Method

Based on the previously described statistical model, the procedure is being tested on the field. The indications taken from the procedure are put into the decision process for the overhauled *PS*.

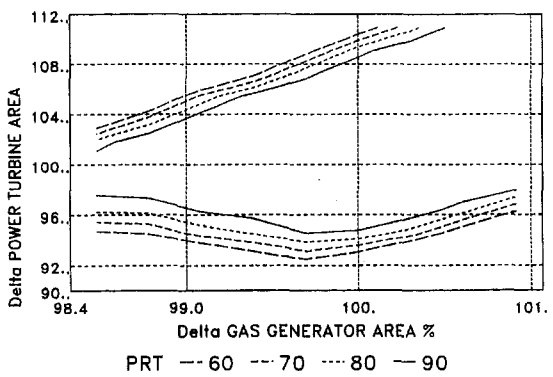

Fig. 12 Distribution of probability to pass the test (NGV_{GG} new)

Downloaded 02 Jun 2010 to 171.66.16.104. Redistribution subject to ASME license or copyright; see http://www.asme.org/terms/Terms_Use.cfm

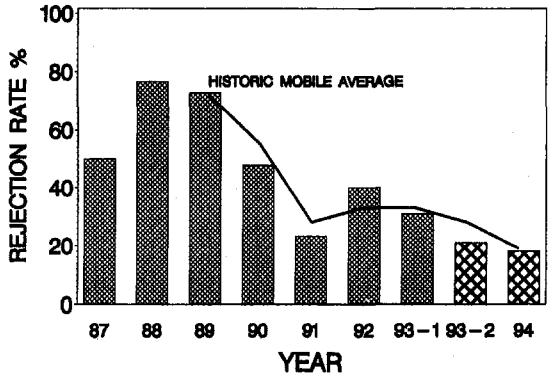

Fig. 13 Rejection rate at first acceptance test of *O/H* power sections

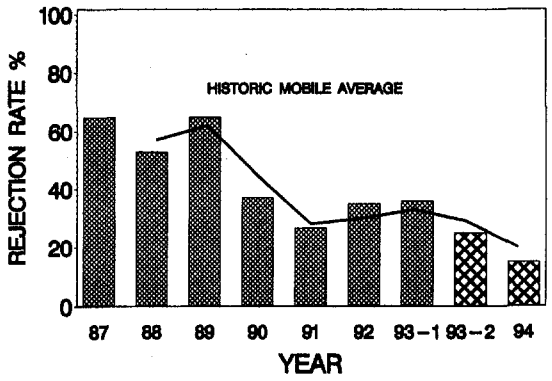

Fig. 15 Rejection rate on total acceptance test for *O/H* power sections

The procedure is currently used in the following way: Once the status of components and some clearances have been defined during the initial phase of the assembly, by running the simulation procedure, it is possible to find which combination, in terms of turbine stator capacities and clearances, can maximize the probability that the engine passes the acceptance test.

The outputs of the simulation are given in terms of turbine stator capacities and a prescribed range of tolerances regarding clearances and seals.

The statistical model can be used with good confidence for the combination of qualitative variables already present in good amount in the data base. The confidence level of the results of procedure is high when the difference between $\mathcal{P}_l$ and $\mathcal{P}_u$ is small, while, in case of high difference, the information for this procedure must be integrated with the results of the engineering model.

Therefore, when the engine has a combination of components and standard of modification different from those contained in an adequate number within the data base utilized for the development of the statistical model, the decisions about the optimal matching are taken according to the indications coming from the thermodynamic model.

Results

In the first two years of application of the method (June 1993–1994) the rejection rate at the first acceptance test for low performance has decreased from 38 to 18 percent as shown in Fig. 13.

The effectiveness of the corrective action on the rejected engines is shown in Fig. 14, where it is possible to see how the rejection rate at the second acceptance test has fallen to zero during last year. The global results, i.e., the rejection rate computed upon all acceptance tests, is shown in Fig. 15, where it is possible to see how the total rejection rate has decreased to 18 percent.

In conclusion, as summarized in Table 1, the application of the method allowed a drastic reduction of the rejection rate at both the first and the second acceptance tests.

The application of this method has a good impact also on the cost and the time spent for the overhaul of the *PS*; in fact, as shown in Fig. 16, the average number of tests performed for each *PS* that passed the acceptance test has been reduced to 1.17.

Another aspect of the application of this method is the impact on the average of the performance for the overhauled power sections.

In fact, if the margin on *NG* is computed as:

$$NG_{\text{Marg}} = 1 - \frac{NG_{\text{AVG}} - NG_{\text{MIN}}}{NG_{\text{MAX}} - NG_{\text{MIN}}}$$

and the margin on EGT as:

$$\text{EGT}_{\text{Marg}} = \text{EGT}_{\text{MAX}} - \text{EGT}_{\text{AVG}}$$

Table 1 Summary of the results on rejection rates (mobile average)

	First Acceptance Test	Second Acceptance Test	Total Acceptance Test
Historical Trend	38.%	47.%	38.%
Application of Method	18.%	9.%	18.%

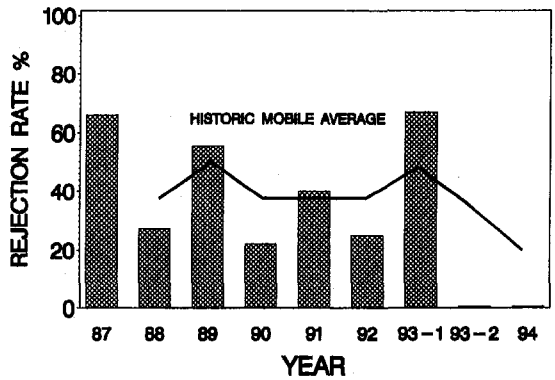

Fig. 14 Rejection rate at second acceptance test for *O/H* power sections

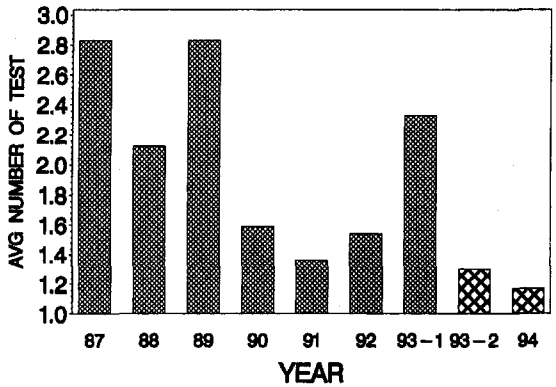

Fig. 16 Average number of tests performed for each accepted *PS*

Downloaded 02 Jun 2010 to 171.66.16.104. Redistribution subject to ASME license or copyright; see http://www.asme.org/terms/Terms_Use.cfm

Table 2 Average margin on performance for accepted *O/H PS*

	Ng Margin (%)	EGT Margin (°F)
Historical	23.	Base
Application of Method	36.	+10%

it is possible to see, from the results shown in Table 2, how the average engine passes the test with a greater margin on *NG* and generally with a lower EGT. The increase in the margins has a good impact on the life of the overhauled *PS*.

Conclusions

When the overhaul process for the PT6T-6 started, the *PS* suffered from a high rejection rate at the acceptance test.

To improve the effectiveness of the overhaul process, a method to reduce the rejection rate has been developed, based on an approach that uses both the thermodynamic model and the statistical model. The first gives an indication about the "average" *PS* while the second can give an indication about the particular class of *PS* configurations.

The first period of application of this procedure gave a good indication as for the significant reduction of the rejection rate of the *PS* at the acceptance test (from 38 to 18 percent on the total of the *PS* tested) and so the procedure has become a routine procedure for the production engines.

Another important result connected with the application of this procedure is that the margins upon *NG* and EGT are increased, with benefits on the overhauled *PS* useful life.

On the basis of the good results obtained with the application of this method on the PT6T-6 power sections, it has been planned to extend and adapt this approach to the other engines of the same family (i.e., PT6T-3 and PT6T-3B) overhauled by Alfa Romeo Avio.

Acknowledgments

The authors wish to thank all the people of Alfa Romeo Avio involved in the overhaul and testing of the Pratt & Whitney PT6T for their contribution to the development and testing of the method.

A particular thanks goes to Dr. V. Luzar for her contribution to the development of the statistical part of this work.

References

Badger, M., Julien, A., LeBlanc, A. D., Moustapha, S. H., Prabhu, A., and Smailys, A. A., 1994, "The PT6 Engine: 30 Years of Gas Turbine Technology Evolution," ASME JOURNAL OF ENGINEERING FOR GAS TURBINES AND POWER, Vol. 116, pp. 322–330.

Doel, D. L., 1994, "TEMPER—A Gas-Path Analysis Tool for Commercial Jet Engines," ASME JOURNAL OF ENGINEERING FOR GAS TURBINES AND POWER, Vol. 116, pp. 82–89.

Macleod, J. D., and Orbanski, B., 1992, "Turbine Rebuild Effects on Gas Turbine Performance," ASME Paper No. 92-GT-23.

Marson, E., 1992, "Effect of Manufacturing Deviations on Performance of Axial Flow Compressor Blading," ASME Paper No. 92-GT-326.

Wheless, K., Malak, M., and Kiker, R., 1990, "JFS190 Turbine Engine Performance Optimized Using Taguchi Methods," AIAA Paper No. 90-2419.

Downloaded 02 Jun 2010 to 171.66.16.104. Redistribution subject to ASME license or copyright; see http://www.asme.org/terms/Terms_Use.cfm

Affordable Nacelle Technologies for Future Turbofans

C. J. Smith
General Electric Aircraft Engines,
Cincinnati, OH 44135

Costs are playing an ever-increasing role in determining what the next generation of aircraft and engines will be. In addition to deciding to what extent wing/engine integration or drag-reducing laminar flow technologies can be employed, etc., the economic impact on both aircraft operation and engines launch and development costs must be evaluated. SFC or fuel burn advantages are no longer dominant to the extent they used to be and for some apparently promising technology concepts the cost disadvantages outweigh the aerodynamic advantages when both effects are transposed into aircraft direct operating costs. In addition, a simple metric has been evolved to rank different technology concepts and prioritize them in order to help determine the most deserving technologies for scarce development funds.

Introduction

Nacelle aerodynamic technology is a well-developed science and arguably offers less opportunity for refinement than does rotating aerodynamics. Large commercial subsonic airliner speeds and the air velocities at the engine inlet have changed little in 30 years, so it would seem that there is not much scope for making large improvements in nacelle technology to reduce engine installation losses significantly. There are, however, numerous ideas for reducing installation losses or drag, but it is important to consider all the implications of the changes a new technology will generate. Cost changes, especially, should be considered, because costs have currently assumed a much more important role, influencing new aircraft sales to a much greater extent than in the past.

A number of promising nacelle technologies have been examined for their possible influences on aircraft fuel burn and direct operating costs (DOC or DOC + I where I is a term to include the interest on money borrowed to purchase the aircraft).

The investigation has been taken a step further by making an assessment of the return on investment of the technology development costs relative to savings that the technology will generate when incorporated into a future commercial airliner fleet. In addition a simple figure of merit has been derived to help apportion limited development funding to the best economic advantage of the candidate aircraft/propulsion concept.

Direct Operating Cost Evaluations

All the applicable changes of SFC, drag, powerplant weight, price and maintenance cost from the various nacelle concepts have been converted into aircraft direct operating costs using "rubber" sensitivities. "Rubber" implies that a reduction in SFC, for example, will require the aircraft to carry less fuel and hence the rubber aircraft can be downsized, with attendant and additional synergistic economies.

These sensitivities are application specific and refer to a particular aircraft flown over a specific mission. The two aircraft used in this paper were an advanced medium range twin flown over a 1000 nautical mile range and a long range quad with a 5000 nautical mile mission. It can be seen that SFC and drag exert greater influence on DOC and weight less influence on DOC at the longer range, Fig. 1.

The items that are included in DOC + I, direct operating cost + interest, fall under three headings; cash DOC − (fuel, crew, maintenance, etc.), depreciation and interest. These are given in more detail together with a tabulation of the economic ground rules used in Fig. 1.

Ranking Factor

The nacelle concepts described in this paper were a few of the many technologies proposed for an advanced gas turbine in a large NASA-sponsored study. A figure of merit was required that could be used to rank this very diversified list of technologies in terms of their value to the airline industry measured against the cost of developing the technology.

The figure of merit selected was

$$\frac{\text{Value to airline} \times \text{Probability of success}}{\text{Development cost}};$$

see Fig. 2. Value to the airline equates directly with aircraft DOC. Probability of success is a subjective judgment on the likely outcome of the development program relative to the target improvement value, and as such relates to the most likely realizable value rather than the maximum possible attainable value. Development cost is all the costs incurred up to the point at which an engine launch decision can be made for an advanced engine incorporating the new technology.

In some instances the new technology had a negative value to the airline, not a cost reduction, in which case the concept was not given a ranking factor and was eliminated from further consideration.

Technology Concepts

1 Two Position Fan Nozzle. In one of the most widely used arrangements for engine thrust reversers, the aft portion of the cowl translates rearward, exposing a cascade that redirects the bypass stream to give it a forward direction and thus generate reverse thrust. This proposal adapts this type of conventional reverser. The first part of the cowl rearward movement is designed not to expose the reverser cascade but to increase the fan nozzle area, by careful design of the nozzle and core cowl profile. Further rearward movement deploys the blocker doors and the reverser cascade is exposed.

If the larger fan nozzle is used for take off and cruise mode, then it is possible to achieve a thrust increase at top of climb, above that of a fixed nozzle engine by closing the nozzle and raising the fan operating pressure ratio. A relatively small change to a conventional thrust reverser allows the moving parts to perform a dual role and offer a useful engine thrust growth.

Contributed by the International Gas Turbine Institute and presented at the 40th International Gas Turbine and Aeroengine Congress and Exhibition, Houston, Texas, June 5–8, 1995. Manuscript received by the International Gas Turbine Institute March 18, 1995. Paper No. 95-GT-402. Associate Technical Editor: C. J. Russo.

Copyright © 1996 by ASME

Downloaded 02 Jun 2010 to 171.66.16.104. Redistribution subject to ASME license or copyright; see http://www.asme.org/terms/Terms_Use.cfm

Economic Ground Rules

80% depreciation over 15 years
10% down payment, 10% residual
6% airframe spares, 17% engine spares
6.0% interest
24.7 year service life
Fuel price = $0.70/USG
Labor rate = $16/mh + 200% burden
1990 dollars
Trips/year = 1300 for 1000 nm
475 for 5000 nm

DOC + I Includes

Cash DOC Items:
Flight crew
Cabin crew
Fuel
Airframe maintenance
Hull insurance
Landing fees
Depreciation:
Airframe
Engine
Interest:

Rubber Sensitivities, Note Application Specific, 1000 nm & 5000 nm

Percent Changes in Parameters to Change DOC by 1%		
Parameter	Percent Change	
	1000 nm	5000 nm
SFC	3.4	2.4
Drag	3.7	2.6
Power plant weight	16.0	25.0
Power plant price	8.9	8.7
Maintenance cost	23.0	27.0

Fig. 1 DOC + I ground rules and "rubber" sensitivities (1000 nm and 5000 nm mission)

Figure 3 identifies the changes that must be made to the thrust reverser, which include:

(*a*) lengthening the travel of the translating cowl
(*b*) modifying the blocker door operation, to keep it stationary for the first part of cowl movement
(*c*) designing the nozzle profile to ensure up to 5 percent area increase with the open nozzle and a passage that converges to the nozzle for all openings.

Considerable savings can be achieved with a variable fan nozzle because of the engine downsizing it permits. A required top of climb thrust level can be achieved with a smaller engine. The take-off thrust of this smaller engine would be restored by running the fan faster. Note that the "smaller" engine here has the same core size but a reduced fan diameter and bypass flow.

Some 0.3 percent sfc increase is to be expected from these changes. It will increase by about 0.1 percent for each of the following reasons:

(*a*) lower bypass ratio
(*b*) reduced fan efficiency. It must be run faster to maintain an adequate stall margin when the nozzle is in the "closed" position
(*c*) bypass duct leakage at the variable nozzle

Downsizing, the engine moves the SFC/thrust bucket to the left and this may or may not improve engine/aircraft cruise thrust matching depending upon the quality of the match with the fixed nozzle configuration. Rematching the engine to exploit the advantages of the variable nozzle, would permit the fan tip diameter to be reduced by 4 percent. This lowers the thrust by about 10 percent. Reducing the nozzle area by 5 percent restores the top of climb thrust.

- Technology Ranking Factor = $\frac{\text{(DOC + I) x Probability of Success}}{\text{Development Cost}}$
- DOC + I impact (rel. to each technology) includes all effects on engine and aircraft (rubberized)
- DOC + I based on a twin engined airlines flying a 1000 nm mission or a quad flying a 5000 nm mission
- Development cost
  - Includes all costs incurred to get to technology availability date (TAD)

Fig. 2 Technology ranking factors

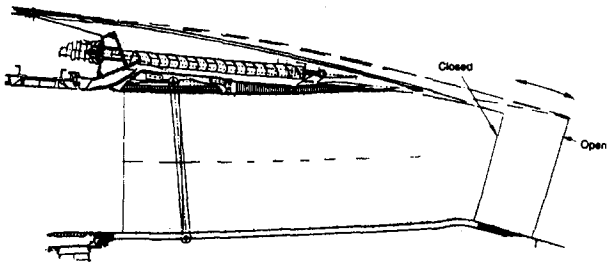

- Dual Function Trans Cowl
- Nozzle Area Increases 5%
- Nozzle Fully Open Before Reverser Cascade Exposed

Fig. 3 Variable area final nozzle

Making appropriate allowances for the extra weight and cost, etc., of the variable nozzle, the net percentage changes resulting from the fan diameter reduction are:

- 1.7 percent power plant weight
- 1.2 percent power plant cost
- .09 percent power plant maintenance cost
- 4 percent nacelle drag

With sensitivities derived from an advanced commercial airliner, the percentage changes were all converted into direct operating cost deltas. Total DOC reduction was about 0.25 percent (even after the 0.3 percent SFC increase previously noted) for a medium range airliner flying a 1000 n.m. mission. The development program will include tests to verify lockouts to prevent inadvertent reverser deployment and a computational fluid dynamics CFD design of the flowpath.

The estimated development program cost was modest and the predicted probability of success high, so the variable fan nozzle scored well in the technology rankings using the simple expression for ranking factor.

2 Hybrid Laminar Flow Nacelle. Drag reduction through the achievement of laminar flow has long been the aspiration of aerodynamicists. In fact considerable successes have been achieved on test flights with a hybrid laminar flow nacelle. The objective is to reduce nacelle external friction drag by 1 to 2 percent of aircraft total drag, a conventional nacelle represents 4–5 percent of aircraft drag.

The source of the improvement lies in the creation of laminar flow over the leading 40 percent of the inlet/fan cowl in order to reduce skin friction drag. Some recontouring of the nacelle together with a limited amount of boundary layer suction is required, Fig. 4. The recontouring provides an extended region

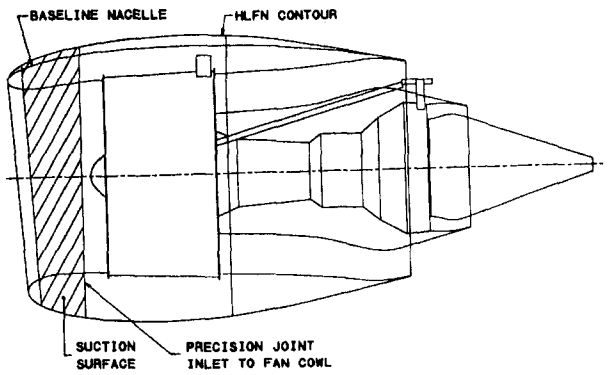

Fig. 4 Hybrid laminar flow nacelle

Downloaded 02 Jun 2010 to 171.66.16.104. Redistribution subject to ASME license or copyright; see http://www.asme.org/terms/Terms_Use.cfm

of favorable pressure gradient relative to a conventional nacelle. Suction is required because laminar flow lip shapes on the forward portion of the nacelle are not compatible with low speed-high angle of attack separation free operation. In accommodating the low-speed angle of attack requirements with conventional lip shapes, laminar flow is possible only with boundary layer suction. Aft of this separation constrained portion of the nacelle, it is possible to maintain natural laminar flow by curvature tailoring. A multitude of small suction holes perforate the cowl skin over about 24 percent of the fan cowl from a plane 9 percent aft of the highlight. A small highly reliable lightweight ejector or a small turbo compressor driven by engine fifth-stage compressor bleed provides the suction.

Nacelle drag reduction is expected to be around 1.5 percent of the total aircraft drag but against this improvement, a 0.12 percent SFC increase exists to provide the engine bleed for the suction turbo compressor. Of more serious consequence is the 3.8 percent weight increase and 18 percent cost increase of the nacelle and pylon. Maintenance costs, incurred through the need to keep the perforations open and insect free, are projected to add an extra 50 cents per engine flight hour to the operating costs.

Converting all these effects into DOC using sensitivities shows that the penalties exceed the rewards. Adoption of the HFLN as it is currently configured would result in an overall cost increase to the airline operator.

Naturally this is a disappointing conclusion after the test successes. Development must address insect coating treatments, and identification of less costly manufacture and construction technologies. Also important is the need to minimize contour mismatches, steps, and gaps at the nacelle joint interfaces, to ensure the boundary layer will remain laminar. This concept was not awarded a ranking because the overall benefit was judged to be negative.

3 Shortened Intake. Additional compromises, relative to those already made on engines about to enter commercial service, can also be made by shortening the inlet, Fig. 5. Reductions in nacelle drag, weight, and cost are possible with a judiciously optimized design. For the shorter nacelle, great care must be taken to ensure that wave drag increases at high cruise Mach numbers is not triggered by increased nacelle curvature associated with shortening the inlet. Also inlet distortion effects in cross-wind operations can not be accentuated beyond the tolerance capabilities of the fan. Wide chord fans of the type likely to be used in an advanced engine exhibit greater distortion tolerance than earlier higher aspect ratio fans, which tends to mitigate the cross-wind risk. The drag of the intake alone is reduced but the overall nacelle drag remains unchanged.

The other changes for the shortened intake have a beneficial effect on aircraft DOC. Projected weight decrease is 1.7 percent less and cost 0.7 percent less. These values translate into a 0.05 percent DOC reduction. Intake nodding loads will be reduced

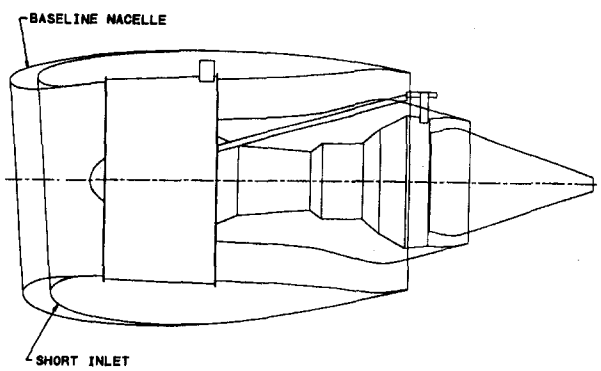

Fig. 5 Short inlet

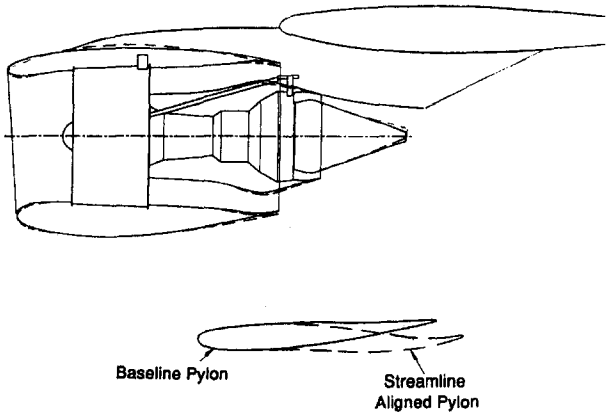

Fig. 6 Flowline nacelle and pylon

with the shorter intake and thus engine carcass bending and subsequently tip rubbing on the compressors and turbines will also diminish. This improvement is not readily quantified without an extensive analysis of engine bending but it could generate as much improvement in DOC as the weight and cost changes. Development testing should include low-speed high angle of attack and cross winds testing performance validation and determination of the influence on high speed drag with the engine inoperative. Ground testing of the engine will assess the acoustic impact of the shortened intake and the influence on operability with the greater pressure distortion that will be present at the fan face. Development costs are not high so this concept achieves a moderate ranking.

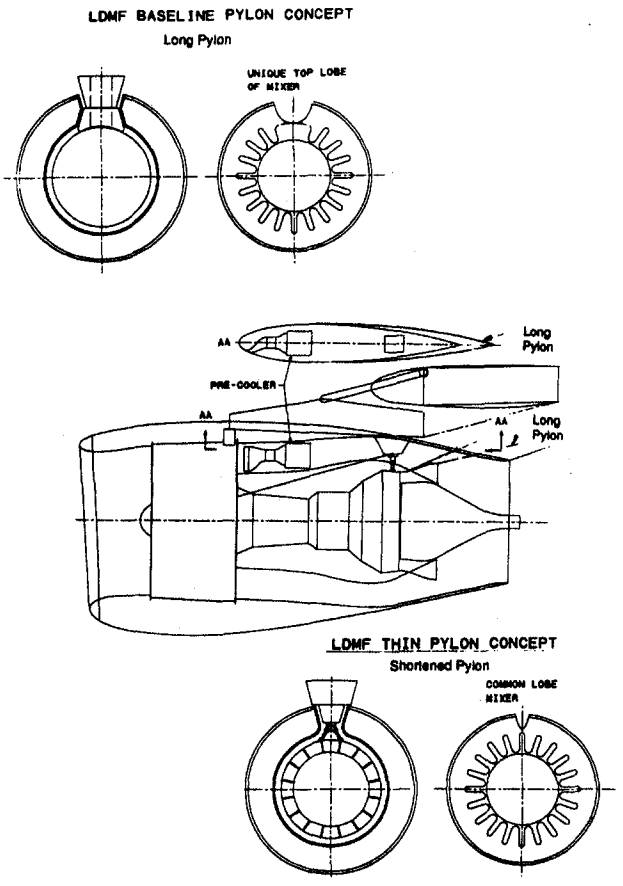

Fig. 7 Long duct mixed flow nacelle

Downloaded 02 Jun 2010 to 171.66.16.104. Redistribution subject to ASME license or copyright; see http://www.asme.org/terms/Terms_Use.cfm

4 Flowline Nacelle and Pylon. Reduced installation drag of the nacelle and pylon are possible if both are recontoured to account for the local flowfield (illustrated in Fig. 6). Minimizing local regions of high velocity induced by the local flowfield of the wing, nacelle, and pylon will lower the overall installed propulsion system drag.

The pylon and nacelle installed losses will be lowered and the aircraft cruise lift/drag ratio raised with a properly designed nonsymmetric fan cowl and nacelle, which, in conjunction with the cambered pylon, improves the wing/nacelle flow field and reduces installed drag.

A drag reduction of 0.6 percent is expected. There will be no change of weight but the nonsymmetric nacelle is estimated to increase the cost by an estimated 8.5 percent. As with the HLFN concept, the economic disadvantage of the higher cost when converted into aircraft DOC outweighs the aerodynamic benefit of lower drag. Without improvements in either manufacturing technology to lower the cost, or dramatic outside influence on airline costs like a large increase in fuel prices, this technology cannot be justified on the aircraft.

Any development program must address manufacturing costs. To support the aerodynamic contentions, three-dimensional Navier–Stokes analysis and design must be performed. This should be followed with an installed wind tunnel test with engine model simulators.

5 Thin Pylon in Long Duct Mixed Flow (LDMF) Nacelle. In a long duct mixed flow engine configuration, the pylon fairing has to surround the rear engine mount located on the rear turbine frame. Conventionally this has been a broad structure and consequently the pylon fairing eliminates one or more of the mixer lobes. Mixer tests have shown that the mixer and nozzle internal performance can be improved by reduced pressure losses and better mixer effectiveness if the pylon can be slimmer, and shorter allowing the pylon to be finished with a slim trailing edge upstream of the mixer; see Fig. 7. This would permit a full circumferential compliment of mixer lobes and also reduced pylon scrubbing and pressure drag.

The reconfigured aft mount and pylon geometry provide a 0.5 percent SFC reduction but the net changes to the nozzle, mixer, and pylon system weigh 3.8 percent heavier, with no change in cost. The resulting DOC reduction is a modest 0.08 percent, though estimated development costs are also modest, so this concept has a good ranking factor.

The development program would focus on the mechanical feasibility. A detailed mechanical design, together with stiffness testing to assess front to back mount deflections and their impact on casing rubs, are necessary to verify the product feasibility of this concept.

Ranking Technology Concepts The five nacelle technologies are compared for a 1000 nm aircraft mission and a 5000 nm aircraft mission on Fig. 8. Both tables are similar but those concepts that offer the greatest improvement in either SFC or drag reduction give the largest improvement with the long mission. The thin pylon in the mixed engine is in this category, as is the hybrid laminar flow nacelle. At 5000 nm the HLFN is a much more attractive concept, though it still carries a small penalty.

Conclusions

- The methodology described in this paper of comparing the overall benefit to the airline economy of a new technology with the development cost incurred by that technology is a useful procedure to help determine a cost-effective distribution of limited development funds.
- The importance of including in the assessment all factors that ultimately have a bearing on airline costs has been highlighted.
- Laminar nacelle flow surprisingly does not offer an aircraft a direct operating cost advantage in this study.
  - When increased manufacturing cost for holes, suction pump, valves, tubing, etc., a sfc penalty for operating the suction system, and increased maintenance costs, are combined, they outweigh the advantage of reduced nacelle drag.
- Low-risk modest payoff concepts are attractive for implementation when they have affordable development cost (i.e., thinned pylon with axisymmetric mixer)
- Of the concepts examined in this study, the best airline operating economy improvement is offered by the variable fan nozzle.

Technology Ranking

	Nacelle Technology	Δ DOC %	Relative Values on Scale of 1-5		
			Probability of Success	Devel Cost	Ranking Factor
1000 NM Mission	1. Two position fan nozzle	0.21	5	5	3
	2. Thin pylon in mixed engine	0.08	5	2	2.5
	3. Shortened intake	0.05	3	4	0.5
	4. Hybrid laminar flow nacelle	-	5	3	-
	5. Flowline nacelle & pylon	-	3	2	-
5000 NM Mission	1. Two position fan nozzle	0.16	5	5	2
	2. Thin pylon in mixed engine	0.16	5	2	5
	3. Shortened intake	0.04	3	4	0.5
	4. Hybrid laminar flow nacelle	-	5	3	-
	5. Flowline nacelle & pylon	-	3	2	-

Note: HLF nacelle & flow line nacelles are better suited to long mission applications than short. At 5000 nm they both have only a small penalty.

Fig. 8 Nacelle advanced concepts

Acknowledgments

The bulk of this work was generated in the course of a NASA-sponsored advanced engine design study made by General Electric Aircraft Engines. The author's gratitude is expressed to both these parties for their permission to publish this paper. Thanks are also expressed to D. Oerhle, D. Yates, and J. Younghans for their help in the preparation of this paper.

References

1 Younghans, J. L., Hoelmer, W., and Stockman, N. O., "Low Speed Effects of Reynolds Number and Lip Geometry on High Bypass Ratio Inlet Performance," Paper No. AIAA-82-0059, 1982.

2 Hoelmer, W., Younghans, J. L., and Raynal, J. C., "Effect of Reynolds Number on Upper Cowl Flow Separation," ICAS-84.1.10.1, 1984.

3 Younghans, J. L., and Lahti, D. J., "Experimental Studies on Natural Laminar Flow Nacelles," Paper No. AIAA-84-0034, 1984.

4 General Electric Aircraft Engines, "Advanced Subsonic Technologies Evaluation Analysis," NASA Sponsored Study—Unpublished, 1994.

Downloaded 02 Jun 2010 to 171.66.16.104. Redistribution subject to ASME license or copyright; see http://www.asme.org/terms/Terms_Use.cfm

Subcritical Crack Growth Life Prediction for Ceramic Components of Advanced Heat Engines

D. C. Wu

A. D. Peralta

M. N. Menon

J. C. Cuccio

AlliedSignal Engines,
Phoenix, AZ 85072

Advanced, high-strength ceramics are finding increasing application in advanced heat engines. To ensure the long-term reliability of components made from these materials, subcritical crack growth (SCG) from inherent flaws has to be taken into account, as this has been identified as the primary failure mode under sustained loading. In analyzing fast fracture data, data censoring is necessary to obtain estimates of the inherent strength distributions for competing failure-causing flaw populations. This is particularly important for ceramic designs, where size scaling is a necessary part of the design analysis. While data censoring has become common for fast fracture data, data censoring involving stress rupture data has yet to be widely applied. This paper describes fast fracture and stress rupture tests performed on an advanced silicon nitride ceramic, the test data and fractography results, censored data analysis for both types of data, derivation of the subcritical crack growth parameters, and application of these parameters to verification specimens. Implications of the findings and recommendations for future studies are also presented.

Introduction

The use of advanced ceramics in heat engines can reduce or eliminate blade cooling, reduce the required containment structure and overall engine weight, and permit operation at higher temperatures with higher efficiency, resulting in reduced fuel consumption, improved performance, and reduced operating costs. However, full-scale production of ceramic components requires improvements in life prediction methodology that can ensure ceramic component integrity in field applications.

In the typical design process employing ceramic components, fast fracture is of initial concern. Once component reliability associated with fast fracture mode is ascertained, component response under sustained loading becomes of prime importance. The fracture of a ceramic component under sustained loading can take place by subcritical crack growth (SCG) from inherent flaws or from flaws generated by creep and oxidation-induced degradation at the surface. How much of the time-to-failure is spent in SCG and how much in crack initiation itself is a matter of speculation at this point. For a given failure process, however, probabilistic methodology can be applied for failure risk assessment.

This paper describes a method for static load life prediction based on analytical modeling of SCG. The approach, material parameter estimation based on uniaxial fast fracture and stress rupture tests, and method verification based on subelement tests are examined.

Approach

The selected approach is based on the premise that fast fracture and stress rupture failures originate from the same material flaws. Fett and Munz (1991) have proposed a method to obtain inferred flaw growth data based on concurrent fast fracture and stress rupture tests. The fast fracture tests yield information on the initial flaw population, which when combined with the stress rupture life distribution yields the crack growth law.

In this approach, the ith value of the lifetime is matched with the ith value of the fast fracture strength, and the crack velocity (da/dt) as a function of the initial applied stress intensity for each specimen is obtained, as in Eq. (1):

$$da/dt = [-2K_i/(Y^2S^2t_f)][d(\ln \sigma/S)/d(\ln t_f)] \quad (1)$$

where:

K_i = initial stress intensity = $K_{Ic}(\sigma/S)$
Y = geometric factor for the internal or surface flaw
S = fast fracture strength
σ = applied stress in the stress rupture test
t_f = time to failure in the stress rupture test
K_{Ic} = fracture toughness.

One complication is that ceramic materials exhibit competing flaw populations: In the simplest case, surface flaws from machining damage, and internal flaws such as inclusions, are the two competing flaw populations. In this paper, censored data analysis will be used to obtain estimates of the inherent strength and lifetime distributions for failures that originate from both competing populations. Censored data analysis is based on the premise that when concurrent flaw populations are present, failure from one flaw population also yields information on failure from the competing population(s) (see Nelson, 1982). Censored data analysis requires that the failure origins of each specimen be identified. In this paper, censored data analysis is combined with the maximum likelihood method to estimate the parameters of the two-parameter Weibull distributions for strength and lifetime distributions. These distributions are then used to determine the crack growth parameters.

For component life prediction, failure risk from fast fracture and SCG needs to be integrated over the entire surface and volume of the component. Except for the simplest components and stress fields, failure risk integration is most easily accomplished with finite element models in conjunction with a risk integration algorithm such as proposed by Evans (1978), and implemented by Peralta et al. (1995).

Contributed by the International Gas Turbine Institute and presented at the 40th International Gas Turbine and Aeroengine Congress and Exhibition, Houston, Texas, June 5–8, 1995. Manuscript received by the International Gas Turbine Institute February 27, 1995. Paper No. 95-GT-236. Associate Technical Editor: C. J. Russo.

Copyright © 1996 by ASME

Downloaded 02 Jun 2010 to 171.66.16.104. Redistribution subject to ASME license or copyright; see http://www.asme.org/terms/Terms_Use.cfm

The failure risk due to fast fracture for internal flaws is evaluated as follows:

$$P_f = 1 - \exp - \{I_V V(\sigma_{Emax}/\sigma_0)^m\} \quad (2)$$

where:

P_f = probability of failure
I_V = multiaxial stress gradient factor (for internally distributed flaws)
V = physical volume
$I_V V$ = effective volume
σ_{Emax} = maximum equivalent stress in the body
σ_0 = second Weibull parameter (characteristic strength for a defined volume)
m = first Weibull parameter or the Weibull modulus.

The equivalent stress may be defined by an appropriate multiaxial criterion; in this paper, the normal stress criterion is used. An analogous equation applies for failure risk from surface flaws. The failure risk at subsequent times needs to incorporate the effect of SCG, which can be expressed in a similar manner as Eq. (1). If it is assumed that the SCG originates from the same material flaws responsible for fast fracture, the failure risk for volume flaws is as described by Ritter (1978) and Cuccio et al. (1994), assuming the SCG equation (Eq. (3)) follows the form: $da/dt = AK^n$:

$$P_{fSCG} = 1 - \exp - \{I_{VSCG} V(\sigma_{Emax}/\sigma_0)^m\} \quad (3)$$

where:

σ_{Emax} = maximum equivalent stress in the body at time t = zero
I_{VSCG} = multiaxial stress gradient factor defined by the time-dependent equivalent stress, $\sigma_E(t)$
$\sigma_E(t)$ = time-dependent equivalent stress = $\sigma_E(0)(1 + Bt\sigma_E(0)^2)^{(1/(n-2))}$
$\sigma_E(0)$ = equivalent stress at time t = zero
B = $(K_{Ic}^{(n-2)}(n-2)AY^2)/2$
t = time
n = SCG exponent
A = SCG constant
Y = flaw geometry factor for internal flaw(s).

An analogous expression applies for failure risk from surface flaws.

Material and Test Setup

Material. The material used in this investigation was a commercially available, hot isostatically pressed (HIPped) silicon nitride, designated as NT154 from Norton Advanced Ceramics, in Northboro, MA. All specimens were produced from a single lot of silicon nitride powder with 4 weight percent yttria added as the densification aid. Cylindrical billets were cold isostatically pressed from the powder and then HIPped to full density. The billets were then given a high-temperature heat treatment to crystallize most of the amorphous grain boundary phase. Tensile specimens of cylindrical buttonhead geometry were diamond ground from these billets; identical specimen geometry was used for both the fast fracture and stress rupture tests. The specimens had gage section dimensions of 6.35 mm diameter and were of 35 mm gage length.

Final grinding on the gage section was performed using a 320 grit diamond wheel in the longitudinal direction. In order to improve the surface strength of all specimens, a post-machining heat treatment (at 982°C for 20 hours) was also performed. All test specimens were fabricated in one processing batch to ensure uniformity.

Test Setup. Concurrent tensile fast fracture and stress rupture tests were conducted at 1204°C on commercial electromechanical tensile testing machines in ambient air. Parasitic bending strains are of special concern in testing ceramic materials, so special care was employed, through the use of self-aligning Instron supergrips and instrumented load rods during the course of testing. Twenty fast fracture tests were conducted at a loading rate of 4005 N/min. The stress rupture tests were conducted at the Mechanical Properties User Center at the Oak Ridge National Laboratory High Temperature Materials Laboratory (ORNL-HTML). The test setup is described in more detail by Menon et al. (1994a).

Specimen displacements were measured over a 25 mm gage length within the 35 mm specimen gage sections with direct-contact extensometers employing SiC probe arms and remote capacitive sensors. A resolution of 1 μm displacement was achieved with this setup.

Several specimens were tested initially to determine the stress level prior to testing the 20 replicate specimens. The purpose of optimizing the stress level was to obtain a reasonable time-to-failure distribution during the stress rupture testing. A stress level of 375 MPa was chosen for the 20 replicate tests.

Data Analysis

The fast fracture strength values from the tests varied from 364.1 MPa to 664.7 MPa, and the stress rupture lives at 375 MPa ranged from 0.4 hours to greater than 500 hours (two tests were suspended after 500 hours testing). In the stress rupture specimens, SCG zones could be identified, as described by Menon et al. (1994b). The specimen fast fracture and stress rupture failure origins were identified through optical and scanning electron microscopy. The internal failure origins in the fast fracture and stress rupture specimens consisted primarily of inclusions. The surface failure origins in the stress rupture specimens were difficult to identify, due to surface oxidation. It was

Nomenclature

A = SCG constant
ASME = American Society of Mechanical Engineers
°C = deg Celsius
DOE = U.S. Department of Energy
HIP = hot isotatic pressing
HTML = high-temperature materials laboratory
I_V = multiaxial stress gradient factor for internal (or volume) distributed flaws
K_i = initial stress intensity
K_{Ic} = fracture toughness
Kt = stress concentration factor
m = first Weibull parameter or the Weibull modulus
m/h = meters per hour
mm = millimeters
MA = Massachusetts
MPa = mega-Pascals
n = SCG constant
NT154 = Norton advanced ceramics HIPped silicon nitride
NYC = New York City
ORNL = Oak Ridge National Laboratory
P_f = probability of failure
S = fast fracture strength
SCG = subcritical crack growth
t = time
t_f = time to failure
U.S. = United States
V = physical volume
Y = geometric factor for internal or surface flaw
σ = applied stress
σ_{Emax} = maximum equivalent stress
σ_0 = second Weibull parameter or the characteristic strength

Downloaded 02 Jun 2010 to 171.66.16.104. Redistribution subject to ASME license or copyright; see http://www.asme.org/terms/Terms_Use.cfm

Table 1 1204°C fast fracture strengths and stress rupture lives (applied load of 375 mPa) with failure origins

FAILURE ORIGIN	STRENGTH, MPA	LIFE, HOURS	FAILURE ORIGIN
Internal	364.1	0.4	Internal
Internal	415.8	0.5	Internal
Internal	423.4	0.8	Internal
Internal	426.1	6	Surface
Internal	450.2	7	Surface
Internal	457.1	12	Internal
Internal	465.4	19	Internal
Internal	479.2	24	Surface
Internal	490.9	40	Internal
Surface*	495.1	43	Surface
Surface	496.4	66	Internal
Internal	506.1	80	Surface
Internal	512.3	120	Surface
Internal	525.4	141	Internal
Internal	539.9	153	Internal
Internal	546.8	253	Surface
Internal	552.3	257	Surface
Internal	586.1	266	Internal
Internal	599.2	(Suspended at 500)	-
Internal	664.7	(Suspended at 500)	-

* Failed from surface pit (atypical surface origin); data point censored.

assumed that the origins of the surface-initiated fast fracture and stress rupture failures were identical. The specimen strength and life test data and the specimen failure origins are listed in Table 1.

Using the failure origin information for data censoring, a two-parameter maximum likelihood Weibull analysis was performed with the strength and life data. The resulting Weibull parameter estimates are listed in Table 2. Weibull plots based on the estimated Weibull parameters and test data are shown in Figs. 1 and 2.

It should be noted that the surface strength estimates relied heavily on censoring, as there was only one surface-originated failure in the fast fracture tests. With the estimates of inherent strength and life distributions, the da/dt versus K relationship can be estimated by assigning median ranks to a virtual data set of strength and life values generated from the appropriate strength and life distributions, and performing regression according to Eq. (1). In the case of the Weibull strength and life distributions, a relationship of the form $da/dt = AK^n$ results. The SCG parameters, A and n, for volume and surface flaws were as follows:

	A, m/h	n
Volume	2.91E-18	16.33
Surface	2.69E-15	14.98

The crack growth rate curves (Fig. 3) based on the A and n parameters indicate that SCG from surface flaws is more severe. Qualitatively, this is consistent with the fact that the surface strengths of the tensile specimens were higher than the volume strengths (indicating smaller surface flaws) while the lifetimes to failure were similar, which requires the surface flaws to grow at a faster rate to "catch up" to the (initially larger) volume flaws. The greater severity of surface SCG can also be rationalized by damage contribution from the oxidizing environment.

Table 2 Weibull parameter estimates from specimen test data

	CHARACTERISTIC STRENGTH, MPA	M (STRENGTH)	CHARACTERISTIC LIFE, HOURS	M (LIFE)
Volume	537.8	7.45	380.6	0.52
Surface	790.0	7.53	348.9	0.58

Model Verification

Two independent subelement geometries were used to assess the validity of the approach. These were: (*a*) notched tensile specimens and (*b*) spin disks. In both cases, the highly stressed surfaces had been transversely machined with respect to the maximum principal stress direction. It was assumed that the subcritical crack growth parameters derived from longitudinally machined specimens could be applied without modification.

Notched Test Specimens. Two ceramic buttonhead notched specimen geometries were tested under constant load at 1204°C. The specimen gage sections are shown in Fig. 4.

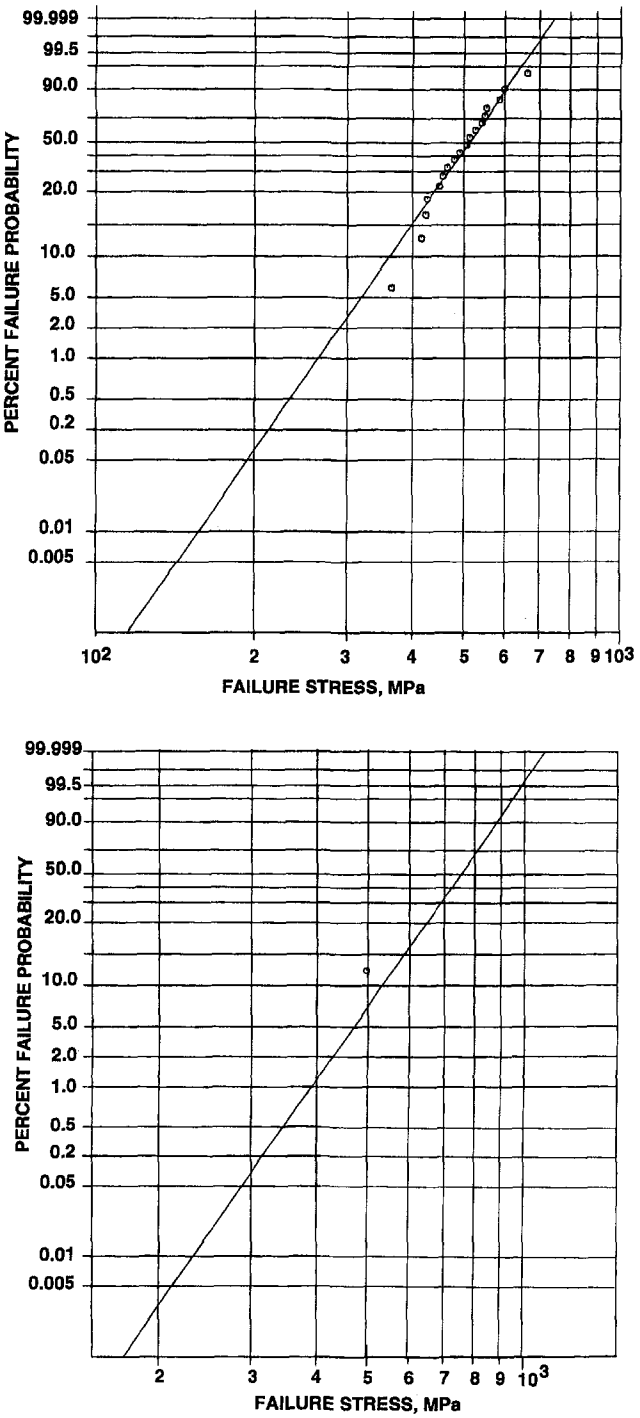

Fig. 1 Weibull plots of fast fracture test results. (A, top) Internal-initiated fracture data: maximum likelihood analysis yields character strength = 537.8 mPa, slope = 7.45; (B, bottom) Surface-initiated fracture data: character strength = 790 mPa, slope = 7.53.

Downloaded 02 Jun 2010 to 171.66.16.104. Redistribution subject to ASME license or copyright; see http://www.asme.org/terms/Terms_Use.cfm

The notches of both specimen designs had the same notch root radii, but different depths relative to the constant-diameter section, resulting in stress concentration values of $Kt = 1.6$ for the shallow notch configuration and $Kt = 2.1$ for the deep notch configuration. In both cases, the grinding direction was perpendicular to the maximum principal stress direction.

The initial flaw distributions were obtained from fast fracture tests of the notched specimens. Finite element models of the two geometries were made; the risk of failure from SCG was assessed using the crack growth constants derived earlier for surface flaws, and internal flaw growth was integrated over the finite element models as a function of time for each loading condition.

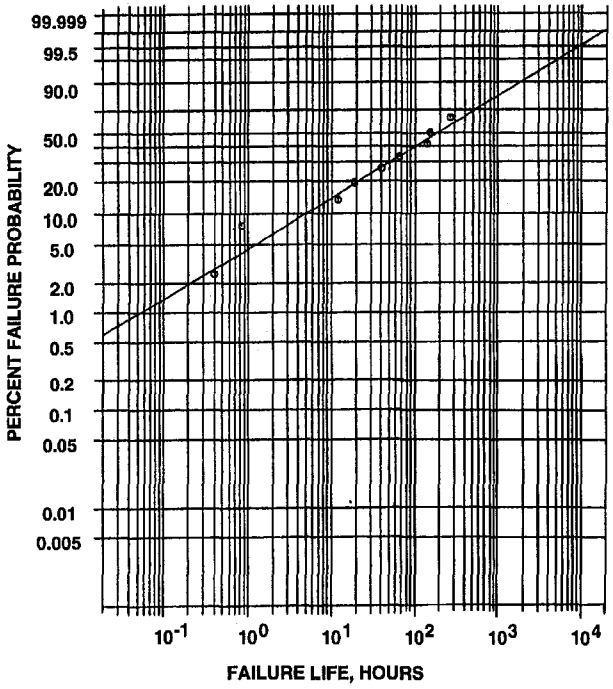

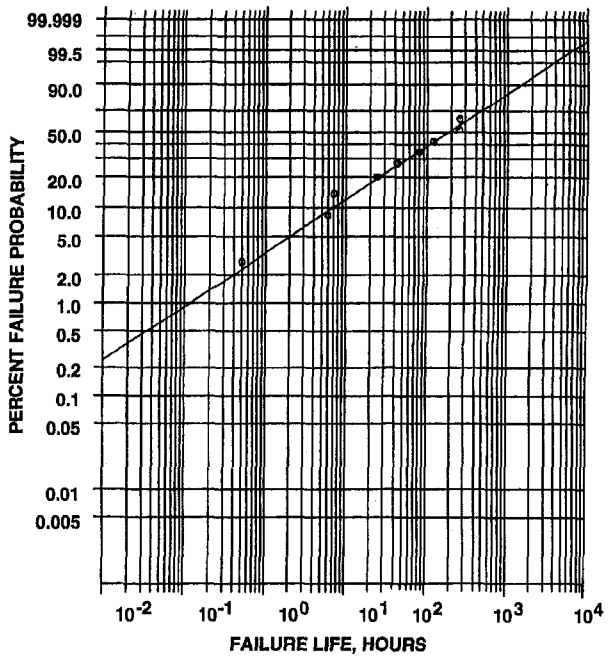

Fig. 2 Weibull plots of censored stress rupture test results. (A, top) Internal-initiated failures at 1204°C/375 mPa; character life = 380.6 H, slope = 0.52; (B, bottom) Surface-initiated failures at 1204°C/375 mPa, character life = 348.9 H, slope = 0.58.

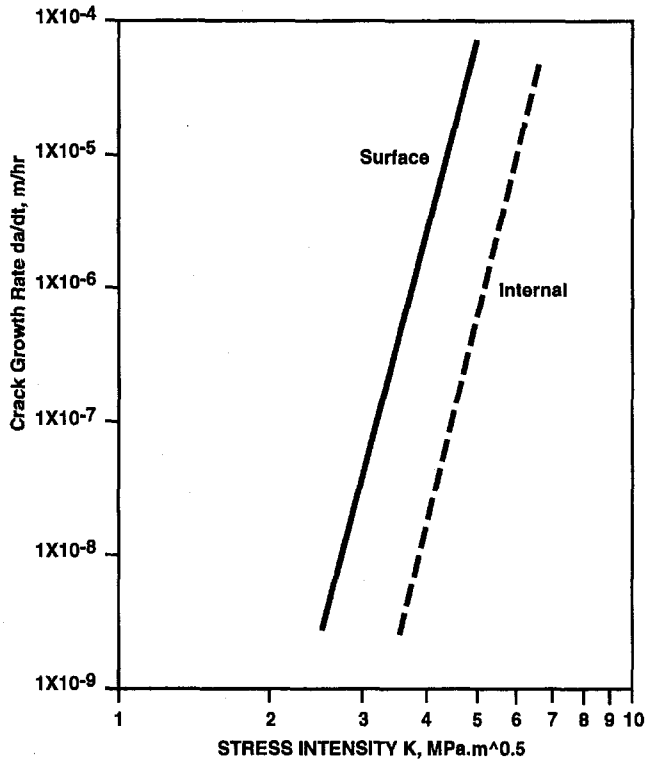

Fig. 3 Comparison of derived crack growth rates for internal and surface flaws tested at 1204°C

All the observed failures were surface-initiated; the predictions were consistent with this observation. In both specimens, the risk of failure from internal flaws at any given time point was always orders of magnitude smaller than that from surface flaws. The life predictions based on Eq. (3) and the test data are shown in Fig. 5. It should be noted that the data exhibited substantial scatter; numerous tests were suspended after 500 hours duration. It should also be noted that, as expected, for a given net section stress, the higher stress concentration ($Kt = 2.1$) specimens exhibited shorter life due to the higher notch root stress.

Spin Test Disks. Six ceramic spin disks of the configuration shown in Fig. 6 were spin tested under constant speed at 1204°C. As with the notched specimens, the initial flaw distribution was determined via fast fracture tests of the spin disks.

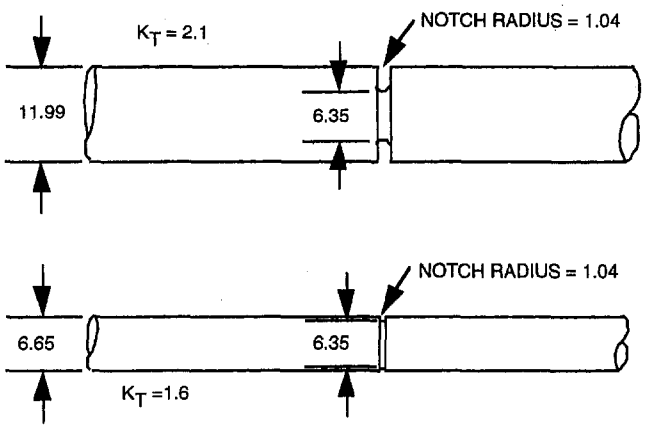

Fig. 4 Notched test specimen configurations (gage sections)

Downloaded 02 Jun 2010 to 171.66.16.104. Redistribution subject to ASME license or copyright; see http://www.asme.org/terms/Terms_Use.cfm

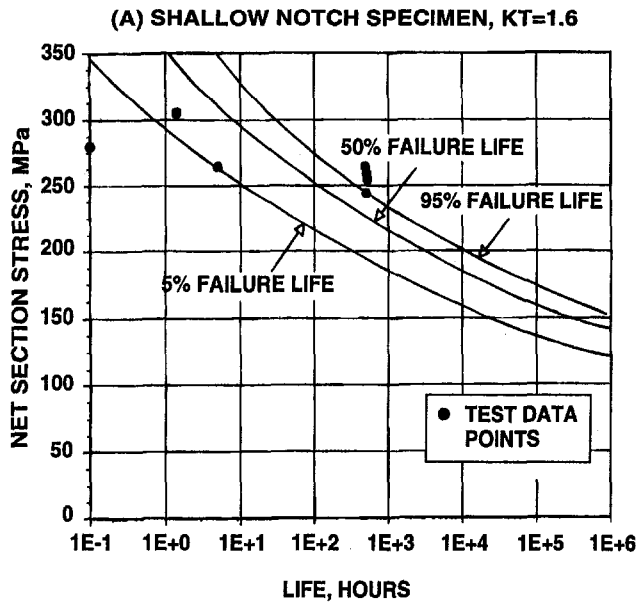

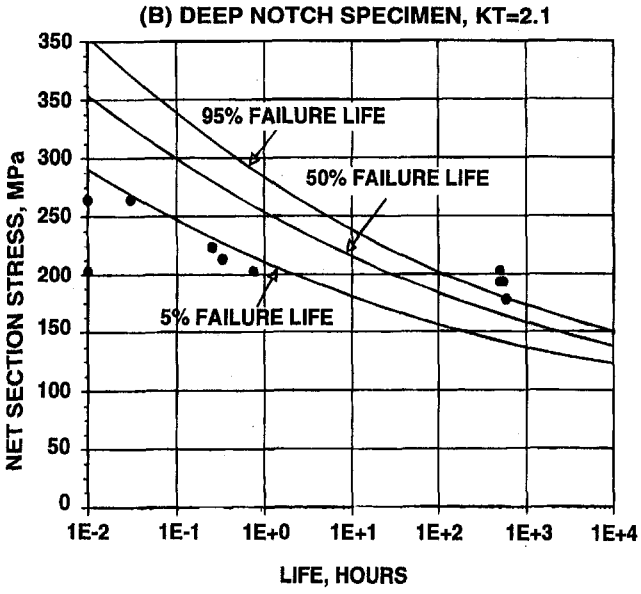

Fig. 5 Notched specimen test results compared with life predictions at 5, 50, and 95 percent probability of failure

The spin disks had higher internal stresses than those at the surface. However, most of the fast fracture failures occurred from surface flaws. This was evidently caused by rough surface finish close to the spindle-to-disk transition on the spin disks, which degraded the surface strength, as described by Cuccio et al. (1995) and Peralta et al. (1995).

The failure risk from SCG was integrated over the finite element model at each of the test conditions, based on the observed surface and volume flaw distributions. The life predictions based on Eq. (3) and the test data are shown in Fig. 7. For the surface failures, the lives were underpredicted; for the single internal failure observed, the life was overpredicted. It should be noted that the sample size was small and that scatter can be expected.

Discussion

Reasonable agreement was achieved between the life predictions and test observations from the verification specimens. In both types of verification test specimens, surface failures dominated, which reiterates the importance of obtaining independent estimates of surface and internal SCG parameters. The value of data censoring and maximum likelihood analysis to estimate the Weibull parameters for competing flaw populations cannot

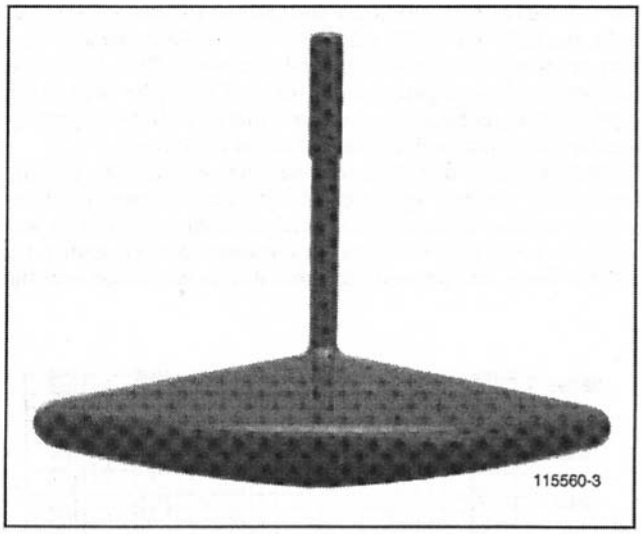

Fig. 6 Spin disk test specimen configuration: disk diameter = 137 mm

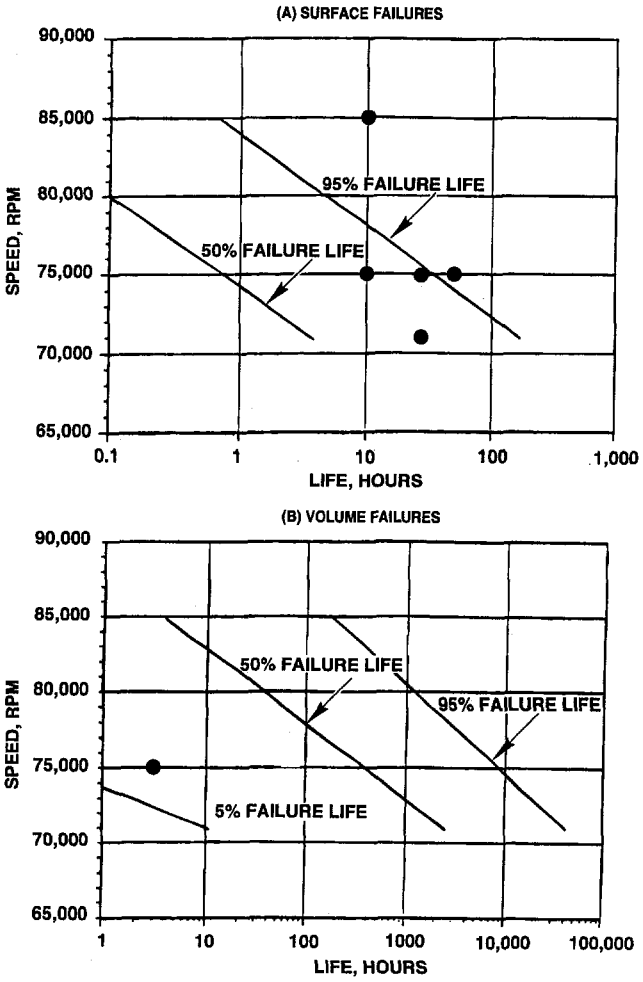

Fig. 7 Spin disk test results compared with life predictions at 5, 50, and 95 percent probability of failure for: (A, top) surface-originated failures, and (B, bottom) volume-originated failures

Downloaded 02 Jun 2010 to 171.66.16.104. Redistribution subject to ASME license or copyright; see http://www.asme.org/terms/Terms_Use.cfm

be overemphasized. The possible causes of discrepancies between the test observations and the life predictions and possible areas for future investigations are described below.

The approach taken in this paper assumes that subcritical crack growth starts at the onset of loading from inherent material and machining flaws and that the crack growth parameters obtained from uniaxial test specimens can be applied to more complex geometries with different surface machining flaw populations. A critical question is whether an incubation period exists prior to crack growth and whether the flaw population changes with time at temperature. This may be answered with explicit crack growth measurements of flaws/cracks that simulate inherent flaws and careful metallographic observations of flaws/cracks as a function of time.

The observed discrepancies between the predictions and observations may also be due to multiaxial stress states in the verification specimens. Future work should include efforts to obtain crack growth information under multiaxial loading conditions.

The predictions made in this paper are based on limited data and median estimates of the crack growth parameters. Future activity should also include derivation of confidence bounds on the crack growth parameters, which can be accomplished through Monte Carlo simulation of both the strength and lifetime distributions.

Conclusions

Independent surface and volume subcritical crack growth (SCG) parameters were obtained from fast fracture and stress rupture test results from identically prepared tensile specimens. The SCG parameters were successfully applied to subelement specimens, with reasonable agreement between the resulting life predictions and test observations.

In order to further develop time-dependent life prediction methods, areas of future activities have been identified. These include: (1) confirmation of the subcritical crack growth approach through validation of the SCG parameters with explicitly measured crack growth rates and metallographic observation of failure-causing flaws as a function of time and temperature; (2) obtaining crack growth rate information under multiaxial loading conditions; and (3) derivation of confidence bounds on the SCG parameters.

Acknowledgments

The work described in this paper was part of the Life Prediction Methodology for Ceramic Components of Advanced Heat Engines program, funded by the U.S. Department of Energy under Contract No. 86X-SC674C. We would like to thank the Department of Energy for financial support and Dr. C. Brinkman of the Oak Ridge National Laboratory for overall program direction. We would like to acknowledge the contributions of Mr. H. T. Fang in careful fractography, Dr. J. Z. Song in notch specimen analysis, and Ms. P. J. Brehm in programming. The contributions of Drs. M. Ferber, A. Wereszczak, and M. Jenkins (now at the University of Washington) of the Oak Ridge National Laboratory High Temperature Materials Laboratory are acknowledged with gratitude.

References

Cuccio, J. C., Peralta, A. D., Wu, D. C., Fang, H. T., Brehm, P. J., Menon, M. N., Strangman, T., Meade, W. D., and Wade, J., 1995, *Life Prediction Methodology for Ceramic Components of Advanced Heat Engines Phase I Final Report,* Oak Ridge National Laboratory report, ORNL/sub/89-SC674/1/V1 & V2, Mar.

Evans, A. G., 1978, "A General Approach for the Statistical Analysis of Multiaxial Fracture," *Journal of the American Ceramic Society,* Vol. 61, Nos. 7–8, pp. 302–308.

Fett, T., and Munz, D., 1991, "Methods of Determining Subcritical Crack Growth by Static Lifetime Tests With Natural and Artificial Cracks," *Journal of Testing and Evaluation,* Vol. 19, No. 6, pp. 461–466.

Menon, M. N., Fang, H. T., Wu, D. C., Jenkins, M. G., Ferber, M. K., More, K. L., Hubbard, C. R., and Nolan, T. A., 1994a, "Creep and Stress Rupture Behavior of Silicon Nitride: Part I, Experimental Observations," *Journal of the American Ceramic Society,* Vol. 77, No. 5, pp. 1217–1227.

Menon, M. N., Fang, H. T., Wu, D. C., Jenkins, M. G., and Ferber, M. K., 1994b, "Creep and Stress Rupture Behavior of Silicon Nitride: Part III, Stress Rupture and the Monkman–Grant Relationship," *Journal of the American Ceramic Society,* Vol. 77, No. 5, pp. 1235–1241.

Nelson, W., 1982, *Applied Life Data Analysis,* Wiley, New York, pp. 347–356.

Peralta, A. D., Wu, D. C., Brehm, P. J., Cuccio, J. C., and Menon, M. N., 1995, "Strength Prediction of Ceramic Components Under Complex Stress States," ASME Paper No. 95-GT-394; accepted for publication in the ASME JOURNAL OF ENGINEERING FOR GAS TURBINES AND POWER.

Ritter, E., 1978, "Engineering Design and Fatigue Failure of Brittle Materials," *Fracture Mechanics of Ceramics,* Plenum Press, New York, Vol. 4, pp. 667–686.

Downloaded 02 Jun 2010 to 171.66.16.104. Redistribution subject to ASME license or copyright; see http://www.asme.org/terms/Terms_Use.cfm

Thermal Shock Analysis and Testing of Simulated Ceramic Components for Gas Turbine Applications

H. Rajiyah

L. P. Inzinna

G. G. Trantina

Mechanics of Materials Program,
GE Corporate Research and Development,
Schenectady, NY 12301

R. M. Orenstein

M. B. Cutrone

Power Generation Engineering,
GE Power Generation,
Schenectady, NY 12301

A ceramic gas seal for a utility gas turbine was designed and analyzed using ANSYS and CARES/LIFE. SN-88 silicon nitride was selected as the candidate material. The objective was to validate the failure prediction methodology using rectangular plates, which were thermally shocked in a fluidized bed. The failure prediction methodology would then be applied to the representative component geometry. Refined ANSYS finite element modeling of both the plate and component geometries was undertaken. The CARES/LIFE reliability analysis of the component geometry for fast fracture was performed for two cases: (I) steady-state thermomechanical loads during normal gas turbine operation and (II) transient thermal shock loading during a turbine trip. Thermal shock testing of alumina disks was performed in order to gain confidence in the testing and analysis procedures. Both notched and unnotched SN88 plates were then tested. Failure modes were identified through flexure tests and data censoring was performed using SAS. Weibull modulus was assumed to be invariant with temperature and the scale parameter was assumed to vary through a scaling variable such that multiple data could be pooled.

Introduction

The methodology for failure and life prediction of monolithic ceramic gas turbine components has been undertaken. Demands to increase turbine output and efficiency and simultaneously reduce NO_x emissions, with both heavy duty and aeroderivative gas turbines, are growing in the power generation sector. Since these multiple requirements could be achieved by operating the gas turbine with a reduction in parasitic component cooling, materials that exhibit high specific strength and stiffness, high thermal conductivity, and good oxidation and corrosion resistance at high temperatures are desirable. Certain monolithic silicon nitride ceramics exhibit these desirable properties but inherent brittleness, variability in strength due to processing and machining operations, and susceptibility to damage from thermal shock, which may reduce component reliability, are the concerns of design engineers.

The intent of the study described was to gain confidence in the predictive methodology for ceramic structures that might be used in gas turbine applications. For the thermal shock studies reported, only fast fracture was considered. SN-88 silicon nitride (NGK Insulators, Ltd., Nagoya, Japan) was selected as the candidate material. Censoring of fracture strength data from four-point bending experiments was performed, and Weibull strength parameters were estimated for relevant failure modes. It was assumed that the Weibull moduli for each failure mode were invariant over a temperature range of 25–1204°C. ANSYS (Swanson Analysis System, Inc., 1986) was used for thermal/structural analysis and CARES/LIFE (Powers et al., 1992) was used for risk integration to predict ceramic component reliability. A stationary gas seal (shroud) for a utility gas turbine was the ceramic component modeled. The thermal and mechanical boundary conditions imposed on the ceramic shroud were taken to be as realistic as possible.

Contributed by the International Gas Turbine Institute and presented at the 40th International Gas Turbine and Aeroengine Congress and Exhibition, Houston, Texas, June 5–8, 1995. Manuscript received by the International Gas Turbine Institute February 27, 1995. Paper No. 95-GT-308. Associate Technical Editor: C. J. Russo.

Alumina disks were tested in thermal shock in order to gain confidence in the predictive methodology. The thermomechanical material properties were obtained from published data. Weibull modulus and characteristic strength of the flaw distribution were estimated from fracture strength data from three-point bending experiments. Failure probabilities for the ceramic shroud were determined for two conditions: (I) steady-state thermomechanical loads during normal gas turbine operating conditions, (II) transient thermal shock loading during a turbine trip. The thermomechanical properties were provided by the material supplier. The strength data was obtained from four-point bending experiments. Thermal shock analyses and testing of notched and unnotched SN-88 plates were performed using the same material properties and Weibull parameters as those used for analyses of the SN-88 shroud.

Data Censoring of SN-88. SN-88 is a sintered silicon nitride containing a fraction of elongated grains for enhanced fracture toughness. Fast fracture data were evaluated to obtain temperature-independent (i.e., combined) Weibull moduli and temperature-dependent Weibull scale parameters for predominant failure modes. Failure modes are defined herein as discrete populations of defects, each of which may be described using the two-parameter Weibull distribution obtained from censored component strength data. These defects are the sites of rapid crack initiation, which occurs when a critical stress intensity is reached or exceeded. Volume-distributed pores (P) and large grains (G) are typical failure modes in silicon nitrides containing elongated grains and were selected for censored analyses of data. It was assumed that each failure mode acted independently and that the failure modes did not change with material lot or with shape and loading of the test piece or component. Data censoring over different temperature regimes for each failure mode was accomplished in SAS (1993) using

$$\frac{\sum_{i=1}^{n} (\sigma_{fi})^m \ln (\sigma_{fi})}{\sum_{i=1}^{n} (\sigma_{fi})^m} - \frac{1}{\gamma} \sum_{i=1}^{\gamma} \ln (\sigma_{fi}) - \frac{1}{m} = 0 \qquad (1)$$

Copyright © 1996 by ASME

Downloaded 02 Jun 2010 to 171.66.16.104. Redistribution subject to ASME license or copyright; see http://www.asme.org/terms/Terms_Use.cfm

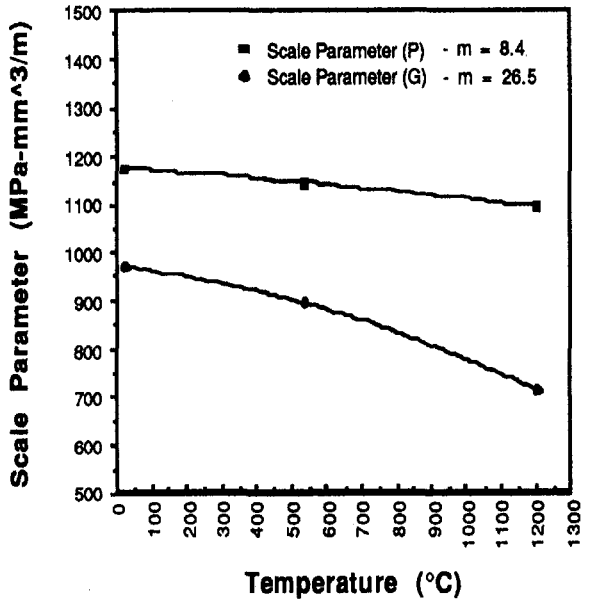

Fig. 1 Weibull scale parameter versus temperature for (A) pores and (B) large grains

and

$$\sigma_\theta = \left[\frac{\sum_{i=1}^{n} (\sigma_{fi})^m}{\gamma}\right]^{1/m} \quad (2)$$

where γ is the number of remaining specimens for the failure mode of interest, n is the total sample size and σ_{fi} is the fracture strength of the ith sample. The Weibull scale parameter σ_0, which is a temperature-dependent material property, was calculated off-line using

$$\sigma_0 = \sigma_\theta * V_e^{1/m} \quad (3)$$

where m is the combined Weibull modulus for pores or large grains over 25–1204°C and V_e is the effective volume of the test piece. Of 90 four-point flexure observations evaluated, 33 fractures originated from pores and 44 fractures originated from large grains. The remaining fractures originated from inclusions or surface, corner or unidentified defects, and were not considered in the analyses. Pore and large grains were also observed as failure origins in tensile tests. The combined Weibull moduli estimated using SAS for volume-distributed pores was 8.4 and for volume-distributed large grains was 26.5. The Weibull scale parameters versus temperature for pores and large grains are given in Fig. 1. These parameters were input to CARES/LIFE to calculate failure probabilities of the SN-88 ceramic thermal shock plates and shroud.

Thermal Shock Test Apparatus. Configuration of the 1-atm proof test rig is shown in Fig. 2. It was comprised of an enclosed oven, which could heat the specimen up to 1500°C, and a fluidized bed of alumina particles, which was used to shock the ceramic component thermally when it was lowered from the oven. Two calibrations were performed using (1) a copper sphere to evaluate one-dimensional heat flow and (2) a copper plate to evaluate two-dimensional heat flow. The heat flow was measured between ~180°C and room temperature. The measured heat transfer coefficients were 307 W/m^2-K for the copper sphere and 398 W/m^2-K for the copper plate. Repeatability of the heat transfer measurements was within ~5 percent for the copper sphere and within 2 percent for the copper plate over two runs each.

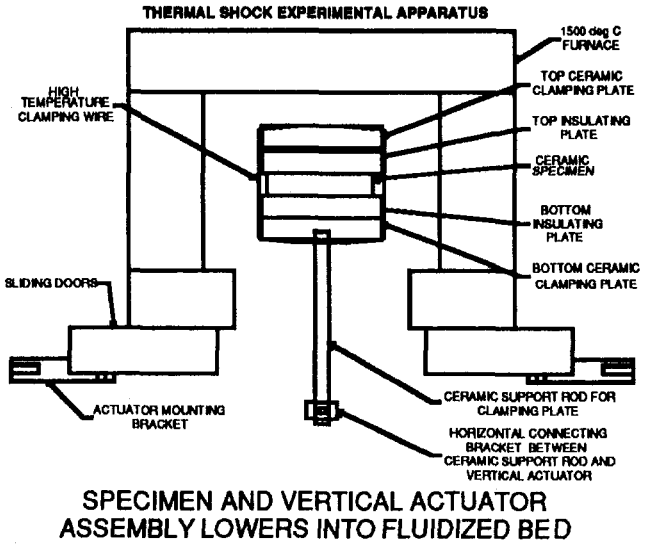

Fig. 2 Configuration of the thermal shock test apparatus

Alumina Disk Failure and Test Predictions. Disks of sintered alumina measuring 63.5 mm in diameter and 11.1 mm in thickness, described by Trantina (1980), were analyzed using CARES/LIFE for fast fracture and quenched in the fluidized bed at successive temperature increments of 50°C until failure. The material tested was from the same lot as the material described by Trantina. It was assumed for this and subsequent testing that the component strength did not change until a critical temperature difference was reached or exceeded, i.e., slow crack growth did not occur during quenches prior to that resulting in catastrophic failure of the test piece. The intent was to gain confidence in the testing and analysis procedures by using a material containing a single volume-distributed failure mode, identified as regions of an uncharacterized second phase. The material properties used for the analysis were taken from Morrell (1985). The estimated Weibull modulus was 8 and the estimated scale parameter was 416 MPa-mm$^{3/m}$ as reported by Trantina (1980). Stresses were calculated by ANSYS 4.4A using a heat transfer coefficient of 398 W/m^2-K on uninsulated surfaces. The comparison between analysis based upon CARES/LIFE and thermal shock tests is given in Fig. 3.

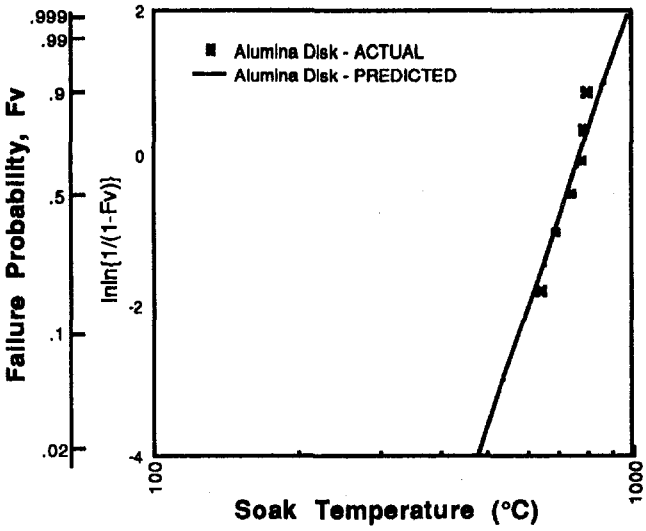

Fig. 3 Failure probabilities of alumina disks predicted using CARES/LIFE and determined from experimental data

Downloaded 02 Jun 2010 to 171.66.16.104. Redistribution subject to ASME license or copyright; see http://www.asme.org/terms/Terms_Use.cfm

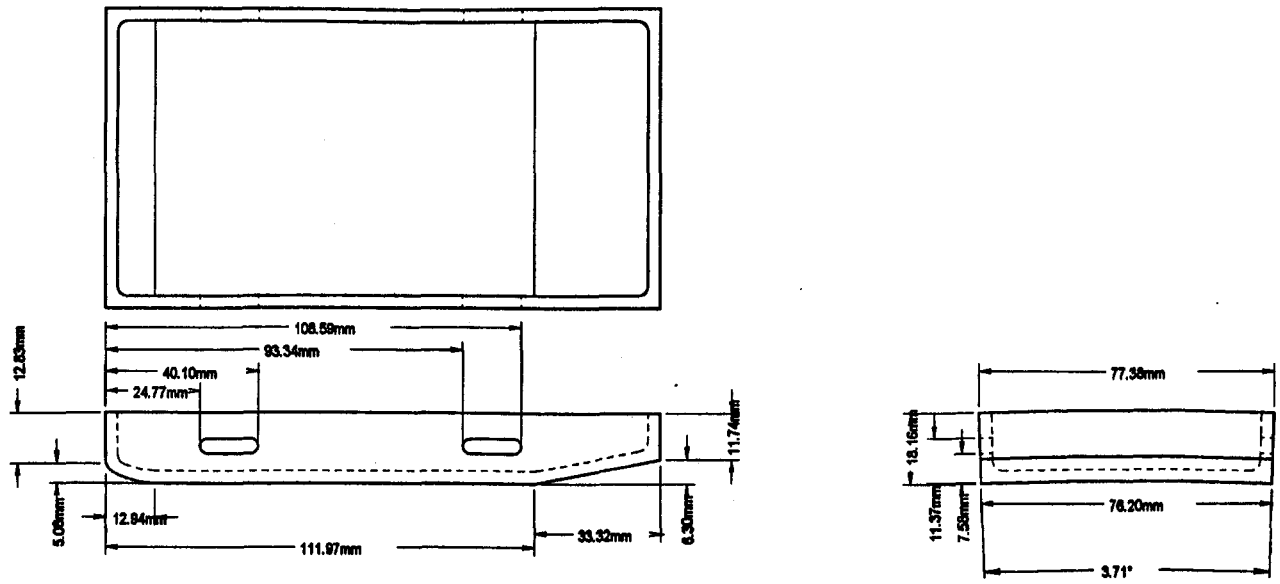

Fig. 4(*A*) (I) Top, (II) side, and (III) front views of the conceptual ceramic shroud model (in mm)

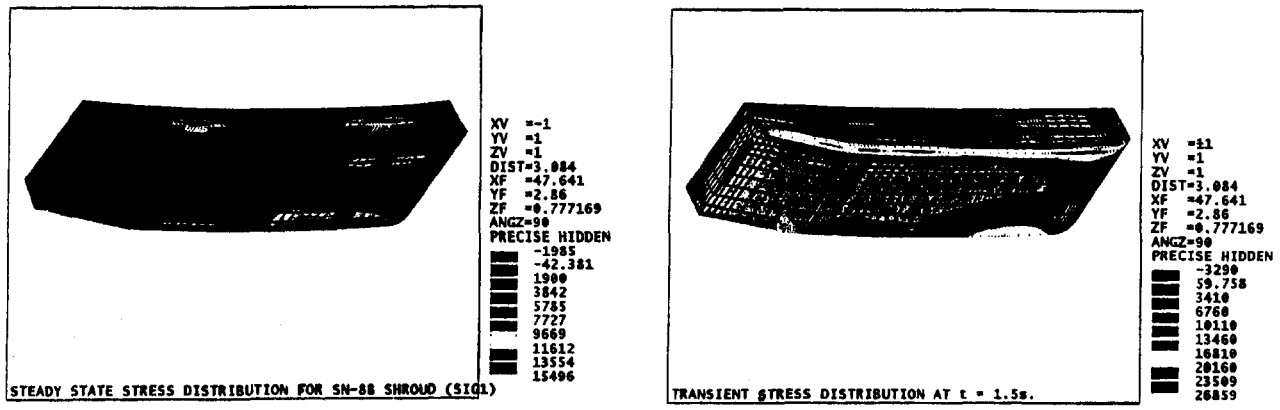

Fig. 4(*B*) Steady-state and transient (t = 1.5 s) stress distributions (in psi) of the SN-88 shroud

Reliability Analysis of the Ceramic Gas Seal (Shroud). A conceptual ceramic shroud was designed as part of the CFCC Phase I Program (DOE/CE/41000-01). The shroud is illustrated in Fig. 4(*A*). The solid model of the shroud was meshed with refined elements wherever necessary using the IDEAS package (Structural Dynamics Research Corp., 1988). The boundary conditions were set to best match the temperature, pressure, and heat transfer conditions known from experience. A reduction in the shroud cooling of ~70 percent relative to the current design was assumed for the thermal analysis. The finite element method (FEM) thermal and stress analysis were performed in ANSYS 4.4A using the temperature-dependent engineering properties of SN-88 in Table 1 (provided by NGK Insulators).

The FEM model constituted one half of the shroud, divided down the axial centerline. The model consisted of 8034 nodes and 6000 eight-noded brick elements. The steady-state and transient (at t = 1.5 s) stress distributions are shown in Fig. 4(*B*). The steady-state temperature of the shroud ranged from 656°C to 994°C. Bulk steady-state temperature of the shroud was 818°C. The maximum steady-state stress was 107 MPa at a temperature of 684°C. The predicted high-stress regions in the steady-state condition were the outer surfaces of holes used for mounting the shrouds to the turbine stator.

The simulation of the full-load turbine trip was performed by assuming that the gas temperature on all surfaces of the shroud decreased instantly to 371°C. The stress analysis was repeated at a minimum time interval of 0.1 second, with the steady-state condition being at t = 0. The maximum transient stress during the turbine trip was 185 MPa at a temperature of 642°C at t = 1.5 seconds. The predicted high stress regions in the transient (trip) condition were the axial edges and the center of the gas side surface.

The reliability analysis for fast fracture was based on the following assumptions: (1) Failure will occur from volume-distributed pores or large grains only (suitable data for analysis

Table 1 Engineering properties of SN-88 sintered silicon nitride

Property	Temperature (°C) 25	200	400	600	800	1000	1200	1400
Density (g/cm^3)	3.52	-	-	-	-	-	-	-
Young's Modulus (GPa)	300	300	300	300	300	290	290	280
Shear Modulus (GPa)	120	120	120	120	120	116	116	112
Poisson's Ratio	0.27	0.27	0.27	0.27	0.27	0.27	0.27	0.27
Coeff. of Thermal Expansion [Note 1] (x 10^{-6}/K)	-	2.2	2.7	3.0	3.3	3.4	3.5	3.5
Thermal Conductivity (W/m-K)	71.1	41.8	33.5	29.3	25.1	20.9	20.9	-
Specific Heat (J/kg-K)	669	837	1004	1130	1213	1255	1297	-

Notes:
1) Measured between 40°C and the temperature indicated.

Downloaded 02 Jun 2010 to 171.66.16.104. Redistribution subject to ASME license or copyright; see http://www.asme.org/terms/Terms_Use.cfm

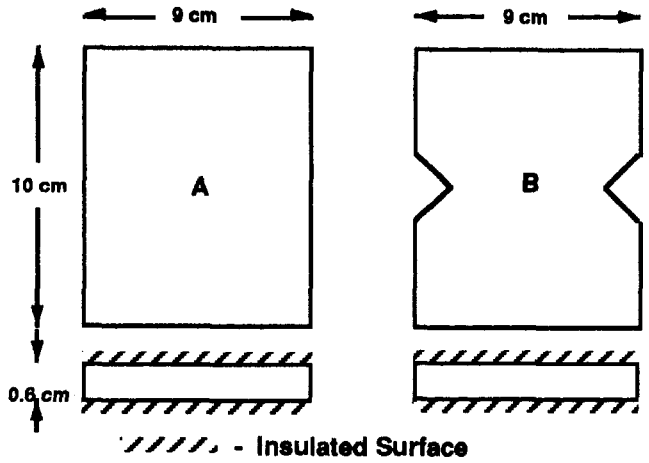

Fig. 5 Unnotched (A) and double-notched (B) SN-88 plate configurations that were thermal shock tested

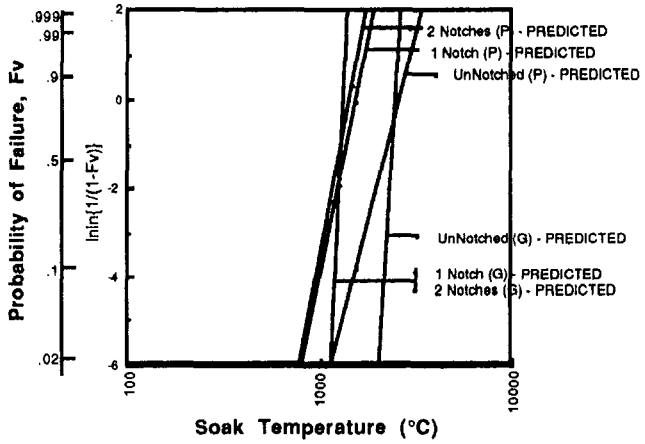

Fig. 6 Failure probabilities of SN-88 plates in proof test rig predicted using CARES/LIFE (G: large grains, P: pores)

of other failure modes that may be present in components was not available at the time of the preparation of this manuscript). These failure modes are randomly distributed and oriented, act independently and do not change with material lot, component geometry or loading conditions. (2) The relative frequency of pores and large grains is the same in the components as in the flexure test specimens. (3) Strength varies linearly with temperature over ranges between experimental data sets. The overall component failure probabilities were obtained by computing the probability of survival (Ps) for each failure mode using CARES/LIFE and using the following expression off-line:

$$P_f = (1 - Ps_1 \cdot Ps_2 \cdot Ps_n) \quad (4)$$

where P_f is the overall component failure probability and Ps_i ($i = 1, \ldots, n$) is the probability of success of the ith failure mode.

The volume-distributed pores and large grains (discussed in Section 1) were assumed to be the failure modes acting in the ceramic shroud. The overall component failure probability due to fast fracture at the steady-state baseload operating point was 0.37 E-7, using an effective volume of 8.5 E-25 cm^3. The overall component probability of failure due to fast fracture at $t = 1.5$ s during a turbine trip was 0.88 E-5, using an effective volume of 10 E-4 cm^3. The strength limiting failure mode was volume-distributed pores in both cases.

Thermal Shock Testing and Analysis of SN-88 Plates. The specifications of the unnotched and double-notched SN-88 plates that were thermal shock tested are shown in Fig. 5. The notches subtend an angle of 90 deg and have a depth of 0.6 cm.

The plates were insulated on both faces to increase the stresses during quenching. Stresses were calculated by ANSYS 4.4A using a heat transfer coefficient of 398 W/m^2-K on uninsulated surfaces for all plate geometries. The stress distribution reached a maximum at $t = 95$ s for the unnotched plate when quenched from 1538°C. The maximum stress in the plate was 362 MPa. This is almost twice the maximum stress predicted for the SN-88 shroud. The stress distribution reached a maximum at $t = 80$ s for the double-notched configuration. The maximum stress, located at each notch, was 876 MPa. The effective volume of the double-notched plate was 5.4 E-4 cm^3. The computed failure probabilities for the pores (P) and large grains (G) failure modes as functions of furnace soak temperature are shown in Fig. 6 for the unnotched, single, and double-notched configurations.

Five unnotched SN-88 plates were shocked to room temperature in the thermal shock rig from temperatures up to 1365°C. The unnotched plates could not be thermally fractured in the thermal shock rig, which was consistent with the prediction that the failure probability was very low at 1365°C. Next, 13 double-notched plates were tested in the rig. The soak temperatures were increased in 100°C increments initially. Later experiments were performed using soak temperature increments of 25°C. All plates were fractured from soak temperatures between 675 and 800°C, although CARES/LIFE analysis predicted thermal fracture at soak temperatures of 1150°C–1350°C. All fractures originated at a notch and propagated to the opposing uninsulated surface. Figure 7 compares the failure probabilities of the double-notched plates in the thermal shock rig and those predicted using CARES/LIFE. The agreement between the predicted and actual probabilities of failure was poor, as discussed below.

The Weibull modulus of the thermally shocked double-notched plates, as estimated from the slope of failure data (Fig. 7) was approximately 25. This would indicate that the failures were controlled by large grains. Only one plate had large grains in the vicinity of the fracture origin. If the majority of failures were controlled by pores, on the other hand, the slope of the failure data should have been significantly lower. Furthermore, the significantly higher actual failure probabilities relative to those predicted for a given soak temperature imply that the flaws that controlled thermal shock resistance were localized at

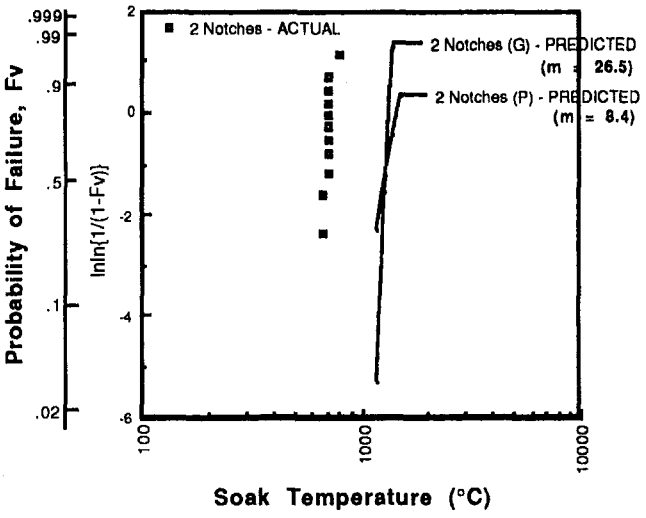

Fig. 7 Failure probabilities of double-notched SN-88 plates predicted using CARES/LIFE and determined from proof testing

Downloaded 02 Jun 2010 to 171.66.16.104. Redistribution subject to ASME license or copyright; see http://www.asme.org/terms/Terms_Use.cfm

the high stress region in the plate rather than randomly distributed, as assumed during the volume reliability analysis.

The notches in the SN-88 plates were machined using a 1200 grit diamond wheel (as compared to 320 grit for most other surfaces) and were hand polished following machining. A post-machining anneal was also supplied to minimize the effect of machining damage. Nonetheless, post-test evaluations revealed that some machining damage was present in the notch regions. This lends itself to a hypothesis that notch machining introduced a new localized failure mode, which considerably reduced the thermal shock resistance of the double-notched plates relative to that predicted from the intrinsic failure modes. Notched flexure strength tests will be performed in the future, which will enable reliability analysis for localized machining damage. This will require modifying the CARES/LIFE code to determine the reliability of components containing oriented flaws.

Conclusions

The following conclusions can be summarized from the work performed:

1 CARES/LIFE predictions agree well with the thermal shock test data for unmachined alumina.

2 The thermal shock test reliability predictions using CARES/LIFE for unnotched SN-88 plates were not contradicted by the experimental data; however, the predicted reliability of the double-notched SN-88 plates was not attained in experiment. It was hypothesized and shown that an additional failure mode was introduced due to machining of notches.

3 The conceptual SN-88 shroud was predicted have very high probabilities of survival for fast fracture under the normal and trip operating loads in the gas turbine, if the assumed failure modes (volume-distributed pores and large grains) control fracture in the component. This hypothesis was based on censored strength data for machined test bars, and must be verified for shroud components that have been formed, densified, and machined using processes relevant to commercial production.

Acknowledgments

The current investigation was supported by the Electric Power Research Institute and Gas Research Institute under contract No. EPRI RP2608-3. The data censoring analyses of S. Roamer of RPI and W. Tucker of GECRD are greatly appreciated. The encouragement of W. Bakker of EPRI and R. Petrich of GRI is also acknowledged. The shroud design was proposed under the DOE Contract No. DE-FC02-92CE 4100.

References

Morrell, R., 1985, Handbook of Properties of Technical and Engineering Ceramics, Part I.

Powers, L. M., Starlinger, A., and Gyekenyesi, J. P., 1992, "Ceramic Component Reliability With the Restructured NASA/CARES Computer Program," ASME Paper No. 92-GT-383.

SAS, 1993, User's Manual, Statistical Analysis System Institute, Inc.

Structural Dynamics Research Corp., 1988, "Finite Element Modeling With IDEAS."

Swanson Analysis System, Inc., 1986, ANSYS Programmer's Manual for Rev. 4.4A.

Trantina, G. G., 1980, "Statistical Fracture Analysis of Brittle Materials in Thermally Stressed Components," in: *Thermal Stresses in Elevated Environments*, D. P. H. Hasselman and R. A. Heller, eds., pp. 229–243.

Downloaded 02 Jun 2010 to 171.66.16.104. Redistribution subject to ASME license or copyright; see http://www.asme.org/terms/Terms_Use.cfm

Effect of Cyclic Loading on the Creep Performance of Silicon Nitride

A. A. Wereszczak

M. K. Ferber

T. P. Kirkland

High Temperature Materials Laboratory,
Oak Ridge National Laboratory,
Oak Ridge, TN

C.-K. J. Lin

Department of Mechanical Engineering,
National Central University,
Chung-Li, Taiwan

Tension–tension cyclic fatigue tests (triangular waveform, σ_{max} = 100 MPa, R = 0.1) were conducted on hot isostatically pressed (HIPed) silicon nitride at frequencies spanning several orders of magnitude (5.6 × 10^{-6} to 0.1 Hz or 10^{-3} MPa/s to 18 MPa/s) at 1370°C in air. The amount of cyclic creep strain was found to be a function of the frequency or stressing rate, with greater strains to failure observed as the frequency or stressing rate decreased. The total strain was viewed as the sum of elastic, anelastic (or transient recoverable), and plastic (viscous or nonrecoverable) strain contributions, after the empirical Pao and Marin model. The plastic strain was found to be the dominant component of the total creep and was unsatisfactorily represented by the Pao and Marin model. To circumvent this, a time exponent was introduced in the plastic strain term in the Pao and Marin model. This modification resulted in good correlation between model and experiment at the slower frequencies examined but overpredicted the cyclic creep strain at the faster frequencies. The utility of using the modified Pao and Marin model to predict cyclic creep response from static creep and strain relaxation tests is described.

Introduction

Many structural components are subjected to cyclic loading at elevated temperatures. For example, a cyclic change in angular velocity of a spinning gas turbine rotor will change the centrifugal force and corresponding stress in a cyclic fashion of any given point within the rotor's material. For lifetime prediction, it is important that the component designer understand the candidate material's response to such a cyclic stressing condition. However, high-temperature, tensile, cyclic fatigue data for structural materials such as HIPed silicon nitride are lacking in the literature. The cyclic creep response and affiliated damage mechanisms of some silicon nitride materials have been methodically examined in tension. However, these studies were conducted on either immature material by today's standards (Liu and Brinkman, 1987) or on material that is no longer commercially available (Lin et al., 1994).

The motive of the present study was to examine the utility of extending values and parameters generated from static creep tests to predict cyclic loading response. Numerous tensile-static creep tests have been reported in the literature the last few years on various silicon nitrides (Ferber and Jenkins, 1992; Ding et al., 1994; Menon et al., 1994); therefore, an extensive database is available for static creep tests. The ultimate goal is to be able to take advantage of the more extensive static creep databases to predict cyclic creep response via an appropriate model.

The present study: (1) extracts data from previously generated static creep tests conducted on a HIPed silicon nitride material, (2) describes strain relaxation tests that were conducted as an analytical supplement, (3) describes how an existing empirical model, which describes static creep, was modified to accommodate dynamic or cyclic loading, (4) predicts the cyclic creep response using information from the static and strain relaxation test sources, and then (5) compares it with experimentally generated cyclic creep responses. Along the way, important insights were made with regard to the role of the viscoelastic or anelastic secondary phase on the cyclic creep performance; these are presented here.

Material Description and Experimental Procedure

PY6 silicon nitride[1] was the material examined in this study. The material contained 6 wt% yttrium oxide as a densification aid. Specimens were cold isostatically pressed, glass-encapsulated, and then HIPed. The as-received microstructure consisted of acicular-shaped grains (typically ≈ 0.7–1.5 μm × 4–10 μm) mixed with equiaxed grains (≈1 μm diameter). These silicon nitride grains were separated by thin layers (≈1–3 nm) of an amorphous yttrium–silicon oxynitride. However, most of the secondary phase was located at multigrain junctions. X-ray diffraction was conducted on the as-received material of one of the test specimens and β-Si_3N_4 was identified along with a trace of α-$Y_2Si_2O_7$ (JCPDS#21-1457). The α-$Y_2Si_2O_7$ phase was mostly at the multigrain junctions.

Button-head tensile specimens (6.35 mm gage diameter and 35 mm gage length) were used. Tension–tension cyclic tests were conducted at 1370°C in ambient air (40–60 percent RH and 25°C). A triangular waveform was used in all tests with $\sigma_{min}/\sigma_{max}$ = R = 0.1 and σ_{max} = 100 MPa. Specimens were loaded at one of several frequencies (or stressing rates) that varied over several orders of magnitude. Test frequencies were 0.1, 0.0056, 0.00056, 0.000056, and 0.0000056 Hz, which corresponded to stressing rates of 18, 1, 0.1, 0.01, and 0.001 MPa/s, respectively. Due to a limitation in the number of specimens, only one specimen per frequency was tested. As a supplement to the cyclic testing, strain (or creep) relaxation tests were conducted at 1370°C. This involved removing a 100 MPa stress from a tensile specimen in a matter of a few seconds and monitoring the strain or creep recovery as a function of time. The motive behind the strain relaxation tests was to examine the relaxation behavior of this material at 1370°C and to correlate it with the cyclic behavior of the material.

All tests were conducted on electromechanical tensile test machines in electronic closed-loop load control.[2] Specimens

Contributed by the International Gas Turbine Institute and presented at the 40th International Gas Turbine and Aeroengine Congress and Exhibition, Houston, Texas, June 5–8, 1995. Manuscript received by the International Gas Turbine Institute February 27, 1995. Paper No. 95-GT-309. Associate Technical Editor: C. J. Russo.

[1] GTE Laboratories, Inc., Waltham, MA (1989–90 vintage).
[2] Model 1380, Instron Corp., Canton, MA.

Copyright © 1996 by ASME

Downloaded 02 Jun 2010 to 171.66.16.104. Redistribution subject to ASME license or copyright; see http://www.asme.org/terms/Terms_Use.cfm

were heated using a compact two-zone, resistance-heated ($MoSi_2$ elements) furnace having six elements per zone. Specimen grips were positioned outside the furnace hot zone. The grips and couplers were tensile-load-activated and were designed to minimize specimen bending. Specimen elongation was measured over a 25 mm gage length using a high-temperature, contact extensometer that employed a capacitance sensor. Extensometer accuracy and stability of approximately 0.5 μm over the 25 mm gage length was achieved. Personal computers were used to acquire load, load error, specimen elongation, and furnace temperature data as a function of time.

Results and Discussion

Modification of the Pao and Marin Model. The empirical Pao and Marin model (Pao and Marin, 1953) was chosen because it was already in a form that could readily accommodate variable stressing conditions in its prediction of creep strain. In the Pao and Marin (PM) model, the total isothermal strain ($\epsilon_{t'}$) at any time is composed of three independent terms: the elastic strain (ϵ_e), the anelastic or transient or recoverable nonelastic strain (ϵ_a), and the plastic or nonrecoverable strain (ϵ_p). This is represented by:

$$\epsilon_t' = \epsilon_e + \epsilon_a + \epsilon_p \tag{1}$$

where

$$\epsilon_e = \frac{\sigma}{E} \tag{2}$$

$$\dot{\epsilon_a} = \frac{d}{dt}(\epsilon_a) = \alpha(C_1\sigma^n - \epsilon_a) \tag{3}$$

and,

$$\dot{\epsilon_p} = C_2\sigma^n, \tag{4}$$

where σ is the applied stress, E is the Young's modulus, α is a variable that is equal to the inverse of the relaxation time constant and is representative of the viscoelastic behavior, and C_1 and C_2 are constants. Equation (3) was proposed by Pao and Marin because they argued that the transient or anelastic strain is not proportional to the stress, but to stress raised to some power. In addition, Pao and Marin acknowledged in Eq. (3) that the anelastic strain rate decreases with an increase in the anelastic strain and approaches zero when the anelastic strain reaches an asymptotic value. From Eq. (3), the relation containing ϵ_a can be rewritten for any function of stress that is dependent on time as:

$$\dot{\epsilon_a} + \alpha\epsilon_a = \alpha C_1\sigma^n = \alpha C_1 F(t), \tag{5}$$

where $F(t)$ can be used to represent any time dependent function of stress. Equation (5) is a first-order differential equation and the solution can be obtained using LaPlace transforms. The solution is

$$\epsilon_a = \alpha C_1 \int_0^t F(t-\xi)e^{-\alpha\xi}d\xi \tag{6}$$

where ξ is the shift or translation time (a property of the LaPlace transform). The solution to Eq. (4) is simply

$$\epsilon_p = \int \dot{\epsilon_p}dt = C_2\int_0^t \sigma^n dt \tag{7}$$

For static creep (σ = constant), the PM model represents the total creep strain as

$$\epsilon_{t'} = \frac{\sigma}{E} + C_1\sigma^n(1 - e^{-\alpha t}) + C_2\sigma^n t. \tag{8}$$

This model may ultimately be used for static, dynamic, and cyclic stressing, as long as the correct time dependence of stress is employed. The PM model predicts that the total strain as a function of time (combining Eqs. (2), (6), and (7)) for any static or nonstatic stressing condition is:

$$\epsilon_{t'} = \frac{\sigma}{E} + \alpha C_1\int_0^t F(t-\xi)e^{-\alpha\xi}d\xi + C_2\int_0^t \sigma^n dt. \tag{9}$$

Equation (9) simplifies to Eq. (8) when a constant stress is applied.

The PM model represents the plastic component of creep as being linearly dependent with time (i.e., a viscouslike, permanent creep response that ultimately represents steady-state creep). As shown in Fig. 1, the plastic component of creep is not linear with time for the Si_3N_4 investigated in the present study. The plastic strain is dependent on time to an exponent less than one. Furthermore, the plastic component of creep con-

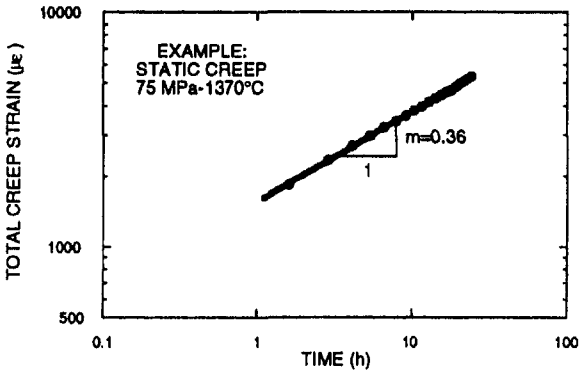

Fig. 1 For PY6 silicon nitride, the plastic component of creep is dependent on time to an exponent less than one

Nomenclature

α = inverse of the relaxation time constant
C_1 = constant that is present in the anelastic strain representation
C_2 = constant that is present in the plastic strain representation
ϵ_a = anelastic strain
$\dot{\epsilon_a}$ = anelastic strain rate
$\epsilon_{a'}$ = maximum anelastic strain for a corresponding change in stress
ϵ_{am} = anelastic strain of the modified Pao and Marin model
ϵ_e = elastic strain
ϵ_p = plastic strain
$\dot{\epsilon_p}$ = plastic strain rate
ϵ_{pm} = plastic strain of the modified Pao and Marin model
ϵ_t = total creep strain of the modified Pao and Marin model
$\epsilon_{t'}$ = total creep strain of the Pao and Marin model
E = Young's modulus
MLR = multilinear regression
MPM = modified Pao and Marin model
n = stress exponent—plastic strain
n' = stress exponent—anelastic strain
PM = Pao and Marin model
q = relaxation time constant
R = minimum to maximum stress ratio
σ = stress
σ_{max} = maximum stress
σ_{min} = minimum stress
$\Delta\sigma$ = change in stress
t = time
ξ = Laplace transform shift or translation time

Downloaded 02 Jun 2010 to 171.66.16.104. Redistribution subject to ASME license or copyright; see http://www.asme.org/terms/Terms_Use.cfm

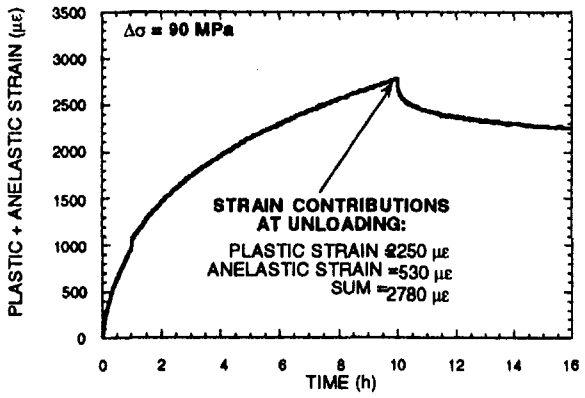

Fig. 2 As the total accumulated strain (ϵ_t) increases, the ratio of ϵ_a'/ϵ_t becomes smaller. ϵ_a' is constant and depends only on the change of stress associated with unloading.

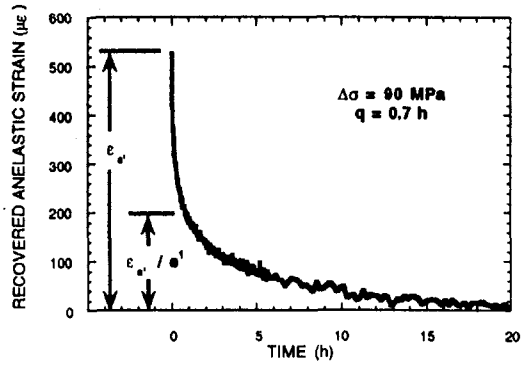

Fig. 4 An example of a strain relaxation test history. ϵ_a' is the total recovered anelastic strain and the relaxation time constant, q, the time it took for 63 percent of ϵ_a' to be recovered.

stitutes a significant contribution to the total creep strain, especially at long times. Figure 2 shows that the magnitude of the total recovered anelastic strain becomes more insignificant as the total creep strain increases with time. This is an important observation because it reveals that the plastic strain eventually becomes the dominant contributor to the total strain at 1370°C in PY6 silicon nitride. A time exponent not equal to one and the eventual dominance of the plastic strain on the total creep strain amplifies the error associated with the assumption that the plastic strain is linearly dependent with time. To address these issues, the PM model was modified in the present study by introducing a time exponent (m) parameter into the plastic strain term (i.e., the third term in Eq. (9)). The modified Pao and Marin (MPM) model then is represented as:

$$\epsilon_t = \frac{\sigma}{E} + \alpha C_1 \int_0^t F(t-\xi)e^{-\alpha\xi}d\xi + C_2 \int_0^t \sigma^n t^m dt, \quad (10)$$

where ϵ_t now represents the total strain for any time. The modified plastic term in Eq. (10) will be referred to as ϵ_{pm}. In addition, a different stress exponent (n') for the modified anelastic strain (ϵ_{am}) was also introduced to account for the possibility that the stress exponent for the anelastic strain term may not be the same as that for the plastic strain term. As an example of this for the case of an applied static stress, $n' \neq n$ in the second term of Eq. (8). Qualitative descriptions of the independent elastic, anelastic, and plastic components for the PM and the MPM models are schematically shown in Fig. 3.

Experimental Results

Strain Relaxation Behavior. Strain relaxation tests were conducted at 1370°C to determine the values of the parameters

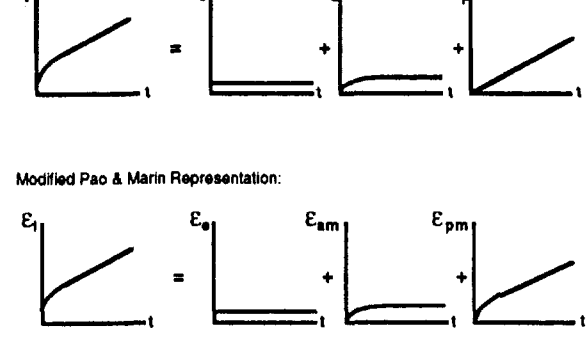

Fig. 3 Examples of qualitative strain responses for an applied static stress are shown for the MP and MPM models

that describe the anelastic strain, ϵ_{am}. The strain relaxation behavior characterized from unloading was taken as congruent to the behavior on loading, which has been previously demonstrated for HIPed silicon nitride (Wereszczak et al., 1994). The strain recovery and the primary creep mechanisms are believed to be equivalent and result from the viscoelastic response of the amorphous grain boundary phase and the sliding of the grain boundaries, which is accommodated by the elastic deformation of the material adjacent to grain asperities between the grains (Lange et al., 1980).

The relaxation time constant (q), α, n', and the constant C_1 were determined. α is simply the inverse of q (i.e., $\alpha = 1/q$). For this test, a tensile stress of 100 MPa was reduced to approximately 7 MPa; it was not completely removed to maintain specimen alignment. Several relaxation tests were conducted to examine any dependence of q on: (1) the hold time (0.1, 1, and 10 h) at 100 MPa prior to load removal, (2) different amounts of total creep strain, and (3) the amount of stress removed ($\Delta\sigma$). It was found that q was independent of the hold time at peak stress prior to unloading and also independent of the total strain accumulated. The total amount of ϵ_a recovered ($\epsilon_{a'}$) was found to be linearly dependent on $\Delta\sigma$ over the changes in stress examined (i.e., $n' = 1$). It exhibited the relation $\epsilon_{a'} \approx 6 \cdot \Delta\sigma$ for 54 MPa $\leq \Delta\sigma \leq$ 93 MPa where $\epsilon_{a'}$ and σ have units of $\mu\epsilon$ and MPa, respectively. An example of a strain relaxation test history is shown in Fig. 4. The elastic load, ϵ_e, is subtracted out from the strain shown in Fig. 4, so the decay shown is strictly due to anelastic recovery, ϵ_{am}. The relaxation time constant is equal to the time it took for 63 percent (i.e., e^{-1}) of $\epsilon_{a'}$ to recover. Although it was debatable whether or not $\epsilon_{a'}$ was indeed ever attained (i.e., $\dot{\epsilon}_a^* = 0$), even after *days* at the unloaded stress, in practicality $\dot{e}_a^* \approx 0$ after ≈4–5 hours. It was determined that $q = 0.7$ h = 2500 s or that $\alpha = 1.4\ \text{h}^{-1} = 0.0004\ \text{s}^{-1}$. A single relaxation time constant was determined to represent the relaxation behavior for the sake of simplicity; however, evidence suggests that a spectrum of relaxation constants may be more representative (Lange et al., 1980; and Arons and Tien, 1980). Combining the data from Fig. 4 with Eq. (7), C_1 was determined to be $2.6 \times 10^{-3}/\alpha$. The obtained values for α, n', and C_1 were used in Eq. (10) for all analysis.

Cyclic Fatigue Behavior. The strain–time histories for the five cyclic fatigue tests are shown in Fig. 5 and compared with previously generated static creep histories (Ferber and Jenkins, 1992). The test matrix, number of cycles, and times to failure are listed in Table 1. As the frequency is slowed, the general trend is toward more extensive total creep strain. Specimens PY6-1 and PY6-2 were tested at the two fastest frequencies and their strain–time histories fell between the range of the static creep histories of specimens tested at 50 and 60 MPa. The average tensile stress of the triangular waveform used in this

Downloaded 02 Jun 2010 to 171.66.16.104. Redistribution subject to ASME license or copyright; see http://www.asme.org/terms/Terms_Use.cfm

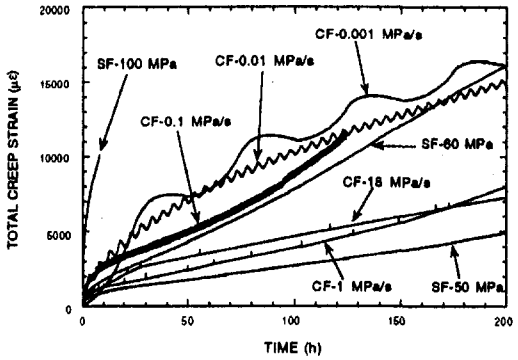

Fig. 5 Strain–time histories of cyclic fatigue tests (CF) compared with static fatigue (SF) strain histories generated in a previous study (Ferber and Jenkins, 1992)

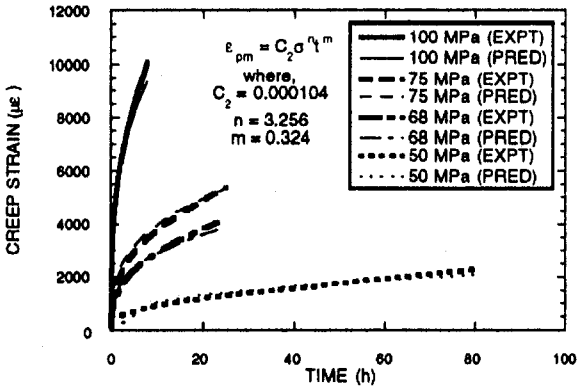

Fig. 6 The variables C_2, n, and m determined from multilinear regression of total creep strain versus time from static creep histories previously generated (Ferber and Jenkins, 1992)

study was 55 MPa, so it is not altogether surprising that the strain–time histories of at least some of the tested specimens fell within this range. Specimens PY6-3, PY6-4, and PY6-5 exhibited more total creep than the static creep test at 60 MPa, even though their average stresses were still 55 MPa. Possible reasons for the greater total creep strains shown by specimens PY6-3, PY6-4, and PY6-5 will be revisited in later discussion. The strain was not continuously monitored with the contact extensometers for tests PY6-1 and PY6-2 to avoid damage to the instrument, so strain was periodically measured at discrete times; these are the "tick" marks present in the strain histories of these two tests.

To determine the values of the parameters associated with the plastic component of the MPM model, ϵ_{pm}, multilinear regression (MLR) was employed on static creep data previously generated on PY6 (Ferber and Jenkins, 1992). MLR on creep strain as a function of stress and time was performed on the natural logarithm of the integrand in the third term in Eq. (10), or

$$\ln(\epsilon_{pm}) = \ln(C_2) + n \ln(\sigma) + m \ln(t), \qquad (11)$$

for static creep stresses of 50, 68, 75, and 100 MPa. It was determined that $C_2 = 0.000104$, $n = 3.256$, and $m = 0.324$. It is noteworthy that the stress dependence on the total creep strain was found to be 3.256 in the present study, while the stress dependence on the minimum creep rate was previously determined to be 4.7 for PY6 at 1370°C (Ferber and Jenkins, 1992). The time exponent of 0.324 is quite close to the 1/3 predicted by the classical Andrade analysis (Andrade, 1914). The experimental data and the fitted curves are shown in Fig. 6. Even though the total strain is plotted as the ordinate in Fig. 6, the use of it (versus *just* the plastic strain) does not affect the slope determination of the plastic creep time exponent (i.e., m) on the log–log plot because the elastic and anelastic contributions are small and effectively constant over the life of the test. These three values of C_2, n, and m were used in Eq. (10) for all analysis.

The MPM model described by Eq. (10) was used to fit the experimental data numerically. The values of the parameters used in the analysis were: $\alpha = 1/q = 0.0004\ s^{-1}$, $C_1 = 0.0026/\alpha$, $n' = 1$, $E = 300$ GPa (43.5×10^6 psi), $C_2 = 0.000104$, $n = 3.256$, and $m = 0.324$. As an illustrative example, Figs. 7(*a*, *b*) show an arbitrary triangular waveform and the prediction of elastic, anelastic, and plastic strain, and their sum, for one cycle of an arbitrary triangular waveform. Units of MPa and $\mu\epsilon$ (or μm/m) were used consistently throughout the analysis.

Table 1 Test matrix and cyclic fatigue results. Triangular waveform described by $R = 0.1$ and $\sigma_{max} = 100$ MPa.

Specimen ID	Freq. (Hz)	Stress Rate (MPa/s)	# of Cycles to Failure	Time to Failure (h)
PY6-1	0.1	18	406600*	1129*
PY6-2	0.0056	1	4939	247
PY6-3	0.00056	0.1	248	124
PY6-4	0.000056	0.01	149.5	747.5
PY6-5	0.0000056	0.001	8.4	419

* Test interrupted, specimen did not fail.

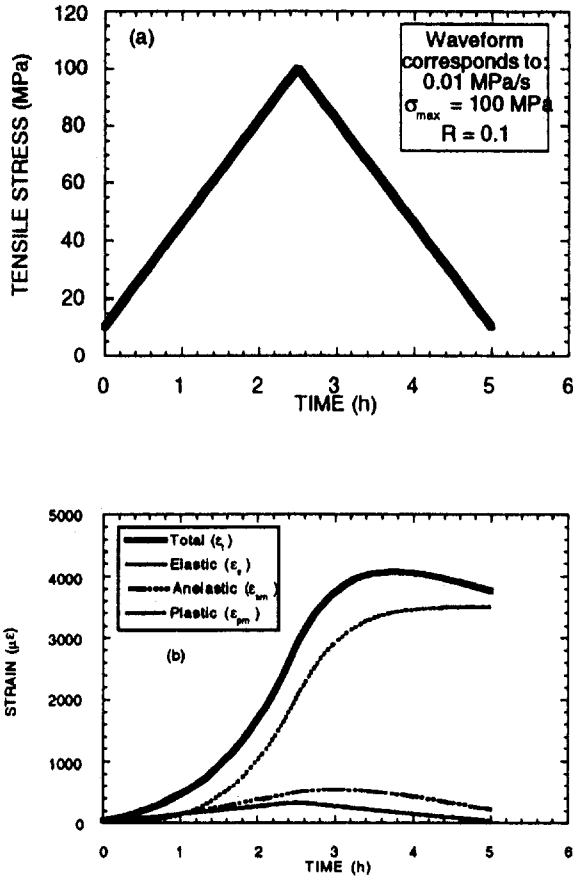

Fig. 7 For an arbitrary triangular waveform (*a*), examples of elastic, anelastic, plastic, and total strains are predicted (*b*) for one cycle using Eq. (10)

Downloaded 02 Jun 2010 to 171.66.16.104. Redistribution subject to ASME license or copyright; see http://www.asme.org/terms/Terms_Use.cfm

The predicted fits for the five specimens tested in this study are shown in Fig. 8 along with the experimental creep strain–time curves. The experimental cyclic creep curves exhibit continued increases in their total strain indicative of creep racheting behavior (Kraus, 1980). A large discrepancy between experimental and predicted cyclic response was observed at faster frequencies or faster stressing rates. This discrepancy lessens as the test frequency was decreased, but it remained substantial for stressing rates equal to and above 0.1 MPa/s, as shown in Figs. 8(*a–c*). Data were only predicted for durations of about 5.5 and 50 hours for specimens PY6-1 and PY6-2, respectively, because computation time was excessive and the discrepancy between experiment and prediction became evident after short times. The magnitudes of total creep strain predicted for 0.01 MPa/s were approximately equal to those of the experiment, as shown in Fig. 8(*d*), although the creep rates were dissimilar throughout the test duration. The prediction of the cyclic creep response was quite good for the 0.001 MPa/s test, as shown in Fig. 8(*e*). The predicted total creep strain profile was coincident with the experimental data up to approximately 175 hours, but the overall increase in the experimental creep rate after 175 h suggested an onset of tertiary creep. Tertiary creep behavior is a phenomenon that is not addressed in the MPM model.

A possible reason why the MPM model overpredicts the cyclic creep strain at faster test frequencies and stressing rates may be due to the changing nature of the material's elastic stress limit. The effective elastic limit[3] is a function of the stressing rate for PY6 silicon nitride and decreases with decreasing stressing rate at 1370°C. This trend has also been reported for hot-pressed silicon nitride (Ohji et al., 1987). The dynamic fatigue, stress–strain history was reported by Lin et al. (1993) for PY6 at 1370°C. That data traversed over thousands of microstrain; however, only the first 800 $\mu\epsilon$ (or 0.08 percent strain) of it are shown in Fig. 9. Four of the five stressing rates shown match rates used in the present cyclic fatigue study; 37 MPa/s was included as a comparison to show a faster stressing rate response. Although it is somewhat of a subjective determination, the effective elastic limit is somewhere between ≈80–100 MPa for 1 MPa/s and as low as ≈30 MPa for 0.001 MPa/s. Note that these stressing rates were used in the present cyclic fatigue tests on specimens PY6-2 and PY6-5, respectively. The MPM model predicts a plastic contribution to the total strain for *all* stresses during each cycle; whereas in the experimental case, there may only be a plastic strain contribution for stresses *above* the elastic limit for that corresponding stressing rate. For cyclic tests PY6-1, PY6-2, and PY6-3, the frequencies or stressing rates were *fast enough* where there was not an appreciable amount of time above the elastic limit for each stressing rate to accumulate the total strain predicted by the MPM model. This lack of acknowledgment of the elastic limit will cause the MPM model to overpredict the total cyclic creep strain consistently at faster frequencies or stressing rates. At the slower stressing rates of 0.01 and 0.001 MPa/s, the relatively low elastic limit coupled with the long times that the stress in each cycle is in excess of it results in more representative predictions of total cyclic creep strain.

Instead of a critical or elastic stress limit argument, the perspective of a threshold strain to explain the cyclic creep behavior also may be used. In this case, plastic strain only accumulates if ϵ_{am} is saturated or reaches some threshold anelastic strain (i.e., ϵ_{pm} increases only if $\epsilon_{am} = \epsilon_{a'}$ or $\epsilon_{am} = \text{const} \cdot \epsilon_{a'}$). The basis for this comes from at least two sources. Lin et al. (1994) experimentally found that cyclic loading of PY6 (0.1 and 10 Hz) at 1370°C always yielded less accumulated creep strain and

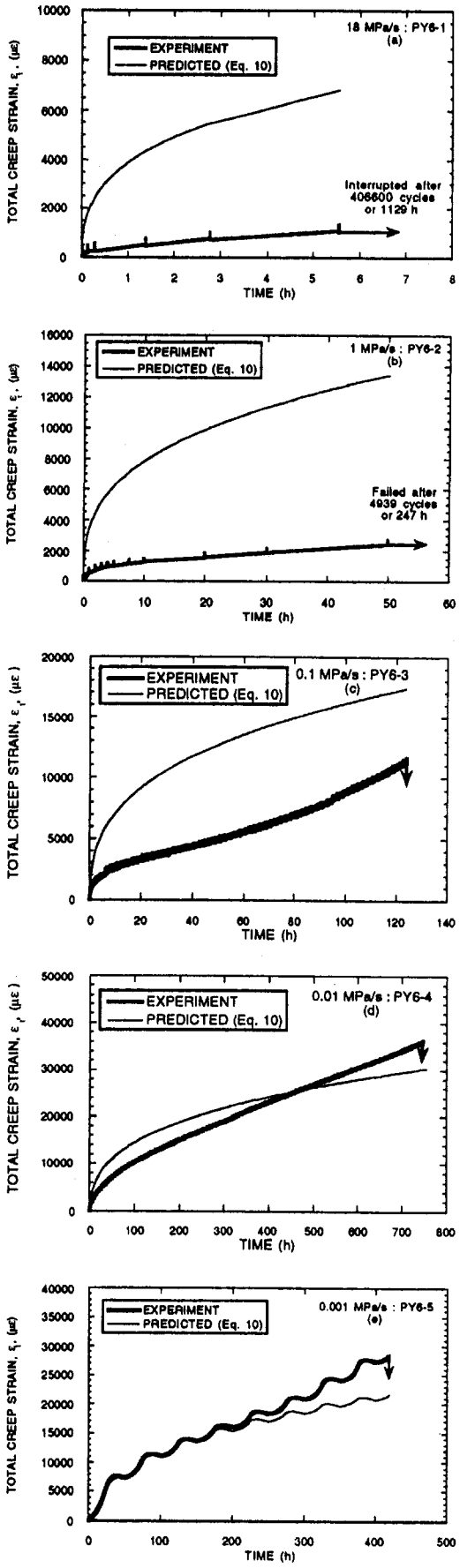

Fig. 8 Experimental cyclic creep strain as a function of time is compared with data predicted using the MPM model for specimens: (*a*) PY6-1, (*b*) PY6-2, (*c*) PY6-3, (*d*) PY6-4, and (*e*) PY6-5

[3] The present reference to an "elastic limit" is somewhat of a misnomer. At elevated temperatures where anelasticity is active, the strain limit describing the onset of nonlinearity is due to elastic plus anelastic effects (Lubahn, 1953). However, for the sake of convenience, this limit in the present study is referred to as the "elastic limit."

Downloaded 02 Jun 2010 to 171.66.16.104. Redistribution subject to ASME license or copyright; see http://www.asme.org/terms/Terms_Use.cfm

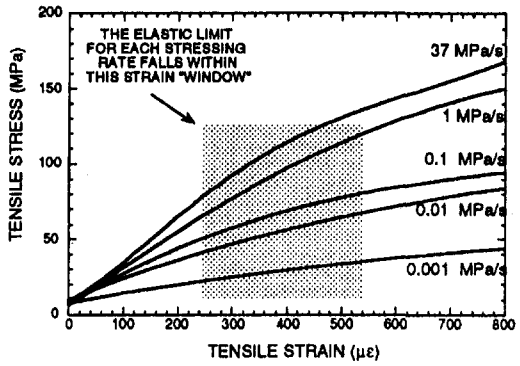

Fig. 9 As the stressing rate is decreased, the elastic limit decreases and plastic creep occurs at lower stresses. Creep strain data are extracted from reported tests (Lin et al., 1993).

longer lifetimes than static loading at comparable stresses. In that study, it was speculated that the viscoelastic or anelastic nature of the secondary phase acted in concert with the fast cyclic loading and unloading to slow the normal accumulation of creep damage. In a second study, cavitation (a permanent or plastic damage mechanism) was shown to account for as much 85 percent of the total creep strain (Luecke et al., 1993); however, the attainment of a small amount of accumulated strain was necessary before cavities were detected. Both these studies support the claim that a critical strain (in this case, an anelastic strain) needs to be attained in order for plastic deformation to become active. This critical strain may indeed be stress dependent in a similar fashion to the dependence of $\epsilon_{a'}$ on the $\Delta\sigma$ from the strain relaxation studies. If the anelastic strain is saturated, then no more anelastic strain can be accommodated and high local stress intensities may develop, which act to nucleate cavities. The MPM model does not take into account that the onset of plastic deformation requires a threshold of anelastic strain to be met; consequently, it will overpredict the plastic strain at faster frequencies or stressing rates where the critical strain is not attained. Indeed there is *some* accumulation of plastic strain evident in Figs. 8(a–c) for the faster frequencies; therefore, for this argument to be valid, an anelastic strain threshold must have been met for each cycle, although the corresponding accumulation of plastic creep was relatively small. Of the arguments based on the plastic strain first requiring the attainment of a critical stress or strain, the latter is more versatile because it can more easily reconcile plastic deformation under fast frequency cyclic and static loading conditions.

In the future, the MPM model will be further refined to predict creep strain whose plastic component only becomes activated once an elastic stress limit is exceeded or an anelastic strain threshold is saturated. This refinement shall correct, or at least lessen, overpredicted creep strains and more accurately reflect cyclic creep response of materials such as PY6 silicon nitride.

Conclusions

The amount of tension–tension cyclic creep strain was found to increase as the frequency or stressing rate of a triangular waveform (σ_{max} = 100 MPa and R = 0.1, average stress of cycle = 55 MPa) decreased for PY6 silicon nitride at 1370°C. For frequencies of 0.1 and 5.6 × 10^{-3} Hz (stressing rates of 18 and 1 MPa/s, respectively), the amount of cyclic creep strain fell within a range bounded by static creep responses of 50 and 60 MPa. The total cyclic creep strain increased continually for comparable times for frequencies of 5.6 × 10^{-4} Hz, 5.6 × 10^{-5} Hz and 5.6 × 10^{-6} Hz (stressing rates of 0.1, 0.01, and 0.001 MPa/s, respectively).

A modified Pao and Marin model was successful at predicting representative low-frequency, cyclic creep responses from data and creep parameters extended from static creep and strain relaxation tests. The model predicted cyclic creep strains similar to those experimentally determined for 5.6 × 10^{-5} Hz. It very accurately predicted the cyclic creep response for 5.6 × 10^{-6} Hz.

The modified Pao and Marin did not satisfactorily predict cyclic creep response at frequencies equal to and faster than 5.6 × 10^{-4} Hz. The model overpredicted the cyclic creep strains at these faster frequencies. The model predicts the contribution of plastic strain for all stresses in the cyclic waveform used; however, it is evident that an elastic stress limit or an anelastic strain threshold needs to be attained *prior* to the accumulation of plastic strain.

Acknowledgments

This research was sponsored by the U.S. Department of Energy, Assistant Secretary for Energy Efficiency and Renewable Energy, Office of Transportation Technologies, as part of the Ceramic Technology Project of the Propulsion System Materials Program, under contract No. DE-AC05-84OR21400 with Martin Marietta Energy Systems, Inc.

The authors wish to thank Dr. B. Gieseke, Dr. H.-T. Lin, and Dr. A. E. Pasto for reviewing the manuscript and for their helpful suggestions and comments. C.-K. J. Lin was a postdoctoral researcher at the High-Temperature Materials Laboratory at the time of this study.

References

Andrade, E. N. da C., 1914, "The Viscous Flow in Metals and Allied Phenomena," *Proc. Roy. Soc.*, Vol. A90, p. 329.

Arons, R. M., and Tien, J. K., 1980, "Creep and Strain Recovery in Hot-Pressed Silicon Nitride," *J. Mat. Sci.*, Vol. 15, pp. 2046–2058.

Ding, J.-L., Liu, K. C., More, K. L., and Brinkman, C. R., 1994, "Creep and Creep Rupture of an Advanced Silicon Nitride Ceramic," *J. Am. Cer. Soc.*, Vol. 77, No. 4, pp. 867–874.

Ferber, M. K., and Jenkins, M. G., 1992, "Evaluation of the Strength and Creep-Fatigue Behavior of Hot Isostatically Pressed Silicon Nitride," *J. Am. Cer. Soc.*, Vol. 75, No. 9, pp. 2453–2462.

Kraus, H., 1980, *Creep Analysis*, Wiley, New York.

Lange, F. F., Clarke, D. R., and Davis, B. I., 1980, "Compressive Creep of Si_3N_4/MgO Alloys, Part 2, Source of Viscoelastic Effect," *J. Mat. Sci.*, Vol. 15, pp. 611–615.

Lin, C.-K. J., Jenkins, M. G., and Ferber, M. K., 1993, "Tensile Dynamic and Static Fatigue Relations for a HIPed Silicon Nitride at Elevated Temperatures," *J. Eur. Cer. Soc.*, Vol. 12, pp. 3–13.

Lin, C.-K. J., Jenkins, M. G., and Ferber, M. K., 1994, "Cyclic Fatigue of Hot Isostatically Pressed Silicon Nitride at Elevated Temperatures," *J. Mat. Sci.*, Vol. 29, pp. 3517–3526.

Liu, K. C., and Brinkman, C. R., 1987, "Dynamic Tensile Cyclic Fatigue of Si_3N_4," *Proc. of the 25th Automotive Technology Development Contractors' Coordination Meeting*, P-209, pp. 189–197.

Lubahn, J. D., 1953, "The Role of Anelasticity in Creep, Tension, and Relaxation Behavior," *Trans. of the A. S. M.*, Vol. 45, pp. 787–838.

Luecke, W., Wiederhorn, S. M., Hockey, B. J., and Long, G. G., 1993, *Silicon Nitride Ceramics*, V287, Mat. Res. Soc. Symp. Proc., I.-W. Chen et al., eds., pp. 467–72.

Menon, M. N., Fang, H. T., Wu, D. C., Jenkins, M. G., Ferber, M. K., More, K. L., Hubbard, C. R., and Nolan, T. A., 1994, "Creep and Stress Rupture Behavior of an Advanced Silicon Nitride: Part 1, Experimental Observations," *J. Am. Cer. Soc.*, Vol. 77, No. 5, pp. 1217–27.

Ohji, T., Sakai, S., Ito, M., Yamauchi, Y., Kanematsu, W., and Ito, S., 1987, "Yielding Phenomena of Hot-Pressed Si_3N_4," *High Temperature Technology*, Vol. 5, pp. 139–144.

Pao, Y.-H., and Marin, J., 1953, "An Analytical Theory of the Creep Deformation of Materials," *J. Appl. Mech.*, No. 6, pp. 245–252.

Wereszczak, A. A., Kirkland, T. P., and Ferber, M. K., 1994, "Stress and Strain Relaxation Behaviour in HIPed Silicon Nitrides," *J. Mat. Sci. Lett.*, Vol. 13, pp. 1469–71.

Downloaded 02 Jun 2010 to 171.66.16.104. Redistribution subject to ASME license or copyright; see http://www.asme.org/terms/Terms_Use.cfm

Combined Helium and Combustion Gas Turbine Plant Exploiting Liquid Hydrogen (LH_2) Physical Exergy

G. Bisio
Energy and Conditioning Department, University of Genoa Via all'Opera Pia 15, A-16145 Genoa, Italy

A. Massardo
Mem. ASME

A. Agazzani
Machines and Energy Systems Institute, University of Genoa, Via Montallegro 1, 16145 Genoa, Italy

The aim of this work is the energy and exergy analysis of a combined plant made up of a conventional gas turbine (heavy-duty or aeroderivative) and a closed helium turbine cycle, which exploits liquid hydrogen (LH_2) as a lower energy source. A helium turbine with the characteristics of the fluid allows us to operate between the usual temperatures of the top turbine waste gas and those of the liquid hydrogen available. In this way the combined system reaches efficiency values greater than every combined system proposed to date. The work contains a detailed analysis of the relative entropy productions of the helium cycle and considerations about the realization and technological aspects of helium turbines.

Introduction

The fossil fuel reserves of primary energy are limited. In addition, energy supply has a considerable impact on the environment, even if some alleged effects are far from being fully established. Consequently, any way of using energy more efficiently and of employing renewable energy sources should be examined thoroughly. Hydrogen produced with renewable energy sources could be a nonpolluting energy carrier for the future.

In the last few years, studies have been carried out concerning the use of hydrogen as an energy vector. Particularly in Germany research is being done on the convenience of producing hydrogen in Canada by means of power from hydroelectric plants and of transporting it to Germany, either in liquid phase or chemically bound, e.g., in toluene (Grawe and Holzer, 1989; Sprengel, 1991). Further research is being carried out on the convenience of producing hydrogen by solar energy, chiefly in North Africa and Saudi Arabia (Grawe and Holzer, 1989; Hassmann et al., 1991).

As regards the transport of liquid hydrogen, this must be vaporized before any exploitation, and it seems convenient to utilize the physical exergy of hydrogen due to its liquid phase at a temperature of 20 K, instead of destroying this exergy in the vaporization with heat obtained from sea water or, even worse, by burning a fraction of the hydrogen.

Several processes have been considered to use the physical energy of liquids at atmospheric pressure by vaporizing, at cryogenic temperatures, e.g., nitrogen, hydrogen, and natural gas (Griepentrog and Weber, 1978; Oshima et al., 1978; Weber, 1989; Bisio and Cerullo, 1992).

Two general alternatives may be envisaged:

(a) direct utilization in cryogenic facilities (cold storage or various process uses);
(b) indirect utilization in the generation of electric power.

Direct utilization poses some problems:

(i) it entails coupling two plants with asynchronous characteristics;
(ii) it is essential to ensure that the operation of the LH_2 (liquid hydrogen) or LNG (liquid natural gas) terminal is not hampered by malfunctions in the plant of the cryogenic customer;
(iii) the available exergy cannot be sufficiently exploited in relation to both its quantity and its temperature level.

Indirect utilization in the generation of electric power avoids the drawbacks of direct utilization and uses the available exergy in a more efficient way.

LH_2, owing to its high exergy value, is specifically suitable for this exploitation by means of a combined system employing a closed-cycle helium turbine with two exergy sources. The former, at temperatures above that of the environment, is given by the waste gas of an open cycle combustion gas turbine, and the latter, at temperatures under that of the environment, is given by the vaporization and superheating of LH_2.

Despite its expense, the helium cycle has been chosen because it is the only suitable fluid due to its very low critical point (4.125 K). It does not present explosion hazards and the technology of helium plants is well developed.

System Layout

The layout of the combined system is shown in Fig. 1. The helium cycle, in which hydrogen vaporization is the heat sink, is represented in Fig. 2 by a temperature (T) versus specific entropy (s) diagram. Point 1, corresponding to the helium compressor inlet, is characterized by a temperature around 50 K. The helium is then compressed (process 1-2). In the recuperator, thermal energy of the turbine outlet (process 5-6) is transferred to the compressed helium (process 2-3). Then in the gas–helium heat exchanger, the helium is heated by the exhaust gas of the combustion turbine (process 3-4) until it reaches its peak temperature (about 770 K). Hence, in the subsequent expansion of helium (process 4-5) the useful power (in addition to that necessary for the compressor) is obtained. The thermal energy outgoing from the helium cycle (process 6-1) vaporizes the hydrogen (compressed by a pump at $p_8 = 10$ MPa) and superheats it to the temperature T_9, over 100 K in the helium–

Contributed by the International Gas Turbine Institute and presented at the 40th International Gas Turbine and Aeroengine Congress and Exhibition, Houston, Texas, June 5–8, 1995. Manuscript received by the International Gas Turbine Institute March 16, 1995. Paper No. 95-GT-298. Associate Technical Editor: C. J. Russo.

Copyright © 1996 by ASME

Downloaded 02 Jun 2010 to 171.66.16.104. Redistribution subject to ASME license or copyright; see http://www.asme.org/terms/Terms_Use.cfm

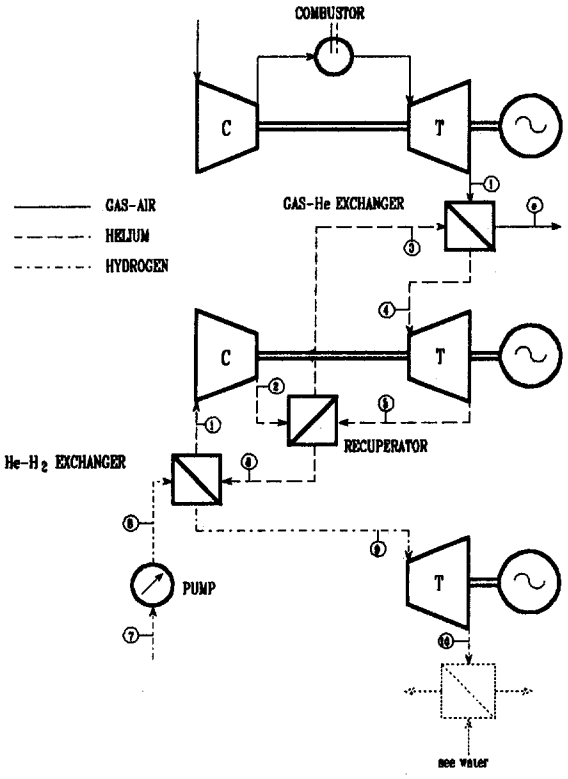

Fig. 1 Layout of the combined plant

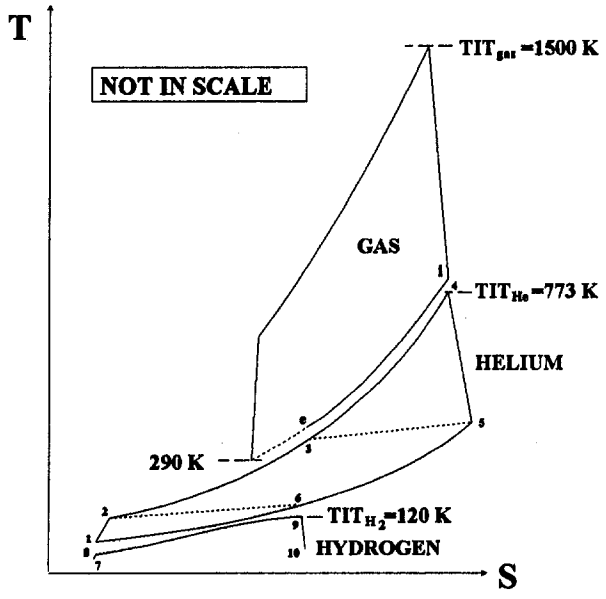

Fig. 2 Temperature-specific entropy diagram of the proposed combined cycle

hydrogen heat exchanger (process 8-9). With the considered data (pressure p_8), liquid hydrogen is transformed into superheated vapor without the system having been separated into two phases (i.e., heating at supercritical pressure).

Moreover, if it is so desired, the hydrogen can be expanded to pressure p_{10} ($\approx$ 0.5 MPa; lower values may cause a very low turbine outlet temperature or even the inlet into the two-phase area) and then, e.g., warmed again with heat obtained from sea water.

A system without hydrogen expansion has also been considered since a hydrogen turbine working at cryogenic temperatures has not been thoroughly evaluated.

Figure 3 shows a preliminary system energy balance. Around 39 percent of the thermal energy employed by the system is converted into electrical energy by the closed helium cycle, around 35 percent by the open gas turbine cycle, around 7 percent by the open hydrogen cycle, for an overall value of around 80 percent. Without hydrogen expansion the overall energy efficiency is around 74 percent.

Thermodynamic Analysis

For estimating the system performances, an extremely fast and flexible code that allows a complete thermodynamic analysis of the plant was developed.

The helium and hydrogen thermodynamic characteristics determine the operative conditions of the system points shown in Fig. 2. The values of functions p (pressure), T (temperature), i (specific enthalpy), s (specific entropy), and ex (specific physical energy) corresponding to the states of helium and hydrogen environment and to the states of the cycles points (1-6 for helium, 7-10 for hydrogen) are estimated utilizing the data of Reynolds (1979), Raznjevic (1970), and Woolley et al. (1948).

Nomenclature

Ex = (physical) exergy, kJ/kg
Ex_a = actual exergy loss, kJ/kg
Ex_{rf} = losable (or reference) exergy, kJ
Ex_u = recovered (and actually usable) exergy, kJ
Ex°_{rf} = losable (or reference) exergy power, kW
Ex°_c = chemical exergy power, kW
ex = specific exergy, kJ/kg
i = specific enthalpy, kJ/kg
L = shaft work per unit mass, kJ/kg
m = mass flow rate, kg/s
P_e = electrical power, kW
P_t = thermal power, kW
p = absolute pressure, MPa
p_o = absolute pressure of the environment
Q = heat transfer per unit mass, kJ/kg
R = recovery factor (defined in the paper)
r = exergy ratio (defined in the paper)
s = specific entropy, kJ/(kg K)
T = temperature, K, °C
T_o = temperature of the environment, K, °C
x = quality
α = thermal efficiency (or effectiveness) of a heat exchanger
β = electrical engine efficiency
η = energy efficiency
σ_a = actual entropy production, kJ/K
σ°_a = actual entropy production rate, kW/K
σ_{rf} = reference entropy production, kJ/K
σ°_{rf} = reference entropy production rate, kW/K
σ_r = relative entropy production (rate)
σ'_{ri} = relative entropy production rate of the single phase i with reference to the parameter σ°_{rf} of the whole system
Φ = exergy efficiency
Φ'_i = exergy efficiency of the single phase i with reference to the parameter Ex°_{rf} of the whole system

Subscripts

g = waste gas
He = helium
H_2 = hydrogen
i = inlet
e = exit

Downloaded 02 Jun 2010 to 171.66.16.104. Redistribution subject to ASME license or copyright; see http://www.asme.org/terms/Terms_Use.cfm

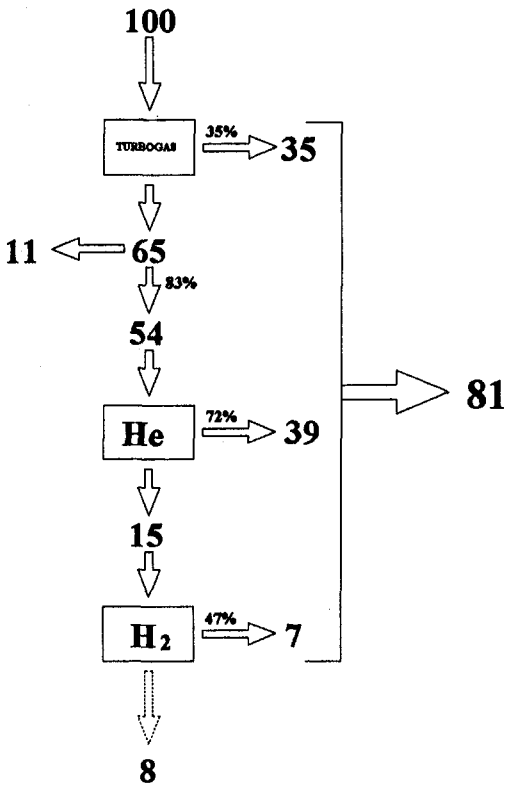

Fig. 3 Combined plant preliminary energy balance

The performance and the characteristics of the top gas turbine cycle were fixed during the system analysis: a cycle with energy efficiency 35 percent and net specific work 295.45 kW/(kg/s) (Farmer, 1994). Table 1 reports the thermodynamic functions at the inlet and at the exit of the exhaust gas heat exchanger.

Pressure losses and component efficiencies are taken into account. The main equations utilized for the thermodynamic analysis are reported in the appendix.

Exergy Analysis of the Helium Cycle. The helium cycle examined in this paper, even if it is formally similar to other power cycles, differs greatly from them on the basis of second-law analysis.

Indeed, one has exergy inlet both by waste energy of the top turbine and by "vaporization" and superheating of hydrogen at low temperatures.

The exergy efficiency of the helium cycle is given by

$$\Phi_{He} = L_{ne}/[(ex_i - ex_e)\, m_g/m_{He} + (ex_8 - ex_9)\, m_{H_2}/m_{He}] \quad (1)$$

Since the exergy coming from the "vaporization" and superheating of the liquid hydrogen can be judged free, it is convenient to consider the ratio r of the exergy of the obtained electrical energy to the exergy coming from the waste gas of the combustion turbine:

$$r = L_{ne}/[(ex_i - ex_e)\, m_g/m_{He} \quad (2)$$

This parameter, however, cannot be called "efficiency."

Table 1 Top turbine waste gas processes

	environment (o")	inlet state (i)	exit state (e)
p - MPa	0.1	0.125	0.115
T - K (°C)	290.15 (17)	813.15 (540)	378.15 (105)
i - kJ/kg	290.3	837.3	379.27
s - kJ/(kg K)	6.838	7.8430	7.0653
ex - kJ/kg	0	255.4	23.02

Table 2(A) Helium cycle

	environment (o)	state 1	state 2
p - MPa	0.1	1.2	8
T - K (°C)	290.15 (17)	50 (- 223.15)	116.23 (-156.92)
i - kJ/kg	1519.0	272.12	636.76
s - kJ/(kg K)	29.7882	15.4471	15.9071
ex - kJ/kg	0	2914.2	3145.4
	state α	state 3	state 4
p - MPa	7.95	7.9	7.8
T - K (°C)	290.15 (17)	355.05 (81.9)	773.15 (500)
i - kJ/kg	1544.9	1882.0	4051.8
s - kJ/(kg K)	20.7062	21.7685	25.8344
ex - kJ/kg	2661.0	2689.9	3680.0
	state 5	state β	state 6
p - MPa	1.3	1.27	1.25
T - K (°C)	398 (124.85)	290.15 (17)	156.73 (-116.42)
i - kJ/kg	2083.3	1523.1	838.07
s - kJ/(kg K)	26.1029	24.5100	21.3405
ex - kJ/kg	1633.6	1535.6	1770.2

Table 2(B) Hydrogen processes

	envir. (o')	state 7	state 8
p - MPa	0.1	.101325 ($x_7 = 0$)	10.2
T - K (°C)	290.15 (17)	20.28 (- 252.87)	28 (-245.15)
i - kJ/kg	4085.8	263.8	430.1
s - kJ/(kg K)	70.18	16.75	16.837
ex - kJ/kg	0	11680.7	11821.8
	state 9	state 10	state 11
p - MPa	10	0.5	10
T - K (°C)	120 (- 163.15)	41.25 (-231.9)	290.15 (17)
i - kJ/kg	1739.1	917.65	4136
s - kJ/(kg K)	38.73	39.864	52.33
ex - kJ/kg	6778.2	5628.1	5229.4

Analysis of the Relative Entropy Productions and Efficiencies of the Helium Cycle Phases. The critical examination of the concept of efficiency led to the definition of an operational domain, in which the process can be achieved (Bisio, 1989). This domain is confined by regions of no entropy production (upper limit) and no useful effects (lower limit). As a reference value, the entropy production corresponding to

Table 3 Main results obtained

L_{ne}	1557 kJ/kg	$P_{eH_2 2}$	5554 kW
η_{He}	0.7140	m_{H_2}	31.73 kg/s
R	0.2595	m_{He}	73.4 kg/s
P_{tHe1}	159190 kW	Φ_{He}	0.4736
$P_{tH_2 2}$	41532 kW	r	1.407
P_{eHe}	114223 kW	η_t	0.806
$P_{eH_2 1}$	25541 kW	F_t	0.767
$Ex_{rf}°$	241199 kW	$\sigma_{rf}°$	831.29 kW/K
Process	σ_{ri}	$\sigma_{ai}°$ (kW/K)	σ_{rf}'
1) 1-2	0.3799	35.76	0.0430
2) 2-3 and 5-6	0.5683	84.59	0.1018
3) 3-4	0.1048	29.33	0.0353
4) 4-5	0.0575	29.77	0.0358
5) 6-1	0.4681	258.17	0.3106

Downloaded 02 Jun 2010 to 171.66.16.104. Redistribution subject to ASME license or copyright; see http://www.asme.org/terms/Terms_Use.cfm

no useful effects, σ_{rf}, is assumed; multiplied by the environment temperature, T_o, it gives, for the selected operational domain, the maximum exergy loss, a parameter called the losable or reference exergy, Ex_{rf}. The actual entropy production, σ_a, multiplied by T_o gives the actual exergy loss, Ex_a. The ratio of the actual entropy production to the reference value is named relative entropy production, σ_r. The difference between the losable and the lost exergies is the recovered exergy, Ex_u. Exergy efficiency is the ratio of the recovered to the losable exergy:

$$\Phi = Ex_u/Ex_{rf} = (Ex_{rf} - Ex_a)/Ex_{rf}$$
$$= (T_o\,\sigma_{rf} - T_o\,\sigma_a)/(T_o\,\sigma_{rf})$$
$$= (\sigma_{rf} - \sigma_a)/\sigma_{rf} = 1 - \sigma_r \qquad (3)$$

Analysis of the Single Phases Separately. We consider the single phases and their relative entropy productions and efficiencies separately.

(A) Process 1-2 (helium compressor). The efficiency, Φ_1, and the relative entropy production, σ_{r1}, are given by:

$$\Phi_1 = (ex_2 - ex_1)/(-L_c), \quad \sigma_{r1} = 1 - \Phi_1 \qquad (4)$$

(B) Processes 2-3 and 5-6 (regenerator). One of the extreme temperatures of the two streams is above and the other is below that of the environment. In our opinion, none of the formulations of exergy efficiency proposed in literature apply to this particular case (Kotas, 1985; Bisio, 1989). Indeed, in both streams the exergy first decreases and subsequently increases, attaining a minimum near the environment temperature (not exactly at the environment temperature, due to small mechanical irreversibilities).

We propose the following. Let us consider states α and β reported in Table 2A:

$$\Phi_2 = [(ex_3 - ex_\alpha) + (ex_6 - ex_\beta)]/[(ex_2 - ex_\alpha)(ex_5 - ex_\beta)],$$
$$\sigma_{r2} = 1 - \Phi_2 \qquad (5)$$

(C) Process 3-4 (exhaust gas heat exchanger).

$$\Phi_3 = m_{He}\,(ex_4 - ex_3)/[m_g\,(ex_i - ex_e)], \quad \sigma_{r3} = 1 - \Phi_3 \qquad (6)$$

(D) Process 4-5 (helium turbine).

$$\Phi_4 = L_t/(ex_4 - ex_5), \quad \sigma_{r4} = 1 - \Phi_4 \qquad (7)$$

(E) Process 6-1 (heat exchanger between helium and hydrogen).

$$\Phi_5 = m_{He}\,(ex_1 - ex_6)/[m_{H_2}\,(ex_8 - ex_9)], \quad \sigma_{r5} = 1 - \Phi_5 \qquad (8)$$

Analysis of the Single Phases With Reference to the Entropy Production Rate of the Whole Helium Cycle. As was already dealt with by Bisio (1994), for the single phases of a cycle, it seems more meaningful to consider as relative entropy production of the phase i, σ'_{ri}, the ratio of the actual entropy production of this phase, σ_{ai}, to the reference entropy production of the whole cycle, σ°_{rf}. In a similar way, an alternative definition of exergy efficiency, Φ'_i, of a single phase with reference to the losable exergy power of the whole system is proposed:

$$\sigma'_{ri} = \sigma^\circ_{ai}/\sigma^\circ_{rf}, \quad \Phi'_i = 1 - \sigma'_{ri} \qquad (9)$$

The reference exergy power of the whole cycle is:

$$Ex^\circ_{rf} = m_{H_2}\,(ex_8 - ex_9) + m_g\,(ex_i - ex_e) \qquad (10)$$

and then the reference entropy production rate:

$$\sigma^\circ_{rf} = [m_{H_2}\,(ex_8 - ex_9) + m_g\,(ex_i - ex_e)]/T_o \qquad (11)$$

Thus, let us consider the actual entropy production rates.

(A) Process 1-2 (helium compressor).

$$\sigma^\circ_{a1} = m_{He}\,[-L_c - (ex_2 - ex_1)]/T_o \qquad (12)$$

(B) Processes 2-3 and 5-6 (regenerator).

$$\sigma^\circ_{a2} = m_{He}\,[(ex_2 - ex_3) - (ex_6 - ex_5)]/T_o \qquad (13)$$

(C) Process 3-4 (exhaust gas heat exchanger).

$$\sigma^\circ_{a3} = [m_g\,(ex_i - ex_e) - m_{He}\,(ex_4 - ex_3)]/T_o \qquad (14)$$

(D) Process 4-5 (helium turbine).

$$\sigma^\circ_{a4} = m_{He}\,[(ex_4 - ex_5) - L_t]/T_o \qquad (15)$$

(E) Process 6-1 (heat exchanger between helium and hydrogen).

$$\sigma^\circ_{a5} = [m_{H_2}\,(ex_8 - ex_9) - m_{He}\,(ex_1 - ex_6)]/T_o \qquad (16)$$

Obviously, the following relations are verified:

$$\sigma_r = \sigma'_{r1} + \sigma'_{r2} + \sigma'_{r3} + \sigma'_{r4} + \sigma'_{r5}, \quad \Phi_{He} = 1 - \sigma_r \qquad (17)$$

The value obtained for the exergy efficiency of the whole cycle is practically coincident with that previously calculated.

Analysis Results

Tables 2(*A*), 2(*B*), and 3 show the results concerning a calculation example of the plant whose assumptions are reported in Table 4. The overall energy efficiency is equal to 80.6 percent, the exergy efficiency 76.7 percent (without a hydrogen turbine 72 and 68.5 percent, respectively). Regarding the single helium cycle, its energy efficiency is extremely high (since the cycle works between very large temperature extremes), about 71 percent, while the exergy value is equal to 47 percent.

The ratio between the electrical power and the mass flow rate of every cycle is noteworthy: obviously the helium cycle gives the higher value, 1556 kW/(kg/s), while the hydrogen cycle and the gas turbine cycle give respectively 630 kW/(kg/s) and 295 kW/(kg/s).

The following figures show the results of a parametric analysis; since the helium cycle is the one that affects the system more, performances have been estimated by varying the helium maximum pressure and the helium recuperator effectiveness, while the assumptions are those reported in Table 4.

Table 4 Main assumptions

inlet chemical exergy power of gas turbine	309400 kW
inlet thermal power of gas turbine	294300 kW
net electrical power of gas turbine	103200 kW
gas mass flow rate	349.3 kg/s
helium maximum pressure	8 MPa
helium minimum pressure	1.2 MPa
helium maximum temperature	773.15 K
helium minimum temperature	50 K
hydrogen maximum pressure	10.2 MPa
outlet hydrogen turbine pressure	0.5 MPa
helium compressor efficiency	0.867
helium turbine efficiency	0.958
hydrogen turbine efficiency	0.95
helium recuperator effectiveness	0.848

Downloaded 02 Jun 2010 to 171.66.16.104. Redistribution subject to ASME license or copyright; see http://www.asme.org/terms/Terms_Use.cfm

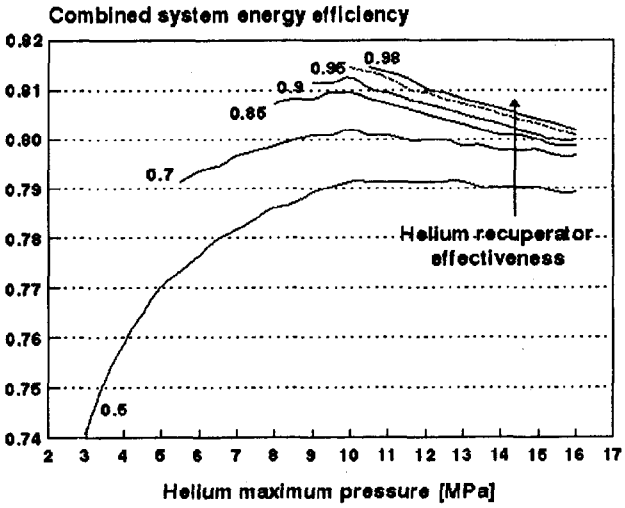

Fig. 4 Helium maximum pressure and recuperator effectiveness influence on combined cycle efficiency

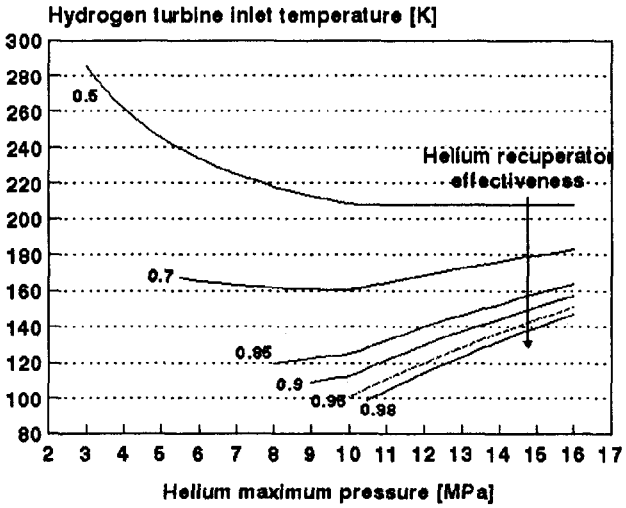

Fig. 6 Hydrogen turbine inlet temperature versus helium maximum pressure and recuperator effectiveness

Figure 4 shows the overall energy efficiency, while the efficiencies of the single helium cycle are shown in Figs. 5(*a*) and 5(*b*). It is interesting to observe that high values of the combined system efficiency are obtained equally utilizing a low helium recuperator effectiveness (0.5); the difference in comparison of the maximum values is around 2 percent. Moreover this permits a relatively small regenerative exchanger. The advantage of having a low recuperator effectiveness can be explained by analyzing Figs. 6 and 7. In fact, as the helium recuperator effectiveness decreases, the hydrogen maximum temperature increases (see Fig. 6) and therefore the hydrogen cycle efficiency increases. This is illustrated by Fig. 7, in which the cycle energy efficiencies are shown versus helium recuperator effectiveness (the helium maximum pressure was fixed equal to 10 MPa).

By varying the recuperator effectiveness from 0.5 to 0.95, the hydrogen cycle efficiency decreases from 56 to 45 percent, the helium cycle efficiency increases from 60 to 76 percent while the overall efficiency increases only slightly from 79 to 81.5 percent. It is also possible to obtain equally high system efficiencies without hydrogen expansion (Fig. 8): around 75 percent for the system energy efficiency, 71 percent for the system exergy efficiency.

Many of the curves shown in the previous figures have not been drawn for helium maximum pressure lower than a certain value, since a minimum limit (20 K) was fixed for the tempera-

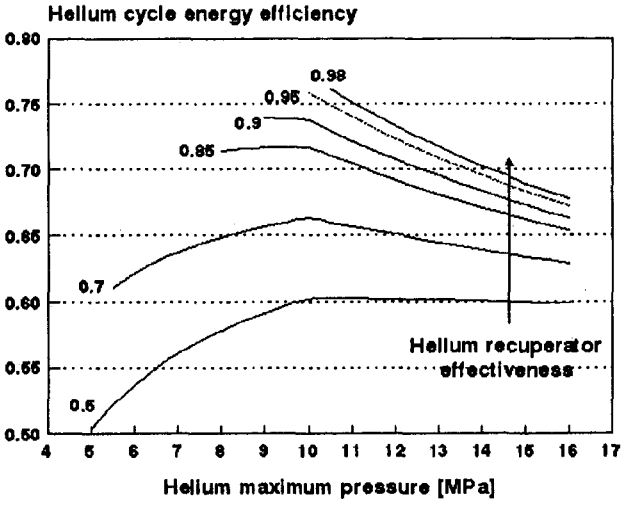

Fig. 5(*a*) Helium cycle energy efficiency versus maximum pressure and recuperator effectiveness

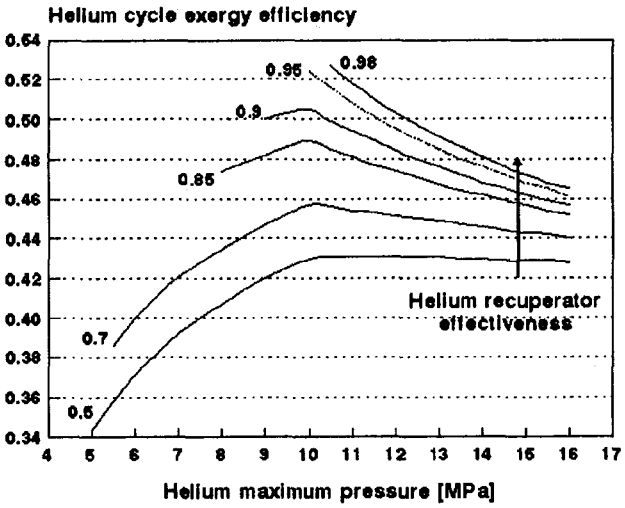

Fig. 5(*b*) Helium cycle exergy efficiency versus maximum pressure and recuperator effectiveness

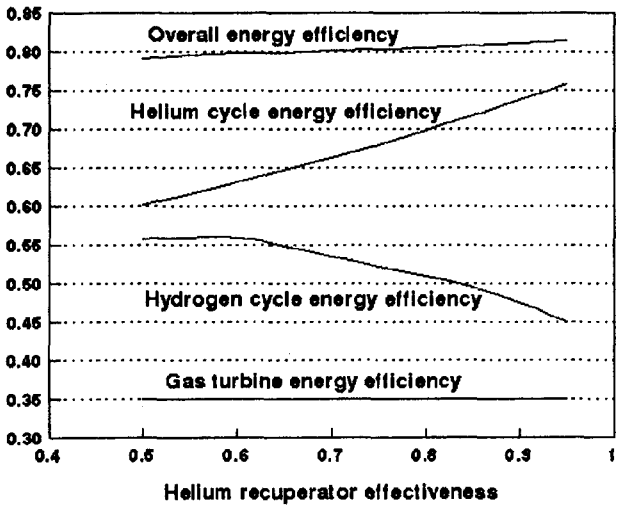

Fig. 7 Cycle efficiency versus helium recuperator effectiveness

Downloaded 02 Jun 2010 to 171.66.16.104. Redistribution subject to ASME license or copyright; see http://www.asme.org/terms/Terms_Use.cfm

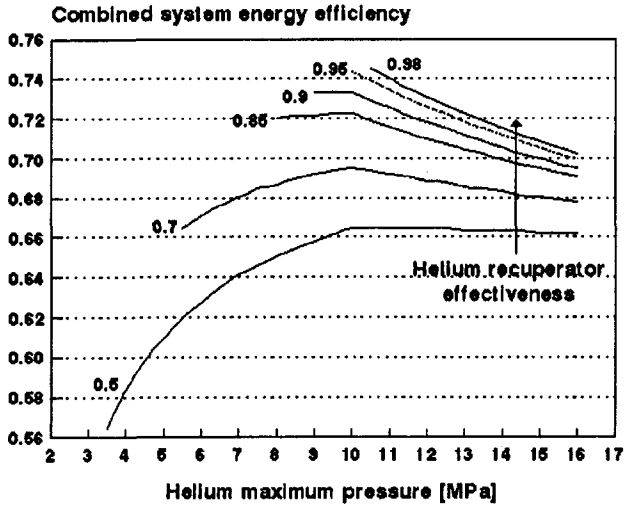

Fig. 8 Combined system (without hydrogen turbine) efficiency

ture difference between the outlet exhaust gas heat exchanger and the cold side outlet helium recuperator (point 3 of Fig. 2).

It is interesting to analyze the entropy production of the helium cycle. From the example shown in Table 3 one notes that the maximum value of entropy production rate takes place in the heat exchanger between helium and hydrogen; this is visualized by the parameter σ'_{r5}, which is much higher than the other parameters σ'_{ri} (even if σ_{r2} is almost equal to σ_{r5}). Figures 9(a) and 9(b) show the relative entropy production of helium phases versus maximum pressure (the recuperator effectiveness is fixed equal to 0.85) and versus recuperator effectiveness (the maximum pressure is fixed equal to 10 MPa). It should be noted that, by varying the maximum pressure, the value of phase 6-1 remains nearly constant, the value of phase 1-2 (compression) increases strongly, that of phase 2-3 and 5-6 (regeneration) decreases strongly, while the values of phase 4-5 (expansion) and 3-4 decrease slightly. Instead, by varying the recuperator effectiveness, the value of phase 2-3/5-6 has a maximum point, the values of phases 4-5 and 1-2 keep nearly constant, the value of phase 6-1 increases slightly, while that of phase 3-4 decreases strongly.

In all results presented here, the conditions of the exhaust gas at the exit of gas–helium heat exchanger have been kept the same. Particularly for the temperature, a value of 379 K was chosen: This allows a recovery of waste heat from the open cycle gas turbine equal to 83 percent. Utilizing a "clean" combustible as, for example, the same hydrogen and decreasing the temperature of the gas to the environment temperature of 290 K, it is possible to recover the whole waste heat (100 percent) and reach a value of the overall energy efficiency near to 90 percent (around 85 percent for the exergy efficiency), while without the hydrogen turbine the obtainable values are respectively 78.7 and 74.9 percent.

Helium and Combustion Gas Turbine

As reported by Farmer (1994), the thermal efficiency of combustion gas turbines has increased steadily over the last half century. Today simple cycle machines are running at over 40 percent efficiency and combined cycles at 55 percent, with an increase to over 58 percent for machines soon to enter service (Korakianitis, 1994a,b). Many new thermodynamic cycles will lead to efficiencies of over 60 percent before the year 2000.

One of the major factors in efficiency advancement has been the continuously increasing level of turbine inlet temperature, made possible by material technology and turbine blade cooling techniques.

The temperature capability of closed-cycle gas turbine has been limited by the external heater. By using a nuclear heat source with the graphite (ceramic) core and a direct cycle gas turbine, this metallurgical limit in the heater is obviated (Fig. 8, McDonald and Etzel, 1994).

The key to the design of the high-efficiency helium turbomachine is the technology from the combustion gas turbine industry, both heavy-duty and aeroderivatives. State-of-the-art technology from these gas turbines is directly applicable to the design of the helium turbomachine, particularly in the areas of design methodology, performance materials, and fabrication methods (Massardo and McDonald, 1995).

With its high specific heat working fluid the helium gas turbine can be characterized by high specific power ($>$ 900 kW/(kg/s)); as an example with a rating of 290 MWe the turbomachine is compact by virtue of the high degree of system pressurization; it is physically smaller than the 226 MWe simple cycle heavy-duty industrial gas turbine that is in utility service today.

The difference between air and helium is manifest in several areas. Combustion machines require fewer compressor and turbine stages. Very high specific power can be realized with helium (at elevated pressure) resulting in a more compact turbocompressor. With a clean closed cycle a very small hydraulic diameter passages can be utilized, which, with high thermal conductivity for helium, results in a very compact recuperator (McDonald, 1994). For systems using a low molecular gas like helium there are areas that will require detailed design attention, namely: seal design to minimize bypass flow; flange design to obviate leakage and electrical insulation in the generator and magnetic bearings windings.

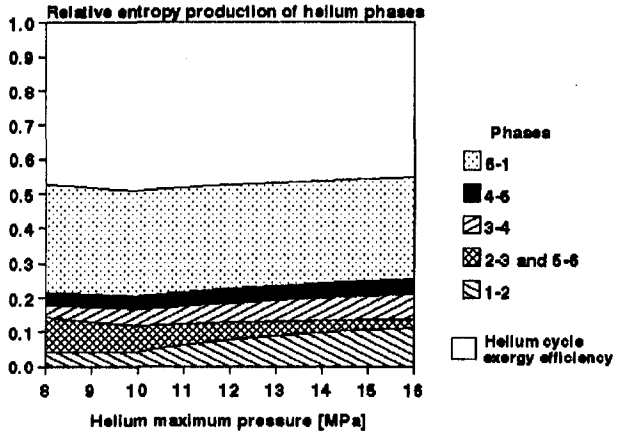

Fig. 9(a) Relative entropy production of helium phases versus maximum pressure (recuperator effectiveness = 0.85)

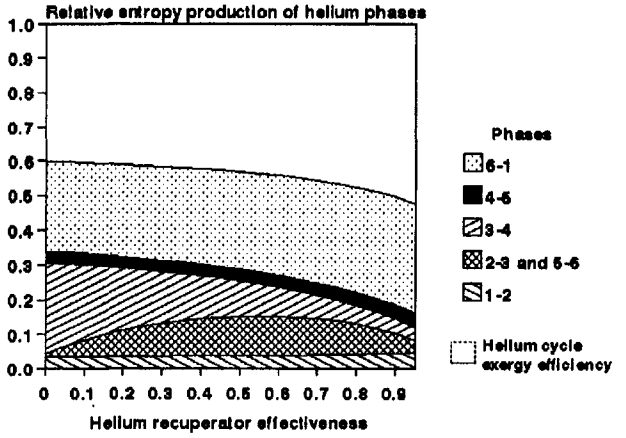

Fig. 9(b) Relative entropy production of helium phases versus recuperator effectiveness (maximum pressure = 10 MPa)

Downloaded 02 Jun 2010 to 171.66.16.104. Redistribution subject to ASME license or copyright; see http://www.asme.org/terms/Terms_Use.cfm

In the context of this paper, the helium gas turbine has two technology bases that are being fully utilized: operating experience from helium cooled reactors and the Oberhausen II gas turbine plants and design know-how from the air-breathing machines, namely, gas turbines and heat exchangers (recuperators and compact aircraft aerospace units).

The possibility of realizing the hydrogen turbine working at cryogenic temperatures has not been thoroughly evaluated; nevertheless it has been employed in space with satisfactory results, particularly with rockets that employ hydrogen as a propellant. In any case it must be remarked that the system without hydrogen expansion also reaches considerable performances.

Conclusions

The main conclusions of this work are the following:

- First of all, it is to be remarked that the helium cycle examined in this paper, though it is formally similar to other usually considered cycles, differs greatly from them on the basis of the second-law analysis. Indeed, one has inlet exergy both by exploiting the waste energy of an open gas turbine cycle and by vaporizing and superheating hydrogen at a temperature under that of the environment. This allows a very great combined system energy or exergy efficiency to be obtained.
- Since the helium cycle works between very large temperature extremes, the recuperator exchanges a considerable thermal power, reaching remarkable size, but the parametric analysis of the system has shown that high plant efficiencies are obtainable even with low values of the helium recuperator effectiveness.
- Positive considerations about the realization and technological aspects of helium turbine have been taken into account.

However, in general, the usefulness of these combined systems is conditioned by various parameters, which are variable in relation to the location of the system (e.g., possible exploitations of LH_2 exergy, existence and size of gas hydrogen storage systems, availability of waste thermal energy).

References

Baehr, H. D., and Schwier, K., 1961, *Die thermodynamischen Eigenschaften der Luft,* Springer-Verlag, Berlin.

Bammert, K., and Deuster, G., 1974, "Das Heliumturbinen-Kraftwerk Oberhausen—Auslegung und Aufbau," *Energie und Technik,* Vol. 26, pp. 1–6.

Bammert, K., Rurik, J., and Griepentrog, H., 1974, "Highlights and Future Development of Closed-Cycle Gas Turbines," ASME JOURNAL OF ENGINEERING FOR POWER, Vol. 76, pp. 342–348.

Bisio, G., 1989, "On a General Statement for Efficiency," *Chemical Engineering Communications,* Vol. 81, pp. 177–195.

Bisio, G., and Cerullo, N., 1992, "Thermodynamic Analysis of Combined Plants Utilizing Helium Turbine With Nuclear Heating and Liquid Hydrogen Refrigerating," *Proceedings of 27th IECEC,* San Diego, Aug. 3–7, Vol. 4, pp. 277–282, SAE, Warrendale, PA.

Bisio, G., 1994, "The Possible Utilization of Low-Temperature Waste Energy Linked With the Exploitation of LNG Physical Exergy," *Proceedings of 29th IECEC,* Monterey, CA, Aug. 7–12, Vol. 4, pp. 1537–1542.

Farmer, B., 1994, *Gas Turbine World,* Vol. 15.

Grawe, J., and Holzer, J., 1989, "Möglichkeiten der Einführung solaren Wasserstoff in Künftige Strom- und Energieversorgungs-systeme am Beispiel der Bundesrepublik Deutschland," *B. W. K.,* Vol. 41, pp. 432–438.

Griepentrog, H., and Weber, D., 1978, "Gasturbinen im geschlossenen Prozess für neue Anwendungsgebiete," *Kerntechnik,* Vol. 20, pp. 537–543.

Hassmann, K., Keller, W., and Stahl, D., 1991, "Perspektiven der Photovoltaik," *B. W. K.,* Vol. 43, pp. 103–112.

Korakianitis, T., and Wilson, D. G., 1994a, "Models for Predicting Performance of Brayton-Cycle Engines," ASME JOURNAL OF ENGINEERING FOR GAS TURBINES AND POWER, Vol. 116, pp. 381–388.

Korakianitis, T., and Béier, K. S., 1994b, "Investigation of the Part-Load Performance of Two 1.12 MW Regenerative Marine Gas Turbines," ASME JOURNAL OF ENGINEERING FOR GAS TURBINES AND POWER, Vol. 116, pp. 418–423.

Kotas, T. J., 1985, *The Exergy Method of Thermal Plant Analysis,* Butterworths, London.

Massardo, A. F., and McDonald, C. F., 1995, "Closed Cycle Gas Turbine Perspective Enabling Technologies From Combustion Turbines—the Key Factor for Future Deployment," presented at the VIII Conference on Complex Energy Systems, Bologna, Italy.

McDonald, C. F., and Etzel, K. T., 1994, "Nuclear Gas Turbine (GT-MHR) Performance Potential," ASME Paper No. 94-GT-416.

McDonald, C. F., 1994, "The Key Role of Heat Exchangers in Advanced Gas Cooled Reactors Plants," *Heat Recovery Systems CHP,* Vol. 14, No. 1, pp. 7–28.

Oshima, K., Ishizaki, Y., Kameyama, S., Akiyama, M., and Okuda, M., 1978, "The Utilization of LH_2 and LNG Cold for Generation of Electric Power by a Cryogenic Type Stirling Engine," *Cryogenics,* Vol. 18, pp. 617–620.

Raznjevic, K., 1970, *Tables et Diagrammes Thermodynamiques,* Editions Eyrolles, Paris.

Reynolds, W. C., 1979, "Thermodynamic Properties in SI," Dept. Mech. Engineering, Stanford University, Stanford, CA.

Sprengel, U., 1991, "Solar Hydrogen Energy Carrier for the Future," German Aerospace Research Establishment, DLR; Solar and Hydrogen Energy Research Center, ZSV; Ministry of Economic Affairs and Technology for the State of Baden-Württemberg, Stuttgart.

Weber, D., 1989, "Strömungsmachinen für hohe und tiefe Temperaturen bei der Kraft-Wärme-Kopplung von Stromerzeugung und Flussigerdgasverdampfung," *Forsch. Ing.-Wes.,* Vol. 55, pp. 155–158.

Woolley, H. V., Scott, R. N., and Brickwedde, F. G., 1948, "Compilation of Thermal Properties of Hydrogen in its Various Isotopic and Ortho-Para Modifications," *J. Res. Nat. Bureau Standards,* Vol. 41, pp. 379–475.

APPENDIX

With reference to helium mass unit, the heat transfers are given by:

$$Q_{34} = i_4 - i_3, \quad Q_{61} = i_1 - i_6 \tag{A1}$$

The turbine and compressor works are given by:

$$L_t = i_4 - i_5, \quad L_c = i_1 - i_2 \tag{A2}$$

The cycle net work is given by:

$$L_n = L_t + L_c \tag{A3}$$

Indicating by β_1 the electrical efficiency, the net electrical work L_{ne} follows:

$$L_{ne} = (L_t + L_c)\,\beta_1 \tag{A4}$$

The energy efficiency of the helium cycle can be written as:

$$\eta_{\mathrm{He}} = L_{ne}/(Q_{34}/\alpha) \tag{A5}$$

where α is the thermal efficiency (or effectiveness) of the heat exchanger of the top turbine exhaust gas.

In addition, the thermal energy Q_{61} is utilized to "vaporize" and superheat the hydrogen with a further recovery factor R:

$$R = |Q_{61}|/(Q_{34}/\alpha) \tag{A6}$$

We use "vaporize" because with the data utilized in this work (Table 2B), liquid hydrogen is transformed into superheated vapor, without separating into two phases.

The outlet thermal power from the open cycle turbine in the waste gas heat exchanger is given by

$$P_{tg} = m_g\,(i_i - i_e) \tag{A7}$$

corresponding to inlet thermal power and a mass flow rate of helium:

$$P_{t\mathrm{He}1} = \alpha P_{tg}, \quad m_{\mathrm{He}} = P_{t\mathrm{He}1}/Q_{34} \tag{A8}$$

The outlet thermal power from the helium cycle is:

$$P_{t\mathrm{He}2} = m_{\mathrm{He}}\,|Q_{61}| \tag{A9}$$

corresponding to mass flow rate of hydrogen:

$$m_{\mathrm{H}_2} = P_{t\mathrm{He}2}/(i_9 - i_8) \tag{A10}$$

The electrical power of the helium cycle is given by:

$$P_{e\mathrm{He}} = m_{\mathrm{He}}\,L_{ne} \tag{A11}$$

The electrical power for pumping liquid hydrogen can be written as:

Downloaded 02 Jun 2010 to 171.66.16.104. Redistribution subject to ASME license or copyright; see http://www.asme.org/terms/Terms_Use.cfm

$$P_{eH_2 2} = m_{H_2} (i_8 - i_7)/\beta_2 \quad \text{(A12)}$$

The energy efficiency of the helium cycle and the pumping of liquid hydrogen is:

$$\eta_{He2} = (P_{eHe} - P_{eH_2 2})/P_{tg} \quad \text{(A13)}$$

The electrical power generated by the hydrogen turbine is:

$$P_{eH_2 1} = m_{H_2} (i_9 - i_{10}) \beta_3 \quad \text{(A14)}$$

With reference to the whole combined system, the energy efficiency, η_t, and the exergy efficiency, Φ_t, can be defined by:

$$\eta_t = (P_{eg} + P_{eHe} + P_{eH_2 1} - P_{eH_2 2})/P_{tc} \quad \text{(A15)}$$

$$\Phi_t = (P_{eg} + P_{eHe} + P_{eH_2 1} - P_{eH_2 2})/Ex_c^\circ \quad \text{(A16)}$$

where

P_{eg} = net electrical power of combustion gas turbine cycle
P_{tc} = inlet thermal power of gas turbine
Ex_c° = inlet chemical exergy power of gas turbine

Downloaded 02 Jun 2010 to 171.66.16.104. Redistribution subject to ASME license or copyright; see http://www.asme.org/terms/Terms_Use.cfm

Mechanisms of Coke Formation in Gas Turbine Combustion Chambers

M. Brandauer

A. Schulz

S. Wittig

Lehrstuhl und Institut für Thermische Strömungsmaschinen, Universität Karlsruhe (T.H.), 76128 Karlsruhe, Federal Republic of Germany

New gas turbine combustor designs are developed to reduce pollutant and NO_x emissions. In these new combustors, the formation of carbonaceous deposits, especially in prevaporizers, affects the reliability and effectiveness of operation. To avoid deposits, a detailed knowledge of the origins and mechanisms of formation is required. To obtain a deeper insight, the phenomena were studied systematically. The deposits under consideration show differing characteristics suggesting more than one formation mechanism in the combustor. Consequently, the primary goal was to identify the formation mechanisms and, subsequently, to simulate the mechanisms under well-defined conditions in bench tests for determining the relevant parameters of deposit build-up. The mechanisms of formation were identified based on the properties of the deposits in the combustion chamber. In order to characterize the deposits, physical and chemical analysis techniques were utilized. In summary, tests and numerical predictions identified two major paths of formation: a deposit build-up resulting from flame products such as soot or coked droplets and a deposit build-up resulting from liquid fuel impinging the wall accompanied with chemical reactions at the wall. The deposits caused by fuel droplet impingement were intensively studied in bench tests. In analyzing the processes, the influence of wall temperature, fuel composition, and the oxygen content in the environment is shown in detail. In addition, the importance of thermal instabilities of the fuel, previously studied under fuel supply system conditions, is demonstrated for a deposit formation inside a combustion chamber.

Introduction

The development of new gas turbines is focused on improvements in thermal efficiency and pollutant emissions. Higher thermal efficiencies are primarily attained by increasing temperatures and pressures. Both parameters favor pollutant formation during the combustion process, if no special measures are taken. Therefore, primarily for combustors burning liquid fuels, new design concepts and fuel preparation systems have to be developed to meet future laws and regulations for pollutant emissions.

Prevaporizing the liquid fuel and mixing it with primary air before it enters the reaction zone of the combustor is a new approach to reduce pollutants. However, in addition to self-ignition of the vaporized fuel and flashback, the formation of carbonaceous deposits affects the reliability and effectiveness of the prevaporizers. Carbonaceous deposits at the wall, for example, reduce the vaporization rates drastically and affect the radiative heat transfer in the combustor. Also, because deposits affect heat transfer from the hot gas flow to the wall, they cause complex wall temperature distributions, thus leading to thermal stresses and damage to the combustor. To avoid deposit formation, detailed information on the mechanisms and the major influencing parameters is imperative. In contrast to previous studies (Starkman et al., 1951; Wear and Hibbard, 1955) in gas turbine combustors that determined different deposits without investigating the formation mechanisms, our new approach considers two different paths of formation: deposits resulting from liquid fuel impinging and reacting at the wall's surface, and from flame products such as soot or coked droplets, which agglomerate at the wall. First of all, criteria to distinguish between the two formation mechanisms were derived based on the deposit properties to determine the formation path. After determining the formation mechanisms, bench tests were performed for identifying the parameters influencing deposit formation.

Consequently, the following approach had to be taken in the present study: Based on observations under real engine conditions accompanied with detailed chemical analyses of the deposits, bench tests under well-defined conditions were required for an understanding of the chemical mechanisms. The methodology of the investigations including the chemical and physical diagnostics as well as the test facilities and the results will be described below.

Methodology and Analysis Techniques

As the experiments under real combustor conditions revealed various deposits suggesting different mechanisms of formation, the primary goal in studying combustor deposits is the definition of the deposit formation path. This can be reached by a systematic analysis of the deposit properties as well as by the numerical simulation of the flow field in the combustor under consideration.

For a complete description of the deposits, various coordinated analysis techniques were applied. To get a first indication on the chemical composition, the specimen were tested by elemental analysis. Using this technique, a C—H—N—O determination can be obtained. For choosen experiments a determination of the sulfur content was done, additionally. In particular, the carbon content provides decisive information about the formation mechanism. Furthermore, based on the results of elemental analysis, further analysis techniques can be chosen effectively. Infrared spectroscopy was applied to identify chemical functionalities in the deposits to get a deeper insight in chemical reactions. Gas chromatography was performed to investigate the fuels as well as the solid deposits, which were dissolved in advance. Although not all components in the deposits can be

Contributed by the International Gas Turbine Institute and presented at the 40th International Gas Turbine and Aeroengine Congress and Exhibition, Houston, Texas, June 5–8, 1995. Manuscript received by the International Gas Turbine Institute February 10, 1995. Paper No. 95-GT-49. Associate Technical Editor: C. J. Russo.

Copyright © 1996 by ASME

Downloaded 02 Jun 2010 to 171.66.16.104. Redistribution subject to ASME license or copyright; see http://www.asme.org/terms/Terms_Use.cfm

dissolved, gas chromatography gives important information about chemical combinations included in the deposits.

To detect whether graphite has formed within the deposits, diffraction patterns of the samples were performed. Furthermore, if graphite does exist, a preferred orientation of the basal planes can be determined using this technique. These patterns distinguish whether deposit formation at the combustor wall is caused by droplet impingement or by intermediate flame particles. Additionally, scanning electron photographs were taken from the samples to characterize the surface morphology of the deposits. Regarding the morphology, a first indication on the path of deposit formation can be obtained (Schirmer, 1970). In applying the different analysis techniques, a systematic and comprehensive characterization of the physical and chemical properties of the deposits was achieved. Considering the results of all analysis techniques, the deposit formation can be deduced and the major question whether the chemical reactions take place at the wall or in the flow field can be answered. The suggested mechanisms can then be confirmed by numerical studies of the flow field in the combustor and a calculation of the fuel preparation.

In the second step, influencing parameters are derived and quantified through deposit formation studies under well-defined conditions. A quantification of the influencing parameters can only be reached by systematic bench tests as under real engine conditions various parameters are interacting and varying, e.g., wall temperatures oscillate with the thermal load and in the course of starting and stopping.

In laboratory experiments, the formation of deposits caused by droplets impinging on the hot combustor wall is simulated under well-defined conditions. In the investigations, the main parameters influencing deposit formation, such as wall temperature, fuel composition, and oxygen content in the environment, are tested. By comparing chemical properties of bench test deposits with those derived from a combustion chamber, it can be determined whether droplet impingement on the combustor wall is one of the relevant mechanisms leading to deposit formation under gas turbine combustor conditions. In case of identical chemical deposit properties, the same chemical reactions will take place under engine conditions and in laboratory experiments.

In demonstrating that identical mechanisms take place in bench tests and combustors, the results of the present study are of far-reaching consequence for deposit formation in real engines, since the results of the bench tests can be applied to real engine conditions. Another advantage of the chosen concept is the fact that the reasons of deposit formation can be determined independently from combustor design and solely on the deposit properties. For example, in considering the elemental analysis, the path of deposit formation under gas turbine combustor conditions can be determined.

Experimental Setup

For the various laboratory investigations, a bench test rig, shown in Fig. 1, was developed. The main objective of the test facility was the simulation of the combustor wall conditions, which include the effects of surface temperature, surface material, and ambient atmosphere. Thus, deposit formation by droplet impingement on the hot combustor wall was investigated. The monodispersed fuel droplets of 0.022 ml volume, generated by a burette, hit the surface of the test specimen. The test specimen with a diameter of 50 mm was heated by an electrical heater element. Maximum surface temperatures up to 1100 K can be achieved for the investigations such that the whole temperature regime for deposit formation was possible.

The temperature was monitored simultaneously by thermocouples and an infrared system. Surface temperature measurements were performed by pyrometry in the vicinity of deposit build-up, which was varnished with a coating exhibiting well-defined emission characteristics. As infrared camera measurements revealed a homogeneous temperature distribution on the specimen surface, temperature measurement by pyrometry beside the deposit formation area provided exact values of the surface temperature at the location of deposit build-up.

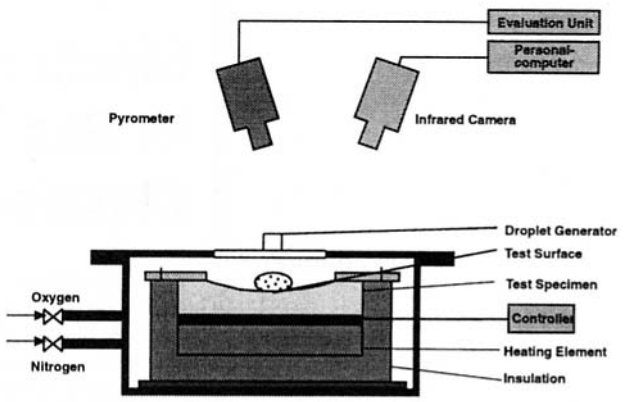

Fig. 1 Schematic of the bench test rig

Furthermore, the test specimen and the location of deposit build-up are enclosed in order to vary the content of oxygen and nitrogen in the test rig. Due to the design of the test rig, near-wall conditions in a combustor including fuel, wall temperature, wall material, and gas atmosphere can be adjusted constantly.

After hitting the heated test specimen, the fuel droplets evaporate and chemical reactions are initiated that lead to the build-up of solid carbonaceous deposits. The evaluation of the test is done gravimetrically by weighing the test specimen before and after the test, respectively. The sensitivity of the gravimetric weighing system is 0.1 mg, so that exact values of deposit mass can be given. Only solid deposits are weighed; gums and deposit precursors are excluded. The design of the present bench test rig provides a quantitative relation between the mass of the deposit and the mass of the fuel, which is of fundamental importance for identifying major influences. As the characteristic quantity, a dimensionless deposit mass is introduced, defined as:

$$w = m_{\text{dep}}/m_{\text{fuel}} \cdot 100 \text{ [percent]}$$

where w denotes the mass ratio of the deposit to the initial test fuel. This dimensionless quantity is established in order to compare tests with different initial fuel masses. The introduction of this dimensionless number is possible as preliminary tests revealed a linear dependence between deposit mass and fuel mass under constant test conditions. Considering deposit mass in the quantification of the major influences is an advantage of the test rig, because other bench test rigs (see Maier and Jantzen 1985) allow only visual evaluation of the deposits. Furthermore, a chemical evaluation by the above-described techniques is done to get information about reactions leading to deposit build-up.

The combustion chamber tests were performed in the film-evaporation research combustor at the Institute for Thermal Turbomachinery. A sketch of the combustor, which is described in detail by Pfeiffer et al. (1991a, b), is given in Fig. 2. The combustor was designed for a thermal load of about 150 kW at a pressure of 4.5 bar with a overall air/fuel ratio of 5.6. Further information on constructional details is given in the above-quoted papers.

The combustor was developed to find new design concepts in reducing NO_x emissions by fuel vaporization and staged combustion. In the following discussion, only a few comments on fuel preparation in the combustor will be made because it affects briefly the deposit formation.

Downloaded 02 Jun 2010 to 171.66.16.104. Redistribution subject to ASME license or copyright; see http://www.asme.org/terms/Terms_Use.cfm

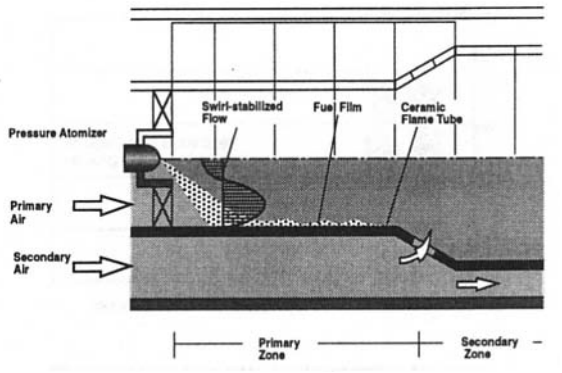

Fig. 2 Schematic of the film evaporation combustor

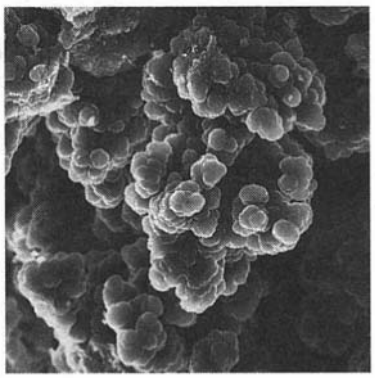

Fig. 4 Scan microscope photograph of deposits in vicinity of nozzle (1 cm = 20 μm)

The fuel (fuel oil) is sprayed by a pressure atomizer toward the inner surface of the flame tube. The droplets impinge on the wall and form a liquid film, which is shear driven by the primary air flow. While spreading, the film evaporates through heat transferred from both the wall and the hot gas flow. The primary air enters the combustion chamber by an axial flow swirler, thus forming a recirculation flow regime for flame stabilization. The fuel vapor mixes with the primary air forming a homogeneous fuel/air mixture in the primary zone.

Deposit Formation in the Combustion Chamber

In the research combustion chamber, deposit formation occurred at two locations. Under certain test conditions, deposit build-up was found not only in the flame tube in the region of the fuel film, but also in the vicinity of the fuel nozzle. A sketch of deposit location is given in Fig. 3.

These deposits were characterized by several analysis techniques to determine their formation mechanisms. To get a first impression of the surface morphology, scanning microscope photographs of both deposits in the flame tube as well as in the vicinity of the fuel nozzle were performed.

Figure 4 shows the deposits near the fuel nozzle. An accumulation of spherical particles, which were initiated in the hot flow field and then agglomerated at the wall surface, became apparent. The diameter of these spherical particles was approximately 4–5 μm. The particles are considerably larger than soot particles, as Müller and Wittig (1991) showed in detailed studies. In contrast, the deposits in the flame tube (see Fig. 5) exhibited an amorphous structure without any particles falling out from the hot gas flow. The differences in the deposits due to their location in the combustor detected by scan microscope were confirmed by their chemical composition.

While the deposits in the vicinity of the nozzle contained about 98 mass percent carbon and 1–2 percent oxygen, the deposits in the flame tube consisted of about 74–80 percent carbon, 20 percent oxygen, 4 percent hydrogen, and small amounts of nitrogen. Based on the results of the elemental analysis, further analysis techniques were done. Thus, from the deposits in the flame tube, infrared spectra were taken in order to obtain more information about functional groups containing hetero-compounds, especially oxygen. The deposits in the vicinity of the fuel nozzle, which consisted almost entirely of carbon, were described by diffraction patterns to identify whether graphitization has occurred in the material. The pattern shown in Fig. 6 demonstrates the presence of some randomly oriented crystallites in the deposits. Thus, these particles have been exposed to extremely high temperatures in the reaction zone of the combustor.

For the initiation of graphitization processes, temperatures beyond 1200 K were required (Heidenreich et al., 1968). However, these temperatures were not reached at the combustor wall where the deposits were found as shown by thermal paints. This hypothesis is supported by the fact that no preferred orientation of the intensity in Fig. 6 is present, which would indicate an orientation of the basal planes in the deposits parallel to the wall surface. Since no preferred orientation occurred, an indication is given that the deposit-forming reactions and graphite formation would take place in a flow field and not at a plain surface (Grisdale, 1953). Therefore, on account on diffraction analysis, deposit formation at the fuel nozzle is primarily caused by particles formed in the hot reaction zone of the combustor.

Summarizing the analyses of the deposits in the vicinity of the fuel nozzle, deposit formation here was caused by flame products as soot or coked droplets, as examined by Urban and Dryer (1990). This conclusion can be supported by analyzing the flow field in the combustion chamber.

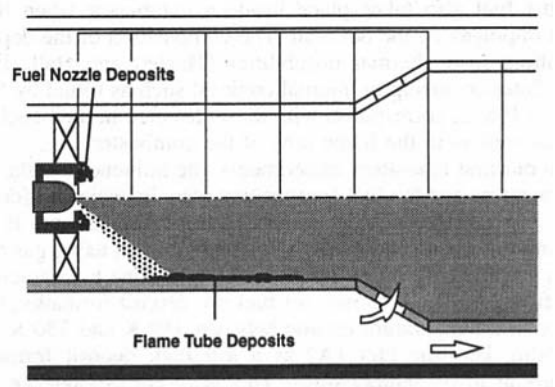

Fig. 3 Sketch of deposit location

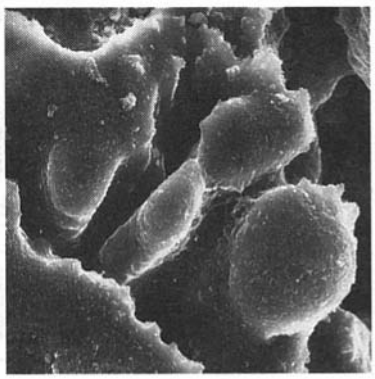

Fig. 5 Scan microscope photograph of the deposits in the flame tube (1 cm = 20 μm)

Downloaded 02 Jun 2010 to 171.66.16.104. Redistribution subject to ASME license or copyright; see http://www.asme.org/terms/Terms_Use.cfm

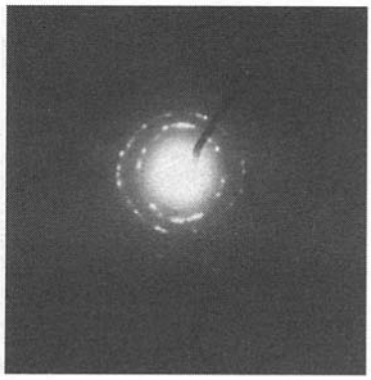

Fig. 6 Diffraction pattern of the deposits in the vicinity of the fuel nozzle

To show the impact of the flow field in the combustor on deposit formation, a numerical calculation was performed. The numerical simulation was done by a finite-volume code developed at the Institute for Thermal Turbomachinery (see Noll, 1993) for computing three-dimensional, turbulent combustor flows. The code uses the standard $k-\epsilon$ turbulence model with high-order discretization. The case discussed in the following represents typical test conditions, where deposit build-up was found (see also Pfeiffer et al., 1991a). In Fig. 7, the flow field in the primary zone of the combustor is shown. In the vector plot the spreading of the recirculation regime within the primary zone becomes apparent. For reasons of clarity, some streamlines are plotted. The streamlines show that the recirculation flow regime spreads back to the fuel nozzle so that hot gas and intermediate flame products can fall out there. In considering the flow field, a transport of small particles, formed in the hot reaction zone of the combustor, toward the vicinity of the fuel nozzle can be determined.

Therefore, regarding both the chemical properties of the deposits as well as the flow situation in the combustor, a deposit build-up at the fuel nozzle by small particles such as soot or coked droplets can be formulated. The size of the particles corresponds with those found by Urban and Dryer (1991), who give a correlation between the initial droplet diameter and the diameter of the coked droplet. Because these authors considered solely heavier fuels, further studies are necessary to validate the assumption that these spherical particles are coked fuel droplets.

The deposits within the flame tube differ distinctly from those in the vicinity of the nozzle. In particular, the high oxygen content, which is identified by elemental analysis as well as by infrared analysis, exhibits similarities with deposits formed through thermal instabilities of hydrocarbons. These mechanisms were studied by Chin and Lefebvre (1993) and Krazinski et al. (1992) under fuel supply system conditions. Both authors investigated deposit formation by heating fuels in tubes outside a combustor. To illustrate that these mechanisms are also relevant inside the combustor for fuel impinging the combustor

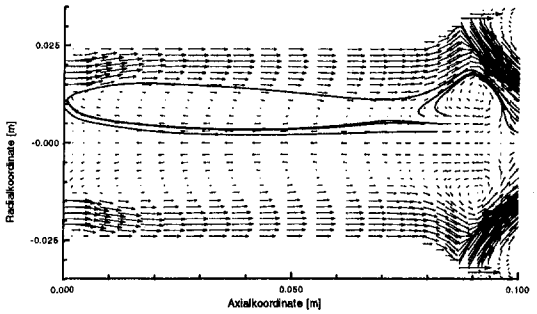

Fig. 7 Computed flow field in the primary zone of the combustor

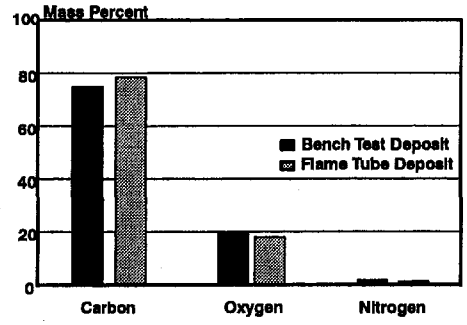

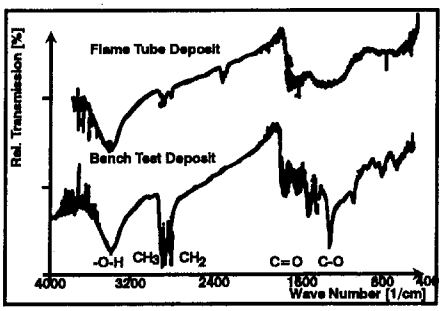

Fig. 8 Chemical characteristics of the deposits in the flame tube and in the bench test rig

walls, the present combustor results were further studied in detail. To verify the hypothesis, the deposits of laboratory experiments are contrasted to those in the film section of the combustor and those found in investigating thermal instabilities of fuels.

Deposit Formation in Bench Tests

In the bench test rig, a deposit formation caused by droplet impingement on the hot combustor wall was simulated. All the tests described below were performed at a pressure of 1 bar. To compare the deposits in the bench tests and those in the flame tube of the previously described combustor, fuel oil was initially utilized. As Fig. 8 shows, both the elemental analyses and the infrared spectra of deposits in the bench test as well as in the film section of the combustor under consideration show good agreement.

In both cases, the deposits consist of approximately 80 percent carbon and 20 percent oxygen. The oxygen is chemically fixed in —OH, C=O, and C—O bonds. Based on the correlation of deposit composition in both test rigs, it can be assumed that identical mechanisms of formation take place and the dependencies found for deposit formation in the bench tests can be applied to combustor conditions. Contrasting the deposit composition to deposits observed in fuel supply systems, it is apparent that the mechanism stemming from thermal instability of the fuel also takes place inside a combustor when liquid fuel impinges on the hot wall. The composition of the deposits resulting from thermal instabilities (Hazlett and Hall, 1981) and those occurring in internal engines, such as found by Ebert et al. (1981), corresponds with those detected in the bench test rig as well as in the flame tube of the combustor.

In our first laboratory experiments, the influences of the wall temperature and the fuel composition were investigated for several gas turbine fuels as well as pure hydrocarbons. Before testing the gas turbine fuels, a detailed analysis using gas chromatography and boiling point curves was done to characterize the fuels. As Fig. 9 shows, for fuel oil, deposit formation takes place in a temperature regime between 450 K and 730 K.

Using kerosine (Jet 1A) as a test fuel, deposit formation occurs at lower temperatures. This is in correspondence with the boiling characteristics of the fuels because the measured

Downloaded 02 Jun 2010 to 171.66.16.104. Redistribution subject to ASME license or copyright; see http://www.asme.org/terms/Terms_Use.cfm

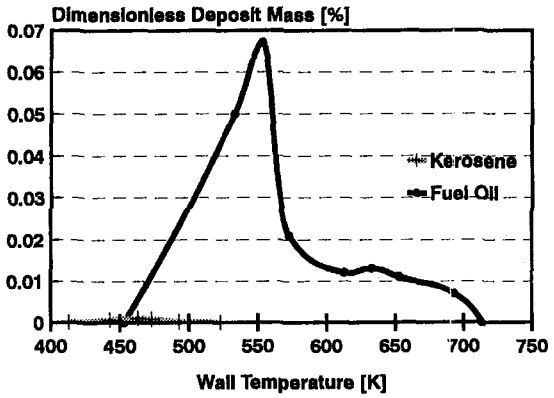

Fig. 9 Deposit formation of gas turbine fuels

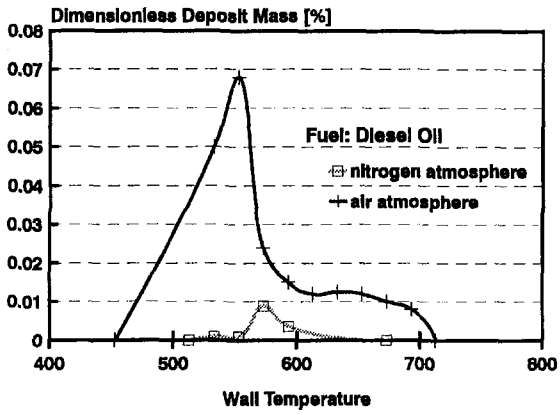

Fig. 11 Influence of ambient atmosphere on deposit formation

boiling range (DIN 51751) of kerosine lies between 413 K and 518 K while fuel oil boils between 450 K and 650 K. Contrasting the deposit mass of fuel oil and the kerosine under consideration, it is apparent that the high-boiling fuel oil contributes more strongly to deposit formation than the kerosine.

To demonstrate that the high-boiling components in the fuel are responsible for deposit formation, the fuel oil was split into two fractions. The components boiling above 613 K were split from the compounds boiling below 613 K. While the high-boiling components contribute very strongly to deposit formation, the fraction boiling below 613 K formed no deposits (see Fig. 10).

From gas chromatography measurements of the high-boiling fuel fraction, no combinations with fewer than 19 carbon atoms were identified. The tendency of the long-chain components in the fuel to form deposits was confirmed by studies with pure hydrocarbons. In these studies considering alkanes, alkenes, and aromatics, it was found that with increasing carbon chain length of the hydrocarbon, deposit formation increases (see Brandauer et al., 1993). As a further result of the investigations with pure hydrocarbons, a first approach to describe the reactions leading to deposit formation can be given. In particular, autoxidation of the fuel plays an important role.

To confirm our reaction path, which indicate a strong influence of oxygen on deposit formation, our studies in an air environment were compared to those in a nitrogen atmosphere. As Fig. 11 indicates, the oxygen in the ambient atmosphere contributes to a high deposit forming tendency. This is confirmed by studies of Hurley (1982), who was unable to find any deposits from liquid fuels under nitrogen tests when he used fuel without oxygen.

In the presence of oxygen, the deposit formation based on fuel oil takes place in a temperature regime between 450 K and 730 K, showing maximum deposit mass at approximately 570 K. At 450 K, the onset of fast autoxidation in the fuel takes place. At temperatures above 570 K both the rate of autoxidation decreases and the droplet vaporization time decreases as shown by our droplet investigations. Both effects lead to a decrease in deposit formation. The time the liquid fuel wets the hot wall strongly affects deposit formation. To determine this fact unequivocally, experiments with various solutions of hexane and hexadecene were performed. Hexane and hexadecene were chosen because hexane forms no deposits and hexadecene contributes strongly to deposit formation. The deposit mass shown in Fig. 12 is thus normalized to the initial hexadecene mass. With increasing hexadecene content in the solution, the dimensionless deposit mass increases. The vaporization time of the two-component droplets, which is also the time for chemical reactions in the liquid fuel, is also plotted in Fig. 12. In this plot, the increase of deposit formation with increasing vaporization time becomes apparent.

The influence of vaporization time also becomes clear when comparing the deposit forming tendency of the high-boiling compounds in the fuel to the fuel oil itself. Our recorded boiling point curves show that above 613 K only 12 percent by volume of the fuel oil boils. Because these combinations are responsible for deposit formation solely, about 8 times more dimensionless deposit mass will be expected in the experiments. However, these combinations cause about 20 times more dimensionless deposit mass (compare Figures 9 and 10) because they exhibit longer vaporization times at the same surface temperature than the fuel oil itself.

In summary, long-chain components in the fuel, which allow long residence times at high surface temperatures, contribute strong to deposit formation. The temperature regime as well as

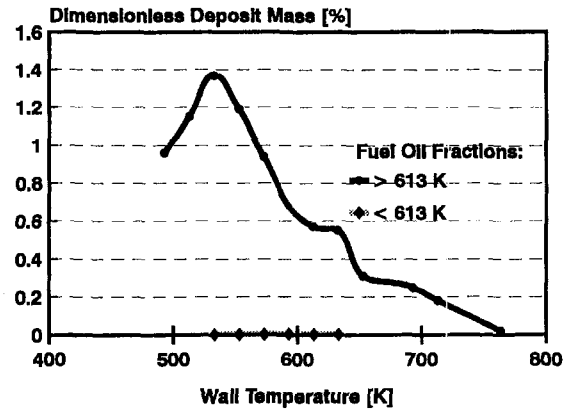

Fig. 10 Deposit formation of fractions of fuel oil

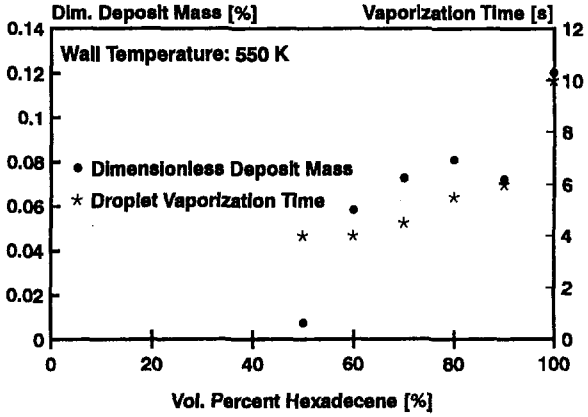

Fig. 12 Influence of vaporization time on deposit formation

Downloaded 02 Jun 2010 to 171.66.16.104. Redistribution subject to ASME license or copyright; see http://www.asme.org/terms/Terms_Use.cfm

the fact of increasing deposit mass with increasing residence time on the surface is in accordance with investigations of Marteney and Spadaccini (1986) in a heated tube. This confirms that identical processes are taking place in the combustor with fuel impinging on the hot wall and during thermal decomposition in a fuel supply system. The increase in deposit formation with rising oxygen concentration in the ambient atmosphere indicates the presence of reactions with oxygen in the formation path of these deposits. Therefore, autoxidation reactions take place in the fuel, as other authors postulate in investigating thermal instabilities of fuels (Krazinski et al., 1992; Roback et al., 1983; Katta et al., 1993).

Conclusions

Deposit formation in gas turbine combustion chambers is found to occur at two locations with different formation mechanisms. In the combustor under consideration, deposit formation originates in the vicinity of the fuel nozzle by accumulation of particles formed in the reaction zone. This is demonstrated by detailed chemical and physical analyses and a numerical simulation of the flow field in the combustor. In contrast, the deposit build-up in the flame tube is caused by the impingement of fuel droplets on the hot combustor wall, accompanied by chemical reactions of the fuel at the wall. Finally, based on the physical and chemical characteristics of the deposits, criteria to distinguish the formation mechanisms inside the combustor were formulated. By simply comparing the elemental analyses, it can be detected whether deposit formation is caused by intermediate flame products or liquid fuel impinging on the combustor flame tube.

Detailed simulation of deposit formation by fuel impingement at the flame tube was accomplished in bench tests. From the apparent chemical similarities between the deposits from bench tests and the deposits in the flame tube, it becomes evident that the study of the relevant parameters for deposit formation in bench tests is permitted. After defining the influence of fuel composition and wall temperature, e. g., a temperature range of approximately 200 K to 300 K depending on fuel composition, it is shown that these deposits are affected by the oxygen concentration in the ambient atmosphere. In further studies the deposit causing combinations in a gas turbine fuel can be identified and the influence of the residence time of the liquid fuel on the hot surface can be determined. Considering the chemical composition and the existing temperature range of deposit formation, it is demonstrated that the thermal instabilities of the fuel, which were investigated in detail under fuel supply system conditions, have a decisive impact on deposit formation in advanced combustors using fuel prevaporization.

Acknowledgments

The research program has been supported by the Arbeitsgemeinschaft Hochtemperaturgasturbine, AG TURBO, initiated by the Secretary of Science and Technology of Germany (BMFT), and the Sonderforschungsbereich 167 by the Deutsche Forschungsgemeinschaft (DFG).

Thanks are given to the Director of the Engler-Bunte-Institute at the University of Karlsruhe, Prof. K. Hedden and to Dipl.-Ing. M. Hutfliess, for carrying out the chemical analyses. Further thanks go to the Laboratory of Scanning Microscopy at the University of Karlsruhe for their support.

References

Brandauer, M., Schulz, A., Pfeiffer, A., and Wittig, S., 1993, "Experimental Study of Coke Deposition Under Gas Turbine Combustor Conditions," *Combustion Science and Technology,* Vol. 89, pp. 265–273.

Chin, J. S., and Lefebvre, A. H., 1993, "Influence of Flow Conditions on Deposits From Heated Hydrocarbon Fuels," ASME JOURNAL OF ENGINEERING FOR GAS TURBINES AND POWER, Vol. 115, pp. 433–438.

Ebert, B. L., Davis, W. H., Mills, D. R., Dennerlein, J. D., 1981, "The Chemistry of Internal Combustion Engine Deposits," presented at American Chemical Society Atlanta Meeting, Mar. 29–Apr. 3, Vol. 26.

Grisdale, R. O., 1953, "The Formation of Black Carbon," *Journal of Applied Physics,* Vol. 24, pp. 1082–1091.

Hazlett, R. N., and Hall, J. M., 1981, "Jet Aircraft Fuel System Deposits," American Chemical Society Atlanta Meeting, Mar. 29–Apr. 3, Vol. 26.

Heidenreich, R. D., Hess, W. M., and Ban, L. L., 1968, "A Test Object and Criteria for High Resolution Electron Microscopy," *Journal Appl. Cryst.,* Vol. 1, pp. 1–19.

Hurley, C. D., 1982, "Carbon Formation by the Pyrolysis of Gas Turbine Fuels in Preflame Regions of Gas Turbine Combustors," ASME Paper No. 82-GT-84.

Katta, V. R., Jones, E. G., and Roquemore, W. M., 1993, "Development of Global Chemistry Model for Jet-Fuel Thermal Stability Based on Observations From Static and Flowing Experiments," presented at the AGARD Meeting on Fuels and Combustion Technology for Advanced Aircraft Engines, Colliferro, Italy, Paper No. PEP-18.

Krazinski, J. L., Vanka, S. P., Pearce, J. A., and Roquemore, W. M., 1992, "A Computational Fluid Dynamics and Chemistry Model for Jet Fuel Thermal Stability," ASME JOURNAL OF ENGINEERING FOR GAS TURBINES AND POWER, Vol. 114, pp. 104–110.

Maier, K., and Jantzen, E., 1985, "Ablagerungen in Flugtriebwerken, Teil I: Erscheinungsformen und Testmethoden," *Zeitschrift für Flugwissenschaft und Weltraumforschung,* Vol. 9, pp. 211–217.

Marteney, P. J., and Spadaccini, L. J., 1986, "Thermal Decomposition of Aircraft Fuel," ASME JOURNAL OF ENGINEERING FOR GAS TURBINES AND POWER, Vol. 108, pp. 648–653.

Müller, A., and Wittig, S., 1991, "Influence of Temperature and Pressure on Soot Formation in a Shock Tube Under High Pressure Conditions," *Proc. 18th Symposium on Shock Waves,* Institute of Fluid Science, Tohoku University, Japan, pp. 759–764.

Noll, B., 1993, "Evaluation of a Bounded High Resolution Scheme for Combustor Flow Computations," *AIAA Journal,* Vol. 30, No. 1, pp. 64–70.

Pfeiffer, A., Schulz, A., and Wittig, S., 1991a, "Principles of the ITS Ceramic Research Combustor: Segmented Flame Tube and Staged Combustion," ASME Paper No. 91-GT-63.

Pfeiffer, A., Schulz, A., and Wittig, S., 1991b, "Design and Development of the ITS Ceramic Research Combustor," *Proceedings of the 1991 Yokohama International Gas Turbine Congress,* Gas Turbine Society of Japan, pp. III-9-15.

Roback, R., Szetela, E. J., Spadaccini, L. J., 1983, "Deposit Formation in Hydrocarbon Fuels," ASME JOURNAL OF ENGINEERING FOR POWER, Vol. 105, pp. 59–65.

Schirmer, R. M., 1970, *Morphology of Deposits in Aircraft and Engine Fuel Systems,* SAE Paper No. 700258.

Starkman, E. S., Catteneo, A. G., and McAllister, A. H., 1951, "Carbon Formation in Gas Turbine Combustion Chambers," *Industrial and Engineering Chemistry,* Vol. 43, pp. 2822–2826.

Urban, D. L., and Dryer, F. L., 1990, "New Results on Coke Formation in the Combustion of Heavy Fuel Droplets," *23th (International) Symposium on Combustion,* The Combustion Institute, pp. 1437–1443.

Urban, D. L., and Dryer, F. L., 1991, "Formation of Coke Particulate in the Combustion of Residual Oil: Particle Size and Mass Prediction From Initial Droplet Parameters," in: *Heat Transfer in Combustion Systems,* Symposium at AIAA/ASME Thermophysics and Heat Transfer Conference, Seattle, pp. 83–88.

Wear, J. D., and Hibbard, R. R., 1955, "Coke Deposition and Smoke Formation in Turbojet Engines," NASA Report RM E55G28.

Downloaded 02 Jun 2010 to 171.66.16.104. Redistribution subject to ASME license or copyright; see http://www.asme.org/terms/Terms_Use.cfm

Jet Fuel Deposition and Oxidation: Dilution, Materials, Oxygen, and Temperature Effects

S. Zabarnick

P. Zelesnik

R. R. Grinstead

Aerospace Mechanics Division,
University of Dayton Research Institute,
Dayton, OH 45469

Quartz crystal microbalance (QCM) and pressure measurements are used for determination of jet fuel thermal stability in a batch reactor. The QCM is able to monitor extremely small amounts of deposition in situ, while the pressure measurements provide qualitative data on the oxidation process. The dependence of the deposition amount was monitored as a function of the oxygen availability for two fuels. Also, the effect of QCM electrode materials was investigated. Deposition and oxidation were compared for the following electrode materials: gold, aluminum, silver, and platinum. We also studied the effect of dilution on oxidation and deposition. Jet fuel was diluted with increasing amounts of hydrocarbon solvent. It was observed that this dilution procedure can help characterize a fuel's effective antioxidant concentration. Fuel dilution is also shown to be a good technique for improving thermal stability characteristics of poor fuels. Additionally we have studied the temperature effect on deposition for two fuels over the range 140 to 180°C.

Introduction

Recent advances in jet aircraft and engine technology have placed an ever-increasing heat load on the aircraft. The bulk of this excess heat is absorbed by the aircraft fuel, as jet fuel is used as the primary coolant for the numerous heat sources. This hot fuel reacts with dissolved oxygen to form oxidized products and deposits. The formation of deposits results in the fouling of fuel lines, valves, actuators, nozzles, and various other aircraft components with the potential to result in catastrophic failure. The recent development of the quartz crystal microbalance (QCM) technique provides an extremely sensitive technique for real-time, in situ measurements of jet fuel thermal oxidative deposition (Klavetter et al., 1993; Martin et al., 1991). The technique is sufficiently sensitive that deposition can be readily measured under realistic turbine engine thermal conditions, unlike the accelerated conditions of temperature and/or time under which most previous measurements have been made. The modification of the QCM system with addition of a pressure transducer has enabled simultaneous real-time, *in situ* measurements of both deposition and oxidation. Recent work has demonstrated the capabilities of the technique in evaluating both jet fuels and potential jet fuel additives (Zabarnick, 1994; Zabarnick and Grinstead, 1994). The ability to measure oxidation and deposition simultaneously provides an ideal environment in which to study the effect of oxygen concentration on the deposition process.

Many current and future military aircraft incorporate an onboard inert gas generating system (OBIGGS) to lower the oxygen level in the fuel tank ullage space. As this OBIGGS can lower the dissolved oxygen concentration present in the fuel, it is important to understand the effect this has on the deposit-forming process. In addition, during the thermal oxidation process in a flowing fuel system, the oxygen concentration in the fuel decreases as the oxidation process continues. Thus, a fundamental understanding of the effect of the oxygen concentration on thermal stability (thermal stability refers to the deposit-forming tendency of the fuel) is essential for designing jet fuel systems. For this purpose we have developed a technique to vary the oxygen level available to the fuel in the QCM system. In this work we will present results showing the effect of varying oxygen concentrations on fuel thermal stability.

On its trek through a complex military fuel system, jet fuel contacts a variety of materials. It is important to understand the effect these materials have on fuel thermal stability. Previous QCM jet fuel thermal stability work has exclusively studied crystal electrodes with gold surfaces (Klavetter et al., 1993; Zabarnick, 1994; Zabarnick and Grinstead, 1994). For the present work we have acquired quartz crystals with electrodes of the following materials: gold, platinum, aluminum, and silver. In this work we study the effect of the crystal electrode material on jet fuel thermal stability for a variety of jet fuel samples.

We have also investigated the technique of fuel dilution to study the effect of varying concentration of the antioxidant and deposit producing molecules naturally present in jet fuels. This technique provides a method for determining the relative effective antioxidant concentrations that are naturally present in various fuels. Fuel dilution also promises to provide a method for inexpensively improving the thermal stability of highly depositing jet fuels.

In modern military aircraft, jet fuel is recirculated through the aircraft fuel system and exposed to various temperatures for various residence times. These temperatures and residence times change constantly during a mission as the throttle is changed and the aircraft maneuvered. Thus, an understanding of the effect of temperature on jet fuel thermal stability is essential to the design of aircraft fuel systems and minimization of fuel system fouling phenomena. In this work we have varied fuel temperature over the range 140 to 180°C while monitoring deposition and oxidation for two different fuels.

Experimental

The QCM experimental apparatus has been described in detail previously and will be described only briefly here (Klavetter et al., 1993; Zabarnick, 1994). Jet fuels are thermally stressed

Contributed by the International Gas Turbine Institute and presented at the 40th International Gas Turbine and Aeroengine Congress and Exhibition, Houston, Texas, June 5–8, 1995. Manuscript received by the International Gas Turbine Institute February 10, 1995. Paper No. 95-GT-50. Associate Technical Editor: C. J. Russo.

Copyright © 1996 by ASME

Downloaded 02 Jun 2010 to 171.66.16.104. Redistribution subject to ASME license or copyright; see http://www.asme.org/terms/Terms_Use.cfm

Table 1 Properties of fuels studied

Fuel Number and Designation	Hydrotreated?	Total Sulfur (ppm)	JFTOT Breakpoint (C)	Other Notes
F-2747 (Jet A-1)	Yes	37	332	Light depositor, fast oxidizer
F-2827 (Jet A)	No	763	282	Heavy depositor, slow oxidizer
F-2980 (Jet A)	No	614	288	Merox treated, moderate oxidizer
Exxsol D80	–	3	–	Pure solvent, very fast oxidizer, very light depositor

in a 100 ml stainless steel Parr pressure reactor. The reactor is modified with an RF feedthrough for attachment of the QCM. The reactor is supplied with gas inlet (below the liquid level) and outlet (above the liquid level) lines. A magnetic stir bar and stirrer are used during the runs to minimize spatial inhomogeneities in species concentration and temperature. The reactor is heated with a clamp-on band heater, which is controlled with a PID temperature controller. A thermocouple is immersed in the fuel to monitor and control the temperature, which can be readily maintained ±0.4°C at 140°C over a 15 hour run. The reactor was also fitted with a Sensotec 0–50 psia pressure transducer for measurement of the reactor headspace pressure. The output of the pressure transducer is read by a digital multimeter (Keithley Model 199/1992).

The quartz crystals used were 5 MHz, 2.54 cm diameter, 0.33 mm thick, AT cut wafers. The QCM crystal is suspended vertically in the fuel in order to minimize gravitational effects on deposition. The crystals are obtained from Maxtek Inc. and are normally manufactured with overtone polished gold electrodes. For the materials work we acquired crystals with electrode surfaces of platinum, aluminum, and silver. The quartz crystal resonator is driven at 5 MHz by a oscillator circuit that was developed by Sandia National Laboratories (Klavetter et al., 1993). This circuit tracks the impedance variations of the crystal in order to determine the resonant frequency of the device. The oscillator frequency output is read by a frequency counter (HP Model 5384A). The change in frequency of the device at constant temperature is related to surface mass deposition on the crystal. The oscillator circuit also provides an amplitude output that indicates crystal damping. The output is read by the digital multimeter. The crystal frequency, reactor temperature, reactor pressure, and crystal damping voltage are monitored at 1 minute intervals over a GPIB bus via a personal computer.

A standard experimental run is conducted by filling the reactor with 60 ml of fuel, then sparging with air for one hour to air saturate the fuel. The reactor is then sealed at one atmosphere and heated to the test temperature. Typically the fuel reaches the test temperature after a 35 to 40 minute heat-up period. After the 15 hour run time, the heater is turned off and the reactor allowed to cool. For the oxygen and temperature effect studies, a slightly different method was used in order better to control the oxygen availability and/or to prevent significant oxygen consumption and deposition during the heat-up period. For these runs the fuel is sparged with nitrogen for one hour in order to purge the fuel of dissolved oxygen. The reactor is then sealed and heated to temperature. Once the fuel has reached temperature, air is added through the gas inlet line and the headspace pressure is monitored to determine the amount of air added. This technique provides a reproducible way of varying the oxygen availability of the reactor for the oxygen studies. It also prevents significant oxidation from occurring during the heat-up period for higher temperature runs.

The theory that relates the measured frequency changes to surface mass has been presented in detail elsewhere (Martin et al., 1991). The frequency change of a crystal immersed in a liquid fuel can be due to two effects: The first results from changes in the surface mass density; the second is due to changes in the liquid density and viscosity. At constant temperature and relatively small extents of chemical conversion, the liquid properties remain constant and the frequency change can be related to surface deposition via the equation

$$\rho_s = -(2.21 \times 10^5 \text{ g/(cm}^2 s)) \frac{\Delta f}{f_0^2} \qquad (1)$$

where f_0 is the unperturbed resonant frequency, Δf is the change in resonant frequency, and ρ_s is the surface mass density (mass/area). In general, the reproducibility of the mass deposition measurements on fuels is limited to ±20 percent for the QCM technique. The fuels studied and some of their properties are listed in Table 1.

Results and Discussion

Oxygen Dependence of Deposition. Here we present results of a study of the effect of oxygen availability on the deposition of a jet fuel. It is well known that the presence of oxygen is required for production of significant quantities of deposits (Hazlett, 1991). In most fuels the removal of oxygen results in a significant decrease in deposit formation. In flowing fuel systems, oxygen may be removed more readily near the hot tube walls; this results in oxygen concentration gradients in both axial and radial directions. Obviously, to understand the deposition process completely the oxygen dependence of deposition needs to be studied. To date, few studies have monitored jet fuel deposition as a function of oxygen availability.

Figure 1 shows the deposition measurements obtained when varying the oxygen availability for fuel F-2980. This fuel was chosen because of its moderate to slow oxygen consumption rate and its significant deposition. Thus both the deposition and oxidation processes could be readily monitored with the QCM and pressure monitoring techniques. Initially, the fuel was sparged with nitrogen to remove any dissolved oxygen. Then, the fuel was heated to 140°C at which time air was added via the gas inlet line at pressures ranging from 0 to 30 psi. The figure shows that the total deposition at the end of the 15 hour run increases with increased oxygen availability. The deposition varies from 0.3 μg/cm^2 for the zero oxygen run to 11.4

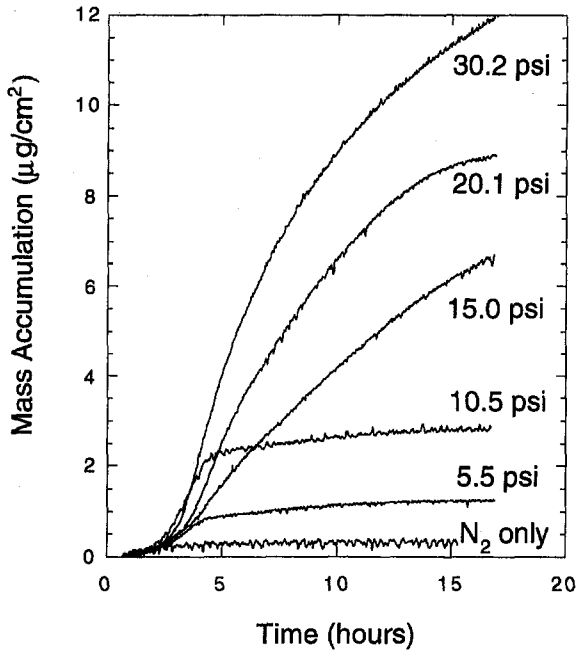

Fig. 1 Plots of mass accumulation versus time at various added air pressures in fuel F-2980

Downloaded 02 Jun 2010 to 171.66.16.104. Redistribution subject to ASME license or copyright; see http://www.asme.org/terms/Terms_Use.cfm

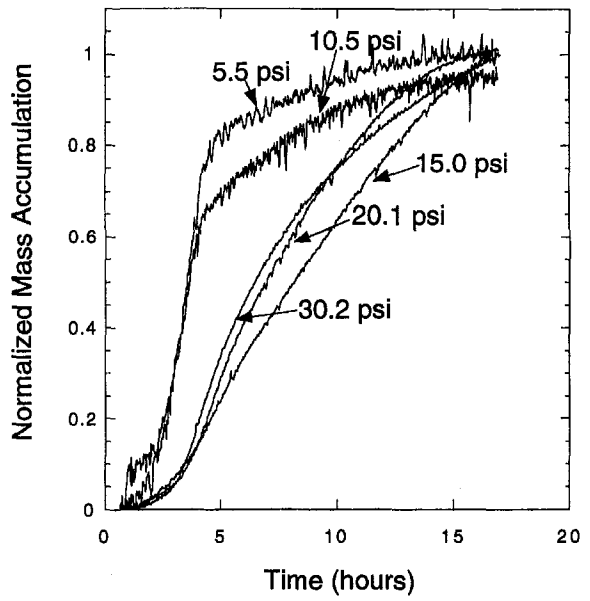

Fig. 2 Plots of normalized mass accumulation versus time at various added air pressures in fuel F-2980

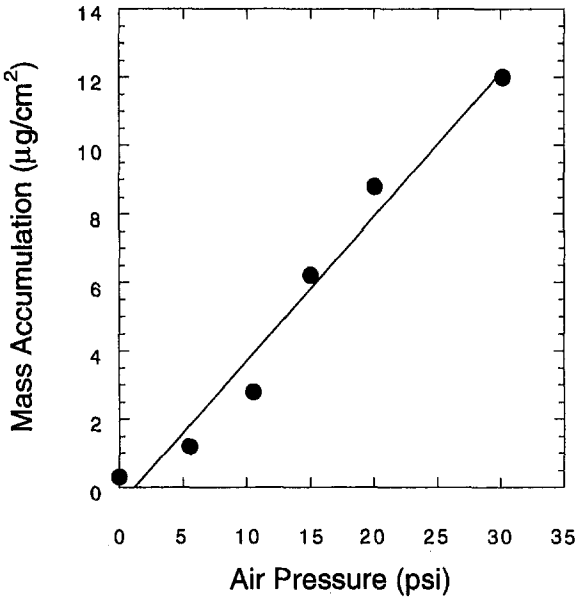

Fig. 3 Plot of final mass accumulation versus air pressure for fuel F-2980

$\mu g/cm^2$ for the 30.2 psi run. Each of the deposition curves shows an initial slow deposition rate up to 2 hours (induction period). The time at which the deposition levels off appears to occur at different times for the various oxygen levels plotted. To illustrate this dependence better, we have normalized each measured deposition by the maximum deposition at the end of each test and plotted the results in Fig. 2. It is apparent that the 5.5 and 10.5 psi runs have shorter early rise times and their depositions begin to level off much earlier than the higher oxygen runs. The 15.0 psi run has the slowest normalized deposit production rate. The corresponding pressure measurements for these runs (not shown) support the previous observation (Zabarnick, 1994) that the deposition production rate and leveling off times correspond well to the oxidation and oxygen consumption processes, respectively. Thus, these normalized deposition plots yield information about the oxidation process. The observed behavior of normalized deposition versus oxygen availability in Fig. 2 is complex but can be rationalized if one considers that the oxygen consumption process generates various product species, some of which may act as antioxidants, such as aldehydes. Thus the slower normalized deposition observed at 15 psi and above may be due to production of significant concentrations of antioxidant species at these higher oxygen conditions. Another possible explanation is that the chemical kinetic oxygen reaction order dependence may be changing as the oxygen availability is increased. That is, there may be a shift from near first-order oxygen consumption (where the oxygen consumption rate is proportional to oxygen concentration) to near zeroth-order (where the oxygen consumption rate is independent of oxygen concentration). The complex diffusion process of oxygen from the headspace of the reactor into the fuel during the test precludes a more exhaustive analysis of oxygen reaction orders.

The final deposition at 15 hours from Fig. 1 is plotted versus oxygen availability in Fig. 3. It appears that the deposition at 15 hours varies linearly with the oxygen availability in the reactor. The deposition varies from 0.3 $\mu g/cm^2$ for the zero oxygen run to 11.4 $\mu g/cm^2$ for the 30.2 psi run. This dependence is also approximately linear for deposition at 5 and 10 hours (not shown). The observed linear dependence of the measured deposition on the oxygen availability at various extents of reactions (reaction times) is a significant result for the fuel system design process if this linear response is universal for all jet fuels. In order to test this supposition, we have also performed these oxygen-dependent studies for a second fuel, F-2827. The final deposition at 15 hours versus oxygen availability for this fuel is shown in Fig. 4. The figure shows that the final deposition is linear over the range 0 to 20 psi added air, but above 20 psi the deposition appears to level. This leveling of the deposition may be due to incomplete oxygen consumption at these higher oxygen availabilities. Unfortunately, the slow oxidation of this fuel precludes use of the pressure measurement technique to confirm this supposition. These results point out that the level of oxygen consumption is an important parameter to monitor in studies of the oxygen dependence of deposition. It is apparent that the oxygen dependence of deposition cannot be represented as a simple linear dependence, especially when studying a varying array of different fuels. Also, under partial oxygen consumption conditions, lowering the oxygen availability does not necessarily result in reduced deposition (see Fig. 1).

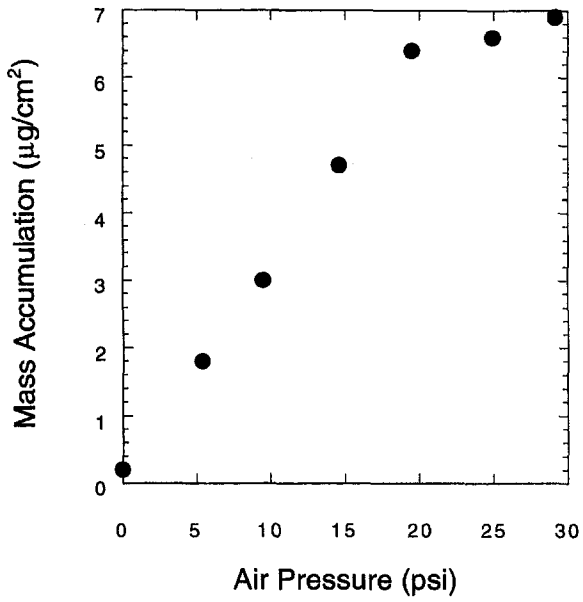

Fig. 4 Plot of final mass accumulation versus air pressure for fuel F-2827

Downloaded 02 Jun 2010 to 171.66.16.104. Redistribution subject to ASME license or copyright; see http://www.asme.org/terms/Terms_Use.cfm

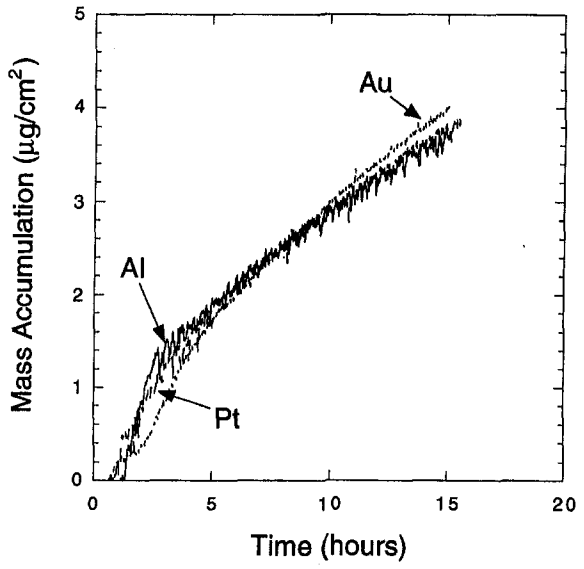

Fig. 5 Plots of mass accumulation versus time for aluminum, gold, and platinum electrode surfaces with fuel F-2827

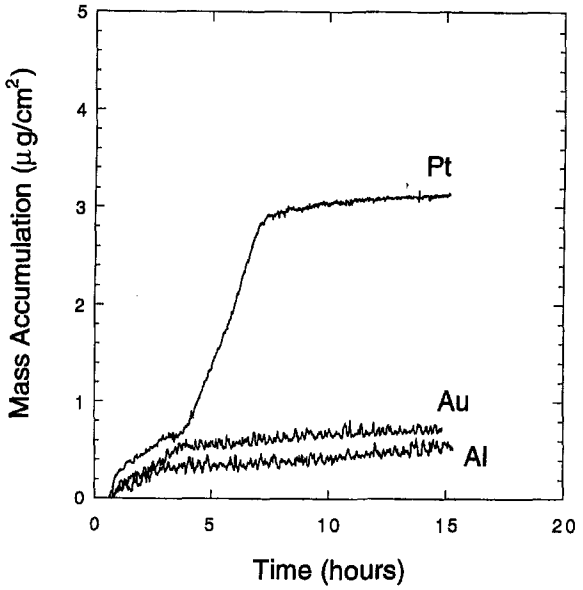

Fig. 6 Plots of mass accumulation versus time for aluminum, gold, and platinum electrode surfaces with fuel F-2747

Materials Effects on Deposition. Although the Parr reactor utilized for these QCM measurements is constructed of stainless steel, the deposition is measured on the surface of the quartz crystal electrode. To date, all QCM jet fuel deposition measurements have used crystals with gold electrodes. In general, gold is a rather unique metal that tends to be relatively unreactive. Also, gold is not used significantly in real jet fuel systems. Thus there is concern that measurements of deposition on gold surfaces do not adequately represent typical deposit processes in real fuel systems. In order to address this concern, we have acquired quartz crystals with electrode surfaces of the following materials: gold (Au), platinum (Pt), aluminum (Al), and silver (Ag). These materials do not necessarily represent common jet fuel system components, but these crystal types were readily available from the manufacturer.

We have studied deposition on crystal electrodes with gold, platinum, and aluminum surfaces for two different fuels (the silver electrode results are presented separately below). Deposition was monitored at 140°C and 1 atm air. The results are shown in Figs. 5 and 6 for fuels F-2827 and F-2747, respectively. Figure 5 demonstrates that in fuel F-2827 deposition is identical for each of the three electrode surface materials. Figure 6 shows that the gold and aluminum electrode show very similar deposition for fuel F-2747, while the platinum electrode experiences significantly higher deposition. Thus, the effect of materials appears to be fuel dependent. Gold and aluminum surfaces appear to yield identical results for both fuels studied. As aluminum is a material commonly found in fuel systems, this result reinforces the relevance of previous measurements of fuel thermal stability with gold electrodes. Platinum is a metal that is not commonly used in aircraft fuel systems. Platinum and platinum complexes are commonly used as catalysts in petroleum refining and other processes; thus, the increased deposition in Fig. 6 may be due to the catalytic activity of the platinum metal. Why does the platinum electrode show increased deposition in fuel F-2747 and not in F-2827? Fuel F-2747 is a rapidly oxidizing fuel (oxygen is consumed within 3 hours at 140°C) while F-2827 is a slowly oxidizing fuel (oxygen consumption takes >15 hours) (Zabarnick, 1994). Also, fuel F-2747 is known to produce significant quantities of hydroperoxides, while fuel F-2827 does not. The Pt surface may be able to catalyze the decomposition of hydroperoxides under these conditions. This would produce free radicals, which would further react with other substances, producing increased deposition. This hypothesis can be tested by monitoring the hydroperoxide concentration during these runs with and without the presence of Pt.

The results for deposition measurements on silver electrodes are shown in Fig. 7. We first tested fuel F-2827, which produced an extremely large surface deposition, 18.1 $\mu g/cm^2$, at the end of the 15 hour run. This is much larger than the deposition observed for the other materials (Fig. 5). Visually, the silver electrode surface did not appear to have a typical carbon deposit; instead, the surface of the electrode appeared to have a very thin blue/black film. To determine if the measured deposition was due to the normal thermal oxidative deposit, we reran the test with the fuel sparged with N_2 to remove O_2. The result is also shown in Fig. 7. Without O_2 present the deposition actually increased; the extremely large deposition actually prevented data from being acquired after 3 hours. It was quite apparent

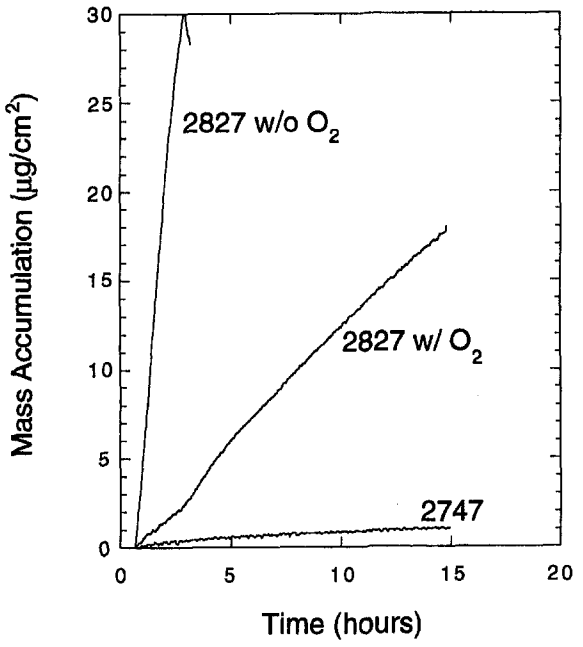

Fig. 7 Plots of mass accumulation versus time with a silver electrode surface

Downloaded 02 Jun 2010 to 171.66.16.104. Redistribution subject to ASME license or copyright; see http://www.asme.org/terms/Terms_Use.cfm

from the magnitude and appearance that this was not a "normal" carbon deposit. It is well known that silver reacts readily with sulfur compounds to form a thin film of silver sulfide (tarnish). In the atmosphere this is primarily caused by hydrogen sulfide, H_2S. Fuel F-2827 has a relatively high sulfur content (see Table 1). To test if sulfur might be responsible for this deposit, we sparged fuel F-2747, a low-sulfur fuel, with N_2 and measured the resulting deposition, as shown in the figure. This low-sulfur fuel yielded a significantly lower deposition of 1.1 $\mu g/cm^2$. In order to confirm that the measured deposition is due to sulfur, we have used Auger spectroscopy to measure the atomic constituents of the surface layer of the crystal electrode for the runs with F-2827 fuel. The analyses confirm the presence of silver sulfide, Ag_2S; the surfaces run with fuel F-2827 consist of 60–70 percent Ag and ≈30 percent S atoms. The surface of the F-2747 crystal was composed of silver almost exclusively (>95 percent). As the only source of sulfur in this system is from the fuel, this technique may provide a very sensitive measure of fuel sulfur.

For use as an analytical technique for sulfur, additional work needs to be done. The linearity of the test with fuel concentration and the effect of temperature need to be determined. Furthermore, the sensitivity of the test to various types of sulfur compounds needs to be measured. Also, the cause of the difference in measured profiles with and without the presence of oxygen, as seen in Fig. 7, needs to be determined. At present it is thought that formation of carbon deposits in the presence of oxygen may explain the lesser formation of deposits. It is believed that the formation of silver sulfide tarnish on silver surfaces occurs by the reaction of sulfur with the surface silver atoms, and subsequent migration of subsurface silver atoms to the surface (Ricciardiello and Riotti, 1972). We hypothesize that the deposition of carbonaceous fuel deposits may cover the surface enough to limit the reaction of sulfur with silver, thus explaining the lower deposition in the presence of oxygen. Another possible explanation is that the presence of oxygen may result in oxidation of these sulfur compounds, which may prevent their reaction with the surface. For maximum sensitivity as an analytical test for fuel sulfur the presence of oxygen should be limited.

Effect of Fuel Dilution. We have studied the effect of fuel dilution on oxidation and deposition by diluting fuel F-2827 with a hydrocarbon solvent, Exxsol D80. Fuel F-2827 is a moderately high depositing fuel and a very slow oxidizer, while Exxsol D80 is a narrow-cut, dearomatized, low-sulfur (3 ppm), aliphatic solvent. A jet fuel such as fuel F-2827 can be thought of as a hydrocarbon solvent, consisting of alkyl aromatics, naphthenes, and paraffins, with small concentrations of other species, such as phenols, sulfur compounds, and nitrogen compounds. These other species are thought to be major players in both the formation of deposits and the inhibition of oxidation (Heneghan and Zabarnick, 1994). Thus, the dilution of a jet fuel with a solvent such as Exxsol D80 in effect reduces the concentration of these species.

We have diluted F-2827 fuel with Exxsol D80 to create mixtures from 100 percent (by volume) Exxsol D80 (referred to here as 0 percent F-2827) to 100 percent F-2827. These air-saturated mixtures were run in the QCM system at the standard conditions of 140°C and 1 atm starting pressure. The results are shown in Fig. 8. The figure shows the very different deposition and oxidation characteristics of the neat fuels, F-2827 and Exxsol D80. After 15 hours Fuel F-2827 produces deposits of 3.6 $\mu g/cm^2$, while Exxsol D80 produces only 0.6 $\mu g/cm^2$. Fuel F-2827 exhibits a nearly constant pressure profile during the run, while Exxsol D80 oxidizes so rapidly (<1 hour) that only a portion of the pressure drop is observed during the constant-temperature run (a majority of the oxidation is thought to have occurred during the heat-up process). We have previously shown the relationship between the pressure decays and oxidation in this system (Zabarnick, 1994). Also in the figure are

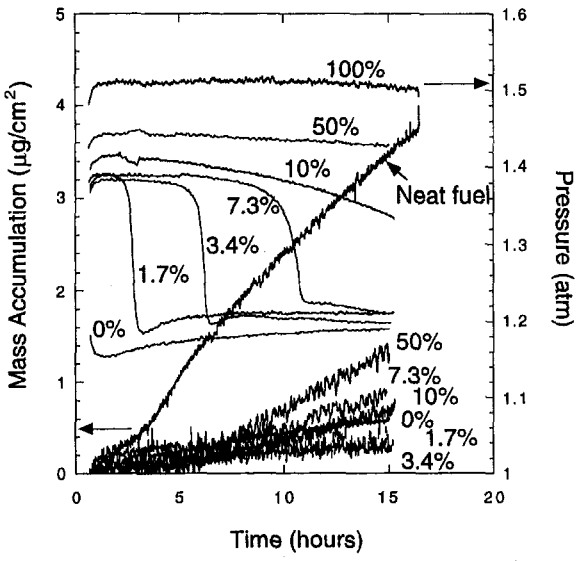

Fig. 8 Plots of mass accumulation versus time for dilution experiments at various percent fuel F-2827 concentrations

shown the results for mixtures composed of 1.7, 3.4, 7.3, 10, and 50 percent fuel F-2827. As the fuel is increasingly diluted, the oxygen removal begins to occur earlier in the run. The 50 percent run shows little pressure decay, while the 10 percent run begins to exhibit a small decay near the end of the run. The 7.3 percent run exhibits oxygen removal near 10 hours, the 3.4 percent run near 6 hours, and the 1.7 percent run near 3 hours. The corresponding deposition measurements show a reduction in deposition for the 50 percent run to 1.3 $\mu g/cm^2$, and at increasing dilutions the depositions scatter around that of the 0 percent run at 0.6 $\mu g/cm^2$. The data of Fig. 8 have implications in three areas: improving the thermal stability of a fuel by dilution, using a slow oxidizing fuel as an antioxidant, and characterizing the "effective" antioxidant concentration of fuels. We will address these individually below.

When we dilute fuel F-2827 to 50 percent we observe that the oxygen removal behavior does not change significantly, while the deposition measured is lower by a factor of ≈2.8. This demonstrates that the mixture of a moderately high depositing fuel with a low depositing fuel can yield a low depositing fuel with a slow oxidation rate. Thus, dilution with an inexpensive hydrotreated fuel may yield a simple and relatively inexpensive method of improving the thermal stability of a highly depositing fuel.

Exxsol D80 is a low depositor but it consumes oxygen quite rapidly. Rapid oxygen consumption is a negative characteristic of a fuel due to the resulting production of peroxides and acids under storage conditions. Mixing Exxsol D80 with relatively small amounts of fuel F-2827 results in a fuel with much delayed oxygen consumption, as seen in Fig. 8. Mixtures with 1.7 percent F-2827 delay oxidation for 2–3 hours, 3.4 percent delays oxidation for 7 hours, while 7.3 percent delays oxidation for 10–11 hours. From this point of view, the addition of small amounts of the slow oxidizing fuel F-2827 to the fast oxidizing "fuel" Exxsol D80 results in inhibition of oxygen consumption. Thus fuel F-2827 acts as an antioxidant when added in small quantities (<10 percent) to Exxsol D80 without significantly affecting deposition detrimentally. This demonstrates that a slow oxidizing fuel can be added to a fast oxidizing fuel to improve oxygen consumption characteristics and storage stability.

The dilution of a fuel with a solvent such as Exxsol D80 can also be used to determine the relative effective antioxidant concentration of the fuel. A characteristic of each individual fuel is the amount of fuel dilution required to bring the time

Downloaded 02 Jun 2010 to 171.66.16.104. Redistribution subject to ASME license or copyright; see http://www.asme.org/terms/Terms_Use.cfm

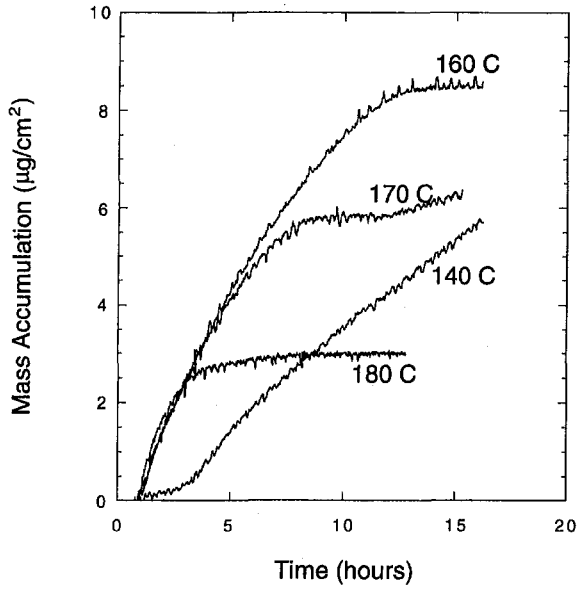

Fig. 9 Plots of mass accumulation versus time for fuel F-2827 over the temperature range 140 to 180°C at 20 psi added air

required for oxygen removal to a given value. Thus by performing this dilution procedure on various fuels and comparing the dilution amount, one can measure a relative effective antioxidant concentration, as the dilution required should be inversely proportional to the effective antioxidant concentration of the fuel. Of course such a relationship between dilution and effective antioxidant concentration is not necessarily linear, but an assumed linearity is sufficient for a relative measure of characterizing fuel antioxidant capabilities. With the current QCM/pressure measurement system this technique would only work on fuels that exhibit significantly delayed oxidation; it would not work on fast-oxidizing fuels. At this time we have not utilized this technique to compare various fuels, but it is a method that provides a way of comparing the relative antioxidant capabilities of fuels.

Effect of Temperature on Deposition. We have investigated the effect of temperature on the deposition of two jet fuels over the temperature range 140 to 180°C. The results are shown in Figs. 9 and 10. These runs were conducted in a similar manner to those described above for the oxygen dependence studies. The fuel was sparged with N_2 gas for one hour to remove the dissolved oxygen present in the fuel and headspace. As seen in the figures, the deposition rates at the higher temperatures are very rapid; the removal of oxygen minimizes deposition during the 45 minute heat-up period when QCM deposition measurements cannot be taken. After fuel heat-up, air is added to the reactor via the gas inlet until a given headspace pressure is reached. It is important to note that the headspace temperature is not measured or controlled, nor is its temperature uniformity known. Thus we do not know if the air bubbled through the fuel that resides in the headspace is at the fuel's temperature or lower. Thus it is difficult to control the oxygen availability of the fuel over a range of temperatures. The worst case situation is if the air actually reaches the fuel temperature; using the ideal gas law, this yields a decrease in oxygen availability of ≈9 percent in going from 140 to 180°C. As the reproducibility of the deposition measurements is greater than 9 percent, these concerns are minimized.

The data of Fig. 9 are for fuel F-2827 with 20 psi of added air. The data of Fig. 10 are for fuel F-2980 with 15 psi added air. Figure 9 shows that as the temperature is increased the rate of deposition appears to increase. This is especially apparent in going from 140 to 160°C. The figure also shows that the time at which the deposition levels off decreases with temperature. At 140°C the leveling has not occurred even at 15 hours, at 160°C leveling occurs near 13 hours, at 170°C leveling occurs near 9 hours, and at 180°C leveling occurs near 4 hours. The leveling off of deposition correlates quite well with the time at which oxygen consumption is complete for a wide variety of fuels (Zabarnick, 1994). Thus the data of Fig. 9 imply that oxygen consumption occurs more rapidly at higher temperatures, which is in agreement with previous observations (Hazlett, 1991). Interestingly, the final deposition at the end of the run displays complex temperature behavior. At 140°C the final deposition is 5.7 $\mu g/cm^2$, at 160°C the final deposition is 8.5 $\mu g/cm^2$, at 170°C the final deposition is 6.3 $\mu g/cm^2$, and at 180°C the final deposition is 3.0 $\mu g/cm^2$. Thus, there exists a temperature at which the deposition is a maximum, in this case 160°C; at both higher and lower temperatures the final deposition is lower. Figure 10 shows similar results for fuel F-2980, except that the peak temperature for final deposition for this fuel is 150°C.

The relationship between the final deposition and temperature is interesting because it appears to conflict with the conventional wisdom that deposition increases with temperature in the autoxidative temperature regime (Hazlett, 1991). This observation was based, for the most part, on devices operated in oxygen availability regimes that are different from the QCM system, as operated in the present work. Two such tests are static flask tests with bubbling oxygen/air and flowing heated tube tests. The flask tests have unlimited oxygen availability and thus the increase in deposits measured versus temperature results from the measurement reflecting the increase in deposition rate with temperature (i.e., the oxidation rate increases with temperature and therefore the deposition rate will reflect this behavior under unlimited oxygen conditions). Figures 9 and 10 show that the deposition *rate* does indeed increase with temperature in the QCM. The complex behavior observed here where the final deposition is lower at the highest temperatures measured is a result of the oxygen limited regime studied here. This behavior is a result of varying deposition with temperature for a given amount of oxygen consumed. The final deposition in an oxygen-limited system represents a measure of the efficiency of generating a given deposition level for a given amount of oxygen. This type of behavior is not monitored in bubbling flask experiments where the fuel has an unlimited oxygen availability.

Flowing heated tube experiments have yet a different regime of oxygen availability. Relatively high temperature and short

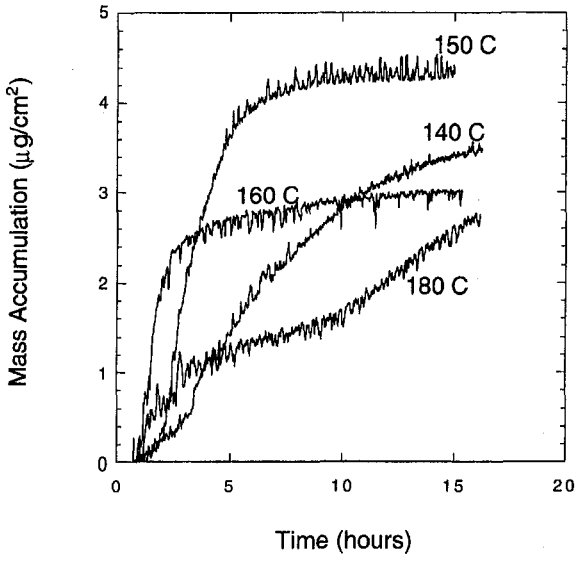

Fig. 10 Plots of mass accumulation versus time for fuel F-2980 over the temperature range 140 to 180°C at 15 psi added air

Downloaded 02 Jun 2010 to 171.66.16.104. Redistribution subject to ASME license or copyright; see http://www.asme.org/terms/Terms_Use.cfm

residence time tests such as the JFTOT (Hazlett, 1991) and the EDTST (Binns et al., 1994) often operate under conditions where oxygen consumption in the bulk fuel is not complete. The relatively short residence time and laminar flow conditions result in oxygen consumption occurring near the tube wall surface, while the bulk fuel does not show significant oxygen removal. The result is that the bulk fuel is able to supply essentially unlimited oxygen for reaction at the surface. Thus the apparent oxygen availability at the surface is unlimited. This results in the deposition versus temperature deposition rates as explained above for the bubbling air/oxygen flask experiments. Recently, other workers have observed a decrease in total deposition versus temperature above 185°C in a flowing heated tube (Jones et al., 1994). These experiments were conducted under very slow flow conditions, where complete oxygen consumption occurs within the tube. Thus the total deposition measured in these slow flow experiments is not dependent on the deposition rate but on the efficiency of deposit production for a given amount of oxygen, similar to the QCM system.

Conclusions

We have used the QCM/pressure measurement technique to study the thermal stability and oxidation characteristics of jet fuel. Both final deposit amounts and deposition rates were found to display complex dependencies on the oxygen availability; in addition, this behavior was observed to be fuel dependent. It was found that gold, aluminum, and platinum electrode surfaces yield similar deposition for fuel F-2827. Gold and aluminum electrodes yield similar results in fuel F-2747, but a platinum electrode gives significantly higher deposition for this fuel. Dilution of a moderate thermal stability fuel with a hydrocarbon solvent improves the thermal stability of the fuel without adversely effecting its oxidation characteristics. Addition of a slow oxidizing fuel to a hydrocarbon solvent can significantly delay oxidation of the solvent. The study of dilution of a slow oxidizing fuel with a hydrocarbon solvent can provide a measure of the relative effective antioxidant concentration of the fuel. Under limited oxygen conditions, we find that the final deposition increases and then decreases over the temperature range 140 to 180°C for two different fuels.

Acknowledgments

This work was supported by the US Air Force, Fuels and Lubrication Division, Wright Laboratories, Wright-Patterson AFB under contract No. F33615-92-C-2207 with Mr. Charles Frayne as technical monitor. We would like to thank Tom Wittberg (UDRI) for performing the Auger spectroscopy analyses.

References

Binns, K., Dieterle, G., Kalt, D., Martel, C., and Williams, T., 1994, "System Evaluation of Improved Thermal Stability Jet Fuels," *presented at the 5th International Conference on Stability and Handling of Liquid Fuels, Rotterdam, the Netherlands.*

Hazlett, R. N., 1991, "Thermal Oxidation Stability of Aviation Turbine Fuels," ASTM, Philadelphia.

Heneghan, S. P., and Zabarnick, S., 1994, "Oxidation of Jet Fuels and the Formation of Deposits," *Fuel,* Vol. 73, pp. 35–43.

Jones, E. G., Anderson, S. D., Goss, L. P., and Balster, W. J., 1994, "The Effect of Additives on the Formation of Insolubles in a Jet A Fuel," presented at the 5th International Conference on Stability and Handling of Liquid Fuels, Rotterdam, the Netherlands.

Klavetter, E. A., Martin, S. J., and Wessendorf, K. O., 1993, "Monitoring Jet Fuel Thermal Stability Using a Quartz Crystal Microbalance," *Energy and Fuels,* Vol. 7, pp. 582–588.

Martin, S. J., Granstaff, V. E., and Frye, G. C., 1991, "Characterization of a Quartz Crystal Microbalance With Simultaneous Mass and Liquid Loading," *Analytical Chemistry,* Vol. 63, pp. 2272–2281.

Ricciardiello, F., and Riotti, S., 1972, "The Corrosion of Fe and Ag in S Liquid at Low Temperature. Effect of S Viscosity," *Corrosion Science,* Vol. 12, pp. 651–659.

Zabarnick, S., 1994, "Studies of Jet Fuel Thermal Stability and Oxidation Using a Quartz Crystal Microbalance and Pressure Measurements," *Industrial and Engineering Chemistry Research,* Vol. 33, pp. 1348–1354.

Zabarnick, S., and Grinstead, R. R., 1994, "Studies of Jet Fuel Additives Using the Quartz Crystal Microbalance and Pressure Monitoring at 140°C," *Industrial and Engineering Chemistry Research,* Vol. 33, pp. 2771–2777.

Downloaded 02 Jun 2010 to 171.66.16.104. Redistribution subject to ASME license or copyright; see http://www.asme.org/terms/Terms_Use.cfm

Surface Effects on Deposits From Jet Fuels

J. S. Ervin

S. P. Heneghan

C. R. Martel

T. F. Williams

University of Dayton, Dayton, OH 45469

Flow experiments in a single-pass heat exchanger using JP-8 and certain additives were initiated under controlled conditions to explore the effects of a metal surface on deposition. The experimental apparatus permitted a unique viewing of the time evolution of deposits at different axial locations under conditions of limited oxygen availability somewhat similar to those in jet aircraft. Scanning electron microscopy was used to examine deposit microstructure. In addition, x-ray photoelectron spectroscopy and Auger electron spectroscopy determined the chemical composition of the deposits. Oxygen concentration measurements in the bulk flow were also performed, and the observed transient oxidation behavior was related to measured time-dependent changes in the deposit. Increasing dissolved oxygen levels and large changes in deposition were characteristic of the induction time. Mechanisms of fouling in the heated and cooled sections were different. Spectroscopic analysis indicated that deposits formed in the heated section had chemical compositions different from those formed in the cooled section. Scanning electron microscopy revealed differences in microstructure between the heated and cooled sections: More uniform deposits formed in the cooled section as a result of once-soluble species becoming insoluble at low temperatures. In addition, the JP-8 additives significantly reduced fouling in the heated section, but their effectiveness in the cooled section, especially after long periods, was unclear.

Introduction

In jet aircraft, fuel is employed as a heat transfer medium to cool the engine lubricant, hydraulic fluids, environmental system, and avionics. Further increases in fuel temperature occur with flow through the main fuel pump and the burner feed arm. Combined, the heat flux from these sources stimulates oxidation reactions, which ultimately result in deposits within fuel lines, on heat exchanger surfaces, and in fuel injectors (Hazlett, 1991). The gradual fouling of tubes within heat exchangers eventually leads to degradation of heat transfer effectiveness since the presence of the deposit increases the thermal resistance between the heated tube wall and the flowing fuel (Johnson et al., 1954; Bradley et al., 1974; Hazlett, 1981; Hazlett and Hall, 1985; Chin and Lefebvre, 1993). Ultimately, if unchecked, the fouling of valves and other close tolerance parts may result in failure of the fuel system. In addition, fouling of fuel nozzles can produce undesirable spray patterns, which cause severe thermal stressing and degradation of the combustor and turbine. Hence, knowledge of the physical structure and chemical properties of deposits, together with an understanding of accumulation mechanisms on metal surfaces, is of great value to jet aircraft designers.

The surface of a heated tube influences the deposition rate by both physical and chemical action, as has been demonstrated by experiment (Hazlett, 1991). The microgeometry of the surface affects the fluid motion near the wall, promoting turbulence and increased mass transport (Smith, 1969; Bradley et al., 1974). Also, the capillary mechanism and the increased surface area as a result of porosity changes are believed to have some role in the observed accelerated deposition rate during long-term testing (Giovanetti and Szetela, 1985; Kamin et al., 1988).

The chemical composition of the tube wall can also determine deposition reactions. For example, Kendall and Mills (1985) and have found that stainless-steel tubes tend to form more deposits than aluminum tubes, and that magnesium migration to the surface of an aluminum tube inhibits fouling. As part of a research program with the United States Air Force involving JP-8 fuels, Lefebvre (1992) found that the deposition rate depends on the metal surface pretreatment. In addition, Heneghan et al. (1985) proposed that a surface-catalyzed peroxide decomposition was responsible for some deposits formed at low temperatures.

Experiments were performed to study fuel deposition under controlled conditions in a forced-flow system in order to investigate effects of the wall and to obtain baseline data on the structure and chemical compositions of deposits after different time periods. Scanning electron microscopy (SEM) is used to examine deposit microstructure, and, in addition, x-ray photoelectron spectroscopy (XPS) and Auger electron spectroscopy (AES) are used to study the chemical composition of the deposits. The experimental arrangement described herein has the unique capability of permitting viewing of the time evolution of deposits under conditions of nonisothermal bulk flow with limited oxygen availability similar to that in jet aircraft.

Apparatus

In the experimental arrangement described in detail by Heneghan et al. (1993) (Fig. 1), fuel at ambient temperature passes from the preconditioning tank by means of a positive displacement diaphragm pump into the first heated block at a pressure of 2.48 MPa; then, eventually, it passes into a cooled block. The insoluble solids were produced by liquid-phase reactions alone since the high pressure maintained the fuel in the compressed liquid state. In the preconditioning tank, the fuel may be sparged with mixtures of nitrogen and oxygen to control the amount of dissolved oxygen and displace argon from the fuel in order to avoid misinterpretations of gas chromatograph measurements. In addition, a positive displacement flow meter monitors the volumetric flow rate of the fuel.

The two heated copper blocks are connected in series and envelope the 316 stainless-steel tubing (180 cm long by 2.16 mm ID by 3.18 mm OD) through which the fuel passes. Each block (46 cm long with a 7.6 cm diameter) can reach tempera-

Contributed by the International Gas Turbine Institute and presented at the 40th International Gas Turbine and Aeroengine Congress and Exhibition, Houston, Texas, June 5–8, 1995. Manuscript received by the International Gas Turbine Institute February 10, 1995. Paper No. 95-GT-103. Associate Technical Editor: C. J. Russo.

Copyright © 1996 by ASME

Downloaded 02 Jun 2010 to 171.66.16.104. Redistribution subject to ASME license or copyright; see http://www.asme.org/terms/Terms_Use.cfm

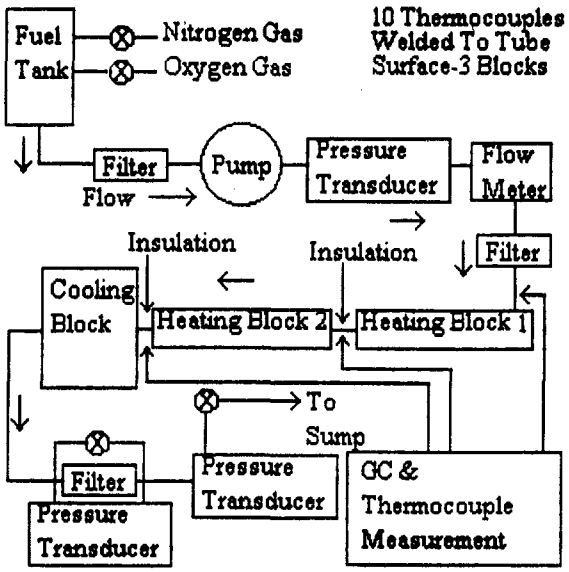

Fig. 1 Experimental apparatus

tures near 770 K and is controlled in such a way that the tube wall temperature distribution remains steady (within ± 2°C). The cooled section consists of an air-cooled copper block (46 cm long with a 7.6 cm diameter), which results in an exiting fuel bulk temperature near ambient. Calibrated type K thermocouples (20 gage) are welded to the outer surface of the stainless-steel tubing to provide the outer tube wall temperature with an uncertainty of ±1°C in both the heated and cooled sections. The stainless-steel tubes (ASTM grade A269/A213) have a surface roughness (arithmetic average) of 8 to 15 min. and are cleaned with Blue Gold alkaline solution in an ultrasonic bath, then rinsed with deionized water prior to use.

Two types of fuels were used: JP-8 and JP-8 with 25 mg/l of BHT (an antioxidant) and 100 mg/l of a dispersant (Betz Process Chemicals 8Q405). The mixture of JP-8 fuel, BHT, and 8Q405 is referred to below as JP-8A. The JP-8 fuel consisted of a Jet A fuel (POSF 2980) and the additives given by military specification MIL-T-83133. The chemical and physical properties of POSF 2980 are listed by Grinstead et al. (1994). Furthermore, Anderson et al. (1994) have identified BHT and 8Q405 as effective deposit-suppressing additives.

Oxygen is detected in-line by means of a Hewlett Packard 5890 Series II gas chromatograph with a microthermal conductivity detector; oxygen concentrations as low as 150 parts per billion can be detected. Oxygen concentrations are measured at the locations shown in Fig. 1: at the inlet of the first heated block, at the inlet of the second heated block, and at the inlet before the cooled block. Details of the installation, fabrication, and calibration of the oxygen analyzer are given by Rubey et al. (1992).

Procedure

In the current experiments, fuel flowed through the apparatus at a rate of 4 ml/min for periods of 0.5, 1.5, 3, 6, 12, or 24 hours. The heated section of the flow loop had bulk temperatures near 493 K for the JP-8 tests and 503 K for the JP-8A tests. A few preliminary tests demonstrated that a slightly higher bulk temperature of 503 K is required to have detectable deposition within the heated section when using JP-8A. The dissolved oxygen measured at the end of the first heated block for the tests involving JP-8A was nearly equal to that for tests with JP-8. In addition, increasing the bulk temperature for the JP-8A experiments resulted in maximum deposition at an axial location in the heated section coincident with that for tests performed with JP-8 alone. The temperature of the cooling block in all cases was held near 25°C.

At the termination of an experiment, the tubes are removed from the system, drained, and rinsed with hexane. They are then dried by flowing filtered, low-velocity nitrogen gas through them. Finally, they are sliced into 50-mm segments. The segments to be analyzed were halved in the axial direction, rinsed in hexane, and dried in a vacuum oven at 120°C for one hour. A Leco (RC-412) multiphase carbon analyzer determined the amount of carbon on half the segments from the carbon dioxide produced from complete combustion of the deposits. SEM determined the deposit microstructure and was used in conjunction with AES and XPS on the remaining segments.

XPS determined the composition of the first three nanometers of the inner tube surface, which was exposed to the thermally stressed fuel. With the AES measurements, a 100-μm-by-100-μm area was raster scanned and internal layers (up to a distance of 150 nm) within the deposit were probed. Uncertainties in the XPS measurements are on the order of 10 percent of the given value. Uncertainties in the absolute value of the composition, with regard to AES profiles of the deposits, are difficult to quantify because of preferential sputtering of certain species. Therefore, only qualitative comparisons can be made between XPS and AES measurements (Wittberg, 1994; Briggs and Seah, 1983).

Results

Axial Temperature and Oxygen Concentration Distributions. The outer tube wall and axial liquid bulk temperature distributions for the JP-8 fuel are given in Fig. 2; the origin corresponds to the inlet of the first heater block. The bulk temperature was steady, save for a moment as the experiment was initiated, indicating no detectable change in heat transfer from the heated blocks to the flowing fuel as the deposit accumulated. The fuel bulk temperature was calculated by finite difference solution of the coupled continuity, momentum, and energy equations using the outer tube wall temperature distribution and the thermal properties of the fuel and tube. The outer tube wall temperature distribution results from a least-squares fit of measured temperatures. The computational procedure, which permits the computation of the bulk temperature, is essentially the SIMPLE algorithm of Patankar (1980) and is described in more detail by Katta et al. (1994) and Krazinski et al. (1992). Turbulent flow conditions were assumed even though the Reynolds number in much of the tube was less than 2300. As described by Katta et al. (1994), buoyancy effects may induce

Nomenclature

AES = Auger electron spectroscopy
ASTM = American Society for Testing and Materials
BHT = butylated-hydroxy-toluene
JP-8A = JP-8 with BHT and 8Q405
JP-8 = POSF 2980 with icing inhibitor, static dissipator, and corrosion inhibitor
$O(z)$ = oxygen composition distribution
POSF 2980 = jet A-neat fuel
SEM = scanning electron microscopy
t = time
XPS = x-ray photoelectron spectroscopy
z = coordinate direction normal to deposit surface
α = spatial mean value of oxygen composition
δ = deposit thickness, nm
δ' = average rate of change in deposit thickness, nm/h
8Q405 = Betz Corp. proprietary dispersant

Downloaded 02 Jun 2010 to 171.66.16.104. Redistribution subject to ASME license or copyright; see http://www.asme.org/terms/Terms_Use.cfm

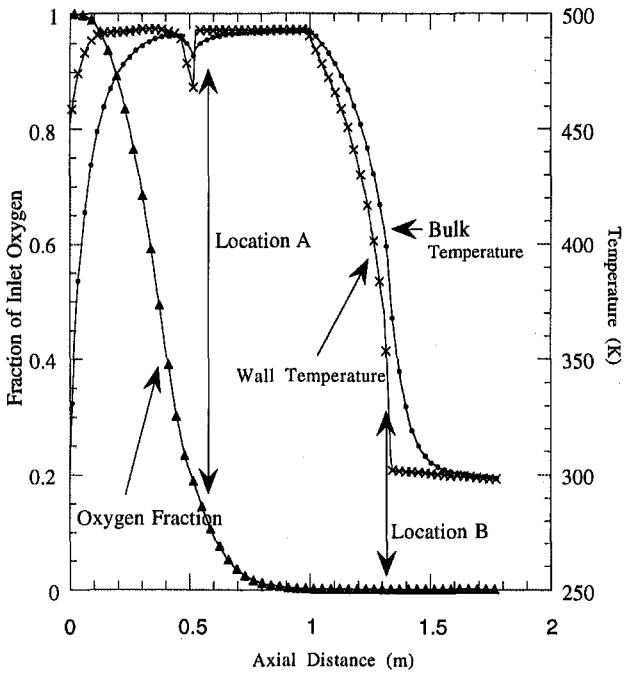

Fig. 2 Bulk oxygen and temperature distributions for JP-8 after 0.5 H

transition to turbulent flow. Furthermore, bulk fuel temperatures measured at different locations were in agreement with computed values (within 3 K). In Fig. 2 and subsequent figures, A and B correspond to local maxima in deposition as determined by carbon burnoff of tube segments, except for the period of 0.5 hours. At location A (near 55 cm), the temperature profile within the tube is essentially fully developed, and the bulk temperature is 493 K for the JP-8 tests and 503 K for the JP-8A tests. At B (near 130 cm), the bulk fuel temperature is 400 K for the JP-8 tests and 410 K for the JP-8A tests. The axial bulk temperature distribution for the JP-8A fuel was similar to that of the JP-8 fuel, except that it was 10°C greater in the heated section and in the entrance region of the cooled section.

Figure 2 shows computed transient oxygen concentrations (after 0.5 hours) ratioed by oxygen concentrations for JP-8 saturated with air. The oxygen concentration computations were performed using the same procedure as that for computation of the bulk temperatures. Measured values of the dissolved oxygen fraction compared well with the computed values. Oxygen distributions for other periods lie to the right of this curve, and oxygen distributions for JP-8A are similar to those of JP-8. In all instances at location A, the concentration of available dissolved oxygen is significantly reduced compared to the inlet conditions; at B, it is depleted.

To investigate the possibility of oxygen diffusion from the tubing or contamination from other sources, the fuel was first saturated with nitrogen gas, then pumped through the heated tubing. Since the oxygen concentration did not increase with time under nearly identical conditions (other than saturating the fuel with nitrogen gas), it was concluded that diffusion of oxygen from the walls was insignificant.

Carbon Mass Determination. In previous investigations such as Marteney (1989), deposit mass was described as a function of time, and the deposition rate increased after large times. Here, it is more physically meaningful to normalize the deposition by the total volume of fuel that has flowed for a given experiment. In Figure 3(a) for JP-8 and Fig. 3(b) for JP-8A, the deposition, determined by carbon-burnoff measurements, is scaled by the volume of fuel flowed for the tube in the first heated copper block. In addition, dissolved oxygen levels are given. The carbon deposition rate for the JP-8A mixture was an order of magnitude lower than that of JP-8.

In Figs. 4(a) and 4(b), the carbon mass, normalized by the inner surface area of the tube, is given for different axial locations, time durations, and fuels. In Fig. 4(a) for the JP-8, as might be intuitively expected, the carbon mass for the 24-hour test is greater than that for the shorter tests. However, the carbon accumulated along the tube after 0.5 hours and then after 1.5 hours is nearly the same; a similar comparison can be drawn between measurements at three and six hours. This seemingly inconsistent behavior is still reasonable since the reproducibility in the determination of the mass of carbon is on the order of ±25 percent. For all the times except 0.5 hours, there are two peak locations in the spatial distribution of the carbon deposit

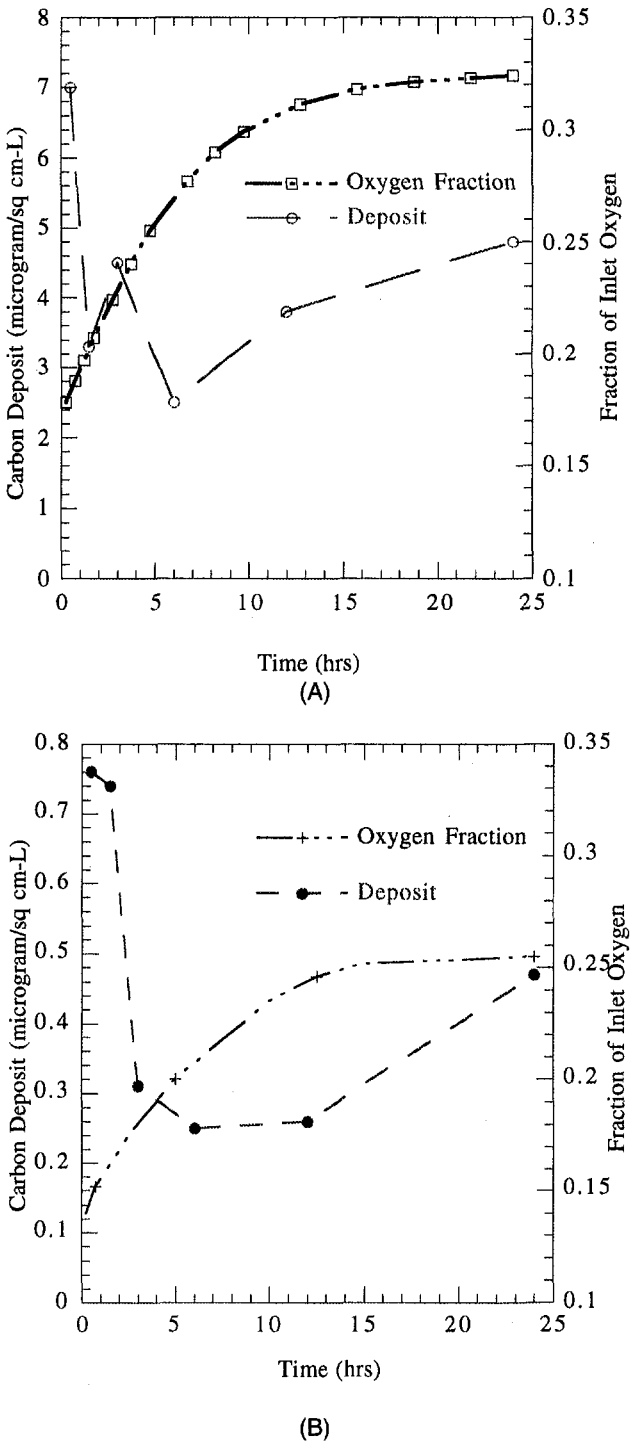

Fig. 3 Carbon deposition and fraction of inlet oxygen, heater block 1: (*A*) JP-8 fuel; (*B*) JP-8A fuel

Downloaded 02 Jun 2010 to 171.66.16.104. Redistribution subject to ASME license or copyright; see http://www.asme.org/terms/Terms_Use.cfm

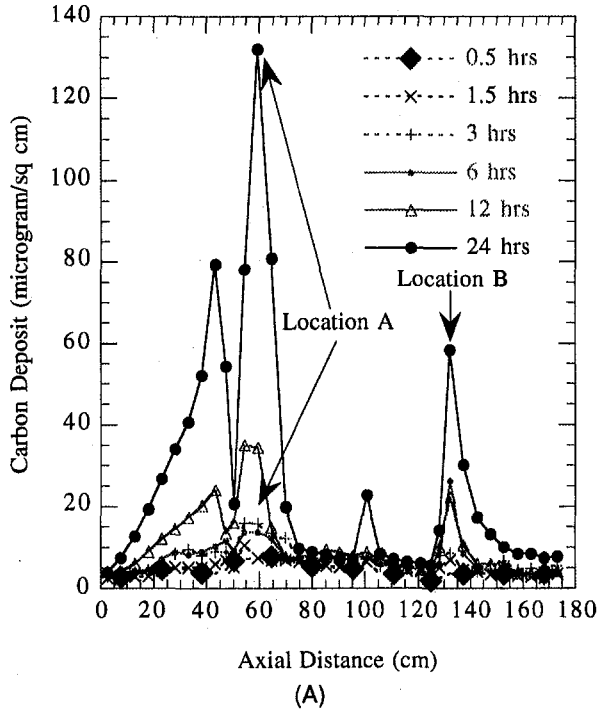

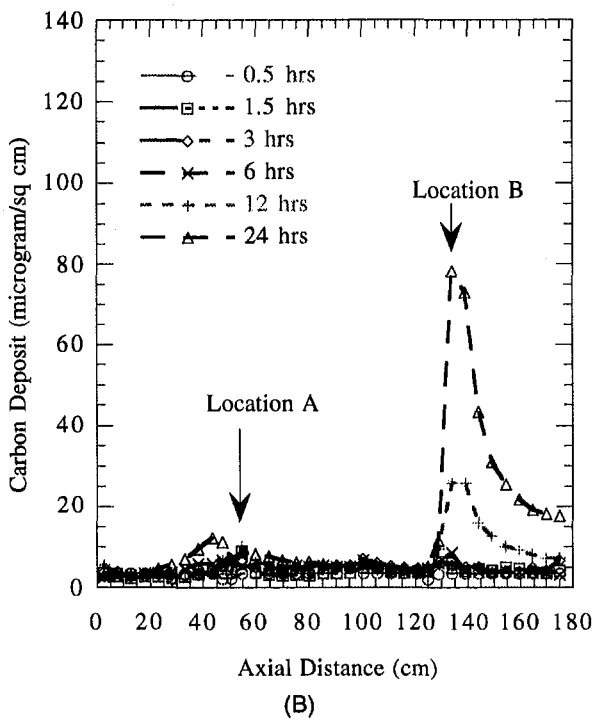

Fig. 4 Carbon deposition: (*A*) JP-8 fuel; (*B*) JP-8A fuel

as described above: locations A and B. In Fig. 4(b) for JP-8A with conditions somewhat similar to those in Fig. 4(a) except for the bulk temperature, locations A and B again correspond to the two maximal peaks in the spatial distribution of carbon.

Scanning Electron Microscopy

JP-8 Fuel. Figure 5(a) is a digitized image of the inner surface of a representative sample of the stainless-steel tube before exposure to thermally stressed JP-8 fuel. Asperities, pits, and grain boundaries are clearly visible. (For Figs. 5(a)–5(c), the magnification is 5000× and a scale of one micron is shown for reference.) Figure 5(b), a photograph of the interior of the tube corresponding to a bulk temperature of 220°C at location A, reveals very fine particles attached to the wall. The pits and microcrevices observed with the blank tube remain distinguishable after three hours of passing heated fuel through the tube. After 12 hours, the features of the underlying tube surface are no longer visible in Fig. 5(c), where the deposit appears to be porous and composed of fine submicron particles. The porosity would seem to be responsible for any accelerated deposit growth since the porous structure would trap fuel largely by capillary action. The trapped fuel would then remain at the higher temperature of the wall deposit for a longer residence time than otherwise might occur if it had not been trapped. Moreover, this porous microstructure has more surface area than that found with a nonporous, smooth deposit for the adhesion of insoluble bulk particles.

In Fig. 5(d), the magnified image (4000×) of location B after three hours shows a flakelike microstructure, which conforms to the topography of the underlying tube surface, and the deposit surface has a roughness length scale smaller than that of the original metal surface but larger than that of the deposits in Figs. 5(b) and 5(c). Similar microstructure is also observed after six-hour and twelve-hour periods.

SEM did not reveal any distinguishable structure on the tube surfaces at locations A and B for periods of 0.5 and 1.5 hours with JP-8.

JP-8A Fuel. For all the tests with JP-8A, the deposit thickness at A was in the range of 10 to 40 nm. As a consequence of this very thin layer, no deposit structure in the heated section was perceptible with SEM, and the magnified images resembled those of the unused tube surface. Figure 5(e) is a SEM image (magnification 3000×) following a 12-hour test from the cooled section at location B. The deposit micrograph, compared to the image of the unused tube of Fig. 5(a), is smooth, suggesting the uniform attachment of polymerized molecules as in the tests without the BHT and 8Q405. There are fissures in the deposit that are most likely the result of sectioning the tube. The large circles at the left side of the photo are cavities that have formed as pieces of the deposit have broken away; the metal surface below is visible within the confines of these circles. The structure of the deposit at B after six hours was similar in appearance to that after twelve hours; for times less than six hours, the microstructure was not discernible.

AES and XPS Analysis

Auger Electron Spectroscopy. AES elemental composition profiles were measured within the deposits for both the JP-8 and JP-8A experiments. In addition, the deposit thickness, δ, which changed only very gradually across the length of each piece of segmented tube, was obtained. As indicated in Figs. 6(a) and 6(b) (following a six-hour test), δ is defined as the distance from the surface exposed to the fuel to the point where the iron and carbon profiles intersect on an AES mapping. The sputter rate for the depth profiles was roughly 8 nm/min, and the maximum depth of profiling into the deposit with a reasonable certainty in the composition was 150 nm.

X-Ray Photoelectron Spectroscopy. Table 1 presents the XPS results for the JP-8 fuel at locations A and B for time durations of 0.5, 1.5, 3, and 6 hours, and an analysis of an unused tube is given for reference. The chemical composition of the deposit surface nearest the flowing fuel at either A or B essentially does not appear to change for periods greater than three hours. The organic acid, ester, aldehyde, and ketone compositions are nearly the same for a given period at A. However, upon comparison of the composition at A with that at B, we find that the organic acid, ester, aldehyde, and ketone composition is lower at B. The alcohol and ether compositions at A and B are similar. The deposit does not cover the tube wall at the end of a 1.5-h period for location B and, as a result, silicon and chromium are still detected.

Downloaded 02 Jun 2010 to 171.66.16.104. Redistribution subject to ASME license or copyright; see http://www.asme.org/terms/Terms_Use.cfm

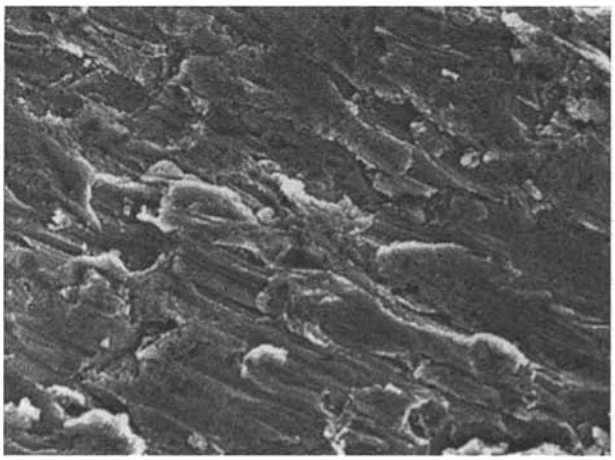

Fig. 5(*A*) Magnification 5000×; scale: 1 micron = ——

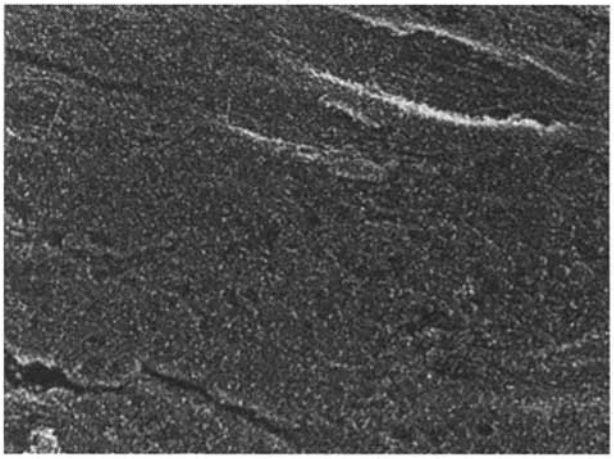

Fig. 5(*B*) Magnification 5000×; scale: 1 micron = ——

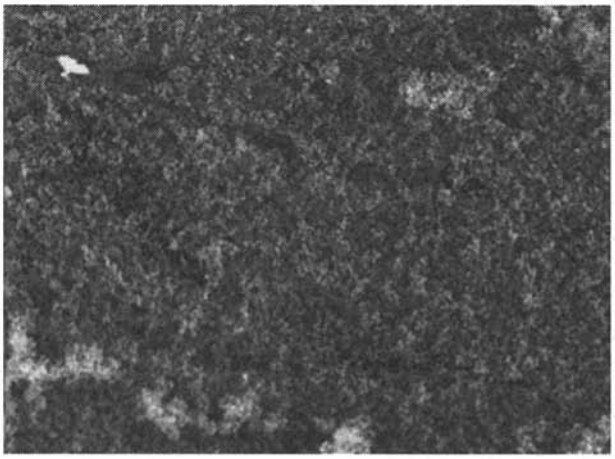

Fig. 5(*C*) Magnification 5000×; scale: 1 micron = ——

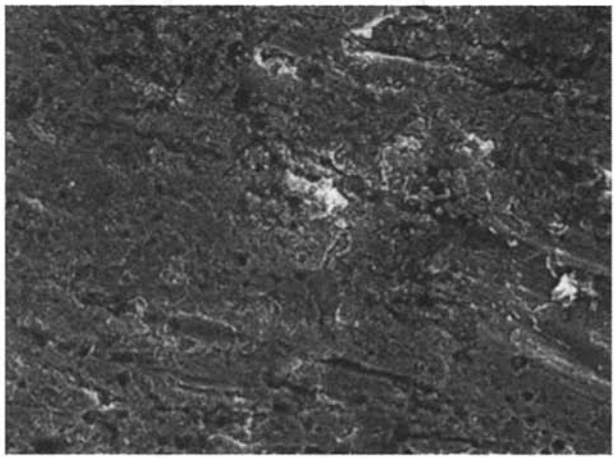

Fig. 5(*D*) Magnification 4000×; scale: 1 micron = ——

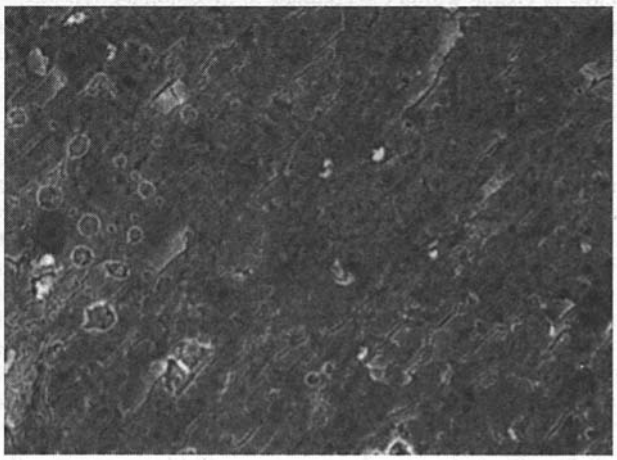

Fig. 5(*E*) Magnification 3000×; scale: 1 micron = ——

Fig. 5 SEM images of tube surfaces at locations A and B: (*A*) unused tube; (*B*) A after 3 h, JP-8 fuel; (*C*) A after 12 h, JP-8 fuel; (*D*) B after 3 h, JP-8 fuel; (*E*) B after 12 h, JP-8A fuel

In Table 2, there are differences in the surface composition between locations A and B, especially with regard to acids and esters, alcohols and ethers, hydrocarbons and elemental carbon, elemental oxygen, sulfur oxides, and sulfides. A comparison of Tables 1 and 2 reveals that the BHT and 8Q405 additives to the JP-8 have changed the chemical composition of the deposits at A with the following trends: CH, C, and C–S are greater with JP-8A, but O and S–O are lower with JP-8A. At B, the following trends are observed: aldehydes and ketones and C–S compounds are greater with JP-8A, but C–O and S–O compounds are lower with JP-8A. These results confirm prior reported measurements for jet fuels (Hazlett and Hall, 1981, 1985).

Discussion

Of particular interest in the AES measurements (Figs. 6(a) and 6(b)) was the elemental oxygen content of the deposit. Since the oxygen composition, $O(z)$, varies spatially, it is convenient to examine the spatial mean value of the oxygen composition, a, as a function of time. Thus,

$$\alpha = \frac{\int_0^{\delta(t)} O(z)dz}{\delta(t)} \tag{1}$$

Hence, the total area beneath the oxygen profile as in Fig. 6(a) is scaled by δ (deposit thickness). Figure 7 presents α for JP-8 and JP-8A. At 0.5 h, the oxygen composition is greater at B than at A because the deposit thickness at B is very thin and the metal surface has an initial oxide layer. It is interesting that the mean oxygen content in the deposit of Fig. 7 decreases as the dissolved oxygen level of Fig. 3 increases during the initial three hours, suggesting that the dissolved oxygen somehow preferentially becomes a constituent of the tube deposits early in testing. (Moreover, this trend in α is further corroborated by

Downloaded 02 Jun 2010 to 171.66.16.104. Redistribution subject to ASME license or copyright; see http://www.asme.org/terms/Terms_Use.cfm

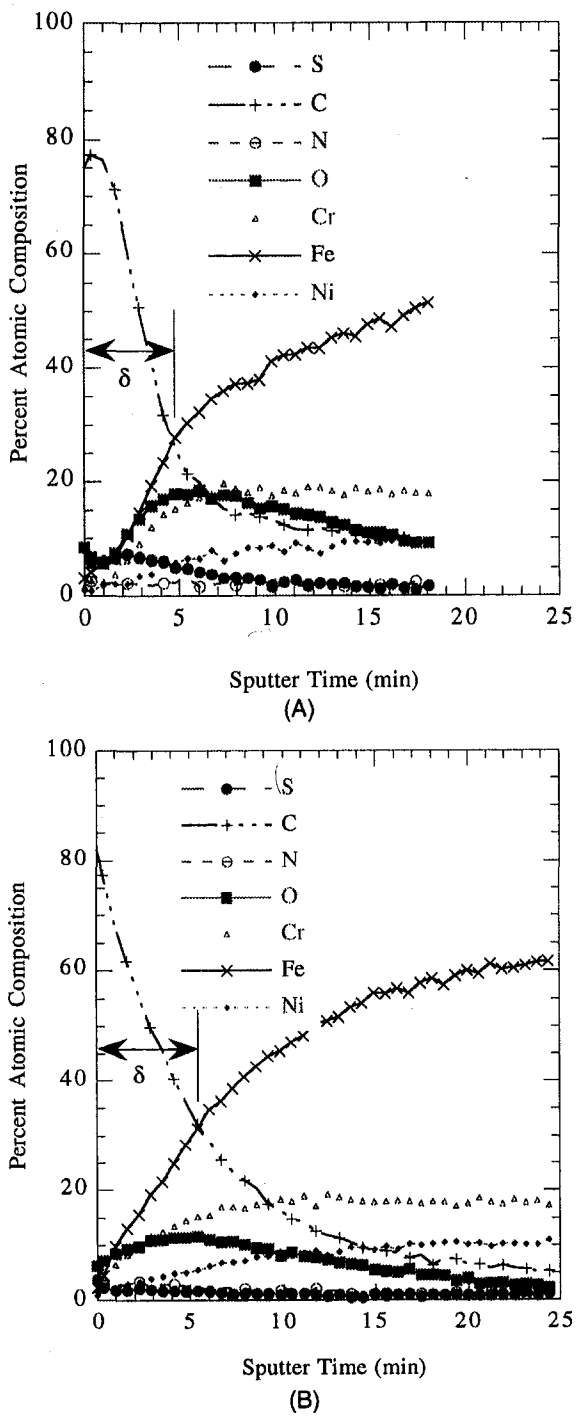

Fig. 6 AES profiles (after 6 hour test) for JP-8 fuel at location: (*A*) A; (*B*) B

the XPS deposit surface measurements in Tables 1 and 2 of O at both locations A and B for JP-8 and JP-8A.) In addition, as shown in Figs. 3(*a*) and 3(*b*), large changes in deposition per volume of fuel occur within the first three hours, are a minimum at the end of about six hours, then begin to increase gradually. These results may be contrasted by what is often ascribed to the induction period: small changes in deposition. The dissolved oxygen levels for both JP-8 and JP-8A increase with changes in the deposition for nearly ten hours, suggesting a relationship between disappearing active sites on the metal surface and the increasing oxygen levels. Similarly, Jones and Balster (1994) have observed changes in measured dissolved oxygen levels during the induction time in a flowing experiment.

JP-8 Fuel Deposits. Location A of Fig. 4 is in the region in which the dissolved oxygen is nearly depleted, but the rate of deposition is relatively high. Immediately downstream of A, the amount of deposition sharply declines. Heneghan et al. (1993a) have observed a similar peak in deposition simultaneously with dissolved oxygen depletion in flowing tests using the present experimental apparatus with certain other aviation fuels. At B, the bulk fuel temperature is nearly 100 K less than the bulk temperature at A. It is suspected that the deposition at B is a consequence of compounds that were soluble at higher temperatures but are now insoluble at lower temperatures. Hence, it might be anticipated that the physical mechanisms of deposition at A and B are very different; these differences will become more apparent with further consideration of the SEM, XPS, and AES measurements.

In the heated section at location A, a very thin (on the order of less than 50 nm) incipient polymolecular film that is detectable with AES forms on the metal surface before the appearance of detectable particles. In the AES measurements of Fig. 6(*a*), beginning with the surface of the deposit nearest the fuel, the local maxima and minima of the sulfur and oxygen distributions follow each other in cases of deposit formation at A, suggesting the presence of sulfur oxides. Their presence is further confirmed by XPS measurements and, perhaps, indicates the action of sulfonic acids. It is believed by many (Kendall et al., 1986; Mushrush et al., 1988; Heneghan and Kauffman, 1994; Kauffman, 1995; Schultz and Gillman, 1994) that sulfur-oxide compounds have some role in the initiation and subsequent growth of deposits under conditions of thermal stressing, as at location A. Furthermore, Kauffman (1995) has suggested a deposition mechanism for straight-run fuels involving phenols and sulfur compounds together with sulfur-oxide reactions at the metal surface. Deposits formed on heated steel wires were found to have sulfur and oxygen AES profiles similar to those measured here for location A.

At later periods at location A, particles formed on the incipient layer of deposit. It is important to note in the SEM image of Fig. 5(*b*) that there is not a continuous layer of particulate matter, but rather the particles are located at specific sites. This might be anticipated since grain boundaries, pits, and crevices all tend to trap impurities and are regions of higher free energy; thus, they are more likely to be nucleation sites. In addition, the observed site-specific formation is somewhat similar to that observed with the acid attack of metallic surfaces whereby the surface is affected at discrete locations, perhaps again suggesting the role of organic acids rather than a deposit film as might result from bulk particle migration to the walls. Similarly, Kendall et al. (1987) describe a layer of lacquer on a metal surface formed in the simulation of an injector feed arm. Microspheres (0.1 μm diameter) of deposit along with agglomerations of microspheres formed a "cauliflower" structure, which may have penetrated the lacquer surface.

The microstructure of the deposit (Fig. 5(*d*)), formed after three hours at location B with a lower bulk temperature of 400 K, is entirely different from that formed in the heated section of the tubing. The deposit is composed of layered lakes rather than fine particles, suggesting an entirely different mechanism for deposition. Moreover, the sulfur and oxygen distributions within the deposit, as determined by AES, appear unrelated. In fact, they move in opposite directions (Fig. 6). It is surmised that these solids are likely the result of polymerized molecules or agglomerates, which precipitate from solution at the lower temperature and eventually adhere to the wall. Schirmer (1970) found that deposits from a wide variety of fuel system simulators consistently were composed of microspheres and structures of randomly packed microspheres approximately 1000 Å in diameter. These microspheres sometimes fused to heated metal surfaces. A similar microsphere structure was observed for JP-8 fuel at location A. However, at location B for both JP-8 and JP-8A fuels, there was no microsphere structure but rather a

Downloaded 02 Jun 2010 to 171.66.16.104. Redistribution subject to ASME license or copyright; see http://www.asme.org/terms/Terms_Use.cfm

Table 1 XPS-determined percent atomic composition: JP-8 fuel

Hours	O-C=O	C=O	C-O	CH,C	O	Fe	N	S-O	C-S	Si	Cr	Total	Total	Total
A														
0	4.8	1.9	5.4	30.2	30.1	14.6	<0.7	0.9	<0.2	7.1	4.1	42.3	<1.1	99.1
0.5	3.7	4.4	5.7	45.1	30.6	5.5	2.4	2.2	0.46	-	-	58.9	2.7	100.1
1.5	4.1	4.6	7.8	49.9	26.1	3.4	1.8	1.6	0.53	-	-	66.4	2.1	99.8
3	4	4.8	6.8	50.4	27.2	2.8	2.1	1.5	0.34	-	-	66	1.8	99.9
6	4.5	4.6	7.3	51	26.2	2.5	1.8	1.7	0.37	-	-	67.4	2.1	100
B														
0	4.8	1.9	5.4	30.2	30.1	14.6	<0.7	0.90.	<0.2	7.1	4.1	42.3	<1.1	99.1
0.5	1.6	1.7	4.5	25.5	44.8	6.8	1.3	1.4	<0.2	8.3	3.9	33.3	<1.6	99.8
1.5	1.7	2.4	4.1	36.4	36.4	5.3	1.7	1.7	0.44	5.5	4.4	44.6	2.1	100
3	1.4	3.1	6.1	58.6	22.2	2.7	3	2.4	0.35	-	-	69.2	2.8	99.9
6	1.4	2.8	6.6	56.4	23.2	3.8	3.1	2.4	0.33	-	-	67.2	2.7	100

O—C=O, acids and esters; C=O, aldehydes and ketones; C—O, alcohols and ethers; CH and C, hydrocarbons and carbon; S—O, sulfur oxides; C—S, sulfides

continuous structure that somewhat resembled micrographs of asphalt formed at much higher temperatures.

JP-8A Fuel Deposits. As might be anticipated, the deposition at A using JP-8A (Fig. 4(*b*)) for periods greater than or equal to three hours is less than that at A for the experiments with JP-8 (Fig. 4(*a*). However, at B, following 12 hours of fuel flow, the amount of deposition was nearly the same as that formed with JP-8. After 24 hours of heating, the deposition at B with JP-8A was actually greater than that at B with JP-8 as in Fig. 4(*a*). Furthermore, the maximum deposition for longer times did not occur near A but rather at B in the cooled section. Hence, the BHT and 8Q405 additives are effective in altering the deposition mechanisms that occur at high temperatures but appear to be ineffective in preventing deposition at low temperatures for long periods under the conditions of the present experiments. The mechanisms of deposition in the cooled section seem to be related to the solubility of the oxidized products; as a result, an antioxidant such as BHT would not be expected necessarily to reduce deposition there.

In Fig. 8, the deposit thicknesses are given as a function of time. The thicknesses for time durations less than six hours are quite small—less than 50 nm. For JP-8, δ at locations A and B could well be represented by a linear relationship between 0.5 and 6 h, and the average rate of increase in the deposit thickness, δ', is roughly 8.3 nm/h for the initial six hours of testing. Following the initial six hours, δ' increases at both A and B, but is much greater in the heated section than in the cooled section. The larger δ' at A may be due to the capillary-trapping mechanism described above, while the lower δ' at B is likely related to the solubility of polymerized molecules. Transient deposit thicknesses are also given for locations A and B for JP-8A. The δ at A for the JP-8A fuel is less than that for the JP-8 fuel, and δ' is roughly 3.3 nm/h. The rate of increase of deposit thickness at B for JP-8A significantly increases after three hours to 50 nm/h, then decreases to 16.7 nm/h between 6 and 12 hours. The reasons for this are, as yet, open to speculation.

Conclusions

Experiments were performed in a forced-flow single-pass heat exchanger to obtain baseline data on the structure and chemical composition of deposits formed after different time periods and to investigate effects of the metal wall. The experimental arrangement permitted viewing of the time evolution of deposits under conditions of nonisothermal bulk flow with limited oxygen. SEM was used for examination of deposit microstructure, and, in addition, XPS and AES were used to study the chemical composition of the deposits. Dissolved oxygen concentration measurements of the bulk flow were performed, and carbon burnoff determined the axial distribution of deposits within the tubes.

This study found the following:

1 Induction time has not been well characterized previously and usually implies a waiting period for "sufficiently measurable" deposition. However, on the molecular scale, deposition is a continuous process regardless of a readily detectable deposit, and induction time may be speculated to be the period in which the catalytic action of the metal surface is dominant and incipient molecular layers form. Here, increasing dissolved oxygen levels and large deposition rates (per volume of fuel) within the tube were characteristic of the induction time.

2 Mechanisms of deposition in the heated and cooled sections were different. AES and XPS analyses indicated that deposits formed in the heated section had chemical compositions different from those formed in the cooled section. In addition, SEM revealed differences in microstructure between the heated and cooled sections: more uniform deposits formed in the cooled section as a result of once-soluble species becoming insoluble at low temperatures.

3 The microstructure of the deposits formed from JP-8A in the cooled section was different from that with JP-8. Moreover, the JP-8 additives significantly reduced fouling in the heated section, but their effectiveness in the cooled section, especially after long periods, is questionable.

Table 2 XPS-determined percent atomic composition: JP-8A fuel

Hours	O-C=O	C=O	C-O	CH,C	O	Fe	N	S-O	C-S	Si	Cr	Total	Total	Total
A														
0.5	3.2	3.7	5.7	45	28.6	6.6	1.9	0.62	0.59	3	1.2	58.2	1.2	100.1
1.5	3.4	3.7	5.3	48.7	26.2	7.2	1.3	0.55	0.58	1.8	1.2	61.7	1.1	99.9
3	3.6	4.8	4.8	52.6	24.1	5.8	2	0.79	0.56	1	-	66.4	1.4	100.1
6	3.9	3.8	6.6	53.4	22.9	4	1.9	1.46	0.51	1.5	-	68.2	2	100
12	3.6	3.7	6.3	54	22.7	4	1.9	1.2	1.2	<0.6	0.8	68.8	2.4	99.4
B														
0.5	2.5	2.9	4	34.8	36.7	7	1.7	0.34	<0.2	6.4	3.3	44.2	<0.5	99.6
1.5	2	3.3	3.5	42.6	31	6.1	1.3	0.63	0.69	5.4	3.6	52.1	1.3	100.1
3	1.5	3.1	3.9	44	30.2	5.7	1.4	1.21	0.42	5.1	3.5	52.9	1.6	100
6	1.4	3.7	4.1	56.4	23.5	4.8	1.9	2	<0.2	<0.6	1.3	65.6	<2.2	99.1
12	0.8	3.3	2.1	65.9	19	2.5	2.2	1.55	0.29	1	1.2	72.4	1.8	99.8

Downloaded 02 Jun 2010 to 171.66.16.104. Redistribution subject to ASME license or copyright; see http://www.asme.org/terms/Terms_Use.cfm

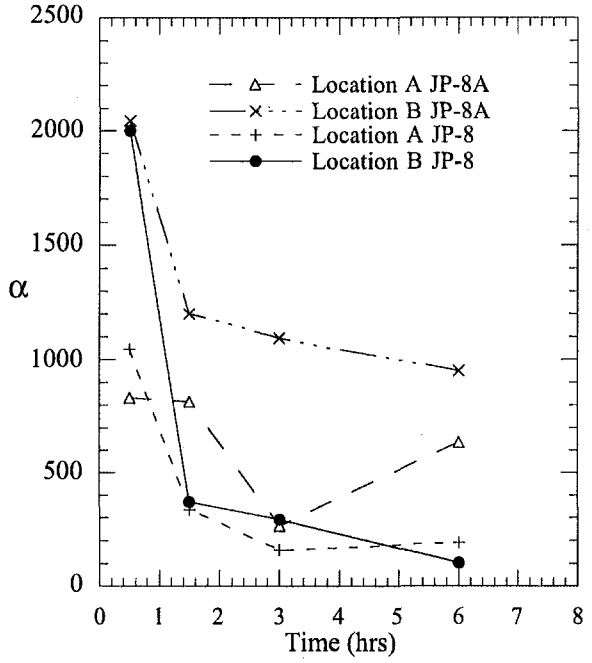

Fig. 7 Spatial mean oxygen content of deposits: JP-8 and JP-8A fuels

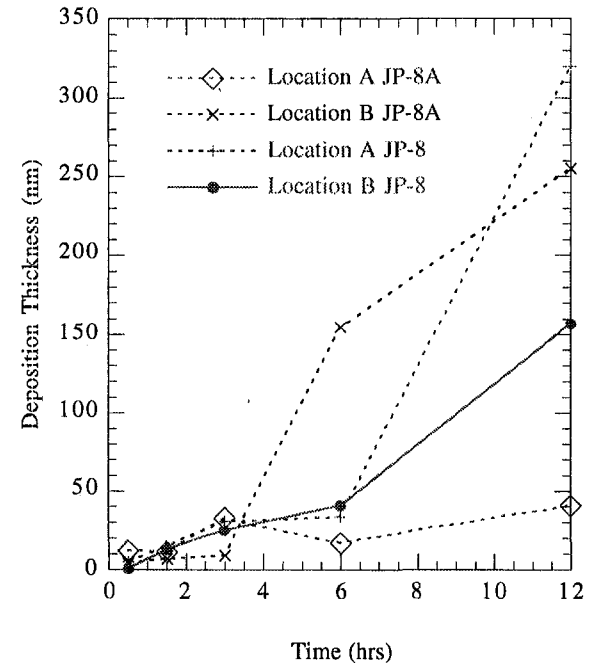

Fig. 8 Deposit thickness at different axial locations and times: JP-8 and JP-8A fuels

Acknowledgments

This work was supported by the U.S. Air Force under Contract No. F33615-92-C-2207 with Mr. C. W. Frayne serving as the technical monitor and Dr. D. R. Ballal as the principal investigator. The authors are grateful for stimulating discussions with Dr. E. G. Jones of Systems Research Laboratories, Dayton, Ohio.

References

Anderson, S., Harrison, W., III, and Roquemore, W., 1994, "Development of Thermal Stability Additive Package for JP-8," presented at the Fifth International Conference on the Handling and Stability of Liquid Fuels, Rotterdam, Netherlands.

Bradley, R., Bankhead, R., and Bucher, W., 1974, "High Temperature Hydrocarbon Fuels Research in an Advanced Aircraft Fuel System Simulator on Fuel AFFB-14-70," AFAPL-TR-73-95, Air Force Aero Propulsion Laboratory, Wright-Patterson Air Force Base, OH.

Briggs, D., and Seah, M., 1983, *Practical Surface Analysis by Auger and X-Ray Photoelectron Spectroscopy,* Wiley, New York.

Chin, J., and Lefebvre, A., 1993, "Influence of Flow Conditions on Deposits From Heated Hydrocarbon Fuels," ASME JOURNAL OF ENGINEERING FOR GAS TURBINES AND POWER, Vol. 115, p. 433.

Giovanetti, A., and Szetela, E., 1985, "Long-Term Deposit Formation in Aviation Turbine Fuel at Elevated Temperature," NASA Report CR-179579, United Technologies Research Center on contract with NASA, Cleveland, OH.

Grinstead, R., Heneghan, S., Striebich, R., and Zabarnick, S., 1994, "Jet Fuel Thermal Stability and Analytic Test Data," UDR-TR-94-20, University of Dayton, Dayton, OH.

Hazlett, R., and Hall, J., 1981, "Chemical Aspects of Jet Fuel Thermal Oxidation Stability," *Fouling of Heat Transfer Equipment,* E. Somerscales and J. Knudsen, eds., Hemisphere, New York.

Hazlett, R., and Hall, J., 1985, "Jet Aircraft Fuel System Deposits," *Chemistry of Engine Combustion Deposits,* L. Ebert, ed., Plenum Press, New York.

Hazlett, R., 1991, *Thermal Oxidation Stability of Aviation Turbine Fuels,* American Society for Testing and Materials, Philadelphia.

Heneghan, S., Martel, C., Williams, T., and Ballal, D., 1993, "Studies of Jet Fuel Thermal Stability in a Flowing System," ASME JOURNAL OF ENGINEERING FOR GAS TURBINES AND POWER, Vol. 115, p. 480.

Heneghan, S., Martel, C., Williams, T., and Ballal, D., 1995, "Effects of Oxygen and Additives on the Thermal Stability of Jet Fuels," ASME JOURNAL OF ENGINEERING FOR GAS TURBINES AND POWER, Vol. 117, pp. 120–124.

Heneghan, S., and Kauffman, R., 1994, "Analytic Tests and Their Relation to Jet Fuel Thermal Stability," presented at the Fifth International Conference on Stability and Handling of Liquid Fuels, Rotterdam, Netherlands.

Johnson, C., Fink, D., and Nixon, A., 1954, "Stability of Aircraft Turbine Fuels," *Ind. Eng. Chem.,* Vol. 46, p. 2166.

Jones, E., and Balster, W., 1994, "Surface Fouling: Short- Versus Long-Term Tests," presented at the Div. Petr. Chem., 208th American Chemical Society National Meeting, Washington, DC.

Kamin, R., Nowack, C., and Darrah, S., 1988, "Thermal Stability Measurements Using the Fiber Optic Modified Jet Fuel Thermal Oxidation Tester," *Proceedings of the 3rd International Conference on Stability and Handling of Liquid Fuels,* Inst. of Petroleum, London, United Kingdom.

Katta, V., Blust, J., Williams, T., and Martel, C., 1994, "Effects of Buoyancy on Heat Transfer and Oxygen Consumption in Fuel-Thermal-Stability Studies," ASME Paper No. 94-GT-346.

Kauffman, R., 1995, "Effects of Sulfur Compounds on the Oxidation of Jet Fuel," ASME Paper No. 95-GT-XX.

Kendall, D., and Mills, J., 1985, "The Influence of JFTOT Operating Parameters on the Assessment of Fuel Thermal Stability," SAE Paper No. 851871.

Kendall, D., Clark, R., and Stevenson, P., 1986, "The Influence of Polar Compounds on the Stability of Jet Fuel," *Proceedings of the 2nd International Conf. on Long-Term Storage Stabilities of Liquid Fuels,* San Antonio, TX.

Kendall, D., Houlbrook, G., Clark, R., Bullock, S., and Lewis, C., 1987, "The Thermal Degradation of Aviation Fuels in Jet Engine Injector Feed-Arms, Part 1—Results from a Full Scale Rig," presented at the Int. Gas Turbine and Aeroengine Congress and Exposition, Tokyo, Japan.

Krazinski, J., Vanka, S., Pearce, J., and Roquemore, W., 1992, "A Computational Fluid Dynamics Model for Jet Fuel Thermal Stability," ASME JOURNAL OF ENGINEERING FOR GAS TURBINES AND POWER, Vol. 114, p. 104.

Lefebvre, A., 1992, "Experimental Studies on Deposit Formation in JP Fuels at High Temperatures," Report No. WL-TR-92-2112, Air Force Aero Propulsion Laboratory, Wright-Patterson Air Force Base, OH.

Marteney, P., 1989, "Thermal Decomposition of JP-5 in Long Duration Tests," Report No. ADB148328, United Technologies Research Center, prepared for Naval Air Propulsion Center.

Mushrush, G., Watkins, J., Hazlett, R., Hardy, D., and Eaton, H., 1988, "Liquid Phase Oxidation of Thiophenol and Indene by *t*-Butyl Hydroperoxide and Oxygen," *Fuel Science and Technology International,* Vol. 6, p. 165.

Patankar, S., 1980, *Numerical Heat Transfer and Fluid Flow,* Hemisphere, Washington, DC.

Rubey, W., Striebich, R., Anderson, S., Tissandier, M., and Tirey, D., 1992, "In Line Gas Chromatographic Measurement of Trace Oxygen and Other Dissolved Gases in Flowing High Pressure Thermally Stressed Jet Fuel," presented at the Symposium on Structure of Jet Fuels III, American Chemical Society, Div. Petr. Chem., San Francisco, California.

Schirmer, R., 1970, "Morphology of Deposits in Aircraft and Engine Fuel Systems," SAE Paper No. 700258.

Schultz, W., and Gillman, A., 1994, "Effects of Sulfur Compounds on a JP-8 Surrogate Fuel," presented at the Div. Petr. Chem., 208th American Chemical Society National Meeting, Washington, DC.

Smith, J., 1969, "Fuel for the SST: Effects of Deposits on Heat Transfer to Aviation Kerosine," *Ind. and Eng. Chem. Process Design and Development,* Vol. 8, p. 299.

Wittberg, T., 1994, University of Dayton Research Institute, private communication.

Downloaded 02 Jun 2010 to 171.66.16.104. Redistribution subject to ASME license or copyright; see http://www.asme.org/terms/Terms_Use.cfm

Surface Fouling in Aviation Fuels: An Isothermal Chemical Study

E. G. Jones[1]

W. J. Balster

J. M. Pickard[2]

Systems Research Laboratories, Inc.,
An Operation of Calspan SRL Corporation,
2800 Indian Ripple Rd.,
Dayton, OH 45440

Surface fouling in aircraft fuel lines that results from autoxidation of aviation fuel remains a serious and very complicated problem. This area has been studied using two Jet-A fuels, POSF-2827 and POSF-2980. The results of a series of dynamic experiments conducted in a single-pass, tubular heat exchanger operated at very slow flow rates under near-isothermal conditions are reported herein. Such studies, by minimizing complications resulting from fluid dynamics and heat flow, constitute a simpler global approach to the chemistry of fouling. The basis for the selection of experimental test conditions is discussed, and data from measurements of dissolved oxygen and surface deposition as a function of fuel stress duration are presented. The effects of parameters such as reaction temperature, tube diameter, experimental test time, and fuel dopants are considered.

Introduction

Aviation fuels, when subjected to heat in the presence of oxygen, undergo degradation from autoxidation reactions, as summarized by Hazlett (1991). Insoluble products formed in these reactions tend to foul heated surfaces, causing reduced efficiency and possible blockage in heat exchangers, hysteresis in servocontrols, and changes in nozzle geometry. As the primary heat sink in modern aircraft, fuel will experience increased thermal stress as aircraft performance is enhanced (Edwards et al., 1992). Each fuel has a unique composition; thus, the chemical reactions describing the autoxidation of one fuel will be different from those of all other fuels. Similarly, the reaction steps from formation of the initial free radical to the final production of insoluble carbonaceous surface deposits or bulk insolubles are too complex to have been outlined for aviation fuels. Minor fuel constituents containing hetero-atoms such as sulfur and nitrogen have been identified either as the primary cause of insoluble formation or as the source of catalysis which can accelerate autoxidation. Also, the conditions of high fuel velocity and nonuniform wall and bulk-fuel temperatures present in fuel lines create complicated fluid-dynamic conditions that are difficult to simulate and that change during each segment of a flight cycle.

Simulating the fuel-stress conditions experienced in fuel lines during flight requires expensive full-scale rigs and large fuel batches. An alternative approach taken in this laboratory has been the use of a simpler near-isothermal flowing test rig (NIFTR) to simulate only the chemical conditions (i.e., the temperature and reaction time) by conducting experiments under near-isothermal conditions. The advantage of this approach is threefold: (1) Many complications from fluid dynamics are removed, (2) wall and bulk-fuel temperatures are the same, and (3) the global aspects of deposition can be described in terms of rate of deposition as a function of reaction time or fuel-stress duration. Since reactions are studied over 100 percent oxygen conversion, an inherent normalization occurs through the use of a fixed amount of reactant, namely, the total amount of oxygen present in air-saturated fuel. It is assumed in this approach that 1 L of fuel stressed to 100 percent conversion will form the same quantity of insolubles as 1000 L of fuel stressed to 0.1 percent conversion. The latter condition more nearly approximates that experienced in an actual aircraft; however, if chemistry is a controlling factor, then the reaction chemistry in controlled isothermal experiments will be the same as that which occurs in the field. This forms the basis for the near-isothermal approach to the study of fuel fouling. Clearly, when isothermal conditions are used, the thermal behavior of fuel must be studied over a range of different temperatures to obtain a broad view of fuel thermal stability.

The goals of the isothermal approach are to (1) isolate the global-chemical processes, (2) collect experimental data that describe the fouling chemistry as a function of reaction time, and (3) compare the thermal behavior of different fuels and establish a baseline for evaluating the efficiency of additives in reducing or delaying surface fouling. Additives such as antioxidants for slowing oxygen consumption, metal deactivators for chelating dissolved metals or passivating tubing walls, and dispersants or detergents for increasing solubility would appear to hold the most promise from a thermal-stability standpoint. Martel (1987) has summarized jet-fuel additives including (in addition to the above) corrosion inhibitors, lubricity improvers, icing inhibitors, static dissipators, and pipeline-drag reducers. Changes introduced by the hindered-phenol antioxidant additive BHT in two Jet-A fuels are presented, and several possible criteria for rating fuels and additives based upon near-isothermal test results are reviewed.

Longer-term goals, not addressed in the current study but a simple extension of the current approach, are to collect data at several temperatures, to derive kinetic parameters that may ultimately describe surface-fouling processes over a broad temperature range, and to use these values in CFD models for predicting fouling under actual aircraft conditions that are difficult to achieve in the laboratory. Models such as those developed by Katta et al. (1993) have been successful in describing surface fouling for several rigs.

This paper describes progress toward obtaining baseline data at 185°C to reflect the surface fouling that occurs in two Jet-A fuels, POSF-2827 and POSF-2980. Included is the establishment of the optimum experimental conditions for studying fouling and for differentiating the fuels in a series. Experimental parameters such as tubing size, reaction-temperature range, sur-

[1] Current address: Innovative Scientific Solutions, Inc., 3845 Woodhurst Court, Beavercreek, OH 45430-1658.

[2] Current address: Kinetica, Inc., P. O. Box 182, Mound Advanced Technology Center, 1 Mound Rd., Miamisburg, OH 45343-0181.

Contributed by the International Gas Turbine Institute and presented at the 40th International Gas Turbine and Aeroengine Congress and Exhibition, Houston, Texas, June 5–8, 1995. Manuscript received by the International Gas Turbine Institute February 10, 1995. Paper No. 95-GT-45. Associate Technical Editor: C. J. Russo.

Copyright © 1996 by ASME

Downloaded 02 Jun 2010 to 171.66.16.104. Redistribution subject to ASME license or copyright; see http://www.asme.org/terms/Terms_Use.cfm

Table 1 Fuel properties

	POSF-2827	POSF-2980
Treatment	Straight Run	MEROX™-treated
JFTOT Breakpoint	266	288
Total Sulfur (%)	0.079	0.061
Freezing Point (°C)	- 43	- 44
Aromatics (%, vol)	19	17
Total Acid No. (mg KOH/g)	0.001	0.001

face conditions, and test duration must be considered. For example, a 6-h test has been found to be adequate for quantifying insolubles and identifying reaction trends in POSF-2827 fuel (Jones and Balster, 1993); however, arguments presented herein indicate that, in general, longer tests of ~70-h duration may be preferable.

Experimental Arrangement

Some general properties of the two fuels are given in Table 1. Although both fuels contain a significant amount of total sulfur, they meet all USAF specifications. POSF-2980 fuel has been treated using the MEROX technique to reduce the mercaptan odor through oxidation to the corresponding disulfide. Both are Jet-A fuels representative of those in commercial service. The antioxidant BHT was obtained from DuPont. Fuels were used as received, with minimal filtration (15 μm) for protection of the syringe pump.

The experiments were conducted using the NIFTR, which has been described previously (Jones et al., 1995; Jones and Balster, 1993). Figure 1 shows the heat exchanger as operated in the extended-pass mode to double the total reaction time. Fuel, which is saturated initially with respect to air and which contains 64 ppm (w/w) of oxygen, is pumped at a pressure of 350 psi through commercial stainless-steel (304) tubing clamped tightly in a 36-in. heated copper block. Most of the experiments were conducted using tubing with dimensions of 0.125-in.-o.d. and 0.085-in.-i.d.; in a few experiments larger tubing with dimensions of 0.25-in.-o.d. and 0.18-in.-i.d. was used. A pair of in-line Ag-membrane filters (0.45 and 0.2 μm) collected the nonadhering bulk insolubles.

Deposition rates were measured in 6-h and ~70-h experiments that were run continuously at a fixed fuel-flow rate; reaction time or stress duration was determined from the flow rate, tube dimensions, and location along the tube axis. The calculated times were reduced by 15 percent to compensate for fuel expansion. When the total test time was increased tenfold, the total volume of fuel increased tenfold. At the end of each test, the heated tube was cut into 2-in. sections, and the quantity of carbon in the deposits was determined from surface-carbon burnoff (LECO RC-412). Deposition rates were determined from the amount of carbon in each 2-in. segment, the increment of stress time within that segment, and the total quantity of fuel used. Each section provides one data point, representing the rate averaged over the entire test time (i.e., 6–70 h). Deposition rate is expressed in units of micrograms of carbon per unit stress time per unit volume of fuel passed through the system. Nonadhering bulk insolubles were quantified by surface carbon burnoff of the in-line filters. Dissolved oxygen was measured in separate experiments using a 32-in. heated tube as a reaction cell and GC detection (Rubey et al., 1992); stress duration was changed by varying the flow rate. Cleaned stainless-steel tubes were used for measurements related to 6-h deposition experiments where deposition occurs primarily on cleaned surfaces. In long-term tests, most deposition occurs on previously fouled surfaces; for comparison with deposition in this case, passivated tubes (Silcosteel, Restek Corporation) were used to minimize catalytic wall effects that occur during oxygen measurements.

Results and Discussion

Selection of Optimum Test Conditions

Temperature Range. In many fuels a close correlation exists between oxygen consumption and deposition; thus, the temperature ranges of interest for oxygen depletion and surface deposition overlap. Experimentally, oxygen depletion can only be measured over a limited temperature range of ~50–60°C for the following reason. At the high-temperature end, the reaction is very rapid, and higher fuel-flow rates are necessary for maintaining short residence times within the heated block. As a result the fuel does not achieve block temperature rapidly, i.e., the experiments depart significantly from isothermal. At the low-temperature end, the reaction is very slow, and residence times on the order of hours are necessary for complete consumption of the dissolved oxygen. Maintenance of GC-detector stability over extended periods of time can introduce significant errors into the measurements. Oxygen depletion in about 15 fuels has been studied in this laboratory, and dissolved oxygen has been found to be completely converted after 1–20 min of stressing at 185°C. The practical temperature range for oxygen measurements using the current techniques is 155–215°C.

Surface-fouling measurements are subject to similar temperature constraints. At the highest temperatures, reaction and subsequent deposition occur over a very narrow time interval; depending upon the fuel-flow rate, deposition occurs only in a limited region of the heated tube. Spatial deposition can be extended through higher flow rates, but at the expense of departure from isothermal conditions. At the lowest temperatures, very slow flow rates must be used for total reaction of the dissolved oxygen. The difficulty arises from the fact that in a 6-h test at 155°C, only about 25 ml of fuel are passed and a limited, minimal amount of deposit is collected. The practical temperature range for near-isothermal surface-fouling experiments is 145–225°C. A temperature of 185°C, the midpoint of the experimental range, was selected as the standard temperature for stressing neat jet fuels to obtain baseline surface deposition and dissolved-oxygen information.

Stress Duration. This parameter is controlled by rates of oxygen consumption and the deposition profile. The primary requirement is to provide sufficient residence time for completion of the oxygen reaction and subsequent deposition within the heated tube. Passing fuel through the heated block once or twice at a flow rate of 0.25 ml/min provides, respectively, 12 and 24 min of stressing at temperature. For the fuels studied, this time is sufficient for complete deposition to occur at 185°C within the heated block.

Test Time. This parameter was established for deposition experiments and determines the total amount of fuel passed through the system. The longer the test time, the greater the

Nomenclature

BHT = 2,6-di-tert-butyl-p-cresol, antioxidant
CFD = computational fluid dynamics
GC = gas chromatograph
JFTOT = jet-fuel thermal-oxidation test
NIFTR = near-isothermal flowing test rig
POSF-2827 = Jet-A fuel, straight run
POSF-2980 = Jet-A fuel, MEROX™-treated
USAF = United States Air Force

Downloaded 02 Jun 2010 to 171.66.16.104. Redistribution subject to ASME license or copyright; see http://www.asme.org/terms/Terms_Use.cfm

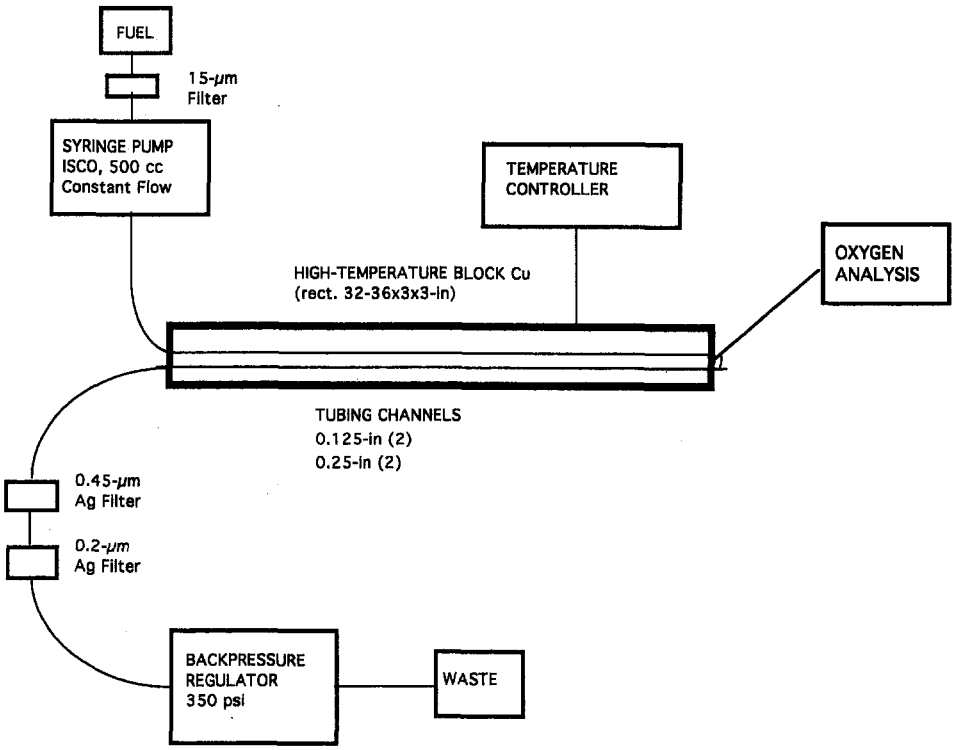

Fig. 1 Schematic diagram of apparatus (NIFTR)

quantity of insolubles formed and the greater the signal/noise ratio. The measured deposition rates represent averages over the total test time. It has been reported (Jones and Balster, 1994a) that the dependence of deposition rate upon stress duration for POSF-2827 aviation fuel changes as the test time is extended from 6 to 70 h. This observation was explained in terms of surface-dependent changes in the rate of oxygen consumption. The initial deposition on clean stainless-steel tubing is governed by a more rapid oxygen loss that is catalyzed by active sites on the cleaned surface. As deposits collect along the walls, active sites become covered, oxygen depletion is no longer surface catalyzed, and its rate and the rate of surface deposition decrease. This is manifested by a reduced deposition rate and a shift in the deposition profile to slightly longer stress times, i.e., residence times. Once the surface is completely covered by deposits, the deposition profile becomes independent of test time.

Figures 2 and 3 show the deposition rate for POSF-2827 and -2980, respectively, as measured in 6-h (initial catalyzed rate) and in ~70-h tests (constant deposition). The rate plotted has been corrected by subtracting the effects of background surface carbon not related to autoxidation. Also shown is the corresponding decay in dissolved oxygen as measured in a cleaned stainless-steel tube and in an inert tube. In general,

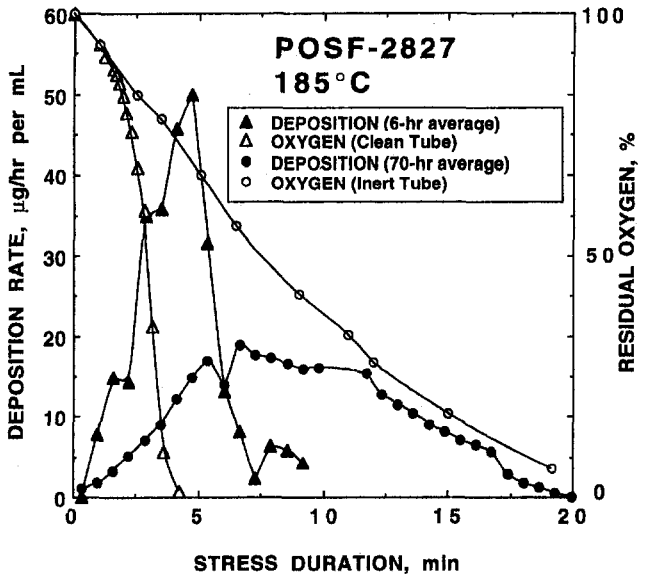

Fig. 2 Deposition rate and residual oxygen versus stress duration for POSF-2827 fuel measured in 0.125-in.-o.d. tubes

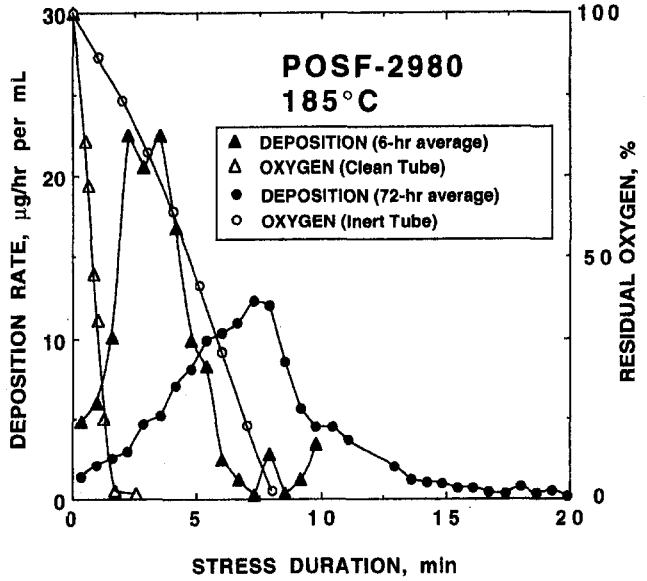

Fig. 3 Deposition rate and oxygen consumption versus stress duration for POSF-2980 fuel measured in 0.125-in.-o.d. tubes

Downloaded 02 Jun 2010 to 171.66.16.104. Redistribution subject to ASME license or copyright; see http://www.asme.org/terms/Terms_Use.cfm

Table 2 Advantages: short- versus long-term testing

Short Term (6 hr)	Long Term (~ 70 hr)
One-day experiment	Weekend experiment
-----	Better signal-to-noise ratio
Deposition on cleaned surfaces	Deposition on fouled surfaces
Faster oxygen reaction (catalyzed)	Slower oxygen reaction (surface passivated)
-----	Reduced baseline correction to rate
Total insolubles per ml constant	Total insolubles per ml constant

POSF-2980 has a slower deposition rate and a faster oxidation rate. The profiles pertain to different conditions. The first (6-h) describes deposition on cleaned stainless-steel tubing, and the second, the deposition mainly on previously fouled surfaces. Evidently POSF-2980 fuel displays deposition changes very similar to those reported for POSF-2827, namely, reduced rate and shift in the deposition profile as the test time is extended. The amount of deposition with POSF-2980 fuel is less and, hence, the surface coverage and passivation will be less than for POSF-2827. Also, regions exist near the entrance and exit of the tubes where deposition is minimal, and these surfaces may continue to catalyze autoxidation.

Table 2 outlines some of the distinct advantages associated with both short- and long-term tests. One of the major considerations is the signal-to-noise ratio. For the current treatment, long-term tests, which better reflect deposition on fouled surfaces were selected to simulate conditions encountered in actual aircraft fuel lines. However, fuels that leave few deposits may never lead to complete coverage of the original surfaces, even in 70-h experiments. It is doubtful that virgin clean surfaces would be common in fuel lines, except for servocontrols where very clean surfaces are required for minimization of hysteresis. In the latter case there may be cause for concern since autoxidation in both of the fuels under study is catalyzed by cleaned surfaces.

Tubing Size. Since deposition in isothermal tests is expressed as a function of stress duration rather than axial tube distance, the rate profiles should be similar in tubing with different internal diameters. The deposition measured for POSF-2827 fuel using larger diameter tubes is shown in Fig. 4. As the test time is extended, the trends observed are the same as those in Fig. 2. Rates are reduced by about a factor of two because of the reduced surface-to-volume ratio. For most studies 0.125-in.

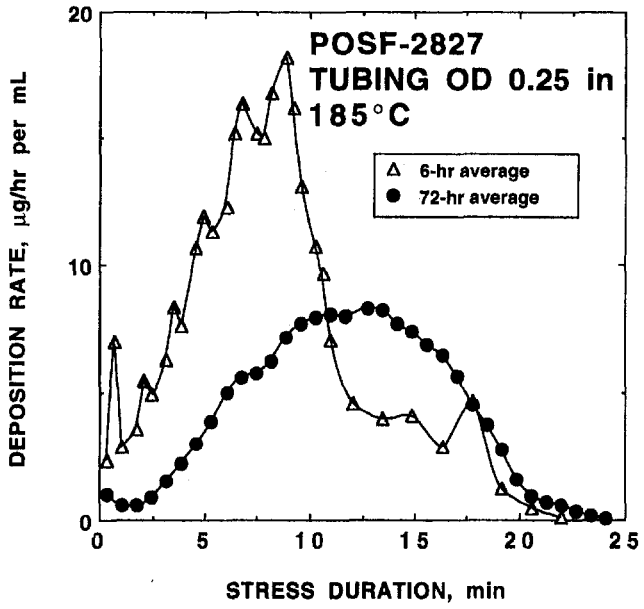

Fig. 4 Deposition rate versus stress duration for POSF-2827 fuel measured in 0.25-in.-o.d. tubes

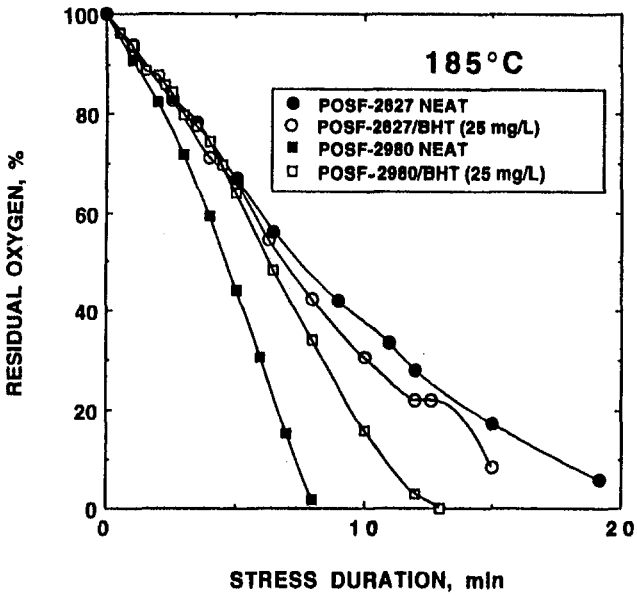

Fig. 5 Oxygen consumption in POSF-2827 and -2980 fuels, neat and with additives

tubes were selected to minimize fuel volume within the heated block and also to minimize the time needed to achieve isothermal conditions. For example, to achieve the same stress time within the heated section using tubing with twice the internal diameter would require a fourfold increase in flow rate. The higher the flow rate, the longer the time required to bring fuel to temperature and the greater the departure from isothermal reaction conditions.

Tubing Surface. The nature of the initial surface is a controlling factor in deposition in 6-h tests; however, once deposits have covered the metal surface, the deposition profile becomes constant. Thus, for long-term tests that produce deposits, the initial tubing surface is not a significant factor. It is for this reason that oxygen measurements were made using inert tubes.

Changes in Deposition Using Antioxidant BHT

POSF-2827 Fuel. The results of oxygen measurements at 185°C using the neat and additized fuel are shown in Fig. 5. Changes introduced by BHT at 25 mg/L fall within the reproducibility of the measurements. The rates are constant down to 30 percent residual oxygen, indicating oxygen nonlimited kinetics. Below 30 percent the rate becomes oxygen limited, as evidenced by tailing. Walling (1957) has summarized the rate expressions for the reaction of oxygen at high (oxygen-nonlimited) and low (oxygen-dependent) concentrations. The presence of certain types of sulfur compounds causes hydroperoxide concentration to remain low. Chain-breaking antioxidants such as BHT (hindered phenol) are ineffective in fuels containing large quantities of naturally occurring autoxidants. POSF-2827 fuel does produce hydroperoxides, but the measured steady-state concentration is very low (<70 μequivalents/L).

The corresponding deposition in the neat and additized fuel is given in Fig. 6. The two profiles are very similar. At this time it is not known whether the slight differences are real or whether they fall within experimental reproducibility. Based upon the similarity of the oxygen curves, it is concluded that BHT does not slow oxygen consumption, nor does it significantly change the surface deposition rate in POSF-2827 fuel.

POSF-2980 Fuel. In contrast to the results given above, BHT significantly slows the rate of oxygen consumption (see Fig. 5). The overall effect is a delay of ~2 min at 50 percent conversion and ~4–5 min at complete conversion. Clearly,

Downloaded 02 Jun 2010 to 171.66.16.104. Redistribution subject to ASME license or copyright; see http://www.asme.org/terms/Terms_Use.cfm

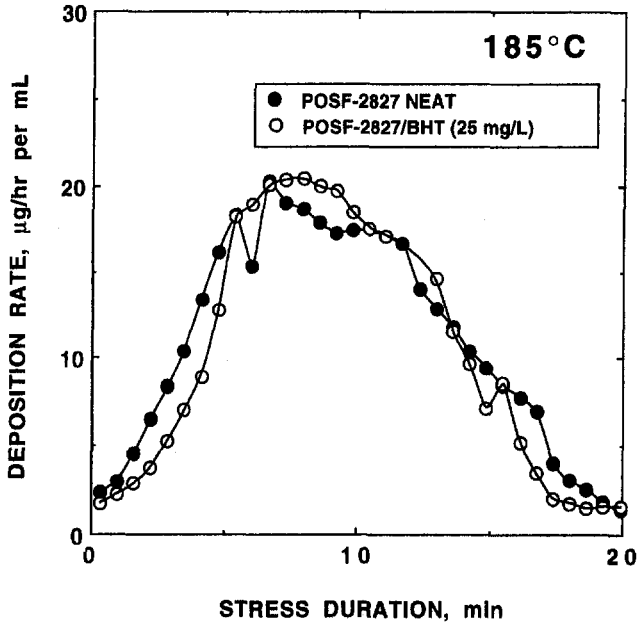

Fig. 6 Deposition rate in POSF-2827 fuel, neat and with additives

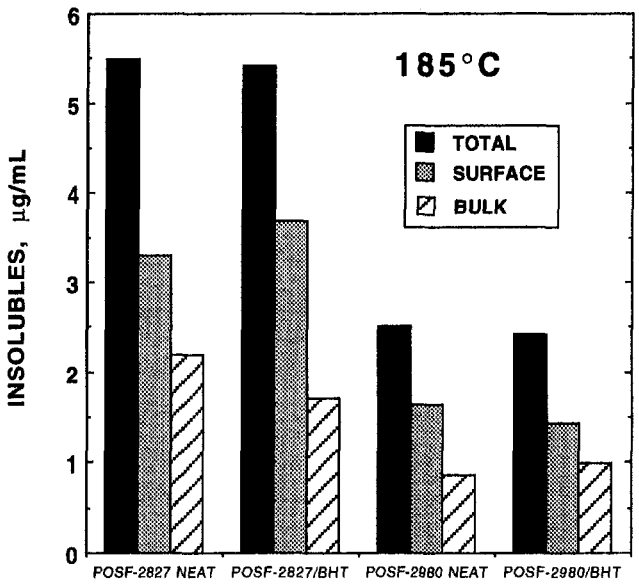

Fig. 8 Quantification of surface, bulk, and total insolubles

fundamental differences exist in the autoxidation of these two Jet-A fuels. The hindered-phenol antioxidant at a concentration of 25 mg/L has a negligible effect on POSF-2827 and yet is very efficient in retarding oxygen reaction in POSF-2980.

The effect of BHT on the deposition profile is shown in Fig. 7. BHT causes a dramatic delay in surface deposition, as might be expected from the oxygen behavior and previous reports of correlation between oxygen reaction and deposition in Jet-A fuels (Jones and Balster, 1994b). The delay in the maximum of the deposition profile is 3–4 min, in reasonable agreement with the oxygen-loss data. However, as with POSF-2827 fuel, the total quantity of deposit (integral under curves) is unaffected by BHT.

Criteria for Comparing Fuels and the Effect of Additives. Based on the previous considerations, two obvious criteria for comparing fuels are the rate of oxygen consumption and the shape of the deposition-rate profile. Other quantitative criteria are the amount of bulk insolubles obtained directly from the in-line filters and the amount of surface insolubles obtained by integrating the area under the deposition profile. These quantities in units of micrograms per milliliter are summarized in the histogram in Fig. 8.

First, consider the impact of BHT. It does not reduce the amount of surface insolubles in POSF-2827 and causes a minor (10 percent) reduction in POSF-2980. BHT delays reaction in POSF-2980; but, given sufficient time to complete deposition, the total surface insolubles remain about the same. In actual service it is doubtful that all oxygen will be converted. This suggests that a more equitable way to assess the impact of BHT may be to compare surface insolubles formed after a limited stress duration, which is equivalent to considering the integral of the surface carbon as a function of stress duration; this is given in Fig. 9 for POSF-2980. Also plotted in this figure is the fractional reduction in surface deposits as a function of stress duration. After 10 min of stressing, BHT has reduced the

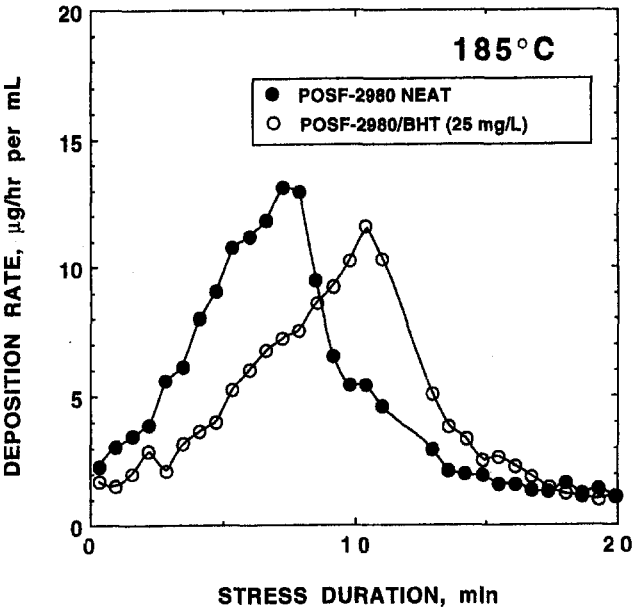

Fig. 7 Deposition rate in POSF-2980 fuel, neat and with additives

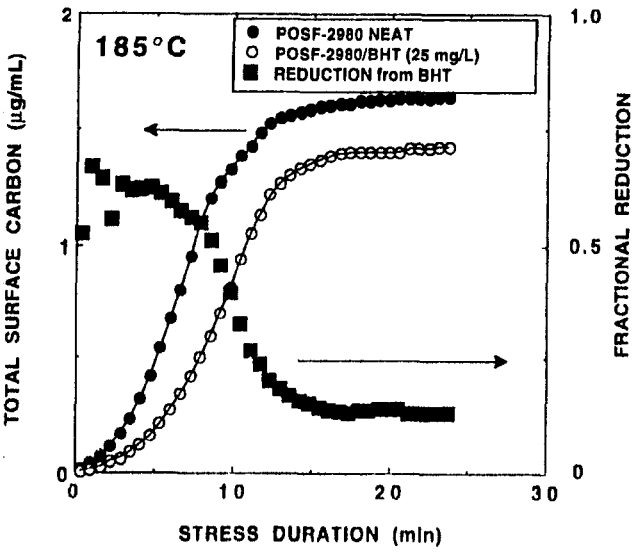

Fig. 9 Plot of total surface carbon (POSF-2980; neat and with additives) and fractional reduction versus stress duration

Downloaded 02 Jun 2010 to 171.66.16.104. Redistribution subject to ASME license or copyright; see http://www.asme.org/terms/Terms_Use.cfm

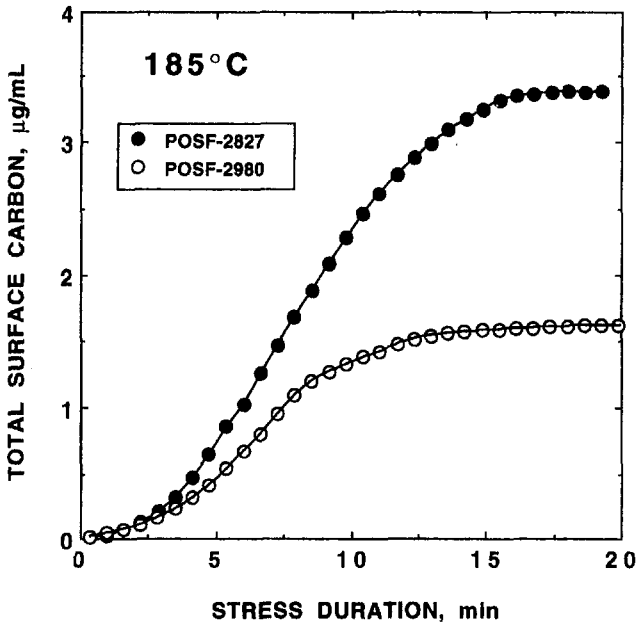

Fig. 10 Plot of total surface carbon versus stress duration at 185°C for POSF-2827 and -2980 fuels

total surface deposits by 35 percent; after only 5 min of stressing, the reduction is 60 percent. Clearly, comparison after shorter stress times best reflects the potential benefits of an antioxidant that serves primarily to delay reaction.

Second, compare the two Jet-A fuels. Figure 8 shows that POSF-2980 fuel produces less surface, bulk, and total insolubles at 185°C than POSF-2827 when these fuels are stressed to complete oxygen conversion and deposition. The difference is approximately a factor of two. However, if the comparison is based on the use of total surface carbon formed over limited stressing as shown in Fig. 10, then the difference between the two fuels is much less for a shorter stress duration. Isothermal test results provide information for comparing fuels using many criteria. It should be noted that all current comparisons relate only to reaction at 185°C. Data collected at other temperatures may rank fuels differently. For example, POSF-2827 fuel has an inverse temperature dependence for total surface insolubles (Jones and Balster, 1994b). It is not known whether POSF-2980 behaves similarly or has a very different temperature dependence. Clearly, refinement of a ranking scheme for fuels and additives is a complicated process.

Finally, Table 2 indicates that short- and long-term tests produce the same amount of insolubles when expressed per unit volume of fuel. For example, the bulk, surface, and total insolubles from 6-h tests with POSF-2827 fuel are 2, 3, and 5 μg/ml, respectively. The corresponding values for POSF-2980 are 0.83, 1.5, and 2.3. These sets of numbers are the same as the long-term values plotted in Fig. 8, within the experimental uncertainty of 10 percent.

Conclusions

Surface fouling that occurs at 185°C in two Jet-A fuels has been studied. Test conditions have been optimized to reflect fuel-dependent differences, and possible criteria have been outlined for ranking fuels and additives based on near-isothermal tests. Unique differences are observed both in the behavior of the neat fuels and in the impact of the antioxidant BHT. Autoxidation of both fuels is catalyzed by cleaned stainless-steel surfaces; the effect is greatly reduced or eliminated by surface passivation that occurs with the accumulation of surface deposits. Fuels that undergo surface catalysis may be of some concern under conditions where clean surfaces are encountered, as in servocontrols.

Acknowledgments

This work was supported, in part, by Wright Laboratory, Aero Propulsion and Power Directorate, Wright-Patterson Air Force Base, Ohio, under USAF Contract No. F33615-90-C-2033. The authors would like to thank Mr. Tim Gootee for performing the surface-carbon analyses, Ms. Lori Balster for making the oxygen measurements, and Mrs. Marian Whitaker for lending editorial assistance. The authors acknowledge valuable discussions with Dr. Larry Goss of SRL, Mr. Steve Anderson of the USAF, and Mr. Wayne Rubey of the University of Dayton Research Institute.

References

Edwards, T., Anderson, S. D., Pearce, J. A., and Harrison, W. E., 1992, "High Temperature Thermally Stable JP Fuels—An Overview," AIAA Paper No. 92-0683.

Hazlett, R. N., 1991, *Thermal Oxidation Stability of Aviation Turbine Fuels,* ASTM Monograph 1, American Society for Testing and Materials, Philadelphia.

Jones, E. G., and Balster, W. J., 1993, "Phenomenological Study of Formation of Insolubles in a Jet-A Fuel," *Energy and Fuels,* Vol. 7, pp. 968–977.

Jones, E. G., Balster, W. J., and Post, M. E., 1995, "Degradation of a Jet A Fuel in a Single-Pass Heat Exchanger," ASME JOURNAL OF ENGINEERING FOR GAS TURBINES AND POWER, Vol. 117, pp. 125–131.

Jones, E. G., and Balster, W. J., 1994a, "Surface Fouling: Short- vs. Long-Term Tests," *Preprints—American Chemical Society, Division of Fuel Chemistry,* Vol. 39(3), pp. 952–957.

Jones, E. G., and Balster, W. J., 1994b, "Formation of Insolubles in a Jet-A Fuel: Temperature Effects," *Preprints—American Chemical Society, Division of Petroleum Chemistry,* Vol. 39(1), pp. 78–81.

Katta, V. R., Jones, E. G., and Roquemore, W. M., 1993, "Development of Global-Chemistry Model for Jet-Fuel Thermal Stability Based on Observations From Static and Flowing Experiments," AGARD Paper No. PEP-19.

Martel, C. R., 1987, "Military Jet Fuels, 1944–1987," Air Force Wright Aeronautical Laboratory Technical Report AFWAL-TR-87-2062, Wright-Patterson Air Force Base, OH.

Rubey, W. A., Tissandier, M. D., Striebich, R. C., Tirey, D. A., and Anderson, S. D., 1992, "In-Line Gas Chromatographic Measure of Trace Oxygen and Other Dissolved Gases in Flowing High-Pressure, Thermally Stressed Jet Fuel," *Preprints—American Chemical Society, Division of Petroleum Chemistry,* Vol. 37(2), pp. 371–376.

Walling, C., 1957, *Free Radicals in Solution,* Wiley, New York.

Downloaded 02 Jun 2010 to 171.66.16.104. Redistribution subject to ASME license or copyright; see http://www.asme.org/terms/Terms_Use.cfm

Modeling of Local Extinction in Turbulent Flames

D. G. Sloan[1]

G. J. Sturgess[2]

Pratt & Whitney,
East Hartford, CT 06108

The Eddy Dissipation Concept (EDC), proposed by Magnussen (1985), advances the concept that the reactants are homogeneously mixed within the fine eddy structures of turbulence and that the fine structures may therefore be regarded as perfectly stirred reactors (PSRs). To understand more fully the extent to which such a subgrid scale stirred reactor concept could be applied within the context of a computational fluid dynamics (CFD) calculation to model local or global extinction phenomena: (1) Various kinetic mechanisms are investigated with respect to CPU penalty and predictive accuracy in comparisons with stirred reactor lean blowout (LBO) data and (2) a simplified time-scale comparison, extracted from the EDC model and applied locally in a fast-chemistry CFD computation, is evaluated with respect to its capabilities to predict attached and lifted flames. Comparisons of kinetic mechanisms with PSR lean blowout data indicate severe discrepancies in the predictions with the data and with each other. Possible explanations are delineated and discussed. Comparisons of the attached and lifted flame predictions with experimental data are presented for some benchscale burner cases. The model is only moderately successful in predicting lifted flames and fails completely in the attached flame case. Possible explanations and research avenues are reviewed and discussed.

Introduction

The provision of adequate stability or lean blowout (LBO) margin is an extremely important design criterion in the development of industrial and aircraft gas turbine engines. It is becoming increasingly more difficult to ensure that adequate stability margins can be maintained in the future because of current design trends toward improved atomization of liquid fuel, high temperature rise, and low emissions combustors, and their associated technologies.

In 1987 the U.S. Air Force established the Combustor Design Model Evaluation (CDME) program, with the goal of improving physical modeling to facilitate design work. Under the CDME effort, a joint industry/government laboratory/university research program was initiated to address lean blowout. A broad description of various experimental and computational facets of this program has been provided in a number of papers (e.g., Roquemore et al., 1991; Sturgess et al., 1991a, b, 1992a, b, 1993a, 1994; Sturgess and Shouse, 1993b).

The present paper is concerned only with the computational component of the program—specifically the modeling of the lean blowout process, the integration of the modeling with computational fluid dynamics (CFD) codes, and the testing and calibration of the modeling against experimental data bases. The complete and direct CFD simulation of the turbulent, nonstationary, and reaction-kinetics characteristics associated with the lean blowout phenomenon in a three-dimensional gas turbine combustor environment is not presently considered to be a viable option. Consequently, the approach adopted for the calculation of lean blowout is to partially uncouple the chemistry from the fluid mechanics and to address each of these problems as a separate modeling issue. This basic philosophy has been applied at two simplistic levels: (1) application of full chemistry via a stirred reactor network established on the basis of CFD analysis of the flow fluid, and (2) utilization of phenomenological and approximated reaction-kinetic extinction modeling within the context of local CFD calculations. Only the latter approach will be discussed herein; the former approach has been highlighted elsewhere (Sturgess et al., 1991a, b).

Background

Much of the combustion modeling concepts developed for local flame extinction has been derived from studies of liftoff and blowout in turbulent, initially non-premixed, jet-flame systems. (The relevancy of such flames to gas turbine combustors and to the experimental vehicles used in the LBO research program is discussed by Sturgess et al., 1994, and Sturgess and Shouse, 1993b.) Although multiple views have been proposed to explain the liftoff/blowoff phenomenon, two of these views (Williams, 1985)—premixed flame propagation and diffusion flamelet theory—generally characterized the perceived extinction behavior.

The diffusion flamelet theory is that advocated by Peters and co-workers (Peters, 1983, 1984, 1985; Janicka and Peters, 1982; Peters and Williams, 1983), involving the subjection of laminar diffusion flamelets to high strain rates. The structure of the laminar diffusion flamelet consists essentially of a thin reaction zone sandwiched between two chemically "inert" outer zones (i.e., air and fuel, respectively). An ensemble of such flamelet entities constitutes the turbulent flow field. Flow processes that lead to stretching of the flame tend to increase the local, instantaneous strain rate (i.e., through the velocity gradient), which in turn is proportional to the composition and conserved scalar gradients. Local extinction is a function of the flame stretch phenomenon, and is assumed to occur when the instantaneous strain parameter exceeds a critical value. The instantaneous "scalar dissipation" rate variable is typically selected as a representative measure of the effects of strain, and may be interpreted as the inverse of a characteristic diffusion time or local residence time. At large values of the scalar dissipation, the heat generation due to chemical reaction is exceeded by the heat loss, due to heat conduction away from the laminar flamelet or rapid interdiffusion of molecules between adjacent microscale vortices or packets. Consequently, local quenching of a reaction mechanism occurs when the turbulent mixing or diffu-

[1] Current address: ABB Combustion Engineering, Inc., Windsor, CT 06095.
[2] Current address: Innovative Scientific Solutions, Inc., Beavercreek, OH 45430-1658.

Contributed by the International Gas Turbine Institute and presented at the 39th International Gas Turbine and Aeroengine Congress and Exposition, The Hague, The Netherlands, June 13–16, 1994. Manuscript received by the International Gas Turbine Institute March 12, 1994. Paper No. 94-GT-433. Associate Technical Editor: E. M. Greitzer.

Copyright © 1996 by ASME

Downloaded 02 Jun 2010 to 171.66.16.104. Redistribution subject to ASME license or copyright; see http://www.asme.org/terms/Terms_Use.cfm

sion time scale is reduced to the same order of magnitude as the chemical reaction time scale. Alternatively stated, the rate at which the reactants are diffusing into the reaction is accelerated to such an extent by the local scalar gradients, that the chemistry is not fast enough to keep pace with it; hence, there is insufficient time for ignition before the temperature and radical species concentrations drop below the local quenching temperature. The diffusion flamelet theory suggests that although the time-averaged concentrations will exhibit an apparent large-scale engulfment or mixing through turbulence, the amount of molecular premixing is insufficient to justify the premixed flame propagation concept.

The alternative and more traditional theory assumes that a lifted, turbulent diffusion flame is stabilized in a region where combustion is controlled by premixing (see Williams, 1985; Janicka and Peters, 1982; Lockwood and Megahed, 1978; Chakravarty et al., 1984; Kalghatgi, 1984; Eickhoff et al., 1985; Byggstoyl and Magnussen, 1985). Even "attached" flames are envisioned as containing a "dark space" between the flame base and the burner rim, in which premixing of fuel and oxidant occur by interdiffusion. In this viewpoint, it is assumed that at the base of a lifted flame, the degree of premixing is large and that the "premixed, laminar" flame base controls the stability of the anchored diffusion flame above it.

Application of premixed theory suggests that the height of the lifted flame corresponds to that location at which the turbulent flame propagation velocity is equal and opposite to the appropriate flow velocity component. If it is assumed that essentially complete premixing on the microscale level occurs, then neighboring vortices of burned and unburned material may be conceptualized. When the volumetric interdiffusion or mixing rate between adjacent Kolmogorov vortices exceeds the volumetric rate of chemical reaction, then the temperature decreases, the turbulent burning velocity drops below a critical value, and local extinction occurs.

Although Dahm and associates (Broadwell et al., 1985; Dahm and Dimotakis, 1987; Dahm and Dibble, 1988) concede that strained flame sheets govern the mechanism leading to liftoff in turbulent diffusion flames, they adopt a somewhat expanded view of premixing in describing the mechanism controlling blowout. During the entrainment process, cold ambient air intertwines with the hot mixture (of products and excess fuel) found in the large-scale structures. The interleafing of the cold air and hot mixture progresses down an inviscid cascade until reaching the Kolmogorov scale. During the cascade process, chemical reaction occurs by molecular diffusion across the strained interfaces. When the cascade reaches the microscale, molecular diffusion homogenizes the remaining cold air and the hot mixture. The fuel concentration in the hot mixture is assumed to be spatially uniform throughout each structure, although the concentration decreases with its Lagrangian age as the vertical structures progress downstream. Hence, two parallel flame processes are occurring simultaneously: combustion in the strained flame sheets, and combustion in the (premixed) homogenized mixtures. In the upstream regions near the nozzle, the resulting homogeneous mixture will still be too fuel rich to induce reaction. However, the strained flame sheets in the upstream region will support combustion (assuming a critical strain threshold has not been exceeded leading to liftoff). In the downstream regions, after successive repetitions of mixing on the scale of the Kolmogorov eddies, the homogenized mixture becomes less fuel rich and more susceptible to combustion. Burning of the homogenized mixtures and the strained flame sheets proceeds simultaneously near the flame tip. Since the fuel-rich, homogenized mixtures are quenched in the upstream regions, it is hypothesized that initial liftoff occurs when the flame sheets exceed a critical strain. However, blowout in the far field is presumed to occur when the dominant homogenized mixtures are extinguished. Extinction in both the strained flame sheets and homogenized mixtures is caused by rapid molecular mixing leading to quenching of the ignitable reactants. However, the former is caused by rapid diffusion induced by excessive scalar gradients, while the latter is prompted by very rapid, large-scale mixing and entrainment.

Although both the laminar diffusion flamelet and premixed models rely on the presence of scalar gradient or mixing intensity to trigger flame extinction, the fundamental combustion processes involved (i.e., diffusion or partially premixed) have not yet been completely resolved. Both models have demonstrated satisfactorily their ability in correlating experimental data and providing insight into the physical mechanisms involved. It is incumbent upon further research efforts to delineate more fully the range over which each has applicability.

Inasmuch as the physical mechanisms leading to liftoff and blowout have not been fully defined, a combustion modeling approach was sought that was potentially applicable to both diffusion and premixed flames and that contained enough of the essential elements of microscale premixing and quenching to be amenable with the prevailing extinction viewpoints.

Eddy Dissipation Concept

The Eddy Dissipation Concept (EDC) of Magnussen (Magnussen and Hjertager, 1977; Byggstoyl and Magnussen, 1985; Magnussen, 1979, 1981a, b, 1985, 1989) is a general model for chemical reaction in turbulent flow. A simplified version of the EDC model, based on infinitely fast chemistry, has been widely used for the calculation of diffusion flames, premixed flames, explosions, flares, transient fire development, and combustion in Otto-cycle engines and gas turbine combustors. Expanded versions of the model, which attempt to include the effects of finite kinetics, have been applied to liftoff of turbulent jet diffusion flames, soot formation and combustion, and NO_x formation.

The EDC model focuses on the physics of the fine-scale turbulence. Microscale processes, exemplified by the dissipation of turbulence into heat and the intimate mixing of reactants on a molecular level, occur within fine eddy structures that have characteristic dimensions on the order of the Kolmogorov microscale. The fine structures may be vortex tubes, sheets, or slabs whose dimensions are small in one or two dimensions, but not in the third. The microscale structures are concentrated in fine-structure regions, which are themselves severely intermittent in a spatial sense and which have a cumulative volume that is only a small fraction of the volume of the fluid.

The eddy dissipation combustion model is based on the concept that the reactants are homogeneously mixed within the fine structures. Therefore, the fine structures are regarded as well-stirred reactors. An illustration of this concept is shown in Fig. 1, where the fluid is partitioned into the fine structures, which define the well-stirred reactors, and the "surrounding fluid," which includes all of the remaining fluid, regardless of turbulence scale. The fine structures are assumed to have a uniform

Nomenclature

m_i = mass fraction of species i
p, P = static pressure
Q = heat load
s = space velocity
T = temperature
V = reactor volume
x, y = Cartesian coordinate directions
y^+ = dimensionless "law-of-the-wall" coordinate
ρ = density
τ = residence time
ϕ = equivalence ratio

Downloaded 02 Jun 2010 to 171.66.16.104. Redistribution subject to ASME license or copyright; see http://www.asme.org/terms/Terms_Use.cfm

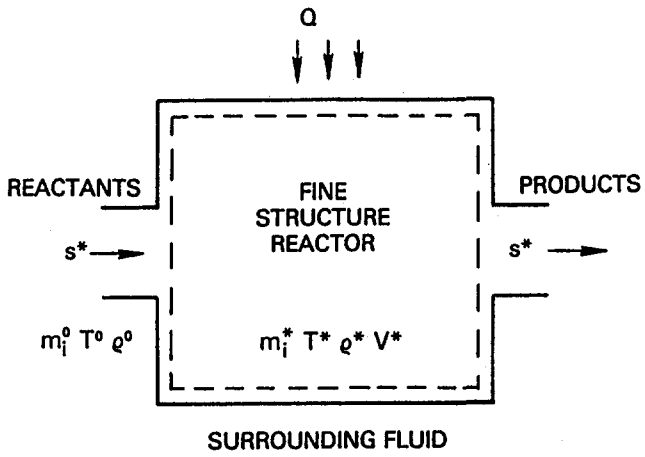

Fig. 1 Schematic illustration of a reacting fine structure (adapted from Magnussen, 1985)

internal composition and temperature, which are determined by the extent of reaction within the subgrid scale reactor. The composition and temperature of the "surrounding fluid" constitute the feed stream conditions to this reactor. To be able to model the chemical reactions occurring within the well-stirred reactors, it is necessary to know the fine-structure volume, as well as the mass exchange rate between the fine structures and the surrounding fluid. The EDC model supplies a system of equations that describes the chemical reaction process within the fine-structure reactors and then relates the microscale parameters to the ensemble-averaged, mean flow field. The ensemble-averaged mean scalar quantities within a local fluid volume (e.g., computational grid cell) are determined by an appropriate linear combination of the fine-structure and surrounding-fluid characteristics.

A full description of the model equations is too extensive to provide at this juncture. However, the required set of EDC model equations, in conjunction with a stirred reactor calculation methodology and "full" chemical kinetics, may be solved for the fine-structure and surrounding-fluid regions of every computational node in the flow field domain. This procedure would, in principle, permit calculation of the pertinent flow field variables in the kinetically limited regime near the onset of the postulated blowout instability.

The key to the success of such an endeavor is the accuracy of the available kinetic mechanisms in the limit of weak extinction, and the extent of the respective computational burdens involved. Since this key is central to both the stirred-reactor network concept and the EDC "sub-grid" stirred-reactor model, the solution methodology and CPU penalty of a stirred-reactor code was investigated, and the predictive accuracy of various kinetic mechanisms was ascertained.

Suitability of PSR Code for LBO Calculation

The stirred-reactor code selected as the vehicle to evaluate the accuracy of the kinetic mechanisms in the limit of extinction was the PSR/Chemkin II code (Glarborg et al., 1988). In the Chemkin PSR code, the system of nonlinear equations is solved by a modified, damped Newton algorithm. If the Newton algorithm fails to converge, the solution estimate is conditioned by a time-integration procedure, which provides initial estimates that are more likely to be within the domain of convergence for Newton's method. Despite the robust convergence features of the Chemkin PSR code, for general purposes the characteristic reaction behavior of the stirred-reactor in the limit of extinction necessitated special modifications to the convergence algorithms. A discussion of the special nature of the extinction point, as well as the arc-length parameterization and continuation methodologies required to calculate it, is relegated to Appendix A.

Kinetic Mechanism Evaluation

The PSR/Chemkin-II code, equipped with both the arc-length parameterization and continuation methodologies, was utilized to evaluate various propane kinetic mechanisms. Propane was selected because its kinetic mechanism has been fairly well established relative to the higher hydrocarbons, and its reaction chemistry behavior resembles that of vaporized JP fuels (design considerations are provided in Sturgess et al., 1992a). Some of the propane kinetic mechanisms evaluated are shown in Table 1. Additional mechanisms include the six-step (global), seven-species mechanism of Jones and Lindstedt (1988), and the eight-step (global/irreversible), eight-species mechanism of Kiehne et al. (1987). However, the former mechanism manifested some unrealistic species concentration behavior near extinction, and the latter could not be solved with the PSR/Newton algorithm because of negative exponents on the species concentrations in the rate expressions (a time-dependent, stiff integrator is required). The Colket (1989) mechanism is a full mechanism, while the Pazcko et al. (1988) partial mechanism contains only those reaction steps that are considered to be important in high-temperature flames. The reduced mechanism, also proposed by Pazcko et al. (1988), consists of relatively complex algebraic expressions formed by the judicious application of partial-equilibrium and steady-state assumptions to the elementary reaction steps. Both the Edelman and Harsha (1978) and Kollrack (1976; Roberts et al., 1972) mechanisms are quasi-global in nature, although the latter mechanism is for JP5 fuel. The Kollrack mechanism was adapted for propane use by both substituting propane thermodynamics for JP5 thermodynamics and by modifying the global steps for the appropriate C:H ratio. The Kollrack mechanism (with propane thermodynamics) was investigated because of its apparent success in predicting propane LBO within the context of a stirred reactor network code (see Sturgess et al., 1991a, b). The Kretschmer and Odgers (1972) empirical expression is based on a one-step stoichiometry relationship for propane. By tabulating the adiabatic temperature rise, activation temperature, and fractional oxygen consumption efficiency as a function of the inlet temperature and the inlet equivalence ratio, the authors were able to calibrate the expression to blowout data from stirred reactors. In order to change the expression into a form that could be inserted into a PSR code and that would provide realistic flame temperatures, it was necessary to modify the stoichiometry relationship by specifying an equilibrium product distribution for the particular equivalence ratio, and then scale the LBO resultant with simple polynomial fits until the resultants matched those of the parent empirical expression.

It can be seen from Table 1 that the full mechanism is approximately two orders of magnitude as CPU intensive as the Kretsh-

Table 1 Propane kinetic mechanism comparison

Mechanism	Number of Species	Number of Reactions*	CPU Seconds** Per Steady-State Solution	30-Step CPU***	Comments
Colket (1989)	51	249-R	1.376	41.3	Full mechanism
Pazcko, Lefdel, Peters (1988)	29	76-I	0.308	9.24	"Partial" mechanism
Pazcko, Lefdel, Peters (1988)	8	5-G	0.045	1.35	Reduced mechanism
Edelman and Harsha (1978)	10	1-G 12-R	0.044	1.32	Quasi-global mechanism
Kollrack (1976) Roberts, et al. (1972)	21	2-G 28-R	0.16	4.8	(a) Quasi-global mechanism (b) Fuel is JP-5
Kretschmer and Odgers (1972) (modified)	7	1	0.015	0.45	Equilibrium product distribution

* I = Irreversible elementary step
R = Reversible elementary step
G = Global step

** CPU on IBM 3090 platform.

*** 20 to 50 steady state solutions may be required to find the extinction point along the reacting branch of the bifurcation curve.

Downloaded 02 Jun 2010 to 171.66.16.104. Redistribution subject to ASME license or copyright; see http://www.asme.org/terms/Terms_Use.cfm

mer and Odgers (1972) one-step mechanism. The reduced mechanism of Pazcko et al. (1988) and the quasi-global mechanism of Edelman and Harsha (1978) also appear to be candidates for consideration on a low CPU-usage basis. Inasmuch as 20 to 50 steady-state solutions may be required to find the extinction points along the reacting branch of the bifurcation curve, the tabular column entitled "30-step CPU" provides an idea of the total CPU required to calculate extinction using the PSR code methodology at a single computational cell during a single gas-phase iteration of a CFD code (see Appendix A). As a basis for reference, the overall CPU time per iteration on a 48 × 45 mesh using a two-dimensional CFD code with the three-species, eddy-breakup combustion model is 1.3 CPU seconds. In such a case, the PSR calculation for even a 10-specie mechanism in a single cell requires as much CPU as an entire gas-phase iteration. Certainly, local application of a PSR calculation or any locally implicit multispecies approach should be done sparingly and selectively.

In order to assess the relative predictive accuracy among the various mechanisms, the PSR calculations were compared with experimental data from the well-stirred reactor experiments of Clarke et al. (1958). The PSR calculations did not take into account possible heat loss. The blowout curve predictions are shown in Fig. 2, plotted in the traditional format of equivalence ratio versus air loading parameter. The experimental blowout points inscribe a typical parabolic profile, with the peak loading occurring near stoichiometric equivalence ratio.

It can be seen from Fig. 2 that the Kollrack mechanism gives results that are generally in good agreement with the Clarke et al. experimental extinction data for lean blowouts; however, there is some fall-off in agreement at low values of combustor loading. (This explains the good agreement obtained by Sturgess et al. (1991b) between experimental LBO data and PSR calculations for a research combustor.) All the other mechanisms give extremely poor agreement at all lean equivalence ratios. For rich equivalence ratios (rich blowouts), both the quasi-global Kollrack and the Edelman and Harsha mechanisms give trends that are qualitatively incorrect; only the "full" and reduced" mechanisms of Paczko et al. are qualitatively correct, while being substantially in error quantitatively.

The predictive accuracy of the Kretschmer and Odgers (1972) empirical expression (unmodified), which was calibrated by comparison with PSR blowout data (including the Clarke et al. (1958) experiments), is shown in Fig. 3. The predictive error and data scatter is typical of the other data sets

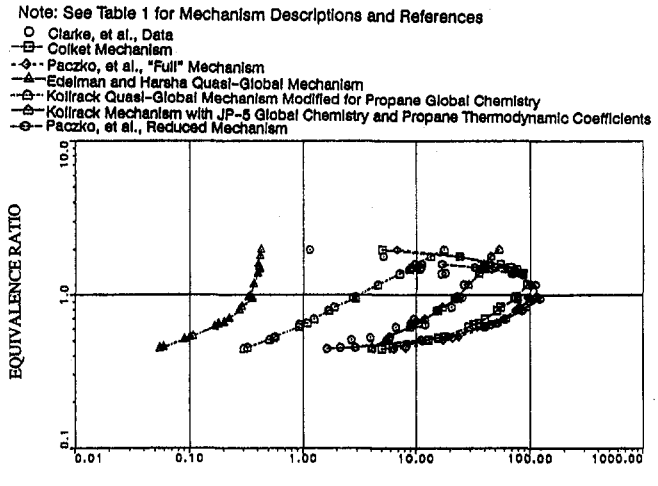

Fig. 2 Comparison of predicted and measured equivalence ratios at extinction as a function of air loading parameter for a well-stirred reactor (injector A of Clarke et al., 1958)

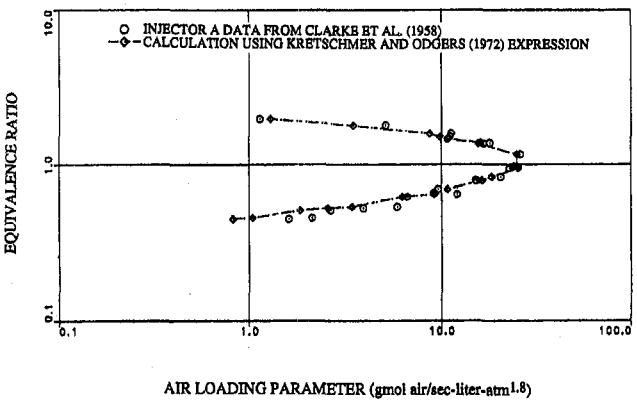

Fig. 3 Comparison of predicted and measured equivalence ratios at extinction as a function of air loading parameter for a well-stirred reactor (injector A of Clarke et al., 1958)

(e.g., injector D, which is not shown) in the Clarke et al. experiments. Given the data scatter represented by the measurements in Fig. 3, it may be concluded that the calibrated ALP expression attains greater predictive accuracy than that exhibited in previous attempts with multistep mechanisms. These predictions now represent the minimum level of accuracy, which other mechanisms or techniques must match in order to be considered for extinction calculations.

It is surprising that at the stoichiometric condition, the full and reduced mechanisms are in error by an approximate factor of 4, which is clearly unacceptable for design purposes. The lack of agreement for the full mechanism, in conjunction with the demonstrated agreement shown for the Kollrack calculation, suggests that this mechanism incorporates a fortuitous assembly of reaction steps and rate constants for the prediction of lean blowouts in hydrocarbon/air mixtures. At least three major factors may have contributed to the observed discrepancies with the data: heat loss, unmixedness, and kinetic mechanism inaccuracies. Although heat losses and imperfect mixing were not quantified in the Clarke et al. experiment, such factors can significantly influence PSR predictions. Spherical reactors of the Clarke et al. type do have heat losses typically greater than 5 percent, and Clarke et al. did observe a pressure loss effect on their data, indicative of less than perfect mixing. Both heat loss and unmixedness, if properly accounted for in the computation, would tend to reduce the peak ALP values of the calculated blowout curve. Although this would decrease the predictive error, it is doubtful that their combined effect could account for the observed (factor of 4) discrepancy with the experiments.

A more plausible explanation for the source of the predictive error is that the hydrocarbon kinetic mechanism may be inadequate in some way. The inadequacy may manifest itself either in terms of the reaction pathways postulated to occur or in terms of the inaccuracy associated with empirical determination of the constants. For example, the pressure dependency may be inadequate for the subatmospheric pressures involved or the concentration dependency for the complex hydrocarbon fragments may be erroneous. For hydrocarbon mechanisms, the ratio constants are known relatively accurately for only a fraction of the total steps. Furthermore, the rate constants are a function of the range of experimental conditions and those conditions are typically removed from blowout conditions.

Extinction Model Methodology

Efforts to predict "perfectly" stirred-reactor (PSR) extinction data demonstrated that neither full nor reduced kinetic mechanisms for propane were able to predict the air loading parameter (ALP) at blowout to within an acceptable degree of error. It was concluded that the discrepancy between the data

Downloaded 02 Jun 2010 to 171.66.16.104. Redistribution subject to ASME license or copyright; see http://www.asme.org/terms/Terms_Use.cfm

and the calculation was most likely due primarily to an inherent inadequacy in the mechanism. These results are indicative of the difficulty of constructing a kinetic mechanism from reaction rate studies available in the literature and applying the mechanism to the relatively unexplored realm of extinction in turbulent flames. For this reason, the simple approach of utilizing a global, single-step rate expression, precalibrated to extinction data, was adopted for use in subsequent extinction calculations. This approach accepts the penalty of loss of wide applicability and versatility (associated with a more complete mechanism) in exchange for improved accuracy in the limit of extinction and substantial cost benefits.

The eddy dissipation concept can be partially implemented as a characteristic time approach, in which the calibrated, single-step rate expressions may be utilized as a stability criterion in conjunction with a fast chemistry model. In this technique, fast or equilibrium chemistry is coupled with the characteristic-time criteria extracted from the EDC model to form a relatively simplistic and CPU-viable prediction package for local extinction in a CFD code.

According to the EDC model, the fine structure or dissipation eddies constitute PSR entities. The local hydrodynamic time scales or residence times corresponding to the fine structure eddies may be calculated from the information supplied through the turbulence model in the CFD code. By calculating the relevant chemical time scale at extinction and comparing it to the hydrodynamic equivalent, the code could, in principle, compute local regions of extinction, and hence, potentially simulate flame lift and blowout.

Chemical Time Scale. The chemical time scale at extinction for propane fuel may be calculated from the Kretschmer and Odgers (1972) empiricism. The expression is based on a stoichiometry relationship (molar basis) for propane given as:

$$\phi C_3H_g + 5(O_2 + aN_2) \rightarrow 3\epsilon\eta CO_2 + 4\epsilon\eta H_2O + (\phi - \epsilon\eta)C_3H_g + 5(1 - \epsilon\eta)O_2 + 5aN_2 \quad (1)$$

where

ϕ = molar equivalence ratio
a = 3.762 moles of N_2/moles O_2 in air
η = ϕ for $\phi \leq 1$
= 1 for $\phi > 1$

and

ϵ = fractional (oxidant) consumption efficiency.

The reaction rate expression is given in terms of the molar rate of disappearance of oxygen as:

$$-r_o = \frac{-dC_o}{dt} = k_o T^m e^{-\mathrm{Tact}/T} C_f^{\alpha} C_o^{\beta} \quad (2)$$

where

r_o = molar rate of disappearance of oxidant (gmol O_2/liter-s)
C_f = molar concentration of fuel (gmol C_3H_g/liter)
C_o = molar concentration of oxidant (gmol O_2/liter)
t = time (s)
k_o = pre-exponential factor based on the oxidant = 1.29×10^{10} ((liters)$^{\alpha+\beta-1}$/(K)^m(gmol)$^{\alpha+\beta-1}$(s))
T = temperature (K)
m = exponent on the temperature
α, β = exponents on the reactant concentrations
Tact = activation temperature (i.e., activation energy divided by the gas constant; in units of K)

For use with blowout curves, the reaction rate equation is couched in terms of an air loading parameter (ALP):

$$\frac{N}{VP^n} = \frac{k_o}{R^n}\frac{(a+1)}{\eta\epsilon}(T_{\mathrm{in}} + \epsilon\Delta T)^{m-n} e^{-\mathrm{Tact}/(\mathrm{Tin}+\epsilon\Delta T)} x_f^{n/2} x_o^{n/2} \quad (3)$$

where

x_f = mole fraction of fuel =

$$\frac{\phi - \epsilon\eta}{5(a+1) + \phi + \epsilon\eta} \quad (4)$$

x_o = mole fraction of oxygen =

$$\frac{5(1 - \epsilon\eta)}{5(a+1) + \phi + \epsilon\eta} \quad (5)$$

n = overall reaction order = $\alpha + \beta$
= 2ϕ for $\phi \leq 1$
= $2/\phi$ for $\phi > 1$
R = universal gas constant =

$$0.08205 \frac{\mathrm{atm - liter}}{\mathrm{gmol - K}}$$

T_{in} = inlet temperature (K)
ΔT = "undissociated" adiabatic temperature rise (K)
V = reactor volume (liter)
P = static pressure (atm)
N = molar flow rate of air into the reactor (gmol air/s)

Kretschmer and Odgers have calibrated the expression to blowout data by tabulating values of the adiabatic temperature rise (ΔT), the activation temperature (Tact), and the fractional oxygen consumption efficiency (ϵ) as a function of the inlet temperature (T_{in}) and the inlet equivalence ratio (ϕ). The tabulation spans inlet temperatures from 300 K to 900 K and equivalence ratios from 0.4 to 2.0.

The extinction residence time (τ^*_{ext}) for the fine-structure eddies may be expressed as:

$$\tau^*_{\mathrm{ext}} = \left(\frac{\rho V}{\dot{m}}\right)^*_{\mathrm{ext}} \quad (6)$$

where ρ is the mass density and $\dot{m}$ is the total mass flow rate into the "reactor." For a given set of reactants (e.g., fuel and air), the extinction residence time is independent of the actual volume (V) specified since the mass flow rate will adjust commensurately to maintain the correct ratio. Consequently, extinction residence times may be calculated solely as a function of the inlet temperature and equivalence ratio.

An example of this calculation using the Kretschmer and Odgers ALP expression (Eq. (3)) is given in Fig. 4. (The waviness of the lines is due to the tabulated constants in the expression.) As expected, the residence times decrease with

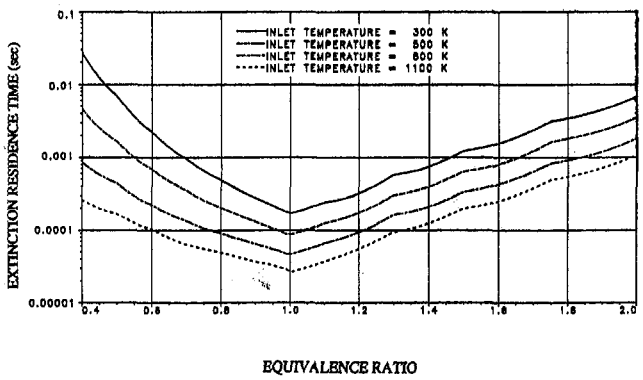

Fig. 4 Extinction residence time as a function of inlet temperature and equivalence ratio as calculated from the Kretschmer and Odgers (1972) ALP expression

Downloaded 02 Jun 2010 to 171.66.16.104. Redistribution subject to ASME license or copyright; see http://www.asme.org/terms/Terms_Use.cfm

increasing temperature and attain a minimum at unity equivalence ratio. The calculated extinction residence times constitute critical chemical time scales. If a local hydrodynamic time scale or residence time is smaller than the prevailing chemical time scale corresponding to extinction, then reaction will not occur and the original reactants entering the PSR are recovered.

Hydrodynamic Time Scale. The fast-chemistry version of the EDC model is based upon a simple, irreversible, one-step chemical reaction rate expression:

(1) mass fuel + (a) mass oxidant →

($1 + a$) mass products (7)

where a is the air-to-fuel stoichiometry ratio on a mass basis. Under fast-chemistry conditions, the limiting concentration of fuel (in a fuel-lean environment) or oxidant equivalents (in a fuel-rich environment) will go to zero in the fine structures or dissipation eddies. Consequently, the mean mass consumption rate of the fuel per unit volume is given as:

$$\bar{R}_{fu} = \frac{\bar{\rho} s \chi \eta}{1 - \gamma^* \chi} (\bar{m}_{\min}) \tag{8}$$

where:

$$\bar{m}_{\min} = \text{minimum of} \left\{ \bar{m}_{fu}, \frac{\bar{m}_{ox}}{a} \right\} \tag{9}$$

$$\chi = \frac{C}{\gamma_\lambda} \left[\frac{\dfrac{\bar{m}_{pr}}{1+a}}{\dfrac{\bar{m}_{pr}}{1+a} + \bar{m}_{\min}} \right] \leq C \tag{10}$$

$$C = \frac{\left(\bar{m}_{\min} + \dfrac{\bar{m}_{pr}}{1+a} \right)^2}{\left(\bar{m}_{fu} + \dfrac{\bar{m}_{pr}}{1+a} \right) \left(\dfrac{\bar{m}_{ox}}{a} + \dfrac{\bar{m}_{pr}}{1+a} \right)} \tag{11}$$

$$\eta = \frac{1}{\gamma_\lambda} \leq \left[\frac{\bar{m}_{\min} + \dfrac{\bar{m}_{pr}}{1+a}}{\bar{m}_{\min}} \right] \tag{12}$$

$$\gamma_\lambda = 2.13 \left(\frac{\nu \epsilon}{k^2} \right)^{1/4} \tag{13}$$

$$\gamma^* = 9.7 \left(\frac{\nu \epsilon}{k^2} \right)^{3/4} \tag{14}$$

$$s = 23.6 \left(\frac{\nu \epsilon}{k^2} \right)^{1/4} \left(\frac{\epsilon}{k} \right) = \frac{1}{\tau} \tag{15}$$

and where χ represents the fraction of the fine structures which are sufficiently heated to react, C is a type of correlation coefficient, η is a heuristic reaction rate modifier, γ^* is the mass fraction of the fine structures in the fluid, and s is a space-velocity for the bulk fluid with units of reciprocal time. The hydrodynamic time scale or residence time in the fine structures is given as:

$$\tau^* = \frac{1}{s^*} = \frac{\gamma^*}{s} = \frac{1}{2.43 \left(\dfrac{\epsilon}{\nu} \right)^{1/2}} \tag{16}$$

An alternate time-scale expression provided in the EDC model, which is a characteristic time scale for the mass exchange between the reacting fine structures and the bulk fluid, can be expressed as:

$$\tau_R = \left(\frac{1 - \gamma^* \chi}{\eta} \right) \tau^* \tag{17}$$

These time scales (τ^*, τ_R or τ) may be compared with the chemical kinetic times scales to establish criteria for the extinction of flames. In regions of the computational domain where zero products exist, the coefficient term of Eq. (17) is equal to unity, and τ_R reduces to τ^*. (This is essentially the case for cells positioned between the nozzle exit and the liftoff height.)

In the present investigation, only τ^* was utilized as the relevant time scale. The chemical kinetic time scale (τ_{ext}) may be found by extracting the residence time at extinction from the calibrated Kretschmer and Odgers ALP expression (see Eq. (3)). Strictly speaking, since the perfectly stirred reactors are represented by the fine structures or dissipation eddies, the "inlet" feed quantities to the PSR are those corresponding to the "surrounding" fluid (see Fig. 1). The mean cell values are a weighted summation of the PSR and surrounding fluid values, e.g.:

$$\bar{\phi} = (\gamma^* \chi) \phi^* + (1 - \gamma^* \chi) \phi^\circ \tag{18}$$

where the asterisk (*) represents the PSR mixture and the degree symbol (°) represents the fluid in the cell surrounding the fine structures. However, since only a partial version of the EDC model is being solved, it is assumed that $\phi \approx \phi^\circ$. Therefore, the "inlet" temperature and equivalence ratio used as feed parameters for the Kretschmer and Odgers PSR extinction expression are simply the local mean quantities. The equivalence ratio used in the model is based on a composite fuel and air, both of which are based on appropriate combinations of products and unburned reactants. Therefore, the equivalence ratio parameter is that which would exist in the absence of reaction for the same flow field (i.e., a mixture fraction type of parameter).

Solution Procedure. The flow chart logic for the extinction calculations using the EDC model is shown in Fig. 5. Following solution of the momentum equations and satisfaction of continu-

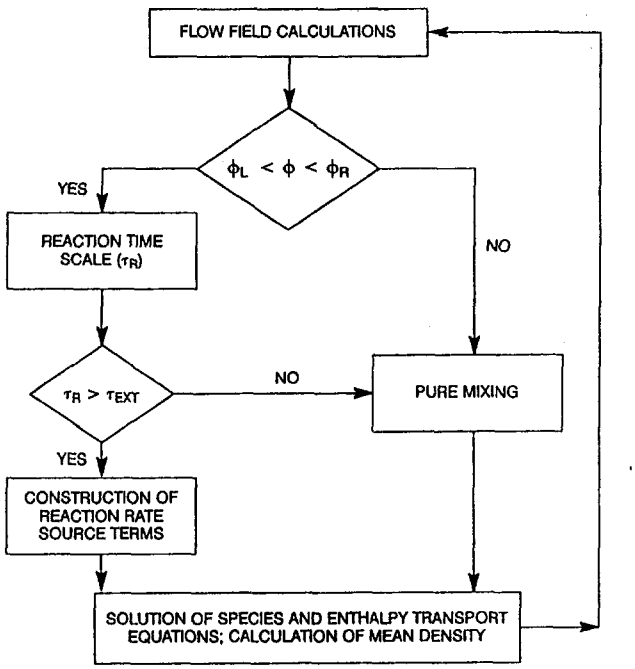

Fig. 5 Flowchart for the extinction calculations using the EDC model (adapted from Magnussen, 1985)

Downloaded 02 Jun 2010 to 171.66.16.104. Redistribution subject to ASME license or copyright; see http://www.asme.org/terms/Terms_Use.cfm

ity, the source terms for the species continuity equation are constructed. Two constraints or gates are applied to the construction of the source terms. First, the local equivalence ratio is compared with prespecified "combustion" limits. Such limits are conceptually distinct from flammability limits. Plots of extinction residence times as a function of equivalence ratio are parabolic in appearance and concave up (see Fig. 4). The rich (ϕ_R) and lean (ϕ_L) combustion limits correspond to asymptotes on each side of the "parabola"-shaped curve or to arbitrarily selected threshold values of extinction residence time. Such combustion limits are a function of the "inlet" feed temperature to the PSR. However, in most of the calculations that follow, unless otherwise specified, constant rich and lean combustion limits were selected that are independent of the inlet temperature. The rich and lean limits were selected as 2.0 and 0.4, respectively; these limits are similar to traditional flammability limits and represent the extent to which the curve fit in the Kretchmer and Odgers ALP expression may be considered to be valid. The local equivalence ratio, which is tested against the combustion limits, is that based on composite, burned-plus-unburned fuel and air. This type of equivalence ratio produces an expanding flame zone, which is closely aligned with the flame zone of the traditional eddy breakup model. Utilization of an equivalence ratio based on unreacted fuel and air alone produces a thin flame sheet over the entire length of the reactor, which is resolved rather poorly with the fixed and coarse grids currently available in CFD codes.

Within the confines of the expanding grid region defined through satisfaction of the combustion limits, a second constraint on the flame zone is applied. The hydrodynamic or PSR residence time (τ^*), or alternatively the "reaction" mass-exchange time scale (τ_R), is calculated and compared with the extinction time scale (τ_{ext}). If the hydrodynamic time scale is smaller than the extinction time scale, then the combustible material within the PSR is not allowed to react, simple mixing occurs, and the reaction rate source term is zero. If the opposite is true, then reaction within the dissipation eddies is permitted, and the reaction rate source terms are constructed from the EDC model relationships. The species and enthalpy transport equations are subsequently solved, density is calculated from its equation of state, and the solution algorithm loops back for another gas-phase iteration.

The fast-chemistry EDC combustion model, with the time-scale methodology described above, were incorporated into the Pratt & Whitney two-dimensional PREACH code (Sturgess, 1983). Additional details regarding the implementation of the model are given in Appendix B.

Dahm and Dibble Liftoff Case

Experimentally measured liftoff heights for a reacting propane–air case are provided by Dahm and Dibble (1988). The gaseous propane enters through a centered fuel tube, which is 3.3 mm in diameter, while the coflowing air stream is enclosed by square duct with side dimensions of 30 cm. The thickness of the fuel tube wall is 0.9 mm. The air stream has an average velocity of 0.58 m/s and a turbulence intensity of 0.4 percent. The propane feed stream is assumed to have a temperature of 260.9 K and turbulence intensities on the order of 6.5 percent. Five finite-difference cells were fitted radially into the primary fuel tube. Two fuel-jet velocities were selected at which to provide liftoff height calculations (20 and 40 m/s). The measured liftoff height at the jet velocity of 40 m/s is approximately 0.132 m, and the measured liftoff height at the jet velocity of 20 m/s is approximately 0.085 m. Since the overall length of the computational domain is 0.8 m and the grid size is 77 × 53, the cell dimensions in the vicinity of the two calculated liftoff height positions are relatively large. The cell length at the upstream liftoff height position is approximately 5 mm, and the cell length at the downstream liftoff height position is on the order of 10 mm. The CFD calculations were axisymmetric.

The liftoff height predictions are shown in Fig. 6. Similarity between the calculated and experimental trend in liftoff height is qualitative only. It can been seen that the flame calculation at the fuel-jet velocity of 40 m/s yields a liftoff height that is in close agreement with the experimental values. On the other hand, the predicted liftoff height at the jet velocity of 20 m/s is somewhat lower than the measured value.

The predicted error in both the point magnitude and the slope of the curve may be attributed to a number of potential sources. The jet growth and development may not be adequately captured due to (a) poor grid resolution in the vicinity of the shear layer, (b) inadequate turbulence and mixing models, (c) failure of a stationary code to simulate low frequency transient characteristics, etc. Certainly, application of the characteristic time approach using crude approximations in the time scale comparison is also a contributing factor. No attempt is made at this juncture to delineate the degree of contributive error from each of the candidate factors.

Flame Lift in a Recirculating Flow Field

Application of the modified two-dimensional PREACH code containing the EDC/time-scale technique to the parabolic flow field of coflowing jets is not by itself a conclusive demonstration of the qualitative efficacy of the concept for flame lift. The concept should also be evaluated in an elliptic flow field, such as that provided by a back step recirculation zone. The unique flame characteristics exhibited by a research step combustor, used in the CDME LBO program (Sturgess et al., 1994), offer a challenging opportunity to further explore the potential of the extinction model.

A schematic of the research step combustor is shown in Fig. 7 and discussed in detail elsewhere (e.g., Sturgess et al., 1992a). A coannular air stream (40 mm O.D.) and fuel jet (30 mm I.D.) feeds air and gaseous propane to a sudden expansion with 55 mm step height. A low Reynolds number set of LDA measurements (SRL, 1990), were made at a constant airflow of 1000 lpm. For the three reacting flow cases (see Table 2), the propane flow ratio was nominally 23, 41, and 63 lpm. For the nonreacting flow case, the "fuel" jet flow rate was 23 lpm of nitrogen. (Nitrogen was used because the molecular-weight equivalent to propane fuel, carbon dioxide, would freeze up the regulators.) The blowout condition was observed at 21 lpm of fuel. For the F23 case ($\phi = 0.59$), the flame was lifted to an observed height of approximately 0.15 m. For the F41 case ($\phi = 1.05$), the liftoff height is approximately 0.10 m. The flame was attached to the edge of the step in the F63 case ($\phi = 1.62$). Since locally laminarized flame regions are observed for Reynolds numbers less than 9000 for free propane jets, the Reynolds numbers in the research step combustor for these flow conditions may be sufficiently low to represent turbulent and transitionally turbulent conditions.

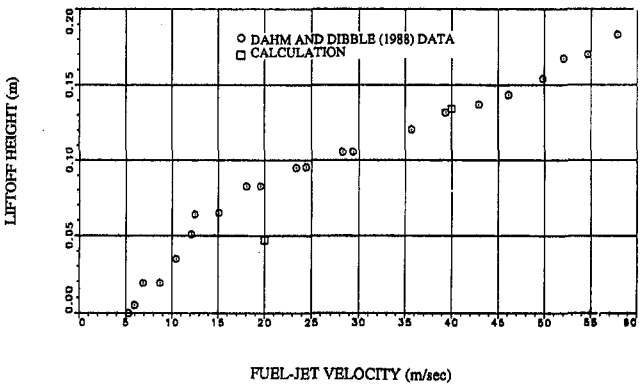

Fig. 6 Comparison of predicted and measured liftoff heights (experimental data from Dahm and Dibble, 1988)

Downloaded 02 Jun 2010 to 171.66.16.104. Redistribution subject to ASME license or copyright; see http://www.asme.org/terms/Terms_Use.cfm

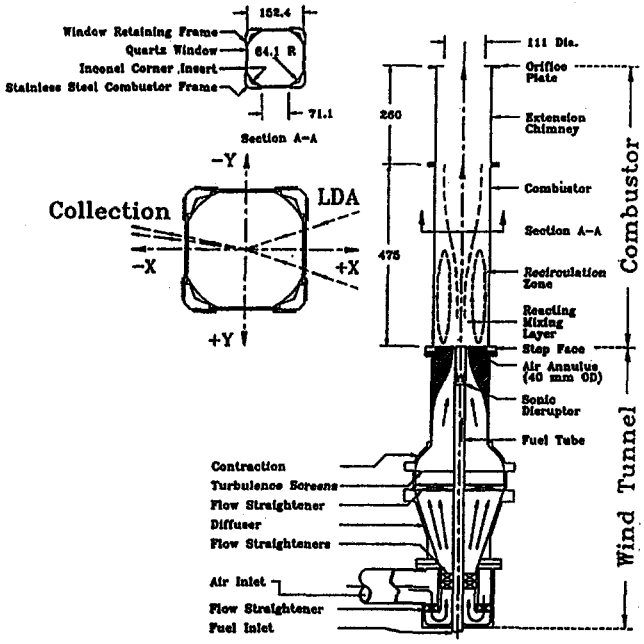

Fig. 7 Schematic of the Research Step Combustor (Sturgess et al., 1992a)

The experimental liftoff height was determined visually, and corresponded to the closest position to the step plane at which flame was observed. (The flame boundary is typically somewhat parabolic, with the closest position in the step shear layer, and of course, is not absolutely stationary.) The liftoff heights are similar to those determined in a companion study of a slightly altered version of the research step combustor. In that study, the visually integrated liftoff heights ranged from 0.16 m to 0.30 m as a function of air flow rate (1200 to 3200 lpm) and equivalence ratio. The flame anchor points fluctuated approximately ±25 mm about the mean axial position and precessed about the symmetry axis; the frequency of the oscillation was less than 60 Hz. The differences perhaps could be associated with the presence, in the fuel tube, of an acoustic isolator (a perforated cone) that increased the turbulence in the fuel jet for the latter tests. To assist in understanding the flame lift and attachment phenomena, planar imaging of instantaneous, laser-induced fluorescence (LIF) emissions of OH have been utilized, as well as thin-film pyrometry (TFP) and Reactive Mie Scattering (RMS).

It has been shown (Roquemore et al., 1991; Sturgess et al., 1991a, 1994) that a centerline recirculation zone is formed at the fuel jet exit due to momentum differences in the fuel and air streams. Because of the relatively low temperatures and high fuel-rich equivalence ratio exhibited in that region, the centerline recirculation zone is unable to support combustion. The experimentally determined centerline reattachment point is between 30 and 35 mm for all cases. For the lifted flames, LIF imaging indicates that a thick flame zone exists in the downstream shear layers, stabilized by the step recirculation zone. When the burner is operated in the fuel-rich mode, the flame is observed to be very stable and is anchored in the fuel–air shear layer by a pilot flame attached to the rearward facing step. The pilot flame is concentrated in vortex structures that shed from the step. Consequently, the flame surface is not continuous but has holes that appear to be located in the braid region of the vortex train. Experimental TFP and LIF measurements indicate that attachment of the pilot flame is intermittent. The temperature peak of the pilot flame is about 5 mm wide and the average radial location of the mean temperature peak is approximately 4 mm (radially outward) from the edge of the step. In the case of the attached flame, intense combustion and mixing occur in the region where the shear layers of the step and fuel jet intersect. The intersection of the shear layers occurs at a distance of about 35 to 40 mm downstream from the confluence plane, and is characterized by vortex merging and a thickening of the flame. In this general vicinity, approximately coincident with the longitudinal extent of the centerline recirculation zone and the vortex merging, the time-averaged attached flame contour assumes an hourglass shape.

The two-dimensional PREACH code with the EDC/extinction model was applied to the four cases of Table 2. The purpose of the investigation was to assess the extent to which a stationary state code and a relatively crude extinction model could capture the lifted and attached flame characteristics exhibited by the experiments. The calculations assumed that the flows in the combustor were perfectly axisymmetric, which they are not. The mesh size used was 77 × 57 for one-half of the combustor from the assumed axis of symmetry; 15 cells were used in the fuel tube, and 5 for the air annulus. The inlet plane was taken as the confluence of the jets, and inlet boundary conditions were estimated from experimental conditions and from an analysis of the measurements taken at an axial station of 7 mm downstream from the step. The initial value taken for turbulent Schmidt number was 0.9. This value is really only appropriate for wall boundary layers; a value of 0.7 has been found appropriate for jet flames, and a value of 0.5 for recirculating flows (Syed and Sturgess, 1980).

N23 Case. LDA measurements of mean and rms velocities were provided at 14 axial positions. Centerline and radial profiles of predicted axial velocity for the nonreacting case are shown in Figs. 8 and 9, respectively. It can be seen that the calculations exhibit accelerated formation of the centerline recirculation zone, relative to the experiment, and the calculated reverse flow velocities are somewhat larger in magnitude. In the centerline recovery region, the experimental results show significantly higher magnitudes of centerline velocity than the calculation demonstrates. This behavior is typical of $k-\epsilon$ model predictions (Sturgess, 1983). At the farthest downstream location (x = 0.350 m), the predicted results may indicate that the experimental reattachment length for the step may be shorter than the calculated reattachment length (8.3 step heights). Perturbations to the inlet velocity profiles and magnitudes did not significantly improve the predictive accuracy. Moving the inlet boundary condition for the fuel tube upstream from the confluence plane served only to induce premature formation of the recirculation zone (although this was observed to experimentally occur for low fuel jet Reynolds numbers (Sturgess et al., 1994)).

The calculated streamline contours (not shown) demonstrate the characteristic hourglass contours arising from entrainment of the secondary air into the lower momentum centerline region.

Table 2 Case description for step research combustor

Case	Fuel	Fuel Flow Rate (SLPM)	Air Flow Rate (SLPM)	Equivalence Ratio	Fuel Tube* Reynolds Number	Comments
N23	Nitrogen	23	1000	-----	1,172	-------
F23	Propane	23	1000	0.59	4,003	Lifted (0.15 m)
F41	Propane	41	1000	1.05	7,135	Lifted (0.10 m)
F63	Propane	63	1000	1.62	10,964	Attached

* Annulus Re No. = 19,870
Duct Re No. = 9,613 (non-reacting)
~ 3,000 (reacting)

Downloaded 02 Jun 2010 to 171.66.16.104. Redistribution subject to ASME license or copyright; see http://www.asme.org/terms/Terms_Use.cfm

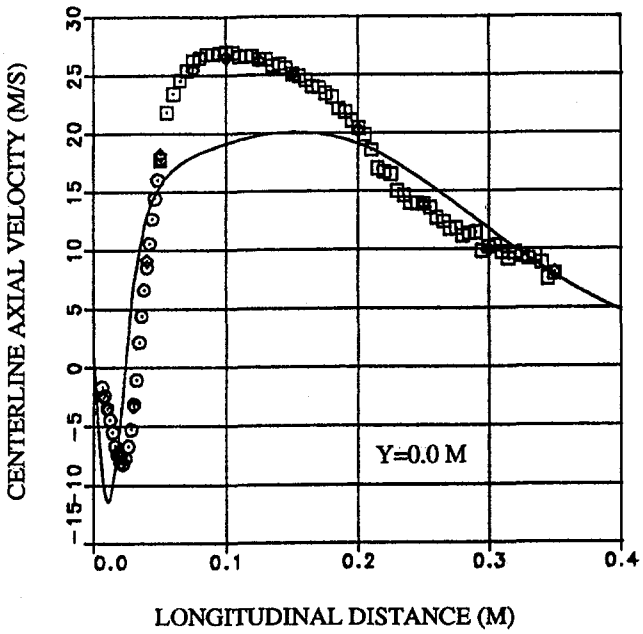

Fig. 8 Comparison of predicted and measured centerline axial velocity profiles for Case N23 (see Table 2); note: Axial extent of computational domain is 0.74 m

While the predictive accuracy is only moderately satisfactory due to a myriad of inlet boundary condition unknowns (see Sturgess et al., 1986) and turbulence model inadequacies, the calculation does calculate qualitatively the "correct" flow features expected from a stationary state analysis. The LDA data predictions for the reacting flow cases are qualitatively very similar and differ primarily in the magnitude of the velocities in the recovery region (due to volumetric expansion).

Eddy Breakup Calculations. To provide a reference base for comparison with the extinction model, the F23 ($\phi = 0.59$) and F63 ($\phi = 1.62$) cases were calculated with the eddy breakup (EBU) model (Magnussen and Hjertager, 1977). The EBU model is a fast-chemistry scheme that permits the fuel and oxidant to react as soon as they mix and form a stoichiometric mixture. Since reaction will occur along the mean stoichiometric contour, it is anticipated that the "flame sheet" will attach within the mixing layer between the fuel and the air. This is illustrated for Case F23 in Fig. 10. As expected the high-temperature flame zone anchors at the edge of the fuel nozzle. Since the F23 ($\phi = 0.59$) case is fuel-lean, the stoichiometric contour intersects the symmetry axis (as evidenced by the high-temperature zone on the centerline). The general trends exhibited by the stoichiometric contours and their coincidence with the high-temperature flame zones are characteristic of the EBU model. Neither the F23 nor the F63 calculations, performed with the EBU model, exhibit the experimentally observed hourglass shape in the streamline contours (not shown). As expected, the mixed-is-burned characteristic of the EBU model prevents it from qualitatively calculating either the lifted or attached pilot flame cases.

Case F23 ($\phi = 0.59$). The calculation characteristics of the fast-chemistry version of the EDC model, standing alone, are very similar to those of the EBU model in that the high-temperature zones will be closely aligned with the stoichiometric contour. However, when the extinction criteria are coupled to the EDC model, the model then acts to exclude reaction in certain areas of the combustor flow field, thus modifying the location of the flame. This effect is illustrated in Fig. 11 for the F23 ($\phi = 0.59$) case. The regions in which reaction is excluded are denoted by the "shaded" areas. The region adjacent to the annulus is too fuel lean for combustion to occur. In like manner, the area adjacent to the fuel tube is outside of the rich combustion limit. The stoichiometric contour divides the fuel lean and fuel rich regions. The third region, "shaded" by horizontal lines, is the zone in which the hydrodynamic residence time is less than extinction time scale. (The extinction region constrained by the time scales actually overlaps into the regions constrained by combustion limits, but the extent of the overlap is not shown.) Although the stoichiometric contour lies entirely within the time-scale constrained region, reaction is not permitted until the fuel emerges downstream of this region. In those

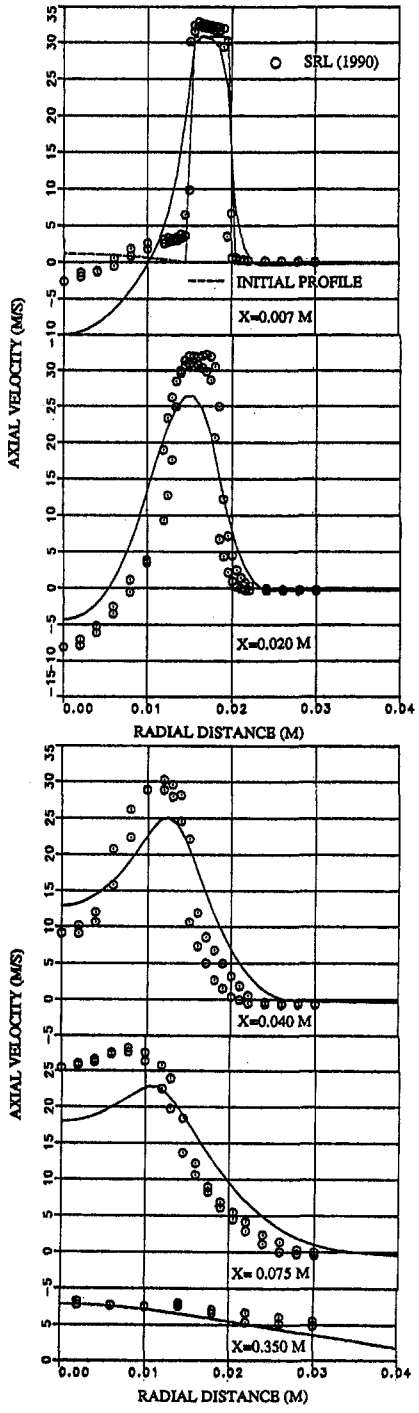

Fig. 9 Comparison of predicted and measured mean axial velocity radial profiles for case N23; note: Radial extent of computational domain is 0.075 m

Downloaded 02 Jun 2010 to 171.66.16.104. Redistribution subject to ASME license or copyright; see http://www.asme.org/terms/Terms_Use.cfm

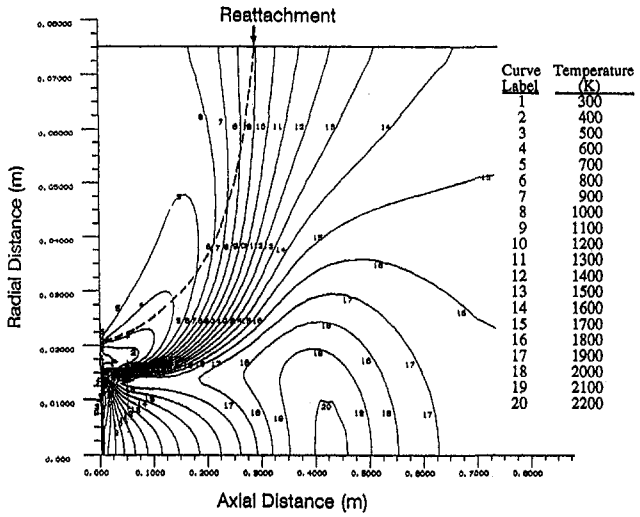

Fig. 10 Temperature field calculated for the research combustor at Case F23 conditions using the EBU model

regions where combustion is permitted, the local equivalence ratio is wholly fuel lean. This observation suggests that when the reaction exclusion regions have become sufficiently large to absorb all of the areas where flammable mixtures prevail, then blowout occurs (as has been computationally verified).

Figure 11 also shows contours that are represented by the log of the absolute value of the fuel reaction rate. Each contour of this modified reaction rate parameter represents an order of magnitude change in the reaction rate relative to an adjacent contour. It can be seen that the highest reaction rate, as expected, coincides with the location that has the highest (lean) equivalence ratio downstream of the reaction exclusion zone. Although reaction is permitted in the recirculation zone along the step, the reaction rates are extremely small as very little unreacted fuel is being recirculated.

The impact of the reaction exclusion zone on the temperature is shown in Fig. 12. The flame is essentially stabilized at the location where the stagnation streamline intersects the fuel-lean constrained region (i.e., in the shear layer region downstream of the step). The calculated anchor position is located in the merged jet/step shear layer at an axial distance of approximately 0.2 m, which exceeds somewhat the value of 0.15 m determined by visual inspection for this case. Since the "flame front" is anticipated to lie along the farthest downstream border of the reaction exclusion zone (see Fig. 11) the flame anchor position varies radially from $x = 0.2$ m near the step recirculation zone to approximately 0.3 m near the centerline. The "parabolic" shape associated with the lifted flame is in accordance with experimental observation.

It should also be noted that the stagnation streamline of the step recirculation zone is entrained into the concentric annular air jet. The hourglass shape of the streamline and the temperature contours that are congruent with it are very reminiscent of the shape of the attached shear layer flame observed during operation of the research step combustor. This same stagnation streamline shape is characteristic of all of the calculations using the lifted flame model. However, the hourglass shape is not exhibited by the stagnation streamline calculated using the EBU model.

Case F41 ($\phi = 1.05$). Figures 13 and 14 display the calculated flame characteristics pertaining to the F41 ($\phi = 1.05$) case. The reaction exclusion regions for the F41 case in Fig. 13 are significantly different from those for the previously discussed F23 ($\phi = 0.59$) case. The F41 case is more fuel-rich than the F23 case; therefore, the fuel-lean constrained region has decreased in size while the fuel-rich constrained region has expanded, relative to the F23 case. The stoichiometric contour does not intersect the centerline as the F23 case did, but is directed toward the chamber wall. The maximum reaction rate parameter is aligned with the stoichiometric contour. Note that

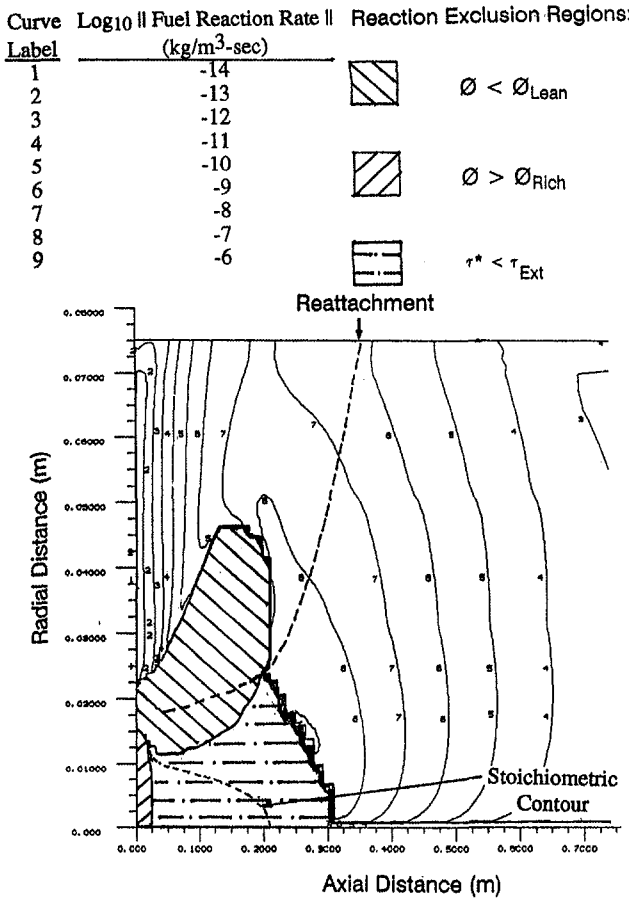

Fig. 11 Reaction exclusion regions and reaction rate parameter field calculated for the research combustor at Case F23 conditions

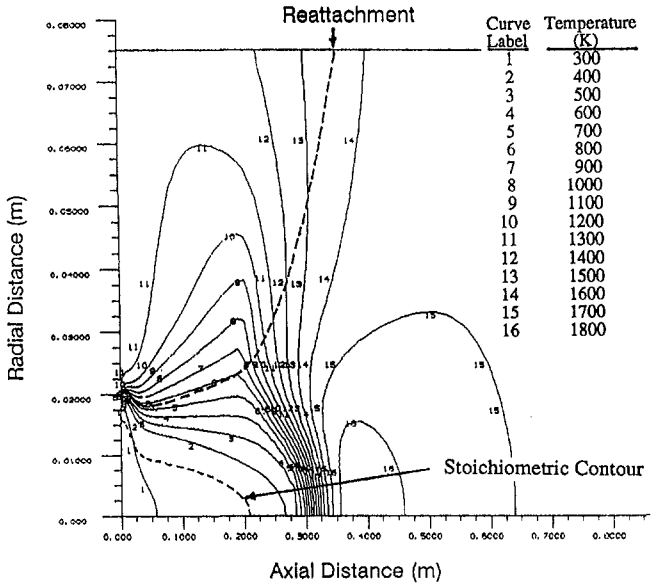

Fig. 12 Temperature field calculated for the research combustor at Case F23 conditions

Downloaded 02 Jun 2010 to 171.66.16.104. Redistribution subject to ASME license or copyright; see http://www.asme.org/terms/Terms_Use.cfm

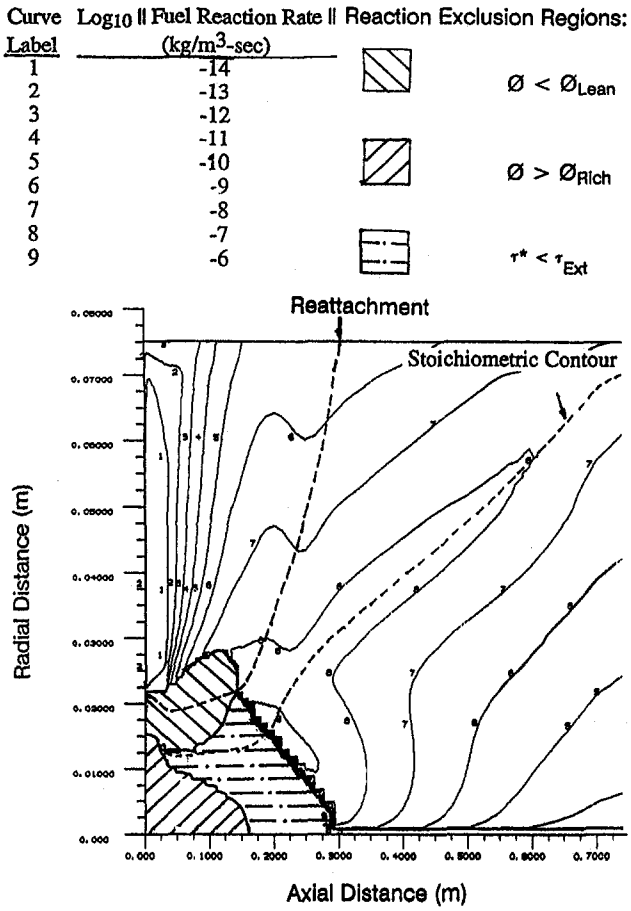

Fig. 13 Reaction exclusion regions and reaction rate parameter field calculated for the research combustor at Case F41 conditions

the fuel reaction rate becomes diminishingly small as the flow recirculates upstream towards the step wall, indicating that negligible fuel survives the transit time from the moment of entrainment into the recirculation zone until the step shear layer is reached. The calculated flame anchor point is again positioned where the stagnation streamline intersects the flame exclusion zone, at an axial distance of approximately 0.14 m. This is somewhat larger than the experimentally observed liftoff height (in the step shear layer) for this case of 0.1 m. The calculated anchor point is again a function of the radius and "parabolically" shaped, varying from $x = 0.14$ m near the step stagnation streamline to 0.29 near the centerline. Relative to the F23 case, the flame both at the anchor point and along the centerline has moved upstream, although only slightly in the latter instance. The temperature contours in Fig. 14 indicate that temperatures, both in the main flow field and in the recirculation zone, have increased substantially, relative to the F23 case, as would be expected for a case with near unity stoichiometry. Experimentally it has been observed that the F41 case represents the demarcation equivalence ratio between the lifted flame regime (at lower equivalence ratios) and the attached flame regime (at higher equivalence ratios).

Case F63 (ϕ = 1.62). Figure 15 illustrates the calculated flame characteristics pertaining to the F63 (ϕ = 1.62) case. Since the F63 case is fuel-rich on an overall equivalence ratio basis, the fuel-lean constrained region has shrunk even further, relative to previous cases, and the fuel-rich constrained region has expanded tremendously. The stoichiometric equivalence ratio intersects the chamber wall near the reattachment point and equivalence ratios have increased in the recirculation zone. The peak reaction rates have shifted to accommodate a change in position of the stoichiometric contour. Unfortunately, although temperatures have increased significantly in the recirculation zone (not shown), the change has not been sufficient to induce the flame to attach to the edge of the step. Experimentally, the F63 flame was observed to attach to the step; furthermore, from photographs (both long exposure and instantaneous LIF) the

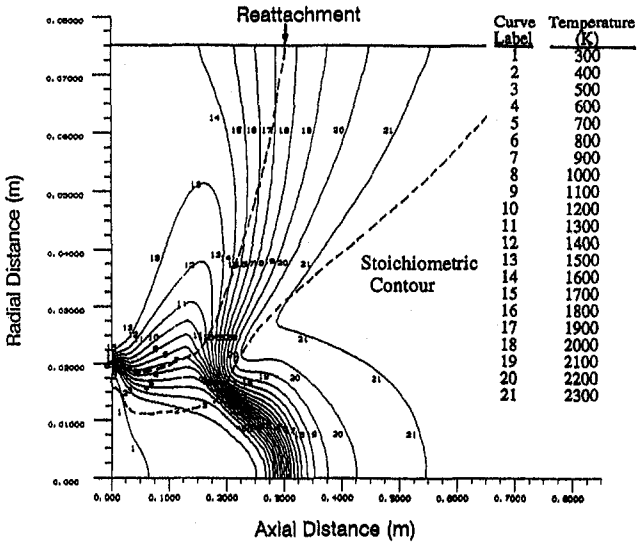

Fig. 14 Temperature field calculated for the research combustor at Case F41 conditions

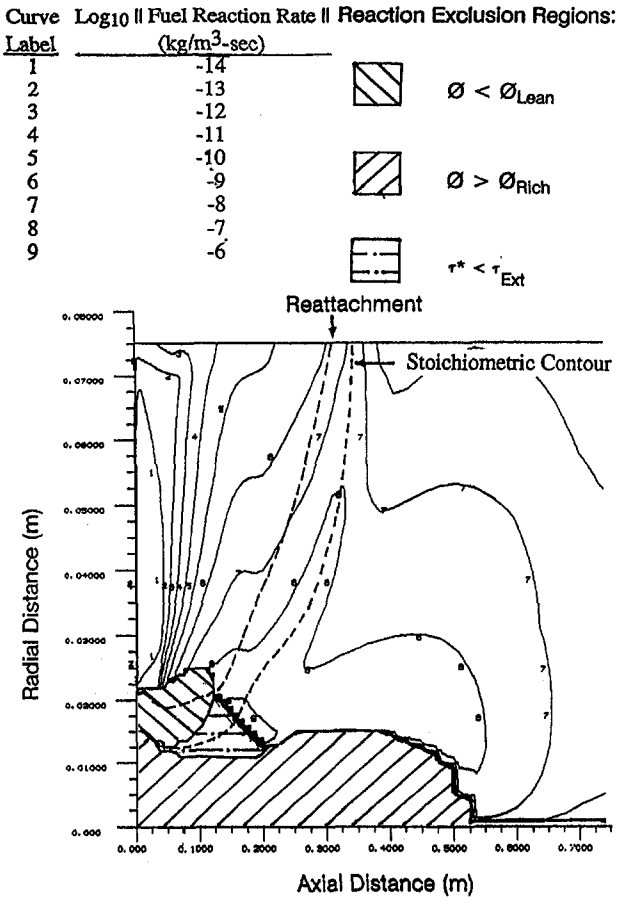

Fig. 15 Reaction exclusion regions and reaction rate parameter field calculated for the research combustor at Case F63 conditions

Downloaded 02 Jun 2010 to 171.66.16.104. Redistribution subject to ASME license or copyright; see http://www.asme.org/terms/Terms_Use.cfm

flame was observed to begin to fill the core of the combustor at an axial distance of about 0.150 m downstream of the confluence plane, which is even farther upstream than the other (lifted flame) cases that have been discussed. The F63 calculation has generated a very fuel-rich core, which delays flame ignition on the centerline and qualitatively contradicts the trend exhibited by the experiments. Clearly, not allowing the rich and lean combustion limits to change as a function of the local temperature, which they are known to be, produces reaction exclusion regions that are not wholly realistic in size.

The poor qualitative agreement for the F63 case prediction of the research step combustor prompted an effort to investigate how the calculation of the attachment process could be improved. It is apparent that the fuel-lean constrained region must somehow be reduced in size before the anchor point can migrate forward to attach to the step, and that more fuel must be recirculated to the step shear layer before it is consumed. A number of case modifications were made in an attempt to ensure this. The extent of mixing was increased by decreasing the turbulent Schmidt/Prandtl number to 0.5, appropriate for recirculating flows. Such a value was found to be appropriate for recirculating flows by Syed and Sturgess (1980). The lean flammability limit was made a function of local temperature, and varied from 0.5 to 0.2; the rich flammability limit was taken as constant at an equivalent ratio of 2.0. The calculations were made using specified wall temperatures for a boundary condition, so that there was heat loss from the combustor. The actual temperatures were based on measurements for attached flame conditions. The specified wall temperature boundary condition showed the existence of extremely severe temperature gradients at the combustor wall and the step. These gradients suggested that wall-quenching of combustion reactions might be the source of the unburned fuel that is recirculated to give the attached flame.

Close to an impervious surface, the luminosity that is associated with visible flame does not extend completely to the surface. The intervening dark region is known as the dead space. Dead space is caused by quenching of chemical reactions due to heat losses to the wall and removal of active radicals. A simplified correlation of wall dead space was incorporated into the two-dimensional PREACH code. The dead space model was applied to the combustor walls and the step, and operated to quench reactions out from the surface to a value of y^+ equal to 100. Attached flame calculations were attempted for 1000 liters/min air and 80 liters/min fuel. This represents a very rich condition ($\phi = 2.05$), for which experimental data are not available, but was chosen to ensure conditions that would be conducive to giving an attached flame regardless of modeling uncertainties.

The calculations for the F80 Case are shown in Figs. 16 and 17. The calculations show that the stoichiometric contour crosses the step recirculation zone and reaches the combustor wall about halfway from the step to the reattachment plane. The stagnation streamlines indicate that the air jet and outer edge of the step recirculation zone move toward the combustor centerline, giving a "waist" at about 40 mm from the jet confluence. The combined combustion criteria exclude chemical reactions from substantial portions of the combustor. The lean combustion limit region has shrunk in size and is wholly encompassed by the time-scale constraint region. The time-scale constraint is now the dominant factor limiting combustion in the step detachment region. The ratio of the hydrodynamic to the chemical extinction time scales would need to be reduced by a factor of 2 or 3 to permit the lean combustion limit to be the primary reaction exclusion agent. The large axial extent of the fuel-rich exclusion region is again clearly erroneous.

Figure 17 presents isotherms that show the severe temperature gradients existing on the step and the combustor walls, and that the recirculation zone is very hot with temperatures exceeding 1500 K. The figure also shows that the main flame is stabilized in the merged step/jet shear layer about 11 cm from the jet confluence. It is rather thick with an axis at a

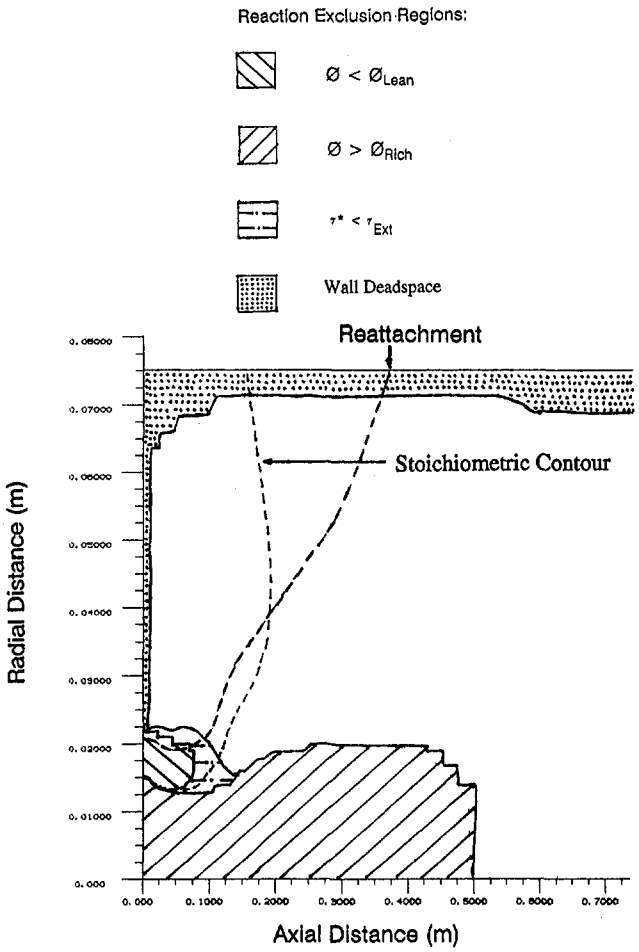

Fig. 16 Reaction exclusion regions calculated for the research combustor at Case F80 conditions

positive angle to the combustor centerline, clearly following the stoichiometric contour across the step recirculation zone. It does resemble the sudden flame sheet thickening observed in the flame photographs (corresponding to F63 measurements), although it is farther downstream. When compared to the instantaneous images of laser-induced OH fluorescence, there is good agreement in position with concentrated islands of reaction in the jet shear layers, that give an apparent sudden thickening of the instantaneous flame.

Although there is more unreacted fuel on the step at the outer edge of the air jet as a consequence of the dead space and thermal boundary, the mixture strength remains inside the reaction exclusion limits. There is no evidence from the isotherms of an attached pilot flame, such as is revealed by the flow visualization.

Concluding Remarks

Based on the apparently inadequate predictive accuracy and CPU-intensive characteristics of the available kinetic mechanisms for propane in the limit of incipient extinction, a composite combustion model was devised for CFD analyses. The model, consisting of a fast-chemistry version of the EDC model and reaction exclusion constraints, was utilized to calculate both lifted and attached flames. In the lifted flame calculations, the model was found to calculate qualitatively the "parabolic" flame contour and the primary flame anchor point positioned in the shear layer, both of which were observed in the research step combustor experiments. However, predictive accuracy of the model was necessarily limited because of its simplicity. In

Downloaded 02 Jun 2010 to 171.66.16.104. Redistribution subject to ASME license or copyright; see http://www.asme.org/terms/Terms_Use.cfm

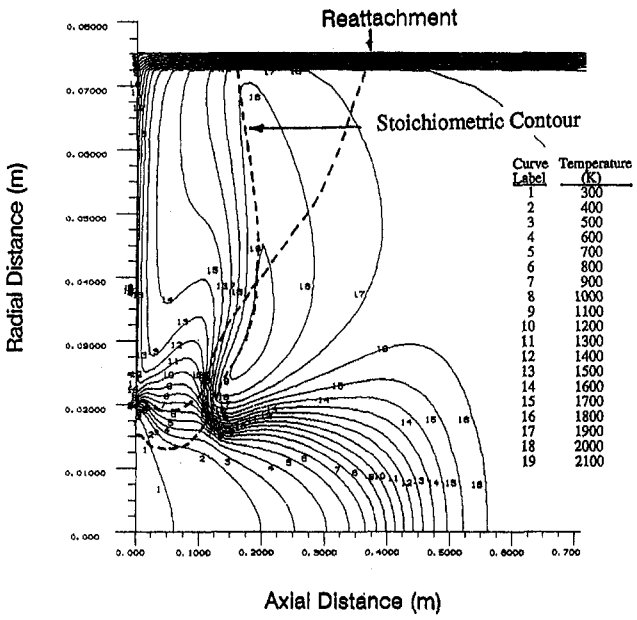

Fig. 17 Calculated temperature field for the research combustor at Case F80 conditions

the attached flame calculation, the model failed completely to generate an attached pilot flame.

The inability to model the attached flame structure in the research step combustor may be ascribed to at least two contributing factors. The first involves the influence of chemical kinetics. The current modeling effort utilized a fast-chemistry model in conjunction with extinction criteria. As an effort was made to bring more and more fuel into the recirculation zone, as evidenced by the relative position of the stoichiometric contour, the one-step, fast chemistry model produced correspondingly higher temperatures within the recirculation zone. The step detachment region must always be fuel lean, in the context of a fast chemistry model and stationary fluid mechanics, since to do otherwise would force the stoichiometric contour to circulate back upon itself (which is impossible). The high temperatures and flame-sheet type calculation associated with a fast-chemistry model essentially preclude any significant unreacted fuel from entraining into the recirculation zone and recirculating to the point of attachment. If it is presumed that it is not pure fuel that is feeding the pilot flame, but rather a hydrocarbon fragment species or CO, then a multistep kinetic mechanism (coupled with a turbulence model) is required to perform the calculation. Survivability of such a reaction intermediate in the recirculation zone would depend upon the specifics of the kinetics and the local conditions in the recirculation zone (e.g., wall deadspace temperature and heat loss), but the possibility should be considered.

Perhaps a more likely factor influencing the attachment phenomenon involves complex, nonstationary transport and mixing considerations. In the research step combustor, at the confluence plane, an annular air stream serves initially to insulate the fuel jet shear layer from the step recirculation zone. The step shear layer does not interact directly with the fuel jet shear layer until the two shear layers merge downstream. It is evident that hydrocarbon fragments or "fuel" species must somehow be crossing the intense flame zone of the merged shear layers and surviving in the step recirculation zone, consisting largely of high-temperature combustion products, for a sufficient length of time to reach and sustain the attached pilot flame. It has been postulated (Roquemore et al., 1991) that entrainment into the step recirculation zone is by an intermittent process involving discrete packets of "unreacted" fuel. The intermittent nature of the entrainment accounts for the intermittent existence of the pilot flame itself. This entrainment process could occur through the holes in the braid regions of the vortices, where stretching leads to local quenching of the flame. The fuel packets must then be transported around or through the recirculation cone in a relatively intact manner until the flame attachment point is reached. Experimental evidence of this phenomenon now exists (Sturgess et al., 1994). Very likely, the true physics underlying the attachment phenomenon will involve some combination of discrete, vortical mixing and reaction kinetics. It is the combined issue of nonstationary species transport and reaction kinetics that CFD analysis must ultimately address to resolve the underlying physics of flame lift and attachment.

Acknowledgments

The authors wish to acknowledge the contributions to this work from their colleagues at Wright-Patterson Air Force Base and Pratt & Whitney. The enthusiasm, encouragement and support of Dr. W. M. Roquemore of Wright Laboratories has been particularly appreciated. The work was supported by the U.S. Air Force Wright Laboratories, under Contract No. F33615-87-C-2822 to Pratt & Whitney, East Hartford, Connecticut. The authors thank Pratt & Whitney Engineering for permission to publish these results.

References

Broadwell, J. E., Dahm, W. J. A., and Mungal, M. G., 1985, "Blowout of Turbulent Diffusion Flames," *20th Symposium (International) on Combustion,* The Combustion Institute, Pittsburgh, PA, pp. 303–310.

Byggstoyl, S., and Magnussen, B. F., 1985, "A Model for Flame Extinction in Turbulent Flow," *Turbulent Shear Flows 4,* L. J. S. Bradberry, F. Durst, B. E. Launder, F. W. Schmidt, and J. H. Whitelaw, eds., Springer-Verlag, Berlin, pp. 381–395.

Chakravarty, A., Lockwood, F. C., and Sinicropi, G., 1984, "The Prediction of Burner Stability Limits," *Combustion Science and Technology,* Vol. 42, pp. 67–86.

Clarke, A. E., Harrison, A. J., and Odgers, J., 1958, "Combustion Instability in a Spherical Combustor," *7th Symposium (International) on Combustion,* Butterworths Scientific Publications, London, pp. 664–673.

Colket, M. B., 1989, Personal Communication, United Technologies Research Center, East Hartford, CT.

Dahm, W. J. A., and Dimotakis, P. E., 1987, "Measurements of Entrainment and Mixing in Turbulent Jets," *AIAA Journal,* Vol. 25(9), pp. 1216–1223.

Dahm, W. J. A., and Dibble, R. W., 1988, "Combustion Stability Limits of Coflowing Turbulent Jet Diffusion Flames," Paper No. AIAA-88-0538.

Edelman, R., and Harsha, P. T., 1978, "Some Observations on Turbulent Mixing With Chemical Reactions," *Turbulent Combustion,* Progress in Astronautics and Aeronautics, Vol. 58, L. A. Kennedy, ed., pp. 55–102.

Eickhoff, H., Lenze, B., and Leuckel, W., 1985, "Experimental Investigation on the Stabilization Mechanism of Jet Diffusion Flames," *20th Symposium (International) on Combustion,* The Combustion Institute, Pittsburgh, PA, pp. 311–318.

Giovangigli, V., and Smooke, M. D., 1987, "Calculation of Extinction Limits for Premixed Laminar Flames in a Stagnation Point Flow," *Journal of Computational Physics,* Vol. 68, pp. 327–345.

Glarborg, P., Kee, R. J., Grcar, J. F., and Miller, J. A., 1988, "PSR: A Fortran Program for Modeling Well-Stirred Reactors," Sandia National Laboratories Report SAND86-8209; UC-4, reprint.

Hottel, H. C., Williams, G. C., and Baker, M. L., 1957, "Combustion Studies in a Stirred Reactor," *6th Symposium (International) on Combustion,* Reinhold Publishing Corporation, New York, pp. 398–411.

Janicka, J., and Peters, N., 1982, "Production of Turbulent Jet Diffusion Flame Lift-Off Using a PDF Transport Equation," *19th Symposium (International) on Combustion,* The Combustion Institute, Pittsburgh, PA, pp. 367–374.

Jones, W. P., and Lindstedt, R. P., 1988, "Global Reaction Schemes for Hydrocarbon Combustion," *Combustion and Flame,* Vol. 73, pp. 233–249.

Kalghatgi, G. T., 1984, "Lift-Off Heights and Visible Lengths of Vertical Turbulent Jet Diffusion Flames in Still Air," *Combustion Science and Technology,* Vol. 41, pp. 17–29.

Kee, R. J., Miller, J. A., and Evans, G. H., 1988, "A Computational Model of the Structure and Extinction of Strained, Opposed Flow, Premixed Methane-Air Flames," *22nd Symposium (International) on Combustion,* The Combustion Institute, Pittsburgh, PA, pp. 1479–1494.

Keller, H. B., 1977, "Numerical Solution of Bifurcation and Nonlinear Eigenvalue Problems," *Applications of Bifurcation Theory,* P. Rabinowitz, ed., Academic Press, New York, New York, 359–384.

Keller, H. B., 1987, *Lectures on Numerical Methods in Bifurcation Problems,* Springer-Verlag, New York.

Downloaded 02 Jun 2010 to 171.66.16.104. Redistribution subject to ASME license or copyright; see http://www.asme.org/terms/Terms_Use.cfm

Kiehne, T. M., Matthews, R. D., and Wilson, D. E., 1987, "An 8-Step Kinetics Mechanism for High Temperature Propane Flames," *Combustion Science and Technology,* Vol. 54, pp. 1–23.

Kollrack, R., 1976, "Model Calculations of the Combustion Product Distributions in the Primary Zone of a Gas Turbine Combustor," ASME Paper No. 76-WA/GT-7.

Kretschmer, D., and Odgers, J., 1972, "Modeling of Gas Turbine Combustors—A Convenient Reaction Rate Equation," ASME JOURNAL OF ENGINEERING FOR POWER, Vol. 94, pp. 173–180.

Law, C. K., 1984, "Heat and Mass Transfer in Combustion: Fundamental Concepts and Analytical Techniques," *Progress in Energy and Combustion Science,* Vol. 10, pp. 295–318.

Lockwood, F. C., and Megahed, I. A. E., 1978, "Extinction in Turbulent Reacting Flows," *Combustion Science and Technology,* Vol. 19, pp. 77–80.

Magnussen, B. F., and Hjertager, B. H., 1977, "On Mathematical Modeling of Turbulent Combustion With Special Emphasis on Soot Formation and Combustion," *16 Symposium (International) on Combustion,* The Combustion Institute, Pittsburgh, PA, pp. 719–729.

Magnussen, B. F., 1979, "Effects of Turbulent Structure and Local Concentrations on Soot Formation and Combustion in C_2H_2 Diffusion Flames," *17th Symposium (International) on Combustion,* The Combustion Institute, Pittsburgh, PA, pp. 1383–1393.

Magnussen, B. F., 1981a, "On the Structure of Turbulence and a Generalized Eddy Dissipation Concept for Chemical Reaction in Turbulent Flow," AIAA Paper No. 81-0042.

Magnussen, B. F., 1981b, "Modeling of Reaction Processes in Turbulent Flames With Special Emphasis on Soot Formation and Combustion," *Particulate Carbon Formation During Combustion,* D. C. Siegla and G. W. Smith, eds., Plenum Press, New York, 321–341.

Magnussen, B. F., 1985, "Heat Transfer in Gas Turbine Combustors—A Discussion of Mathematical Modeling of Combustion, Heat and Mass Transfer With Emphasis on Heat Transfer in Gas Turbine Combustors," AGARD Conference Preprint No. 390, *Heat Transfer and Cooling in Gas Turbines,* Paper No. 23.

Magnussen, B. F., 1989, "Modeling of Pollutant Formation in Gas Turbine Combustors Based on the Eddy Dissipation Concept," presented at the CIMAC Conference in Tainjin, China, 4–8 June.

Paczko, G., Lefdel, P. M., and Peters, N., 1988, "Reduced Reaction Schemes for Methane, Methanol and Propane Flames," *21st Symposium (International) on Combustion,* The Combustion Institute, Pittsburgh, PA, pp. 739–748.

Peters, N., 1983, "Local Quenching Due to Flame Stretch and Non-premixed Turbulent Combustion," *Combustion Science and Technology,* Vol. 30, pp. 1–17.

Peters, N., and Williams, F. A., 1983, "Liftoff Characteristics of Turbulent Jet Diffusion Flames," *AIAA Journal,* Vol. 21(3), pp. 423–429.

Peters, N., 1984, "Laminar Diffusion Flamelet Models in Non-Premixed Turbulent Combustion," *Progress in Energy and Combustion Science,* Vol. 10, pp. 319–339.

Peters, N., 1985, "Partially Premixed Diffusion Flamelets in Non-Premixed Turbulent Combustion," *20th Symposium (International) on Combustion,* The Combustion Institute, Pittsburgh, PA, pp. 353–360.

Roberts, R., Aceto, L. D., Kollrack, R., Teixeira, D. P., and Bonnell, J. M., 1972, "An Analytical Model for Nitric Oxide Formation in a Gas Turbine Combustor," *AIAA Journal,* Vol. 10(6), pp. 820–826.

Roquemore, W. M., Reddy, V. K., Hedman, P. O., Post, M. E., Chen, T. H., Goss, L. P., Trump, D., Vilimpoc, V., and Sturgess, G. J., 1991, "Experimental and Theoretical Studies in a Gas-Fueled Research Combustor," AIAA Paper No. AIAA-91-0639.

Seydel, R., 1988, *From Equilibrium to Chaos,* Elsevier Science Publishing Company, New York.

Sturgess, G. J., 1983, "Aerothermal Modeling Phase I," Final Report, NASA Rept. CR-168202.

Sturgess, G. J., Syed, S. A., and McManus, K. R., 1986, "Importance of Inlet Boundary Conditions for Numerical Simulation of Combustor Flows," *International Journal of Turbo & Jet Engines,* Vol. 3, pp. 43–55.

Sturgess, G. J., Sloan, D. G., Roquemore, W. M., Reddy, V. K., Shouse, D., Lesmerises, A. L., Ballal, D. R., Heneghan, S. P., Vangsness, M. D., and Hedman, P. O., 1991a, "Flame Stability and Lean Blowout—A Research Program Progress Report," *Proc. 10th ISABE,* Nottingham, United Kingdom, pp. 372–384.

Sturgess, G. J., Heneghan, S. P., Vangsness, M. D., Ballal, D. R., and Lesmerises, A. L., 1991b, "Lean Blowout in a Research Combustor at Simulated Low Pressures," ASME Paper No. 91-GT-359.

Sturgess, G. J., Sloan, D. G., Lesmerises, A. L., Heneghan, S. P., and Ballal, D. R., 1992a, "Design and Development of a Research Combustor for Lean Blowout Studies," ASME JOURNAL OF ENGINEERING FOR GAS TURBINES AND POWER, Vol. 114, pp. 13–19.

Sturgess, G. J., Heneghan, S. P., Vangsness, M. D., Ballal, D. R., and Lesmerises, A. L., 1992b, "Isothermal Flow Fields in a Research Combustor for Lean Blowout Studies," ASME JOURNAL OF ENGINEERING FOR GAS TURBINES AND POWER, Vol. 114, pp. 435–444.

Sturgess, G. J., Heneghan, S. P., Vangsness, M. D., Ballal, D. R., Lesmerises, A. L., and Shouse, D., 1993a, "Effects of Back-Pressure in a Lean Blowout Research Combustor," ASME JOURNAL OF ENGINEERING FOR GAS TURBINES AND POWER, Vol. 115, pp. 486–498.

Sturgess, G. J., and Shouse, D., 1993b, "Lean Blowout Research in a Generic Gas Turbine Combustor With High Optical Access," ASME Paper No. 93-GT-332.

Sturgess, G. J., Hedman, P. O., Sloan, D. G., and Shouse, D., 1994, "Aspects of Flame Stability in a Research Dump Combustor," ASME Paper No. 94-GT-496.

Syed, S. A., and Sturgess, G. J., 1980, "Validation Studies and Combustion Models for Aircraft Gas Turbine Combustors," *Proc. ASME Symp. Momentum and Heat Transfer Processes in Recirculating Flows,* B. E. Lauder and J. A. C. Humphrey, eds., ASME HTD-Vol. 13, pp. 71–89.

Systems Research Laboratories, Inc., 1990, Unpublished Data from Step Research Combustor, Wright-Patterson Air Force Base, Dayton, OH.

Williams, F. A., 1985, *Combustion Theory,* 2nd ed., The Benjamin/Cummings Publishing Company, Inc., Menlo Park, CA, pp. 408–410.

APPENDIX A

Extinction Point Calculation

The reaction behavior of a well-stirred reactor (WSR) may be described by a plot of the reaction temperature (or burning ratio) versus the residence time (or Damköhler number). The resultant S-shaped curve (shown in Fig. A-1), where the residence time (τ) has been selected (for present purposes) as the independent branching parameter that is utilized for positional mapping purposes along the extinction curve, may be interpreted in the following manner (see Law, 1984).

For a residence time (τ) equal to zero, the flow is chemically frozen and the unreacted feed stream to the WSR is recovered. By gradually increasing the residence time along the lower branch of the **S** curve, weak chemical reaction is possible. With a continuous increase in the residence time, a point will be reached (τ_{ign}), beyond which the only possible solution lies on the upper branch. The upper branch represents the locus of all possible burning states. As the residence time approaches infinity, the solution asymptotically approaches the state of chemical equilibrium. The lower turning point, at which the system suddenly transits from the lower to the upper branch, is designated as the ignition point. Physically, the rate of heat release in the reactor at the ignition point temperature has increased to the extent that it can no longer be balanced by the heat transport rate. This in turn leads to an increase in the reaction zone temperature, which induces a coupled increase in the reaction rate, culminating in the runaway event of ignition. The feedback mechanism proceeds very rapidly because of the exponential temperature dependence of the Arrhenius kinetics.

In a similar manner, if the residence time is continuously decreased along the upper branch, a point is reached (τ_{ext}), beyond which intense burning ceases to be possible and the system transits precipitously to the solutions on the lower branch. The upper turning point may consequently be identified as an extinction point. At the extinction point, the temperature in the reactor has decreased to a value at which the rate of heat release is no longer sufficient for an appreciable amount of

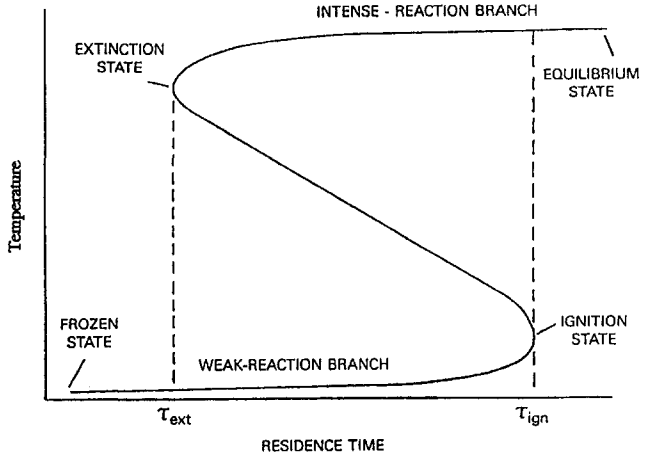

Fig. A-1 Characteristic S-shaped curve showing all possible modes of well-stirred reactor behavior

Downloaded 02 Jun 2010 to 171.66.16.104. Redistribution subject to ASME license or copyright; see http://www.asme.org/terms/Terms_Use.cfm

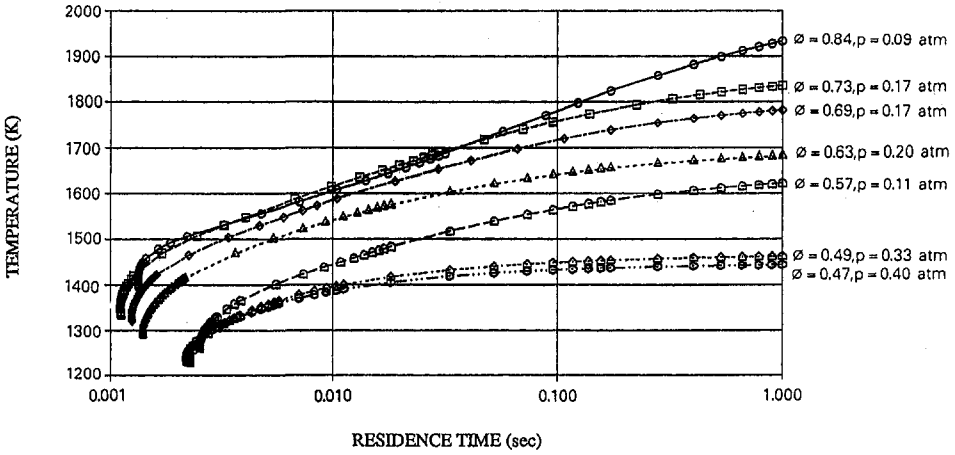

Fig. A-2 Calculated solution points using a PSR code and the arc-length continuation procedure for various reactor considerations (reactor conditions from Hottel et al., 1957, and propane kinetic mechanism from Colket, 1989)

reaction to occur in the residence time available. The intermediate branch, between the ignition and the extinction turning points, represents a locus of nonphysical solutions.

Each of the branches on the **S**-shaped curve for the well-stirred reactor constitute a locus of critical or "equilibrium" points. It is apparent that the upper, intense-reaction branch of the **S** curve is a locus of computed stable or attractive critical points. The intermediate branch of the **S** curve is an unstable or repelling branch, as evidenced by its nonphysical solutions. Calculations with various kinetic mechanisms indicate that the determinant of the Jacobian matrix is positive on the upper branch and negative on the intermediate branch. The extinction point is a turning or limit point that is singular, which causes the Newton algorithm to become more ill-conditioned as extinction is approached. Since the turning point singularity precludes successful convergence of a typical solution algorithm (e.g., Newton technique), an alternate method known as arc-length parameterization must be employed. The method has been developed in a number of sources (Seydel, 1988; Keller, 1977, 1987) and has been applied to various extinction problems (Kee et al., 1988; Giovangigli and Smooke, 1987). This method deletes the independent parameterization involving the residence time and absorbs it as another dependent variable. The augmented vector of dependent variables is now considered to be a function of a new and arbitrary independent parameter s where the parameter s is usually chosen to approximate the arc-length of the solution branch. The arc-length is considered to be a function only of the temperature within the reactor and the residence time.

This change-of-variable procedure, in which τ becomes a dependent variable and the arc-length becomes an independent parameter, essentially introduces a coordinate system transformation such that the turning point singularity disappears. Although the original Jacobian matrix is singular at the extinction point, the singularity associated with the augmented Jacobian matrix is removed. Thus, in principle, it is possible for a continuation method to calculate discrete critical points along the stable branch of the extinction curve, step through the turning point location, and then continue calculations along the unstable branch without experiencing ill-conditioned behavior in the Jacobian matrix.

Although the arc-length parameterization has been useful in enhancing the robustness of the Newton algorithm in the immediate vicinity of the turning point, it does not guarantee that initial estimates to the solution at each critical point will be within Newton's domain of convergence. Consequently, a desirable feature of a continuation procedure would include some methodology for predicting reliable solution estimates at each subsequent position along the branch. In a "predictor-solver" strategy, the predictor component (Euler technique) uses the solution information available at Point 1 to construct a better approximation to the actual solution at Point 2; the solver component (e.g., Newton's method) consists of applying an iterative scheme to the initial approximation until convergence is attained at Point 2. The "predictor-solver" strategy, in conjunction with various step-length controls, constitutes an arc-length continuation methodology.

The PSR/Chemkin-II code, equipped with both the arc-length parameterization and continuation methodologies, may be utilized to trace the **S**-shaped extinction curve. An example of an extinction point calculation is shown in Fig. A-2. As currently implemented, the residence time is decreased in discrete intervals at a constant equivalence ratio, pressure, temperature, and inlet composition until extinction occurs. The largest residence times correspond to a state of near-equilibrium chemistry. To ensure absolute robustness, it is oftentimes necessary to start the calculation near equilibrium. The calculation then proceeds down the reacting branch, with each successive step or point representing a successful solution of the PSR code for the given residence time. Initial guesses for subsequent steps are found by the predictor-solver technique in the arc-length continuation methodology from previous solutions. Relatively small step sizes are required in the vicinity of the extinction point for resolution purposes; interpolation for the blowout point is performed using a quadratic curve fit procedure. It should be noted that a substantial number of steady-state solutions are required to reach the extinction point from the equilibrium point, which may constitute a severe CPU burden. If the PSR calculation procedure were to be implemented within a CFD code, then each curve (in Fig. A-2) would represent the chemistry calculation of extinction for a single computational cell during a single iteration.

APPENDIX B

Model Implementation

Although in principle the application of the EDC/time-scale modeling technique is relatively straightforward, in practice the implementation of the procedure poses some problems that are enumerated below:

1 Experimentation with flame-lift calculations has demonstrated that, during the course of the iterations, certain cells may have equivalence ratios or residence times that are almost

Downloaded 02 Jun 2010 to 171.66.16.104. Redistribution subject to ASME license or copyright; see http://www.asme.org/terms/Terms_Use.cfm

identical in magnitude to the flame extinction limits. Consequently, perturbations to the flow field caused by the numerics, the solution algorithm, or fluctuating patterns in the convergence history may cause the reaction in a cell to turn abruptly on and off. Since every cell impacts upon other cells around it, this "flickering-flame" behavior may influence enough of the computational domain to induce an adverse and oscillatory effect upon the convergence characteristics. In order to partially mitigate this abrupt transition from a reaction state to a nonreaction state, or vice versa, the reaction rates were modified by a clipped sinusoidal or ramp-lime function, which allowed the blowout (or ignition) process to occur gradually over a diffused combustion limit. For example, for rich combustible mixtures, the ramp-type function may be applied in a smooth fashion between the actual rich limit of 2.1 and a value slightly displaced from it (e.g., 2.0).

2 In an actual "stationary" diffusion flame, the existence of a stoichiometric contour in the flame sheet region is intuitively obvious. However, in a calculation of that flame, the computational grid may not satisfactorily resolve the location of the stoichiometric contour. Poor resolution of the flame sheet may produce nonmonotonic variations in the local equivalence ratio or extinction criteria, resulting in an apparent flame spottiness. Consequently, in calculations of the extinction residence time, an inlet equivalence ratio of unity is presently used in every cell where the combustion limits are satisfied.

3 The extinction time scale (τ_{ext}) is a function of the local mean temperature and an equivalence ratio equal to unity (see Note 2 above). Therefore, in the comparatively isothermal region between the jet and the anchor point of a lifted flame, the extinction time scale should remain relatively constant. As shown in Fig. B-1, the hydrodynamic time scale (τ^*) will be much lower than the extinction time scale in the high shear region near the jet exit, but will increase monotonically with axial distance along the stoichiometric contour. At the liftoff height and in the vicinity of the stoichiometric contour, the hydrodynamic time scale will be equal to the extinction time scale, reaction will occur, and temperatures will rise abruptly. With an increase in temperature, the laminar viscosity increases and the density decreases. In the flame region, the entrainment flux increases by a significant amount, and the dissipation rate usually increases accordingly. All of these factors, with the possible exception of the dissipation rate, tend to increase the hydrodynamic time scale in a flame zone. On the other hand, the extinction time scale decreases with an increase in temperature (see Fig. 4). Since reaction is permitted to occur whenever $\tau^* > \tau_{ext}$, the fact that τ^* increases with an increase in temperature while τ_{ext} decreases with an increase in temperature, tends to augment the difference in magnitude between the two time scales and serves to "lock in" or stabilize the flame at the calculated anchor point. Consequently, during the course of the iterations, if the extinction criteria are based on local cell conditions, the calculated flame may anchor itself and lock into a high-temperature region, which region might otherwise have been only a transient artifice of the solution procedure or a residual flame zone from a previous computation. The "lock-in" to the high-temperature region may prevent the flame from migrating to its true equilibrium position, as has been observed.

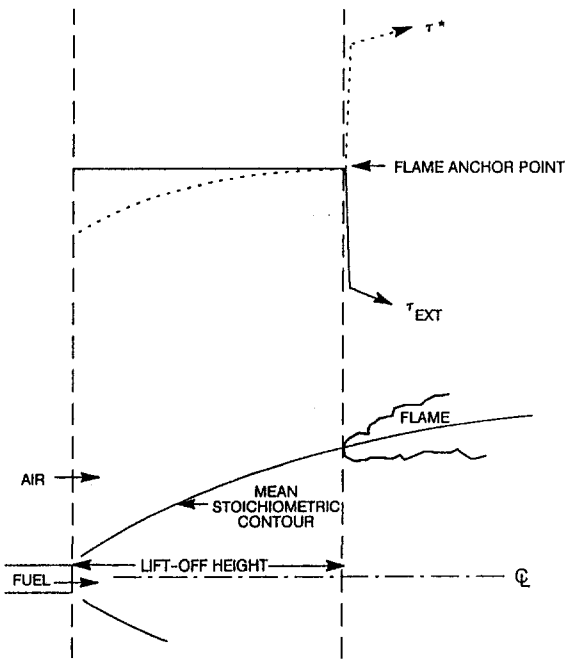

Fig. B-1 Representation of the EDC extinction criterion at the flame anchor point

To overcome this problem, an upwinding procedure is used in which the extinction criteria τ^* and τ_{ext} are functions only of the properties of that neighbor cell that provides a mass flux into the cell in question and has the lowest temperature of any neighboring cell. The rationale for this approach is based on the premixed flame concept of flame stabilization, wherein the anchor point constitutes a location at which the turbulent flame propagation velocity is equal and opposite to the appropriate flow velocity component. At the flame stabilization surface, the flow feeding the perfectly stirred reactors, represented by the dissipation eddies, is to a large degree composed of the unreacted species components coming from the region immediately upstream. Flame stabilization is, in this sense, a planar phenomenon and not a volume (i.e., finite-difference cell phenomenon). Only the extinction criteria are upwinded; the reaction rate source terms are a function of the local cell properties.

Downloaded 02 Jun 2010 to 171.66.16.104. Redistribution subject to ASME license or copyright; see http://www.asme.org/terms/Terms_Use.cfm

Study of Flame Stability in a Step Swirl Combustor

M. D. Durbin

M. D. Vangsness

D. R. Ballal
Fellow ASME

University of Dayton,
Dayton, OH 45469

V. R. Katta
Innovative Scientific Solutions, Inc.,
Dayton, OH 45430

A prime requirement in the design of a modern gas turbine combustor is good combustion stability, especially near lean blowout (LBO), to ensure an adequate stability margin. For an aeroengine, combustor blow-off limits are encountered during low engine speeds at high altitudes over a range of flight Mach numbers. For an industrial combustor, requirements of ultralow NO_x emissions coupled with high combustion efficiency demand operation at or close to LBO. In this investigation, a step swirl combustor (SSC) was designed to reproduce the swirling flow pattern present in the vicinity of the fuel injector located in the primary zone of a gas turbine combustor. Different flame shapes, structure, and location were observed and detailed experimental measurements and numerical computations were performed. It was found that certain combinations of outer and inner swirling air flows produce multiple attached flames, a flame with a single attached structure just above the fuel injection tube, and finally for higher inner swirl velocity, the flame lifts from the fuel tube and is stabilized by the inner recirculation zone. The observed difference in LBO between co- and counterswirl configurations is primarily a function of how the flame stabilizes, i.e., attached versus lifted. A turbulent combustion model correctly predicts the attached flame location(s), development of inner recirculation zone, a dimple-shaped flame structure, the flame lift-off height, and radial profiles of mean temperature, axial velocity, and tangential velocity at different axial locations. Finally, the significance and applications of anchored and lifted flames to combustor stability and LBO in practical gas turbine combustors are discussed.

Introduction

A prime requirement in the design of a modern gas turbine combustor is good combustion stability, especially near lean blowout (LBO), to ensure an adequate stability margin. For an aircraft engine, combustor blow-off limits are encountered during low engine speeds at high altitudes over a range of flight Mach numbers and a good design ensures that the combustor steady-state burning remains within the operating envelope. This envelope should be extensive enough to encompass the under- and overshoots associated with the different response rates to the throttle movements of the fuel system and the rotating machinery. For an industrial combustor, requirements of ultralow NO_x emissions coupled with high combustion efficiency demand operation at or close to LBO, thereby eroding the safety margins. Therefore, a fundamental study of flame stability in a model step swirl combustor (SSC) has important practical applications, and this provided a strong motivation to undertake the present investigation.

The physical mechanisms responsible for the stabilization of a flame on the fuel injector lip (in the near-field region) are not fully understood. In the past, the stabilization mechanism of free jet diffusion flames has been investigated by Vanquickenborne and van Tiggelen (1966), Gollahalli et al. (1985), Pitts (1988, 1990), Bradley et al. (1990), Takahashi et al. (1984, 1990), and Takahashi and Goss (1992). A prime goal of these investigations was to predict flame blowout accurately. For example, Vanquickenborne and van Tiggelen (1966) developed the stabilization criterion that the total approach velocity should be balanced by the turbulent burning velocity of the mixture. Takahashi et al. (1984) found that the local velocities in the vicinity of an attached flame are laminar, and the flame stability mechanism is the balance of the total approach velocity in the attached flame zone with the laminar burning velocity of the mixture. However, in a modern annular gas turbine combustor, the flame is stabilized by producing a swirl-induced recirculation zone in the flow field. This zone is generated by a combination of three mechanisms: an axial swirling air jet associated with each fuel introduction, sudden expansion of the axial swirling jets as they enter the primary zone, and back pressure provided by an array of radial air jets at the end of the primary zone. An SSC was designed to reproduce this type of complicated recirculation flow pattern. This paper discusses the different shapes, structure, and location of the stabilized flame in the SSC and how these various factors affect LBO.

Test Facility

The SSC. Figure 1 shows a schematic diagram of the SSC, which has a 150 × 150-mm cross section with rounded corners, length of 754 mm, and a step height of 55 mm. The SSC provides a geometrically simple, optically accessible research combustor capable of reproducing the fuel–air mixing pattern downstream of the airblast atomizer located in the dome region of a modern annular gas turbine combustor. The SSC also offers independent control over inner and outer airstreams. The SSC was mounted on a vertical combustion tunnel with a three-axis traversing mechanism.

Fuel was supplied to the combustor by the annular fuel tube (20 mm i.d. and 29 mm o.d.), which is coaxially sandwiched between swirling airstreams: the inner air jet (20-mm-dia) and the outer annular air jet (29 mm i.d. and 40 mm o.d.). The combustor exit has a 45 percent blockage orifice plate on top, which simulates the back pressure exerted by the dilution jets in a practical gas turbine combustor (see Sturgess et al., 1990). The SSC has quartz windows on all four sides to permit visual observations and laser diagnostics measurements. The stationary helical vane swirlers were located 25 mm upstream from the burner tube exit in each of the air passages. The inner swirler has six vanes with a central 1.4-mm-dia hole to prevent the flame from anchoring to the swirler. The outer swirler has

Contributed by the International Gas Turbine Institute and presented at the 40th International Gas Turbine and Aeroengine Congress and Exhibition, Houston, Texas, June 5–8, 1995. Manuscript received by the International Gas Turbine Institute February 10, 1995. Paper No. 95-GT-111. Associate Technical Editor: C. J. Russo.

Copyright © 1996 by ASME

Downloaded 02 Jun 2010 to 171.66.16.104. Redistribution subject to ASME license or copyright; see http://www.asme.org/terms/Terms_Use.cfm

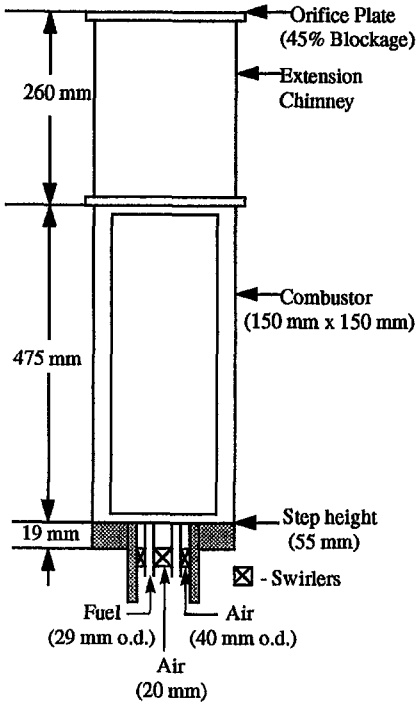

Fig. 1 Schematic diagram of a step swirl combustor

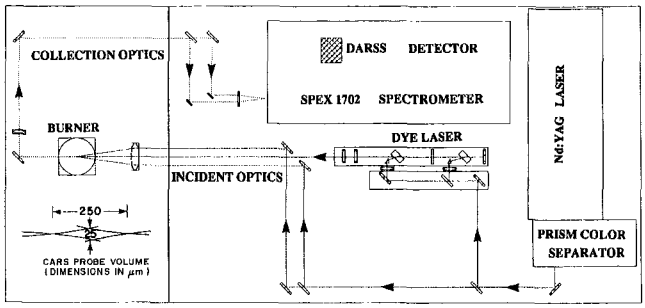

Fig. 2 Schematic of the CARS system optics

twelve vanes. Inner swirler lengths are 25 and 19 mm, respectively, for 30 and 45 deg swirlers; outer swirler length was 32 mm for the 30 deg swirler. Swirler lengths and number of vanes were adequate to ensure that the air closely follows the swirl vane angle. The swirlers were precision-fabricated in a rapid prototype manufacturing process known as stereolithography. These swirlers performed satisfactorily at the level of high temperatures present in the SSC.

Instrumentation

CARS System. Figure 2 shows a schematic of a Coherent Anti-Stokes Raman Spectroscopy (CARS) optics system, which was used for nonintrusive flame temperature measurements. Pan et al. (1991) have provided detailed information on

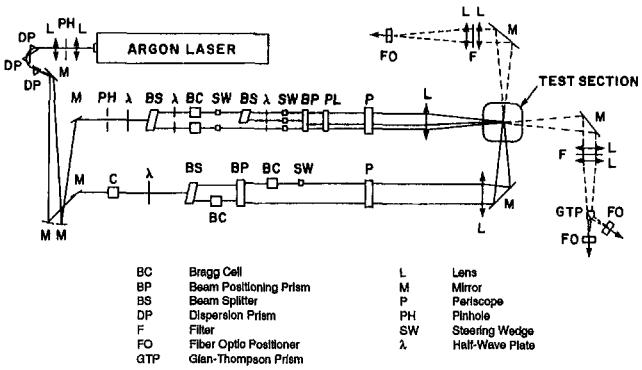

Fig. 3 Schematic of the LDA system optics

CARS measurements. Briefly, the CARS signal was generated by combining two 30 mJ doubled Nd:Yag beams at 532 nm and one 25 mJ broad band dye laser beam centered at 607 nm and pumped by the same Nd:Yag laser. The pulse laser and detector camera run at 10 Hz. A Boxcars configuration with an ellipsoidal probe volume approximately 25 μm (dia) $\times$ 250 μm (length) was used for collecting the signal. The detector is a Princeton Instruments intensified 576 $\times$ 384 charge coupled device (CCD). The intensifier is triggered by a Princeton PG-10 pulser. A Princeton ST-130 controller operates the camera and the detector chiller. The collection process is controlled by Princeton's ST-130 CSMA software package running on a personal computer. Spectra are fit to a library of spectra by a nonlinear fitting routine running on a personal computer. A total of 250 samples were taken for each CARS temperature measurement.

LDA System. Figure 3 illustrated the optical setup of the LDA system. Nonintrusive velocity measurements were made using a Dantec Fiber-Flow LDA system. Essentially, this LDA system is an upgraded version of the system used by Durbin and Ballal (1996). The two-dimensional LDA system uses the 514 nm and 488 nm lines from an argon-ion laser. The laser output is directed into a Dantec Fiber flow transmitter where the colors are separated and directed to optical fiber couplers by a Bragg cell operating at 40 MHz. The four beams are guided to the probe via polarization preserving fibers. The recollimated and focused laser beams cross to produce an ellipsoidal probe volume approximately 100 μm (dia) $\times$ 1000 μm (length). A fluidized-bed seeder was used to inject submicron-sized (97 percent $<$ 1 μm) ZrO_2 particles into each burner tube passage. Velocity biasing was resolved by seeding one passage at a time in a manner similar to Takahashi et al. (1992). The forward scattered signal is collected and separated by dichroic mirrors before it is detected by photomultiplier tubes and processed by individual TSI burst counters. Typical coincident sampling rates exceeded 1 kHz in flames. A total of 2048 coincident samples were collected for each velocity measurement. Custom-designed software was used to reduce the data on a personal computer. Three-component noncoincident velocity measurements were made with the two-dimensional LDA system by scanning in the transverse and radial directions to get axial and

Nomenclature

k = turbulent kinetic energy
Re = Reynolds number
T = mean temperature
U, W = mean axial and tangential velocities, respectively
X, Y, Z = transverse, radial, and axial directions, respectively
ϵ = turbulent-energy dissipation rate
θ = swirl vane angle
ϕ = overall equivalence ratio

Subscripts

f = fuel
i = inner
o = outer

Downloaded 02 Jun 2010 to 171.66.16.104. Redistribution subject to ASME license or copyright; see http://www.asme.org/terms/Terms_Use.cfm

Table 1 Test matrix for the step swirl combustor experiments (all tests at room temperature and atmospheric pressure)

Variable	Range
Inner vane angle, θ_i, degrees	0, 30 and 45
Outer vane angle, θ_O, degrees	30
Vane configuration	co and counter-swirl
Inner air velocity, U_i, m/s	14.4
Re	18.0×10^3
Outer air velocity, U_O, m/s	8.6
Re	14.8×10^3
Fuel velocity, U_f, m/s	2.5
Re	3.2×10^3
Equivalence ratio, ϕ	0.9
Fuel	methane

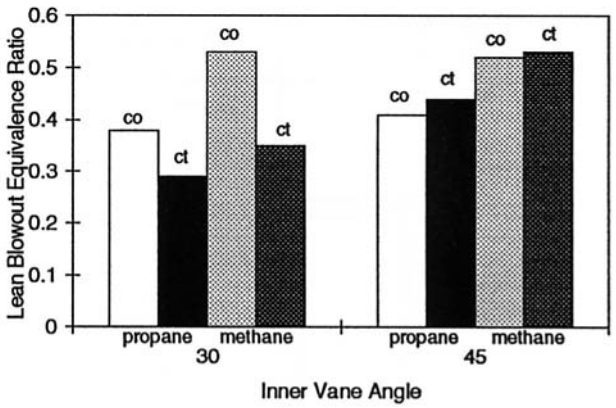

Fig. 4 Lean blowout data comparing inner vane angle, co-swirl (co) and counter-swirl (ct), and methane with propane. Test conditions were θ_o = 30°, ϕ = 0.9, U_i = 14.4 m/s, U_o = 8.6 m/s, U_f = 2.5 m/s.

tangential velocities, and axial and radial velocities, respectively.

Test Conditions. Table 1 lists all the test conditions. Durbin and Ballal (1996) have shown that increasing the inner vane angle increases turbulent mixing and strengthens the inner recirculation zone; these changes dramatically affect the flame structure and the stability characteristics. Therefore, experiments were performed to reveal the differences in flame structure by changing the inner vane angle. Test conditions were also chosen to compare: (*i*) attached versus lifted flames and (*ii*) co-versus counterswirl configurations.

Experimental measurements included flame photography, three-component mean and rms velocities, mean and rms temperatures, and LBO. The LBO data were collected by maintaining a constant airflow rate, heating the combustor to a near steady-state temperature at stoichiometric fuel–air ratio, and then gradually decreasing the fuel flow rate until blowout occurred. This is a standard procedure that has been adopted in our laboratory since the work of Sturgess et al. (1991).

Turbulent Combustion Model

A time-dependent axisymmetric model, which solves axial- and radial-momentum equations, continuity, swirl, turbulent energy (k), turbulent-energy dissipation (ϵ), and enthalpy and species conservation equations was used to simulate the flowfield in the SSC. The standard isotropic $\kappa-\epsilon$ turbulence model was incorporated into this code. Details are described by Katta and Roquemore (1993) and Katta et al. (1994). Briefly, in this turbulence model, density (ρ) was obtained by solving the state equation while pressure field at every time step is determined from pressure Poisson equations. Even though all the governing equations were solved in an uncoupled manner, the turbulence and species conservation equations are coupled through the source terms during the solution process to improve the stability of the algorithm.

In the present analysis of reacting flows, a simple global-chemical-kinetics model involving methane, oxygen, water, carbon dioxide, and nitrogen was used as follows:

$$CH_4 + 2\,O_2 + N_2 \Rightarrow CO_2 + 2\,H_2O + N_2. \qquad (1)$$

The specific reaction rate for Eq. (1) was written in Arrhenius form with an activation energy of 20 kcal/mole and pre-exponential of 2.0×10^{19} $m^6/mole^2/s$. These rate constants were determined by predicting the lift-off of a 8 m/s laminar methane jet flame (Katta, 1995).

An orthogonal, staggered grid system with varying cell sizes in both the z and y directions was utilized. The momentum and swirl equations were integrated using an implicit Quadratic Upstream Interpolation for Convective Kinematics with Estimated Streaming Terms (QUICKEST) numerical scheme (Katta et al., 1994; Leonard 1979), which is third-order accurate in both space and time and has a very low numerical diffusion error. On the other hand, the species, enthalpy, and turbulence-energy conservation equations, which have relatively large source terms, were integrated using the hybrid scheme of Spalding (1972). By rearranging the terms, the finite-difference form of each governing equation at all grid points was written as a system of algebraic equations, which was then solved by using Alternative Direction Implicit (ADI) technique. The time increment, Δt, was determined from the stability constraint and maintained as a constant during the entire calculation. The pressure field at every time step was accurately calculated by simultaneously solving the system of algebraic pressure Poisson equations at all grid points using the LU (Lower–Upper) decomposition technique.

Temperature- and species-dependent thermodynamic and transport properties were used in this formulation. The enthalpy of each species was calculated from polynomial curve-fits, while the viscosity, thermal conductivity, and diffusion coefficients of the species were estimated from the Leonard–Jones potentials. Measured velocity profiles were used at the fuel and air inflow boundaries. All other flow variables (k, ϵ, mass fractions, and T) along these boundaries were assumed to be distributed uniformly. A simple extrapolation procedure (Katta et al., 1994) with weighted zero- and first-order terms was used to estimate the flow variables on the outflow boundary. The usual no-slip, adiabatic, and chemically inert boundary conditions were applied at the walls. Wall functions were used for determining the gradients of the flow variables near the walls.

Results and Discussion

Experimental Observations

Flame Stability. LBO data were collected for all test conditions. In addition, some propane LBO data were collected to examine fuel effects on flame stability. Figure 4 shows LBO data comparing co- and counterswirl and propane with methane. These differences will be discussed after examining flame characteristics utilizing long exposure flame photographs taken with a 35-mm camera. Figure 5(a–e) reveal dramatic flame structure differences in the five test configurations. The only two variables in test conditions for the five cases were inner vane angle and co- or counterswirl configuration. Test conditions were θ_o = 30 deg, ϕ = 0.9, U_i = 14.4 m/s, U_o = 8.6 m/s, U_f = 2.5 m/s, using methane fuel.

Figure 5(a) shows that no swirl in the inner air stream produces a long tubelike central flame structure. The 30 deg outer swirl produces an outer flame structure, which approximates the 30 deg pattern. The attached flame appears to be stabilized

Downloaded 02 Jun 2010 to 171.66.16.104. Redistribution subject to ASME license or copyright; see http://www.asme.org/terms/Terms_Use.cfm

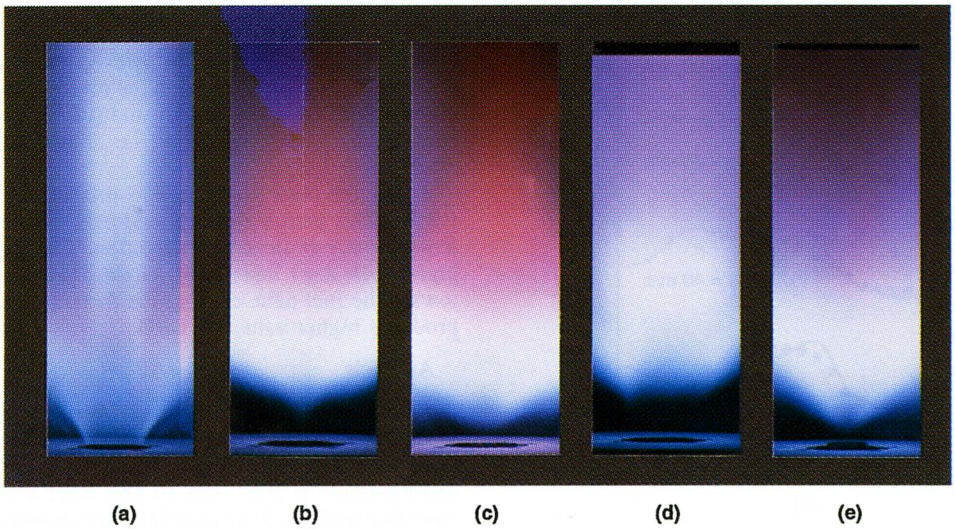

Fig. 5 Photographs illustrating the flame structure for (*a*) θ_i = 0 deg, (*b*) θ_i = 30 deg coswirl, (*c*) θ_i = 45 deg coswirl, (*d*) θ_i = 30 deg counterswirl, and (*e*) θ_i = 45 deg counterswirl. Test conditions were θ_o = 30 deg, ϕ = 0.9, U_i = 14.4 m/s, U_o = 8.6 m/s, U_f = 2.5 m/s, methane.

at the inner air side of the fuel tube and also at the outer air side of the fuel tube. Small traces of flame structure outside the outer air stream are also visible and this can only occur if the fuel penetrates the fast-moving outer air stream or if the fuel recirculates in the outer recirculation zone before burning. It is suspected that the dynamic characteristics of the turbulent flow bring packets of fuel into the recirculation zone and these packets, in turn, burn in the mixing layer of the outer air and the recirculation zone. Sturgess et al. (1991) have observed similar results for a flame stabilized in the outer recirculation zone. This dynamic turbulent exchange phenomenon is more dramatic for an outer vane angle of 60 deg, which produces a stronger outer recirculation zone.

Figure 5(*b*) shows a flame photograph with coswirl configuration and 30 deg inner vane angle. The flame is lifted, there is premixing at its base, and it stabilizes with a dimple shape within the inner recirculation zone. The flame lifts because the inner air stream penetrates the fuel stream with a velocity too high for an attached flame to stabilize and the flame is blown downstream. Also, the inner recirculation is caused by the inner air stream pushing out toward the wall, leaving a low-pressure region in the central portion of the combustor. Chen and Driscoll (1988) have made similar observations on the formation and structure of an inner recirculating vortex. Figure 5(*c*) shows that increasing the inner vane angle from 30 deg coswirl to 45 deg coswirl widens the flame shape and decreases the lift height. This occurs because an increase in vane angle increases the size and strength of the inner recirculation zone but it does not change the stability mechanism; i.e., flame is still stabilized within the inner recirculation zone.

Figure 5(*d*) shows the flame structure for 30 deg inner vane angle counterswirl. The flame has a bulbish shape above the fuel tube. Decreasing the fuel flow velocity causes the flame attachment just above the fuel tube. Figure 5(*e*) shows that

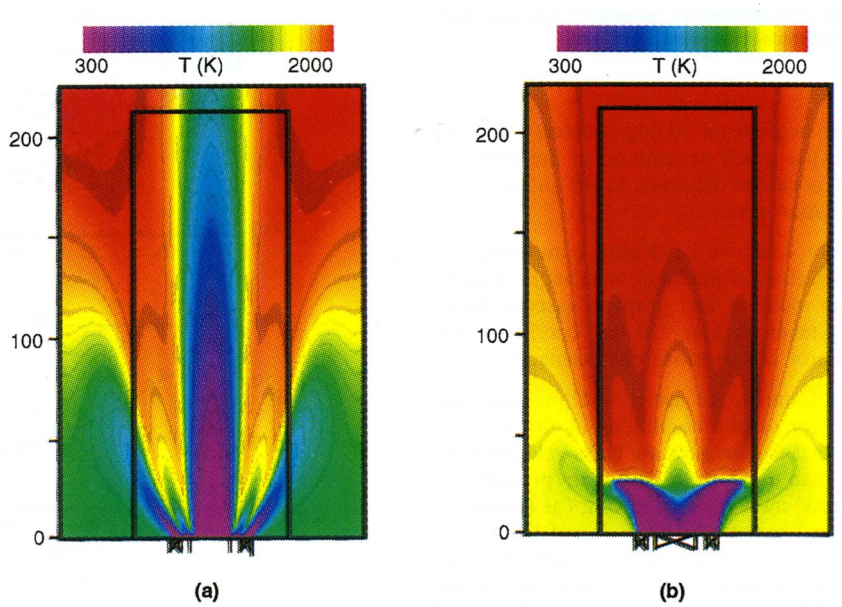

Fig. 6 Computed temperature distribution in SSC for (*a*) θ_i = 0 deg and (*b*) θ_i = 30 deg coswirl. Test conditions are identical to Figs. 5(*a*) and 5(*b*), respectively.

Downloaded 02 Jun 2010 to 171.66.16.104. Redistribution subject to ASME license or copyright; see http://www.asme.org/terms/Terms_Use.cfm

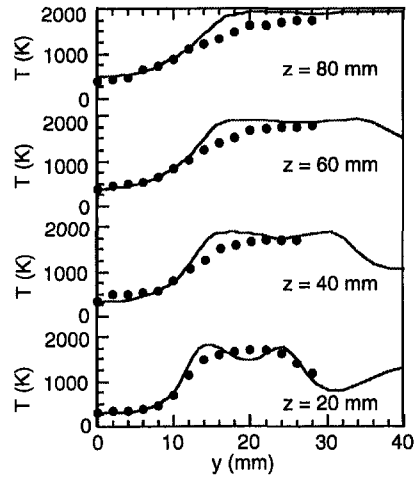

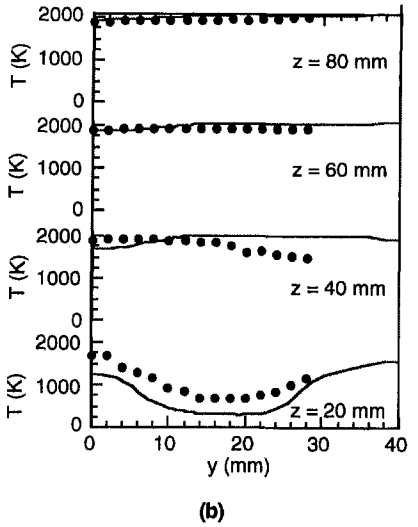

Fig. 7 Radial temperature profiles at different axial locations for (*a*) θ_i = 0 deg, and (*b*) θ_i = 30 deg. Test conditions correspond with Figs. 5(*a*) and 5(*b*), respectively. ● Experimental,—computational.

increasing the inner vane angle from 30 deg counterswirl to 45 deg counterswirl causes too much penetration of the inner air into the fuel zone and this causes the flame to lift and stabilize within the inner recirculation zone.

Lean Blowout. Figure 4 shows LBO data comparing co- and counterswirl for two values of the inner vane angle, namely 30 and 45 deg, for both methane and propane gaseous fuels. The propane data were taken at identical test conditions for comparison purposes. Three observations can be made:

1 LBO values were found to be lower with propane fuel than with methane fuel for all the conditions of the tests. A plausible explanation is that the air/methane mass velocity ratio $(\rho U)_a/(\rho U)_m$ is higher than the corresponding air/propane ratio; this produces enhanced methane–air mixing (as compared to propane-air mixing) and hence a higher value of LBO. Figures 5(*b*), 5(*c*), and 5(*e*) for methane flames clearly show an evidence of premixing at the flame base followed by a lifted flame structure stabilized in the inner recirculation zone.

2 For a 30 deg inner vane angle, LBO values were lower for counterswirl as opposed to coswirl flow direction. This result arises because for the counterswirl flow, shearing braids cause lower air velocities just above the fuel tube leading to an attached flame (which has a lower value of LBO); in contrast the coswirl flow gives higher axial mean velocity directly above the fuel tube, causing the flame to lift from the fuel tube thereby compromising flame stability; i.e., higher values of LBO are obtained.

3 As the inner vane angle is increased from 30 to 45 deg, LBO values increase correspondingly and also LBO becomes less sensitive to swirl flow direction. This happens because the higher (45 deg) inner swirl angle directs more inner airflow toward the fuel tube, causing the flame to lift. This lifted flame produces higher values of LBO.

Analysis

Flame Stability—Computed Results. Predictions were made for different flow conditions using the turbulent combustion model described earlier. Results in the form of temperature distributions for zero- and 30 deg inner coswirl cases (corresponding to Figs. 5(*a*) and 5(*b*) are shown in Figs. 6(*a*) and 6(*b*), respectively. Measured axial, radial, and tangential velocity profiles at the exits of the inner-air and fuel tubes and turbulent mass-averaged outer air velocity obtained from the volu-

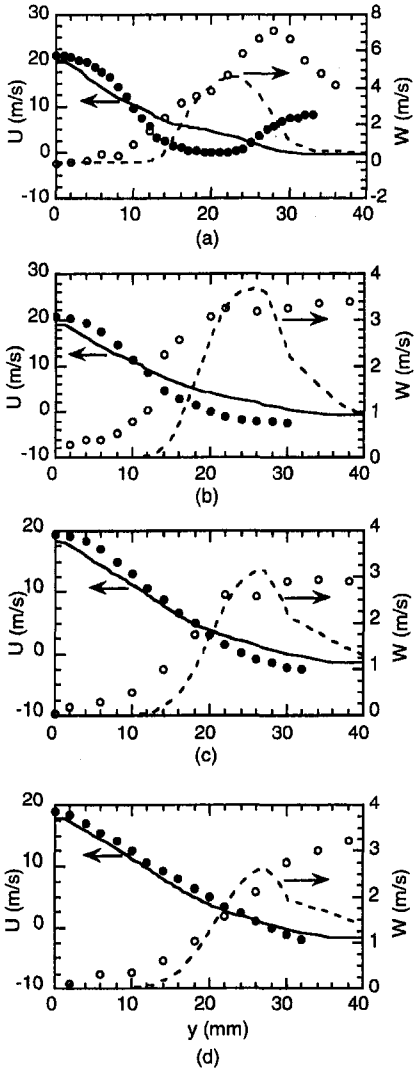

Fig. 8 Calculated and measured velocities for θ_i = 0 deg case at axial locations (*a*) 20 mm, (*b*) 40 mm, (*c*) 60 mm, and (*d*) 80 mm. Circles and lines represent measured and computed velocities, respectively.

Downloaded 02 Jun 2010 to 171.66.16.104. Redistribution subject to ASME license or copyright; see http://www.asme.org/terms/Terms_Use.cfm

metric flow rate provided the inlet boundary conditions for these predictions. Figures 6(*a*) and 6(*b*) show the predicted flame images, i.e., temperature distributions corresponding to flame photographs shown in Figs. 5(*a*) and 5(*b*). Note, the inner box marked on the computed-flame images corresponds with the dimensions of the flame photographs. The following observations were made from the calculated temperature fields: (*i*) In Fig. 6(*a*) (zero inner swirl), the computations correctly predicted the locations of flames on either side of the fuel jet. (*ii*) In Fig. 6(*b*) (30 deg coswirl), a recirculation bubble develops inside the inner air jet and it produces the dimple-shaped flame, and (*iii*) the lift-off height for case (*ii*) predicted by the model matches well with the experimental data. These computations support the qualitative observations on flame photographs described above.

The calculated radial temperature profiles at different axial locations are compared with the measured data in Figs. 7(*a*) and 7(*b*) for zero swirl and 30 deg swirl cases, respectively. In Fig. 7(*a*), in the absence of swirl, the inner air jet spreads gradually, leading to a long tubelike inner flame. Both the calculations and measurements show that the temperature at the center of the SSC over the measurement range (z = 0 to 80 mm) is nearly the same as that of the room temperature air.

Figures 8 and 9 illustrate a comparison between predicted and measured velocities for the zero and 30 deg swirl cases, respectively. Axial (U) and swirl (W) velocity components were compared at different axial locations. For the no-swirl case, calculated velocity profiles agreed well with the experimental data. With 30 deg inner swirl, the measured swirl velocity was generally higher than the predictions, especially in the regions $Y > 22$ mm. Since the outer air was not seeded and the outer velocity profile was approximated, there are discrepancies at locations radially away from the outer jet.

In summary, our simple turbulence model with a single-step global-chemical-kinetics provides a reasonable prediction of flame shape and location, flame temperatures, and axial and swirl velocities. Wherever differences exist between predictions and measurements, an explanation is offered and further investigations along those lines are proceeding.

Flame Shape, Structure, and Location. From the examination of numerous flame photographs and the detailed numerical computations, flame stability in the SSC at the tested flow conditions primarily depends upon the attached flame and the lifted flame processes as sketched in Fig. 10 and described below. Sturgess et al. (1991) and Sturgess and Shouse (1993) have found that studies of such fundamental flame stability processes have great relevance to flame stability in modern annular gas turbine combustors.

1 Multi-attached flame. This type of attached flame is sketched in Figs. 10(*a, b*). As shown in Fig. 10(*a*), for the combination of strong outer swirl (60 deg) and zero inner swirl, the flame is simultaneously attached at three locations: (*i*) inner air side of the fuel stream, (*ii*) outer air side of the fuel stream, and (*iii*) outside of the outer air stream. It may be postulated that the dynamic characteristics of the flow bring packets of fuel into the outer recirculation zone, then burn in the mixing layer of the outer air and the recirculation zone. As the strength of the outer air swirl is decreased (30 deg) the attached flame structure shifts to that sketched in Fig. 10(*b*) where the flame no longer has an attachment on the outer sir side of the fuel stream.

2 Single-attached flame. Figure 10(*c*) illustrates this single attached flame structure. This type of attached flame is observed for low inner (30 deg) and outer (30 deg) counterswirling air flows. Such flow conditions cause the collapse of the twin attached flame structure sketched in Fig. 10(*b*) to a

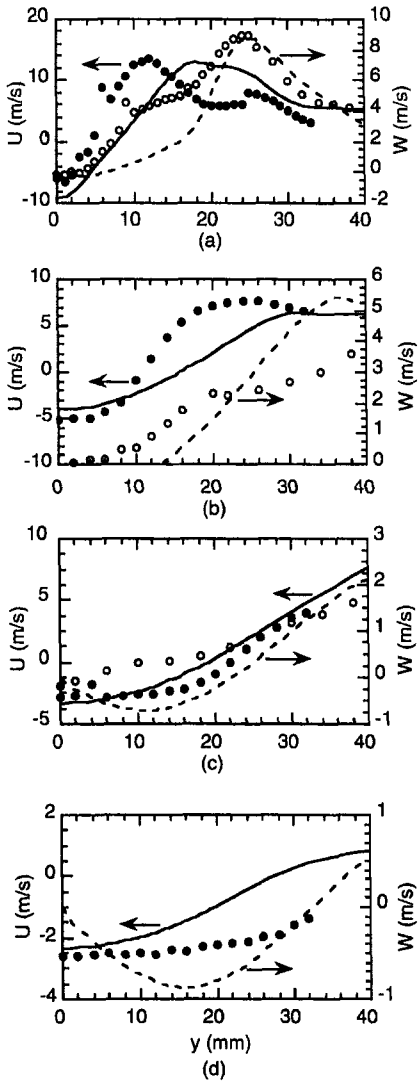

Fig. 9 Calculated and measured velocities for θ_i = 30 deg case at axial locations (*a*) 20 mm, (*b*) 40 mm, (*c*) 60 mm, and (*d*) 80 mm. Circles and lines represent measured and computed velocities, respectively.

single attachment just above the fuel tube. This type of attached flame was also observed for the coswirl configuration but at a lower combustor loading.

3 Lifted flame. Figure 10(*d*) illustrates this type of flame; also it is observed in the photographs of Figs. 5(*b*), 5(*c*), and 5(*e*). The flame lifts from the fuel tube lip because of the high mean axial velocity in the near-field region above the fuel tube. The lifted flame is stabilized by the inner recirculation zone. However, increasing the swirl intensity and/or combustor loading only slightly changes flame stability, i.e., LBO values remain fairly constant for lifted flames. This is because the lifting of a flame is usually accompanied by a premixing of fuel and air at the base of the flame. This premixing compromises the stability of the lifted flame over that of an attached flame, i.e., LBO values are higher for a lifted flame than for an attached flame.

Now, it is also clear that the observed difference in LBO between co- and counterswirl configurations, as shown in Fig. 4, is primarily a function of how the flame stabilizes. Counterswirl conditions readily produce an attached flame for moderate inner swirl intensity (30 deg); however, both configurations produce lifted flames for higher swirl intensity (45 deg) and for this

Downloaded 02 Jun 2010 to 171.66.16.104. Redistribution subject to ASME license or copyright; see http://www.asme.org/terms/Terms_Use.cfm

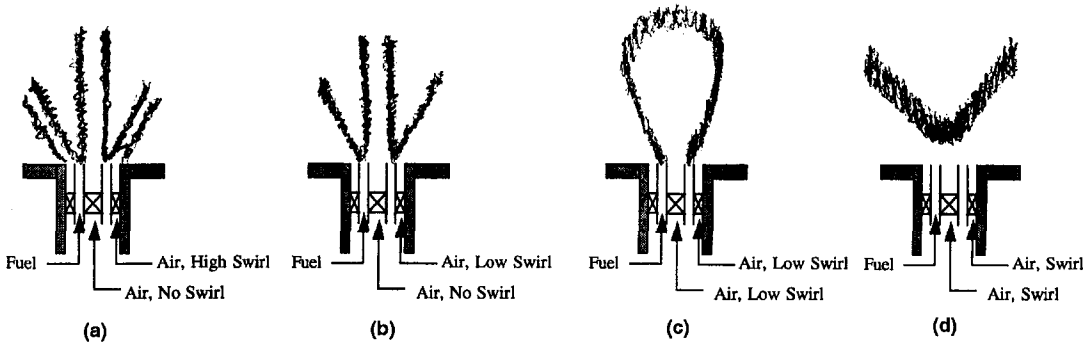

Fig. 10 Sketches illustrating the flame shape, structure, and location in the SSC

latter condition the LBO values are very similar. Finally, Sturgess et al. (1991) and Sturgess and Shouse (1993) have elucidated the significance and applications of anchored and lifted flames to practical gas turbine combustor stability and LBO. They observe three basic flame conditions: a thin sheathlike pilot anchored flame, a shear layer flame associated with the inner and outer recirculation zones, and a lifted main flame, which allows considerable premixing of reactants to take place prior to combustion. These observations further confirm the relevance and importance of the present work to practical gas turbine combustors.

Conclusions

An SSC was designed to reproduce the swirling flow pattern present in the vicinity of the fuel injector located in the primary zone of a gas turbine combustor. Different flame shapes, structure, and location were observed and detailed experimental measurements and numerical computations were performed.

1 For the combination of strong outer swirl and zero inner swirl, a multiple attached flame exists simultaneously over the fuel and air injection tubes. As the strength of the outer air swirl is decreased and that of the inner swirl increased, the flame structure gradually shifts to a single attachment above the fuel injection tube.

2 For higher inner swirl velocity, the flame lifts from the fuel tube and is stabilized by the inner recirculation zone. Premixing of fuel and air at the base of the flame compromises the stability of the lifted flame over that of an attached flame, i.e., LBO values are higher for a lifted flame than for an attached flame.

3 The observed difference in LBO between co- and counterswirl configurations is primarily a function of how the flame stabilizes. Counterswirl conditions readily produce an attached flame for moderate inner swirl intensity; however, both configurations produce lifted flames for higher inner swirl intensity and for this latter condition the LBO values are very similar.

4 Computations based upon a turbulent combustion model correctly predict the attached flame locations, the development of an inner recirculation zone, which produces a dimple-shaped flame structure, and finally the flame lift-off height. The calculated radial mean temperature profiles at different axial locations agreed well with the measured CARS temperature. Also, the calculated velocity profiles agree reasonably well with the LDA measurements of mean axial and mean tangential velocities. These computations show the presence of a strong inner recirculation zone in the SSC, provide the location of the reattachment point of this recirculation bubble, and confirm the transport of combustion products upstream.

Finally, Sturgess et al. (1991) and Sturgess and Shouse (1993) have elucidated the significance and applications of anchored and lifted flames to practical gas turbine combustor stability and LBO. This confirms the importance and relevance of the present work to gas turbine combustors.

Acknowledgments

This work was supported by the U.S. Air Force, Wright Laboratory, Fuels and Lubrications Division, Aero-Propulsion and Power Directorate, Wright Patterson Air Force Base, Dayton, OH, under contract No. F33615-92-C-2207, with Mr. Charles W. Frayne serving as the Air Force Technical Monitor. The authors wish to thank Mr. W. John Schmoll for the custom LDA processing software.

References

Bradley, D., Gaskell, P. H., and Lau, A. K. C., 1990, "A Mixedness-Reactedness Flamelet Model for Turbulent Diffusion Flames," *Twenty-Third Symposium (International) on Combustion,* The Combustion Institute, p. 685.

Chen, R. H., and Driscoll, J. F., 1988, "The Role of the Recirculation Vortex in Improving Fuel–Air Mixing Within Swirling Flames," *Twenty-Second Symposium (International) on Combustion,* The Combustion Institute, p. 281.

Durbin, M. D., and Ballal, D. R., 1996, "Studies of Lean Blowout in a Step Swirl Combustor," ASME JOURNAL OF ENGINEERING FOR GAS TURBINES AND POWER, Vol. 118, pp. 72–78.

Gollahalli, S. R., Savas, O., Huang, R. F., and Rodriguez Azara, J. L., 1985, "Structure of Attached and Lifted Gas Jet Flames in Hysteresis Region," *Twenty-First Symposium (International) on Combustion,* The Combustion Institute, p. 295.

Katta, V. R., and Roquemore, W. M., 1993, "Numerical Method for Simulating Fluid-Dynamic and Heat-Transfer Changes in Jet Engine Injector Feed-Arm Due to Fouling," *Journal of Thermophysics and Heat Transfer,* p. 651.

Katta, V. R., Goss, L. P., and Roquemore, W. M., 1994, "Numerical Investigations of Transitional H2/N2 Jet Diffusion Flames," *AIAA Journal,* Vol. 32, p. 84.

Katta, V. R., 1995, internal report in preparation.

Leonard, B. P., 1979, "A Stable and Accurate Convective Modeling Procedure Based on Quadratic Upstream Interpolation," *Computational Methods in Applied Mechanics and Engineering,* Vol. 19, p. 51.

Pan, J. C., Vangsness, M. D., Heneghan, S., and Ballal, D. R., 1991, "Scalar Measurements of Bluff Body Stabilized Flames Using CARS Diagnostics," ASME Paper No. 91-GT-302.

Pitts, W. P., 1988, "Assessment of Theories for the Behavior and Blowout of Lifted Turbulent Jet Diffusion Flames," *Twenty-Second Symposium (International) on Combustion,* The Combustion Institute, p. 809.

Pitts, W. P., 1990, "Large-Scale Turbulent Structures and the Stabilization of Lifted Turbulent Jet Diffusion Flames," *Twenty-Third Symposium (International) on Combustion,* The Combustion Institute, p. 661.

Spalding, D. B., 1972, "A Novel Finite Difference Formulation for Difference Expressions Involving Both First and Second Derivatives," *International Journal for Numerical Methods in Engineering,* Vol. 4, p. 551.

Sturgess, G. J., Lesmerises, A. L., Heneghan, S. P., and Ballal, D. R., 1990, "Design and Development of a Research Combustor for Lean Blowout Research," ASME JOURNAL OF ENGINEERING FOR GAS TURBINES AND POWER, Vol. 114, p. 13.

Sturgess, G. J., Sloan, D. G., Roquemore, W. M., Shouse, D., Lesmerises, A. L., Ballal, D. R., Heneghan, S. P., Vangsness, M. D., and Hedman, P. O., 1991, "Flame Stability and Lean Blowout—A Research Program Progress Report," Paper No. 91-7037, *Proceedings of Tenth ISABE,* Nottingham, United Kingdom.

Sturgess, G. J., and Shouse, D., 1993, "Lean Blowout Research in a Generic Gas Turbine Combustor With High Optical Access," Paper No. 93-GT-332, to appear in the *Transactions of the ASME.*

Downloaded 02 Jun 2010 to 171.66.16.104. Redistribution subject to ASME license or copyright; see http://www.asme.org/terms/Terms_Use.cfm

Takahashi, F., Mizomoto, M., Ikai, S., and Fukati, N., 1984, "Lifting Mechanism of Free Jet Diffusion Flames," *Twentieth Symposium (International) on Combustion,* The Combustion Institute, p. 295.

Takahashi, F., Schmoll, W. J., and Vangsness, M. D., 1990, "Effects of Swirl on the Stability and Turbulent Structure of Jet Diffusion Flames," Paper No. AIAA-90-0036.

Takahashi, F., and Goss, L. P., 1992, "Near-Field Turbulent Structures and the Local Extinction of Jet Diffusion Flames," *Twenty-Fourth Symposium (International) on Combustion,* The Combustion Institute, p. 351.

Takahashi, F., Vangsness, M. D., and Belovich, V. M., 1992, "Conditional LDV Measurements in Swirling and Non-swirling Coaxial Turbulent Air Jets for Model Validation," Paper No. AIAA-92-0580.

Vanquickenborne, L., and van Tiggelen, 1966, "The Stabilization Mechanism of Lifted Diffusion Flames," *Combustion and Flame,* Vol. 10, p. 59.

Downloaded 02 Jun 2010 to 171.66.16.104. Redistribution subject to ASME license or copyright; see http://www.asme.org/terms/Terms_Use.cfm

A. J. Scalzo

R. L. Bannister

Power Generation Business Unit,
Westinghouse Electric Corporation,
Orlando, FL 32826

M. DeCorso[1]
Media, PA 19063

G. S. Howard[1]
Charlottesville, VA 22902

Evolution of Westinghouse Heavy-Duty Power Generation and Industrial Combustion Turbines

This paper reviews the evolution of heavy-duty power generation and industrial combustion turbines in the United States from a Westinghouse Electric Corporation perspective. Westinghouse combustion turbine genealogy began in March of 1943 when the first wholly American designed and manufactured jet engine went on test in Philadelphia, and continues today in Orlando, Florida, with the 230 MW, 501G combustion turbine. In this paper, advances in thermodynamics, materials, cooling, and unit size will be described. Many basic design features such as two-bearing rotor, cold-end drive, can-annular internal combustors, CURVIC[2] clutched turbine disks, and tangential exhaust struts have endured successfully for over 40 years. Progress in turbine technology includes the clean coal technology and advanced turbine systems initiatives of the U.S. Department of Energy.

Historical Perspective

Westinghouse, a major supplier of steam turbines since the beginning of the 20th century (Bannister and Silvestri, 1989), obtained the experience it needed to develop land-based power generation combustion turbines through its entry into the jet engine business. In March of 1943, the first wholly American designed and manufactured jet engine went on test at Westinghouse, 15 months after obtaining a letter of intent from the United States Navy. The engine (designated WE19A) had a thrust of 1130 lb (513 kg) and weighed 827 lb (375 kg). Without any knowledge of German, British, or other United States activity, Westinghouse developed the first American jet engine with an axial compressor, an annular combustor, a turbine, and a jet exhaust nozzle. The device resembled the Whittle engine developed in England, but there were major differences, in that an axial flow compressor was used, along with a "submerged" combustion chamber; i.e., completely surrounded by compressor flow.

An improved version of the engine, the WE19B, was test flown at Patuxent Flight Test Center in January 1944 as a booster unit on a Chance Vought Corsair. It delivered 1365 lb (620 kg) of thrust, weighed 731 lb (332 kg), and one year later, as the J30, was used to power the Navy's first jet fighter, the McDonnell Douglas FH-1 Phantom. Sixty-one (61) Phantom planes were equipped with the J30 engine.

The J34, a 34-in.-dia engine that delivered 3000 lb (1362 kg) of thrust, was the last major serial production aero engine built by Westinghouse. It was used extensively by the Navy in the McDonnell Banshee. Overall, Westinghouse supplied the engines for 1223 Navy jets before exiting the business in 1960.

Westinghouse's experience with land-based gas turbines started in 1945 with the development of a 2000 hp gas turbine generator set (W21) that consisted of a single reduction gear, compressor, 12 combustors and turbine (Putz, 1948). A thermal efficiency of 18 percent lower heating value (LHV)[3] was obtained. By 1948, Westinghouse had built a 4000 hp gas turbine locomotive with the Baldwin Company that used two of these units. Initial operation was on the Union Railroad burning distillate fuel oil. Later operation was on the Pittsburgh and Lake Erie Railroad using residual oil fuel.

In the late 1940s, the United States Navy wanted to develop a back-up for the nuclear submarine power plant. Westinghouse received a contract designated "Wolverine" to develop a gas turbine engine for surface, snorkel, and submerged operations. A gas turbine engine of 7500 shaft horsepower was designed to operate in open, semi-closed, and closed cycle modes. In the semi-closed mode, oxygen was supplied to the cycle from the snorkel. While in the submerged mode (fully closed cycle) oxygen was supplied and CO_2 gas was discharged overboard. Engine testing was done at the United States Naval Test Laboratory in Annapolis, Maryland, during the early 1950s. While the power plant met all contract requirements, the success of the nuclear submarine program eliminated the need for "Wolverine."

By 1954, gas turbine power plants were becoming a practical and economic reality for particular applications in the power industry. Westinghouse was offering three basic gas turbine designs for power generation that had a rotor inlet temperature of 1350°F (732°C) (Putz, 1954). The units were rated at 3500 kW, 5000 kW (with a regenerator), and 15,000 kW (with a regenerator and intercooler). The latter unit was designed for a full-load simple cycle efficiency of 29 percent compared to the full-load efficiency of 21 percent for the 5000 kW unit.

West Texas Utilities helped pioneer combustion turbine baseload generation with a 5000 kW unit that was installed in 1952 (Cox, 1957). In 1954, another 5000 kW combustion turbine was installed. The waste heat from this unit was used for feedwater heating until 1959 when it was incorporated into a fully fired combined-cycle system. This system generated 39 MW in the steam cycle and 5 MW in the combustion cycle.

The Westinghouse single-shaft, two-bearing, combustion turbine with a reduction gear was first introduced in 1952 as the W81 at 5.5 MW (Stephens, 1952). In 1967, the W251A introduced major innovations such as minimum peak stress turbine

[1] Westinghouse Electric Corporation Retiree.

[2] Gleason Works.

Contributed by the International Gas Turbine Institute and presented at the 39th International Gas Turbine and Aeroengine Congress and Exposition, The Hague, The Netherlands, June 13–16, 1994. Manuscript received by the International Gas Turbine Institute March 4, 1994. Paper No. 94-GT-488. Associate Technical Editor: E. M. Greitzer.

[3] All efficiency values in this paper will be LHV.

Copyright © 1996 by ASME

Downloaded 02 Jun 2010 to 171.66.16.104. Redistribution subject to ASME license or copyright; see http://www.asme.org/terms/Terms_Use.cfm

blade roots, and cooled low alloy steel turbine disks. Today there are over 300 gear-driven units operating in both simple, combined, and cogeneration cycle modes with the current W251 B12 rated at 48 MW.

The first direct drive combustion turbine (W201) at 20 MW was introduced in 1960. A modified W201 combustion turbine was used in 1960 as part of a blast furnace system at U.S. Steel's Chicago Works. The successful development program included design, development, and manufacture of a special casing configuration to remove compressor discharge flow efficiently and deliver it externally to the engine (Krapf and Stephens, 1958). Gases from the blast furnace were burned and ducted back to the turbine through a special duct and scroll.

In 1962, Westinghouse designed the first "packaged" combustion turbine power plant, which was delivered to the City of Houma. The "packaged" power plant concept is retained today in the ECONOPAC[4] system. This simple-cycle package includes the combustion turbine engine assembly; generator and exciter; starting package; inlet and exhaust systems; and plant auxiliary equipment. It is constructed in modules for easy shipment and installation. The ECONOPAC system is also the base for cogeneration and other heat recovery applications.

In 1967, a supercharged direct drive W301 at 25 MW in a heat recovery application was installed at West Texas Utilities San Angelo's Power station and achieved over 39 percent in combined cycle efficiency, the highest in the United States for a number of years.

The first direct drive W501 combustion turbine went into service in 1968 at the Dow Chemical Company with a rating of 42 MW. Many basic design innovations were introduced on the W501A including unique cooled, filtered rotor cooling systems and tilting pad bearings. By 1974, fifty-seven 501s were operating. The 501 technology has grown steadily over 25 years. The current production engine, W501D5 is now being offered with an ISO rating of over 118 MW, the 501F is at 160 MW, and the 501G, introduced in 1994 (Southall and McQuiggan, 1995) at 230 MW. The "F" technology includes increases in airflow and firing temperature, improved component efficiencies, and advances in materials, turbine cooling, and dry low NO_x. Currently, there are about 300 direct drive units in operation. A complete listing of all models sold is shown in Table 1 where total service hours is seen to exceed 47 million.

For over 30 years, Westinghouse has had licensee arrangements with several combustion turbine manufacturers, the major ones being Fiat Avio in Italy and Mitsubishi Heavy Industries (MHI) in Japan. These partners have contributed to the development of the combustion turbine with Westinghouse, particularly in the 50 Hz market; i.e., the TG50 of Fiat Avio and the MW 701 of MHI, 50 Hz versions of the Westinghouse W501 Model. During the late 1980s and early 1990s, a trilateral alliance was formed among Westinghouse, Fiat Avio, and MHI to replace the old licensee/licensor arrangement. The alliance provides for joint development of combustion turbines and sharing of technology. The 501F and the 50 Hz 701F are the first engines developed under this partnership arrangement.

Westinghouse Engine Technology Evolution

Westinghouse model designations initially meant the horsepower output in thousands followed by the number of shafts with letters denoting whether the engine was intercooled, regenerated, reheated, or extracted. Therefore, W201RE would mean 20,000 hp, single shaft, regenerated, with cycle air extraction. Later engine evolution, accelerated by materials and cooling improvements, invalidated such designations.

It should be noted that in this paper, the term "firing temperature" for uncooled engines will be defined as the average temperature leaving the combustors and entering the turbine. This neglects the effect of turbine inlet leakage and first-stage vane cooling and will be confined to first and second-generation engines. For all engines discussed in the third through fifth generations, rotor inlet temperature (RIT) will be used to define the temperature level. RIT is the flow weighted mean total temperature relative to a stationary plane immediately upstream of the first-stage rotor blades. The basic reason for the change is to include the effects of cooling air used by the row 1 vane.

Westinghouse combustion turbine evolution will be presented as follows:

First Generation. This period of the mid-1940s was heavily influenced by jet engine and steam turbine philosophies and will be confined to the W21 engine.

Second Generation. This period spanned from the late 1940s to the mid-1960s and generated many major design innovations that have been retained in our present designs.

Third Generation. The "Northeast Blackout" of 1965 initiated this generation that saw an explosion of design effort and introduced air cooling, higher firing temperatures, improved materials, and precision cast components. In addition, innovative concepts such as cooled, filtered rotor cooling air and rotor blade cooling and low alloy turbine disks, were introduced.

Fourth Generation. The fourth generation covered the 1970s and the 1980s, a period that was severely impacted by the "Oil Embargo" and the Fuel Use Act. Essentially the combustion turbine market disappeared until the Fuel Use Act was repealed and the Public Regulatory Policies Act of 1978 (PURPA) was upheld. The latter part of this generation saw the introduction of increased firing temperatures and improvements in materials, cooling, and efficiency. The W501D5, introduced in 1983, became the largest and most efficient 60 Hz single shaft combustion turbine in the world at 100 MW and over 33 percent efficiency for a simple cycle plant.

Fifth Generation. This generation covers the late 1980s to the present and starts with the 501F advanced combustion turbine with an RIT of 2300°F (1260°C). Units in this generation will extend the air flow limits of last row turbine blades, the temperature limits of row 1 turbine vanes, and the flow limits of row 1 compressor blades through the use of advanced materials and cooling.

First Generation. The jet engine designers needed a high-pressure, high flow facility, for combustor and turbine aerodynamic development. A lightly loaded 23-stage axial flow compressor was designed to meet the needs of the air supply facility. This test compressor together with a 12 can interconnected combustion system and an eight-stage turbine formed the first industrial combustion engine at 2000 hp. The air flow was 35.5 lb/sec (16.1 kg/s) at a pressure ratio of 5, a firing temperature of 1250°F (677°C), and a power output of 2070 hp at an efficiency of 18 percent (Mochel, 1947). The unit was a single shaft, three bearing design with a design speed of 8750 rpm. The external load was driven from the compressor end of the engine.

After a development period, the engine was first applied (1948) as a twin set in a locomotive built by Baldwin and Westinghouse (Stephens and Young, 1989). The engines burned either diesel fuel or residual oil. The locomotive was used as a demonstrator and ran on several railroads, but was never placed in commercial service. Although the locomotive operated at a cost approximately 5 percent less than a diesel locomotive, the capital costs were not competitive. The locomotive was subsequently scrapped, but both turbines were sold for further operation. The left-hand unit was sold to the city of Larned, Kansas, as one of the early decentralized peak shaving plants and the right-hand unit became the world's first intercooled steam injected plant driving an air compressor at

[4] Westinghouse Electric Corporation.

Downloaded 02 Jun 2010 to 171.66.16.104. Redistribution subject to ASME license or copyright; see http://www.asme.org/terms/Terms_Use.cfm

Table 1 Westinghouse supplied combustion turbines

Model	No. of Units	Rating (kW)	Installed Capacity (kW)	Oper. Year	Mech. Drive	60 Hz	50 Hz	Service Hours*
W21	5	1,300	6,500	1949	3	5	0	500,000
W31	6	2,200	13,200	1956	6	0	6	600,000
W41	8	3,100	25,000	1961	4	7	1	800,000
W52	14	3,800	52,400	1956	2	14	0	1,400,000
W62	15	5,500	83,000	1961	13	15	0	1,500,000
W72	17	6,300	107,100	1961	17	1	16	1,700,000
W81	30	5,500	155,400	1952	17	30	0	3,070,345
W82	12	6,000	72,300	1962	12	0	12	1,200,000
W92	29	8,200	231,500	1960	27	29	0	2,900,000
W101	83	7,450	607,600	1961	54	70	13	8,306,630
W121	2	8,950	19,000	1959	1	2	0	200,000
W122	1	10,215	10,200	1967	0	1	0	100,000
W171	39	16,425	509,900	1961	1	28	11	2,184,371
W191	182	17,300	3,044,500	1965	14	127	55	8,596,174
W201	3	18,650	62,600	1960	0	3	0	296,022
W251	195	49,100	5,626,700	1967	1	147	48	4,322,303
W301	32	23,850	938,100	1964	0	27	5	1,638,369
W352	7	27,900	190,900	1979	4	7	0	665,227
W501	227	159,000	13,929,466	1968	0	227	0	7,192,050
W701	8	136,900	1,095,200	1992	0	0	8	0
TOTAL	915		26,780,566		176	740	175	47,171,491

* Service hours are estimated as of 12/31/92

Hopewell, Virginia. The first baseload service of the engine was as a pipeline gas booster pumper on The Mississippi River Fuel Company System in March 1949. This was a dual fuel application burning either oil or gas with the capability of changing to either fuel at full load, an industry first. This particular engine, the first combustion turbine in the world to achieve 100,000 operating hours, was retired after more than 150,000 hours of operation when the gas line was retired.

W21 combustor baskets were contained in individual pipelike enclosures connecting compressor discharge to turbine inlet, as shown in Fig. 1, and bore little resemblance to the Westinghouse aviation gas turbine design, which was an annular combustor, but used the wall cooling arrangement (wiggle strips) from the aviation design. The wiggle strip concept of wall cooling was unique; it interposed a corrugated strip of metal between two cylindrical sections of combustor that permitted the injection of cooling air; it is structurally superior to a single cylinder because the increased section modulus provides superior buckling characteristics and proved to be a fundamental cooling feature that is still being used in current Westinghouse turbines. Also, casings were horizontally split (like steam turbines) instead of the axial stacking used by the jets. Late production units introduced the CURVIC coupled rotor structure, as shown in Fig. 2, to align disks and transmit torque.

Second Generation. In the late 1940s, Westinghouse formed a design group independent of the aircraft group to develop gas turbines for land based applications. Engineering studies indicated that with the high-temperature materials then available, a firing temperature of 1350°F (732°C) was feasible for baseload duty (100,000 hr life). In response to a market survey, the first engine developed was a 5000 kW single-shaft, simple-cycle engine. This engine had a design speed of 5740 rpm, an air flow of about 125 lb/s (57 kg/s) at a pressure ratio of 6.25.

The second-generation engine design eliminated the undesirable center bearing and placed the combustion system inside a pressure vessel. Overall, this design had the following improvements:

- Elimination of center bearing removed a fire hazard and simplified shaft alignment.
- Compressor flow from the diffuser provided impingement and convective cooling of the transition duct.
- Flow into this plenum-type enclosure attenuated flow disturbances to and from the compressor.
- The annular plenum effect provided damping of combustor pressure fluctuations (this became valuable in later years when limits of combustor stability were approached when using water injection for NO_x control).
- Improved cross-flame tube connections were provided for.
- The inclined position for the combustors and transitions was permitted, thus facilitating the center bearing removal by shortening the span length.
- Combustors and cross-flame tubes were completely encased in relatively cool compressor discharge air, thereby eliminating a multitude of pressure connections and potential fire hazard.

In addition to the combustion system changes, the 5000 kW (W81) combustion turbine, introduced in 1952, contained the following basic mechanical design features, illustrated in Fig. 3:

- Individually replaceable turbine and compressor rotor blading without removal of the rotor.
- Inner shrouded diaphragm construction for turbine and compressor stationary blading to permit servicing with rotor in place.
- Support of the exhaust bearing housing by six tangential struts that rotate the housing during thermal transients and maintain shaft alignment without the need of cooling.

The W81 16-stage compressor design was the result of extensive analytical and laboratory development. While the free-vortex design of the early compressor had the advantage of minimizing the effect of neglecting some terms in the Euler equa-

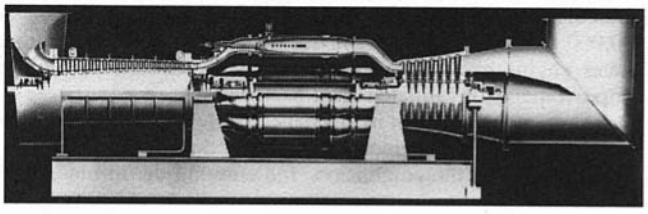

Fig. 1 Cross section of W21 combustion turbine

Downloaded 02 Jun 2010 to 171.66.16.104. Redistribution subject to ASME license or copyright; see http://www.asme.org/terms/Terms_Use.cfm

tions, the result was many stages at relatively low blade tip speeds. In addition, theoretical studies indicated that a design of 50 percent reaction, with a flow coefficient of about 0.55, would give a stage of maximum efficiency. By setting up a preswirl entering the first rotating blade, the blade relative velocity could be significantly reduced and high reaction obtained. This would allow an increase in blade speed with the consequent reduction in the number of compressor stages required for a given pressure ratio. The vortex pattern selected was a compromise between little change in reaction radially and blade shock losses. This vortex pattern specified the mean stage absolute swirl constant and made the axial velocity relatively constant radially. A positive energy gradient was added from blade hub to tip in the first few stages, the energy addition was kept constant in the middle stages, and the gradient removed in the last stages.

Other design techniques used were to specify flow area blockage factors and to use NACA 65 blade sections on a circular arc mean line for the higher Mach number front stages and NACA (4-digit) sections elsewhere. The resulting design was successful except that the starting surge margin was inadequate; therefore, an interstage bleed was added. The average stage efficiency was about 89 percent.

The aerodynamic design of the five-stage turbine was taken mainly from Westinghouse aircraft engine design practice using a free-vortex swirl distribution and constant work radially with a last stage designed for axial velocity outflow. A minimum reaction was maintained at the blade hub sections to prevent suction side separation. All blade sections were designed to provide smooth accelerating flow passages. The average stage efficiency was about 90 percent and the matching of the compressor and turbine flow characteristics was excellent; i.e., the design points of the two components coincided at the engine design point. The engine produced 5700 kW at the generator terminals at a firing temperature of 1350°F (732°C) and a thermal efficiency of about 21 percent. The prototype engine, sold to West Texas Utilities, went into commercial service in 1952. This unit was the first utility application of a Westinghouse combustion turbine.

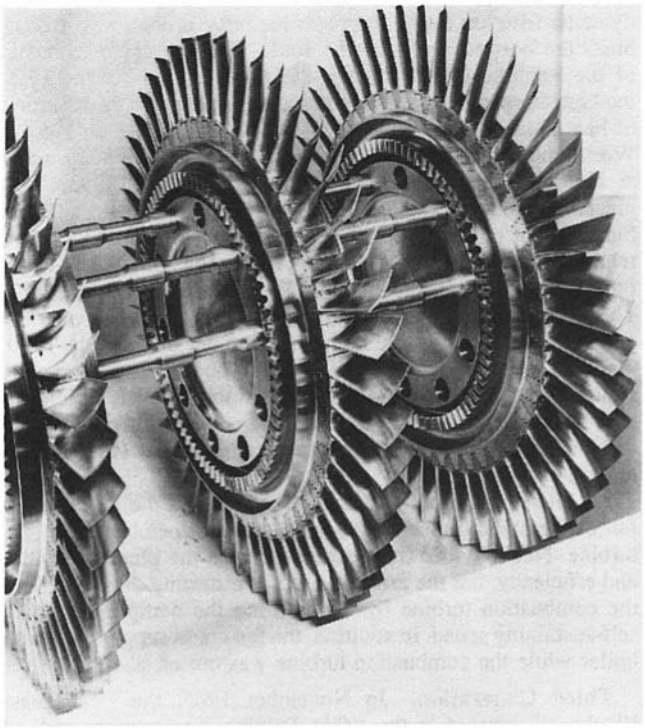

Fig. 2 CURVIC coupled turbine disks

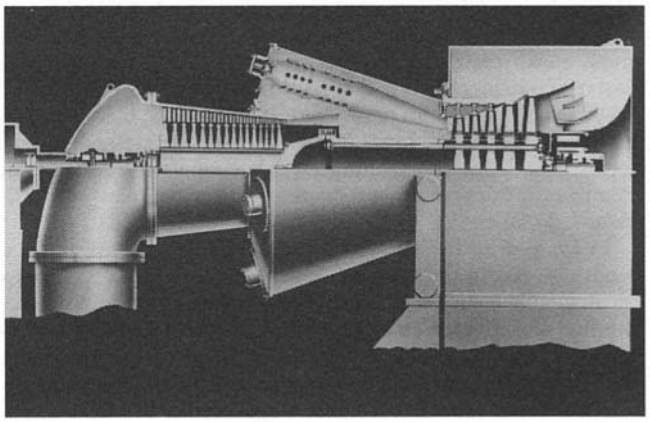

Fig. 3 Cross section of W81 combustion turbine

Marketing studies indicated there were many differing applications for combustion turbines from power generation and transportation, to mechanical drives. Engineering cycle studies were made to determine the best cycle arrangements for the various applications. A summary of those studies, at a 1400°F (760°C) firing temperature, is shown in Fig. 4. Component efficiencies, pressure losses, and heat exchanger effectiveness for these studies were state of the art.

With the successful completion of the 5000 kW design, a line of mechanical drive engines, using the same basic blading as the 5000 kW engine, was designed. For pipeline pumping, a unit was designed with regeneration and a free power turbine (Stephens and Bruce, 1955). The regenerative engine produced about 5400 hp at the turbine coupling with an efficiency of approximately 30 percent. The cycle pressure ratio was 4.2, the compressor speed was 6000 rpm, and the firing temperature was 1350°F (732°C). The regenerative units did not perform in the field as expected, primarily because leakage and pressure loss were greater than expected. This same unit was also modified to be used without regeneration.

To make the engines more competitive with steam plants and other prime movers, it was necessary to use a more efficient cycle. As shown in Fig. 4, a gain of about 12 percent could be

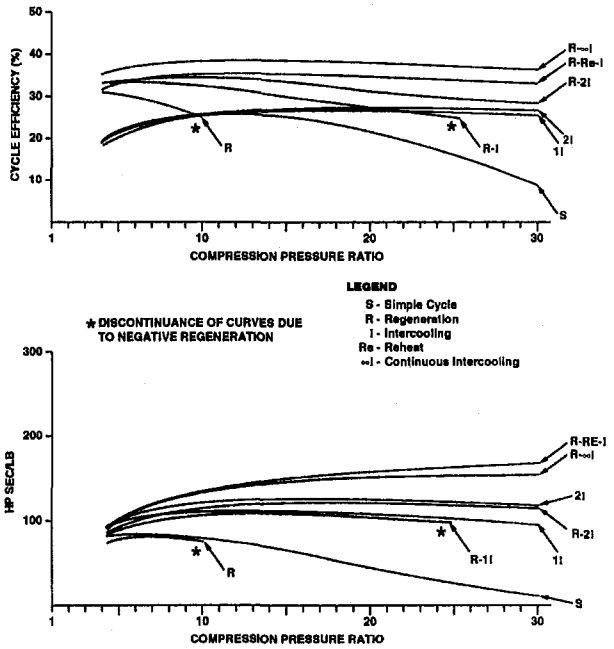

Fig. 4 Summary of engineering cycle studies at 1400°F

Downloaded 02 Jun 2010 to 171.66.16.104. Redistribution subject to ASME license or copyright; see http://www.asme.org/terms/Terms_Use.cfm

obtained by adding intercooling to the regenerative cycle resulting in 34 percent efficiency, which made it competitive with small steam plants. A 15,000 kW engine was designed as a two-shaft, intercooled, and regenerative engine with the load taken from the high-pressure shaft. By taking the load from the 3600 rpm high-pressure shaft, the low pressure (LP) shaft was made variable speed resulting in little dropoff in turbine inlet temperature at part load and, therefore, excellent part-load efficiency.

In 1954, prior to the cancellation of the 15,000 kW project, work was begun on a single-shaft simple-cycle 3600 rpm gas turbine. This engine was later to become the W201 gas turbine, the first direct drive (no gear) Westinghouse combustion turbine. In the W201, the aerodynamic design of the successful 5000 kW engine compressor was modified slightly by eliminating the energy gradient so that stages could be more easily added or removed from the basic design. In addition, lightly loaded stages for high efficiency were adopted for these engines. Design techniques were also improved by refining empirical factors. As high-temperature materials advanced, the allowable turbine inlet temperature was increased, thus improving output and efficiency. By the end of the 1950s, firing temperatures had risen to 1450°F (788°C) at baseload. Also, the W31 and the W121 at 3000 hp and 12,000 hp, respectively, both single-shaft engines, were designed following the same philosophy developed in the W201.

In the middle 1950s, Westinghouse designed a blast furnace blower to supply 125,000 ft^3/min (3540 m^3/min) of air at about 2.5 atmospheres gage pressure, and burning blast furnace gas at about 100 Btu/scf (3700 kJ/scm). The blower was a modification of the W201 in which the blast furnace air was extracted from the compressor discharge and the fuel gas supplied to the engine through a shaft-driven fuel compressor. The fuel compressor was a modified compressor from the W31 engine. The engine and it's performance are shown in Figs. 5 and 6, respectively. Turbine blading, turbine disks, compressor disks, and recuperator were taken from the 15,000 kW unit. This was a very successful design from an engineering point of view, but the market disappeared when oxygen-blown furnaces displaced the old air-blown ones.

In the late 1950s, production for the direct-drive W201 was initiated. The W201 was the forerunner of the W301 and the W501 line. Also, the W121 was improved to the W171 by eliminating the excess quote margin and increasing firing temperature to 1450°F (788°C). In the early 1960s, a zero stage was added to the 14-stage W171 compressor to create the W191

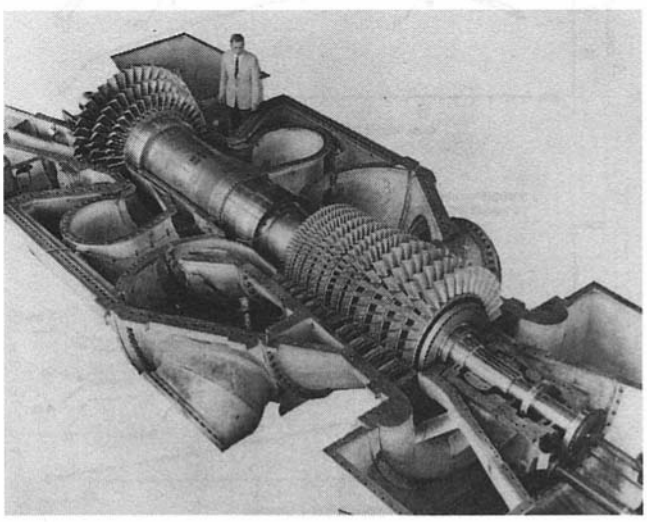

Fig. 5 Blast furnace engine

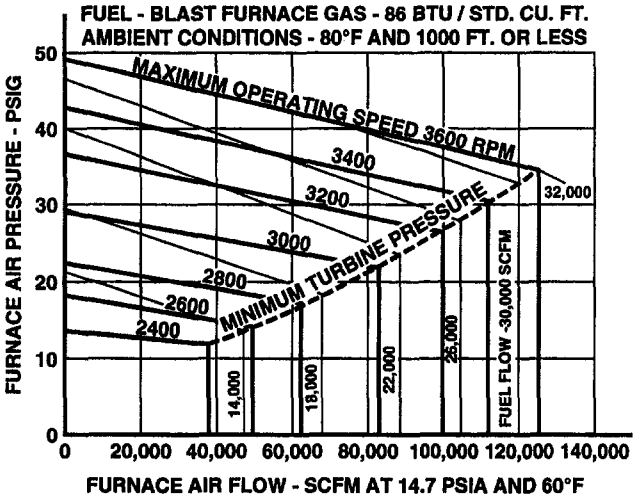

Fig. 6 Performance of blast furnace engine

and the firing temperature of the W31 was increased to 1450F (788°C) to create the W41.

President Eisenhower's Administration started the "Atoms for Peace Program." An interesting outgrowth of this program was the "Marine Gas Cooled Reactors Program" (designated MGCR) that was expected to power a nuclear powered commercial ship. The power plant was to be a helium-cooled reactor as the heat source, coupled with a closed-cycle gas turbine. Westinghouse was selected to provide the turbomachinery for the power plant and the design proceeded to development testing and engine design. However, when the reactor development lagged, the program was canceled. The turbomachinery presented no severe aerodynamic problems and was actually much easier to design than air breathing machinery due to the fact that helium is a light monatomic gas and the speed of sound through it is very high. The engine was rated at 20,000 hp, at an expected efficiency of 31 percent.

Combined gas and steam plants had been developed as early as the locomotive engine, but the 1960s saw the development of the combined cycle. The combined cycle is an ideal thermodynamic solution to the thermal efficiency problem as it combines the best attributes of the Joule–Brayton cycle with that of the Rankine cycle; namely, the addition of heat energy at the high temperature of the combustion turbine and the rejection of heat at the low temperature of the steam turbine. In 1967, a Westinghouse supercharged combustion turbine (W301), rated at 25 MW with a firing temperature of 1450°F (788°C), was placed in operation at West Texas Utilities San Angelo's Power Station. Hot turbine exhaust gases were used in a heavy fuel, reheat boiler (1500 psi, 1000°F [10.3 MPa, 537°C]), which furnished steam to drive an 85 MW turbine (Cox et al., 1967). The plant achieved an annual average efficiency of over 39 percent, the highest in the U.S. for a number of years. In 1990, this plant with over 23 years of successful operating experience, continued to demonstrate that good combined cycle efficiency over a broad load range can be obtained with a combustion turbine combined with a heavy fuel, reheat boiler (Stephens et al., 1990).

An interesting feature of this plant was that the forced draft fan of the steam power plant was used to supercharge the gas turbine. Not only did this feature increase the plant capability and efficiency, but the fan was used as a starting device to start the combustion turbine by windmilling the compressor up to self-sustaining speed. In addition, the fan could supply the steam boiler while the combustion turbine was out of service.

Third Generation. In November 1965, the "Northeast Blackout" ushered in the "Gas Turbine Age" as gas turbine manufacturers were swamped with peaking power plant orders.

Downloaded 02 Jun 2010 to 171.66.16.104. Redistribution subject to ASME license or copyright; see http://www.asme.org/terms/Terms_Use.cfm

Development of gas turbines accelerated as technical staffs expanded. Blade and vane cooling, pioneered by the aircraft engine industry, became available to the industrial engine builders. In response to a need for larger, more efficient engines, Westinghouse developed the W251 and the W501 engines.

The 20 MW W251A, introduced in 1967, was a single-shaft, two-bearing, combustion turbine with reduction gear to accommodate either 60 Hz or 50 Hz for simple or combined cycle applications. Many basic design features proven reliable over many years were retained along with the two-bearing, single-shaft concept. Most noteworthy of these are the CURVIC coupled turbine disks, tangential exhaust bearing struts, blades and stationary vanes that are field removable with the rotor in place, and a compressor end drive. The evolution of the W251 is shown in Table 2.

The compressor of the W251A was taken from the W191, a rear stage added to allow an increase in engine pressure ratio, and a new three-stage turbine designed with higher blade speeds to replace the old five-stage turbine. The first-stage turbine vane was cooled with compressor discharge air. The baseload RIT was increased to 1575°F (857°C) from 1450°F (788°C) increasing the output power by 16 percent at constant heat rate. The first engine was placed in commercial peaking service at Detroit Edison in 1967. The W251A introduced the following improvements for the first time in a Westinghouse design:

- New five-serration, minimum peak stress root design with root extensions to eliminate three-dimensional stress concentration.
- Precision cast turbine vane segments of cobalt-base material (X45) to eliminate structural weld concerns with the nickel-base welded diaphragm assemblies.
- Single turbine blade ring concept with roll out feature to provide service of turbine stationary parts with the rotor in place.
- Extensive use of turbine cooling including the row 1 vane segment, all three rows of turbine disks, and blade rings together with associated stationary flow path parts.
- Segmented ring segments over the rotor blade tips to allow free thermal expansion.
- Interstage seal housing supported from the vane segments on radially oriented keys to allow independent thermal growth of the seal housing to minimize running seal clearances.
- Use of cooled and filtered compressor discharge air for rotor cooling.
- Use of NiCrMoV turbine disc material.
- Compressor bleed extractions for selected cooling of turbine vanes and disk cavities to provide the lowest cost air for duty required.

The W251AA used the W251A compressor with an added front and aft stage to increase the airflow and pressure ratio while using the same turbine except improved row 1 vane cooling to permit a modest increase in RIT to 1640°F (893°C).

The W501 genealogy begins with the 30 MW W301, which began commercial operation in 1960. Unlike previous smaller, higher speed engines, the W301, like the W201, was directly connected to the generator without a gear.

Table 3 traces the development of the 501 family from the W501A to the fifth generation 501F model. The W501A was designed to meet a 42 MW need of the Dow Chemical Company by utilizing the proven, high-performance, 15-stage W301 compressor, with an added front and aft stage to increase the air flow and pressure ratio, and a newly designed four-stage turbine to replace the old five-stage turbine. Dow required a cold-end drive because their system design was a single train of combustion turbine, steam turbine, and generator with the steam turbine providing combustion turbine starting. Also, the hot-end drive was undesirable because a flexible coupling was required. They also preferred two bearings, which provided an excellent match with Westinghouse turbine design philosophy. In addition, the W501A introduced the following improvements:

- Variable inlet guide vane to provide exhaust temperature control on heat recovery applications and to improve starting characteristics.
- Individual blade rings with a roll-out feature to provide independent field service of each stator and seal system with rotor in place.
- Unique cooled, filtered rotor cooling concept utilizing "air separator" rotor component to confine rotor cooling air.
- Unique fore and aft blade seal plates to prevent cooling air leakage and service of blades with rotor in place.
- Four-pad, tilting pad bearings to eliminate any possibility of bearing instability from "oil whip" phenomenon.
- Compressor rotor utilizing a hollow shaft with shrunk on disks to reduce stresses and improve rotor dynamics.

The 60 MW W501AA in 1971 used a newly designed, higher flow, higher pressure ratio compressor with the W501A turbine

Table 2 W251 evolution

Engine	W191	W251A	W251AA	W251B	W251B2	W251B8	W251B10	W251B12
First Startup Date	1961	1967	1969	1971	1973	1978	1983	1990
Power, MW Class	18	20	26	31	34	36	40	48
Rotor Inlet Temp., °F	1450	1575	1640	1806	1806	1911	1985	2100
Air Flow, lb/s	270	270	353	353	353	353	345	372
Pressure Ratio	7	8	10	10	11	11	14	15
No. Comp. Stages	15	16	18	18	18	18	19	19
No. Turb. Stages	5	3	3	3	3	3	3	3
No. Cooled Rows	0	1	1	3	3	3	4	4
Exhaust Temp., °F	777	850	850	930	898	962	941	990
Heat Rate, Btu/kWh; (ISO Gas)								
Simple Cycle	13,430	13,775	13,130	12,540	12,265	11,980	10,980	10,600
Combined Cycle	9,600	9,840	9,040	8,600	8,400	7,900	7,400	7,100

Downloaded 02 Jun 2010 to 171.66.16.104. Redistribution subject to ASME license or copyright; see http://www.asme.org/terms/Terms_Use.cfm

Table 3 W501 evolution

Engine	W501A	W501AA	W501B	W501D	W501D5	W501D5	501F
First Startup Date	1968	1971	1973	1975	1981	1995	1993
Power, MW Class	42	60	80	95	107	118	160
Rotor Inlet Temp.,F	1615	1630	1819	2005	2070	2150	2300
Air Flow, lb/s	548	744	746	781	781	830	960
Pressure Ratio	7.5	10.5	11.2	12.6	14	14.8	14.6
No. Comp. Stages	17	17	17	19	19	19	16
No. Turb. Stages	4	4	4	4	4	4	4
No. Cooled Rows	1	1	3	4	4	5	6
Exhaust Temp., F	885	798	907	982	987	1006	1083
Heat Rate, Btu/kWh; (ISO Gas)							
Simple Cycle	12,600	11,600	11,180	10,925	10,270	10,040	9,590
Combined Cycle	9,000	7,990	7,350	7,025	6,950	6,900	6,600

at essentially the same RIT. Another major design change was a reduction in combustor shell diameter in order to facilitate shipping the engine fully assembled, a feature which has been retained on subsequent models. The combustor was set parallel to engine axis, resulting in an S-shaped transition duct. A secondary benefit of this system was a reduction in pattern factor or peak temperature due to increased mixing.

A significant improvement in engine performance was due to the new axial exhaust system. The axial exhaust system allowed waste heat recovery systems to be located directly downstream of the turbine exhaust, avoided high duct losses, and accommodated a longer and more efficient turbine diffuser.

Many engineering studies were made to determine the optimum cycle to minimize the cost of electricity. Some of the more promising ones (intercooled, multiple shafts, reheat, steam injected, water injected at various locations) were studied in great detail. In the final analysis, the simple cycle gas turbine combined with a steam bottoming cycle was the most widely accepted in the market. The missing link was higher firing temperatures. Figure 7 is a summary of some of those studies. (The question of more efficient cycles is currently being revisited in the advanced turbine systems program discussed later in the paper.)

As shown by Fig. 7, the combined cycle is superior to the regenerated cycle by a significant amount. The pressure ratio of the gas turbine that yields maximum specific power (power output per pound of air flow) also gives optimum combined cycle efficiency. This is a most interesting conclusion and shows that for simple cycle gas turbine engine applications, a high pressure ratio engine is the economic choice, such as for aircraft propulsion. For the same firing temperature levels, the lower pressure ratio gas turbine engine is superior for combined cycle applications. Since the 1970s Westinghouse engines have been designed to be optimum for combined cycle applications and these engines are also excellent for peaking applications, where first cost dominates, since they yield the maximum power for a given amount of hardware. The figure also indicates the dominant role of turbine inlet temperature on both power output and combined cycle efficiency.

Fourth Generation. In this era, the W251B used the same compressor as the W251AA, but with RIT increased to 1806°F (986°C). In addition to further improvement in row 1 vane cooling, the row 1 blade and row 2 vane segment were cooled for the first time in a Westinghouse design. At this point material changes were made such as the row 1 blade made as a casting for the first time with cooling passages integrally cast.

The W251B2 represented additional design improvements in the turbine that produced increased performance, while using the same W251AA compressor with no increase in RIT. The continuation of growth represented in this model consisted of adding a single vane with further improvements in cooling, restaggering of the turbine blade path for an increase in pressure ratio, improvements in cooling flow management, and an improvement in row 2 vane cooling. The single vane was designed to permit service without removing the casing cover, an industry first.

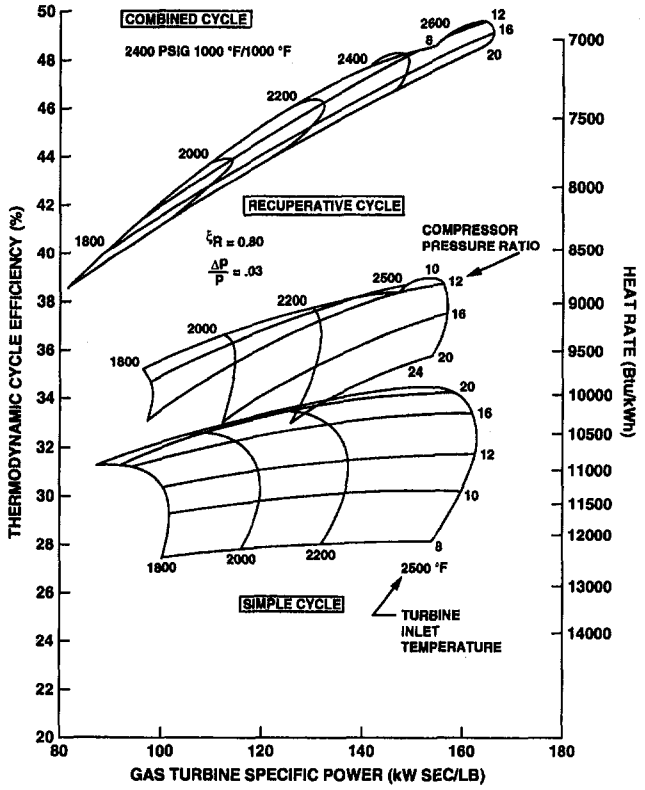

Fig. 7 Summary of combined cycle studies

Downloaded 02 Jun 2010 to 171.66.16.104. Redistribution subject to ASME license or copyright; see http://www.asme.org/terms/Terms_Use.cfm

The W251B8 used the W251AA compressor with performance improvement from an increase in RIT to 1911°F (1044°C) brought about by a redesigned combustion system for improved temperature profile into the turbine, and additional improvements in row 1 vane cooling. Also, the compressor used coated diaphragms for improved performance as well as to retard degradation from ingested contaminants, and rows 1 and 2 turbine vanes and blades were coated for corrosion protection.

The 80 MW W501B, in 1973, was a planned growth step of the W501 model with the principal change being an increase in RIT to 1819°F (993°C). In addition to increased row 1 vane cooling, cooling was added to the row 1 blade and row 2 vane and material was changed, as required, on other rows to compensate for higher gas temperatures. Provision was added for removal of combustors and transition pieces without a cover lift.

The 95 MW W501D was a continuation of the planned growth program for the W501 frame. A further increase in RIT to 2005°F (1096°C) was made possible by advances in turbine cooling technology. Two stages were added to the aft end of the W501B compressor for higher pressure ratio in order to optimize efficiency in combined cycle operations. Cooling was added to the row 2 turbine blade along with increased cooling in upstream stages and material changes as required.

The W501D5 achieved additional performance gains from improvements in component efficiencies, conservation of cooling air energy, and a modest increase in RIT. Compressor performance was improved by increasing the number of diaphragm seal points from two to four, by use of coated diaphragms with improved surface finish, and by restaggering airfoils to improve work distribution. Turbine performance was improved by reducing exit velocity and swirl, by reducing incidence losses, and by better stage work distribution. Stator cooling air was extracted from three compressor bleed points in order to use air at the lowest suitable pressure available. Improvement in detail design reduced internal cooling flow leakage by 12 percent compared to the earlier W501D. In addition, cooling was improved for the first two vanes and blades. Other features provided improved reliability and availability by virtue of improvement in parts' life and easier maintenance and inspection such as a single row 1 vane. In the compressor, the aerofoil-shroud joint was redesigned for increased strength in key diaphragm stages. The combustor cooling technique using the standard "wiggle strip" corrugation was improved by the extended lip, as shown in Fig. 8. This extension improved the tenacity of the convective heat transfer coefficient and reduced downstream temperatures by 200°F (111°C) (Scalzo et al., 1983).

The last engine models of this generation were the W251B 9/10 and the W501D5. Both engines used the same basic compressor, the W251 compressor being a 0.67 scale of the W501. In combined cycle applications the engine's potential efficiency approaches 50 percent. The power capability of these engines is more than 2.5 times that of their third generation antecedents and the efficiency was increased by about 0.33.

The last model engines of this generation utilized streamline curvature calculation methods to solve the Euler equations, with energy loss models developed from a very large experimental data base. The result was compressors with average stage efficiencies approaching 93 percent and cooled turbines with excellent characteristics.

The power rating of a combustion turbine engine is limited by the amount of flow that can be passed by the last stage blade row of the turbine component. Stress capability of the last row turbine blade material at operating temperature and aeroelastic blade limits determines the flow area of the last stage, while leaving axial velocity and density of the exhaust gases, in addition to flow area, determines engine flow. The next generation of engines, the F series and beyond, will be flow-limited designs.

Fifth Generation. The fifth generation engines were designed with the aid of complete three-dimensional computer codes, some of which solve the Navier–Stokes equations. The 501F at 160 MW and 2300°F (1260°C) firing level approaches 55 percent thermal efficiency in combined cycle applications.

The 501F, shown in Fig. 9, is a 3600 rpm heavy-duty combustion turbine designed to serve the 60-Hz power generation needs for utility and industrial service in the 1990s. It was jointly developed by Westinghouse and Mitsubishi Heavy Industries, Ltd. (Scalzo et al., 1989). Designed for both simple and combined cycle applications, it will operate on all conventional combustion turbine fuels as well as with coal-derived low-Btu gas produced in an integrated gasification combined cycle (IGCC) power plant.

The 501F rotor is of bolted construction supported by two, two-element tilting-pad bearings for load carrying and an upper half-fixed bearing. This provides inherent stability of the tilting pad with the reliability of the plain bearing, thus eliminating the top pad fluttering problem that has led to local babbitt fatigue distress. The thrust bearing is a double-acting Kingsbury thrust bearing that uses leading edge groove (LEG) lubrication system.

The compressor rotor is comprised of a number of elements, spigoted and bolted together by 12 through bolts. The turbine rotor section is made up of disks bolted together by 12 through bolts and using CURVIC clutches. This turbine rotor design has amassed over 40 million hours of reliable service in all sizes of combustion turbines. The compressor is a 16-stage axial flow design of 14 pressure ratio that is based on the highly successful W501D5 compressor. A four-stage turbine was selected to maintain moderate aerodynamic loadings even at the increased firing temperature.

Blade rings have been added in the compressor for stages 7–16. Similar to those used in the turbine, they have a high thermal response independent of the outer casing, can be aligned concentric to the rotor to prevent blade rubs and minimize clearance, and therefore maximize performance as well as enhance maintainability of stationary parts.

Flow and pressure coefficients of the 501F compressor have been kept similar to the D5 compressor by increasing the mean diameter of the stages to accommodate the 20 percent increase in flow. In addition, the rear stages of the new compressor have larger diameters to help balance spindle thrust. Interstage bleeds are used for starting and for supplying cooling air to the turbine stationary blading and interstage cooling system. Rotor blades are double circular arc designs in the first four stages. The stators and all other rotor blades are conventional W65 airfoil sections.

The design of the 501F turbine has maintained moderate aerodynamic loadings in spite of the increased inlet temperature by choosing a four-stage turbine with higher peripheral speed compared to the W501D5. The first and second-stage blades

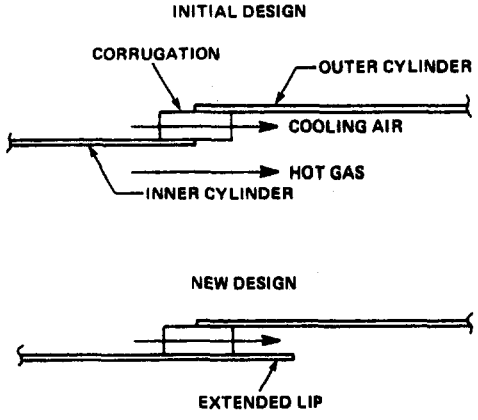

Fig. 8 Extended lip improved combustor cooling

Downloaded 02 Jun 2010 to 171.66.16.104. Redistribution subject to ASME license or copyright; see http://www.asme.org/terms/Terms_Use.cfm

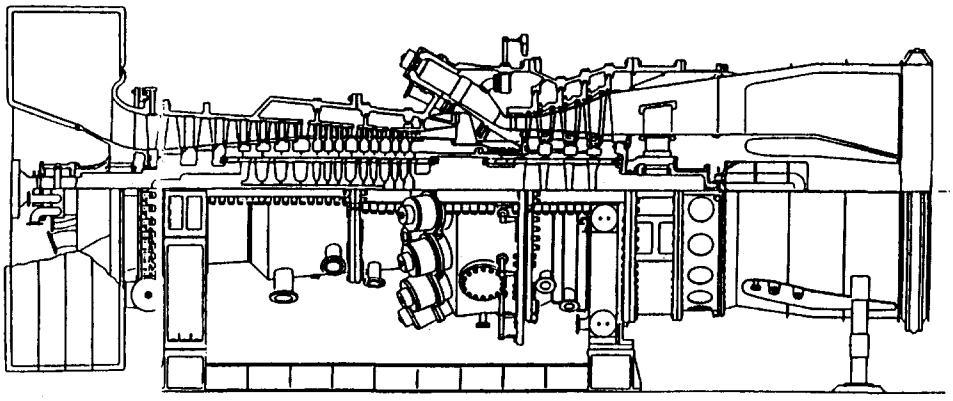

Fig. 9 General configuration of 501F combustion turbine

are the free-standing type, while the third and fourth stages utilize integral "Z" tip shrouds. The use of a shrouded system is a departure from past design practice on the 501 series, but has been in use on the W352.

The first turbine stationary row consists of precision-cast, single-vane segments. There are precision-cast, two-vane segments in the second turbine station row while the third and fourth turbine stationary rows are precision-cast three-vane and four-vane segments, respectively.

Cooling circuits for the turbine section, displayed in Fig. 10, are similar to those used on the W501D5. Rotor cooling air is provided by compressor discharge air extracted from the combustor shell. This air is externally cooled and filtered before returning to the torque tube casing for seal air supply and for cooling of the turbine disks as well as the first, second, and third-stage turbine rotor blades. The row 1 vane cooling design is shown in Fig. 11. This highly effective configuration, which evolved directly from the W501D5 design, utilizes state-of-the-art concepts with three impingement inserts in combination with an array of film cooling exits and a trailing edge pin fin system. The first stage blade is cooled by a combination of film cooling and convection techniques via multipass, turbulated, serpentine passages, with pin fin cooling in the trailing edge exit slots. The cooling circuitry is shown in Fig. 12.

The fifth generation also produced improvements in the W251B10 and the W501D5 models. Introduced in 1990, the W251B12 improvements included modest increases in airflow, pressure ratio, and firing temperature. To accommodate these changes, double circular arc compressor blade profiles were used for the first two blade rows, compressor stages were restaggered, and cooling was improved for the first turbine vane and first rotor blade. Current rating is 48 MW at a simple cycle efficiency of 32 percent (Diakunchak, 1989). The improved W501D5, introduced in 1995, also will include modest increases in airflow, pressure ratio, and firing temperature. Compressor changes were scaled from the W251B12 and cooling was improved for the first three vanes and the first two rotor blades. In addition, the increase in airflow required that the row 4 blade be changed to a "Z" tip shroud similar to the 501F design. Rating of the improved W501D5 will be 118 MW at a simple cycle efficiency of 34 percent.

Cooling Evolution

The evolution of the W501 and the W251 was highly dependent upon improvements in cooling technology as shown in Fig. 13. Without cooling, the maximum RIT would be under 1800°F (982°C). Figure 11 depicts this evolution for row 1 vane, from the early W501A in 1968 to the highly sophisticated cooled design used in the 501F. Similarly, rotor blade cooling has evolved from spanwise holes of the W501B to a sophisticated multipass, turbulated, pin-fin, film cooled design of the 501F. These advances in cooling technology were beyond the published state of the art; hence, a comprehensive development program was required to verify the latest blade and vane cooling designs and to provide a broad base for future designs.

For example, parametric design information on various vane internal cooling features was generated in atmospheric pressure rigs, with the geometry scaled up to effect Reynolds number simulation (Scalzo et al., 1981). Tests were run over a wide range of test parameters using basic test rigs such as the leading

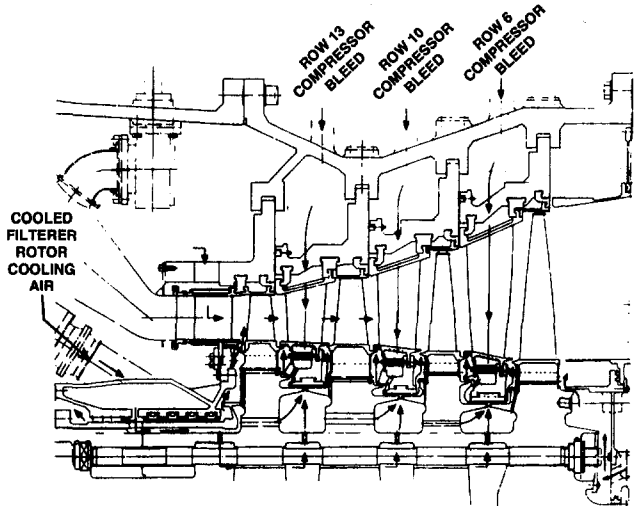

Fig. 10 Cooling circuits for the 501F combustion turbine

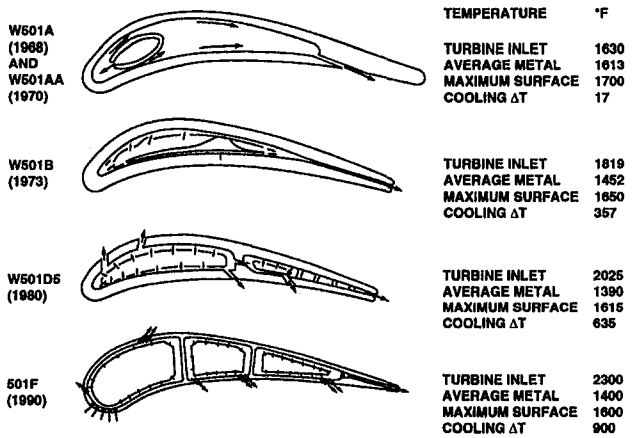

Fig. 11 Evolution of cooling technology

Downloaded 02 Jun 2010 to 171.66.16.104. Redistribution subject to ASME license or copyright; see http://www.asme.org/terms/Terms_Use.cfm

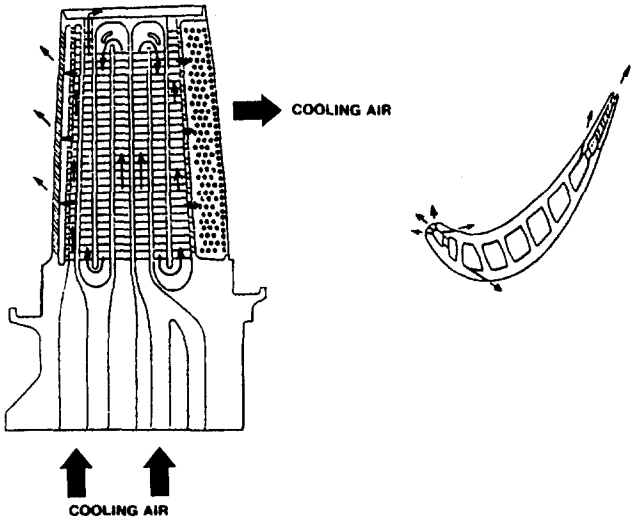

Fig. 12 Cooling circuitry of first-stage blade used in 501F

edge rig shown in Fig. 14. The insert nose in the leading edge heat transfer rig can be replaced so as to vary target distance, radius, and hole array. Actual leading edge cooling geometries have been tested as well as a range of geometries for the generation of parametric design information. In addition to atmospheric model tests, design verification tests were run on production vane segments at full operating temperature and pressure in a full-scale vane cooling rig.

Final verification of blade and vane temperatures were obtained from a fully instrumented full-load engine tests utilizing over 1400 pressure and temperature sensors. Comparisons were made to rig data to update the technology data base. Rotating blades and disks were monitored via telemetry (Scalzo et al., 1986; Gabriel and Donato, 1986).

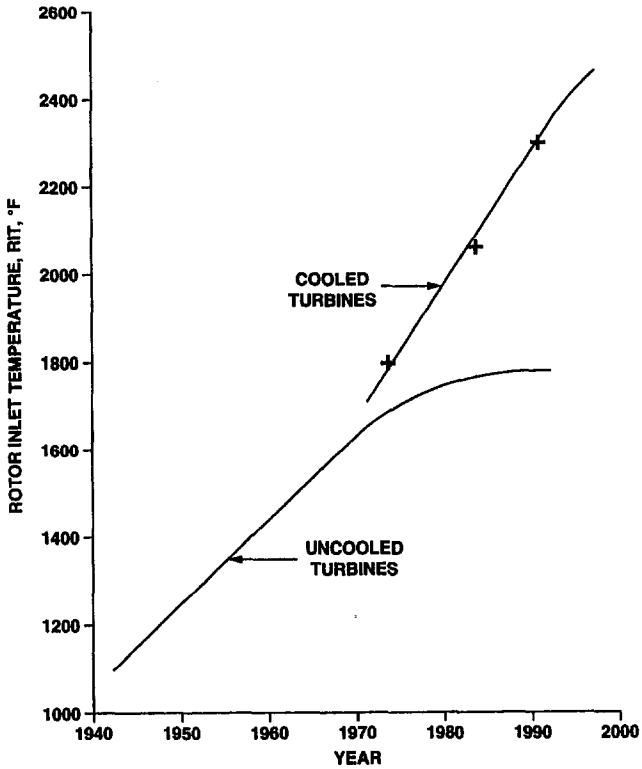

Fig. 13 Firing temperature trend

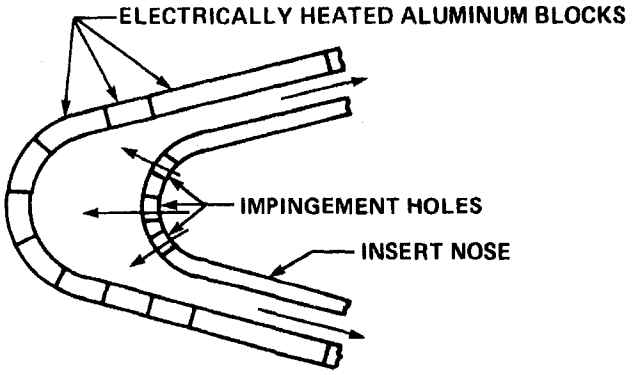

Fig. 14 Insert nose in the leading edge heat transfer rig

Material Evolution

In the early years (1950s to 1960s) materials were selected from available in-house steam turbine and jet engine experiences. However, since aero-engines enjoy a pristine environment, many of these materials were not the best choice for the more corrosive fuels and operating environments of the land-based gas turbine. Also, inspection intervals for aero-components are more frequent as dictated by governmental regulations, while intervals in combustion turbines are being driven up to 24,000 hours by commercial considerations. For these and other reasons, material selection criteria, problems encountered, and developed solutions, would fill several volumes and are beyond the scope of this paper; however, a few pertinent comments will be made.

Compressor Area. Steam turbine and aero-engine experience at the time of the initiation of the Westinghouse combustion turbine (1948 with the W21) dictated using a 12 percent chrome material for rotating and stationary blading because of its high strength, good corrosion resistance, and superior damping characteristics. This rationale is still valid today with standard strength 12 percent chrome material the choice for all compressor rotating blades and diaphragms, with the exception of first two rotating blades in the 501F, which use 17-4 PH, a 17 percent precipitation hardened stainless steel. Sermetel 5380DP[5] coating is currently used in the compressor to retard corrosion. To inhibit fretting, CuNiIn coating is used on blade roots. Compressor rotor materials have essentially retained the low-alloy steel materials based on steam turbine experience.

Combustor Area. The 25-20 series and 18-8 series stainless steel materials were used in early engines; however, Hastelloy X,[6] a high-temperature nickel-base alloy, became the standard for combustor baskets and transition ducts in the late 1960s. This material has been highly successful when kept below 1550°F (843°C) metal temperatures. For turbines with the increased firing temperatures used in the 1980s and later, the transition duct material was changed to IN617[7]; however, the standard combustor basket material is still Hastelloy X. IN617 provided a more stable higher strength material that required no pre- or post-heat treatment as was required by some sheet alloy candidates.

Turbine Stationary. Early designs utilized welded structures in AISI 310, a 25-20 austenitic stainless steel that had excellent resistance both to corrosion and to oxidation at elevated temperatures, but had limited strength capabilities.

A change to the higher strength, nickel-base, IN713 used successfully by aero-engines, met with unsatisfactory results

[5] Sermetech International Inc.
[6] Hayes International.
[7] International Nickel Company.

Downloaded 02 Jun 2010 to 171.66.16.104. Redistribution subject to ASME license or copyright; see http://www.asme.org/terms/Terms_Use.cfm

because of a lack of oxidation/corrosion resistance. A change to another precision cast nickel-base alloy, U500,[8] resolved the corrosion concern, but the integrity of the welded structure was limited.

In 1967, Westinghouse introduced precision cast, cobalt-base, X45 turbine vane segments. This material was a modification of Haynes Stellite 31 used for years in aero engine turbine blades. It was the standard for precision cast turbine vane segments up to 1975, when the W501D was introduced with Westinghouse's ECY768 material in row 1. ECY768 is a cobalt-base alloy with higher creep strength and oxidation/corrosion resistance than standard X45 material. This improved cobalt-base alloy has become the standard for all row 1 vane segments and some selected row 2 and row 3 vane segments. Beginning in about 1975, diffusion and overlay coatings have been used selectively to enhance oxidation/corrosion resistance, as dictated by application.

Turbine Rotating. Various forged nickel-base alloys, and even 12 percent chrome materials, were used for early combustion turbine blades. Today nickel-base alloy Inconel X-750 remains the choice for many last row blades. Increases in firing temperatures necessitated changing to the higher strength Udimet nickel-base alloys in the mid-1970s. U520 forgings and cast U500 became the standard materials for front turbine stages. (All turbine blades are free-standing except for rows 3 and 4 of the 501F and row 4 of the improved W501D5.)

The 1980s and 1990s saw a move from forgings to higher strength cast IN738 material for front end blading, because the complex cooling configurations could not be produced in machined, forged blades. As with the turbine stationary, diffusion, and overlay coatings have been used for rotor blades. Future advanced engines will see a move to directionally solidified (DS) and to single crystal (SC) blading together with advanced coatings.

Turbine Disks. Early combustion turbine disks used a variety of materials including AISI 422, 19-9, and Discalloy 24 (Westinghouse-developed, austenitic alloy similar to A286). Selected cooling of the disk rims was required to prevent creep and notch sensitivity type concerns. To avoid these concerns, Westinghouse developed, in the mid-1960s, a unique cooling system for turbine rotors. High-temperature, high-pressure compressor discharge air is taken outside the engine where it is cooled and filtered before returning to the turbine rotor. This cooled, filtered air provides the rotor with a blanket of protection from hot blade path gases and supplies filtered cooling air to all disk rims as well as cooled airfoils. Filtration eliminates excessive contaminants that could block critical, intricate cooling passages of today's advanced combustion turbines. A reliable steam turbine material, NiCrMoV, was selected because of its high strength and outstanding fracture toughness. When cooled below 750°F (400°C), this material has infinite life because it is below the creep and aging thresholds. Also, its outstanding fracture toughness accommodated standard ultrasonic qualification and, therefore, did not require overspeed spin pits to qualify the forging as is the case for some materials. Since the mid-1960s, NiCrMoV disks integrated into the Westinghouse filtered, cooled air cooling system have generated over 20 million hours of problem free operation.

Mechanical Evolution

The evolutionary Westinghouse design philosophy has resulted in operational reliabilities of over 99 percent and unit availabilities of over 95 percent. Many of the basic design features have stood the test of over four decades of design evolution. These design innovations were identified in previous sections of the paper; for example, cooled, filtered turbine cooling air with NiCrMoV turbine disks. However, several will be expanded in this section; i.e., single row 1 vane, integral compressor vanes, and minimum peak stress turbine blade roots.

Single Row 1 Turbine Vanes. In the early 1970s, the row 1 vane segment of the W251B2 was introduced as a single vane that could be serviced along with baskets and transitions through the combustor basket openings with the casing cover and enclosure roof in place. Other advantages of this design were structural thermal stress at 25 to 50 percent of a three-vane structure and improved casting quality (Hultgren, 1981; Scalzo et al., 1988). Entering a log/log plot displaying the low cycle fatigue (LCF) of a nickel-base alloy or cobalt-base alloy, LCF is increased by over a factor of 10 when stress is reduced 50 percent. In addition, a single vane facilitates higher quality castings compared to multivane castings. For advanced turbines, the inner shroud is supported from the inner casing to limit axial and circumferential displacements, thus controlling flow angles.

Compressor Integral Vane. Selected diaphragm rows on current product models incorporate an integral airfoil/shroud design with four point seals on a removable seal carrier as shown in Fig. 15. Critical structural weld joints are eliminated by use of the integral structure. Also, the airfoil thickness/chord ratio is tapered to produce an optimized aero/mechanical design; i.e., high at the tip required mechanically and acceptable aerodynamically, and low at the hub, required aerodynamically and acceptable mechanically. Endurance strength of the structure is equal to base-metal properties as shown in Fig. 16. This design also provides for service of compressor diaphragms with the rotor in place, as in past designs.

Turbine Blade Roots. In 1963, one of the top priority design goals was to develop an improved turbine blade root more suitable for higher firing temperatures and increased dynamic loadings expected in the third generation designs. Earlier designs were simply scaled from existing steam turbine and aero technology sources. There was also a desire to incorporate the new root design using NiCrMoV material as described in the preceding materials section. Three basic objectives were identified; i.e., provide a thermal barrier, eliminate three-dimensional stress concentration, and minimize peak stresses. Using an extended root or extension isolates the root from flow path temperatures, thus providing a thermal conductive barrier. Also, it eliminates three-dimensional stress concentration resulting from the transfer of bending or dynamic moments from an airfoil shape to the root neck (Scalzo, 1992).

Minimizing peak stresses required the knowledge of two-dimensional stress distribution in irregular shapes. Since there

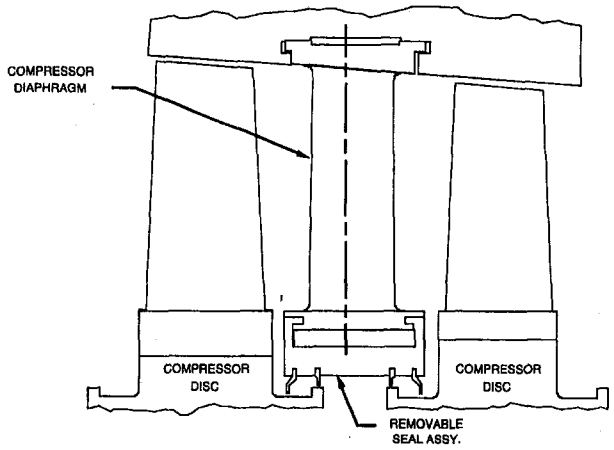

Fig. 15 Integral diaphragm design

[8] Special Metals Company.

Downloaded 02 Jun 2010 to 171.66.16.104. Redistribution subject to ASME license or copyright; see http://www.asme.org/terms/Terms_Use.cfm

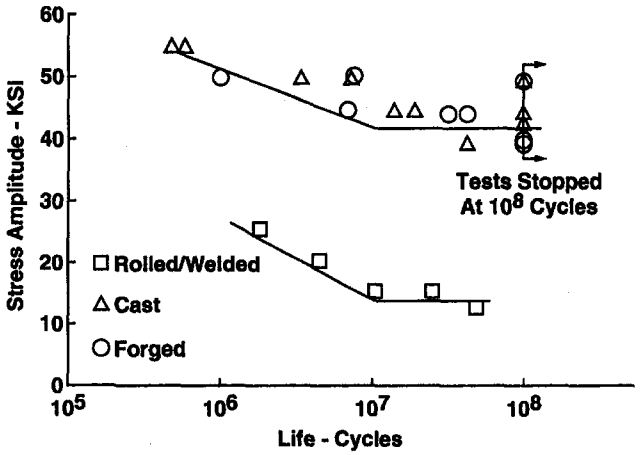

Fig. 16 Endurance strength of diaphragm designs

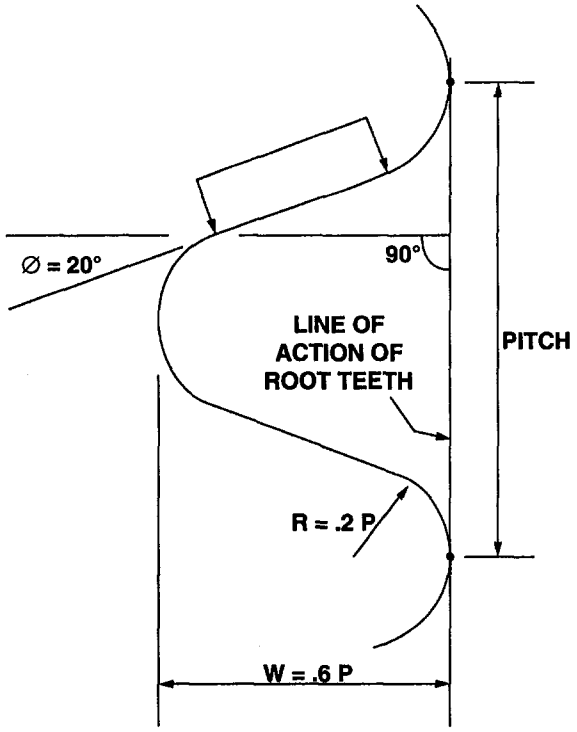

Fig. 18 Root tooth proportions for minimum peak stress under direct load

were no finite element analysis programs available in the early 1960s, a general method for the determination of two-dimensional stress distribution in irregular shapes subjected to body and surface forces was developed using the finite difference method to represent the governing fourth-order partial differential equation together with suitable boundary conditions. A mainframe computer was used to solve the multitude of equations using the over relaxation technique (Scalzo, 1963). Parametric analyses similar to Fig. 17, developed to determine the optimum tooth shape for minimum peak stress, resulted in Fig. 18. This was used to establish the root configuration for the W251A combustion turbine shipped in 1967, and has been used successfully for every Westinghouse combustion turbine since that time.

Combustion Design Evolution

Overall Geometry. In selecting the can-annular design, the W21 designers drew on the early experimental combustor can experience of the jet engine group even though the jets eventually selected an annular combustor. Sets of holes placed at the upstream end provided primary air sufficient for stoichiometric burning and another set of holes placed some distance downstream provided dilution air, bringing the stream temperature down to the required burner outlet temperature (BOT). (Note that BOT is the same value as the "firing temperature" used in the first and second generation.)

All engines have used can-annular combustors except for a silo-type combustor installed in the blast furnace unit. The rationale that supports the can-annular design is still valid after 45 years. Advantages of this concept are:

- Shipped fully assembled with engine, thus reducing field cost.
- Facilitated full-scale laboratory testing.
- Can be developed to provide a preferential radial temperature profile, thus satisfying rotating blade requirements.
- Provides a lower "hot spot" by control of circumferential temperature gradients to improve turbine vane life.
- Generates a discrete harmonic content, thus minimizing blade vibratory design requirements.

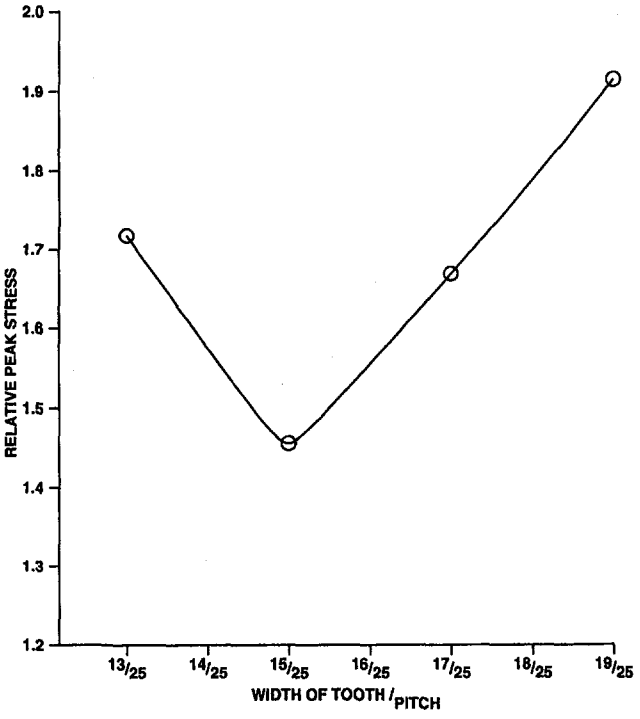

Fig. 17 Stress versus width of tooth/pitch

Fuel Injection. The basic concept of fuel injection and ignition has been maintained from the W21 up to present engines, with the exception of the new advanced low-NO_x designs. Key elements are a pressure atomizing liquid fuel nozzle with a concentric atomizing air-assist used for starting. Gas fuel is injected via a concentric set of orifices. To prevent undesirable combustor noise, the orientation of fuel injection vectors must be compatible with the essential recirculation stabilization pattern required to anchor the flame front (Scalzo et al., 1990). In models built after the mid-1970s, mechanical flow dividers were used to meter liquid fuel equally to each combustor. When required for emissions control, water is injected through the air atomizing ports of the liquid nozzle or premixed, steam is injected either premixed with gaseous fuel or via a separate set of orifices.

Downloaded 02 Jun 2010 to 171.66.16.104. Redistribution subject to ASME license or copyright; see http://www.asme.org/terms/Terms_Use.cfm

Ignition. The ignition scheme used on the earliest combustor designs was a spring-loaded spark plug in each can, which retracted as combustor pressure built up to operating conditions; and cross-flame tubes provided ignition between cans. This belt and suspenders approach was used because, with the large distance between adjacent cans, cross-firing was not reliable. In later engines, with combustors being nested closer together (W251A model and later), cross firing was more effective and spark ignition was provided for only two cans (for redundancy) and cross-firing lit the others. In early designs the cross-firing occurred through tubes attached to each combustor at the combustor flame zone, with one tube fitting inside the other in a sliding fit. In more recent models, this arrangement has been replaced by hard-connected flexible tubing. The retractable spark plug approach remained basically the same with improvements made to the spark plug, the retracting piston, and the electrical power to the plug.

In the earlier engines, flame-on indication was provided by thermocouples protruding into each transition section, which recorded BOT as well as other control input functions. When the BOT increased to that required for the W251AA engine and succeeding models, this arrangement had to be abandoned due to the impact of the higher temperature environment on sensor life. The flame-on detection is now by an optical sensor, which views the combustor flame zone through a port. Other control supervisory functions are taken up by thermocouples placed in the blade path downstream of the last turbine blade row. These exhaust blade path thermocouples also monitor each combustor to protect rotating blades against harmful harmonics (Scalzo, 1992).

Special Fuels. Combustion turbines have the capability to burn a wide variety of fuels. Combustor and fuel injector design modifications have been able to accommodate fuels that have included: natural gas, blast furnace gas, coal gas, distillate fuel, residual fuel, crude oil, methanol, propane, coal derived liquids, and shale oil (Pillsbury, 1974; Pillsbury et al., 1978, 1979; Seglem and DeCorso, 1980; Ambrose et al., 1984). Burning fuels that have potentially corrosive elements require that fuel contaminant specifications be set (Wenglarz and Menguturk, 1982). The Westinghouse Research Laboratory was equipped with corrosion evaluation test rigs where actual fuels were burned, making accurate determinations of fuel element corrosion levels on the combustor and other turbine hot parts. This work at the Research Laboratory was key to setting the ASTM D2880 and ASME B-133 fuel contaminant specifications now in use industry wide (DeCorso et al., 1971; Hussey et al., 1973). Use of these various fuels in the future will now be subject to more stringent emission regulations.

Emissions. The first emission concerns to impact combustor designers began with exhaust visibility (smoke) in 1966. As a result, the W171 and W191 combustors were modified to produce a smokeless design (DeCorso et al., 1967). In the early 1970s, EPA began to develop regulations that dealt with NO_x emission levels. In local areas of California more stringent emission regulations were passed. In the Los Angeles Air Pollution Control District (LAAPCD) regulations (rule 67) called for particulate emissions of no more than 10 lb/hr (4.54 kg/h) regardless of plant size, and a NO_x regulation which required 32 ppmv from a W501 engine. Particulate levels were minimized by adhering to established fuel specifications (Carl et al., 1975) and limiting sulfur content in the fuel, since the Los Angeles particulate measurement technique counted sulfur compounds. (Many current regulations require NO_x to be 25 ppmv or lower, regardless of engine size.)

Working in cooperation with the Westinghouse Research Laboratory, a theoretical understanding of NO_x formation was gained and a NO_x formation model was developed and verified by laboratory and field testing. This model proved to be invaluable in predicting the effect of combustor operating parameters on NO_x formation. It was capable of giving NO_x emission effects due to combustor operating parameters; it also accurately predicted the effect on NO_x emission of various fuels, fuel bound nitrogen, water injection, and steam injection (Hung, 1974; Vermes, 1974). With the NO_x model as a guide, combustion laboratory test time was greatly reduced and valuable insight into potential low-NO_x approaches was provided.

In order to meet the 32 ppm NO_x regulation for W501 turbines, water injection for NO_x control was designed, tested, and proven in the laboratory, and then in a full-scale field test (Ambrose and Obidinski, 1972), in what is believed to be the first application of water injection for NO_x control. Subsequent design and testing also confirmed the use of steam for NO_x control, with steam being less effective, pound for pound, than water.

Dry Low-NO_x. Dry low-NO_x development schemes were explored in the three areas; i.e., premixed lean combustion, rich-lean combustion, and catalytic combustion. Small scale Research Laboratory tests had confirmed that very low-NO_x levels were attainable by premixing the air and fuel. Premixing means in this context that the air and fuel are mixed on a molecular level. A practical scheme to use premixing was devised and given the name of "hybrid combustor" because it utilized the dual approach of a premixed fuel/air stream and a pilot flame zone, which burned in the diffusion flame mode. The term "hybrid combustor" is now commonly used in the industry to refer to this type of low-NO_x combustor. An example of an early design tested is shown in Fig. 19 (Mumford et al., 1977). This design was the basis for the lean, premix combustor design used in the MW701D combustion turbine (Aoyama and Mandai, 1984). Advanced versions of this design are now operating in the 701F (50 Hz scale of the 501F) engines in Japan with NO_x emissions less than 25 ppmv. This design is currently being developed further to produce less than 15 ppmv by the late 1990s.

Another approach to NO_x reduction utilized the rich-lean burn principle, which did not require premixing and was effective for cases where the fuel contained fuel-bound nitrogen (FBN). The premixing or water/steam injection approach is defeated by the presence of significant amounts of FBN. In rich-lean burning, the burning is staged to occur in a fuel-rich zone where the oxygen deficiency prevents NO_x formation; in a second lean zone that follows the rich zone, burning of the products from the rich zone are completed at a temperature low enough to prevent NO_x formation. The multi-annular swirl burner (MASB) was developed, which had the capability of operating as a rich-lean burner, as well as in the lean burn mode. This combustor was successfully operated at the Waltz Mill, PA coal gas test site (Lew et al., 1982) and is now under development as a topping combustor for an advanced PFB cycle program (Garland and Pillsbury, 1992).

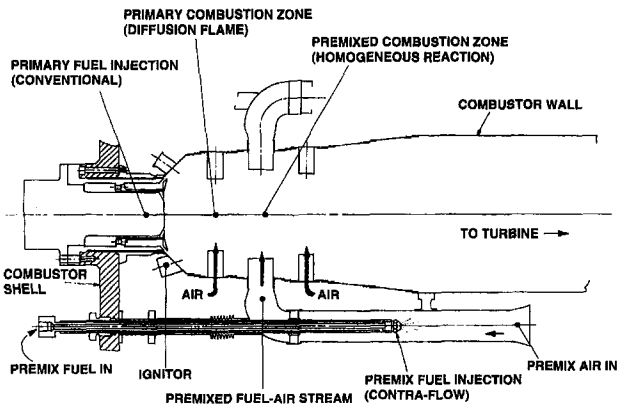

Fig. 19 Hybrid burner

Downloaded 02 Jun 2010 to 171.66.16.104. Redistribution subject to ASME license or copyright; see http://www.asme.org/terms/Terms_Use.cfm

The prospect of ultralow-NO_x using catalytic combustion was first evaluated in 1971. Tests run at the Research Center confirmed that virtually zero emissions could be attained and that very uniform temperature patterns were possible (DeCorso et al., 1977). A very active program included testing of catalytic combustors at full-scale conditions (Hung et al., 1978; Scheihing et al., 1982). Although NO_x was in single digits, the mechanical integrity of the substrate was very unsatisfactory. After the oil embargo sharply curtailed market activity, development effort in low emissions tapered off through the early 1980s; however, activity has surged again in the 1990s with advanced designed catalytic systems currently under review.

Clean Coal Technology

Combustor design and testing first took place in the mid-1970s under United States Government sponsorship for a projected coal gas plant for Public Service of Indiana. Full-scale test facilities were built in which combustors modified for coal gas use were tested with actual coal gas compositions encompassing air blow gasifier and oxygen blown gasifier gas (Pillsbury, 1974). This development supported the joint Westinghouse/Dow Chemical Co. program to burn medium Btu (239 Btu/scf [8890 kJ/scm]) coal gas; first, in a W191 trial engine; and, later in W501D5 turbines at the Dow Chemical Co. IGCC plant in Plaquemine, LA (Hendry and Pillsbury, 1987). These two 104 MW units are operating in a Dow Chemical developed oxygen-blown integrated gasification combined cycle (IGCC) that includes a cold gas cleanup system (Morrison and Pillsbury, 1989). These combustion turbines have operated with average availabilities in excess of 95 percent (Geoffroy and Amos, 1991). The plant, operated over 100,000 hours, has demonstrated the ability of combustion turbines to be adapted to this type of gasification technology.

Most commercial size gasification projects have used high-purity oxygen rather than air as the oxidant for the gasifiers. Recent IGCC evaluations have looked at using the combustion turbine air compressor to supply air for the air separation unit. Typically, this air stream is sent to a high-pressure air separator unit, which produces oxygen for gasification and high-pressure nitrogen for combustion turbine NO_x control. The diluent nitrogen lowers the flame temperature and, therefore, lowers the NO_x.

Other concepts being developed at Westinghouse include incorporating combustion turbines in a coal-fueled combined cycle for second generation pressurized fluidized bed (PFB), and direct coal-fired (DCF) combined cycle configurations. IGCC, PFB, and DCF concepts require a fuel gas cleanup system to remove particulates, sulfur, and alkali (Newby and Bannister, 1994). Low-NO_x levels are obtained through use of advanced combustion processes (Scalzo et al., 1991).

Pressurized Fluidized Bed. Under a DOE-sponsored program, Westinghouse is developing a MASB topping combustor that will be used in the second generation PFB topping combustor (Domeracki et al., 1994). The entire combustion air quantity is introduced into the combustor through axial flow, concentric vane rows. The MASB utilizes vitiated air at 1600°F (871°C) for cooling. Thermal NO_x levels of less than 10 ppm have been measured for a burner outlet temperature of 2300°F (1260°C).

In addition to the topping combustor, Westinghouse is developing and supplying integrated gas turbine systems that will interface with PFB plants and incorporate the functions of hot gas filtration, alkali vapor removal, hot gas piping and control, and turbine compression and expansion (Newby et al., 1994).

Direct Coal. In a direct coal-fueled concept, ash and sulfur are to be removed from the coal during the combustion process. Air from the combustion turbine driven compressor flows into the pressurized slagging combustor and into a topping combustor. About one-third of the air is directed to the slagging combustor for utilization in the sub-stoichiometric combustion of the coal fuel. Two-thirds of the compressor discharge air goes directly to the topping combustor where the low-Btu fuel gas is fired under lean-burn conditions. One advantage of this split is that the majority of the primary combustion process only has to handle one-third of the total air flow required by the combustion turbine. The slagging combustor operates at temperatures high enough to melt or vaporize the inert ash constituents in the coal. Westinghouse worked with Textron Defense Systems under a DOE contract to demonstrate the feasibility of this concept (Bannister et al., 1992). Test results confirmed 99 percent carbon conversion with NO_x levels under 50 ppmw. The next step in the development of this process is to integrate various hardware components into an operating cycle in a pilot plant.

Current and Future Trends

In cooperation with United States Department of Energy's Morgantown Energy Technology Center, a Westinghouse led team is working on Phases 2 and 3 of an eight-year, four-phase Advanced Turbine Systems (ATS) Program to develop the technology required to provide a significant increase in natural gas-fired combined cycle power generation plant efficiency (Bannister et al., 1995).

Efficiencies for large natural-gas-fired combined-cycle systems for the utility market have been demonstrated at 54 to 55 percent. Even though manufacturers will make improvements in the 1990s, pursuing the historic trend, shown in Tables 2 and 3, efficiency levels could reach a plateau for simple and combined cycle plants. Cycle innovations, a 2600°F (1427°C) combustion turbine RIT, reduced cooling air usage, steam cooling, improved component efficiencies, together with improved material/coating systems are needed to achieve combined cycle efficiencies in the 60 percent range for natural gas-fired utility machines (Briesch et al., 1995).

ATS using natural gas is to be commercially available by the year 2000. Coal-derived fuel concepts are candidates for the post-2005 power-generation market. The final design will be fuel flexible in that it will operate on natural gas, but also be capable of being adapted to operate on coal, coal-derived, or biomass fuels (Newby et al., 1995).

Summary and Conclusion

The Westinghouse evolutionary combustion turbine design philosophy has always maintained reliability and maintainability as major considerations. Many basic design innovations have been retained after over four decades of evolution, thereby attesting to the soundness of their selection. Future advancements in firing temperature, materials, cooling, and cycles must also satisfy reliability/maintainability requirements.

Westinghouse has actively worked with industry and the government for over three decades in developing the use of coal as a clean fuel for power generation. The company is currently actively supporting clean coal technology programs in advanced IGCC, first generation PFB, and second generation PFB plants.

Acknowledgments

The authors acknowledge the hundreds of customers who through their never-ending demand for better products have fostered many of the improvements presented in this paper. The authors are also indebted to hundreds of Westinghouse steam and combustion turbine engineers who have also contributed to the development of combustion turbine technology.

References

Ambrose, M. J., and Obidinski, W. S., 1972, "Recent Field Tests for Control of Exhaust Emissions From a 35 MW Gas Turbine," ASME Paper No. 72-JPG-GT-2.

Downloaded 02 Jun 2010 to 171.66.16.104. Redistribution subject to ASME license or copyright; see http://www.asme.org/terms/Terms_Use.cfm

Ambrose, M. J., Costello, R. F., and Schreiber, H., 1984, "Utility Combustion Turbine Evaluation of Coal Liquid Fuels," ASME Paper No. 84-JPGC-GT-13.

Aoyama, K., and Mandai, S., 1984, "Development of a Dry Low NO_x Combustor for a 120 MW Gas Turbine," ASME JOURNAL OF ENGINEERING FOR GAS TURBINES AND POWER, Vol. 106, pp. 795–800.

Bannister, R. L., and Silvestri, G. J., 1989, "Evolution of the Central Station Steam Turbine," *Mechanical Engineering,* Feb., pp. 70–78.

Bannister, R. L., Newby, R. A., and Diehl, R. C., 1992, "Developing a Direct Coal-Fired Combined Cycle," *Mechanical Engineering,* Dec., pp. 64–70.

Bannister, R. L., Cheruvu, N. S., Little, D. A., and McQuiggan, G., 1995, "Development Requirements for an Advanced Gas Turbine System," ASME JOURNAL OF ENGINEERING FOR GAS TURBINES AND POWER, Vol. 117, pp. 724–733.

Briesch, M. S., Bannister, R. L., Diakunchak, I. S., and Huber, D. J., 1995, "A Combined Cycle Designed to Achieve Greater Than 60 Percent Efficiency," ASME JOURNAL OF ENGINEERING FOR GAS TURBINES AND POWER, Vol. 117, pp. 734–741.

Carl, D. E., Obidinski, E. S., and Jersey, C. A., 1975, "Exhaust Emissions From a 25-MW Gas Turbine Firing Heavy and Light Distillate Fuel Oils and Natural Gas," ASME Paper No. 75-GT-68.

Cox, A. R., 1957, "Gas Turbine Generating Experience of West Texas Utilities Company," ASME Paper No. 57-GTP-11.

Cox, A. R., Henson, L. B., and Johnson, C. W., 1967, "Operation of San Angelo Power Station Combined Steam and Gas Turbine Cycle," *Proceedings American Power Conference,* Vol. 29, pp. 401–409.

Diakunchak, I. S., 1989, "The CW251B12 Gas Turbine Engine," ASME Paper No. 89-GT-119.

DeCorso, S. M., Hussey, C. E., and Ambrose, M. A., 1967, "Smokeless Combustion in Oil-Burning Gas Turbines," ASME Paper No. 67-PWR-5.

DeCorso, S. M., Lee, S. Y., and Young, W. E., 1971, "Laboratory Procedures for Evaluating High Temperature Corrosion Resistance of Gas Turbine Alloys," ASME JOURNAL OF ENGINEERING FOR POWER, Vol. 93.

DeCorso, S. M., Mumford, S. E., Carrubba, R., and Heck, R., 1977, "Catalysts for Gas Turbine Combustors—Experimental Test Results," ASME JOURNAL OF ENGINEERING FOR POWER, Vol. 99, No. 2, pp. 159–167.

Domeracki, W. F., Dowdy, T. E., and Bachovchin, D. M., 1994, "Topping Combustor Development for Second, Generation Pressurized Fluidized Bed Combined Cycles," ASME Paper No. 94-GT-106.

Gabriel, F. K., and Donato, V., 1986, "Telemetry Measurement of Combustion Turbine Blade Vibration in a High Temperature Environment," ASME Paper No. 86-GT-207.

Garland, R. V., and Pillsbury, P. W., 1992, "Status of Topping Combustor Development for Second-Generation Fluidized Bed Combined Cycles," ASME JOURNAL OF ENGINEERING FOR GAS TURBINES AND POWER, Vol. 114, pp. 126–131.

Geoffroy, G. A., and Amos, D. J., 1991, "Four Years Operating Experience Update on a Coal Gasification Combined Cycle Plant With Two 100 MW Class Gas Turbines," presented at the Combined Heat and Power and Independent Power Producers Conference, United Kingdom.

Hendry, R. L., and Pillsbury, P. W., 1987, "Commercial Demonstration of the Dow Gasification Process in an Integrated Combined Cycle Cogeneration Application," *Proceedings, American Power Conference,* Vol. 49, pp. 149–153.

Hultgren, K. C., 1981, "Use of 3-Dimensional Finite Element Model in Design of First Stage Turbine Vane Segments," CIMAC Paper No. GT-19, 14th International Congress on Combustion Engines, Helsinski.

Hung, W. S. Y., 1974, "Accurate Method of Predicting the Effect of Humidity or Injected Water on NO_x Emissions From Industrial Gas Turbines," ASME Paper No. 74-WA/GT-6.

Hung, W. S. Y., Dickson, W. H., and DeCorso, S. M., 1978, "Preliminary Design Analysis of a Catalytic Ceramic Structure in a Turbine Combustor," ASME Paper No. 78-WA/GT-10.

Hussey, C. E., Lee, S. Y., and Young, W. E., 1973, "Operation of Gas Turbines on ASTM3-GT Fuel," *Manual on Requirements, Handling, and Quality Control of Gas Turbine Fuel,* ASTM STP 531, American Society for Testing and Materials, pp. 3–21.

Krapf, G. H., and Stephens, J. O., 1958, "Gas Turbines for Blast Furnace Blowing," ASME Paper No. 58-GTP-14.

Lew, H. G., DeCorso, S. M., Vermes, G., Carl, D., Havener, W. J., Schwab, J., and Notardonato, J., 1982, "Low NO_x and Fuel Flexible Gas Turbine Combustors," ASME JOURNAL OF ENGINEERING FOR POWER, Vol. 104, No. 2.

Morrison, E. M., and Pillsbury, P. W., 1989, "Coal Generated Synthetic Gas," ASME Paper No. 89-GT-257.

Mumford, S. E., Hung, W. S. Y., and Singh, P. P., 1977, "A Potential Low NO_x Emission Combustor for Gas Turbines Using the Concept of Hybrid Combustion," ASME Paper No. 77-GT-15.

Newby, R. A., and Bannister, R. L., 1994, "Advanced Hot Gas Cleaning System for Coal Gasification Processes," ASME JOURNAL OF ENGINEERING FOR GAS TURBINES AND POWER, Vol. 116, pp. 338–344.

Newby, R. A., Domeracki, W. F., McGuigan, A. W., and Bannister, R. L., 1994, "Integration of Gas Turbine Systems Into Pressurized Fluidized Bed Combustion Combined Cycles," ASME Paper No. 94-GT-333.

Newby, R. A., Archer, D. H., and Bannister, R. L., 1995, "Conversion of an Advanced Natural Gas-Fueled Combustion Turbine to Coal-Base Fuel Applications," ASME Paper No. 95-GT-162.

Pillsbury, P. W., 1974, "A High Pressure Coal Gas Combustor Testing Program," ASME Paper No. 74-PWR-11.

Pillsbury, P. W., Cohn, A., Mulik, P. R., and Stein, T. R., 1978, "Investigating Combustion Turbine Burner Performance With Coal-Derived Liquids Having High Full-Bound Nitrogen," ASME Paper No. 78-GT-126.

Pillsbury, P. W., Cohn, A., Mulik, P. R., Singh, P. P., and Stein, R. T., 1979, "Fuel Effects in Recent Combustion Turbine Burner Tests of Six Coal Liquids," ASME Paper No. 79-GT-137.

Putz, T. L., 1948, "Operation and Test Experience With an Experimental 2000-HP Gas Turbine," *American Power Conference,* Vol. 10, pp. 355–363.

Putz, T. L., 1954, "Gas Turbines for the Power Industry," *Proceedings American Power Conference,* Vol. 16, pp. 293–298.

Scalzo, A. J., 1963, "Numerical Solution for the Two-Dimensional Stress Distribution in Irregular Shapes," Westinghouse Electric Corporation Report E-1420, Orlando, FL.

Scalzo, A. J., Holden, P. C., and Howard, G. S., 1981, "Westinghouse 501D Combustion Turbine Engine," ASME Paper No. 81-GT-32.

Scalzo, A. J., Howard, G. S., and Holden, P. C., 1983, "Field Test of the W501D, a 100 MW Combustion Turbine," ASME Paper No. 83-GT-174.

Scalzo, A. J., Allen, J. M., and Antos, R. J., 1986, "Analysis and Solution of a Nonsynchronous Vibration Problem in the Last Row Turbine Blade of a Large Industrial Turbine," ASME JOURNAL OF ENGINEERING FOR GAS TURBINES AND POWER, Vol. 108, pp. 591–598.

Scalzo, A. J., Antos, R. J., and Fukue, I., 1988, "Operating Experience Complements New Technology in Design of Advanced Combustion Turbine," ASME Paper No. 88-JPG/GT-1.

Scalzo, A. J., McLaurin, L. D., Howard, G. S., Mori, Y., Hiura, H., and Sato, T., 1989, "A New 150 MW High Efficiency, Heavy-Duty Combustors Turbine," ASME JOURNAL OF ENGINEERING FOR GAS TURBINES AND POWER, Vol. 111, pp. 211–217.

Scalzo, A. J., Sharkey, W. T., and Emmerling, W. C., 1990, "Solution of Combustor Noise in a Coal Gasification Cogeneration Application of 100-MW-Class Combustion Turbines," ASME JOURNAL OF ENGINEERING FOR GAS TURBINES AND POWER, Vol. 112, pp. 38–43.

Scalzo, A. J., Amos, D. J., Bannister, R. L., and Garland, R. V., 1991, "Coal-Fueled Programmes Gather Pace," *Modern Power Systems,* Vol. 11, No. 6, pp. 55–59.

Scalzo, A. J., 1992, "High-Cycle Fatigue Design Evolution and Experience of Freestanding Combustion Turbine Blades," ASME JOURNAL OF ENGINEERING FOR GAS TURBINES AND POWER, Vol. 114, pp. 284–292.

Scheihing, P. E., Piaia, T. A., Pillsbury, P. W., and Kitaplioglu, O., 1982, "Full-Scale Catalytic Burner Testing With No. 2 Oil for Combustion Turbine Application," ASME Paper No. 82-JPGC-GT-20.

Seglem, C. E., and DeCorso, S. M., 1980, "Alternate Fuels Capability of Gas Turbines for Pipeline and Industrial Applications," presented at the 7th Annual Technology Conference and Exposition, Washington, DC.

Southall, L. R., and McQuiggan, G., 1995, "New 200 MW Class 501G Combustion Turbine," ASME Paper No. 95-GT-215; accepted for publication in the *Transactions of the ASME.*

Stephens, J. O., 1952, "Gas Turbine Power Plant Designs," *Proceedings American Power Conference,* Vol. 14, pp. 267–271.

Stephens, J. O., and Bruce, D. F., 1955, "5,000 Horsepower Dual Shaft Gas Turbine Power Plant," *Proceedings American Power Conference,* Vol. 17, pp. 342–349.

Stephens, J. O., and Young, W. E., 1989, "A Super High-Speed Combined-Cycle Locomotive," *Turbomachinery International,* July/Aug., pp. 26–30.

Stephens, J. O., Little, D. A., Hunt, P. J., and Stanaland, R., 1990, "Efficient Part-Load Combined Cycle Operations," *Proceedings 19th Turbomachinery Symposium Texas A&M,* pp. 31–36.

Vermes, G., 1974, "A NO_x Correlation Method for Gas Turbine Combustors Based on NO_x Formation Assumptions," ASME Paper No. 74-WA/GT-10.

Wenglarz, R. A., and Menguturk, M., 1982, "Use of Cascade and Small Turbine Tests to Determine Erosion of Utility Turbines," ASME JOURNAL OF ENGINEERING FOR POWER, Vol. 104, pp. 58–63.

Downloaded 02 Jun 2010 to 171.66.16.104. Redistribution subject to ASME license or copyright; see http://www.asme.org/terms/Terms_Use.cfm

Benefits of MS 6001B Gas Turbine in Cogeneration: The UEM Power Plant Case

P. M. Remy
Usine d'Electricité de Metz (UEM), Metz, France

Y. M. Boissenin

M. M. Molière

European Gas Turbines, Belfort, France

Long before the neologism "Cogeneration" was coined (around 1978), UEM's Chambière Power Plant—which dates back to the turn of the century—was already supplying the city of Metz, east of France, with combined heat and power. In 1992, Chambière experienced a major turning point in its history with the installation of a new unit based on one MS 6001B "Heavy Duty" gas turbine. This model, rated 38 MWe-ISO and burning natural gas or fuel oil, has become the core of a new cogeneration unit exhibiting outstanding performance:

- *efficiency higher than 80 percent (LHV) providing a 20 percent energy saving in comparison to a conventional plant*
- *low pollutant emissions (NO_x, CO, HC) and low contribution to the greenhouse effect (CO_2).*

The gas turbine has been equipped with two steam injection devices, for $DeNO_x$ and power augmentation, respectively, resulting in a very flexible system. After describing the power plant and giving its main achievements in the fields of energy and emissions, the paper briefly presents several improvements intended to protect both the turbine and the environment.

Introduction

Any creation of new power and heat generating units, or an upgrading of existing units leads investors to carefully compare the different solutions available.

Cogeneration installations are selected more and more frequently for their multiple advantages. Solutions based on heavy-duty gas turbines prove very attractive (Boissenin, 1992).

The Metz utility (UEM), which has a long experience with diverse generating equipment, has chosen to install one MS 6001B (or Frame 6B) gas turbine and one Heat Recovery Steam Generator (HRSG) for the Chambière plant extension. The power plant is entirely indoors, as shown in Fig. 1.

Key Dates for Chambière

The UEM is one of 175 privatized electric utilities in France. Since the turn of this century it has been distributing electricity in the Metz region, and has, moreover, been active in the generation of hydraulic and thermal power.

Since 1956 the UEM has developed district heating as a new activity, initially using a conventional boiler room, and since 1961 using the combined heat and power plant at Chambière. This power plant, which since 1971 also recovers the steam produced by the city's household waste incineration plant, simultaneously produces electricity for the Metz region electricity grid (280 MWe and 1.3 TWh/year) and heat for district heating (180 MWth and 250 GWh/year).

Since Chambière's creation, the UEM has always sought to develop and perfect its combined production system. More progress was made in 1992 with the installation of one 38 MW Frame 6 gas turbine, running on natural gas fuel with distillate as a back up.

The main fuel types of the 300 MW thermal power plant, that is, coal, heavy oil, light distillate, and natural gas, allow production of one third of the distributed electricity, meet district heating network requirements, and ensure a safe supply of primary energy.

Why Extend the Chambière Plant?

In 1990, the UEM's basic activity, electricity production, and distribution represented 85 percent of the company's turnover. There is still strong potential for development:

- the likely evolution of European regulations and correlatively of national regulations will not be unfavorable toward independent and decentralized utilities
- the necessity to develop energy savings, to smooth out electric grid load curves (so as to lop peak demand), and to protect the environment will renew interest in decentralized production, therefore in combined heat and power and in peak thermal production.

The UEM considered that the optimization of its economic and strategic configuration depends on the development of its self-production of electricity, in power and energy, and on the valorization of the cogeneration asset. Furthermore, the Chambière installations were between 20 and 30 years old and were no longer reliable enough to meet the same production level.

Why a Gas Turbine?

At the start, all technical possibilities were envisaged. The aim was to maintain the required reliability for Chambière and to increase the potential output of the UEM in favorable economic terms. The field of study was therefore vast.

Out of the twenty or so solutions studied, those based on gas turbines running on natural gas or fuel oil led to a better rate of internal profitability of 20 percent (payback of 5 years).

Moreover, the evolution of EEC directives allowed for the use of natural gas for electricity production.

So, it was decided to complete the studies on the basis of one gas turbine with one HRSG. The addition of a condensing steam turbine was also planned in order to maintain a significant

Contributed by the International Gas Turbine Institute and presented at the 39th International Gas Turbine and Aeroengine Congress and Exposition, The Hague, The Netherlands, June 13–16, 1994. Manuscript received by the International Gas Turbine Institute February 15, 1994. Paper No. 94-GT-421. Associate Technical Editor: E. M. Greitzer.

Copyright © 1996 by ASME

Downloaded 02 Jun 2010 to 171.66.16.104. Redistribution subject to ASME license or copyright; see http://www.asme.org/terms/Terms_Use.cfm

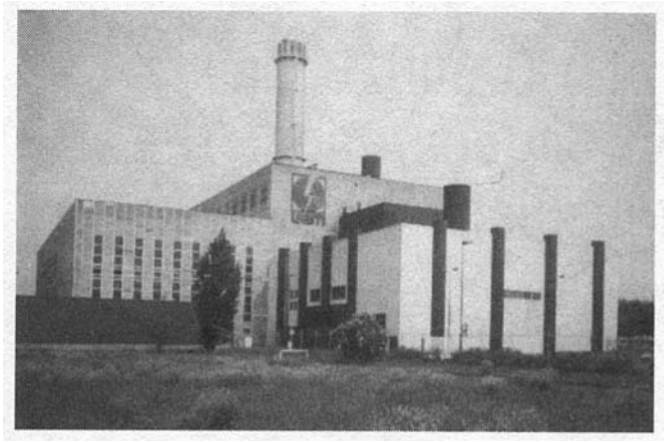

Fig. 1 General view of Chambière Power Plant with extension on the right

consumption of coal from the Lorraine region, so as to support the mining activity, without losing sight of the profitability target of the project.

Main Elements of Extension and Key Dates

We studied one MS 6001B gas turbine rated 38 MWe (51 MWe at peak load with steam injection and low ambient), one 75 MWth HRSG, and one 16 MWe condensing steam turbine, for which the orders were signed in February and March 1991. The project has been carried out over a very short period of time.

- October 1990: engineering contract signed
- October 1991: start of civil works
- October 1992: start of commercial operation

Chambière Before the Extension

The thermal power plant has constantly evolved since its creation and may be represented as the juxtaposition of different types of production able to function separately or as a whole:

- heat production using conventional intermediate pressure boilers (12 bar, 325°C)
- conventional electricity production using a condensing steam turbine driven by intermediate pressure steam
- cogeneration of heat and power associating high pressure (60 bar, 465°C) boilers and extraction backpressure steam turbines
- electricity production using emergency generator sets (2 × 1 MW).

Intermediate-pressure steam, used for district heating or by the condensing steam turbine, may originate from:

- the neighboring household waste incineration plant
- steam bleeding from the extraction backpressure turbines: steam that has already been used for electricity production
- intermediate pressure boilers that also ensure heat production safety.

Low-pressure steam (1.5 bar and 2.5 bar) from the backpressure turbines is used to reheat the district heating water. Figure 2 shows a diagram of the power plant.

Chambière After the Extension

The gas turbine has its own exhaust stack and can therefore operate independently to produce electricity alone (peak shaving if required by the grid).

The temperature of the gas turbine exhaust gases is between 520 and 565°C. The energy contained in the gases is recovered in a relatively complex HRSG according to the different operational possibilities of the Chambière power plant.

From upstream to downstream of the gases circuit, the recovery takes place:

- first, in the form of high-pressure steam, which can be used in the extraction backpressure turbines (in cogeneration) or by intermediate pressure expansion for the condensing steam turbine (combined production), or for the district heating network (in cogeneration)
- next, in the form of intermediate-pressure steam for the condensing steam turbine (combined production) or for the district heating network (in cogeneration)
- last, in the form of reheated water from the district heating network via a heater situated just in front of the exhaust gas outlet in the stack (in cogeneration).

The new condensing steam turbine was installed to make best use of the availability of intermediate-pressure steam according to the time of the year, either in conventional electricity production (boilers + condensing turbine), or in combined production (gas turbine, HRSG, condensing turbine).

The system consisting of the gas turbine, HRSG, and other structures at Chambière has an efficiency of over 80 percent in the cogeneration configuration, and approaching 50 percent in the combined cycle configuration.

The thermal output of the Chambière boilers has gone up approximately from 220 MW to 300 MW:

- electrical output has increased from 30 MW to 100 MW
- the annual electricity capacity (estimation for 1993) has increased from 100 GWh to nearly 400 GWh (of which 200 GWh for the gas turbine).

The energy requirements of the power plant from the beginning of 1993 are covered for approximately:

- 9 percent using 80,000 tons/year of housework waste
- 40 percent by the combustion of 75,000 tons/year of coal
- 50 percent burning natural gas (700 GWh/year HHV)
- 1 percent burning heavy and distillate oils (emergency generator sets).

The multiple energy sources contribute to security of supply for the power plant as well as an optimized economic decision.

Pursuit of the economic optimum leads to continuous adaptation of the power plant's operation to the multiple objectives imposed upon it. In particular the decisions to be made are influenced by:

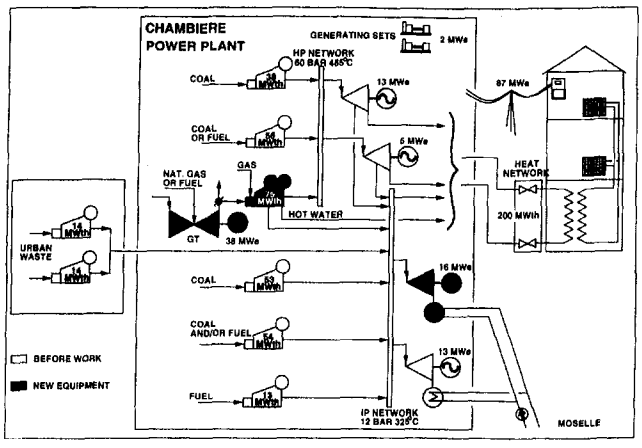

Fig. 2 Diagram of the Chambière power plant

Downloaded 02 Jun 2010 to 171.66.16.104. Redistribution subject to ASME license or copyright; see http://www.asme.org/terms/Terms_Use.cfm

Table 1 MS 6001B gas turbine standard performance

Site conditions	- ISO - Natural gas fuel - 100% base load			
Pressure drops	- Inlet : 100 mm WC - Exhaust : 62 mm WC			
Steam injection	t/h	0	11.3	24.7
Power output	MW	38.5	41	43.8
Heat consumption	GJ/h	440.6	454.6	470.7
	MW	122.4	126.3	130.7
Heat rate	kJ/kWh	11 445	11 090	10 740
GT exhaust				
- Gas flow	t/h	503	515	528
- Temperature	°C	538	533	528
- NOx (15% O_2)	ppm vd	152	42	<42
	g/GJ	264	73	<73
- CO (15% O_2)	ppm vd	≤ 10	≤ 10	≤ 10

- choice of fuel, taking into account that all the steam from the household waste incineration plant must be used
- selection of equipment to be used (gas turbine, cogeneration, intermediate pressure boiler, condensing steam turbine).

For electricity production the public network purchase price must also be considered, as the price of electricity varies in great proportions depending on the tariff periods and fixed bonus.

The Chambière power plant has in fact over 100 possible operating combinations, used to the best profitability of its production means. A central control room is a precious aid to operation.

Frame 6 GT at the Core of the New Cogen Unit

Frame 6 Gas Turbine Identity. This is a heavy-duty gas turbine model manufactured by European Gas Turbines since 1979. More than 425 units are in operation throughout the world. This 40 MW class gas turbine is designed for use in both 50 Hz and 60 Hz networks, and is suitable for different applications (simple cycle, combined cycle, and cogeneration).

The gas turbine generator set is a complete thermal power plant which may be installed outdoors or indoors. Its performances are shown in Table 1.

The equipment set, delivered in factory-assembled compartments and systems, is mainly made up of:

- the gas turbine compartment (cross section shown in Fig. 3) including the lubricating system common to the gas turbine and the generator
- the generator compartment (50 Hz or 60 Hz networks)
- the control compartment from which local operation can be performed. In a combined cycle, remote control can be carried out from the central control room
- the air inlet system, which includes filter, silencer, and ducts
- the exhaust system, which includes ducts, silencer and expansion joints. In the basic arrangement, the exhaust is lateral and a direct stack for the exhaust gases allows simple cycle operation of the gas turbine. At the base of the bypass stack, there is a damper allowing the gases to be directed either to the bypass or to the HRSG. This bypass allows the use of the gas turbine during the HRSG installation. It also facilitates start and increases operation flexibility.

Its start is fast, with a synchronization to the grid in 12 minutes and full load reached after a further 4 minutes.

For base load and natural gas operation, NO_x emissions are 152 ppm vd, at 15 percent O_2 without treatment and can be reduced to 42 ppm with water or steam injection, or to 25 ppm using Dry Low NO_x combustion chambers.

Steam Injection and Its Effects. Steam injection in gas turbines is a proven technique, which is presently making a comeback (Smith, 1993).

Whether carried out at the compressor outlet, for power augmentation purposes, or in the combustion chambers, for $DeNO_x$ purposes, steam injection both reduces NO_x emissions by lowering the combustion temperature and increases the output by expansion in the turbine.

In terms of output, both types of injection have similar effects, the power augmentation being proportional to the steam flow, but the result in terms of efficiency is different according to the thermodynamic system considered:

- In simple cycle, for one Frame 6 gas turbine at base load (ISO) and for a steam flow of 1 ton/hour:

  (*a*) the increase in output is approximately 0.57 percent for an increase in heat consumption of only 0.29 percent,
  (*b*) the reduction in heat rate is therefore 0.28 percent.

- When considering the overall combined cycle, steam injection has a negative result, as it is carried out to the detriment of the steam cycle. However, steam injection for power augmentation is an advantage for the additional flexibility it provides in a complex cogeneration unit such as the one at Chambière.

Regarding the $DeNO_x$ function, it has been observed that one ton of steam injected into the combustion chambers has virtually the same effect as three tons injected into the compressor outlet.

This experimental figure reflects the ratio between the stoichiometric combustion air flow (injection into the flame) and the total gas turbine air flow that corresponds to the combustion, dilution, and cooling functions (injection into the compressor outlet).

In heat recovery, the gas turbine exhaust gas characteristics are also modified as a result of injection:

(*a*) the exhaust gas flow is increased by virtually the same amount as the injected flow (5 percent maximum),

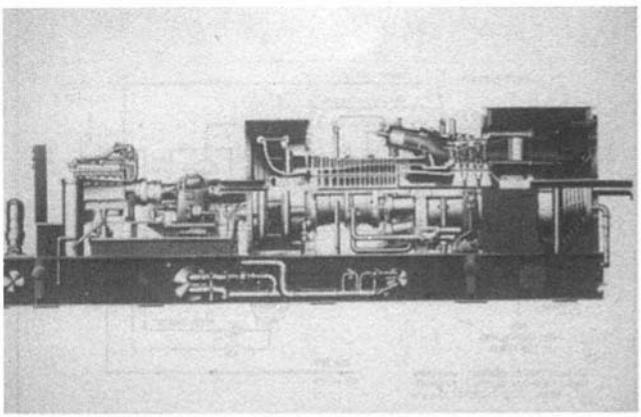

Fig. 3 Cross section of the MS 6001B gas turbine

Downloaded 02 Jun 2010 to 171.66.16.104. Redistribution subject to ASME license or copyright; see http://www.asme.org/terms/Terms_Use.cfm

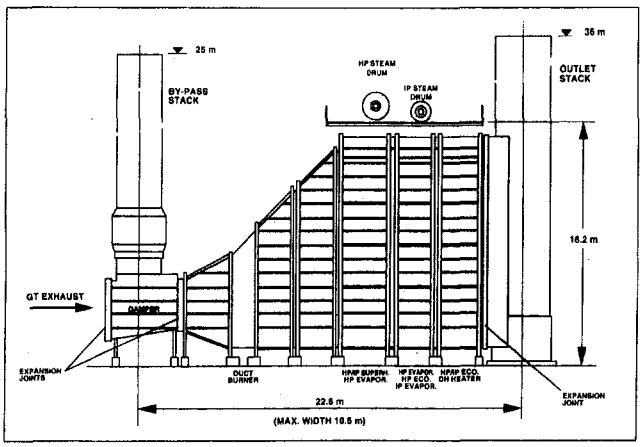

Fig. 4 Bypass and heat recovery steam generator

(*b*) the exhaust gas temperature is reduced by 5°C (10°C maximum with 5 percent injection),
(*c*) the specific heat of gases is slightly increased.

These three changes allow the steam characteristics to remain almost unchanged in the boiler.

Other Important Components of the New Cogen Unit

The HRSG. The HRSG is natural circulation designed with horizontal gas flow and vertical tube bundles. It is equipped with natural gas postcombustion used for peak demand. Figure 4 shows a general view of the HRSG and exhaust gas bypass.

The heat exchanger sections are the HP and IP circuits, respectively, at 63 bar and 13 bar (or 21 bar depending on type of operation) as well as the district heating water heater. Figure 5 shows a diagram of the different heat exchanger tube bundles. The main HRSG performance is shown in Table 2.

The deaerator-feedwater tank is situated next to the boiler.

Condensing Steam Turbine. This newly installed turbine, rated 16 MWe, receives steam from the IP network at 12 bar and 325°C in parallel with the existing 13 MWe turbine. This IP steam (as shown in Fig. 2) originates from:

- either household waste incineration plant boilers
- conventional boilers at Chambière, on coal and/or fuel
- the newly installed HRSG
- or last, from extraction of the two backpressure turbines of 13 and 5 MWe.

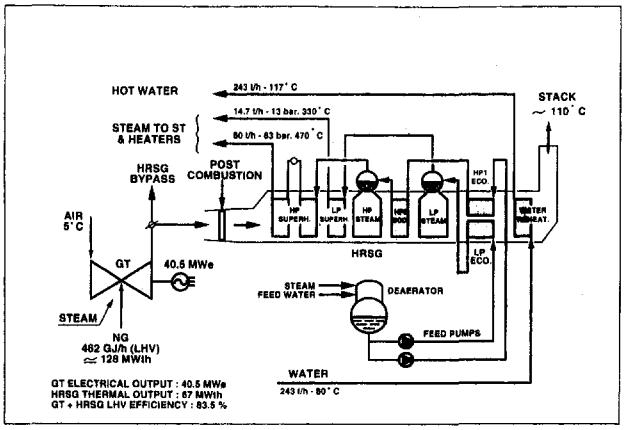

Fig. 5 Schematic diagram of the new UEM cogen unit

Table 2 Chambiere HRSG performance

Gas turbine at 100% base load, on natural gas, ISO conditions, without postcombustion.

Steam injection on GT	t/h	0	10.5	24.7
Exhaut gases pressure drop in the boiler	mm WC	190	200	210
Gas turbine				
. Output	MW	38.15	40.5	43.5
. Heat consumption	GJ/h	440.6	454.4	472
. Exhaust gases	t/h	503	513.5	528
	°C	540	535	530
. Inlet press. drop Δp	mm WC	120	120	120
. Exhaust press. dropΔp	mm WC	250	260	270
. NOx (15% O2)	ppm vd	152	42	< 42
Gases at boiler inlet				
. Flow	t/h	503	513	528
. Temperature	°C	538	533	528
HP steam production				
. Flow	t/h	59.5	60.7	62.9
. Pressure	bar a	63	63	63
. Temperature	°C	470	469	468
IP steam production				
. Flow	t/h	14	10.4	11.6
. Pressure	bar a	12	21	21
. Temperature	°C	338	368	360
District heating water heater				
. Flow	t/h	243	243	243
. Inlet/outlet temp.	°C	80/115	80/121	80/124
. Output	MWth	10.1	11.6	12.5
Stack Temperature	°C	108	113	115.5

The turbine condenser is cooled using water from the River Moselle. It's main performance is:

- Inlet steam flow t/h 82
- Inlet steam pressure bar 12
- Inlet steam temperture °C 325
- Output at generator MWe 16
- Condenser pressure mbar 50

Benefits of the Extension in Energy Terms

The total installed power has been tripled and the heat capability has been increased by almost 50 percent.

Power plant efficiency has been improved due to the use of natural gas in the gas turbine, which allows the use of a water heater for the district heating circuit. This reduces the stack temperature to approximately 110°C.

The increase in efficiency and energy recovery allows, with the same result, a reduction

- in primary energy consumption (energy savings in coal, fuel-oil, and natural gas at Chambière)
- in atmospheric pollution and other emissions (liquid and gaseous waste and ashes).

In 1993, primary energy consumption at Chambière will represent around 1200 GWh. If Chambière did not exist, the primary energy consumption would be over 1600 GWh to meet the same

Downloaded 02 Jun 2010 to 171.66.16.104. Redistribution subject to ASME license or copyright; see http://www.asme.org/terms/Terms_Use.cfm

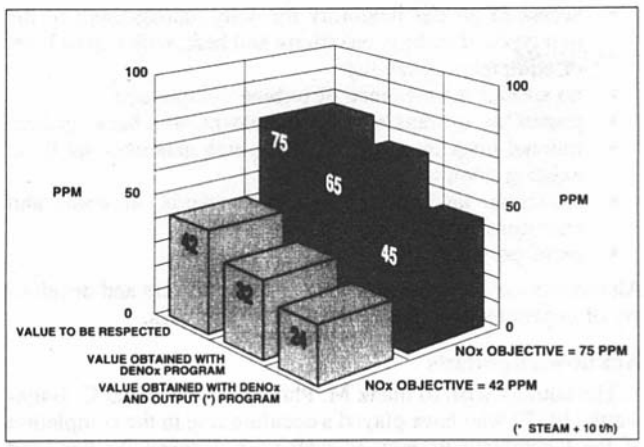

Fig. 6 Gas turbine NO_x emissions

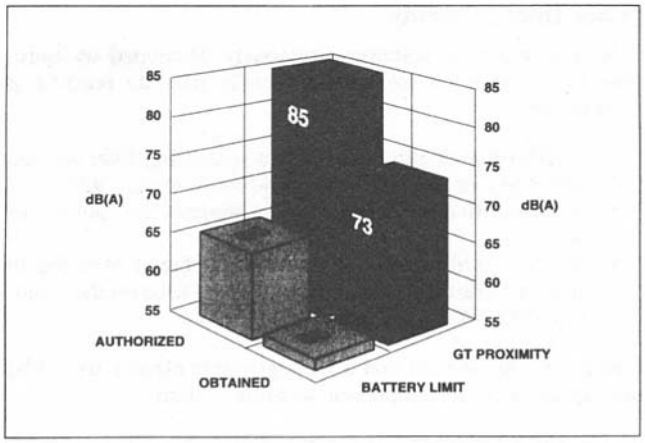

Fig. 7 Gas turbine generating set noise emissions

needs for electricity and district heating, that is to say one third higher.

This energy saving, which adds to a yearly amount of 55,000 coal equivalent tons, demonstrates the advantage of Chambière with regard to protecting the environment, since with the selected energy arrangement polluting emissions are reduced by 25 percent.

Protecting the Environment

Reducing Gas Turbine Emissions. Particular attention has been paid to this point.

Two different options for NO_x have been fixed: 75 ppm (normal maximum value to be respected) and 42 ppm (maximum value to be respected in the case of abnormal local pollution).

The strategy, which was drawn up with the help of both steam injection systems, is the following:

$DeNO_x$ program. Injection of $DeNO_x$ steam flow automatically piloted by the gas turbine control curve according to the fuel flow (an image of load and atmospheric conditions) to obtain the selected NO_x objective, with a substantial margin. The $DeNO_x$ program is applied permanently; the operator is only able to select one of the predefined NO_x options.

Power Augmentation Program. Any surplus steam from the entire cogeneration unit, may be injected into the gas turbine.

An Extensive Emission Checkup. A measuring campaign carried out using natural gas between 70 and 100 percent of gas turbine baseload led to the following results (Fig. 6).

- the $DeNO_x$ program attains the objectives of 75 and 42 ppm with a 15 to 25 percent margin
- the two programs applied simultaneously assure a 40 percent reduction in the selected NO_x emissions level, for an "output" steam flow of 10 t/h
- CO and CH_4 emissions are below 1 ppm whatever the global steam flow injected
- CO_2 emissions are below 100 g/MJ in baseload
- an increased power output of 14 percent using steam injection causes an increase in gas turbine CO_2 emissions of only 7 percent.

Noise Reduction. The turbine super package was designed to reduce noise levels to a minimum. In addition, the gas turbine building has been overinsulated in order that any increase in external noise levels may not disturb the neighborhood.

Owing to specific solutions built into the overall design such as the acoustic enclosure of the generating set and the complex building lagging for low-frequency noise absorption, remarkable performances have been achieved.

A series of readings has in fact revealed very low noise levels internally and externally, as shown in Fig. 7. As an example, the levels recorded correspond to those of a restaurant, respectively with or without musical animation. For this project, the design engineer was awarded a prize for the protection of the environment by the French FNGEEE.[1]

Integration of New Buildings on Site. Great attention has been paid regarding the aesthetics of the new building, for maximum integration into the environment.

What is more, an architectural study is presently underway taking into account on a larger scale the Chambière site (existing power plant, new buildings, coal and fuel storage areas) in the environment, with the aim of making this site a pleasant landmark on the access road to Metz city.

Emissions and Waste From the Pre-existing Equipment. Apart from gas turbine emissions, the user has devoted around $5 million (1990) to reduce pollution caused by existing equipment: reduction in liquid waste from ash treatment, dust removal from boiler smoke, renovation of fuel storage areas, etc.

Global Result. The introduction of the gas turbine and the work carried out have led to an important improvement in the global impact of gaseous emissions, as shown in Fig. 8.

[1] Fédération Nationale de la Gestion des Equipments, de l'Energie et de l'Environnement.

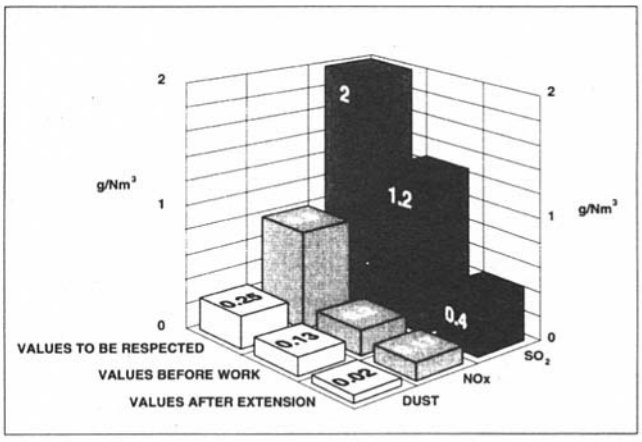

Fig. 8 Atmospheric emissions

Downloaded 02 Jun 2010 to 171.66.16.104. Redistribution subject to ASME license or copyright; see http://www.asme.org/terms/Terms_Use.cfm

Other Improvements

Several technical solutions previously developed by European Gas Turbines have been especially put into practice at Chambière:

- a lube oil mist eliminator with a coalescing filter with an efficiency of over 97 percent (Molière et al., 1993)
- a sodium-free water treatment to suppress any hot corrosion risk
- a new, highly oxidation-resistant oil brand intended to minimize turbine maintenance, already used on the prototype MS 9001F gas turbine (216 MW).

Finally, it was decided that a biodegradable cleaner would be used in the off-line compressor washing system.

Conclusion

Owing to the various technical options selected and notably to the selection of a Frame 6 gas turbine, the objectives set for the new Chambière cogeneration unit have been fully achieved:

- increase in power and heat generation capacity to meet needs
- reduction in fuel heat consumption
- access to greater flexibility for daily management of the two types of energy, electricity and heat, with a high level of equipment reliability
- no special maintenance of turbine components
- possibility to transfer, at any moment, to a back up fuel
- rational integration of the gas turbine generator set in an existing complex power plant
- reduction, far beyond required standards, of waste and emissions into the environment
- rapid project implementation.

All these issues are carefully analysed by planners and developers of cogeneration schemes sited in urban areas.

Acknowledgments

The authors wish to thank M. Philippe (UEM) and C. Bannwarth (EGT) who have played a deciding role in the completion of the Chambière project, as well as J. Worsey for her kind assistance.

References

Boissenin, Y., 1992, "Cogeneration and Energy Savings," *GEC Alsthom Technical Review,* No. 10.

Molière, M., Gérome, Y., and Truong, L. S., 1993, "Turbine Lube Oil Mists: an Approach to the Generation Mechanism and an Investigation of Elimination Systems," ASME Paper No. 93-GT-249.

Smith, L. D., 1993, "Watering Down Gas Turbines," *Modern Power Systems,* p. 17, June.

Downloaded 02 Jun 2010 to 171.66.16.104. Redistribution subject to ASME license or copyright; see http://www.asme.org/terms/Terms_Use.cfm

Advances in Steam Path Technology

J. I. Cofer, IV
GE Power Generation,
General Electric Co.,
Schenectady, NY 12345

For many years, GE has been conducting research to understand better the loss mechanisms that degrade the aerodynamic performance of steam turbine stages, and to develop new computational fluid dynamics (CFD) computer programs to predict these losses accurately. This paper describes a number of new steam path design features that have been introduced in the GE steam turbine product line to improve turbine performance and reliability. These features include diaphragms with contoured sidewalls, advanced vortex blading with compound tangential lean, new continuously coupled last-stage buckets with improved aerodynamic efficiency and reliability, improved downward and axial flow exhaust hoods, and better steam leakage control devices. The benefits of these new features for both new units and retrofits of existing units are discussed. In addition, the paper discusses the new generation of three-dimensional viscous CFD analysis codes being used to develop new design concepts, including codes developed by GE as well as those obtained externally. Also described are the extensive laboratory test programs being conducted to validate the CFD codes and verify the predicted efficiency gains for new design features. Last, the paper describes new and unique state-of-the-art steam path design automation and optimization tools that dramatically reduce the design cycle time for new advanced aerodynamic designs.

Introduction

Turbine Efficiency Losses. The thermodynamic performance of a steam turbine is primarily determined by the design of the steam path components, which include the valves, inlet, nozzles, buckets, steam leakage control devices, and the exhaust. Because the efficiency of the entire power plant cycle is highly dependent on the efficiency of the steam turbine, it is important to minimize aerodynamic and steam leakage losses in the turbine steam path, in both rotating and stationary components. Figure 1 shows the types of efficiency loss that occur in a typical turbine stage and the approximate percentage that each type contributes to the total stage loss. Nozzle and bucket aerodynamic profile losses, secondary flow losses, and leakage losses account for roughly 80 to 90 percent of the total stage losses.

Nozzle and bucket profile losses can be significant if the blade shapes are not optimized for the local operating conditions. Profile losses are driven by surface finish, total blade surface area, airfoil shape and surface velocity distributions, and proper matching between nozzle and buckets to minimize incidence losses.

Equally significant losses can be caused by the complex secondary flows (Fig. 2, adapted from Langston, 1980) that are generated as the viscous boundary layers along the inner and outer sidewalls of the steam path are turned through the blade rows. These complex, three-dimensional flows must be thoroughly understood before effective methods can be developed to reduce the associated losses.

Steam leakage through the seals between stationary and rotating components of the turbine constitutes an efficiency loss because the leakage flow does not contribute to the work output of the stage. This loss can be quite significant, particularly at bucket tips. In short high-pressure (HP) stages, the tip leakage loss is driven by the high stage pressure levels and the relatively larger amount of radial clearance area compared to the nozzle flow area. In taller intermediate (IP) and low-pressure (LP) stages, the tip leakage loss is driven by the higher reaction levels at the bucket tips, which increases the pressure drop across the bucket tip. Steam leakage through the diaphragm shaft packing and the shaft end packing also causes losses, but these are generally of lesser magnitude than tip leakage losses.

Equal attention must be paid to the losses in stationary flow path components, such as inlets, valves, and exhausts. Any pressure drop that occurs in these components constitutes a loss in available energy and a reduction in work output.

Key Elements of GE Aerodynamic Development Programs. For many years, development efforts have been under way to better understand and reduce the various losses listed above. The objective of this long-term program is to develop specific design features, for both new turbines and retrofits of existing units, that maximize overall turbine efficiency while maintaining a high degree of reliability and cost effectiveness. Most aspects of this multifaceted development program are being conducted in cooperation with other company components such as aircraft engines, gas turbine, and corporate research and development (CRD). The four key elements of our overall aerodynamic development program are:

- The development of better computational fluid dynamics computer programs, which allow more accurate predictions of the complex behavior of the steam flow in the turbine.
- The development of new design concepts to improve efficiency, by using the CFD codes.
- An extensive laboratory test program to validate the CFD codes and verify the predicted efficiency gains.
- The development of a suite of powerful design automation and optimization tools to allow implementation of advanced aerodynamic design features on a custom basis to maximize efficiency for each specific application in short design cycle times.

This paper will review recent advances in steam path technology resulting from these development initiatives and the impact of these advances on current steam turbine designs.

Contributed by the International Gas Turbine Institute and presented at Cogen-Turbo Power, Vienna, Austria, August 23–25, 1995. Manuscript received by the International Gas Turbine Institute May 25, 1995. Associate Technical Editor: C. J. Russo. ASME Paper No. 95-CTP-2.

Copyright © 1996 by ASME

Downloaded 02 Jun 2010 to 171.66.16.104. Redistribution subject to ASME license or copyright; see http://www.asme.org/terms/Terms_Use.cfm

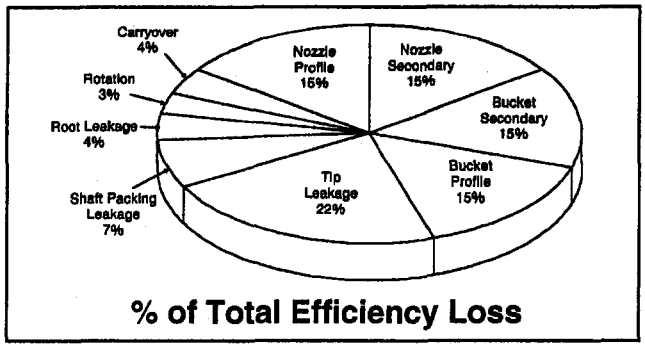

Fig. 1 Typical HP turbine stage efficiency losses

CFD Methods

In order to utilize the available energy of the steam fully for maximum efficiency, the three-dimensional flow field throughout the turbine must be accurately predicted. In particular, a better understanding is needed of the effects of wet steam, viscosity, and unsteady rotor–stator interactions if the remaining losses are to be reduced. Recent advances in the development of computational fluid dynamics computer programs have provided us with the tools we need to achieve better designs with reduced cost and shorter design cycle time.

Viscous Euler CFD Code. In the early 1980s, the GE steam turbine, gas turbine, and aircraft engine businesses began a long-term joint research program with CRD to study secondary flow phenomena using a combined analytical and experimental approach. Analytical investigations included the development of complex computational fluid dynamics computer codes based on three-dimensional formulations of the inviscid Euler equations and the viscous Navier–Stokes equations. The initial inviscid code was developed by CRD and called the EULER3D program (Holmes and Tong, 1985). A viscous code that included turbulence models was later developed by GE Aircraft Engines and called the Viscous Euler program (Turner and Jennions, 1993; Turner et al., 1993).

Comprehensive experimental investigations were conducted to test the validity of the predictions made by the EULER3D code. These tests utilized CRD's large-scale wind tunnel test facility, shown in Fig. 3, and the results are described in detail by Holmes and Warren (1985). In this study, EULER3D predictions of the flow in a subsonic turbine nozzle cascade were compared to cascade test data, including lampblack and oil flow visualization studies. Comparisons were made for nozzles with both parallel and diverging sidewalls, and the code was able to predict inviscid flows in turbine blade passages quite well.

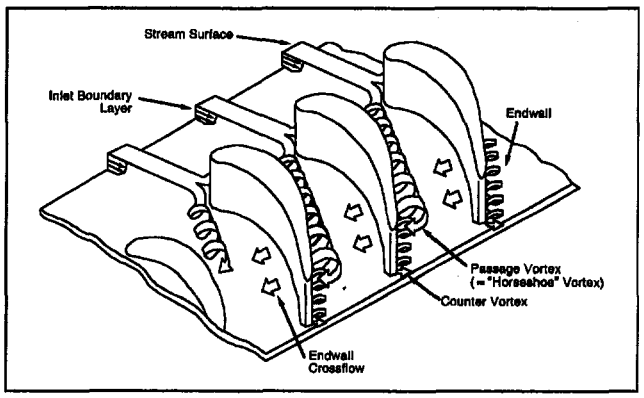

Fig. 2 Secondary flow in turbine nozzle cascade

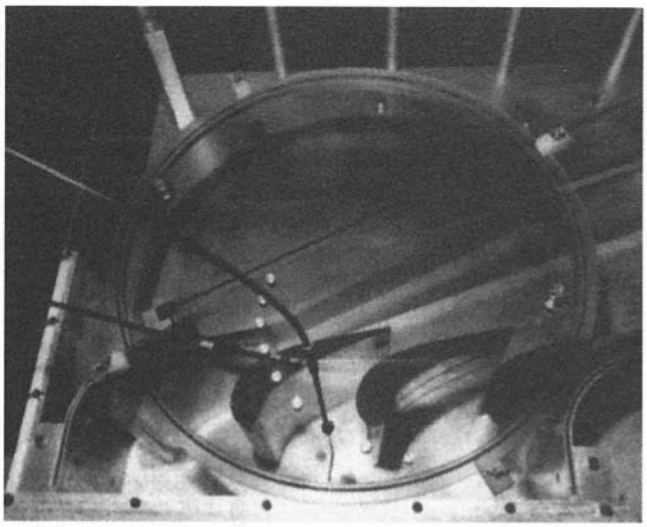

Fig. 3 Nozzle cascade wind tunnel

A unique flow visualization method was developed for the wind tunnel facility to aid in understanding the physics of secondary flows. The flow particle trajectories shown in Fig. 4 were obtained by shining a strobe light on helium-filled zero-buoyancy soap bubbles injected into the flow. Figure 4 clearly shows one leg of the "horseshoe" vortex spiraling around the nose of a nozzle cascade with parallel sidewalls.

In the last few years, the Viscous Euler code has replaced EULER3D as the analysis code of choice for a wide variety of turbomachinery design problems. Improvements in computer technology have made it practical to run viscous codes such as Viscous Euler on a network of high-powered workstations, without the need for supercomputers.

Figure 5 shows the Viscous Euler calculation grid on a blade-to-blade plane for a high-pressure bucket vane. A similar calculation grid is generated for the nozzle passage, and a complete stage solution is obtained by automatically iterating between the nozzle and bucket solutions as they run in parallel on separate workstations. For a complete three-dimensional solution, up to 250,000 grid points might be needed in each blade passage to resolve the details of the secondary flows accurately. Figure 6 shows Mach number contours for this same vane in subsonic flow, and the trailing edge wake is clearly visible.

Figure 7 shows a comparison of calculated and measured total pressure contours on a plane perpendicular to the turbine axis just downstream of an intermediate pressure nozzle with

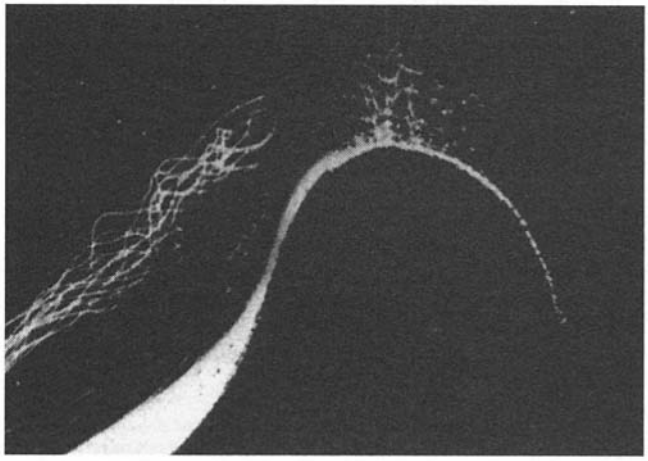

Fig. 4 Helium bubble traces in nozzle cascade

Downloaded 02 Jun 2010 to 171.66.16.104. Redistribution subject to ASME license or copyright; see http://www.asme.org/terms/Terms_Use.cfm

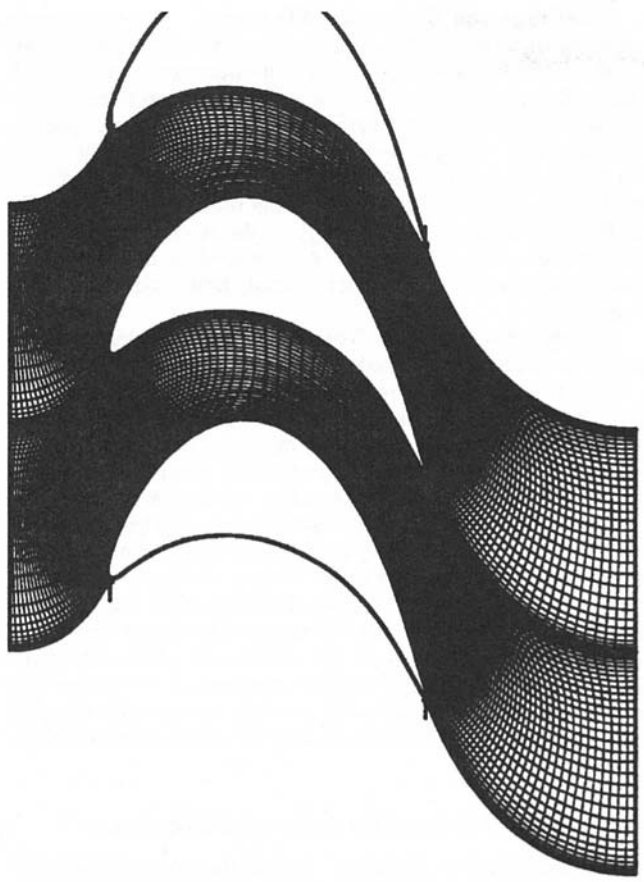

Fig. 5 HP bucket Viscous Euler calculation grid

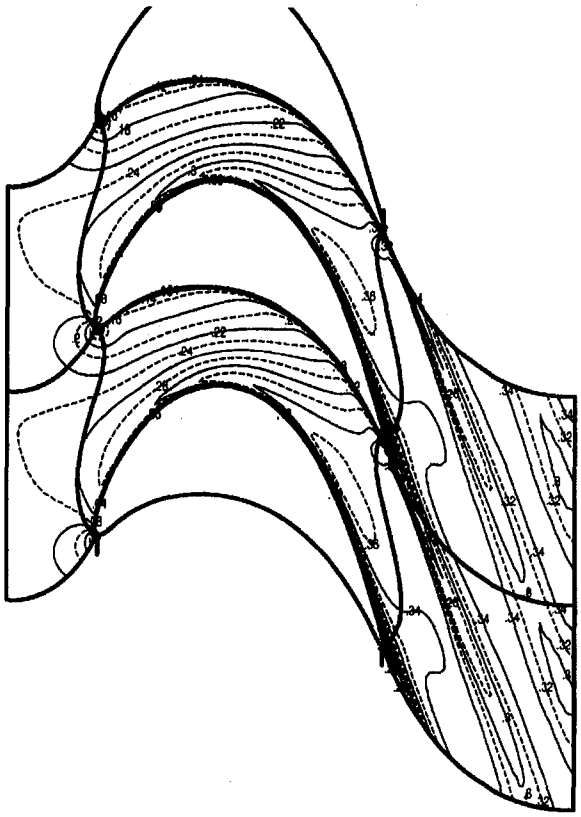

Fig. 6 HP bucket Viscous Euler Mach number contours

compound tangential lean. The calculated contours were generated from a Viscous Euler solution for the stage shown in Figs. 29 and 30. The measured contours were generated from traverse data obtained for the same stage with a small probe inserted between the nozzle and bucket in the subsonic air test turbine in the GE Aerodynamic Development Laboratory in Schenectady, New York (Figs. 27 and 28, described later in this paper). The Viscous Euler results agree remarkably well with the test results.

Comparisons with the CRD wind tunnel data, as well as with a variety of rig test data on aircraft engine and steam turbine stages, have shown that the Viscous Euler code accurately predicts the complex three-dimensional flow in turbine blade passages in both subsonic and transonic conditions, including the details of the secondary flows. This code is now used extensively to optimize aircraft engine turbine and compressor designs, as well as to develop advanced aerodynamic designs for steam and gas turbines.

NOVAK3D CFD Code. With improvements in computing power, the time required to obtain a Viscous Euler solution has been reduced to an acceptable level. However, the Viscous Euler code performs its calculations on a fixed structured grid, which the user must create prior to running the code. Consequently, a significant amount of time must be spent manually building and refining the calculation grid to ensure a valid solution in regions of rapidly changing flow quantities. If the user does not have an adequate knowledge of the solution in advance, he may not place grid points in the correct locations to resolve the flow properly. To eliminate the need for manual grid generation and refinement, CRD developed a code called NOVAK3D (Connell et al., 1993; Connell and Holmes, 1993; Braaten and Connell, 1994) that solves the three-dimensional time-averaged Navier–Stokes equations just as Viscous Euler does, but with an unstructured adaptive grid that automatically adjusts itself as the solution progresses to resolve areas of rapidly changing flow quantities. Figure 8 compares a Viscous Euler structured grid with a series of successively refined NOVAK3D grids. Figure 9 shows the calculation grid generated by the NOVAK3D code on a blade-to-blade plane for a transonic nozzle vane. More grid points have automatically been added in regions of high blade surface curvature, in the wake region, and in the region of the shock wave attached to the vane trailing edge. Because the grid refinement algorithm places grid points only where they are needed, creating a dense grid in regions of rapidly changing flow quantities and a coarser grid elsewhere, the code produces a more accurate solution in less computa-

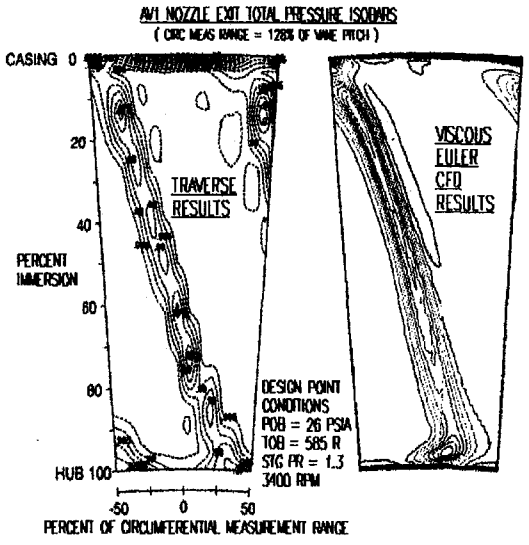

Fig. 7 IP nozzle Viscous Euler results and comparison to test data

Downloaded 02 Jun 2010 to 171.66.16.104. Redistribution subject to ASME license or copyright; see http://www.asme.org/terms/Terms_Use.cfm

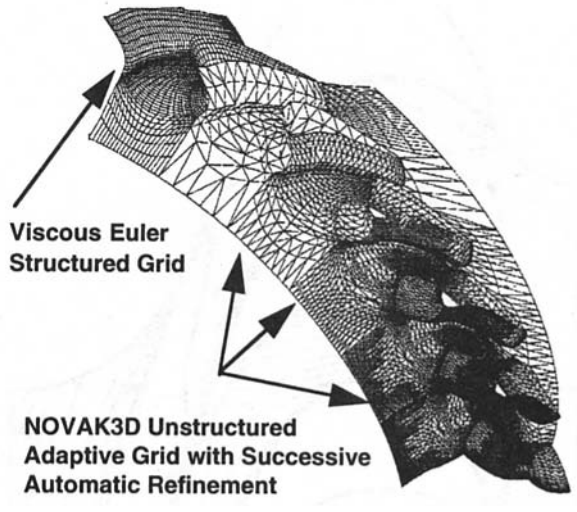

Fig. 8 Comparison of structured and unstructured grids in CFD codes

tional time. The code has been configured to accept solid model geometry input from computer-aided design programs in a variety of standard formats. With NOVAK3D's automatic grid generation, designers can obtain solutions to complex problems in a small fraction of the time that it would take with structured grid codes. Examples of the use of NOVAK3D to obtain flow solutions in such complex geometries as exhaust hoods and valve bodies are discussed later in this paper.

A three-dimensional physical model of wet steam behavior is currently under development for incorporation into NOVAK3D. This model will include detailed three-dimensional wet steam effects, such as homogeneous and heterogeneous moisture droplet formation and growth, droplet trajectories, and condensation shocks. The code will then be used to develop improved moisture removal devices for wet steam turbine stages. Better moisture removal devices will provide two significant benefits: improved efficiency, since stage efficiency improves about 1 percent for every additional 1 percent of moisture that is removed, and reduced bucket erosion. An extensive experimental program is planned to validate the wet steam CFD model to be incorporated in NOVAK3D.

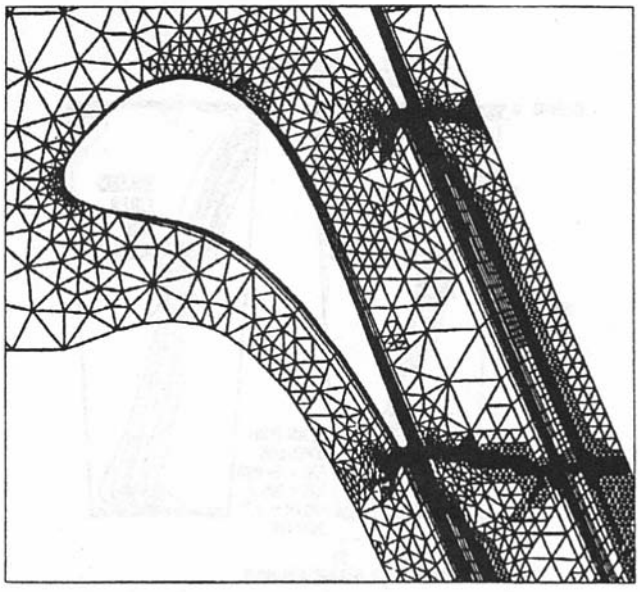

Fig. 9 NOVAK3D refined calculation grid for transonic nozzle

Multistage and Unsteady CFD Codes. A better understanding of unsteady flow effects and rotor–stator interactions is needed if the losses associated with them are to be reduced. The influence of these effects on performance has been implicitly accounted for in our traditional turbine performance prediction methods through the use of empirical correlations based on laboratory and field test data. However, it has been difficult to develop specific design features that reduce these losses due to the high expense and difficulty of the required testing. For this reason, renewed effort has been placed on developing the analytical capabilities to predict unsteady flows and rotor–stator interactions.

In early 1994, GE Power Generation and GE Aircraft Engines used the unsteady flow code developed by Rai and Madavan (1990) to analyze a steam turbine stage with a compound lean nozzle. Because the time required to achieve a solution with unsteady codes is still excessive, more recent efforts have focused on the calculation of steady-state multistage solutions using the passage-average approach of Adamczyk et al. (1990).

Losses due to shock waves, wakes, hub and tip leakage flows, and secondary flows propagate downstream and influence the performance of successive stages. Figure 10 shows some initial results from the Adamczyk code obtained for the third stage in a group of advanced vortex HP stages. The figure on the left shows vorticity contours at the nozzle exit plane, while the figure on the right shows vorticity contours at the bucket exit plane. Detailed comparisons of the code results with test data will be performed to validate the code for steam turbine applications.

New Design Features for Improved Efficiency

Advanced Vortex Blading. Before the advent of powerful computers and modern CFD codes, the complete, three-dimensional form of the equations governing the flow inside a turbine stage could not be used for practical design purposes. Designers were forced to make simplifying assumptions about the flow to reduce the equations to a manageable form. Dating back to the 1950s, GE steam turbine stages traditionally have been designed using a true free vortex radial flow distribution. In this type of design, the radial components of velocity are neglected and the assumption is made that the product of radius and tangential velocity is constant. These assumptions greatly simplify the equations and result in a flow characterized by constant axial velocity and constant work at all radii in the blade row. For shorter stages, free vortex designs with tapered and twisted nozzles and buckets can be very efficient, and considerably more efficient than purely cylindrical stages. For longer stages, however, the free vortex design often results in extremely

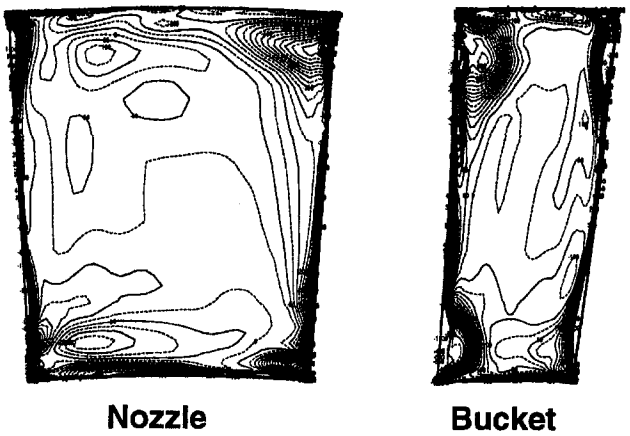

Fig. 10 Multistage CFD analysis—vorticity at stage 3 nozzle and bucket exit

Downloaded 02 Jun 2010 to 171.66.16.104. Redistribution subject to ASME license or copyright; see http://www.asme.org/terms/Terms_Use.cfm

twisted buckets that are difficult to design mechanically, and it produces high tip reactions that lead to high tip leakage losses.

The CFD codes available today allow accurate solutions of the fully three-dimensional viscous Navier–Stokes flow equations, and designers are no longer bound to the free vortex concept. In 1984, GE initiated a development program to investigate various "controlled vortex" design concepts, in which the radial flow distribution is tailored to maximize the efficiency of individual stages. This program was accelerated in 1990 and expanded to include the design and testing of a number of "advanced" vortex stage designs that began with the controlled vortex concept and incorporated variable tangential lean into the nozzles. Many of these concepts have been derived from advanced aircraft engine design technology, and were developed jointly with GE Aircraft Engines using the Viscous Euler CFD code. An extensive ongoing test program has been under way since 1990 to verify the predicted efficiency gains for these new concepts. All of these concepts share the following characteristics:

- The radial flow distribution is tailored to maximize efficiency based on the individual stage geometry and operating conditions.
- The total nozzle surface area has been reduced relative to a conventional design by using fewer nozzles per 360 deg with better aerodynamic profile shapes that retain the same total mechanical strength as a conventional design. In many cases, the number of nozzles in the diaphragm has been reduced by as much as 50 percent. This provides a net reduction in profile loss with no loss in mechanical integrity.
- Variable tangential or compound lean is used in the nozzles when it produces a significant gain in overall stage efficiency.
- Root reaction is increased in varying degrees to improve bucket root performance, and tip reaction is generally decreased relative to a free vortex design to reduce tip leakage.

Due to the quite different operating conditions in HP, IP, and LP stages, different concepts are used in each type of stage. In the HP section, stage pressure ratios are about 1.2. This pressure ratio is not limited by aerodynamic considerations, but rather by the pressure loading across the diaphragm at the high pressure levels occurring in the HP section. Consequently, nozzle cross sections must be relatively larger in size than bucket cross sections to carry the mechanical load. Figure 11 shows a typical advanced vortex HP stage. Figure 12 compares the radial distribution of reaction and flow angle for this design to a conventional free vortex design. In the advanced vortex design, overall stage reaction has been increased somewhat, although more at the root than at the tip, and root reaction is limited to about 10 percent to minimize thrust on the rotor. The flow angle relative to the axial direction has been decreased at the root and increased at the tip to shift flow radially inward toward the root. The flow angle shift at the root allows a more efficient, less cambered bucket root section to be designed, as shown in Fig. 5. The nozzle and bucket for each stage are carefully designed as a matched set to eliminate bucket incidence angle losses. Due to the relatively low velocities in the stage (see Fig. 6), the small size and strength of the secondary flow vortices, and the short blade height, nozzle lean has not proven to be an effective loss reduction method in this type of stage. A major program is currently under way to develop new design concepts to improve the efficiency of high-pressure stages further using a combination of CFD analysis and testing in our single-stage subsonic air turbine and the multistage low-speed research turbine at GE Aircraft Engines (Figs. 34 and 35, described later in this paper).

In the IP section, stage pressure ratios are generally in the range of 1.2 to 1.3. Velocities are somewhat higher than in HP

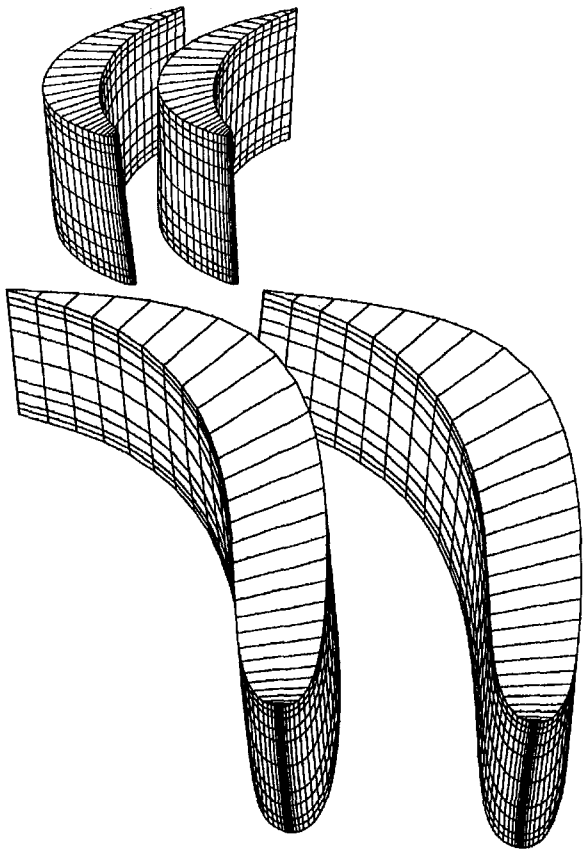

Fig. 11 Advanced vortex HP nozzle and bucket

stages, and blades are longer and more twisted. Figure 13 shows a typical advanced vortex IP stage. Figure 14 compares the radial distribution of reaction and flow angle for this design to a conventional free vortex design. In these stages, the flow is biased away from the sidewalls toward the more efficient midsection of the blade by increasing the throat at the pitchline, producing a nozzle that is slightly overcambered at the root and tip relative to the pitchline shape. Compound lean has been introduced in the nozzle to reduce the secondary flow losses, and root reaction has been increased to allow a more efficient, less cambered bucket root section to be designed. As in the HP stage, the nozzle and bucket for each IP stage are carefully designed as a matched set to eliminate bucket incidence angle losses. The radial flow distribution in the nozzle is determined using numerical optimization techniques described later in this paper. Stage test results obtained in the subsonic air turbine have demonstrated that advanced vortex stages of this type are the most efficient we have ever built.

Our analytical studies have shown that redistributing the flow radially and leaning the nozzle have only a weak effect on overall nozzle efficiency—the losses are simply redistributed. However, if the vortexing and lean are done in the proper combination, they can reduce the size and strength of the secondary flow vortices entering the bucket, particularly at the root, which leads to substantial improvements in bucket efficiency. The nozzle and bucket must be designed as a matched set to take full advantage of the benefits of blade lean.

In the LP section, stage pressure ratios are high enough to produce transonic velocities in the last few nozzles and buckets. Buckets are long and highly twisted, and diaphragm outer sidewall slant angles can approach 50 deg. The advanced vortex design concept used in the early LP stages is the same as that used in IP stages, as depicted in Fig. 13. In taller LP stages, some modifications are made to the IP design concept to produce the

Downloaded 02 Jun 2010 to 171.66.16.104. Redistribution subject to ASME license or copyright; see http://www.asme.org/terms/Terms_Use.cfm

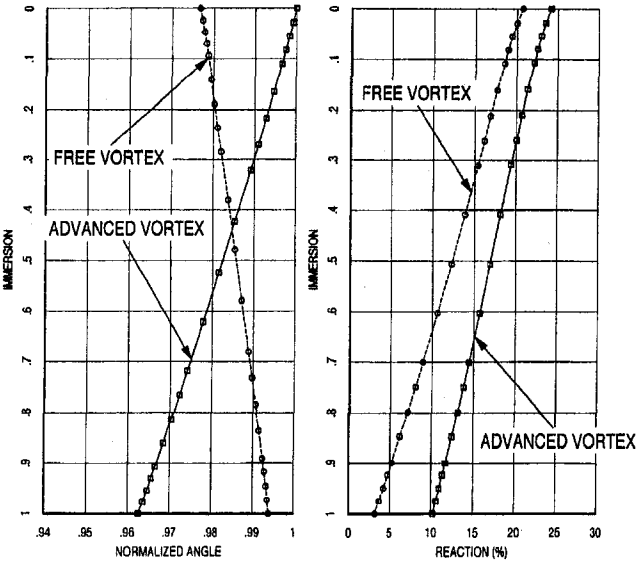

Fig. 12 HP stage nozzle exit angle and reaction distributions

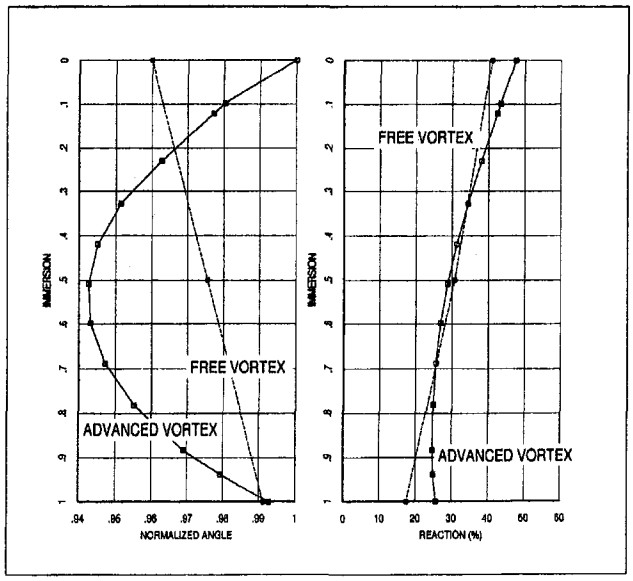

Fig. 14 IP stage nozzle exit angle and reaction distributions

nozzle shown in Fig. 15. First, the point of maximum bow in the blade is moved closer to the root to put more lean at the root, where it has the most benefit, and less at the tip. Second, a small amount of axial sweep is added to the nozzle leading edge to minimize the nozzle axial width over most of the length of the blade, thus reducing profile losses. The last-stage nozzle, and in some cases the next to the last nozzle, typically has straight tangential lean, with no bowing. In transonic nozzles, the transonic portion near the root is designed with a converging–diverging cross section to minimize shock losses.

Each individual advanced vortex stage in a customer's specific application is custom-designed to optimize its efficiency in conjunction with the other stages in the turbine section. Off-the-shelf blades are seldom used, because this necessarily involves compromising the efficiency of the design to fit the existing blading. The design automation and optimization tools that allow us to do this in a very short design cycle time are described later in this paper. Concurrent with the development of new aerodynamic design concepts, modern manufacturing technologies such as five-axis NC machining, precision forging, and precision casting are being utilized to allow advanced vortex blade shapes to be made in a cost-effective manner and in shorter manufacturing cycle times.

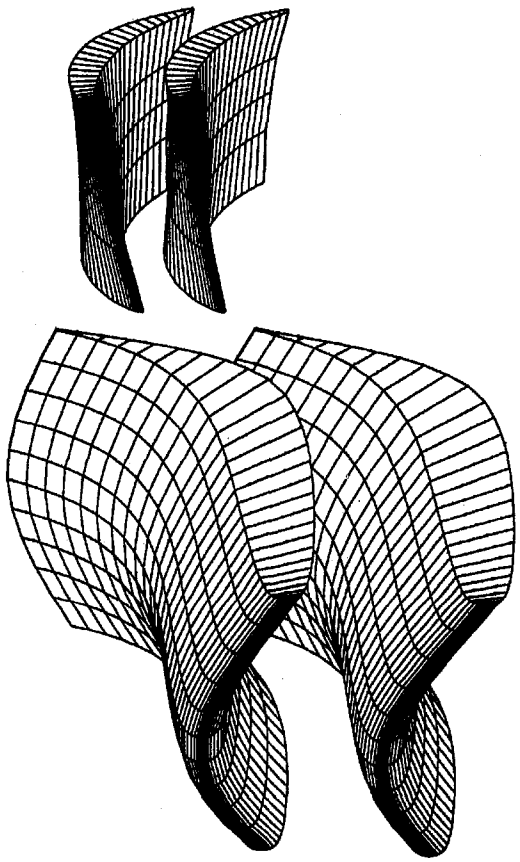

Fig. 13 Advanced vortex IP nozzle and bucket

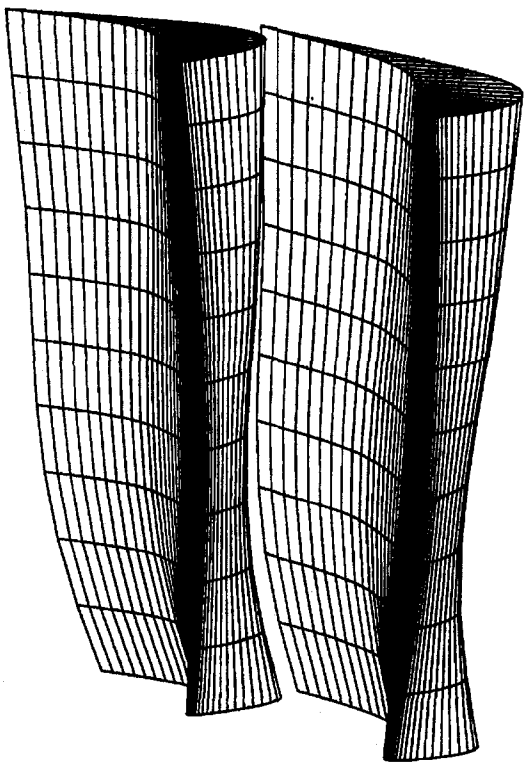

Fig. 15 Advanced vortex LP nozzle

Downloaded 02 Jun 2010 to 171.66.16.104. Redistribution subject to ASME license or copyright; see http://www.asme.org/terms/Terms_Use.cfm

Overall stage efficiency gains of 2 to 2.5 percent have been achieved on advanced vortex stages relative to our conventional free vortex designs, which are already very efficient. This includes the combined effects of reduced nozzle count, improved profile designs, optimized radial flow distribution, nozzle lean, and improved bucket tip seals. Advanced vortex stage designs are offered as a standard feature on all new utility-type fossil reheat steam turbines rated 200 MW and above. They can also be applied to fossil reheat turbines rated below 200 MW and to combined-cycle reheat turbines, and they are available for retrofit in HP, IP, and LP stages.

40-in. (1016 mm) Titanium Last-Stage Bucket. The last-stage bucket is one of the most important contributors to the performance and reliability of the steam turbine. Our last-stage buckets all share a common continuously coupled design technology, and they range in size from a 20-in. (508 mm) 3600 rpm bucket to a 48-in. (1219 mm) 3000 rpm titanium bucket. Design features of this family include:

- Improved vane profiles, including a convergent–divergent supersonic passage design with high solidity.
- Improved radial mass flow distribution to optimize efficiency.
- Improved tip leakage control that permits moisture removal.
- Continuously coupled covers, either side entry or over-and-under. These covers provide structural coupling and damping, and also control vane tip flow passage geometry for the reduction of leakage, secondary flow, and shock losses.
- Optimum location of midspan connection for structural damping and vibration control, either a loose tie wire or a nub-sleeve connection.
- Self-shielded erosion protection. No separate attachment of shielding is necessary due to the use of high strength erosion-resistant materials with excellent toughness characteristics and a proven service record.

With the last-stage buckets typically producing 10 percent of the total unit output, and up to 15 percent in some combined-cycle applications, improvements in last-stage efficiency can significantly impact the output of the total unit. Retrofitting an older last-stage design with a modern diaphragm and last stage bucket can typically improve heat rate and output by up to 1 percent. Replacement of an older LP turbine steam path with a modern steam path design can improve heat rate by an additional 1.0 to 1.5 percent. O'Connor et al. (1988) and Morson (1990) describe the family of modern last-stage buckets in more detail. The modern buckets can be retrofit into most existing units.

A recent addition to the 3600 rpm family is a 40-in. (1016 mm) titanium last-stage bucket, described by Morson et al. (1988). A series of rigorous mechanical tests of the new bucket were recently completed on the test rotor shown in Fig. 16, and all design criteria were met. A 48-in. (1219 mm) version for 3000 rpm application is also available.

Contoured Sidewalls. In the early 1980s, experimental investigations were conducted by CRD and the steam turbine business to determine the effects of outer sidewall contours on secondary flow losses. Prior research (Dejch et al. 1960) suggested that outer sidewall contours other than straight-parallel could have a beneficial effect on stage efficiency. A properly designed sidewall contour reduces secondary flow losses by reducing the cross-channel pressure gradients, thereby reducing the strength of the secondary flows. The contour also reduces the size of the loss region near the inner sidewall, and reduces nozzle profile losses due to the lower velocity at nozzle inlet. Contoured sidewalls are typically used in the first stage of a turbine section.

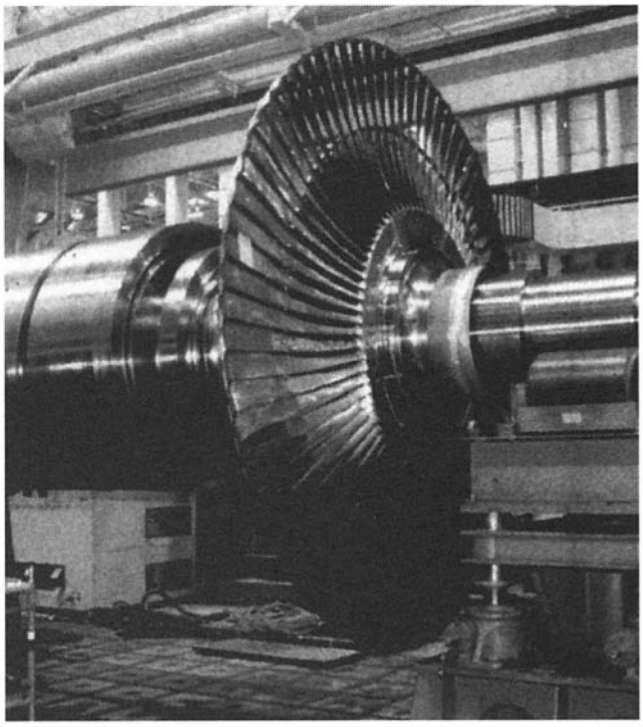

Fig. 16 40-in. (1016 mm) titanium last-stage buckets

GE's first running stage test of a steam turbine using contoured sidewalls was performed in 1983. This test was performed on a small low-energy, two-stage commercial mechanical drive turbine that included a converging sidewall contour on the first stage and a diverging-converging contour on the second stage. The contours were designed using guidelines presented by Dejch et al. (1960). An overall efficiency gain of 0.7 percent was realized. Wind tunnel cascade tests conducted in 1984 by CRD produced a diverging–converging sidewall contour that increased stage efficiency by 1 percent. An improved method for optimizing the shape of the contour for a given stage was also developed by CRD during this time period based on experimental results and extensive CFD analysis. In a parallel effort, a running stage test of a contoured sidewall was conducted in 1985 in the subsonic air turbine. The stage efficiency with the sidewall contour proved to be 1.5 percent greater than that for the equivalent stage with cylindrical sidewalls, as shown in Fig. 17. Subsequent tests on improved contoured sidewalls yielded gains of up to 2 percent in stage efficiency.

Contoured sidewalls are routinely used in mechanical drive turbines, ships service turbine-generator sets, and in the HP, IP, and LP sections of large fossil and nuclear power generation turbines, for both new units and uprate applications. A typical application might include contoured sidewalls in up to eight stages in the machine, depending on the turbine configuration, for an overall turbine efficiency gain ranging between 0.25 and 0.50 percent due to the contouring alone.

A family of sidewall contours has also been developed for the new solid particle erosion-resistant nozzle designs described by Sumner et al. (1985). The contours improve efficiency and, at the same time, increase the resistance of the nozzle to SPE damage. These contours are available for new and retrofit nozzle box designs for control stage and first reheat stage applications.

Bucket Tip and Shaft Packing Seals. An extended effort, until recently mostly experimental in nature, has been directed toward finding ways to minimize leakage through bucket tip and shaft packing clearances. Bucket tip leakage controls have typically utilized a single spill strip mounted on the upstream

Downloaded 02 Jun 2010 to 171.66.16.104. Redistribution subject to ASME license or copyright; see http://www.asme.org/terms/Terms_Use.cfm

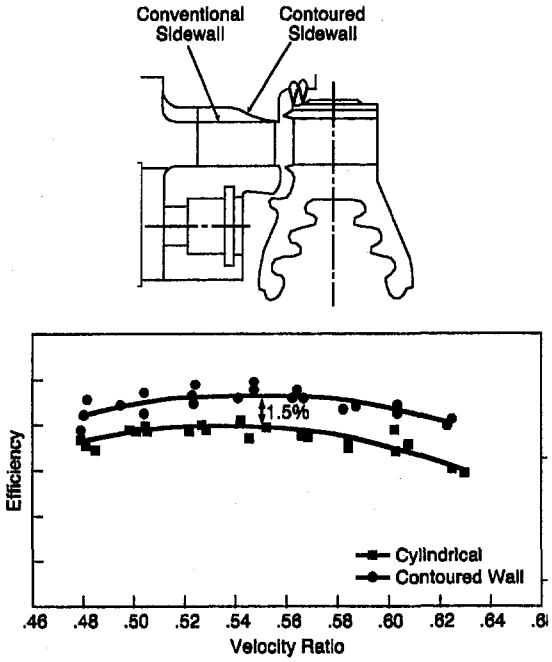

Fig. 17 Contoured sidewall test data

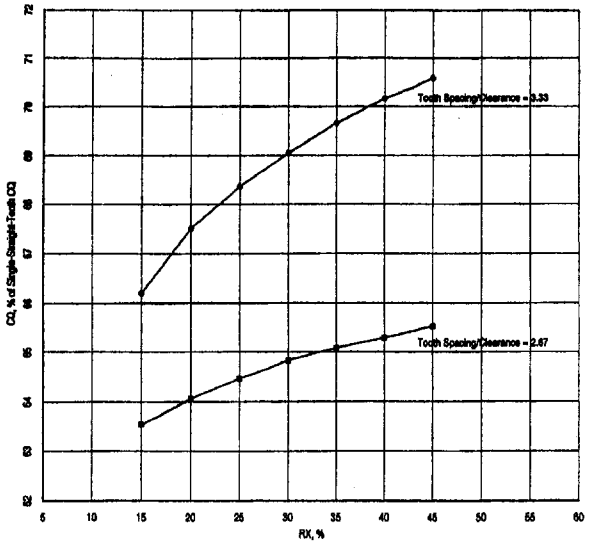

Fig. 18 Slant tooth bucket tip seal test results—optimum tooth spacing

side of the bucket shroud, or two spill strips mounted on either side of the bucket cover tenon. Leakage along the shaft is controlled by packings containing multiple teeth located between the diaphragms and the shaft and at the ends of the shaft. Leakage can be reduced by either reducing the radial clearance between stationary and rotating components, or by designing the seal geometry to create a tortuous path that induces turbulence and restricts the flow.

Experimental data on leakage control has been obtained largely through two-dimensional stationary air tests (such as the rig shown in Fig. 33) rather than more expensive three-dimensional rotating steam tests. Stationary air tests allow a much larger variety of leakage control configurations to be tested at relatively low cost. However, we have developed a unique, cost-effective method for testing new bucket tip seal concepts in our subsonic air turbine, by shrink-fitting a thin ring containing the tip seal geometry onto the outer rim of the blisk test wheel (described later in this paper). By testing the wheel with and without the new seal, the effects of the seal can be isolated.

Over the years, GE has tested a great variety of bucket tip seal configurations. The test results show that leakage flow is substantially reduced when a stepped or high-low spill strip is used. The configuration currently used on the majority of HP and IP bucket tip seals includes steps with double teeth on both the upstream and downstream sides of a recessed tenon. The application of these improved radial tip leakage controls improves sustained efficiency as well, because any damage to the improved controls due to a rub results in less increase in leakage than an equivalent rub to a single radial tip spill strip. Slant teeth also help to reduce leakage flow, as long as the proper tooth spacing has been selected. Figure 18 shows test data recently obtained in our seal test rig that illustrates the importance of choosing the optimum ratio of tooth pitch to radial clearance to minimize leakage flow.

All modern GE 20-in. (508 mm) last-stage buckets and larger now include a radial spillband on the bucket cover to maintain a tight radial clearance and minimize tip leakage flow. This spillband improves stage efficiency by as much as 3 percent depending on bucket length, which is equivalent to about 0.3 percent in overall turbine efficiency.

To complement our experimental program, we are now using a commercially available three-dimensional viscous code called STAR-CD to perform detailed parametric analyses of new bucket tip leakage control configurations. Figure 19 shows velocity vectors calculated by STAR-CD at the leading edge of a flat bucket cover with slant teeth mounted on the casing. The code clearly shows the vortex structures in the leakage path. The code is used as a numerical test vehicle to identify promising seal configurations that warrant testing in either the stationary seal test rig or the subsonic air turbine.

A new area we are investigating in more detail is the effect of the tip seal leakage flow on the downstream blade rows as the leakage flow reenters the steam path. The flow leaking over the top of the bucket cover enters the tip seal passage with a high tangential velocity component. While the tortuous path through the seal geometry reduces the axial component of the leakage flow, it does relatively little to affect the tangential component. As the leakage flow re-enters the steam path on the downstream side of the bucket, the still largely tangential flow must mix with the largely axial flow leaving the bucket. This generates mixing losses and can lead to incidence angle problems in the downstream nozzle. Traverse measurements of stage exit swirl angle obtained in the subsonic air turbine have confirmed this behavior, as shown in Fig. 20. We have refined the tip leakage models in our quasi-three-dimensional flow solver to reflect this behavior (also shown in Fig. 20). This allows designers to account for this effect more effectively in the pre-

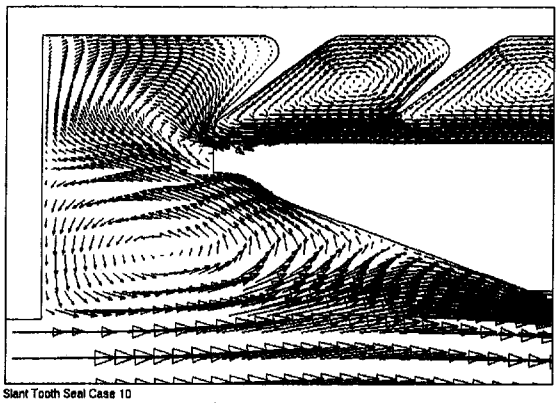

Fig. 19 CFD analysis of bucket tip seal passage—velocity vectors

Downloaded 02 Jun 2010 to 171.66.16.104. Redistribution subject to ASME license or copyright; see http://www.asme.org/terms/Terms_Use.cfm

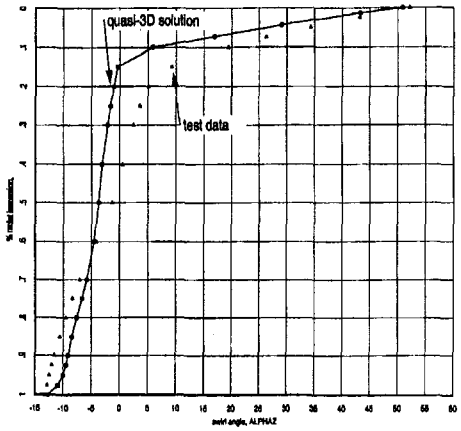

Fig. 20 Influence of tip seal reentry flow on stage exit flow angle—comparison of quasi-three-dimensional analysis to test data

liminary design of multistage turbines. The behavior of re-entering tip seal flow is also being thoroughly investigated in the low-speed research turbine tests on HP stages mentioned earlier.

Exhaust Hoods. Poor aerodynamic design of the exhaust casing or hood can produce a large pressure drop from the last-stage bucket exit to the hood exit. This pressure drop constitutes an efficiency loss because it represents energy that cannot be used by the turbine to produce power. A well-designed hood can diffuse the flow, causing the static pressure to increase from the last-stage bucket exit to the hood exit flange to match the fixed condenser pressure. This pressure recovery gives the turbine an effective back pressure that is lower than the condenser pressure, so that more energy is available for producing power. In this manner, a good diffusing hood can produce a significant overall gain in efficiency.

In downward flow configurations, the exhaust hood must turn the flow downward 90 deg before it enters the condenser inlet. In the patented GE hood design concept, structural support plates inside the hood are used to partition the total flow area into smaller passages in which flow diffusion can be carefully controlled. Carefully designed flow guides and vanes are used to improve the aerodynamic performance of the hood further. Internal flanges, support struts, pipes, and other protrusions into the flow passages that cause efficiency losses and generate noise are removed or minimized.

GE's approach to exhaust hood design in the past has been purely experimental. To optimize a new design, the internal flow passages of the hood were duplicated in an exact scale model, which was tested in an air flow test facility at GE's Aerodynamic Development Laboratory. Since the early 1960s, literally dozens of different exhaust hood models in hundreds of different configurations have been tested, and a performance prediction and design method based on various hood geometry parameters has been developed from this extensive test data base.

Axial flow exhausts have significant size and efficiency advantages over downward flow exhausts. They are simpler to design and build, and can be much more efficient diffusers than downward flow exhausts. The velocity distribution at the exhaust flange can also be made quite uniform, resulting in improved condenser performance.

Axial flow hoods lend themselves to a more analytical design approach because of their simpler geometry compared to downward flow hoods. A paper by Sovran and Klomp (1967) has been particularly useful. GE has designed many axial flow hoods based on this paper, and laboratory tests on scale models have confirmed the excellent performance of these designs.

Our approach to exhaust hood design has improved dramatically in the last two years, with the advent of CFD codes that are capable of accurately modeling the complex geometry and flow phenomena inside exhaust hoods. Figure 21 shows a computer-generated solid model of the internal components of a downward flow diffusing exhaust hood that had been tested in the laboratory using lampblack and oil to visualize the flow. Figure 22 shows sample results from an analysis using the STAR-CD code, in this case velocity vectors and magnitudes. The code was able to predict the visualized flow features and measured pressure recovery very well. Because STAR-CD uses a structured grid approach, generating the solid model and the calculation grid took several man-months. However, this was less time than it took to build the original air test scale model, and the analysis yielded far more detailed information about the flow inside the hood than was obtained in the laboratory model tests. Numerous design refinements have already been incorporated into our downward flow hood designs as a result of using CFD analysis.

The NOVAK3D CFD code has proven to be an extremely useful tool for the analysis of complex stationary flow components such as exhaust hoods. Because it eliminates the need for time-consuming manual grid generation and refinement, solutions to complex problems can be obtained in a fraction of the time required with structured grid codes. Figure 23 shows an analysis of an axial flow hood that contains a number of struts, pylons, and pipes. The conical outer wall has been removed for clarity, and only the surface grid is shown. Once the surface model of the hood was created using a CAD program, NOVAK3D was able to create a grid and converge to a solution in only five days on a single workstation. Figure 23 also shows "flow ribbons" that follow streamtubes through the flow, which indicate that the flow is generally well behaved throughout the hood.

The NOVAK3D code was used to redesign the large pylons supporting the hood to eliminate large regions of separated flow downstream of the pylons. The top of Fig. 24 shows velocity vectors around the original pylon. A packing seal pipe is located downstream of the pylon in a region of massive separation. The bottom of Fig. 24 shows the redesigned, more streamlined pylon. The packing seal pipe has been relocated inside the new pylon, and the region of separation has been eliminated.

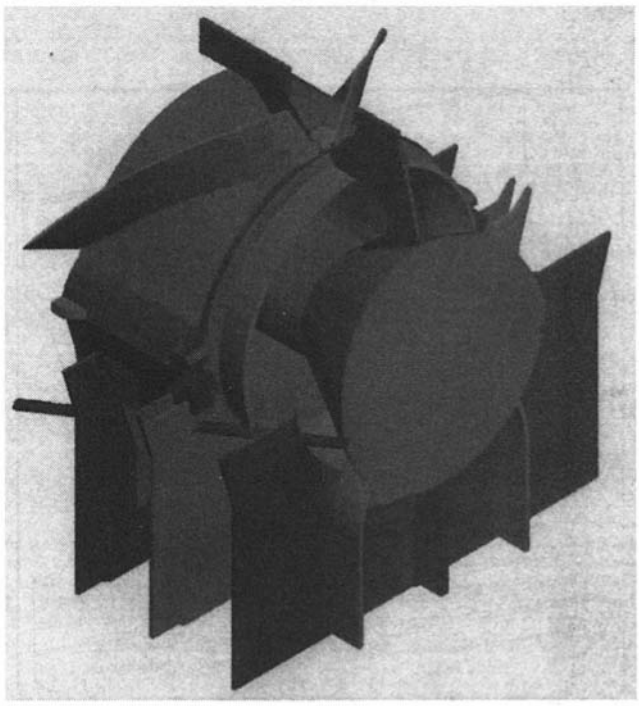

Fig. 21 Solid model of downward-flow exhaust hood for CFD analysis

Downloaded 02 Jun 2010 to 171.66.16.104. Redistribution subject to ASME license or copyright; see http://www.asme.org/terms/Terms_Use.cfm

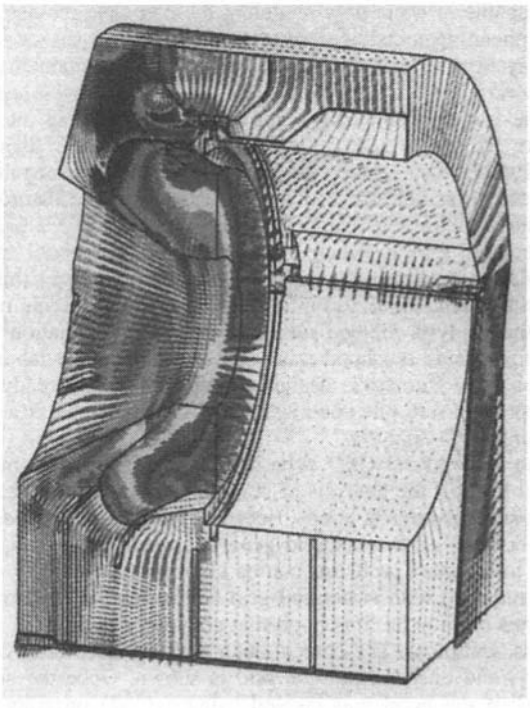

Fig. 22 Velocity vectors in downward-flow exhaust hood

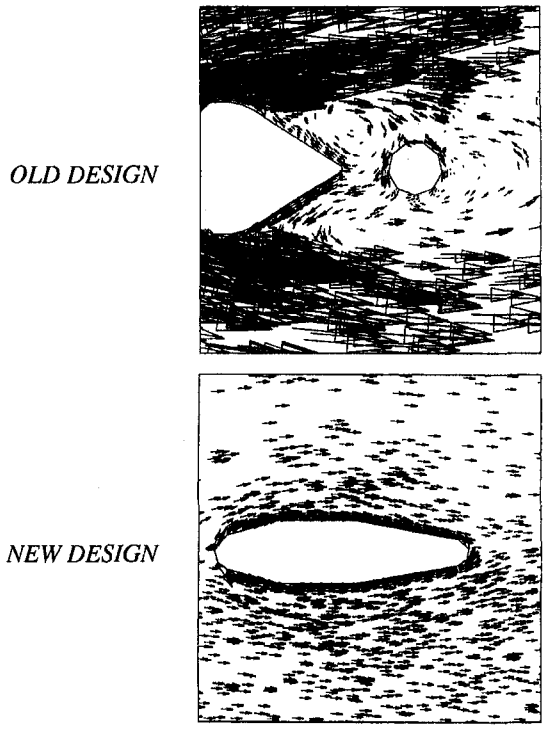

Fig. 24 NOVAK3D analysis of flow near struts in axial-flow exhaust

Valves and Inlets. A new development program has been initiated to develop more efficient and cost-effective inlet and valve designs using the NOVAK3D code to analyze the flow in the complicated geometries of these components. Figure 25 shows the surface grid generated by NOVAK3D for a steam turbine bypass valve that previously had been air tested in GE's Aerodynamic Development Laboratory. Figure 26 compares the valve flow coefficient calculated by NOVAK3D at two different valve lifts to the air test data, and it shows that NOVAK3D is able to predict the flow coefficient quite well. The NOVAK3D solution has provided many valuable insights into the behavior of this valve and others, and improvements are being implemented.

Laboratory Test Programs

Subsonic Air Turbine. The principal test vehicle used for the development of new stage design concepts is the subsonic air turbine located in GE Power Generation's Aerodynamic Development Laboratory in Schenectady, New York. This rig, shown in Figs. 27 and 28, permits the quick and accurate evaluation of turbine test stages at actual operating speeds and pressure ratios using compressed air as the working fluid. In addition to traditional performance testing, nozzle and stage exit traversing as well as laser-assisted data acquisition procedures are employed to collect more detailed flow field information. Numer-

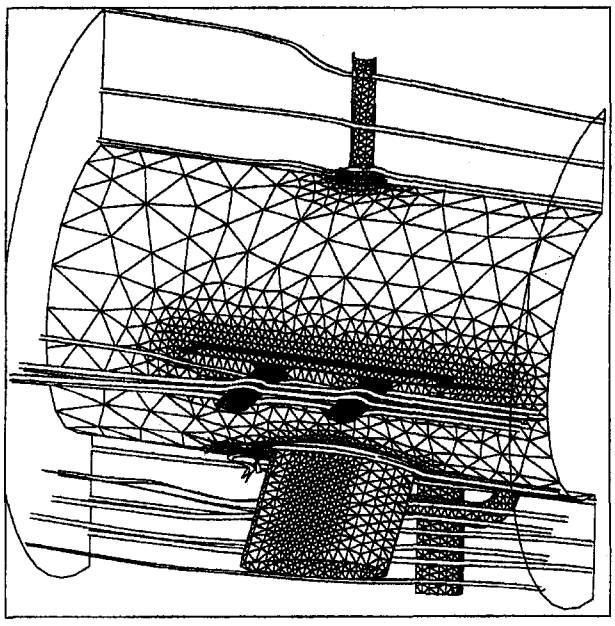

Fig. 23 NOVAK3D analysis of axial-flow exhaust with "flow ribbons"

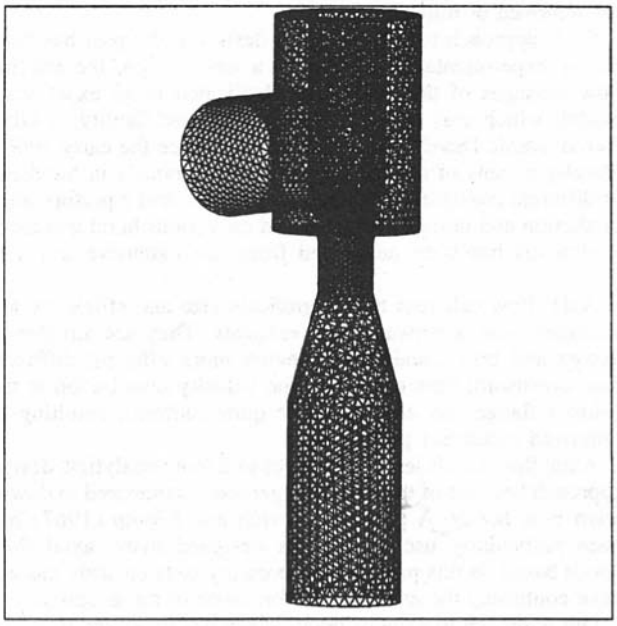

Fig. 25 NOVAK3D grid for bypass valve

Downloaded 02 Jun 2010 to 171.66.16.104. Redistribution subject to ASME license or copyright; see http://www.asme.org/terms/Terms_Use.cfm

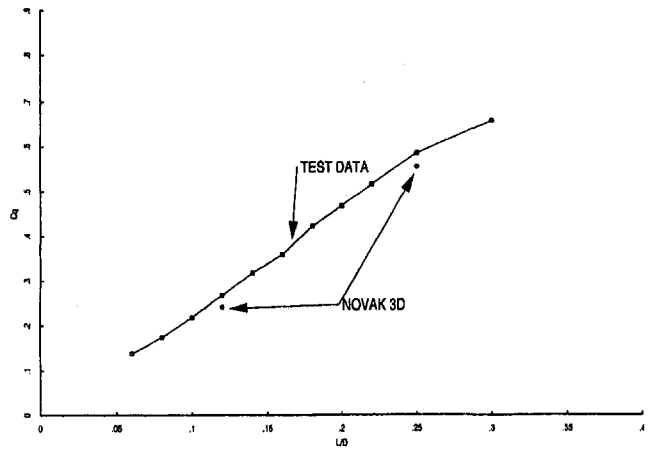

Fig. 26 NOVAK3D analysis of bypass valve—comparison of calculated flow coefficient with test data

ous new configurations have been tested in this facility over the past three years to confirm that significant efficiency gains have been achieved, and to validate the CFD codes.

The facility is arranged as a closed loop. A 4810 HP centrifugal compressor is used to circulate the air around the loop, and a smaller makeup air compressor permits the desired stage inlet pressure to be maintained. Prior to reaching the test section, the air supply passes through a water-cooled heat exchanger to permit the stage inlet temperature to be accurately maintained. A hydraulic actuation system slides the inlet plenum apart from the exhaust scroll, permitting easy access to the test stage. Test wheels are about 38 in. (965 mm) in diameter overall and have active blade lengths in the 2-in. (50.8 mm) to 5-in. (127 mm) range. Shaft speeds vary between 2000 and 4800 rpm. Figure 29 shows a typical air turbine test diaphragm with compound lean nozzles designed for an intermediate pressure stage, while Fig. 30 shows the test wheel for the same stage.

A water-cooled inductor type dynamometer that is supported on hydrostatic oil pads is used to measure the shaft torque developed by the wheel. An enhanced accuracy rotary torque meter provides an additional torque reading for comparison and redundancy. A coupling that permits axial movement is used for the gear-driven positioning of the wheel relative to the diaphragm. This feature is particularly useful for accurately setting the nozzle-to-bucket axial gap and it provides a way to study the effect of changing the edge-to-edge distance easily. A bearing load loss cell system floats the entire stub shaft and bearing assembly on a hydrostatic oil film. This permits the torque loss due to bearing friction to be determined accurately during all running conditions.

Traversing at nozzle and bucket exit planes is done using thermocouple probes for temperature measurement, and three-hole wedge and cobra probes with autonulling features for pressure and flow angle measurements. A recent innovation in the facility allows laser-Doppler velocimetry and laser light plane flow visualization techniques to be used to further our knowledge of the flow mechanisms responsible for improved stage designs. An instrumentation tunnel that includes a five-axis traverse mechanism (shown in Fig. 31) permits the accurate positioning of laser probes and a mirror for directing the laser light into the interior of a nozzle passage. The laser light passes through a specially designed fused silica window installed in the outer wall of the diaphragm. Figure 32 shows a vortex structure at the exit plane of a leaned nozzle visualized with the laser light plane technique. The laser light plane data acquisition system is currently undergoing development to improve its ability to capture video images of flow features with greater clarity. This technique, along with the laser-Doppler velocimetry, is providing additional data for validating the CFD codes used to design and evaluate alternative aerodynamic design concepts.

Air turbine test wheels, such as the one shown in Fig. 30, are produced as a "blisk" (short for "bladed disk"), in which the wheel, buckets, and integral bucket covers are machined out of a single disk of metal with a high degree of precision. The blisk construction eliminates the time-consuming operations associated with assembling individual buckets on the wheels, and reduces the manufacturing time by more than 50 percent. Before a new design concept is committed to test hardware, plastic parts are made using a stereolithography process to visualize new components with complex shapes, and to perform manufacturing producibility studies. By using these rapid prototyping methods, we have dramatically reduced our development cycle time for new aerodynamic design concepts, and have accelerated the introduction of new high-efficiency features into our product line.

Tip Seal Test Rig. New noncontacting leakage control devices are tested in the rig shown in Fig. 33 using compressed air. The rig accommodates stationary two-dimensional models of seal geometries that are machined into 6-in.-long (152 mm) flat plates. These seal strips feature straight, slant, stepped, high-low and other tooth arrangements in combination with smooth and contoured bucket cover or shaft surfaces. For bucket tip seal tests, the test section in the rig can simulate the leakage flow that goes over the bucket cover and through the bucket tip seal, as well as the main flow that goes under the cover and contributes to the stage output. The leakage flow is measured using an ASME orifice plate, while the main flow is measured using an ASME flow nozzle. The pressure level in the main flow and the pressure ratio across the seal can also be varied separately.

CFD analyses are used along with this rig to screen potential seal design candidates. Figure 18 shows typical data obtained in the rig in a recent test series designed to determine the optimum tooth spacing for a slant tooth bucket tip seal. Figure 19 shows the equivalent CFD analysis using the STAR-CD code. The more promising candidates are then tested on a running stage in the air turbine.

Low-Speed Research Turbine. The multistage low-speed research turbine (LSRT) shown in Fig. 34 is located at the GE Aircraft Engines Aerodynamics Research Laboratory in Cincinnati, OH. It is used to test large-scale models containing up to three stages in an environment where very detailed measurements of the flowfield can be made. A cross section of the LSRT is shown in Fig. 35. The LSRT has a constant casing

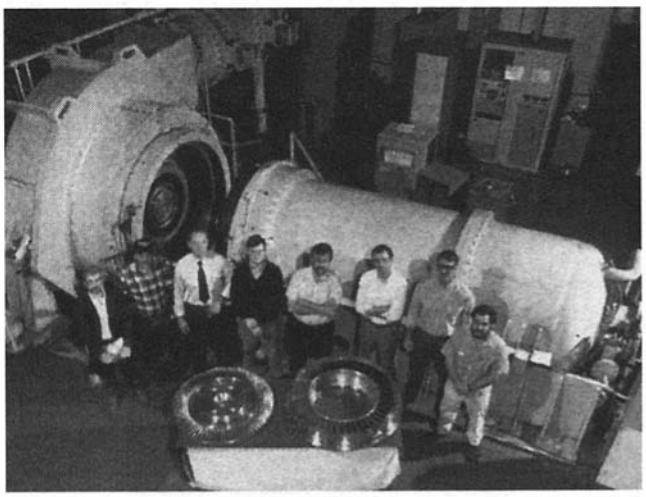

Fig. 27 Subsonic air turbine test facility

Downloaded 02 Jun 2010 to 171.66.16.104. Redistribution subject to ASME license or copyright; see http://www.asme.org/terms/Terms_Use.cfm

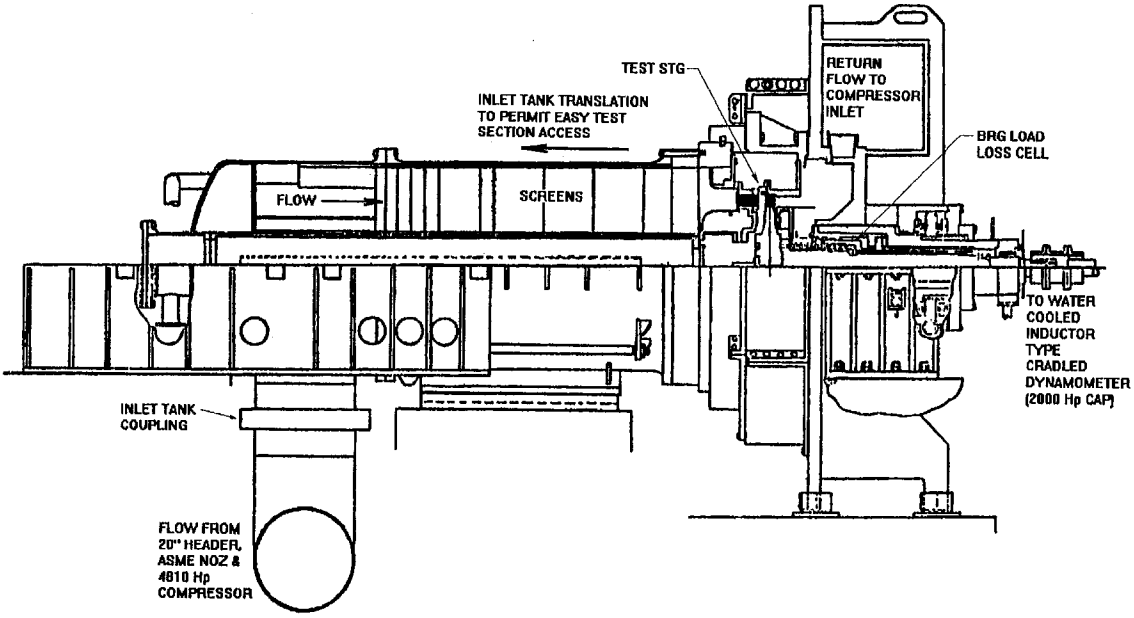

Fig. 28 Cross section of subsonic air turbine test facility

diameter of 60 in. (1.524 m), a vertical axis of rotation, a calibrated intake system, and Plexiglas casing windows, which mount into large steel casings. Ambient air is pulled from the inlet at the top through the turbine blading and into a large plenum beneath the turbine. This air, which is drawn through the blading by a large centrifugal blower located next to the plenum, causes the turbine to rotate. The power generated by the test turbine is used to assist in driving the blower, saving roughly one-third of the power requirements for the facility. The design tip speed for the turbine is 161 ft/sec (49.1 m/s) at 616 rpm.

The rate of mass flow through the turbine is controlled by a set of variable inlet guide vanes on the blower and by variable air-bleed valves in the outer cylinder. The blower exhausts the air from the turbine into an air-handling/mixing system outside the laboratory. This system mixes the exhaust air with outside ambient air in varying proportions before it is returned to the lab building, thereby maintaining a constant temperature and pressure environment in the lab.

Individual nozzles and buckets are precision-molded from high-strength plastic and assembled into rings and disks, thus allowing a wide variety of turbine geometries to be modeled. The airfoils are large enough to be instrumented with a matrix of static pressure taps. A rotating scanivalve and slipring allow measurements to be made in the rotating frame. A variety of measurement techniques, including laser-Doppler velocimetry, are used to gather detailed information about the flowfield. As mentioned earlier, the LSRT is currently being used to test new design concepts specifically targeted to improve the efficiency of high pressure stages.

Design Automation and Optimization

For new turbine designs, it is often necessary to perform numerous labor-intensive and time-consuming design iterations before all design requirements are met. The turbine stages in a given section must be optimized to produce maximum efficiency, while at the same time mechanical and producibility requirements must be met.

To achieve dramatic reductions in design cycle time, CRD has developed a unique and innovative workstation-based tool for the fast design of blade cross sections. In this tool, called Bezblade, blade cross-sectional shapes are described in parametric form as smooth Bezier curves. Through a user-friendly graphic interface, shown in Fig. 36, the aerodynamic designer has direct control over familiar geometric design parameters such as blade stagger, passage throat, blade thickness, cross-sectional area, and leading and trailing edge wedge angles. The blade shape can be changed by either using a mouse to drag the Bezier curve control points, by dragging sliding controls representing each design parameter, or by directly typing in

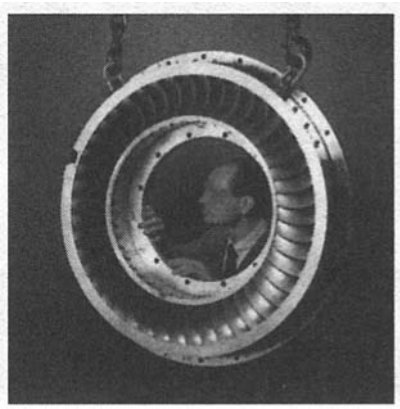

Fig. 29 Advanced vortex test diaphragm

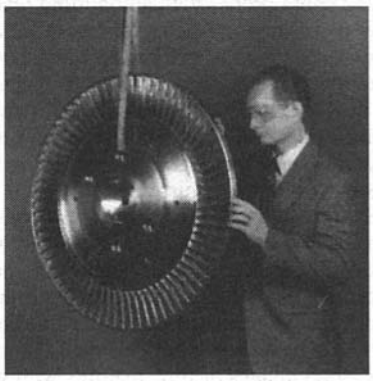

Fig. 30 Advanced vortex "blisk" test wheel

Downloaded 02 Jun 2010 to 171.66.16.104. Redistribution subject to ASME license or copyright; see http://www.asme.org/terms/Terms_Use.cfm

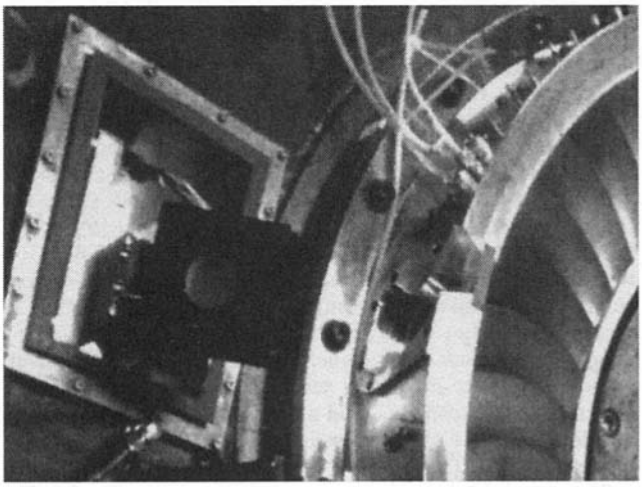

Fig. 31 Laser tunnel and optics in subsonic air turbine

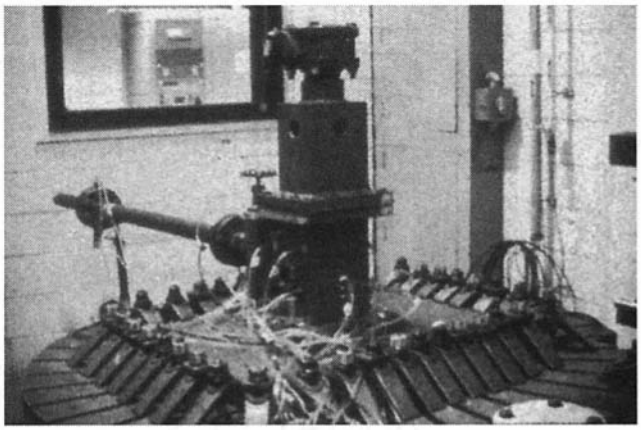

Fig. 33 Tip seal test rig

the parameter values. The Bezier curve representation allows individual parameters to be varied without requiring fine tuning of the other parameters to achieve reasonable shapes. The program is coupled to a fast two-dimensional flow solver that allows the designer to manipulate the blade shape and receive quick feedback on the effect of the shape change on the blade surface Mach number distribution. Individual blade cross sections can be radially stacked to form a complete blade, and curves are automatically plotted of the various blade geometry parameters as functions of radius. By directly modifying these curves using the mouse, the stackup can be quickly smoothed out to produce the final blade shape.

A significant improvement was made to Bezblade by coupling it to a two-dimensional version of NOVAK3D and using a linear perturbation method to compute sensitivities of the flow solution to the positions of each of the Bezier control points. Once the sensitivities have been computed, the designer can manipulate the blade shape and receive immediate, real-time updates on the effect of the shape change. The blade surface Mach number distribution changes literally as fast as the designer can change the shape with his mouse.

Bezblade has been used with great success to design advanced vortex stages for production units. While this design tool has dramatically reduced design cycle time, the design engineer must still use Bezblade in a manual, iterative fashion until he is satisfied that he has achieved an optimum design, and he must visually evaluate the quality of the blade design. To achieve further reductions in cycle time in the optimization process, we have made use of a design optimization computer program developed by CRD called Engineous (Powell et al., 1990). GE's many uses of Engineous are described by Ashley (1992). Engineous is a user-friendly generic software shell that automatically iterates design programs until constraints and design goals are met. Engineous captures human design knowledge in a "knowledge base" by querying the engineer for the required rules. It does not attempt to replace the designer, but retains the knowledge of different specialists in multiple disciplines. When design knowledge is incomplete, which is often the case with rapidly changing technology, Engineous combines its own intelligent searching heuristics with the existing knowledge to solve the problem. It performs the tedious work required to iterate design and analysis codes (such as manipulating and editing input data, running programs, and scanning output files), and it applies design knowledge to modify design parameters. By delegating this work to Engineous, engineers can realize a

Fig. 32 Laser light plane flow visualization

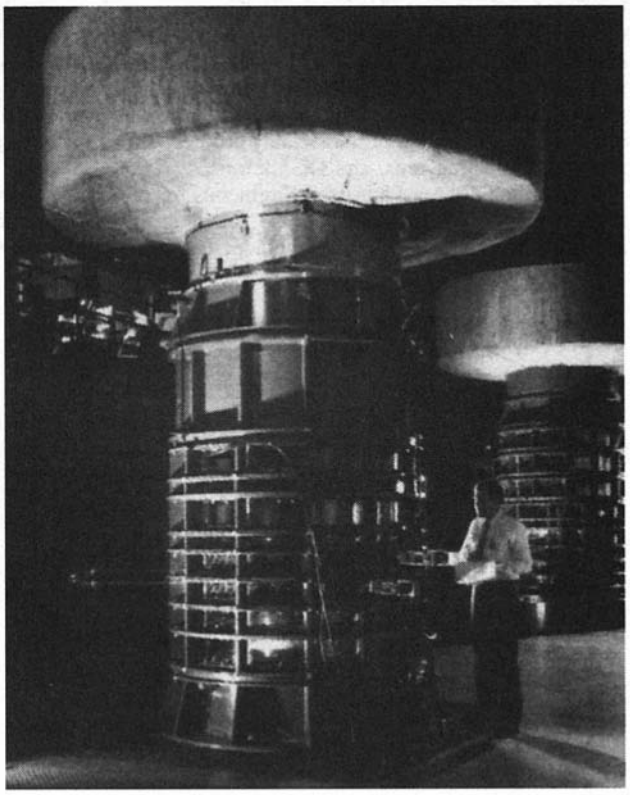

Fig. 34 Low-speed research turbine test facility at GE Aircraft Engines

Downloaded 02 Jun 2010 to 171.66.16.104. Redistribution subject to ASME license or copyright; see http://www.asme.org/terms/Terms_Use.cfm

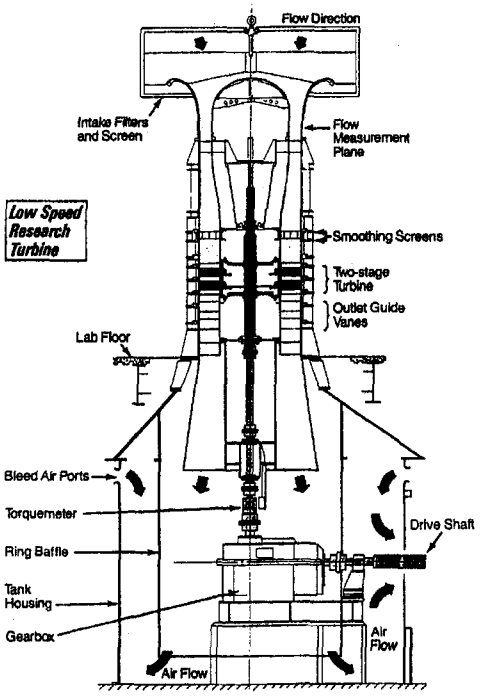

Fig. 35 Cross section of low-speed research turbine test facility

10:1 improvement in the time required to develop a new design, can minimize human error, and can achieve improved designs.

Because Engineous is automated, it can explore many more design options and parameter trade-offs in a given period of time. Additionally, the program's own searching heuristics and numerical optimization techniques often turn up new design solutions that designers had not thought of before. Engineous can also couple design codes from many disciplines, such as aerodynamics and mechanical design, to effectively balance interrelated and often conflicting goals. The program dynamically displays its results as they unfold, allowing designers to analyze solutions during and after the run, applying their own judgment to the problem. The program has been used successfully by many GE components for the design of such products as aircraft engine centrifugal compressors and turbines, superconducting generators, cooling fans, and DC motors.

GE Aircraft Engines has used Engineous for preliminary turbine stage layout (Lee et al., 1993; Goel et al., 1993) with a better than five to one improvement in design cycle time. Encouraged by this success, GE Power Generation coupled a quasi-three-dimensional throughflow program to Engineous, so that the radial flow distribution in Advanced Vortex stages could be optimized. Engineous automatically runs a sequence of six design codes to optimize the radial flow distribution for a given stage in only a few hours running on a workstation, a procedure that used to take an engineer several weeks to do manually.

Based on the success of an early attempt by GEAE to use Engineous to design airfoil sections (Shelton et al., 1993), GE Power Generation and CRD developed an automated workstation-based system that uses Engineous to optimize three-dimensional blade profiles to maximize efficiency while meeting all mechanical design requirements. The system was created by coupling Engineous to Bezblade, a two-dimensional flow solver, a knowledge base containing aerodynamic and mechanical design rules and constraints, and a number of other blade design utilities. This suite of programs is known as the Turbine Airfoil Design System (TADS).

The overall blade design process is illustrated in Fig. 37. The initial layout of the turbine section is done by the Thermodynamic Layout Program (TLP) module, which generates thermodynamic data including entrance and exit flow angles for all of the blade rows based on a quasi-three-dimensional streamline calculation. This layout incorporates the effect of blade lean and other advanced vortex features. An engineer sets up an initial baseline blade design file based on TLP output, and launches TADS. For each bucket design, five cross sections equally spaced from root to tip are designed simultaneously on five separate workstations to reduce the design cycle time. For each of these cross sections, Engineous changes the blade cross-sectional shape using Bezblade, runs the flow solver, evaluates the output, and makes new changes to the shape based on the results of its last change. It continues to iterate on the design until it achieves maximum blade "quality," which is defined as a combination of factors that ensure that the optimum blade surface Mach number distribution is achieved, and that the blade shape is radially smooth. The most difficult element in the system to develop was the translation of the designer's visual subjective perception of the design into an analytic evaluation that the computer could perform.

The designer can monitor the optimization process for each cross section by calling up the workstation screen shown in Fig. 38. The current blade shape is displayed in the lower left window, and the corresponding blade surface Mach number plot is displayed in the lower right window. The blade quality parameter is displayed in the upper right window. Figure 39 illustrates the type of shape changes made by the system during the optimization process. These windows are updated every few seconds

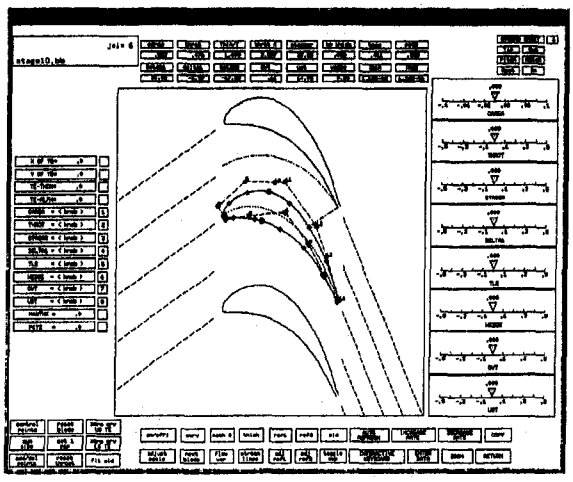

Fig. 36 Bezblade screen

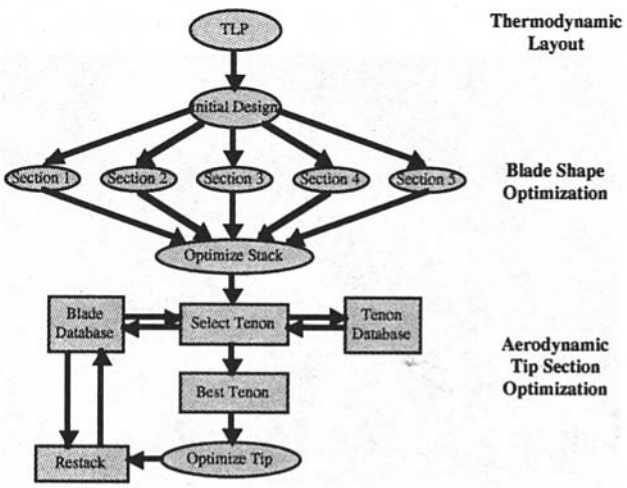

Fig. 37 TLP/TADS blade design process

Downloaded 02 Jun 2010 to 171.66.16.104. Redistribution subject to ASME license or copyright; see http://www.asme.org/terms/Terms_Use.cfm

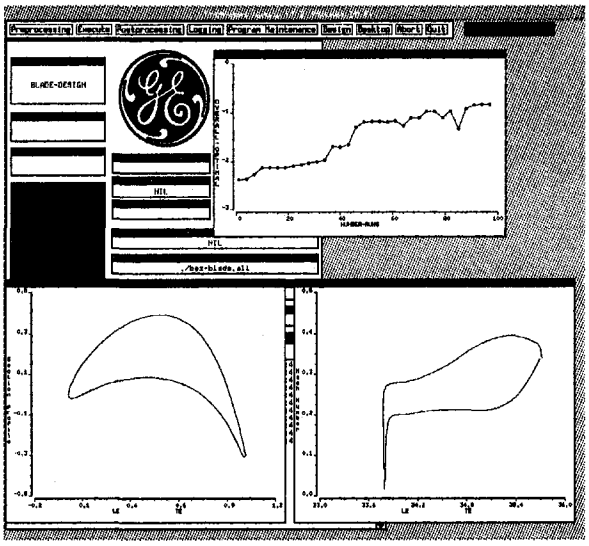

Fig. 38 TADS/Engineous screen

as the optimization proceeds. Typical cross-sectional designs require one to four hours of execution time, depending on the quality of the initial baseline design.

Once the five cross sections have been designed, TADS brings them together and uses Engineous to smooth out the blade stackup. The system then enters the tenon database and selects a tenon that meets mechanical design requirements and fits on the bucket tip section as closely as possible. If the tenon cross section is larger than the vane tip section, Engineous redesigns the tip section to fit around the tenon, and then modifies the vane below the tip section to achieve a smooth blend. Figure 40 shows a typical intermediate pressure bucket designed by the system.

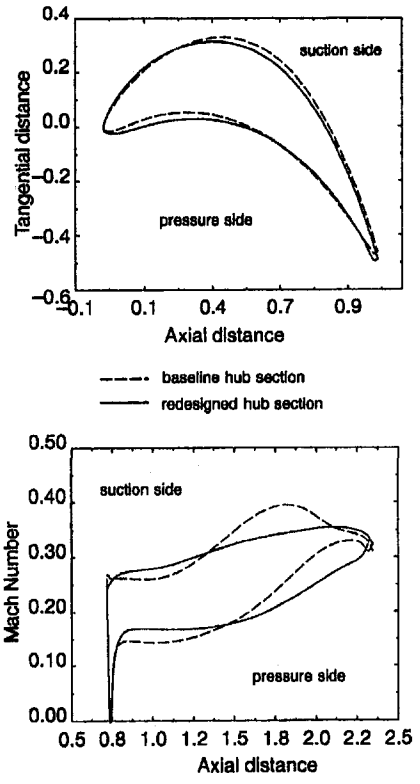

Fig. 39 Results of TADS blade shape optimization

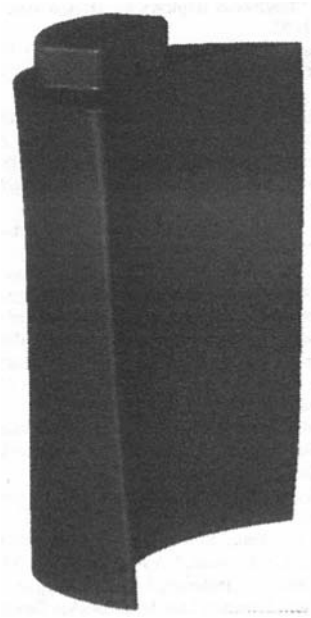

Fig. 40 Solid model of typical bucket designed by TADS

This system is now used to design all advanced vortex buckets for production units. A fifteen-to-one reduction in design cycle time has already been achieved, and further gains continue to be made as the system is refined. By incorporating mechanical design constraints into the system, TADS allows us to design fully customized turbines that exactly meet the needs of each individual customer in considerably less time than it took in the recent past, and with no compromise in mechanical integrity and reliability. This remarkable design tool also allows us to respond to retrofit opportunities more quickly, thus giving our customers more options for improving existing designs.

Summary

In this paper, recent advances in GE steam path technology have been described. Advanced computational fluid dynamics codes are being used to develop new aerodynamic design concepts to improve efficiency dramatically. Extensive laboratory test programs are being performed to verify the predicted efficiency gains of new design features, and to validate the CFD codes. Unique design automation and optimization tools have been developed that allow fully customized turbines to be designed in short cycle times to meet the needs of individual customers.

Acknowledgments

I wish to thank the Steam Turbine 3D Aero Team for all the hard work described in this paper: R. Jones, R. Markytan, E. Paz, D. Rockefeller, S. Ruggles, H. Singh, J. Stampfli, and L. Willey. I also wish to thank the people at CRD who have contributed much to the success of the program: M. Braaten, S. Connell, S. Goel, G. Holmes, and S. Lamson. None of this work would have been possible without the strong support of R. Couchman, General Manager of the Steam Turbine Design & Development Engineering Department, and P. Friesen, Steam Turbine Product General Manager. Last but not least, I thank my wife Sharon and children John and Emily, for their patience and support.

References

Adamczyk, J. J., Celestina, M. L., Beach, T. A., and Barnett, M., 1990, "Simulation of Three-Dimensional Viscous Flow Within a Multistage Turbine," ASME *Journal of Turbomachinery*, Vol. 112, pp. 370–376.

Downloaded 02 Jun 2010 to 171.66.16.104. Redistribution subject to ASME license or copyright; see http://www.asme.org/terms/Terms_Use.cfm

Ashley, S., 1992, "Engineous Explores the Design Space," *Mechanical Engineering,* Feb., pp. 49–52.

Braaten, M. E., and Connell, S. D., 1994, "A 3D Unstructured Adaptive Multigrid Scheme for the Navier–Stokes Equations," GE CRD Report No. 94CRD146.

Connell, S. D., and Holmes, D. G., 1993, "A 3D Unstructured Adaptive Multigrid Scheme for the Euler Equations," AIAA Paper No. 93-3339.

Connell, S. D., Holmes, D. G., and Braaten, M. E., 1993, "Adaptive Unstructured 2D Navier–Stokes Solutions on Mixed Quadrilateral/Triangular Meshes," ASME Paper No. 93-GT-99.

Dejch, M. E., et al., 1960, "Method of Raising the Efficiency of Turbine Stages With Short Blades," *Teploenergetika,* Feb., pp. 18–24.

Goel, S., Gregory, B. A., and Cherry, D. G., 1993, "Knowledge-Based System for the Preliminary Aerodynamic Design of Aircraft Engine Turbines," Society of Photo-optical Instrumentation Engineers, *Applications of Artificial Intelligence, Knowledge-Based Systems in Aerospace and Industry,* Orlando, FL, Apr. 13–15.

Holmes, D. G., and Tong, S. S., 1985, "A Three-Dimensional Euler Solver for Turbomachinery Blade Rows," ASME JOURNAL OF ENGINEERING FOR GAS TURBINES AND POWER, Vol. 107, pp. 258–264.

Holmes, D. G., and Warren, R. E., 1985, "Detailed Studies of Inviscid Secondary Flows," GE CRD Report No. 85CRD133; presented at the 1985 ASME Winter Annual Meeting, Nov. 18.

Langston, L. S., 1980, "Crossflows in a Turbine Cascade Passage," ASME JOURNAL OF ENGINEERING FOR POWER, Vol. 102, pp. 866–874.

Lee, H., Goel, S., and Tong, S. S., 1993, "Toward Modeling the Concurrent Design of Aircraft Engine Turbines," ASME Paper No. 93-GT-193.

Morson, A., Williams, J. C., Pedersen, J. R., and Ruggles, S. G., 1988, "Continuously Coupled 40-Inch Titanium Last Stage Bucket Development," GE Power Generation Turbine Technology Reference Library Paper No. GER-3590.

Morson, A., 1990, "Steam Turbine Long Bucket Developments," GE Power Generation Turbine Technology Reference Library Paper GER-3647.

O'Connor, M. F., Williams, J. C., Dinh, C. V., Ruggles, S. G., and Kellyhouse, W. W., 1988, "An Update on Steam Turbine Redesigns for Improved Efficiency and Availability," GE Power Generation Turbine Technology Reference Library Paper No. GER-3577.

Powell, D. J., Skolnick, M. M., and Tong, S. S., 1990, "Engineous: A Unified Approach to Design Optimization," *Applications of Artificial Intelligence in Engineering,* Vol. 1, Computational Mechanics Publications, Southampton, United Kingdom, pp. 137–157.

Rai, M., and Madavan, N., 1990, "Multi-airfoil Navier–Stokes Simulations of Turbine Rotor-Stator Interaction," ASME *Journal of Turbomachinery,* Vol. 112, pp. 377–384.

Shelton, M. L., Gregory, B. A., and Lamson, S. H., 1993, "Optimization of a Transonic Turbine Airfoil Using Artificial Intelligence, CFD and Cascade Testing," ASME Paper No. 93-GT-161.

Sovran, G., and Klomp, E. D., 1967, "Experimentally Determined Optimum Geometries for Rectilinear Diffusers With Rectangular, Conical or Annular Cross-Section," in: *Fluid Mechanics of Internal Flow,* G. Sovran, ed., symposium held at General Motors Research Laboratories in Warren, MI, Elsevier Publishing Co.

Sumner, W. J., Vogan, J. H., and Lindinger, R. J., 1985, "Reducing Solid Particle Damage in Large Steam Turbines," *Proceedings of the American Power Conference,* Vol. 47, pp. 196–212; also published as GE Power Generation Turbine Technology Reference Library Paper No. GER-3478A.

Turner, M. G., and Jennions, I. K., 1993, "An Investigation of Turbulence Modeling in Transonic Fans Including a Novel Implementation of an Implicit k–ϵ Turbulence Model," ASME *Journal of Turbomachinery,* Vol. 115, pp. 249–260.

Turner, M. G., Liang, T., Beauchamp, P. P., and Jennions, I. K., 1993, "The Use of Orthogonal Grids in Turbine CFD Computations," ASME Paper No. 93-GT-38.

Downloaded 02 Jun 2010 to 171.66.16.104. Redistribution subject to ASME license or copyright; see http://www.asme.org/terms/Terms_Use.cfm

Modeling of (Cogeneration) Power Plants on Time-Dependent Power Demands of the Consumer

M. Witzani
ÖMV Cogeneration,
Vienna, Austria

P. Pechtl
Enter Software Inc.,
Graz, Austria

This paper presents a planning tool where rigorous plant performance models are used to produce accurate plant performance data reflecting real plant operation under the loads specified by load demand curves. Cumulative figures such as total fuel consumption and production efficiency serve as the basis for a subsequent detailed economic analysis. Basic inputs to the model are the energy demand curves for a specific site on a daily, hourly, or even per minute basis. The plant performance model takes into account the varying load levels, ambient conditions, fuel price, and revenues from electric power delivered off-site. The load/performance simulator calculates plant performance and basic economic parameters at each point in time of the load demand curve to exactly match the given energy demand (Fig. 1). The results are critical economic data like cumulated fuel consumption and expenses, total energy production, and overall averaged plant efficiency. The performance model delivers detailed plant performance data on an overall plant as well as component level. The results reflect real plant operation under all varying conditions, hence produce highly significant performance and economic parameters.

Introduction

Increasingly stringent power production economics requires very accurate planning tools at an early stage of the design of cogeneration power plants. The more accurate the evaluation the engineer carries out in the planning phase, the better the overall plant economics will be. Computer simulation offers a viable tool to provide accurate data in a very short time, not only for the plant performance, but also for the plant economics. Energy supply is nowadays accomplished with cogeneration plants for simultaneous supply of thermal and electrical energy at the site of energy use. Recent advancements in power generation technology suggest gas turbine-based cogeneration facilities in combined and single-cycle configuration, with heat recovery steam generators. This technology allows one to configure such facilities in great variety. It is very difficult to select the most economic plant configuration, which depends not only on the technology used and the energy demand characteristics, but also on various economic parameters, such as fuel price, electricity rates etc.

Rigorous performance and economic analyses have to be carried out to provide a database for relevant decisions. This paper describes an analysis tool and a method to analyze various plant configurations in terms of plant performance and economics, not only for one specified load point but for all possible states of operation imposed by the varying load demand. Basic economic parameters like cumulated fuel consumption, incurred fuel cost (also as a function of prices varying over time and season) as well as collected revenues from electricity and thermal energy sales are determined simultaneously. These basic economic parameters serve as the input for an economic investment analysis in terms of capital costs, return of investment, and the like. The latter is not part of this presentation, for it is a fairly standard procedure. The point is to provide the most accurate input parameters for the investment analysis, which is the purpose of the method described here.

Usual engineering practice of the analysis of plant economics takes into account only one or two averaged load points (summer and winter) as a representative load state basis. Simple extrapolations are made over the whole operating period.

On the other hand, sophisticated methods have been developed to carry out economic analysis and optimization (Frangopolus, 1990a, b), using techniques such as linear programming, to find an optimal configuration, design, and operational strategy. However, to decrease computation time, these methods take into account very simplistic performance models for the equipment involved. These are either constant energy conversion efficiencies (Frangopolus, 1990a, b) for boilers and turbines or fairly simplistic equations (Yokoyama, 1995). Also, the analysis methods (Frangopolus, 1990a, b; Yokoyama 1995) are based on load duration curves rather than on detailed load demand curves.

The method presented here takes into account detailed load demand profiles over the period of interest (see Fig. 7) and evaluates plant parameters based upon true simulation of plant performance. Each individual energy form (steam and power) is considered at its correct demand level at the appropriate time. The development of such an integrated load/performance model offers the opportunity to analyze different plant configurations simultaneously producing input parameters for a subsequent economic analysis in terms of capital cost and return of investment. As such the method presented here could be used to verify results from a general purpose optimization system, as mentioned above.

Performance Model

Plant Performance Model. This modeling technique requires simulation models, which feature two important qualities. The first quality is to provide a modular structure so that a plant model can be quickly adopted to represent various power plant configurations.

Contributed by the International Gas Turbine Institute and presented at Cogen-Turbo Power, Vienna, Austria, August 23–25, 1995. Manuscript received by the International Gas Turbine Institute May 20, 1995. Associate Technical Editor: C. J. Russo. ASME Paper No. 95-CTP-48.

Copyright © 1996 by ASME

Downloaded 02 Jun 2010 to 171.66.16.104. Redistribution subject to ASME license or copyright; see http://www.asme.org/terms/Terms_Use.cfm

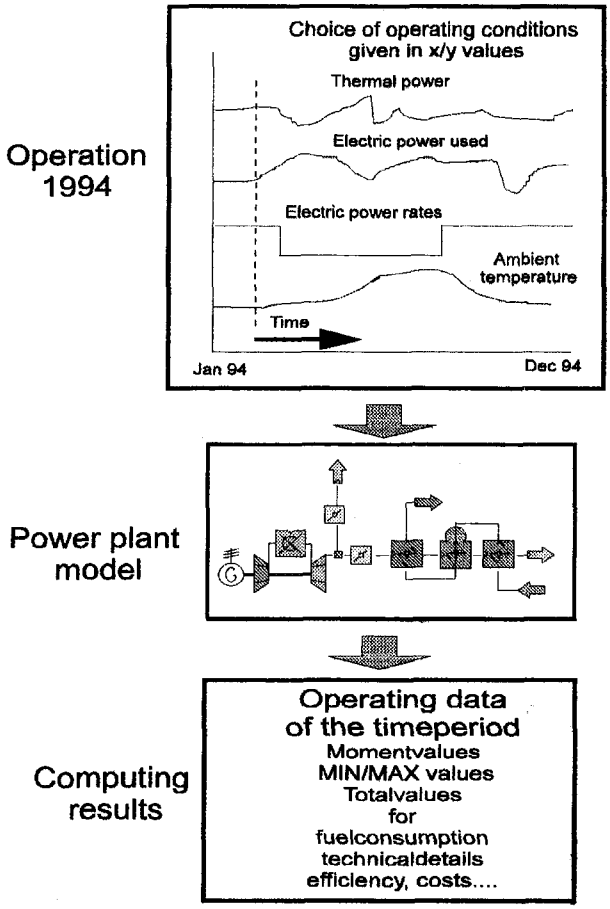

Fig. 1 Modeling of cogeneration power plants on load curves

The second quality is that the simulator has accurate mathematical models, which can be executed in two modes: (1) the design mode and (2) the off-design or rating mode. The off-design mode is necessary for plant performance predictions under varying load demand.

Tools such as the GateCycle computer software code (Erbes and Gay, 1989) help by providing an accurate analytical framework that includes all the necessary relations for modeling gas and steam turbines, pumps, heat exchanger equipment, and the like.

With this modular power plant analysis tool, it is very easy to quickly create models for various plant configurations. All unit operations are available in the library. The user selects each unit operation from a library, arranges them on a graphic drawing page, and draws the connecting steam, gas, and water lines to finalize the plant configuration. Figure 2 shows a sample of unit operation models available in a library and a power plant model composed of some of the unit operations. An extensive database offers more than 100 data sets to model various gas turbines available on the market. In the design phase of the performance model it is very easy to exchange one turbine with another. Calculations are carried out on the same basis and the results are very comparable.

The analysis code can be operated into two distinct modes, the design mode and the off-design mode. In each mode, heat and mass balances are established. In the design mode, physical parameters of the various unit operations are determined. These may be a heat exchange surface area, a steam turbine flow capacity, etc. In the off-design or rating mode, the physical characteristics of the model are fixed to represent a power plant "as built."

Plant Operation Control. A spreadsheet program (Fig. 3) provides the basic framework to contain all data relevant for the operation of the plant. Also, the detailed energy demand curves are residing in the spreadsheet model. Through an interface developed particularly for this application, the plant performance analysis code may be called by a spreadsheet procedure with automatic "two-way" data transfer. The performance analysis code is such just a subfunction of the spreadsheet.

A "power plant operation" procedure, programmed in terms of spreadsheet macros, "runs" the power plant for each individual load point of the load demand curve. The operation macros determine the current settings in terms of extraction steam to satisfy a thermal energy demand and the load level for power production. It transfers these demands and the ambient conditions to the model database. After setting those parameters it invokes an analysis run and retrieves the performance results. A complete analysis may require as many as a couple of hundred performance runs. It may be run overnight; no interaction of the user is necessary at this point. The results are used to establish the time-dependent plant performance data, needed for the integration and formation of the economic parameters.

Analysis Methodology

Client Data. Particular care must be taken when selecting the relevant database. The modeling results, as accurate as they may be, are only as relevant as these data. For further considerations the data can be distinguished in three sets. These are

1 site conditions
2 design criteria
3 time-dependent data such as load demand curves, cyclic ambient conditions, electricity revenues, fuel price, etc.

The site conditions and design criteria are considered when generating the plant performance model and preselecting the plant configurations suitable for the clients site. The load demand curves are input to the combined load/performance analysis where any model is run for the various load conditions. A subsequent analysis of plant economics leads to the final deci-

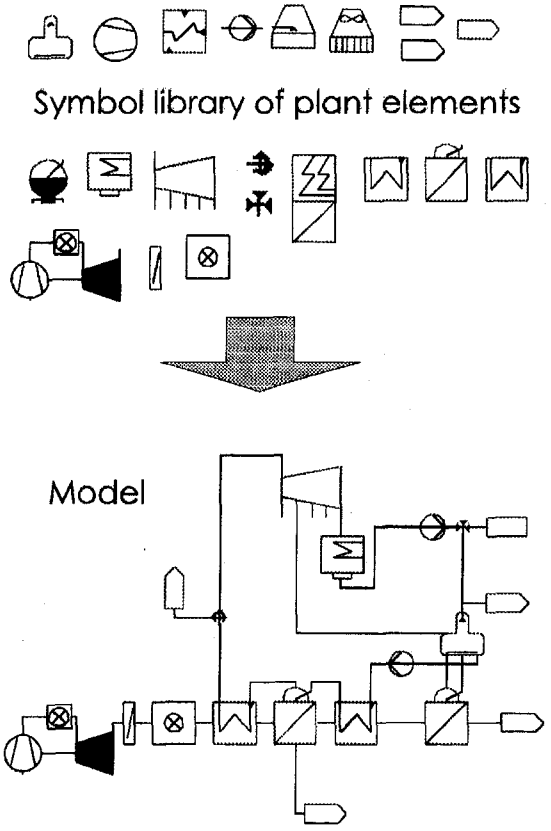

Fig. 2 GateCycle unit operations library and power plant model

Downloaded 02 Jun 2010 to 171.66.16.104. Redistribution subject to ASME license or copyright; see http://www.asme.org/terms/Terms_Use.cfm

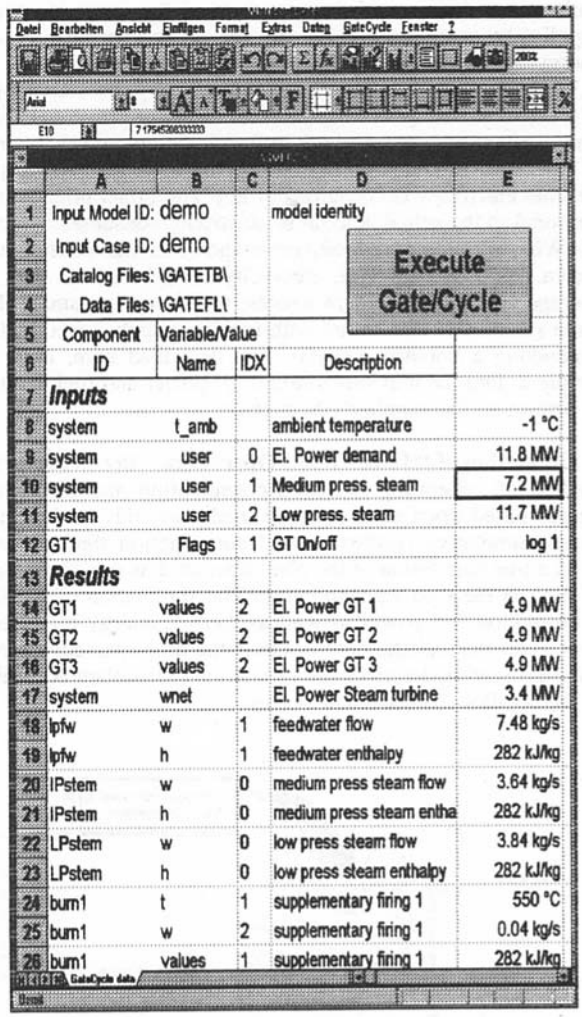

	A	B	C	D	E
1	Input Model ID: demo			model identity	
2	Input Case ID: demo				
3	Catalog Files: \GATETB\				
4	Data Files: \GATEFL\				
5	Component	Variable/Value			
6	ID	Name	IDX	Description	
7	*Inputs*				
8	system	t_amb		ambient temperature	-1 °C
9	system	user	0	El. Power demand	11.8 MW
10	system	user	1	Medium press. steam	7.2 MW
11	system	user	2	Low press. steam	11.7 MW
12	GT1	Flags	1	GT On/off	log 1
13	*Results*				
14	GT1	values	2	El. Power GT 1	4.9 MW
15	GT2	values	2	El. Power GT 2	4.9 MW
16	GT3	values	2	El. Power GT 3	4.9 MW
17	system	wnet		El. Power Steam turbine	3.4 MW
18	lpfw	w	1	feedwater flow	7.48 kg/s
19	lpfw	h	1	feedwater enthalpy	282 kJ/kg
20	IPstem	w	0	medium press steam flow	3.64 kg/s
21	IPstem	h	0	medium press steam entha	282 kJ/kg
22	LPstem	w	0	low press steam flow	3.84 kg/s
23	LPstem	h	0	low press steam enthalpy	282 kJ/kg
24	burn1	t	1	supplementary firing 1	550 °C
25	burn1	w	2	supplementary firing 1	0.04 kg/s
26	burn1	values	1	supplementary firing 1	282 kJ/kg

Fig. 3 MS-EXCEL spreadsheet model as "plant operator" with data interface area to GateCycle power plant simulator

sion as to which plant configuration provides the most economic choice.

Site Conditions, General Data. The general data provide the basis for a preselection of plant configurations. Several sources exist to establish relevant site conditions. These are primarily the client, the gas supplier, the local utility company, and local authorities. Further data are gathered at site visits. The site conditions comprise ambient conditions, sea level, voltage level, site access, available space, plant layout, cooling water supply, etc. Several constraints may exist, concerning plant emissions, cooling water supply, and the like.

Design Criteria. Design criteria are plant capacity, process steam pressures and temperatures, flow rates, etc. Equipment data for steam, gas turbines, and heat exchange equipment from vendors are considered when the plant performance model is generated. As a consequence, vendor data for various equipment are an integral part of the general data set (ISO-data for gas turbine performance, ambient temperature dependence, etc.).

Time-Dependent Data. Time-dependent data are:

1 Load demand curves for electric power and thermal energy.
2 Varying ambient conditions.
3 Revenues from electricity sales.
4 Fuel price.
5 Electricity price.

A survey with the client results in his specific pattern of energy consumption. The clients facility and energy usage might be monitored over a period of time. It is important to pick a representative time period to make valid extrapolations. Representative time periods can be: selected days, weeks, or even the whole period of a month or a year. During this period data are taken. The more frequent data sets are recorded, the more accurate the final result will be. This survey delivers detailed data for the electrical power demand and any thermal energy demand in terms of process steam flow rates, pressure, and temperature.

For gas turbine-based plants records of the ambient temperature are also of importance. Unless measured, the local weather forecast institutes supply this information. Surplus electricity generated usually is sold to the outside grid. The achievable price depends on the utilities own demand situation. Consequently, the price the utility company will pay for extra electricity will vary over time. Costs for fuel gas and electricity bought from the utility may also vary over the considered time span on a daily or seasonal basis.

Data Preparation. Once all necessary data have been collected, they have to be prepared for processing in the load/performance models. Ideally the data are readily available on electronic media like a file on a disk. Unfortunately the thermal and electric power consumption are often recorded in form of graphs or are recorded in form of numbers at constant time steps. New EDV technology such as scanners and optical character recognition software enables the user to input the data in a somewhat automated manner.

Establishing the Performance Models for Various Plant Configurations. At this stage a regular plant design process takes place. Models of various plant configurations are established and analyzed. Technical feasibility and rough economic estimates support the preselection of possible plant configurations. First economic parameters can be determined with averaged "representative" load points in a traditional manner. Obvious differences in operational and cost effectiveness deliver first decision criteria.

Existing Energy Supply System. Usually good documentation exists about the performance and economics of the current energy supply situation, which conveniently serves as the basis for a comparison of a current system with a new facility.

A performance model of the existing facility run through the load/performance simulator helps to establish this consistent basis. Real plant performance data, retrieved from the client's operational records, serve as the input for the simulation model. The plant configuration is well known, and can easily be represented with the unit operation modules found in the general power plant simulator. Once the performance model of the existing plant has been generated, it will be cycled through the recorded load demand curves.

The results (power, thermal energy delivery, and total fuel consumption) can easily be compared with the real data from the past. This step is important to verify the significance of the model, particularly for the client.

New Generation Facility. The site conditions, design criteria, and engineering experience suggest a few possible plant configurations. A certain capacity can be satisfied with a plant in single-cycle or combined-cycle configuration. It can be a one train GT/HRSG plant or a multiple train plant. The steam turbine part can be configured as a back-pressure or a condensing turbine. For each of these configurations, a plant performance model has to be prepared, considering real equipment.

In the design mode all vendor information is used to establish a realistic performance model.

The design conditions are established with the client. Either base load or average load levels serve as the design basis for equipment sizing. If peaking capabilities are important peaking

Downloaded 02 Jun 2010 to 171.66.16.104. Redistribution subject to ASME license or copyright; see http://www.asme.org/terms/Terms_Use.cfm

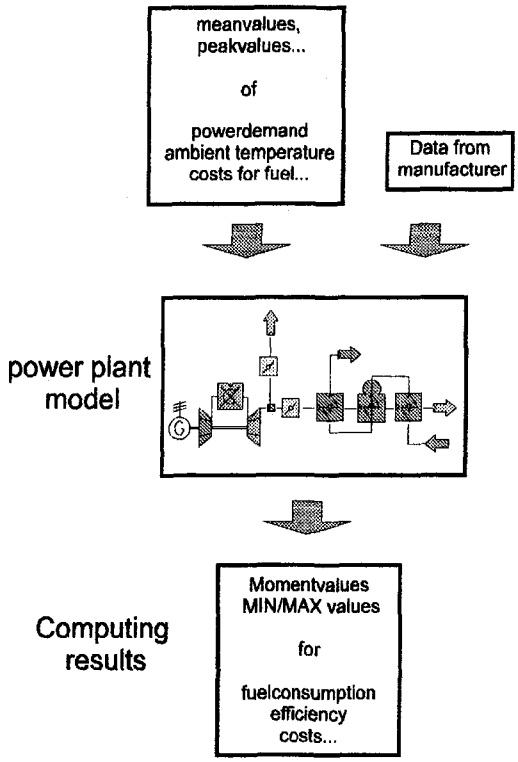

Fig. 4 Design phase for various power plant configurations using modular simulator

rates may also be used for equipment sizing. Figure 4 shows the basic steps involved in that design process. The results of this step are physical parameters of the equipment such as heat exchange surfaces and steam turbine flow capacities.

A gas turbine database allows one to select model parameters for many commercially available engines and provides basic engine behavior with regard to changing load and ambient conditions as well as steam or water injection rates.

Evaluation on Certain Operating Points. This is the first approach to define a possible configuration of the power plant to be designed. This step designs the elements according to their maximal and minimal operating conditions (see Fig. 4). At this stage a rough estimate about the possible designs can be made. It is also possible to compare two or more configurations to find out the advantages and disadvantages.

Technical Evaluation. Off-design analysis runs of the models covering minimum and maximum load states teach us about the ability of the selected equipment to operate at these extreme conditions. This step may show that a certain piece of equipment is not able to handle the situation, exceeding, e.g., maximum flow rates or temperatures established by a vendor. Changes to the design may be necessary and require some iteration. At this point design heat and material balances have been established for each configuration. The technical feasibility for all plant configurations considered is also proven.

Economic Evaluation. Based upon the results of the design steps and the technical feasibility, the basic economics can be evaluated. Averaged operating conditions will give a first estimate of energy and fuel costs. The usual practice of economic evaluation would take the results from such an average condition and multiply numbers over the considered time span to produce the cumulative cost/production figures for a certain time span. The conclusions drawn from such a simplified method may not always be correct.

Possible errors show easily when calculating the primary energy costs. A decision whether a cogeneration unit should be built or not relies on the comparison of the costs of energy supplied by some utility company versus the expected costs of energy due to the production in a cogeneration plant.

The utility's costs for electricity are in many cases composed of a constant base price ($/year) and an offset price ($/kWh). The constant base price relates to the maximum power in terms of kW drawn at one point in time and has to be paid regardless, whether electricity is consumed or not. The offset price is proportional to the actual amount of electricity consumed in terms of kWh. An average load state never shows the maximum power drawn. As a consequence, electricity costs based on such an average load state result in figures, which are too small. The same situation is also found with fuel gas supply costs. Unless conducting a detailed analysis, like described here, it is not simple to find the maximum values for power and fuel demand to determine the supplier's base price.

Simulation of "True" Plant Operation. In contrast to the method of generating averaged consumption and production figures based upon some average load state, this method produces cumulative production and consumption figures based upon a true simulation of the plant operation at any given point of time in the load demand curve. The summation of the fuel consumption and power as well as thermal energy production rates gives the realistic numbers over the time span considered. The next section describes the simulation of the plant according to the detailed load demand curves.

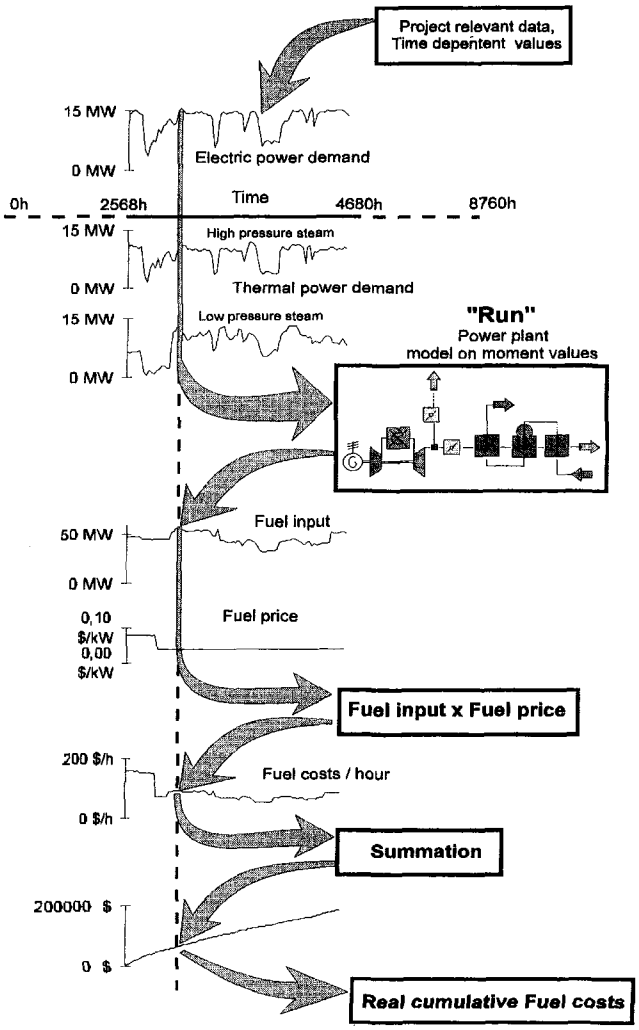

Fig. 5 Steps for the load/performance analysis based on the "true" plant performance

Downloaded 02 Jun 2010 to 171.66.16.104. Redistribution subject to ASME license or copyright; see http://www.asme.org/terms/Terms_Use.cfm

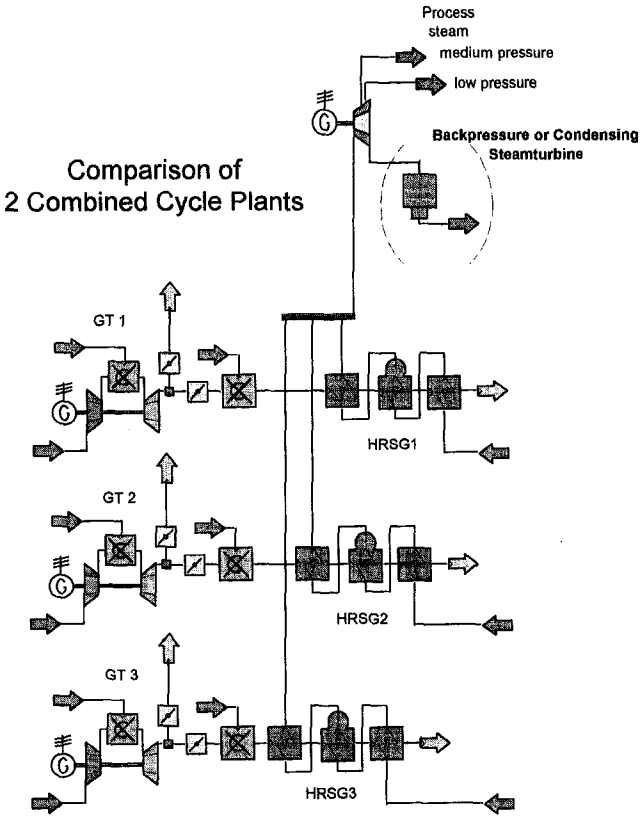

Fig. 6 Power plant configuration, showing three trains of GT–heat recovery boilers and a back-pressure or optional condensing steam turbine

Running the "True" Analysis

At this step, each power plant model is "operated" by computer simulation like a real plant under the varying load demand. The operator routine of the load/performance simulator automatically conducts a series of runs according to the load demand profile. Performance results of each run are stored and made available for later analysis. Figure 5 shows the steps involved. The interface routines between operator routine and the plant performance model allows us to execute as many runs as necessary, in an automated manner.

The performance parameters at each point of time in the load demand curve are the fuel consumption rate, the power production rate, thermal energy supply rate, and conversion efficiency. The integration routine forms the cumulative fuel consumption and power production figures. Taking into account the time-dependent fuel price, electricity price, and revenue, the cumulative costs and revenues for fuel and electricity are formed simultaneously.

Technical Evaluation. All operational data are available over the considered time span. This gives a very good insight in the real operation of the plant envisioned. Results can be used to: (1) estimate true mean values, (2) find actual peak load levels and flow rates, (3) find the most probable operational state of the plant. This information can be used to reselect pieces of equipment. A pump might be chosen with a size and characteristics, which operates at the optimal operating point (sweet spot) most of the time. On the other hand, the fully documented runs for existing plants and several new plant configurations offer a very good basis for the comparison.

Economic Evaluation. Due to the sophisticated, realistic performance modeling the "true" technical data available lead to a very good database for the economic analysis. The decision can safely be made as to which plant configuration offers the most economic choice at a certain site. As an example, the user can consciously decide whether or not a less expensive, however less flexible cogeneration facility is more economical, than a combined cycle block, which is more expensive but operates more efficiently.

If a performance model of an existing plant had been prepared, it would be run through the load/performance model to establish the performance and economic parameters. The cost effectiveness of each proposed change of the energy supply facility can be easily compared.

Beyond that, design studies that consider very detailed questions can be carried out quickly and realistically. Questions such as, is it favorable to install a more expensive yet more efficient pump, can easily be answered. We just run two models (one can easily be generated from the other by copying and changing) through the economic simulator and compare the final economic key parameters like the true costs of energy taking into account the lower operating costs and the higher capital costs due to higher investment.

Case Study

A new cogeneration facility shall satisfy the energy demand as of the last year's load (see Fig. 6). Figure 7 displays input data in terms of load demand curves for electricity and process steam.

The following situation was used to investigate. The electricity base price, which relates directly to the maximum power, drawn from the utility, is relatively expensive. High plant availability would reduce the need to demand power from the utility grid, hence lower the base price for electricity from outside. This drove the decision for a three-train GT/supplementary fired HRSG configuration, feeding steam into one steam turbine, displayed in Fig. 1 of the appendix. In case one GT fails or is maintained, only a portion of the electricity demand has to be supplied by the utility. The question to investigate was whether to install a condensing steam turbine or a back-pressure steam turbine.

In one case (case 2), with the condensing steam turbine, process steam would be supplied by extraction from the steam turbine. Varying process steam demand would be satisfied by varying extraction rates. The remainder of the steam would generate power, which in turn would be delivered to the utility grid. In case of a gas turbine failure or maintenance, increased supplementary firing would not only make up for missing steam but also allow to increase power production in the steam turbine to make up for the gas turbine power. A substantial saving in electricity costs could be realized at the expense of substantial higher investment.

In the other case (case 1), a much cheaper installation, using a steam turbine in back-pressure operation, would supply low-pressure process steam from the exit of the turbine. Varying process steam demand will be satisfied with varying firing rates in the heat recovery steam generators. Below a certain minimum (no firing) excess steam would be blown off or the exhaust gas would partially bypass the HRSG. The cheaper investment is counterbalanced by a significantly less efficient operation. In case of a gas turbine failure, the missing power cannot be made up by increased steam turbine production and has to come from the outside utility grid. In Fig. 8 two diagrams show the calculation results from the two plant types. The diagram in the middle relates to the installation with the back-pressure steam turbine (case 1), the diagram in the lower part relates to the installation with the condensing steam turbine (case 2). The diagrams show the overall efficiency and the excess power delivered to or received from the utility grid (negative power means utility supply). Note that these simulation results reflect real power plant behavior, hence have a high significance. With this setup any scenario may be investigated at minimum effort, changing demand characteristics as well as different operation strategies.

The electricity curve in case 1 clearly shows that under some circumstances power has to be delivered from the utility grid

Downloaded 02 Jun 2010 to 171.66.16.104. Redistribution subject to ASME license or copyright; see http://www.asme.org/terms/Terms_Use.cfm

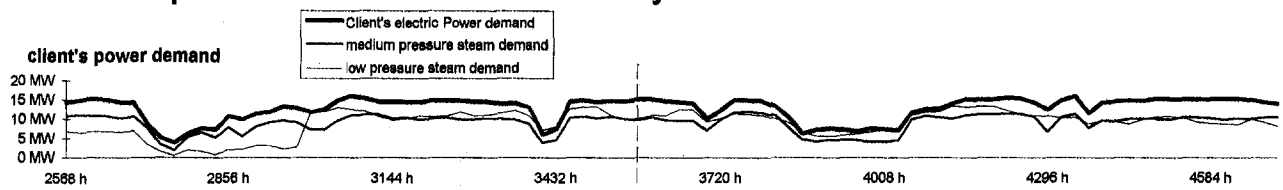

Fig. 7 Sample load demand curves for electric power demand, and medium and low-pressure steam demand

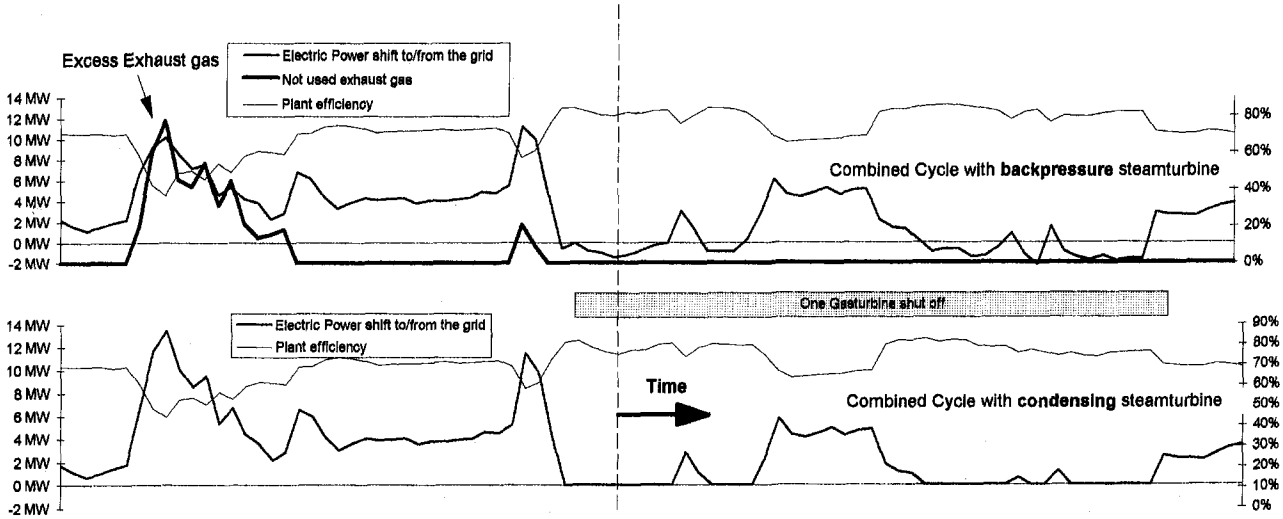

Fig. 8 Results from the load/performance model for case 1 (upper curve) and case 2 (lower curves)

(in right part of the diagram). Also, in some instances, not all of the thermal energy contained in the exhaust gas can be used and is wasted (in the left part of the diagram).

The electricity curve in case 2 shows that under no circumstances will power be drawn from the utility grid. Even in the case of one gas turbine shut down, the power needed by the plant can be produced. Off-site delivery may go to zero, but no power comes from the utility grid. Different scenarios lead to different conclusions; what to discuss would exceed the purpose of this presentation. However, generally, the analysis indicated that the demand pattern plays a significant role on the overall economics of the cogeneration facility. Strongly varying process steam demand favors the condensing installation; relatively constant process steam demand favours the back-pressure installation.

Conclusion

A very powerful tool and methodology for planning and designing power plants has been presented here. It comprises rigorous plant performance modeling and simulating true power plant operation as well as accurate calculation of economic parameters. Based upon the quality of the operational data made available, the quality of the economic analysis is very high. Strategic and design decisions can easily be made on grounds of a reliable economic database. Particularly, after the final economic analysis, the quality of answers to the following questions increases substantially:

1 What is the economics of a new cogeneration facility?
2 Is it worthwhile to replace the existing plant with a new one; what is the incentive?
3 What is the most economic plant configuration on a certain site (simple cogeneration, gas turbine in single or combined cycle)?
4 What is the most economic lay out for particular plant elements?
5 Can the desired load demand pattern be satisfied?
6 Basic design questions, like how many gas turbines should be employed, should there be a steam turbine in back-pressure operation or a condensing steam turbine with steam extraction, or no steam turbine at all?

References

Erbes, M. R., and Gay, R. R., 1989, "GATE/CYCLE Predictions of the Off-Design Performance of Combined Cycle Power Plants," *Simulation of Thermal Energy Systems,* ASME AES-Vol. ???/HTD-Vol. 124, pp. 43–51.

Frangopolus, C. A., 1990a, "Intelligent Functional Approach: A Method for Analysis and Optimal Synthesis-Design-Operation of Complex Systems," *Proceedings, Future for Energy—Flowers 90,* pp. 597–609.

Frangopolus, C. A., 1990b, "Optimization of Synthesis-Design-Operation of a Cogeneration System by the Intelligent Functional Approach," *Proceedings, Future for Energy—Flowers 90,* pp. 597–609.

Ito, K., Yokoyama, R., and Matsumoto, Y., "Optimal Operation of Cogeneration Plants With STEAM-Injected Gas Turbine," ASME JOURNAL OF ENGINEERING FOR GAS TURBINES AND POWER, Vol. 117, pp. 60–66.

Yokoyama, R., and Ito, K., 1995, "Multi-objective Optimization in Unit Sizing of a Gas Turbine Cogeneration Plant," ASME JOURNAL OF ENGINEERING FOR GAS TURBINES AND POWER, Vol. 117, pp. 53–59.

APPENDIX

Hard- and Software Requirements

All software used to built this analysis tool runs on a IBM (or compatible) PC under Windows 3.1 (or Windows for Workgroups) with the following minimum recommended hardware:

- Personal computer with 486 or Pentium processor
- 8MB RAM or more
- 250 MB hard disk

Less powerful configurations will end up using longer calculation time.

Downloaded 02 Jun 2010 to 171.66.16.104. Redistribution subject to ASME license or copyright; see http://www.asme.org/terms/Terms_Use.cfm

Air Bottoming Cycle: Use of Gas Turbine Waste Heat for Power Generation

O. Bolland

M. Førde

Division of Thermal Energy and Hydropower, Norwegian University of Science and Technology, Trondheim, Norway

B. Hånde

Oil Engineering Consultants, Sandvika, Norway

This paper presents a thermodynamic analysis of the Air Bottoming Cycle (ABC) as well as the results of a feasibility study for using the Air Bottoming Cycle for gas turbine waste heat recovery/power generation on oil/gas platforms in the North Sea. The basis for the feasibility study was to utilize the exhaust gas heat from an LM2500PE gas turbine. Installation of the ABC on both a new and an existing platform have been considered. A design reference case is presented, and the recommended ABC is a two-shaft engine with two compressor intercoolers. The compression pressure ratio was found optimal at 8:1. The combined gas turbine and ABC shaft efficiency was calculated to 46.6 percent. The LM2500PE gas turbine contributes with 36.1 percent while the ABC adds 10.5 percent points to the gas turbine efficiency. The ABC shaft power output is 6.6 MW when utilizing the waste heat of an LM2500PE gas turbine. A preliminary thermal and hydraulic design of the ABC main components (compressor, turbine, intercoolers, and recuperator) was carried out. The recuperator is the largest and heaviest component (45 tons). A weight and cost breakdown of the ABC is presented. The total weight of the ABC package was calculated to 154 metric tons, and the ABC package cost to 9.4 million US$. An economical examination for three different cases was carried out. The results show that the ABC alternative (LM2500PE + ABC) is economical, with a rather good margin, compared to the other alternatives. The conclusion is that the Air Bottoming Cycle is an economical alternative for power generation on both new platforms and on existing platforms with demand for more power.

Introduction

The driving force in Norway for the interest in the Air Bottoming Cycle (ABC) is the CO_2 tax on the use of fuel in gas turbines on oil platforms in the North Sea. This CO_2 tax is currently 11.8 cent/Sm^3 fuel gas (or 0.80 NOK/Sm^3 gas). The annual payment of CO_2 tax from one LM2500PE gas turbine is approximately 4.4–5.1 million US$ (30–35 million NOK). The gas consumed by gas turbines on the oil platforms could alternatively be sold, and the value would be to approximately 7.4–8.8 cent/Sm^3 (0.50–0.60 NOK/Sm^3). The CO_2 tax and the sales value of the gas then amount to as much as approximately 20 cent/Sm^3.

Reduced fuel consumption can be achieved by using a combined gas turbine/steam turbine cycle. This type of combined cycle has gained widespread acceptance in the land-based power generating industry and is definitely a "proven technology." On oil platforms in the North Sea, a number of studies on using combined cycles have been conducted, but the typical result of these has been that a combined gas turbine/steam turbine cycle is not economical, despite the high CO_2 tax. Even if such a combined cycle offers a high fuel-to-power conversion efficiency, the cost due to the high weight of the equipment (especially the heat recovery steam generator) has been found to be too high. The cost of weight of equipment is very high on an oil platform, and therefore implementation of fuel reduction initiatives should take place with lightweight equipment.

The ABC together with a topping gas turbine cycle is another type of combined cycle. It offers an efficiency close to that of a combined gas turbine/steam turbine cycle, and offers the potential for lower weight compared to the combined gas turbine/steam turbine cycle. It has in the past not been paid much attention to, and the main reason for that is probably the rapid technological improvement during the last two decades and the commercial success of the combined gas turbine/steam turbine cycle.

What Is the Air Bottoming Cycle? Like the steam bottoming cycle in a combined cycle, the ABC may utilize heat rejected from a gas turbine. A general flowsheet diagram of the ABC is shown in Fig. 1. Ambient air (1) is drawn through a filter and is compressed in the low-pressure compressor (LPC). The air is then cooled (3–4) before it is further compressed in an intermediate compressor (IPC). Again the air is cooled (5–6) before the final stage of compression in the high-pressure compressor (HPC). In Fig. 1 the process shown has the compression divided into three sections with two intercoolers. It is of course possible instead of having two intercoolers to use one or three or even more intercoolers. This is a question about what is practical and a balance between cost and benefit of having more intercoolers.

The compressed air (7) is heated in a heat exchanger before it enters (8) a turbine. In the turbine the air is expanded while shaft work is generated. After the turbine the air is exhausted to a stack. The work generated in the turbine is sufficient to drive the compressor and a generator. A gear between the turbine shaft and the generator may be necessary.

The ABC offers the possibility to provide to an external process compressed air at moderate temperatures (7*a*) and/or compressed hot air (8*a*). The ABC may be a closed or partially closed cycle by recycling the air (9*a*).

In the literature extensive surveys can be found on the use and thermodynamic potential of a variety of power cycle working fluids where heat sources are latent and/or sensible heat (Pettersen, 1987; Hornnes and Bolland, 1991). However, air as a bottoming cycle working fluid has not been paid much attention to. Most notable are probably the patents by Farrell

Contributed by the International Gas Turbine Institute and presented at Cogen-Turbo Power, Vienna, Austria, August 23–25, 1995. Manuscript received by the International Gas Turbine Institute June 20, 1995. Associate Technical Editor: C. J. Russo. ASME Paper No. 95-CTP-50.

Copyright © 1996 by ASME

Downloaded 02 Jun 2010 to 171.66.16.104. Redistribution subject to ASME license or copyright; see http://www.asme.org/terms/Terms_Use.cfm

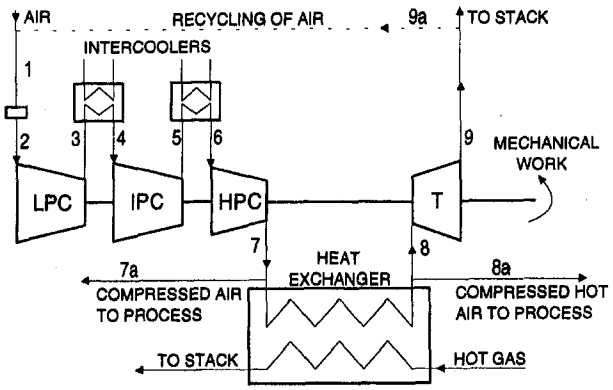

Fig. 1 A schematic diagram of a possible configuration of the air bottoming cycle

(1988, 1992). Also others like Pettersen (1987), Wicks et al. (1992), Walker et al. (1992), and Weston (1993) have proposed and discussed bottoming cycles with air as the working fluid.

Alternatives to Using the ABC. On oil platforms there will in the next years be a few options to using simple-cycle gas turbines for power generation. One of them is the ABC as described in this paper, but there are also other alternatives that may be competitive with the ABC. These are:

High-temperature, high-pressure-ratio simple-cycle gas turbines: The development of gas turbines has now come to the point where efficiencies in excess of 40 percent are achievable in the near future. Examples are the LM6000PA (≈40 MW), the FT8 (≈26 MW), and the Trent (≈51 MW).

Combined gas turbine/steam turbine cycles: Current design practice is not suitable for being applied on oil platforms. However, there is a potential toward a more compact lightweight design, especially for the heat recovery steam generator (Sæther, 1993). The use of the "once-through" concept, together with close packing of short finned tubes (serrated fins) with a small diameter, enables a significant weight reduction.

The combined gas turbine/steam turbine cycle offers the highest efficiency potential for the power generating alternatives on oil platforms, which at present would be in the range 47–49 percent.

Intercooled recuperated gas turbine: Rolls-Royce and Westinghouse are now developing an intercooled and recuperative gas turbine (WR-21) for the US Navy. The power output will be 21-22 MW and the efficiency approximately 42 percent at full load and with favorable part-load performance (Shepard et al., 1995; Hawkins et al., 1994).

Computational Models and Design Methods

In the following, models and design philosophy are presented for the present work. These include models for both component design and cycle analysis.

Cycle Analysis. The ABC uses a gaseous working fluid, which implies both gas compression and expansion (a Brayton cycle). In connection with recovery of sensible heat from a gas turbine topping cycle, the disadvantage with the ABC is that the compression of the working fluid restricts how much heat can be recovered. In the ABC the heat is picked up between the compressor and the turbine, and it is actually the compressor discharge temperature that determines how much heat can be recovered. To overcome this restriction, the compressor may be intercooled whereby the compressor discharge temperature is lowered.

In the present work the flow rate of the ABC is determined by fixing the $\dot{m}c_P$ ratio between the cold and hot sides to unity. The reason for this is that for a given power output from the ABC, the heat transfer area required is at a minimum when this ratio is unity.

Traditional first-law analysis based upon component performance characteristics coupled with energy balances invariably leads to a correct final answer. However, such analysis cannot locate and quantify the sources of loss that lead to that result. This is because the first law embodies no distinction between work and heat, no provision for quantifying the quality of energy. These limitations are not a serious drawback when dealing with familiar systems, since an intuitive understanding of the different parametric influences on system performance and second-law qualitative appreciation of "grade-of-heat" and effect of pressure loss can be developed. When analyzing novel and complex thermal systems, however, such an understanding should be supplemented by more rigorous quantitative methods. Second-law analysis, or exergy analysis, provides these tools. Second-law analysis is no substitute for first-law analysis; rather it is a supplement. In the present work results using both first and second-law calculations are presented.

The exergy of a flow stream for a given pressure (p_1) and temperature (T_1) is given by Eq. (1):

$$e(p_1, T_1) = h_1 - h_a - T_a(s_1 - s_a) \quad (1)$$

where the index a denotes the ambient condition. The term $(s_1 - s_a)$ can for an ideal gas, which is the case for the ABC, be written

Nomenclature

c = chord, m
C_L = lift coefficient
C_M = Mach number correction factor
c_P = specific heat capacity, kJ/(kg K)
D_{eq} = equivalent diffusion ratio
e = exergy, kJ/kg
h = enthalpy, kJ/kg
H = wake form factor
h_B = blade height, m
i = incidence, deg
M = Mach number
$\dot{m}$ = flow rate, kg/s
n_s = specific speed, rad/s
p = pressure, Pa
$\dot{Q}$ = volumetric flow rate, m^3/s
R = radius, m
R_g = gas constant, kJ/(kg K)
s = entropy, kJ/(kg K)
t = tip clearance, m
T = temperature, K
U = tangential velocity at mean line, m/s
V = absolute velocity, m/s
W = relative velocity, m/s
Y = specific work for a turbine stage, J/kg
β = flow angle, deg
θ = momentum thickness, m
ρ = density, kg/m^3
σ = solidity (chord/spacing)
ψ = pressure coefficient
ω = rotational speed, rad/s
φ = flow coefficient
$\bar{\omega}$ = pressure loss coefficient $\omega = \Delta p^2/\rho V^2$

Subscripts and Superscripts

0 = stagnation
1 = inlet
2 = outlet
a = ambient
p = profile
S = dynamic
tip = tip clearance
w = annulus
Z = axial direction
∞ = vector mean velocity
$\bar{}$ = averaged

Downloaded 02 Jun 2010 to 171.66.16.104. Redistribution subject to ASME license or copyright; see http://www.asme.org/terms/Terms_Use.cfm

$$s_1 - s_a = \int_{T_a}^{T_1} c_P \frac{dT}{T} - R_g \int_{p_a}^{p_1} \frac{dp}{p}. \quad (2)$$

To quantify the loss of exergy for a component, an exergy balance around the component is applied. The difference in exergy between the ingoing and outgoing streams will then be the loss of exergy. The loss of exergy is caused by heat exchanger temperature differences, "mismatched" heat exchanger temperature profiles, heat losses, pressure losses, mixing losses, mechanical losses, generation of entropy in compression and expansion processes, and rejection of exergy to the surroundings (Bolland, 1991).

Compressor. A mean line prediction method (MLPM) was used to model the flow through the compressor. NACA 65 profiles are assumed at this preliminary design stage. Each blade row forms a control volume, which has to satisfy conservation of mass, momentum, and energy. Viscous effects are included by the use of empirical correlations. The method demands that every blade row be described with inlet/outlet angles, blade height, spacing, chord, and outer/inner radius. The weakness of the method is that three-dimensional effects (including hub and tip effects) are only taken into account by using rough empirical laws. Uniform axial velocity in each cross section was assumed. This can be achieved with a free vortex tangential velocity distribution. The intention here is to list the empirical correlations used in the compressor flow model. Further details concerning the correlations can be found from Hånde (1992).

The losses in a compressor blade row can be categorized into profile losses, annulus losses, secondary losses, and tip clearance losses.

The profile losses are caused by boundary layer development on the blade surfaces. A highly recognized method for predicting these losses at design point operation was developed by Lieblein (1959). The profile total loss coefficient depends on the momentum thickness growth on the blade surface, which in turn is closely related to the diffusion of the blade. The model of Lieblein was modified by assuming that zero incidence corresponds to the minimum loss condition, and by using the axial velocity correction suggested by Klapproth (1959), the *corrected equivalent diffusion ratio* with the assumptions of NACA 65(A10) blades becomes:

$$D_{eq} = \frac{V_1}{V_2}\left[1.12 + 0.0117(i)^{1.43} + 0.61\frac{\cos^2\beta_1}{\sigma}\left(\tan\beta_1 - \frac{V_{Z2}}{V_{Z1}}\tan\beta_2\right)\right] \quad (3)$$

The relation between momentum thickness θ and D_{eq} is:

$$\frac{\theta}{c} = 0.005 + 0.01(D_{eq} - 1.3) + 0.025(D_{eq} - 1.3)^6 \quad (4)$$

The high power of the last term gives the sudden rise in momentum thickness caused by boundary layer separation at high D_{eq}. The relation between momentum thickness and profile loss coefficient is:

$$\bar{\omega}_p = 2C_M\left(\frac{\theta}{c}\right)\frac{\sigma}{\cos(\beta_2)}\left(\frac{\cos(\beta_1)}{\cos(\beta_2)}\right)^2 \frac{\frac{2H_2}{3H_2 - 1}}{\left(1 - \left(\frac{\theta}{c}\right)\frac{\sigma H_2}{\cos(\beta_2)}\right)^3} \quad (5)$$

The form factor effect, the last fraction in Eq. (5), contributes in most cases less than 10 percent of the profile losses and is neglected here. The profile losses are corrected for Mach number effects by using the following:

$$C_M = 1 + a\mathrm{M}^2 \quad (6)$$

where C_M = correction factor for Mach number effects, a = 0.1 (stator) and a = 0.3 (rotor). Equation (6) is a rough curve fit of Koch and Smith's method (1976) for solidity of 1.35, maximum thickness-to-chord ratio of 0.06, trailing-edge-thickness-to-chord ratio of 0.01, diffusion factor of 0.45, and Reynolds number of 10^6.

The correlations used for annulus $\bar{\omega}_w$ (Eq. (7)), secondary $\bar{\omega}_{sec}$ (Eq. (8)), and tip clearance $\bar{\omega}_{tip}$ (Eq. (9)) losses are based on the recommendations of Grieb et al. (1975). The loss factors are assumed to be independent, and the total loss factor is the sum of individual loss factors (Eq. (10)).

$$\bar{\omega}_w = 0.01\left(\frac{c}{h_B}\right)\left(\frac{W_\infty}{W_1}\right)^2 \quad (7)$$

$$\bar{\omega}_{sec} = 0.016C_L\left(\frac{c}{h_B}\right)\frac{1}{\cos(\bar{\beta})}\left(\frac{\bar{W}}{W_2}\right)^2 \quad (8)$$

$$\bar{\omega}_{tip} = 0.60C_L\left(\frac{t}{h_B}\right)\left(\frac{c}{h_B}\right)\frac{1}{\cos(\bar{\beta})}\left(\frac{\bar{W}}{W_2}\right)^2 \quad (9)$$

$$\bar{\omega} = \bar{\omega}_p + \bar{\omega}_w + \bar{\omega}_{sec} + \bar{\omega}_{tip} \quad (10)$$

Surge inception is determined by the use of the *effective static pressure rise coefficient* as described by Sovran and Klomp (1967), Koch (1981), and Hånde (1992).

The effective flow area is the geometric area times a blockage factor. This blockage factor accounts for the effects of blade thickness, boundary layer, and wakes. This factor was set to 0.9.

Turbine. The ABC turbine is designed by using a mean line prediction method base on one-dimensional parameters. The parameters are; the pressure coefficient ψ (or blade loading coefficient) (Eq. (11)), the flow coefficient ϕ (Eq. (12)), and the specific speed n_s (Eq. (13)).

$$\psi = \frac{Y}{\frac{1}{2}U^2} = \frac{c_P(T_{01} - T_{02})}{\frac{1}{2}U^2} \quad (11)$$

$$\phi = \frac{V_Z}{U} \quad (12)$$

$$n_s = \omega\frac{\dot{Q}^{1/2}}{Y^{3/4}} \quad (13)$$

where the indices 1 and 2 denote in and out of a stage, respectively.

The values for isentropic efficiency as a function of flow and pressure coefficients are taken from Smith's diagram (Sayers, 1990). This diagram gives the efficiency at the design point. For this specific study Smith's diagram is applied in a rather conservative manner. The turbine polytropic efficiency is estimated to 90 percent (total-to-total), which is 1–2 percentage points below that of the diagram for each stage.

For the three-dimensional design of the turbine stage, the free-vortex method is applied, which gives constant work from hub to tip over the blade. Furthermore, at this stage of the preliminary design it is assumed that the blade height is equally distributed on each side of the mean diameter of the blade. This may have to be redistributed in the final design analysis.

Intercoolers. The intercoolers are supposed to be of the "compact heat exchanger" type. The cold and hot fluids flow in finned channels arranged next to each other, and they are

Downloaded 02 Jun 2010 to 171.66.16.104. Redistribution subject to ASME license or copyright; see http://www.asme.org/terms/Terms_Use.cfm

separated by thin plates. The heat transfer surface geometry and design method are based on the work of Kays and London (1984).

Exhaust Gas to Air Heat Exchanger. The heat of the gas turbine exhaust is recovered and transferred to the compressed air between the compressor and turbine of the ABC. For this application there are two different types of heat exchanger that can be used: regenerators and recuperators. In a recuperator, heat is transferred through walls that separate the flows. In a regenerator, the heat transfer surface is alternately exposed to the two flows. Kays and London (1984) list three advantages that regenerators have over recuperators:

1 A much more compact heat transfer surface can be employed.
2 The heat transfer surface is substantially less expensive per unit of transfer area.
3 Because of the periodic flow reversals, there are no permanent flow-stagnation regions and, consequently, the surface tends to be self-cleaning. The self-cleaning feature has been demonstrated by Ljungstrom-type air preheaters used in central station plants employing lowest grade of coal.

A fourth advantage is that regenerators require only light-gage containment for the low-pressure exhaust gas over most of their volumes. Recuperators require heavy-gage containment over their entire volumes. Kays and London (1984) also list two disadvantages of regenerators compared to recuperators:

1 There is some mixing of the hot and the cold fluids because of leakage and carryover.
2 If the fluids are at different pressures, as in the ABC, the sealing problem of a regenerator is a difficult one.

Additionally one can say that recuperator design for this type of application and size range is a much more proven technology compared to that of regenerators.

Some fluid mixing is acceptable for regenerators in gas turbine systems; however, leakages have been unacceptably high—over 4 percent of the compressor flow in many cases. This is because the seal designs have been poor. This is why recuperators have been favored over regenerators for gas turbine systems. With a proper seal design it is possible to have leakages at about 3 percent. An air leakage of 3 percent reduces the combined gas turbine and ABC efficiency approximately 1 percentage point.

The core of the regenerator is smaller and weighs less than the core of a recuperator. The slats in a regenerator are not required to support any pressure difference, and may be as thin as 25 μm. The plates of a recuperator are typically about 200 μm thick (Wilson and Kupratis, 1994). The fact that the regenerator's slats are eight times thinner makes the core at least eight times lighter (Beck, 1994). Second, the thinner slats offer a smaller area for core heat conduction in the flow direction. Conduction reduces heat exchanger effectiveness, so the flow length in a plate-fin recuperator must be longer to compensate for the effects of conduction. This means that to achieve the same pressure drop across the core, the recuperator's plates must be spaced farther apart than the regenerator's slats, and this will increase the size of the recuperator.

In the present work it was chosen to go for a recuperator and not a regenerator. The most important reasons for this decision are the efficiency reduction caused by air leakage from a regenerator, and that large recuperators are a more proven technology compared to regenerators for this application. When or if regenerators become a more mature technology in this size range, it is indeed an interesting option for the ABC because of the high NTU number required in order to obtain a high cycle efficiency.

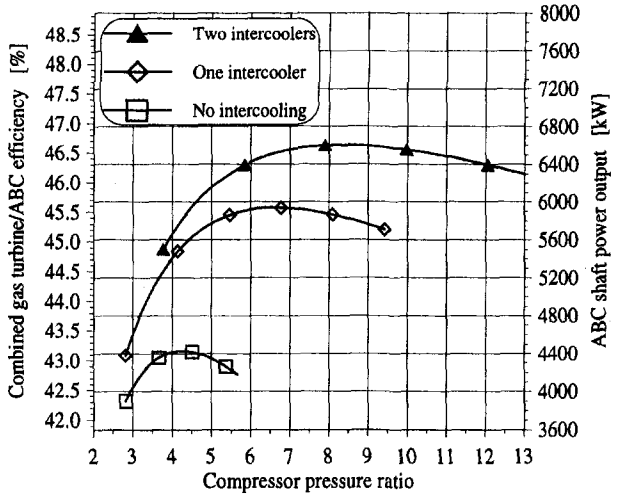

Fig. 2 Efficiency and ABC power output as function of compressor pressure ratio for no intercooling, one and two intercoolers

As for the intercoolers, the heat transfer surface geometry and design-method for the recuperator are based on the work of Kays and London (1984).

ABC Cycle Analysis

Number of Intercoolers. From a thermodynamic point of view the ABC should have an isothermal compression. This is of course difficult from a practical point of view. However, a larger number of intercoolers is wanted, up to a point where the benefit of an extra intercooler is balanced with the parasitic losses. When considering practical design and construction of the ABC, the question reduces to whether one or two intercoolers should be used. A comparison between different numbers of intercoolers and compressor pressure ratios is shown in Fig. 2. In the present work two intercoolers are chosen as well as a total compressor pressure ratio of 8:1 (including the intercooler pressure losses), which are based on the results presented in Fig. 2. With one intercooler the ABC power output peaks at a pressure ratio of approximately 6:1. With no compressor intercooling, the combined gas turbine/ABC efficiency peaks at a pressure ratio of approximately 4:1. The difference in combined gas turbine/ABC efficiency between using one or two intercoolers is slightly above 1 percent.

Number of Spools. The ABC engine can be designed as a single-shaft or two-shaft engine. In that respect an important point is how the topping gas turbine will be operated and what part-load performance is required. In order to fit in as an advantageous option on oil platforms, it is unquestionable that the ABC should be able to operate well at gas turbine part-load.

In the following a general qualitative comparison is made between a steam bottoming cycle and the ABC at part-load operation of the topping gas turbine. At part-load operation of the topping gas turbine (assuming a multispool engine) both exhaust gas flow rate and temperature are decreased compared to full-load operation. Both these types of bottoming cycle consist of three major process steps that influence the performance: compression, heat exchange from the topping to the bottoming cycle, and expansion.

Compression: The work of compression (feedwater pumps) is small in a steam bottoming cycle and may be regarded as unchanged at part load because of its small influence on plant efficiency. In a gas turbine cycle, the work of compression typically constitutes half of the turbine work (as high as 70 percent for the ABC). At part load it is highly important for an axial compressor to have the optimal combination of speed,

Downloaded 02 Jun 2010 to 171.66.16.104. Redistribution subject to ASME license or copyright; see http://www.asme.org/terms/Terms_Use.cfm

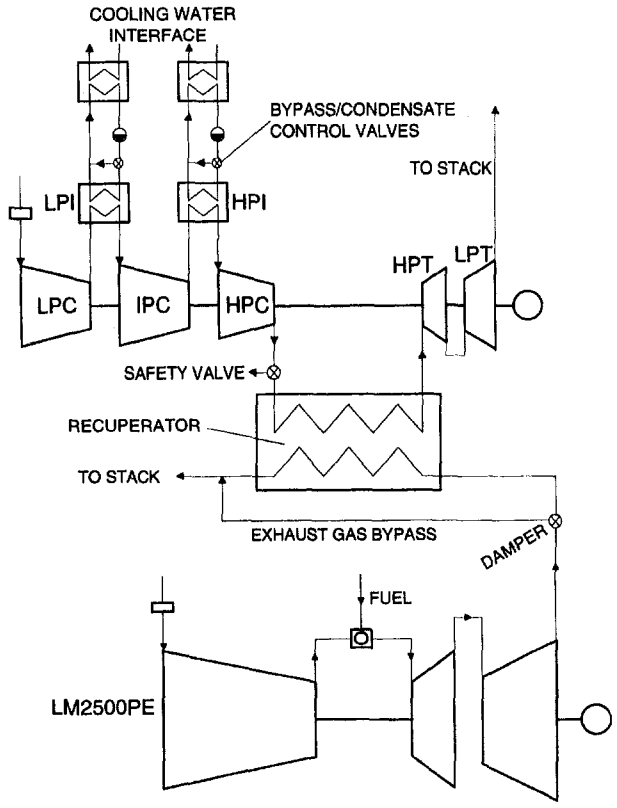

Fig. 3 Flowsheet diagram for the LM2500PE gas turbine and ABC

flow rate, and pressure ratio. Otherwise the efficiency drops off significantly. A two-shaft engine will in principle be better than a single-shaft engine in this respect. A single-shaft compressor would have to run at constant speed, and this is of course a disadvantage at part load. The part-load performance of the ABC compressor was estimated and it was found that the compressor has very steep constant-speed lines in a compressor map diagram. At part load the pressure ratio will decrease, but if constant speed is assumed, the compressor flow rate is more or less maintained. If the flow rate is maintained at constant speed and reduced pressure ratio, the compressor efficiency decreases significantly. The steep constant-speed line in the compressor map is caused by the intercoolers, which reduces the cumulative effects of "disturbances" through the compressor. Even if an axial compressor is operated at the most favorable conditions at different loads, the compressor efficiency is reduced to some extent and thus accordingly reducing the plant efficiency.

Heat transfer from the topping to the bottoming cycle: For a steam bottoming cycle, the steam generation is reduced as well as steam pressure (assuming sliding pressure operation) and steam temperature. The steam generation is mainly a function of heat transfer. The heat exchanger in the ABC acts in principle different from a steam generator in the sense that it is *not* the heat transfer that decides the flow rate on the cold side but rather the compressor. If using a single-shaft ABC engine with a more or less a constant flow rate at part load, the air exit temperature from the heat exchanger is reduced a lot more than the gas turbine exhaust temperature. For a two-shaft ABC engine where the flow rate is reduced at part load, the heat exchanger air exit temperature is maintained closer to the exhaust gas temperature.

Expansion: A steam turbine operates over a wide range of flow rates at rather high part-load efficiencies (sliding pressure operation). The ABC turbine with its low pressure ratio (compared to a steam turbine) is much more sensitive to changes in flow rate and pressure ratio with respect to efficiency. If a single-shaft engine is used, meaning more or less constant flow rate and low air temperature, the pressure ratio at part load is reduced significantly. If using a single-shaft engine, the difference between the compressor discharge temperature and the turbine inlet temperature will be small at part load and thus result in a small shaft work. The pressure ratio is also reduced significantly at part load for a two-spool engine because the flow rate reduction is more important than the more or less maintained turbine inlet temperature compared to using the single-shaft engine (according to the choked nozzle equation, the turbine inlet pressure is proportional to flow rate and proportional only to the square root of temperature). Concerning the part-load performance of the turbine, it is advantageous with a reduction in both flow rate and temperature (two-spool engine), instead of only temperature reduction at constant flow rate (single-spool engine).

It can be concluded that a combined gas turbine/steam turbine plant will operate at higher part-load efficiencies than the combined gas turbine/ABC. In order to reduce this difference, a possibility would be to use variable first row stator vanes in the turbine. Next it can be concluded that the part-load performance of a two-spool ABC engine will clearly be better than a single-shaft engine.

From a more general point of view, one can say that if the topping gas turbine is a two-spool (or three-spool) engine, the ABC should be a two-spool engine. On the other hand, if the topping gas turbine is a single-spool engine, the ABC also should be single-spool in order to match the flow rate of the ABC to that of the topping cycle.

Results From the Cycle Calculation. In the following the final cycle design is presented. The assumptions as well as site conditions for the cycle analysis are given in Appendices A.1-3. For the cycle calculations it was emphasized to use accurate models for the thermophysical properties of the air (Olikara and Borman, 1975). The referendum temperature for enthalpy of air was set to 25°C. A cycle flowsheet diagram is shown in Fig. 3.

A summary of the plant performance is given in Table 1. The pressure ratios for the different compressor modules were chosen after an optimization with respect to cycle efficiency.

The shaft power output from the ABC was calculated to 6.6 MW. This extra power increases the power generation efficiency from the simple cycle gas turbine efficiency of 36.1 percent to a combined cycle shaft efficiency of 46.6 percent. The ABC adds 10.5 percent points to the simple-cycle gas turbine efficiency.

Table 1 A summary of the plant performance data

Gas turbine net power output	22643	kW
ABC shaft power output	6605	kW
ABC power output at generator terminals	6407	kW
ABC auxiliary power requirements	67	kW
ABC net power output	6340	kW
Combined gas turbine/ABC power output	28983	kW
Gas turbine fuel consumption	1.3132	kg/s
Gas turbine efficiency	36.10	%
ABC cycle efficiency[1]	23.23	%
ABC cycle efficiency[2]	10.53	%
Combined gas turbine/ABC shaft efficiency	46.63	%
Net combined gas turbine/ABC efficiency	46.21	%

[1] Ratio between ABC shaft power output and the heat transferred from the gas turbine exhaust
[2] Ratio between ABC shaft power output and the gas turbine fuel energy input

Downloaded 02 Jun 2010 to 171.66.16.104. Redistribution subject to ASME license or copyright; see http://www.asme.org/terms/Terms_Use.cfm

Table 2 The balance of energy flows going in and out of the ABC "control volume"

Gas turbine exhaust gas heat (in)[1]	37825.1	kW
ABC net power output	6340.5	kW
Generator losses	198.2	kW
Mechanical losses	46.6	kW
Auxiliary power requirements	66.5	kW
Compressor inlet air flow	1231.4	kW
LP intercooler heat rejection	3510.6	kW
HP intercooler heat rejection	4942.0	kW
Heat loss from recuperator & ducts	56.9	kW
ABC turbine stack heat rejection	12045.1	kW
Gas turbine exhaust stack heat rejection	9387.6	kW
Sum of outgoing flows (out)	37825.2	kW

[1] The referendum for enthalpy by which the heat is calculated, is 25 °C

A complete energy flow breakdown for the ABC "control volume" is given in Table 2. It is shown how the heat transferred in the recuperator is converted to other energy flows.

In Table 3 an exergy loss breakdown is shown. The compressors constitute 14 percent of the total losses, the intercoolers 13 percent, the recuperator with ducting 11.1 percent, the turbine 11.2 percent, and the stack losses (both from the ABC and the gas turbine) constitute 47.3 percent of the total losses. The exergy efficiency of the ABC is 36.8 percent when using the gas turbine exhaust exergy as a reference.

When comparing the numbers in Tables 2 and 3 one can easily distinguish between what appears to be the losses given by a traditional first-law analysis, and the true losses resulting from a second-law analysis.

A sensitivity analysis was carried out, and the main conclusion is that for the final design of the ABC engine, engineering efforts should be put into designing for highest possible turbine and compressor efficiencies.

Component Design

Compressor Design. The compressor design process applied consists of two phases, determination of main dimensions and the more detailed preliminary design. In the design of the main dimensions, one determines number of stages, speed, and diameter by using dimensionless design parameters. The determination of these parameters is based on: recommended design rules as found in the literature (Øverli, 1992) and predicted values from actual compressor designs. The number of stages is determined by selecting a maximum pressure ratio (or head) per stage. In this case a maximum pressure ratio of 1.25 per stage was used. This resulted in three stages each for the LPC and IPC and four stages for the HPC. Inner and outer blade radius is determined by selecting the inlet hub/tip ratio 0.6 and the inlet axial Mach number 0.45.

The rotational speed can be found by selecting a flow coefficient (axial velocity/rotational velocity). Recommended values 0.4-0.5 for the low-pressure stages and 0.4-0.3 for the high-pressure stages. The ABC compressor consists of three serial coupled units. These units will be coupled on the same shaft, running with the same speed, 8500 rpm. As a compromise the selection of design speed was based on the IPC unit. As a result the design speed for the LP unit is somewhat higher than optimum and the design speed for the HP unit is slightly lower than optimum. The main dimensions of the flow path of the compressor is shown in Fig. 4.

The *preliminary design* is based on the main dimensions, and is obtained with the mean line prediction method as previously described. The purpose is to determine rotor blade angles, stator blade angles, blade height, blade chord, and blade spacing.

The following design criteria have been used to determine the blade geometry:

- Reasonable constant head per stage
- First-stage inlet relative Mach number between 0.75 and 0.8
- Equivalent diffusion ratio (D_{eq}) below 1.7 for all blades
- Constant or slightly decreasing axial velocity through each unit.

Chord and spacing have been selected by careful study of gas turbine axial compressor design. Stator blade angles have been determined to give zero incidence for both stator and rotor. No use of variable geometry has been evaluated. The computational results are given in Appendix A.4.

As an alternative to the current design, it would be possible to use a centrifugal HPC instead of axial type compressor. This would be a simpler and less expensive design, though the performance would be somewhat poorer compared to an axial HPC.

Turbine Design. The preliminary design for the turbine covered two different options; a one-spool engine running at 8500 rpm, and a two-spool engine with a HP turbine at 8500 rpm and a LP turbine (or power turbine) at 3000/3600 rpm. For the second option the HP turbine has to be designed to match the compressor work, which reduces the freedom in the design of the different turbine stages. As discussed earlier, it was concluded that the two-spool alternative is the preferred one.

The pressure coefficient (Ψ) is set between 2.0 and 3.0 and the flow coefficient (ϕ) target is approximately 0.6. Keeping the pressure coefficient as high as possible reduces the blade tip diameter but increases the blade loading and thereby reduces the polytropic efficiency. The flow coefficient has to be set to an optimum between blade height and meridional flow velocity. Lowering the flow coefficient gives a lower meridional velocity and thereby lower losses related to velocity, but on the other hand the blade height will be larger and imply a more complicated blade design.

For the 3000 rpm power turbine the maximum exit turbine diameter is approximately 1.5 m and including housing and dressing the maximum diameter can be as much as 1.8 m. For the 3600 rpm power turbine the exit turbine diameter is approximately 1.3 m and including housing and dressing the maximum diameter will be 1.6 m. The 3000 rpm two-spool option is about 0.6 m larger in diameter than a one-spool turbine (at 8500 rpm) would be, and the 3600 rpm two-spool option is 0.4 m larger. The main geometric parameters for the ABC turbine are shown in Fig. 4.

Table 3 Exergy balance of the ABC

Gas turbine exhaust gas exergy (in)[1]	17222.4	kW
ABC net power output	6340.5	kW
Generator losses	198.2	kW
Mechanical losses	46.6	kW
Auxiliary power requirements	66.5	kW
Compressor inlet air flow	0	kW
Air filter	57.7	kW
LP compressor	494.9	kW
LP intercooler[2]	564.1	kW
IP compressor	430.6	kW
HP intercooler[2]	863.3	kW
HP compressor	595.5	kW
Recuperator & ducts[3]	1206.4	kW
Turbine	1215.8	kW
ABC turbine stack loss	3068.3	kW
Gas turbine exhaust stack loss	2074.1	kW
Sum exergy losses & net work (out)	17222.4	kW

[1] Ambient condition: T=281.15 K (8 °C) and p=1.013 bar.
[2] Includes both rejection of heat and pressure loss
[3] Includes the heat transfer loss and pressure losses for both air and exhaust gas.

Downloaded 02 Jun 2010 to 171.66.16.104. Redistribution subject to ASME license or copyright; see http://www.asme.org/terms/Terms_Use.cfm

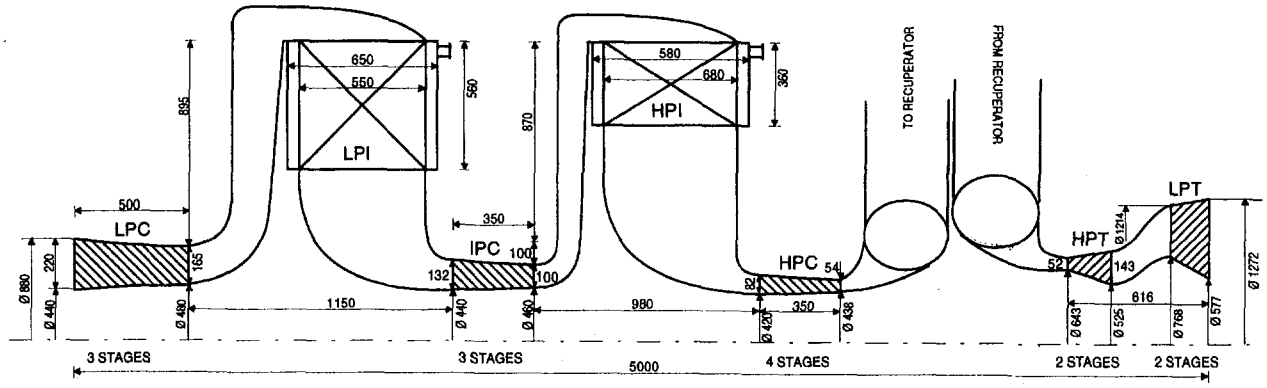

Fig. 4 A sketch of the ABC engine

Intercooler Design. A multipass crossflow configuration was chosen for both intercoolers. The compressor air makes one pass and the cooling water makes two passes in each intercooler. An alumina alloy, AA 6082 T6, was chosen as the core material (Solheim, 1994). This alloy is often used in offshore applications. The density is 2710 kg/m^3 and the thermal conductivity is 170 W/(m K). The intercoolers are designed as modules; where 12 modules form a ring around the compressor body for each of the two intercoolers (see Fig. 5). The main design data for the intercoolers (1 out of 12 modules) are shown in Table 4. The air side pressure drop was allowed to be 2 percent for each of the intercoolers. Nearly half of this pressure drop is related to the heat exchanger core, while the remaining pressure drop is due to diffuser, bends, and headers.

Recuperator Design. In the present study a design of a recuperator for the ABC was made. A comparable design is that of the recuperator, which is going to be used in the WR-21 intercooled and recuperated gas turbine from Rolls-Royce and Westinghouse (Ricket, 1994; Shepard et al., 1995; Hawkins et al., 1994). The design made in the present study is to a large extent similar to that of the WR-21. The WR-21 recuperator is designed as a plate-fin heat exchanger with an effectiveness of approximately 90 percent and weighing approximately 18 metric tons. The main difference between the WR-21 recuperator and the ABC recuperator is the ratio between the heat capacities $\dot{m}c_P$ of the hot and the cold fluids. For a gas turbine with air cooling, a certain percentage of the compressor air (the cooling air) does not go through the recuperator. The specific heat capacity of exhaust gas is about 4–5 percent higher than that of the air at relevant temperatures. The $\dot{m}c_P$ ratio will probably be somewhere between 0.75 and 0.85 for a gas turbine recuperator, while for the ABC this ratio was found optimal at unity. When comparing these two recuperators for the same effectiveness and same heat transfer, the NTU number will be significantly higher for the ABC recuperator. This means that the ABC recuperator will be notably larger than a gas turbine recuperator.

The details from the present recuperator design are shown in Table 5. Surface type P9 or 9.03 was chosen for the exhaust gas side and P13 or 19.86 for the air side (Kays and London, 1984). For the current design an alloy steel was chosen instead of ordinary steel (conductivity of 20 W/(mK)). The WR-21 recuperator is going to be made of 14Cr4MO stainless steel, which was preferred to the more expensive Incoloy 800 (Shepard et al., 1995). If there will be more corrosion than expected, the rather expensive INCO 625 is the preferred material. The recuperator core weight and volume were in the present study calculated to 42.4 metric tons and 53.6 m^3, respectively. Efforts were made to design a compact recuperator, which is evident when considering the relatively high number for heat transfer area per volume.

In Fig. 6 the influence of recuperator effectiveness on cycle efficiency and recuperator weight is shown, where an $\dot{m}c_P$ ratio of 1 is assumed. There are two curves for the recuperator weight; one for alloy steel and one for ordinary steel. The difference in weight between these two options is around 6 metric tons for a recuperator effectiveness of 90 percent. As the recuperator effectiveness is increased, the cycle efficiency increases linearly. The recuperator weight increases exponentially as the

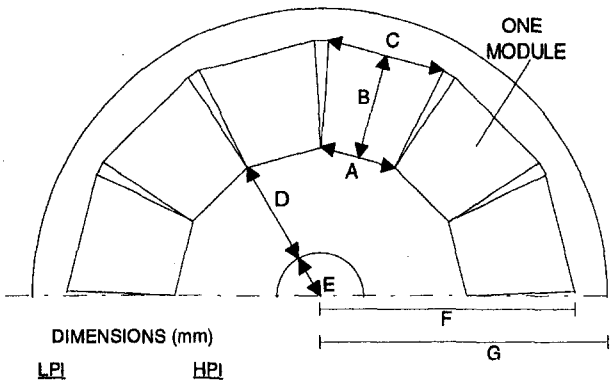

DIMENSIONS (mm)

LPI	HPI
A = 383	A = 486
B = 541	B = 370
C = 650	C = 650
D = 520	D = 730
E = 220	E = 210
F = 1300	F = 1323
G = 1450	G = 1420

Fig. 5 A view of the intercooler modular design in the axial direction of the ABC engine

Table 4 Intercooler design data: The numbers are for one module out of 12 parallel ones for both the LP and HP intercooler

	LPI		HPI	
	air	water	air	water
Flow rate [kg/s]	5.994	4.208	5.994	6.046
Inlet pressure [bar]	1.897	2.0	3.561	2.0
Inlet temperature [°C]	72.68	13.0	93.48	13.0
Film coeff. [W/(m^2 K)]	149.9	2383	225.3	2447
Fin efficiency [-]	0.905	0.693	0.865	0.687
Mass flux [kg/(m^2 s)]	37.98	121.1	59.45	112.7
Reynolds number [-]	6981	338.1	10495	314.7
Total film coeff. [W/(m^2 K)]	121.0		166.7	
Resistance ratio air/water-side	7.4		5.22	
Core volume [m^3]	0.145		0.119	

Downloaded 02 Jun 2010 to 171.66.16.104. Redistribution subject to ASME license or copyright; see http://www.asme.org/terms/Terms_Use.cfm

Table 5 Recuperator design data

	Exhaust gas	Air
Flow rate [kg/s]	69.24	71.93
Inlet pressure [bar]	1.033	8.012
Inlet temperature [°C]	527	114.8
Film coeff. [W/(m^2 K)]	49.8	121
Fin efficiency [-]	0.567	0.798
Mass flux [kg/(m^2 s)]	4.31	15.90
Reynolds number [-]	662.5	1002
Fin frequency [m^{-1}]	355.3	781.9
Plate spacing [mm]	20.9	6.35
Fin thickness [mm]	0.203	0.152
Heat transfer area/volume [m^2/m^3]	800.5	1841
Total film coeff. [W/(m^2 K)]	21.3	
Resistance ratio exhaust/air-side	2.28	
NTU [-]	9.12	
Heat transfer effectiveness [%]	90.4	
Plate thickness [mm]	0.2	
Core volume [m^3]	53.6	
Core weight [kg]	42400	

recuperator effectiveness goes up. If the recuperator weight is to be reduced from the present value of 42 metric tons down to, say, 20 metric tons, the recuperator effectiveness must be reduced to approximately 82 percent. The combined gas turbine and ABC efficiency is then reduced from 46.6 to approximately 44.7 percent.

When comparing the weight of the present recuperator design to the weight of a regenerator, there is a difference by a factor of approximately 4–5.

Cost and Economics of the ABC

A weight and cost estimation of the components in the ABC was carried out. The results are summarized in Table 6. The net present value of the added efficiency/power by the ABC at constant fuel consumption was calculated to 9 million US$. This is approximately the same as the predicted cost of the ABC (9.4 million US$).

An economic analysis was carried out. Different cases were defined and comparisons were made between these. Some general parameters for the economic calculations are given in Appendix A.4. The *reference case* for comparison is the ABC together with an LM2500PE gas turbine. It is assumed that the

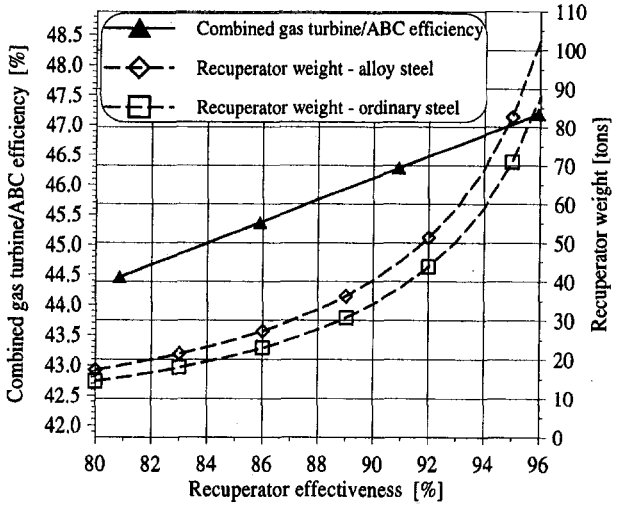

Fig. 6 Combined gas turbine/ABC efficiency and recuperator weight as function of recuperator effectiveness

Table 6 Cost estimates for the ABC components

Component	Cost	Weight
	Mill. US$	Metric tons
Air inlet system	0.294	10.6
ABC engine (without intercoolers)	4.412[1]	30.0
Intercoolers	0.206	3.0
Recuperator	2.941	45.0
Generator including enclosure	0.809	20.3
Ducting, dampers and stack	0.403	37.4
Cooling water pumps	0.011	0.7
Sea water heat exchangers	0.077	5.2
Other	0.206	2.0
Total	**9.359**	**154.2**

[1] The production cost may be approximately 1/3 of this number

other cases must give the same power output as for the combined LM2500PE and ABC (29 MW). On this basis two cases (1-2) were defined for an installation on a new oil platform, and one case was defined for a retrofit case on an existing platform (3). The cost of installing equipment of this type on a new platform was estimated to 47 US$/kg (Rasmussen, 1994). The cases are:

Reference case: 1 × LM2500PE + ABC. The weight and cost of the LM2500PE are estimated to 125 metric tons and 11.3 MUS$, respectively. The weight and cost of the ABC are estimated to 154 metric tons and 9.4 MUS$. The power output and efficiency are 29 MW and 46.2 percent, respectively.

1 *The reference case compared to using 2 × LM2500PE.* These two gas turbines are assumed to operate on part load such that the power output equals that of the reference case. The gas turbines will be operating at an efficiency of 32.7 percent. The weight of these two gas turbines including all equipment is estimated to 250 metric tons. The total cost is estimated to 22.6 MUS$.

2 *The reference case compared to using an LM2500+.* It is assumed that this gas turbine will operate at full load with an efficiency of 37.0 percent. The cost and weight of an LM2500+ are estimated to 13.5 MUS$ and 150 metric tons, respectively. The LM2500+ is an upgraded and partly redesigned version of the LM2500PE. The main difference between these two is that LM2500+ has a new stage added in front of the compressor, which increases the air flow approximately 20 percent. The pressure ratio is raised from 18 to 23, and the efficiency is increased 1–2 percent compared to the LM2500PE (all these numbers are preliminary).

3 Assuming that on an existing platform is an LM2500PE. The two alternatives to be considered consist of: (*a*) ABC is installed beside an existing LM2500PE, assuming that there is enough space available and that the platform structure can take the extra weight of the ABC. (*b*) The existing LM2500PE is exchanged with a new LM2500+. According to GE it will be possible to exchange only the engine itself, and other components like the air intake system do not have to be changed. These two alternatives would give the same power output. The cost and weight of the ABC is assumed equal to that of the ABC in the reference case. The cost of the LM2500+ is estimated to 6.2 MUS$. The platform-related cost for exchanging the LM2500PE with the LM2500+ is estimated to be equal to that of a new installation, meaning that the weight (150 metric tons) is multiplied with the specific cost of weight used in the present study.

One should note that the assumption of equal power output means that for case 1 there will be invested in surplus power that is *not* given any value in the economical analysis.

The results of the economic comparison of the cases are presented in Table 7. It should be noted that the numbers for

Downloaded 02 Jun 2010 to 171.66.16.104. Redistribution subject to ASME license or copyright; see http://www.asme.org/terms/Terms_Use.cfm

Table 7 Results from the economic comparison between the LM2500PE/ABC and the other cases

Case	1	2	3
	2×LM2500PE new platform	1×LM2500+ new platform	1×LM2500+ existing platform
NPV capital costs [MUS$]	0.6	-13.3	-3.4
NPV CO_2-tax [MUS$]	21.8	13.1	13.1
NPV fuel gas cost [MUS$]	15.0	9.0	9.0
NPV Total [MUS$]	37.4	8.9	18.8
Annuity [MUS$/year]	4.1	1.0	2.1
Simple payback [years]	-	5.5	1.4

net present value (NPV) and annuity in Table 7 are calculated by subtracting the key number values of the present case from those of the reference case. The net present value of the capital cost is negative when the investment cost of the reference cost is higher than that of the present case (as for case 2 and 3).

The results in Table 7 show that all cases gave a positive net present value. The simple payback time was calculated to 5.5 and 1.4 years for cases 2 and 3, respectively. For case 1 the investment cost for the reference case was found less, and thus no payback time was calculated.

Conclusions

The conclusion is that the Air Bottoming Cycle is an economical alternative for power generation on both new platforms and on existing platforms with demand for more power.

The recommended ABC is a two-shaft engine with two compressor intercoolers. The pressure ratio was found optimal at 8:1. A recuperator is recommended instead of a regenerator for the heat transfer from the gas turbine exhaust gas to the compressed air of the ABC.

The combined gas turbine and ABC shaft efficiency was calculated to 46.6 percent. The LM2500PE gas turbine contributes with 36.1 percent while the ABC adds 10.5 percent points to the gas turbine efficiency. The ABC shaft power output is 6.6 MW when utilizing the waste heat of an LM2500PE gas turbine. For a final design of the ABC, the compressor and turbine efficiencies are very important to get as high as possible with respect to cycle power output and efficiency.

The preliminary compressor and turbine design has shown that an axial intercooled compressor and an axial turbine, which are adapted to the air bottoming cycle for an GE LM2500PE, can be built using conventional design practice.

At present it is suggested to use a recuperator and not a regenerator for the ABC.

A weight and cost breakdown of the ABC is presented. The total weight of the ABC package was calculated to 154 metric tons, and the ABC package cost to 9.4 mill. US$.

An economic examination for three different cases was carried out. The results show that the ABC alternative (LM2500PE + ABC) is economical, with a rather good margin, compared to the other alternatives.

Acknowledgments

Norsk Hydro, Kværner Energy, and the Research Council of Norway supported this work.

References

Beck, S., 1994, "Creare Baleen Regenerator," Memorandum, Creare Inc.

Bolland, O., 1991, "A Comparative Evaluation of Advanced Combined Cycle Alternatives," ASME JOURNAL OF ENGINEERING FOR GAS TURBINES AND POWER, Vol. 113, pp. 190–197.

Farrell, W. M., 1988, "Air Cycle Thermodynamic Conversion System," United States Patent No. 4,751,814.

Farrell, W. M., 1992, "Air Cycle Thermodynamic Conversion System," European Patent Specification 0 208 162 B1.

Grieb, H., Schill, D. G., and Gumucio, R., 1975, "A Semi-empirical Method for the Determination of Multistage Axial Compressor Efficiency," ASME Paper No. 75-GT-11.

GTPRO v.6.5, 1994, commercially available gas turbine database and power cycle design program, Thermoflow Inc., Wellesley MA, USA.

Hånde, B. M., 1992, "Simulation of Steam Injected Gas Turbines," Doctoral Thesis, University of Trondheim, ISBN 82-7119-401-1.

Hawkins, W. J., Mathieson, D., Bruce, C. J., and Socoloski, P., 1994, "System Development Test Program for the WR-21 Intercooled Recuperated (ICR) Gas Turbine Engine System," ASME Paper No. 94-GT-186.

Hornnes, A., and Bolland, O., 1991, "Power Cycle Working Fluids," SINTEF-report STF15 A91041, Trondheim, Norway.

Kays, W. M., and London, A. L., 1984, *Compact Heat Exchangers,* 3rd ed., McGraw-Hill.

Klapproth, J. F., 1959, Discussion of paper by Lieblein listed elsewhere in this reference list, ASME *Journal of Basic Engineering,* Vol. 81, p. 398.

Koch, C. C., and Smith, L. H., 1976, "Loss Sources and Magnitudes in Axial-Flow Compressors," ASME JOURNAL OF ENGINEERING FOR POWER, Vol. 98, No. 3.

Koch, C. C., 1981, "Stalling Pressure Rise Capability of Axial Flow Compressor Stages," ASME JOURNAL OF ENGINEERING FOR POWER, Vol. 103, No. 4.

Lieblein, S., 1959, "Loss and Stall Analysis of Compressor Cascades," ASME *Journal of Basic Engineering,* Vol. 81, No. 3.

Olikara, C., and Borman, G. L., 1975, "A Computer Program for Calculating Properties of Equilibrium Combustion Products With Some Applications to I.C. Engines," SAE Paper No. 750468, Feb.

Øverli, J. M., 1992, *Strømningsmaskiner (Turbomachinery),* Vol. 3, 2nd ed., Tapir, Trondheim.

Pettersen, J., 1987, "Bunnprosesser for gassturbin-kraftverk (Bottoming Cycles for Gas Turbine Power Plants)," Diploma Thesis, Division of Refrigeration, Norwegian Institute of Technology.

Rasmussen, J. B., 1994, personal communication, Norsk Hydro T&U.

Ricket, R., 1994, personal communication, Westinghouse Electric Corporation, ICR Design Engineering.

Sayers, A. T., 1990, *Hydraulic and Compressible Flow Turbomachines,* McGraw-Hill, New York, p. 236.

Shepard, S. B., Bowen, T. L., and Chiprich, J. M., 1995, "Design and Development of the WR-21 Intercooled Recuperated (ICR) Marine Gas Turbine," ASME JOURNAL OF ENGINEERING FOR GAS TURBINES AND POWER, Vol. 117, pp. 557–562.

Solheim, K. S., 1994, personal communication, Norsk Hydro Aluminium Structures.

Sovran, G., and Klomp, E. D., 1967, "Experimentally Determined Optimum Geometries for Rectilinear Diffusers With Rectangular, Conical or Annular Cross-Section," *Fluid Mech. of Internal Flow,* Elsevier Publishing, Amsterdam.

Sæther, S., 1993, "Combined Cycles With Compact Heat Recovery Steam Generators," SINTEF Report STF15 A93111, Trondheim, Norway.

Walker, G., Kremer, J., Fauvel, R., Reader, G., and Bingham, E. R., 1992, "Stirling Bottoming Cycle for the Gas Turbine Exhaust Streams of Pipeline Compressor Stations," *Proceedings of the 27th Intersociety Energy Conversion Engineering Conference,* San Diego, CA, Aug.

Wicks, F., Berven, G., and Marchionne, D., 1992, "A Combined Cycle With Gas Turbine Topping and Thermodynamically Ideal Gas Turbine Bottoming," *Proceedings of the 27th Intersociety Energy Conversion Engineering Conference,* San Diego, CA, Aug.

Wilson, R. A., and Kupratis, D. B., 1994, "Future Vehicular Recuperator Technology Projections," ASME Paper 94-GT-395; accepted for publication in the ASME *Journal of Turbomachinery.*

Weston, K. C., 1993, "Dual Gas Turbine Combined Cycles," *Proceedings of the 28th Intersociety Energy Conversion Engineering Conference,* Atlanta, GA.

APPENDIX

A.1 Site Conditions

In this study a specific location on an oil platform in the North Sea was chosen for a possible implementation of the ABC. Site conditions typical on an oil platform were chosen as: ambient temperature = 8°C, ambient relative humidity = 60 percent, ambient air pressure = 1.013 bar, cooling water temperature = 8°C, generator speed = 60 Hz.

A.2 Topping Gas Turbine

The LM2500PE gas turbine is the most commonly used gas turbine in the Norwegian sector of the North Sea. This gas turbine was chosen as the topping cycle for the ABC. Performance and exhaust gas data are given in Table 8. A typical fuel gas composition was used. The source of the LM2500PE data is GTPRO (1994).

A.3 Computational Parameters

Ambient temperature = 8°C, ambient air pressure = 1.013 bar, compressor pressure ratio: LPC = 1.91, IPC = 1.91, HPC

Downloaded 02 Jun 2010 to 171.66.16.104. Redistribution subject to ASME license or copyright; see http://www.asme.org/terms/Terms_Use.cfm

Table 8 LM2500PE performance and exhaust gas data (GTPRO, 1994)

Fuel consumption		1.3132	kg/s
Exhaust gas flow rate		69.24	kg/s
Exhaust gas temperature		527	°C
Compressor inlet pressure loss		10	mbar
Turbine exhaust pressure loss		20	mbar
Generator terminal power output		22935	kW
Gas turbine auxiliary power		111	kW
Miscellaneous plant auxiliaries		181	kW
Net power output		22643	kW
Net efficiency		36.1	%
Exhaust gas:	Nitrogen - N_2	75.15	vol-%
	Argon - Ar	0.90	vol-%
	Oxygen - O_2	13.74	vol-%
	Carbondioxide - CO_2	3.36	vol-%
	Water - H_2O	6.85	vol-%

= 2.28, compressor inlet temperature: LPC = 8°C, IPC = 25°C, HPC = 25°C, turbine inlet temperature = 490°C, turbine polytropic efficiency = 90.0 percent, turbine exit pressure drop = 4 mbar, compressor inlet pressure drop = 10 mbar, recuperator air side pressure drop = 160 mbar, recuperator heat loss = 0.2 percent, recuperator air loss = 0.0 percent, pressure drop intercoolers: LP = 2.0 percent, HP = 2.0 percent, mechanical efficiency = 99.3 percent, generator efficiency = 97.0 percent, auxiliary power ([percent] of net power) = 1.0 percent; computational interest rate = 7 percent, economical life time = 15 years, operational hours per year = 8000 h, fuel gas CO_2 tax = 11.76 cents/Sm^3, fuel gas sales value = 8.09 cents/Sm^3.

A.4 Compressor Design Details

Low-Pressure Compressure—LPC

Inlet rotor angle	Outlet rotor angle	Blade height [m]	Spacing [m]	Chord [m]	R_{outer} [m]	R_{inner} [m]
50	37	.220	0.047	0.065	0.440	0.220
53	37.7	0.190	0.046	0.06	0.420	0.230
55	39	0.165	0.044	0.05	0.405	0.240

Stage	T_{02} [K]	T_{S2} [K]	T_{S1} [K]	p_{02} [bar]	Work [kW]
0	281.1	267.4	267.4	1.003	—
1	302.3	278.1	261.4	1.271	1532
2	324.8	302.9	285.4	1.591	1633
3	246.5	325.9	309.1	1.916	1577

LPC polytropic efficiency (total-to-total): 88.3, work: 4742 kW, exit pressure: 1.916 bar.

Intermediate-Pressure Compressor—IPC

Inlet rotor angle	Outlet rotor angle	Blade height [m]	Spacing [m]	Chord [m]	R_{outer} [m]	R_{inner} [m]
47	27	0.132	0.045	0.04	0.352	0.220
48	26	0.116	0.042	0.038	0.340	0.224
50	27	0.100	0.040	0.035	0.330	0.230

Stage	T_{02} [K]	T_{S2} [K]	T_{S1} [K]	P_{02} [bar]	Work [kW]
0	298.1	282.6	282.6	1.883	
1	321.0	298.6	280.2	2.403	1658
2	343.2	321.4	304.5	2.971	1612
3	366.2	345.3	327.6	3.596	1669

IPC polytropic efficiency (total-to-total): 89.7, work: 4938 kW, exit pressure: 3.596 bar.

High-Pressure Compressor—HPC

Inlet rotor angle	Outlet rotor angle	Blade height [m]	Spacing [m]	Chord [m]	R_{outer} [m]	R_{inner} [m]
48	20	0.0820	0.036	0.033	0.292	0.210
48	19	0.0700	0.034	0.032	0.284	0.214
48	19	0.0610	0.031	0.030	0.278	0.217
48	20	0.0540	0.028	0.028	0.273	0.219

Stage	T_{02} [K]	T_{S2} [K]	T_{S1} [K]	p_{02} [bar]	Work [kW]
0	298.1	284.0	284.0	3.536	—
1	322.5	302.7	283.4	4.574	1768
2	345.5	325.7	308.3	5.678	1672
3	367.5	347.6	331.5	6.883	1594
4	388.1	368.4	353.5	8.062	1498

HPC polytropic efficiency (total-to-total): 89.0, work: 6530 kW, exit pressure: 8.062 bar.

Downloaded 02 Jun 2010 to 171.66.16.104. Redistribution subject to ASME license or copyright; see http://www.asme.org/terms/Terms_Use.cfm

J. P. Ehrhardt
Naval Sea System Command,
Amphibious Warfare Program,
Washington, DC

S. K. Spring
Gas Turbine Branch,
Carderock Division Naval
Surface Warfare Center,
Philadelphia, PA 19112

Component and Procedural Improvements for the T-62T-40-7 Gas Turbine in the LCAC Fleet

The Sundstrand Power Systems T-62T-40-7 Gas Turbine Auxiliary Power Unit (APU) was adapted from an aircraft-borne APU to a marine application on the U.S. Navy's Landing Craft Air Cushion (LCAC). Although the LCAC APU experienced less operating time than its aircraft version, the environmental conditions that exist cause unusual wear and component failures. Component and procedural improvements have been developed to extend the reliability of the T-62T-40-7 on board the LCAC.

Introduction

The Landing Craft Air Cushion (LCAC) is the U.S. Navy's high-speed amphibious landing craft capable of operating over land, water, and ice. The craft are transported in and launched from well-deck equipped amphibious ships of the LSD 36, LSD 41, LPD, LHA, and LHD classes. The primary mission for the LCAC is amphibious warfare to provide quick and over-the-horizon transport of personnel, cargo, and equipment of a U.S. Marine task force from ship to shore. The lift and speed capabilities of the LCAC are provided from aero derivative Textron Lycoming TF40B turbines for main propulsion and Sundstrand Power Systems (SPS) T62T-40-7 (T-62) gas turbine generator sets for auxiliary power. Extensive engineering has gone into protecting the engine with air filtration to remove water, airborne salt, and sand, but unexpected engine mechanical problems occur that are unique to the craft environment and operating platform (Fig. 1).

While on cushion the gas turbine air inlets are about 15 ft (5 m) above the water surface. The sea state and speed of the craft subject these inlets to a constant deluge of sea water spray. On land, the beach sand is blown by the lift cushion air and the propellers into every part of the craft. If there is a slight crack or opening in between inlet filters or engine housing seals, water, salt and sand will find their way into these crevices to create potential problems for the gas turbine engines. Even in the well deck of the lift ship, inlet air is contaminated with exhaust soot and smoke that passes through the air filters as the craft light off and prepare to embark on a mission. In comparison to the protected confines of other naval gas turbines in larger ships, the LCAC main propulsion engines, Textron-Lycoming TF40B, and the auxiliary engines, SPS T-62, probably experience the most severe environmental conditions of any current U.S. Navy gas turbine engines.

In these particular case studies of the SPS T-62 engine, the engine mechanical failures are unique to the LCAC installation, even though this engine has had numerous hours of operation on aircraft applications, and a 500-hour LCAC acceptance test.

There are two T-62 auxiliary power units on board the LCAC used for electrical power, and bleed air for the main engine starting and anti-ice heating of the propeller shrouds. The gas turbine engine's rated output power is 150 shaft horsepower (SHP) at a standard 59°F (15°C) day with zero bleed air at 61,091 rpm (100 percent rated speed), or 100 SHP and with 40 lb/min bleed airflow. The generator's rated output voltage, current, and load is 120/208 volts AC, 167 amps, 60 kW, respectively, at a 400 Hz frequency.

The engine has a single shaft with centrifugal compressor and turbine. The load on this turbine varies with the electrical power and the bleed air demands. The electrical power requirement is the primary load while bleed air is throttled for exhaust gas temperature (EGT) control (see Fig. 2).

Component Improvements

T-62 Labyrinth Oil Seal. One of the earliest and most perplexing problems encountered with the T-62 engine on the LCAC is the high oil consumption because of leakage around the labyrinth seal of the compressor bearing (see Fig. 3). This failure has accounted for about 43 percent of T-62 engine removals from the craft in the past seven years.

The labyrinth oil seal is pressurized by compressor discharge air from the backside of the impeller through three equally spaced lengthwise grooves in the rotor shaft (i.e., buffer air grooves). When the engine is removed and disassembled for oil leakage, the buffer air grooves are completely filled and blocked with a black residue. The blockage of these air passages during engine operation allows lubricating oil to be sucked out of the bearing past the labyrinth seal into the compressor air stream, losing about 2 quarts (1.75 liters) of oil per hour. Chemical analysis of the black residue was conducted on several engines and found to contain the following elements: a majority of carbon with silicon, chlorine, sodium, and trace iron and sulfur. The source of this residue came from three probable faults:

- Oil coking after shutdown;
- Ingestion of exhaust gases during operation (sulfur was found in some residue samples);
- Compartment or air filter bypass of inlet air (some samples contained only sand and salt).

From this analysis, we felt that there was a multiple of failure mechanisms, and developed designs that would correct them.

The first design improvement was to change the labyrinth seal O-ring configuration from a face seal to a circumferential design. This change helped reduce the number of premature engine removals that occurred around 100 hours of operation. During disassembly of these engines, the dimensions of the parts were correct, but the assembly tolerances allowed for insufficient compression of the rubber face seal and looseness around the outside diameter. At the recommendation of our repair facility, Naval Aviation Depot, Cherry Point and our engineering facility, Naval Surface Warfare Center Carderock Division (NSWC-CD), we have been replacing this seal with

Contributed by the International Gas Turbine Institute and presented at the 39th International Gas Turbine and Aeroengine Congress and Exposition, The Hague, The Netherlands, June 13–16, 1994. Manuscript received by the International Gas Turbine Institute February 9, 1994. Paper No. 94-GT-168. Associate Technical Editor: E. M. Greitzer.

Copyright © 1996 by ASME

Downloaded 02 Jun 2010 to 171.66.16.104. Redistribution subject to ASME license or copyright; see http://www.asme.org/terms/Terms_Use.cfm

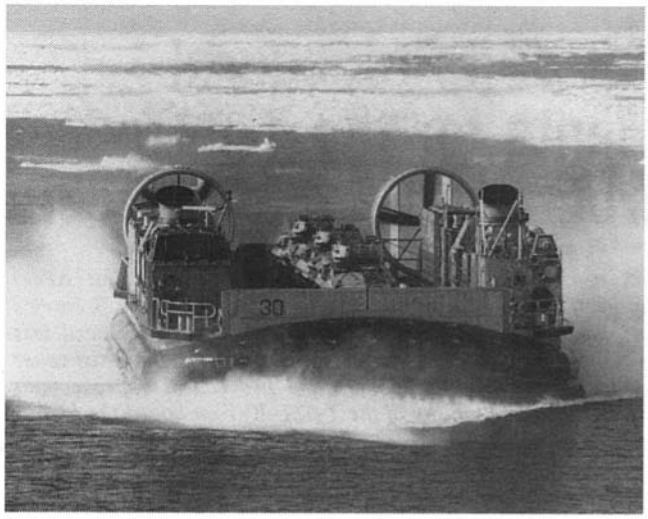

Fig. 1 LCAC on cushion in Bering Sea

a navy aircraft engine circumferential seal configuration during depot repair.

The second change was to add a delta pressure gage and alarm for the last-stage engine inlet "Duralife" filter. The engine manufacturer's technical position was that exhaust soot was ingested from the T-62 eductor opening when the filter is clogged or blocked and the fire doors accidently close (see Fig. 4). The alarm alerts the crew to replace the filters, or check the fire door opening.

The third change was to redesign the compartment bolted-accessed hatch to a quick-opening configuration. By chance, it was found that the LCAC crews were reattaching the top hatch with a third of the 56 bolts required (for easier access to the engine) and often without gaskets. This was found to be a major source of salt and sand contamination, when water and sand entered through the gaps of the unbolted sections of the hatch.

Oil coking after engine shutdown is still a potential source of contamination in the air grooves because of the heat transfer through the shaft from the turbine impeller. During recent baseline measurements for oil loss with the labyrinth and carbon seals, engine motoring causes excessive oil seepage/blow-by around the unpressurized shaft grooves. Engine motoring for turbine cooling is currently required at shutdown EGT temperatures of 400°F (204°C) or above. Since shutdowns average about 400°F, we are contemplating raising the motoring/cooling temperature to reduce the probability of flooding the grooves at shutdown, and also to reduce the number of starter failures discussed in later sections of this paper.

While these design changes were being developed, an intermediate maintenance procedure was implemented to clean the buffer air passages in the shop (without removing the impeller) using a solvent and small wire rods. This procedure reduces the cost and increases the availability for what would normally be a depot repair.

In the long term, we will be testing a carbon seal and bellows seal that would replace the labyrinth design and negate the requirement for a buffer air passage.

Carbon and Bellows Seals. The replacement of the labyrinth seal by either a carbon or a bellows seal is an intricate design change to the T-62. As mentioned above, this change is in response to the numerous oil leakage failures of the labyrinth bearing seal. NSWC-CD, along with two seal manufacturers, has designed two alterative seals. The carbon seal is designed and manufactured by EG&G Sealol, and the bellows seal is designed and manufactured by Metal Fab Corp. Both designs are intended to be a direct replacement for the existing labyrinth seal and to function properly without the need for secondary air pressure. Both the seals were selected in part because they are presently being used in other gas turbine applications.

The carbon seal is similar in design to the existing labyrinth seal with the exception of the inner labyrinth "teeth," which have been removed and replaced by a cracked carbon element (Fig. 5). The carbon element was designed to expand with the shaft in order to apply a constant sealing pressure on the shaft though the entire engine heating and expansion process.

The bellows seal uses a silica element to contact a wear ring. The wear ring is attached to the shaft. The silica element is held concentrically around the shaft using a small bellows spring assembly (Fig. 6).

The seals will be evaluated in the test cell on normal engines and oil consumers, as well as in the fleet. There were not enough test cell data at the time of this paper to select a seal design; however, the carbon seal has shown improved resistance to oil consumption.

Start Bypass Valve. Corrosion can occur everywhere on the craft, and especially around the inlet air paths of the gas turbines. Susceptible areas of external corrosion can be cleaned by external fresh water rinses to remove excess salt coating. On the internal parts of the turbine, the manufacturer must take the marine environment into account when considering the material of the part. The current T-62 bypass valve is used to unload to atmosphere the compressor discharge pressure of the engine under reduced loads. The valve is made of cast aluminum and corrodes severely around the electrical connectors. Internal pitting has also occurred to restrict internal valve movement. This particular case is an example of an original aircraft component being used in a marine environment.

Two design changes have been initiated: A cap has been installed on the end of the air discharge at 01 deck to prevent sea water accumulation in discharge line; and the valve body has been changed to a cast corrosion resistant steel.

Cold Weather Heaters. In 1987, the LCAC was tested in a cold weather chamber at temperatures from 40°F (4°C) to −30°F (−34°C). The purpose of this test was to verify the operation of the craft installed cold weather equipment and to identify any unique problems with the craft machinery in a cold/arctic environment.

For the gas turbines, fuel heaters have been installed in the main fuel tanks, and the T-62's have additional starting fuel tank heaters, to prevent diesel fuel wax accumulation in fuel lines and filters. From a cold craft condition, the T-62 starting fuel is heated with DC power. Once the fuel is heated, the APU is started; it generates AC power used to heat the fuel in the craft main fuel tanks.

Two starting problems occurred during the cold weather test: engine flame-outs and EGT overtemperature shutdowns. Using DFM (NATO Symbol F-76), the cold fuel between the start tank and the fuel control would not atomize properly, and flamed out during ignition. Normally, three start attempts were required before warmed start-tank fuel achieved a successful

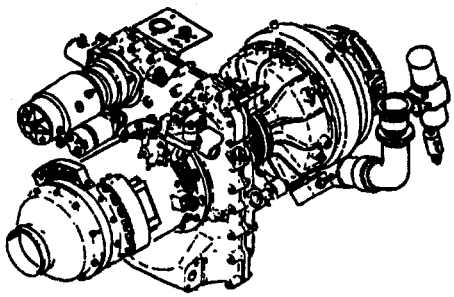

Fig. 2 T-62T-40-7 gas turbine generator set

Downloaded 02 Jun 2010 to 171.66.16.104. Redistribution subject to ASME license or copyright; see http://www.asme.org/terms/Terms_Use.cfm

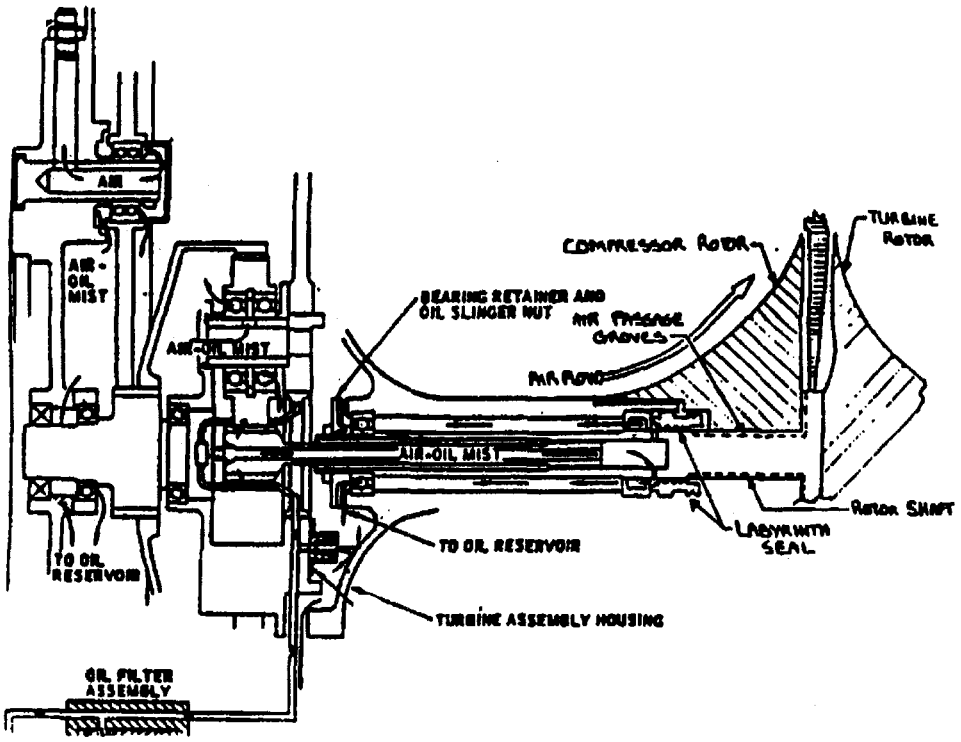

Fig. 3 Labyrinth seal design

start. The second problem, EGT overtemperature, was caused by internal icing of the fuel control diaphragm springs. This control uses compressor discharge pressure (CDP) to regulate the fuel for engine speed control (Fig. 7). During a start sequence, the fuel flow could not be regulated and the subsequent rich fuel flow caused combustion over temperature. At extreme temperatures, below 10°F (−12°C), a hand-held heat gun was needed to defrost the fuel control.

To correct these problems, line heaters were installed between the start fuel tanks and the fuel control to correct the flame-out problem and make for easier starts. As part of an arctic temperature modification for the main engines and T-62's, rubber-molded heater pads were designed using an external AC powered source for overnight (layup) heating.

LCAC tests were conducted in the Bering Sea in March 1992. The fuel line heaters were sufficient to start the T-62's with easily DFM fuel, and are now a permanent engine modification.

Electrical Starters. On-board batteries provide 24 volts DC power to the T-62 electric starters. The starters are used to motor the engine for prestart purging, starting, cool-down after operation, and, whenever the craft is operated at sea, a water, or detergent wash cycle. The duty cycle is a 30 second run followed by a 2-minute cool down, for a maximum of three cycles, before a mandatory 30-minute cool down period. The number of starts/motors cycles has averaged one start/motor per hour of operation on the LCAC.

The starter configuration is quite simple and is similar to an ordinary truck starter. However, with the additional demands of motoring for cooling and water washing, the reliability of the starter has been poor. There are two different vendor designs for the starters: a Delco-Remey unit which went out of production in 1989; and its replacement, an EEMCO unit. The Mean Time Between Failures (MTBF) is 850 hours for the Delco and 550 hours for the EEMCO. The primary failure of mode both starters has been armature burning/overtemperature, although both designs use a class H insulation, currently the highest rating with a maximum material temperature design limit of 350°F (178°C).

The criticality of these failures became apparent with the introduction of the EEMCO starter into the fleet. Previously, the Delco starter was a lower-cost part that could be inexpensively repaired by local armature shops. With the EEMCO unit, the purchase cost more than quadrupled and the armature is not repairable.

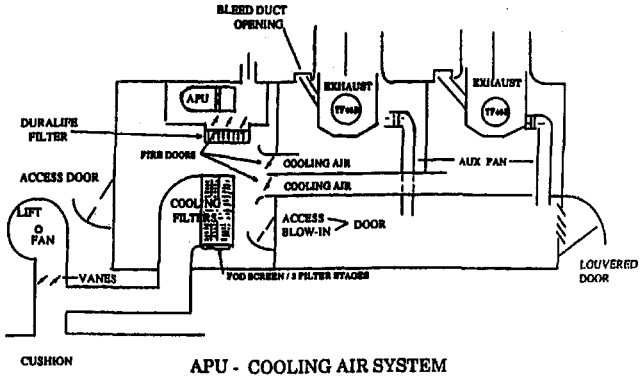

Fig. 4 APU engine compartment—view of duralife filter and fire doors

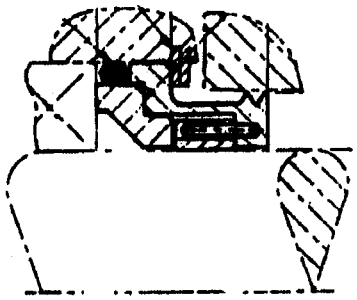

Fig. 5 Cracked carbon seal

Downloaded 02 Jun 2010 to 171.66.16.104. Redistribution subject to ASME license or copyright; see http://www.asme.org/terms/Terms_Use.cfm

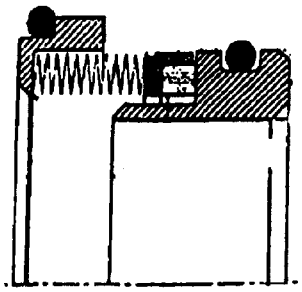

Fig. 6 Bellows ceramic seal

A test program was initiated to evaluate maximum APU module temperatures, in-rush and motoring currents, voltage drop, and starter casing temperatures to find whether failures were induced by craft electrical systems, or operating temperatures. Briefly, maximum in-rush current measured about 450 amps with a decaying average of 300 amps, module temperatures reached a maximum of 75°C (167°F), and starter casing temperatures of about 135°C (275°F). Armature temperatures could not be measured in a craft setup. No substantial conclusions could be derived from these test data except that there were extreme starter loads and reduction of rotational speed from compressor drag during the wash cycle. From our analysis, both starters are undersized to meet the motoring and wash requirements of the LCAC.

The obvious solution to this problem is to find another starter; however, there are none on the market. A change to the motoring and wash requirements had to be initiated. Motor times were reduced to 15 seconds for cooling, but, from fleet experience, wash cycles could not be reduced. With the introduction of an on-line wash system (Patterson and Spring, 1992), there is a means to reduce motoring cycles. Until the permanent on-line wash design change has been incorporated on all craft, a portable injection method (Fig. 8) has been developed to reduce the severity of wash motoring on the starter. On the one craft that already had an on-line system installed, no starter failures have occurred with about 800 hours of operation.

Fuel Manifold Assembly. The T-62 uses a rigid, small tube fuel manifold assembly that has six fuel nozzles brazed at the tubing ends (Fig. 9). The tubes are about 0.5 cm in diameter and are formed in an arc to fit around the combustor housing. The tubes are flexed somewhat to align the nozzles with the combustor ports, and are attached with swivel nuts. During factory assembly and, especially, on craft installations where the manifold is installed from the top of the engine and bent around the exhaust duct, the manifold tubing can be over stressed at the nozzle attachments.

Around mid-1990 on the craft number 037, a series of manifold tube failures occurred at the six o'clock nozzle position. On several occasions when a nozzle broke, the APU compartment flooded with fuel, creating a dangerous fire hazard on the craft. Fortunately, when a nozzle breaks there is not sufficient fuel to maintain speed and combustion, and the engine will automatically shut down. Failures at this position were attributed to high cycle fatigue (HCF) from engine vibration and the high preload stress of nozzle misalignment and attachment.

Crews were immediately advised to check for fuel leakage whenever there was an automatic engine shutdown. Sundstrand developed an urgent design change of the manifold material from stainless steel to a more resilient Inconel 625, and added dampening clamps to the assembly. Additionally, the nozzle collars were rounded to allow self-alignment at installation.

Further, a vibrational survey and strain analysis was conducted by NSWC-CD on a test cell engine, a second craft (i.e., LCAC 025), and both LCAC 037 T-62 engines for comparison of static and dynamic loads on the engine fuel manifold (Naval Ships Warfare Center, 1993). Strain gages were installed with the grids aligned as closely as possible to the nozzle fillet surface for maximum sensitivity. Strain data were acquired at startup and at load, and with bleed air activated. Data was also measured during installation to determine static stress in nozzle connection.

For vibration analysis accelerometers were installed in three directions (vertical, axial, and transverse) on the turbine and gearbox and in the vertical and axial directions on the generator.

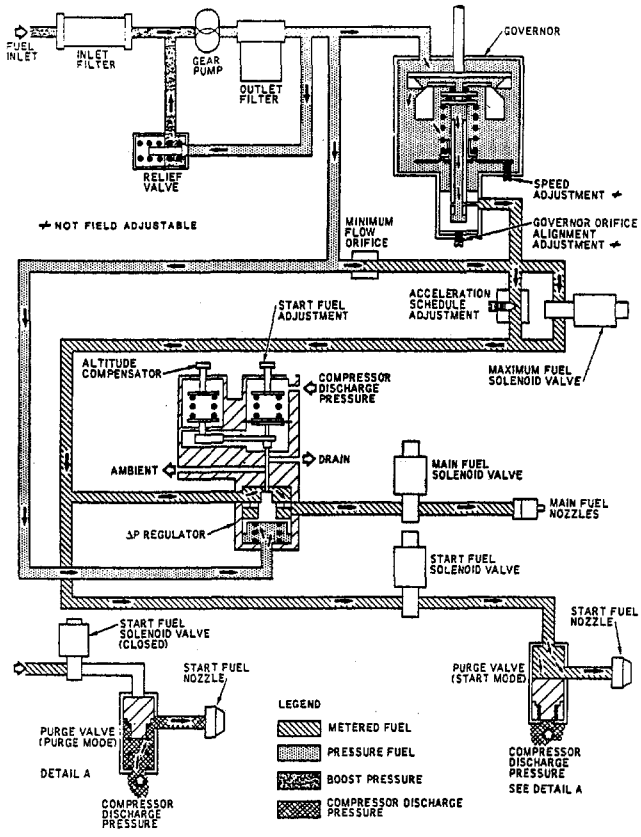

Fig. 7 APU fuel system schematic

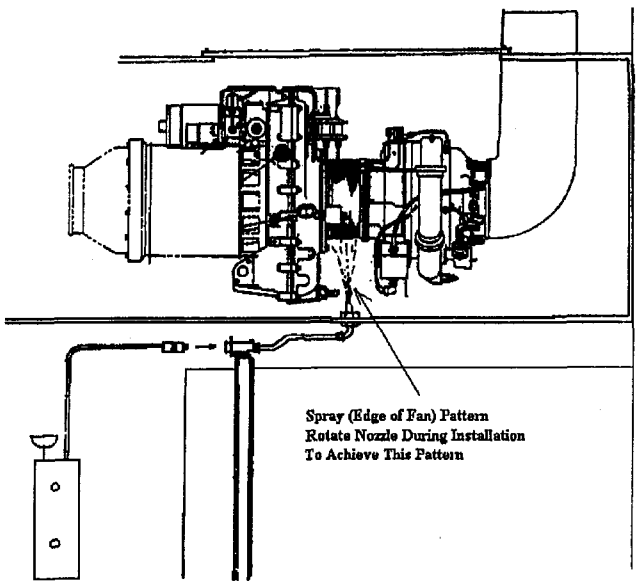

Fig. 8 Portable APU on-line wash method

Downloaded 02 Jun 2010 to 171.66.16.104. Redistribution subject to ASME license or copyright; see http://www.asme.org/terms/Terms_Use.cfm

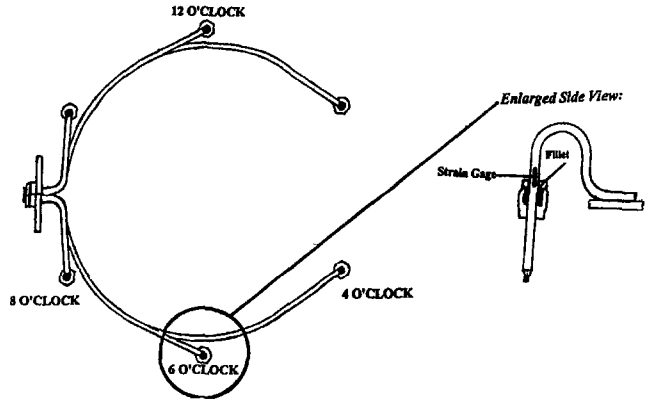

Fig. 9 Hard tube fuel manifold assembly

For comparison purposes, these locations are identical to those selected for the T-62 test cell engine and on LCAC 025.

Goodman Diagrams were constructed from the static bending stress, thermal stress, and varying dynamic stresses. Static and thermal stresses were not significant, but would vary greatly between different installations. Of all the engines tested, LCAC 037 engines experienced significantly higher dynamic strain measurements, particularly at the turbine 8X rotational blade rate. Moreover, review of the test data indicates that the dynamic stress increased with increasing electrical (kW) load, as illustrated in Fig. 10. As shown, nozzle fatigue failure is probable at the 6 o'clock position for loads above 40 kW.

Because of the high vibrational stress measured on LCAC 037 fuel manifold, NSWC-CD investigated an alternate flexible manifold design currently used on the T-62 engines of the U.S. Army hovercraft, LACV-30. The flexible manifold is easier to install and remove from the engine, and less likely to be stressed in a vibrational mode. Two flexible manifolds have been installed on LCAC 037 for the past eight months for prototype testing.

Procedural Improvements

LCAC Performance Analysis System (LPAS). The controls for the LCAC are a fly-by-wire design and are centrally located in the starboard cabin. The operating crew consists of the craftmaster; an engineer, a navigator, a deck mechanic, and a load master. Of the LCAC operating crew, the engineer has the responsibility for the starting, operating, condition monitoring, and record keeping requirements for all machinery on the craft. For real time condition monitoring the LCAC is built with an alarm and monitoring system (AMS), which processes remotely sensed data from transducers on all critical equipment into an alarm and sensor keyboard, and digital video display at the engineer's station in the starboard cabin.

During operations, the starboard cabin becomes a center of hyperactivity between the craftmaster, navigator, and engineer, especially during maneuvers in and out of the well deck. Often critical operating data cannot be logged by the engineer because of other demands for the control and operation of the craft machinery. Later, during failure analysis or mishap critiques, valuable data have been lost and conclusions can only be drawn from crew debriefs. Also, for gas turbine engine condition monitoring, data have not been adequately recorded on an historical basis that could show degradation or loss of efficiency. In the case of the APUs, which have only a minimal data transducers, condition monitoring is now limited to EGT changes over time. From the crew's point of view, there is no way to foresee an impending failure.

From this experience, a computer-based trend analysis system, known as LPAS, is being developed to process operational data from the AMS. Positional data from the craft's global positioning system (GPS) will be combined into a comprehensive data bank for machinery performance condition monitoring and mishap analysis. This data system will chronicle all alarms; track engine start, stop, and run times; document real-time equipment casualties; and with GPS data, provide full incident reconstruction with craft position, speed, and heading.

One advantage of using LPAS data is the ability of the crews to expedite trouble shooting and corrective maintenance. Further, as the database is compiled on the gas turbines, relevant trend graphs can be produced to determine engine performance. It should be noted that the LCAC gas turbines have neither torque meters nor fuel flow meters, which will make LPAS an important tool in condition monitoring and preventive maintenance.

Engine Lubrication and Preservation. The LCAC gas turbine engines use lubricating oil that currently complies to the specifications of Military Standard, MIL-L-23699, Revision D (NATO Code 0-156). Operationally, this synthetic oil has functioned satisfactorily in both hot and cold environments. However, because this oil has no preservation properties, maintenance and lay-up procedures have been developed to assure periodic oil wetting of the internal bearings, gears, etc. For example, the gas turbine engines are required to be either motored every two weeks, or removed from the craft for preservation and storage.

In early 1992, Naval Air Warfare Center issued a qualification report (Naval Air Warfare Center, 1992) for Castrol Aerojet 5 synthetic jet oil, which met the requirements of Military Specification, MIL-L-23699D, and contains additives for corrosion inhibition. Unlike earlier brands of additives, such as Bray Co, which is added to oil only for engine storage, and flushed before reuse of engine, Castrol Aerojet 5 can provide both the lubrication and thermal requirements, and internal corrosion protection.

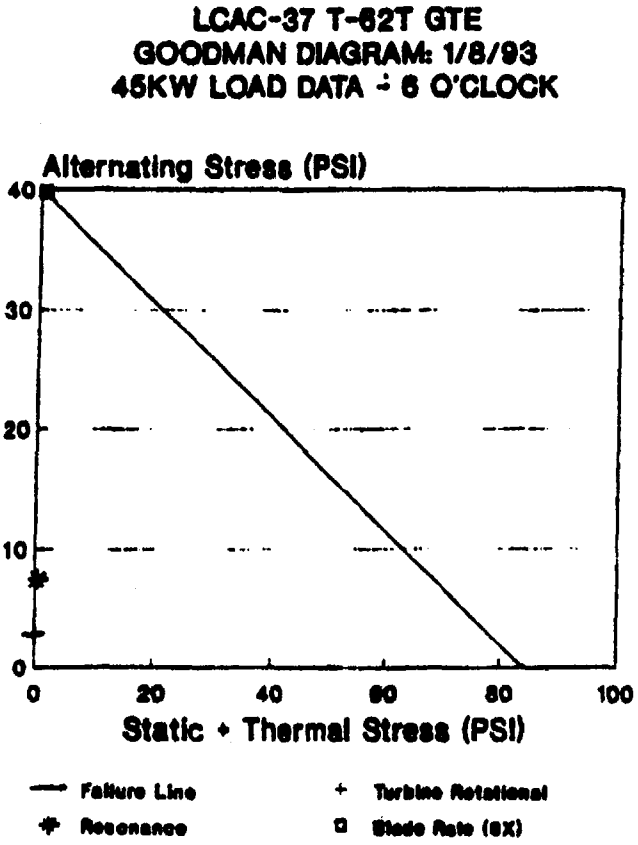

Fig. 10 Dynamic stress at 45 kW

Downloaded 02 Jun 2010 to 171.66.16.104. Redistribution subject to ASME license or copyright; see http://www.asme.org/terms/Terms_Use.cfm

This oil meets a proposed Revision E to MIL-L-23699 specification.

Sundstrand has approved Castrol Aerojet 5 oil suitable for use on the T-62 turbine. Additionally, all reduction gears will use and be preserved with this oil, which means a substantial reduction in maintenance upkeep and time for the LCAC maintenance crews.

On-Line Washing. On-line or running compressor washing has been utilized in the gas turbine field for several years. The aviation industry has used this process with much success. Initially, an on-line wash system was installed on two APUs for evaluation in the fleet. This system was very successfully and, as a result, a craft-alterations package was developed to install on fleet craft.

Benefits from the on-line wash system include: reduced starter wear, reduced maintenance time, and increased corrosion protection. The starter is not used during the on-line method of washing as it is with the crank method of washing. With a fully automatic on-line wash system, only the craft engineer is needed to wash the engine. This process also eliminated the need to disconnect the engine fuel control CDP line that can fill with water during the current deluge wash. Finally, with the removal of salt from the engine and the corrosion inhibitors in the cleaning solutions, engine corrosion can be controlled.

Testing of the on-line wash procedure required analysis of the thermal stress effects, and compressor cleaning effectiveness. The T-62s on the prototype craft were borescoped to verify the baseline condition of the turbine and compressor sections. Neither borescope inspection revealed any unusual conditions in the engines. After a few hundred hours of operation and approximately 150 washes, the engines were borescoped and found to be internally clean with no noticeable defects in the turbine. One of the T-62s was removed due to high oil consumption (labyrinth seal blocked) and returned to the depot for repair. During this repair, the rotating components were critically inspected for stress cracks. Neither the compressor nor the turbine wheel showed any harmful effects from the wash cycling.

The cleaning effectiveness was measured by the percentage of degradation in the engine performance. Baseline operating parameters were measured and compared to postevaluation parameters and there was no measurable EGT increase or performance degradation during the evaluation period.

Corrosion Control. The salty and wet environment for the T-62 on board the LCAC significantly affects fasteners and the electrical hardware on the engine. Procedural changes have been developed to wash and coat exposed parts to reduce maintenance and increase reliability of the engine.

Overhaul procedures at NADEP Cherry Point has also included the repainting of the gearbox due to problems from extended exposure to saltwater. A daily external fresh water wash procedure could reduce or eliminate the need for this costly repair step. Engine accessibility, as noted in a previous section, was very limited in the original craft design; therefore, daily washes and inspections could not be done.

T-62 Test Cell. A significant engineering asset for testing and evaluating engine hardware is the test cell located at the Naval Surface Warfare Center, Philadelphia. The test cell has bleed air and electrical load capacities to simulate craft installation. A computer-based data acquisition system is installed to monitor all engine, generator, and test cell parameters.

The capability of having a controlled environment allows for accurate test measurement and calibration. The environmental features include: humidity control, soot ingestion, salt mist injection, compressor inlet air temperature control, fuel temperature control, and ambient engine cooling air temperature.

Summary and Conclusion

For a high-speed and lightweight surface craft application, such as the LCAC, an aero derivative gas turbine is aptly suited for the power plants to provide high horsepower at a low weight ratio. However, being an aircraft engine, they have minimal improvements for the marine environment. To mitigate the severe marine environment, it is necessary that the craft builder provide adequate external protection, clean fuel, clean filtered combustion and cooling air, vibration isolation, power limits, and most importantly a good maintenance plan with easy access for cleaning and trouble isolation.

In the severe environment under which the LCAC operates, operating machinery will continually degrade. Maintenance is required to detect degradation through inspection and servicing. A majority of the T-62 engine problems can be attributed to the lack of servicing on a daily basis because the access into the compartment was impractical (e.g., the 56 bolt hatch), or often extremely labor intensive and time consuming, for example engine water washing. If the maintenance chore is too difficult, even the most dedicated sailor will tend to ignore the maintenance task.

Experience on the LCAC has shown that the Sundstrand T-62-40-7 gas turbine is a capable and reliable power plant, if it is adequately protected and maintained in this harsh environment. The selection of a gas turbine for hovercraft use should consider the following design criteria:

(a) Corrosion resistant materials should be used throughout—including external accessories, electrical connectors, and fasteners;

(b) The engine compartment should be secure during operation to protect the engine from unfiltered/contaminated combustion air. Yet, for maintenance, it should be designed for easy access to engine components;

(c) Internal compressor cleaning should include the "on-line" wash capability to reduce motoring wear on the starter, and reduce maintenance down time and workload for the crews;

(d) During extended down times, the engines can corrode internally from condensation accumulated through exposed ports/openings. Since engines are not removed for preservation, a method to protect the installed engines is needed, such as using the "on-line" wash nozzles to spray preservative into the gas path, and using a preservative oil, like Castrol Aerojet 5, internally for bearing and gear protection. With the test cell facilities at Naval Surface Warfare Center Carderock Division, Philadelphia, we have been able to develop practical solutions for the T-62 problems, and to verify them on a test engine at a minimal cost.

References

Naval Ships Warfare Center—Carderock Division, 1993, Preliminary Report of 1 Mar. 93, LCAC-37 Vibration Survey.

Naval Air Warfare Center, 1992, Aircraft Division, Trenton, NJ, "Qualification of MIL-L-23699D Aircraft Engine Oil, Castrol Aerojet 5," Final Report NAWCADTRN-LR-PE-92-7, 3 Jan 92.

Patterson, J., and Spring, S., 1992, "On-Line Detergent Washing: Reducing the Environmental Effects on the LCAC Gas Turbine Engines," ASME Paper No. 92-GT-269.

Downloaded 02 Jun 2010 to 171.66.16.104. Redistribution subject to ASME license or copyright; see http://www.asme.org/terms/Terms_Use.cfm

The Installation, Testing, and Lessons Learned of the TF40B Gas Turbine Test Facility

J. S. Patterson

H. Harris

Naval Surface Warfare Center,
Carderock Division,
Philadelphia, PA

The TF40B Gas Turbine Test Facility is the only dedicated Landing Craft, Air Cushion main propulsion engine test complex available to the U.S. Navy. This facility, located at the Naval Surface Warfare Center, Carderock Division (NSWCCD) in Philadelphia, PA, began operation in August, 1992. Since then, the test engine has logged approximately 230 starts and 350 operating hours. This paper will present the installation, testing, and lessons learned of the TF40B test facility. The installation section will discuss the modifications made to the existing test facility to accept the TF40B engine. The test section will include the Foreign Object Damage (FOD) screen evaluation, both on-line and crank wash detergent fluid evaluations, cold weather fuel testing, engine vent line testing and Aerojet 5 oil evaluation. The lessons learned section will include problems related to the electric starter, waterbrake, inlet and exhaust systems, data acquisition system, instrumentation control panel, and the test cell equipment arrangement.

Introduction

The AlliedSignal TF40B gas turbine engine is a direct drive, high-speed turbine engine used for main propulsion in the Landing Craft, Air Cushion (LCAC) class vessels. The LCAC is a high-speed, ship to shore, over the beach, amphibious landing craft. The craft is designed to carry a 120,000 lb (54,431 kg) payload and can travel at speeds in excess of 40 knots. The craft is designed to transport personnel, supplies, equipment, and weapons systems from host ships to the shore and across the beach for a dry landing. Each craft is outfitted with four TF40B engines, used to drive the lift fans and propellers. At the present time, there are 72 craft in the Fleet, stationed at either Assault Craft Unit Four (ACU-4), Little Creek, Virginia, or Assault Craft Unit Five (ACU-5), Camp Pendleton, California.

In Fiscal Year 1991, NSWCCD was funded by Naval Sea Systems Command (NAVSEA) to design and construct a test facility for the TF40B engine. Construction was started in June 1991 and the engine was installed in May 1992. The test site officially began operation on August 19, 1992.

Test Site Installation

To minimize design and construction costs, the TF40B gas turbine engine (Serial Number LE-40262) was installed in an existing test site at NSWCCD. This site, known as the Small and Medium Gas Turbine Test Facility, as shown in Fig. 1, was originally built in 1969 to test a Solar Saturn T1020S gas turbine engine. The facility was dormant after the completion of the AlliedSignal AGT 1500 Salt Ingestion Test in 1984.

To reduce operating and maintenance costs, a second gas turbine engine was installed in the test cell. The second engine, the Turbomach T-62T gas turbine, is used as an Auxiliary Power Unit (APU) on the LCAC for electrical power generation and starting energy for the pneumatic starter on the TF40B. This installation, however, has resulted in numerous logistic, maintenance, and operational problems, which are discussed in the "Lessons Learned" section of this paper.

Contributed by the International Gas Turbine Institute and presented at the 40th International Gas Turbine and Aeroengine Congress and Exhibition, Houston, Texas, June 5–8, 1995. Manuscript received by the International Gas Turbine Institute March 7, 1995. Paper No. 95-GT-310. Associate Technical Editor: C. J. Russo.

Test Site Specifications. The test facility contains two explosion proof test cells that have an operating range of 100 to 10,000 shaft horsepower. The facility is equipped with a fully automatic fire suppression system, a 2000 gallon (7571 liters) fuel oil storage tank, and an Alfa-Laval Model MAPX 205T-20 fuel oil purifier. Auxiliary systems include 120/240VAC, 28VDC and 60/400 Hz electrical service, city and river water, and low-pressure shop air. The cell is also equipped with an 8000 lb (3629 kg) overhead crane.

Test Site Modifications. To facilitate the installation of the TF40B engine, the cell was stripped to its bare walls. Due to the extended period of inactivity, nearly every system needed to be rebuilt or upgraded. These systems included the electrical, fuel transfer and purification, low-pressure shop air, city and river water, engine loading and controls, fire suppression, air inlet, and exhaust ducting.

The original site plans called for the installation of the entire LCAC engine module. This included the engine housing, air inlet filtration system and all auxiliary and support systems. However, due to space and funding limitations, the TF40B engine was the only main propulsion component installed, along with its essential support equipment and control system.

Engine Mounting and Loading System. The TF40B is coupled directly to a high-speed 5000 shaft hp (3728 kW) Model 106-080-002 Kahn waterbrake, which provides a torque load to the engine. The waterbrake is controlled by remote activated pneumatic V-notched ball valves in both the supply and drain water lines. The waterbrake is cantilevered off the front of the engine. The engine and waterbrake are mounted to a steel I-beam support frame, which was designed in-house using a finite element stress analysis program. The frame is solid mounted to the T-block foundation. The engine installation is shown in Fig. 2.

Test Cell Ducting. The engine draws its intake air directly from the test cell. Exhaust gases are ducted through a stainless steel collector and stack to atmosphere. To minimize costs, the existing test cell inlet stack was used. A remote activated louver was added to the inlet system to upgrade the fire suppression system. The existing exhaust collector was modified for this installation. This collector was connected to the existing exhaust stack. The engine was coupled to the collector by means of a

Copyright © 1996 by ASME

Downloaded 02 Jun 2010 to 171.66.16.104. Redistribution subject to ASME license or copyright; see http://www.asme.org/terms/Terms_Use.cfm

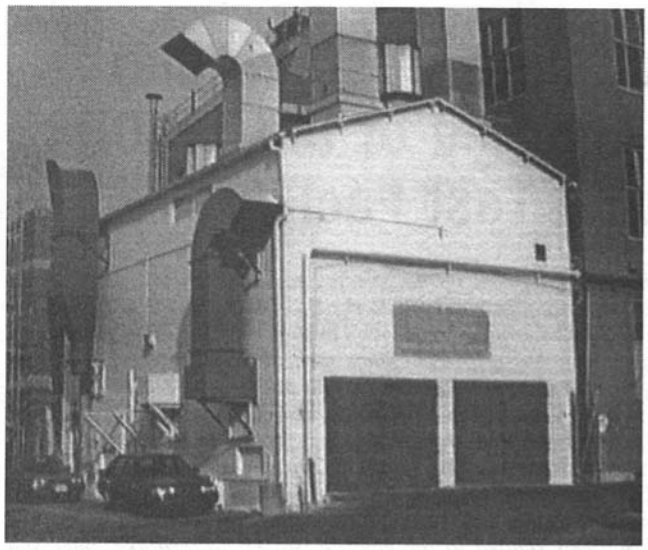

Fig. 1 Small/medium gas turbine facility

modified LCAC diffuser. In this design, there is no direct physical connection between the diffuser and collector, which permits thermal growth and vibration isolation. However, the lack of a physical connection allows an excessive amount of exhaust gases to return back into the test cell. This causes the compressor blades to foul with carbon and accelerate the crank wash and on-line detergent wash intervals. In addition, these exhaust gases increase the ambient temperature within the test cell, which degrades the performance of the engine.

Engine Control System. On the craft, the engines are controlled and monitored by the Modular Control Box (MCB). The MCB is a solid state unit that contains the following cards: system power supply, temperature monitor, gas producer and power turbine speed monitors, engine sequence, malfunction monitor, fuel control isolation analog, and utility panel. The test cell engine also uses the same electronic control unit. The outputs of the control box are then split between a control console panel and a computer-based data acquisition system.

The control panel contains six analog gages to monitor exhaust gas temperature (EGT), oil pressure and temperature, control voltage, gas producer (N1) speed, and power turbine (N2) speed. The panel also contains pertinent engine caution and shutdown alarms, as well as the waterbrake controls. The computer-based data acquisition system displays and records all major engine and test cell operating parameters. The test operator uses this system to operate and monitor the engine.

Tests Performed

The following is a summary of tests performed in the TF40B test facility. These tests include the on-line and crank wash detergent fluid evaluations, foreign object damage (FOD) screen evaluation, cold weather fuels testing, engine vent line test, and Aerojet 5 oil evaluation.

On-Line Detergent Fluid Evaluation. On-line detergent washing of the compressor section of the gas turbine engine is accepted in the aerospace industry and the industrial power generation industry, as an effective means of maintaining optimum operational characteristics with minimum maintenance time. Due to the harsh environment the LCAC operates in, the on-line detergent wash system is extremely beneficial to this craft.

On-line detergent washing is accomplished by injecting an atomized mixture of detergent and distilled water, at a constant pressure into the inlet air ducting of the running engine. The cleaning fluid is drawn into the engine by the suction effect of the compressor assembly.

The purpose of this test was to evaluate several water-based detergents on their effectiveness in cleaning the TF40B gas turbine compressor assembly by on-line detergent washing. This test also verified the design of the TF40B on-line detergent wash nozzles.

Test Cell Installation. A schematic of the test cell installation is shown in Fig. 3. The detergent and distilled water are mixed in a 16 gallon (61 liter) holding tank, which is pressurized to 65 psig (4.48 bar). The system is activated by depressing a latching push button installed in the engine control console. The push button opens a solenoid valve, which allows the solution to flow from the tank through a 15 μm strainer and branch into the two nozzle blocks. Each block contains two 0.25 gallon per minute (0.95 liter per minute) spray nozzles, which have a droplet mean volume diameter of 800 μm at 60 psig (4.14 bar). The duration of each wash was three minutes. To simulate the operating conditions of the LCAC, the engine was subjected to salt water and carbon contaminants.

Salt water was fed into the running engine by a nebulizer. The water was made to military standard MIL-C-85704. The

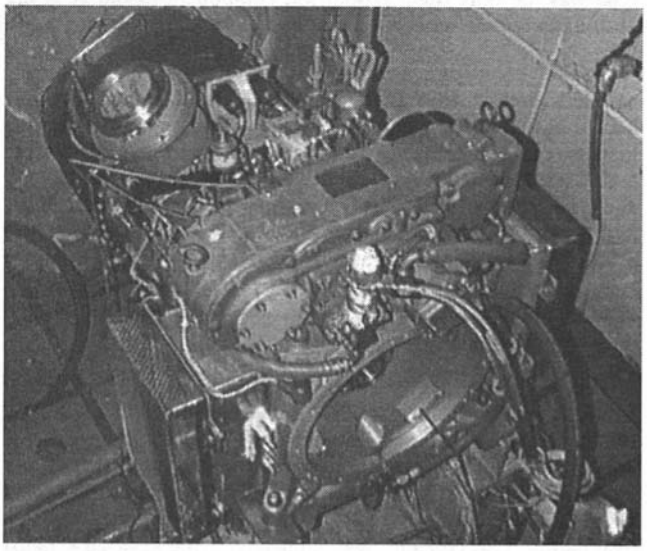

Fig. 2 TF40B test cell engine

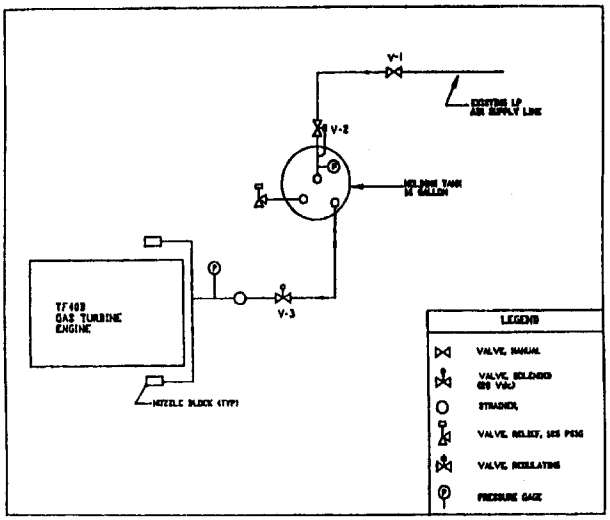

Fig. 3 On-line wash schematic

Downloaded 02 Jun 2010 to 171.66.16.104. Redistribution subject to ASME license or copyright; see http://www.asme.org/terms/Terms_Use.cfm

amount of salt injected into the engine (FES) was calculated using the following equation:

$$FES = PPM_D \times F_A/(W_S \times 10^6)$$

where PPM_D is the desired salt concentration in parts of salt per million parts of air by weight, F_A is the average inlet airflow rate in pounds/hour and W_S is the weight of the salt in the salt solution in pounds/gallon. On average, the engine ingested approximately 0.003 gallons/hour (0.011 liters/hour) of salt. Carbon was introduced by means of the peripheral gap that existed between the engine diffuser and exhaust collector. This gap permitted exhaust gases to back flow into the test cell, resulting in carbon re-ingestion. The amount of contaminates entering the engine was not a concern, because the purpose was to enhance compressor fouling as quickly as possible.

Test Results. There were several benefits derived from evaluating the on-line fluids in the controlled environment of the test cell. These included the ability to measure compressor fouling and the level of airborne contaminants accurately, the ability to record and analyze the engine parameter data from each detergent and the ability to easily video borescope the internal condition of the engine. As a result of this test, the military specification MIL-C-85704, "Cleaning Compound, Turbine Engine Gas Path," was updated to include recommended detergents for online detergent cleaning. These detergents included EDC R-2701, R-MC, Turboclean 2, Turbotect 920 and 950, and ZOK-27. In addition, the on-line detergent wash nozzles were proven to be effective in flow rate and spray pattern.

Crank Wash Detergent Fluid Evaluation. Due to environmental restrictions imposed by the state of California, the US Navy is required to reduce and eventually eliminate most types of solvent-emulsion based engine gas path cleaners. As a result, the Navy is actively pursuing this objective by evaluating the use of water-based crank wash detergents.

Test Cell Installation. NSWCCD tested two water-based detergents (EDC R-2701 and R-MC T-70) for cleaning the TF40B by detergent crank washing. The engine was injected with salt water and engine exhaust gases to foul the compressor assembly. The engine was degraded by 4 percent in power then crank washed using a water-based detergent. Washing was accomplished using a portable detergent wash cart in accordance with the TF40B Maintenance Requirement Card (MRC) 2341 R-6. This process was done five times per detergent.

Test Results. As a result of the test cell operations the two fluids, previously qualified for on-line detergent washing, were also qualified for crank washing. This determination was based on the results obtained from borescope inspections and the engine parameter data analysis. Long term plans call for qualifying additional fluids during the coming year.

FOD Screen Evaluation. The TF40B installed on the craft do not have a last chance FOD screen, to protect the engine from foreign objects entering the compressor assembly. As a result, there have been numerous incidents of FOD to the engines. To minimize repair and maintenance costs, NSWCCD investigated the possibility of installing a FOD screen into the engine's inlet air system.

Figure 4 shows the prototype design for these screens. The two wedge-shaped screens were designed to mount directly to the engine air inlet plenum. A wedge-shaped design was utilized to provide for the largest possible surface area. The screen chosen was a coarse three strands per inch, 0.054 inch (1.37 millimeter) CRES 316 stainless steel material. The solidity (S), a nondimensional parameter for the relative area blocked by the screen, was determined by the following equation:

$$S = 1 - (A_O/A_T)$$

where A_O is the open area of screen and A_T is the total area of screen. As air passes through the screen, it is accelerated. Jets of relatively high velocity form behind the openings and intersperse with wakes of relatively low velocity behind the elements. As the flow passes downstream, the jets and wakes mix to yield an uniform flow. The solidity of this FOD screen varied due to the change of surface of the screen at any given plane perpendicular to the air flow. At the nose of the FOD screen, the solidity was approximately 0.019. Beyond the nose, the solidity increased to 0.022.

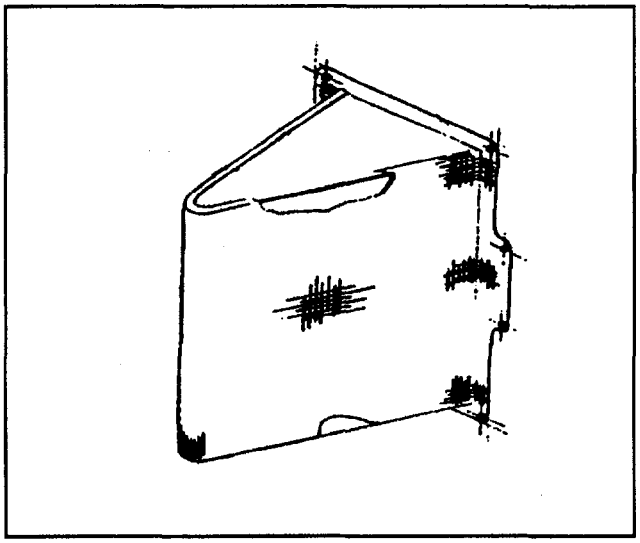

Fig. 4 TF40B FOD screen

The objective of the test was to determine if a wedge-shaped inlet FOD screen attached to the engine inlet plenum would affect the operating performance of the engine, by disturbing the inlet air flow.

Test Installation. A partial LCAC air intake duct system was assembled to the engine. The intake duct system consisted of the instrument test section, FOD screen, straight section, and 90 deg elbow. The test section ducts were installed to the engine bell mouths and contained the pitot tubes, which recorded the inlet air average airflow velocity pressure. The FOD screens were attached to the test section ducts and inserted through the straight ducts. The final section of the intake ducts were the 90 deg elbows. One end of the elbow was attached to the straight duct, and the other end was opened to the atmosphere. This installation is shown in Fig. 5.

Test Results. Engine performance data and inlet duct air velocity pressures were recorded at several different power points, with and without the FOD screens installed. The methods used to determine the FOD screens affect on the engine included the engine performance data (shaft horsepower and specific fuel consumption), air inlet duct velocity profile (with and without the screens), and the pressure drop calculations. Test results indicated that the wedge-shaped FOD screen did not lower the shaft horsepower, raise the specific fuel consumption, or disturb the air flow into the engine.

Cold Weather Fuels Test. LCACs operating in cold weather experienced difficulty in starting and operating the TF40B engines. In this environment, the engines experienced longer start times and failed starts. In addition, during these cold starts, a large amount of smoke was discharged from the engine exhaust into the well deck of the host ship. The excess smoke created a health hazard for the well deck personnel, in addition to increasing the inlet filter clogging rate as a result of exhaust re-ingestion.

Downloaded 02 Jun 2010 to 171.66.16.104. Redistribution subject to ASME license or copyright; see http://www.asme.org/terms/Terms_Use.cfm

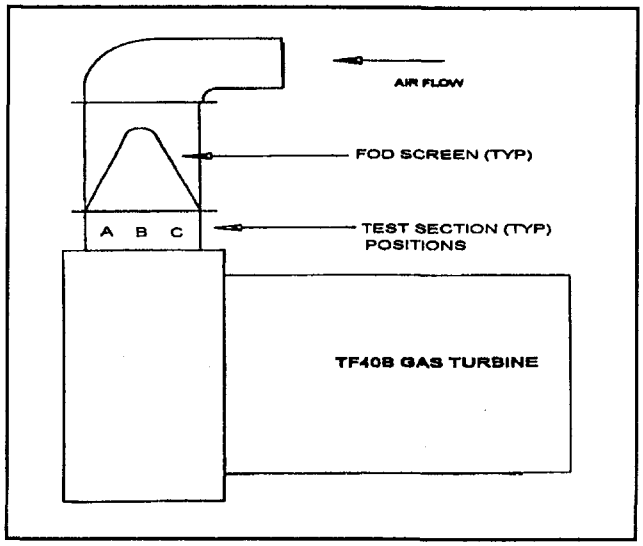

Fig. 5 FOD screen test installation

NSWCCD was tasked to perform cold start testing for the engine, using both JP-5 and DFM fuel oils. This included identifying the cold start characteristics of the engine, evaluating the exhaust gases and particles emitted from the engine while burning JP-5 and DFM and identifying the fuel characteristics of both fuel oils.

Test Cell Installation. The TF40B gas turbine was operated in a cold weather scenario using both JP-5 and DFM fuel oils. Exhaust gases were analyzed, and engine start times and performance data were recorded and fuel samples were taken. To simulate a cold weather environment, prior to testing, the heat in the test cell was secured to cool the engine and the fuel transfer system. One hour prior to light off, the cell cooling fan was energized to further reduce the ambient temperature. During the start process, the fuel temperature, ambient temperature, time to ignition, time to idle and amount of visual smoke were recorded. Exhaust gases were analyzed to measure the levels of O_2, CO, CO_2 and NO_X. JP-5 and DFM fuel samples were taken and analyzed for color, specific gravity, flash and pour point, carbon residue, and viscosity.

Test Results. The results of this test revealed that JP-5 fuel improved the cold weather start capability and reduced the amount of visible smoke present during the start sequence by 75 percent. However, there was no increase in start times for DFM versus JP-5. The emissions test revealed that JP-5 reduced the particle emissions above 1 μm by 400 percent and decreased the NO_X emissions by 24 percent. The analysis of the fuel oils revealed that all samples were within reference limits.

Engine Vent Line Test. In the current design of the LCAC engine lube oil vent line system, the engines are directly connected to the craft waste drain system, which has presented a problem to the TF40B. A number of incidents have occurred where a clogged oily drain line has caused waste fluid to flow back into the TF40B engine oil sump via the engine vent line. In October 1993, LCAC-014 experienced catastrophic oil system dilution when the craft oily waste system clogged, causing fluid to back into the TF40B oil sump.

Test Cell Installation and Test Results. The test cell engine was instrumented to record pressure within the Inlet Housing Module (IHM) at various engine power levels. Pressures within the IHM will also provide the pressure within the engine vent line. The purpose of this test was to determine whether the vent line modification restricted the engine from discharging oily mist or air vapor. In addition, accurate IHM pressure readings were required to assure that a vacuum would not occur which could suck oil from the engine. Results indicated that the TF40B engine vent line could be hard piped into the exhaust collector without any adverse effects to the engine.

Aerojet 5 Oil Evaluation. The TF40B engines installed on the LCAC experience a high mortality rate of the number 6 and 7 bearings. The primary cause of the failures has been corrosion of the rolling elements and raceways. The Navy recently qualified Castrol Aerojet 5 oil, which has a corrosion inhibiting additive to military specification MIL-L-23699. Laboratory testing on this oil revealed that it retards the corrosion of bearings in environments of 100 percent humidity and cyclic temperatures.

Test Cell Installation. The Aerojet 5 oil was evaluated in the test cell engine from May 1993 to August 1994. During that time, the engine was operated for a total of 233 hours. The oil was periodically analyzed (a total of 12 samples were taken) to test for physical and chemical changes, water determination, and oil health by emission spectroscopy. In addition, two corrosion ball tests were performed to measure the level of the corrosion inhibiting agent.

Test Results. Results of the chemical analysis revealed that all the samples were within established reference limits for appearance, total water content, total acid number, viscosity, flash, and pour point. The viscosity of the oil was very stable; however, the readings were at the low end of the acceptable range. In addition, the oil did not retain or attract a considerable amount of water. Results of the spectrographic analysis, which measures the level of wear metal elements in the oil, revealed that all the samples were within established reference limits. The purpose of this analysis was the determine the type and level of wear within the engine. Results of the corrosion ball tests revealed that both samples were within acceptable reference limits. Test results revealed that the oil successfully passed the test criteria, with no significant performance degradation. As a result, the oil was approved for TF40B use.

Lessons Learned

There have been many lessons learned during the design, construction and operation of the TF40B test facility. The following section outlines a few of these key issues.

Work Shop/Storage Facility and Repair Planning. Any test facility constructed should have a dedicated shop area, to permit engine disassembly and repairs. This facility does not have such an area. Any major engine work requires removing the engine from the cell and transporting it across the Philadelphia Naval Base to the gas turbine rework facility. By moving the gas turbine, two problems arise. First, it takes a major effort of time and manpower to remove and transport the gas turbine, and second, there is the possibility of engine damage.

In addition to an adequate shop area, storage space for tools, test equipment, consumable, and spare parts is critical. Initially, there was no adequate storage space in the test facility, but we have recently added a mezzanine level above the control room, dedicated for storage.

Finally, to operate and maintain the engine properly, funds should be set aside for the purchase of special tools, spare parts, and consumables. Initially, we were unable to set aside funds for the purchase of the special tools, which hampered our ability to perform inspections and tests. However, during the past year, we have purchased a complete set of special tools for the engine.

Engine Auxiliary Systems. Whenever possible, the test facility should duplicate the site/craft installation. The most important lessons learned here were related to the use of an electric starter, waterbrake, and the existing inlet and exhaust ductwork.

Downloaded 02 Jun 2010 to 171.66.16.104. Redistribution subject to ASME license or copyright; see http://www.asme.org/terms/Terms_Use.cfm

TF40B Electric Starter. On the LCAC, the TF40B engines are started with a pneumatic air turbine starter. However, due to funding and parts availability restrictions, we used an electric start system. This system included a modified electric starter, four 12VDC batteries hooked up in series and in parallel to provide 24VDC, and a rectifier used to recharge the batteries and to provide additional start current. Due to low line losses, however, the system was too efficient and provided excessive voltage and current to the starter. This excessive energy over-torqued both the accessory drive gear and pinion, resulting in a catastrophic engine failure. To alleviate this problem, an air turbine starter was installed on the test cell engine.

Waterbrake. When the TF40B engine is operated above 95 percent N2 speed, the waterbrake becomes unstable. This causes the N2 to fluctuate, making it difficult to control the engine. This condition is a result of pressure fluctuations within the inlet supply line. As a result, the supply line cannot provide enough water pressure to the waterbrake at high engine speeds. To correct this problem, the waterbrake inlet system will be redesigned to remove all unnecessary line restrictions and an in-line boost pump will be installed to increase the water supply pressure.

Inlet and Exhaust Systems. Another major area where the test site does not duplicate the LCAC installation is the inlet and exhaust systems. The lack of an inlet system (ducting and air filtration) severely limits testing capabilities. Also, the lack of a filtration system tends to cause the compressor to foul more quickly, increasing both maintenance costs and manpower requirements.

The test cell exhaust system has caused numerous problems and delays. The engine was coupled to the existing exhaust collector, by means of a modified LCAC diffuser. This collector was connected to the existing exhaust stack. In this design, there is no direct physical connection between the diffuser and collector, which permits thermal growth and vibration isolation. However, the lack of a physical connection allows an excessive amount of exhaust gases to return back into the test cell. This tends to foul the compressor blades with carbon and accelerate the crank wash and on-line detergent wash intervals. In addition, these exhaust gases increase the ambient temperature within the test cell, which degrades the performance of the engine.

Data Acquisition System (DAS). The DAS installed in the test facility was a general all purpose system. The software used was not designed for a gas turbine test site, but for general data gathering. This software does not provide on-line trending or diagnostic capabilities. The hardware consists of a simple 286 IBM computer. While the system was adequate for this application, data collection and sorting were labor intensive. To improve this situation, a new system will be installed that uses the most up-to-date computer hardware and software components available and will provide real time data recording, performance trending, and diagnostic capabilities.

Instrumentation Control Panel. The instrumentation control panel does not have all the necessary gages that the operator needs to run the engine. Specifically, the waterbrake controls were not included in the instrumentation panel, but on the DAS. This has caused numerous problems, because the engine could not be safely operated without the DAS in operation.

Test Cell Equipment Arrangement. To save design time and construction cost, the test facility contains both the TF40B and the T-62T gas turbine engines in the same cell. This arrangement has lead to several maintenance and logistic problems. These problems include the inability to operate more than one engine at a time, because of limitations of the DAS, as well as engine availabilities and scheduling conflicts. In addition, exhaust gases from the TF40B engine back flow into the T-62T engine through the common exhaust ducting. Finally, the lack of physical space limits the expansion of either engine within the test cell.

Conclusions

- A gas turbine facility should be designed to include adequate work and storage space.
- Special tools for the gas turbine along with spare parts and consumables should be procured before the test site is in operation.
- The test facility should duplicate site/craft installation, if funding permits.
- Attention should be paid to design details for the auxiliary systems.
- The data acquisition system should be the most up-to-date computer hardware and software available.
- The test cell should only contain one engine.
- The instrumentation control panel must contain all the gages necessary to operate the engine safely.

Summary

Overall, the construction, operation, and maintenance of the TF40B test facility has been quite an undertaking. Constructing, operating, and maintaining a test cell requires much planning, coordination, and above all, sufficient funding. However, the authors believe that the benefits derived from the test facility clearly outweigh the cost and problem encountered. Finally, the authors believe that there exists a genuine need for this test facility in the LCAC program.

Acknowledgments

The authors would like to take this opportunity to thank the engineering and shop personnel at NSWCCD who assisted in the design, construction, operation, and maintenance of the TF40B test facility. In particular, the authors would like to recognize the contributions of Wes Norton and Roger Yee, Code 9335, to this paper.

Downloaded 02 Jun 2010 to 171.66.16.104. Redistribution subject to ASME license or copyright; see http://www.asme.org/terms/Terms_Use.cfm

Aero Engine Test Experience With CMSX-4® Alloy Single-Crystal Turbine Blades

K. P. L. Fullagar

R. W. Broomfield

M. Hulands

Aerospace Group,
Rolls-Royce plc,
Derby, United Kingdom

K. Harris

G. L. Erickson

S. L. Sikkenga

SPS Technologies,
Cannon-Muskegon Corp.
Muskegon, MI 49443

A team approach involving a turbine engine company (Rolls-Royce), its single-crystal casting facilities, and a superalloy developer and ingot manufacturer (Cannon-Muskegon), utilizing the concepts of simultaneous engineering, has been used to develop CMSX-4 alloy successfully for turbine blade applications. CMSX-4 alloy is a second-generation nickel-base single-crystal superalloy containing 3 percent (wt) rhenium (Re) and 70 percent volume fraction of the coherent γ' precipitate strengthening phase. Its finely balanced composition offers an attractive range of properties for turbine airfoil applications. In particular the alloy's combination of high strength in relation to creep-rupture, mechanical and thermal fatigue, good phase stability following extensive high temperature, stressed exposure and oxidation, hot corrosion and coating performance, are attractive for turbine engine applications where engine performance and turbine airfoil durability are of prime importance. The paper details the single-crystal casting process and heat treatment manufacturing development for turbine blades in CMSX-4 alloy. Competitive single-crystal casting yields are being achieved in production and extensive vacuum heat treatment experience confirms CMSX-4 alloy to have a practical production solution heat treat/homogenization "window." The creep-rupture data-base on CMSX-4 alloy now includes 325 data points from 17 heats including 3630 kg (8000 lb) production size heats. An appreciable portion of this data was machined-from-blade (MFB) properties, which indicate turbine blade component capabilities based on single-crystal casting process, component configuration, and heat treatment. The use of hot isostatic pressing (HIP) has been shown to eliminate single-crystal casting micropores, which along with the essential absence of γ/γ' eutectic phase, carbides, stable oxide, nitride and sulfide inclusions, results in remarkably high mechanical fatigue properties, with smooth and particularly notched specimens. The Re addition has been shown not only to benefit creep and mechanical fatigue strength (with and without HIP), but also bare oxidation, hot corrosion (sulfidation), and coating performance. The high level of balanced properties determined by extensive laboratory evaluation has been confirmed during engine testing of the Rolls-Royce Pegasus turbofan.

Introduction

Increased operating temperatures and higher rotational speeds resulting in increased component stresses are primary goals in the continuing development of the gas turbine to provide improved fuel efficiency and power-to-weight performance. Cost reduction, from improvements in turbine component producibility and process yield, and through gains in airfoil component durability, is an additional objective.

During the last 15 years, turbine inlet temperatures have increased by 278°C (500°F). About half of this increase is due to a more efficient design for the air cooling of turbine blades and vanes, while the other half is due to improved superalloys and casting processes [1].

The greatest advance in metal temperature and stress capability for turbine blades in the last 30 years has been the result of the development of single-crystal superalloy, casting process, and engine application technology pioneered by Pratt and Whitney Aircraft (PWA) [2–20].

PWA reports [21] that the F100-PW-220 fighter engine has an increased durability core section, which makes a major contribution to the PW-220's record of safety and reliability, with a shop visit rate of only 2.2 occurrences per 1000 engine flight hours (EFH) (U.S. Air Force Service), in-flight shutdowns of 0.026 per 1000 EFH, 95 percent fully mission capable, 0.6 maintenance manhours (base level) per EFH, proven in seven and a half years and greater than 750,000 EFH of service. The engine core, which features first and second-stage single-crystal blades and vanes in PWA 1480 alloy [2], is approved and has demonstrated 4000 cycles before required hot-section inspection. The Turbo-Union (Rolls Royce, MTU, & Fiat) RB-199 engine now utilizes SRR 99 alloy [6, 7] for the single-crystal *HP* and *IP* turbine blades, which have demonstrated excellent performance in service in arduous desert conditions.

The compositions of the first-generation single-crystal superalloys, which have attained turbine engine application status, are shown in Table 1. These alloys are characterized by similar creep-rupture strength. However, they exhibit differing single-crystal castability, residual gamma/gamma prime (γ/γ') eutectic phase content following solutioning, propensity for recrystallization during solution heat treatment, absence or presence of carbides, impact and mechanical fatigue properties (HCF and LCF), environmental oxidation, and hot corrosion properties and density.

Turbine engine experience with the first-generation single-crystal alloys has resulted in process developments being combined with second-generation alloy development, to improve and maximize overall properties of the turbine airfoil components [23]. Microstructures can be optimized to be fully solu-

Contributed by the International Gas Turbine Institute and presented at the 39th International Gas Turbine and Aeroengine Congress and Exposition, The Hague, The Netherlands, June 13–16, 1994. Manuscript received by the International Gas Turbine Institute February 8, 1994. Paper No. 94-GT-169. Associate Technical Editor: E. M. Greitzer.

Copyright © 1996 by ASME

Downloaded 02 Jun 2010 to 171.66.16.104. Redistribution subject to ASME license or copyright; see http://www.asme.org/terms/Terms_Use.cfm

Table 1 First-generation single-crystal superalloys

Alloy	Nominal Composition, wt. % Cr	Co	Mo	W	Ta	V	Cb (Nb)	Al	Ti	Hf	Ni	Density kg/dm³
PWA 1480 (2)	10	5	-	4	12	-	-	5.0	1.5	-	BAL	8.70
René N-4 (3,4)	9	8	2	6	4	-	.5	3.7	4.2	-	BAL	8.56
SRR 99 (6,7)	8	5	-	10	3	-	-	5.5	2.2	-	BAL	8.56
RR 2000 (6,7)	10	15	3	-	-	1	-	5.5	4.0	-	BAL	7.87
AM1 (9)	8	6	2	6	9	-	-	5.2	1.2	-	BAL	8.59
AM3 (20)	8	6	2	5	4	-	-	6.0	2.0	-	BAL	8.25
CMSX-2® (12,15)	8	5	.6	8	6	-	-	5.6	1.0	-	BAL	8.56
CMSX-3® (12,15)	8	5	.6	8	6	-	-	5.6	1.0	.1	BAL	8.56
CMSX-6® (16)	10	5	3	-	2	-	-	4.8	4.7	.1	BAL	7.98
AF 56 (8)	12	8	2	4	5	-	-	3.4	4.2	-	BAL	8.25

Table 2 Second-generation single-crystal alloys

Alloy	Nominal Composition, wt. % Cr	Co	Mo	W	Ta	Re	Al	Ti	Hf	Ni	Density kg/dm³
CMSX-4® (23,24)	6.5	9	.6	6	6.5	3	5.6	1.0	.1	BAL	8.70
PWA 1484 (18)	5	10	2	6	9	3	5.6	-	.1	BAL	8.95
SC 180 (34)	5	10	2	5	8.5	3	5.2	1.0	.1	BAL	8.84
MC2 (35)	8	5	2	8	6	-	5.0	1.5	-	BAL	8.63
René N-5 (22)	7	8	2	5	7	3	6.2	-	.2	BAL	NA

tioned and HIP'ed, to contain neither γ/γ' eutectic phase, nor regions of incipient melting, carbides, nor microporosity [23, 24]. The published compositions of the second-generation single-crystal alloys are shown in Table 2.

The Rolls-Royce Pegasus vectored-thrust turbofan powers all variants of the British Aerospace/McDonnell Douglas Harrier short take-off and vertical landing (STOVL) aircraft (Fig. 1). It features high thrust-to-weight ratio, single engine simplicity, fast throttle response, contrarotating *HP* and *LP* spools to minimize gyroscopic couple, high flow *HP* air bleed for the aircraft reaction control system and swiveling exhaust nozzles for vectored thrust-swept arc of 98 deg and other important design features shown in Fig. 2.

The Pegasus 11-61 (designated the F 402-RR-408 in the U.S.) is the latest and most powerful variant of the engine. Rated at 105.3 KN (23,690 lb) thrust at ISA + 15°C, the significant thrust increase over earlier variants improves the short take-off performance of the Harrier II particularly in hot and high conditions by over 20 percent, specific excess power at 1524 m (5000 ft)/Mach 0.75 by 85 percent and vertical landing (VL) payload on a tropical day by 100 percent with a 10 percent improvement in VL aircraft weight.

The Harrier II [AV-8B] STOVL close support mission is particularly arduous for the engine with multicycle, high-temperature lift conditions with some hot gas ingestion, combined with high-power combat maneuvering. The turbine blades and coatings are given a "hard ride" in terms of high temperature creep, thermal and mechanical fatigue, oxidation and hot corrosion (sulfidation). Hot corrosion is of concern to ship-embarked Harrier operations. This application seemed ideal to evaluate the single-crystal turbine blade capabilities of CMSX-4 alloy (13, 23–25). CMSX-4 was selected by Rolls-Royce on the basis of both overall combination of properties and the performance of a single uncoated blade in an early Adour engine demonstrator unit. This single-crystal, complex cooled blade ran for 8745 idle-maximum cycles at a first-stage vane outlet maximum gas temperature of 1800–1850 K [1527°C (2781°F)–1577°C (2871°F)] and was deemed suitable for further running based on post-engine test examination.

Alloy Melting

The optimized vacuum induction refining procedures developed for CMSX-2® and CMSX-3® alloys and discussed in [12], were used to produce the 23 V-3 furnace 8000 lb (3630 kg) heats of CMSX-4 alloy, melted to date (Nov. 1993). Table 3 shows the C, S, [N], and [O] contents of these heats, which include three 50 percent revert/50 percent virgin heats. Studies by several single-crystal casters demonstrate that high [N] and [O] levels in single-crystal superalloy ingot adversely affect single-crystal casting yield due to grain defects [26]. The presence of [O], [N], and S master alloy impurities is known to transfer nonmetallic inclusions, such as aluminum oxide, and nitrides and sulfides of tantalum and titanium, to single-crystal parts [27].

The extensive development of the vacuum induction refining process for the CMSX-4 alloy ingot combined with clean single-crystal casting processes have resulted in both clean alloy and airfoil castings in terms of stable oxide dross or refractory inclusions. This is confirmed by production of over 30,000 single-crystal turbine airfoil castings ranging from 0.25 mm (0.010 in.) thick Lamilloy® crystalfoils, hybrid CastCool® blades and vanes, to large shrouded turbine blades up to 160 mm (6.3 in.) in length for the new 80,000 lb thrust commercial turbofan engines, with attendant high process yields and low levels of grain defects [23].

Manufacturing Development

The Rolls-Royce (RR) Company Research & Development Foundry (CRDF) collaborated with Cannon-Muskegon (CM) during the engineering development stage of CMSX-4 alloy (circa 1987) through to finalizing the aim chemistry in 1989. The aim chemistry optimization phase targeted maximization of creep-rupture response of the alloy utilizing multistep 99 percent + solution heat treatment procedures [28], optimized high-temperature aging heat treatment [29] and ensuring alloy microstructural phase stability following extensive high-temperature, stressed exposure. The desired fully heat treated γ' microstructure is shown in Fig. 3.

Nomenclature

γ = gamma phase
γ' = gamma prime phase
MFB = machined-from-blade
HP = high pressure
IP = intermediate pressure
EFH = engine flight hours
HCF = high cycle fatigue
LCF = low cycle fatigue
TCP = topologically close-packed phase
SEM = scanning electron microscope
TEM = transmission electron microscope
TTT = transformation–time–temperature curve
H_z = frequency in cycles per second
K_T = stress concentration factor
TFCIL = thermal fatigue crack initiation life
TF = thermal fatigue
SOT = stator vane outlet gas temperature
ASMET = accelerated simulated mission endurance test
C = carbon
S = sulfur
[N] = combined nitrogen
[O] = combined oxygen
ISA = International Standard Atmosphere (15°C)

Downloaded 02 Jun 2010 to 171.66.16.104. Redistribution subject to ASME license or copyright; see http://www.asme.org/terms/Terms_Use.cfm

Fig. 1 Radar-equipped Harrier II Plus

The CRDF work encompassed all aspects of alloy evaluation from assessing its single-crystal castability performance on a range of development military/civil engine turbine blades and vanes, to development of productionized vacuum heat treatment processes (solution and high-temperature age) and the provision of single-crystal test bars for determination of the mechanical and physical property design data-base.

The CRDF used small bore (140 mm (5.5 in.) diameter cooling plate), withdrawal-type furnaces [6], with additional instrumentation, for the single-crystal castability studies. These furnaces have high-frequency electric induction melting in single shot, rigidized ceramic fiber crucibles with automatic bottom pouring (Fig. 4).

No significant single-crystal casting problems were found with either 181 kg (400 lb) or 3630 kg (8000 lb) vacuum induction refined heats of CMSX-4 alloy, in terms of grain defects such as "freckles," high angle boundaries (HAB's), recrystallization (RX), alloy-core/shell reactions or stable oxide dross-type inclusions. The CMSX-4 single-crystal turbine blades manufactured by the CRDF have performed satisfactorily in rig and development engine testing out to 5000 cycles. Extensive cut-up microstructural assessment of single-crystal airfoils in the alloy cast by the CRDF and vacuum heat treated under CRDF control, ensured the solution heat treatment was developed to achieve full γ' and γ/γ' eutectic solutioning within a temperature "window" suitable for production vacuum heat treatment furnace loads. Additionally, the incorporation of the optimized high-temperature (1140°C (2085°F)) primary age into the solution heat treat cycle, commensurate with the quench rate from the solution temperature [24], generated an electro-etch response permitting surface grain defects to be detected with high sensitivity.

Transfer to production of the single-crystal casting and heat treatment technology for CMSX-4 from the CRDF to the RR Precision Casting Facility (PCF) was initiated in 1989. This proceeded without any major problems culminating in the "buy-off" of CMSX-4 alloy and the single-crystal airfoil castings by RR Manufacturing and the generation of a full material specification, MSRR 7248, in June 1992.

The PCF single-crystal casting process utilizes the same small bore furnaces as in the CRDF and an ethyl silicate bonded Zircosil (zirconium silicate) mold system applied by automated conveyers and robots. The molds incorporate ceramic filters. The majority of blades are produced using a grain selector

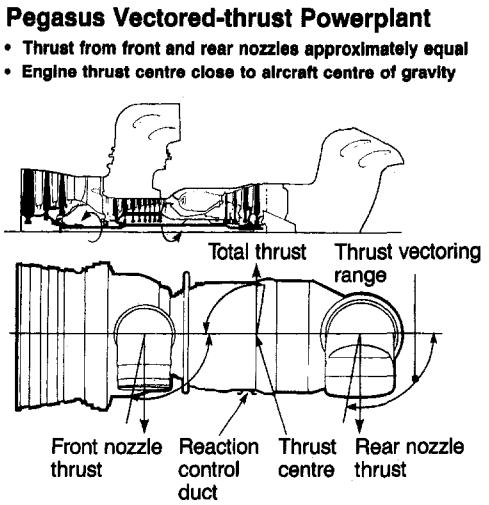

Fig. 2 Pegasus vectored-thrust powerplant:
• Thrust from front and rear nozzles approximately equal
• Engine thrust center close to aircraft center of gravity

Table 3

CMSX-4® Alloy 8000 lb. (3630 kg) V-3 Furnace 100% Virgin Heats

	C, S, [N] & [O] Contents (wt. ppm)			
Heat	C ppm	S ppm	[N] ppm	[O] ppm
V 7927	20	6	3	1
V 8053	19	5	2	1
V 8054	15	6	3	1
V 8154	21	3	2	2
V 8194	17	4	2	2
V 8195	18	4	2	2
V 8256	15	2	1	1
V 8276	19	2	1	2
V 8277	20	2	1	2
V 8291	14	2	1	2
V 8311	17	2	1	2
V 8312	19	2	1	2
V 8330	24	2	2	1
V 8331*	18	2	2	2
V 8351	21	2	1	1
V 8393	24	3	1	2
V 8394*	32	4	1	2
V 8432	19	2	1	2
V 8433	19	2	1	2
V 8455	23	2	1	2
V 8479	21	2	1	2
V 8480	17	1	1	1
V 8481*	17	2	2	1

*50% virgin/50% foundry revert heats

Downloaded 02 Jun 2010 to 171.66.16.104. Redistribution subject to ASME license or copyright; see http://www.asme.org/terms/Terms_Use.cfm

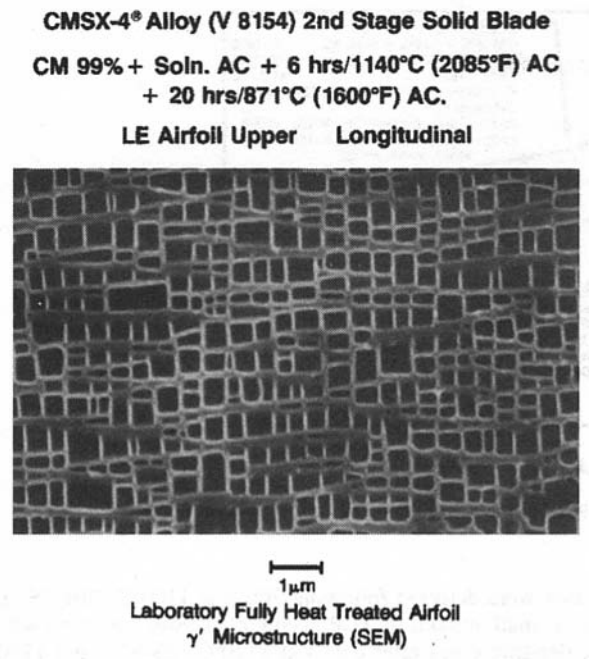

Fig. 3

system. However, double orientation controlled blades are now being produced using seeding techniques to maximize the material properties to specific engine applications. After casting, the CMSX-4 blades are processed to remove the mold materials and ceramic cores prior to solution heat treatment. New handling techniques have been developed at all stages prior to heat treatment, so as to eliminate causes of recrystallization.

The production solution heat treatment/homogenization cycle has been developed and optimized in conjunction with CM and vacuum heat treatment subcontractors to ensure that optimum microstructure/microchemistry and mechanical property response is achieved. Following PCF Laboratory evaluation, this has led to temperature and cooling rate control limits, which confidently ensure that microstructure/homogenization and mechanical property criteria are met. Once a solution heat treatment furnace's characteristics have been established, mechanical testing is relaxed and heat treatments are monitored by control limits and microstructure. Over 180 such solution heat treatments have been accumulated to date without a rejection.

The blades produced have low grain defect reject rates as CMSX-4 alloy is not prone to "freckle" formation. The small-diameter high-gradient furnaces allow accurate and repeatable control of the solidification conditions. Specific blades are also HIP'ed in order to reduce the sites for fatigue initiation, in particular the micropores. Such blades are solution heat treated prior to HIP'ing and given a short time solution treatment following HIP to achieve optimum γ' precipitate size. This cycle has been developed and optimized to minimize cost while ensuring that the mechanical properties are achieved.

Including the manufacturing development program, nearly 40 tons (88,000 lbs) of CMSX-4 alloy from 20 different CM heats have been cast by the PCF into 18,000 blades (Nov. 1993). The range of blades manufactured vary from solid to complex cored parts for the RR Tay, RB 211, Trent, Pegasus, and EJ 200 engine applications. The heats have demonstrated very tight aim chemistry control, which has contributed to the consistent performance CMSX-4 alloy has achieved within the PCF.

The PCF experience with CMSX-4 has shown it to be capable of achieving high yields with the manufacturing process. New turbine blade components have been launched with initial yields in excess of 85 percent. The behavior of CMSX-4 under the PCF casting conditions is now well understood.

Material Properties

The main difference between CMSX-4 alloy and first-generation single-crystal alloys such as CMSX-2 [12], PWA 1480 [2] and SRR 99 [6, 7] is the addition of 3 percent Re, and a corresponding reduction in tungsten (W) and chromium (Cr)

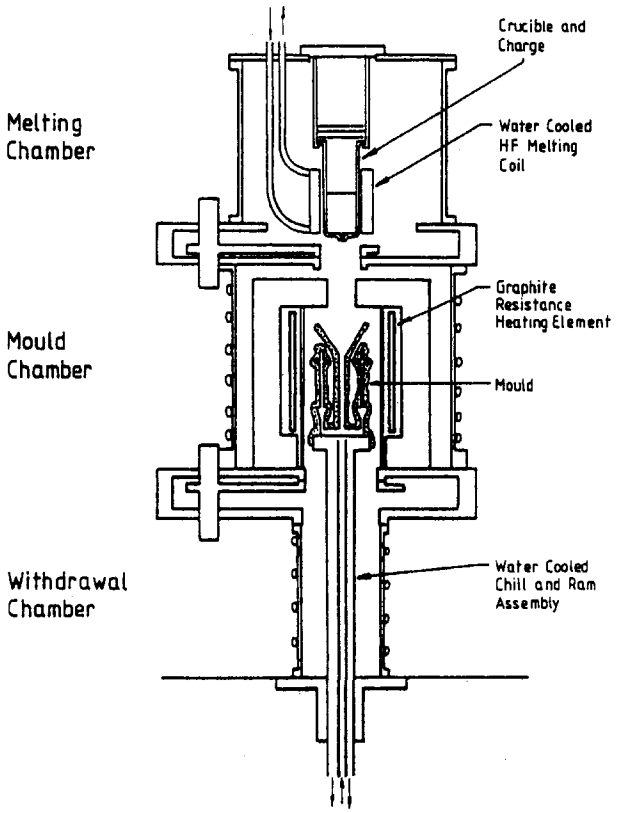

Fig. 4 Configuration of the single-crystal furnace [6]

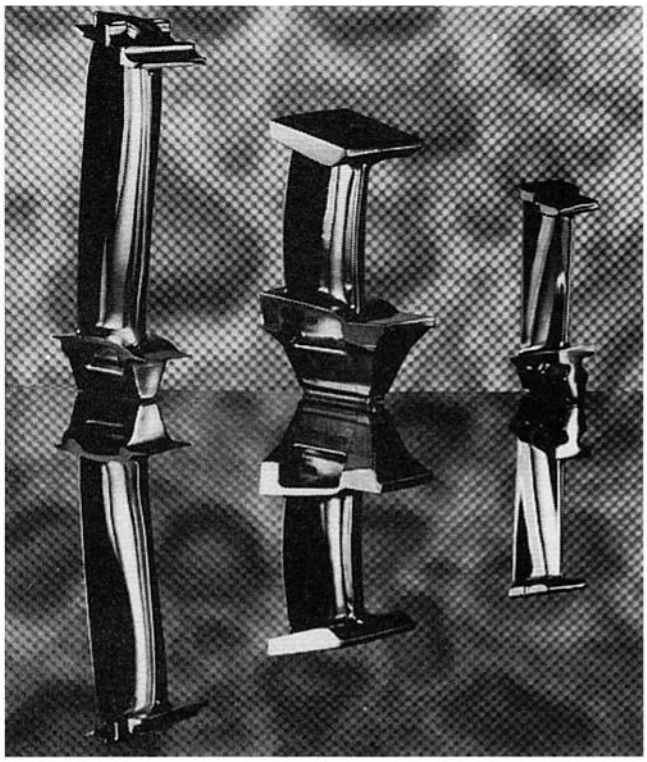

Fig. 4 (Cont.) Typical single-crystal turbine blades cast in CMSX-4 alloy

Downloaded 02 Jun 2010 to 171.66.16.104. Redistribution subject to ASME license or copyright; see http://www.asme.org/terms/Terms_Use.cfm

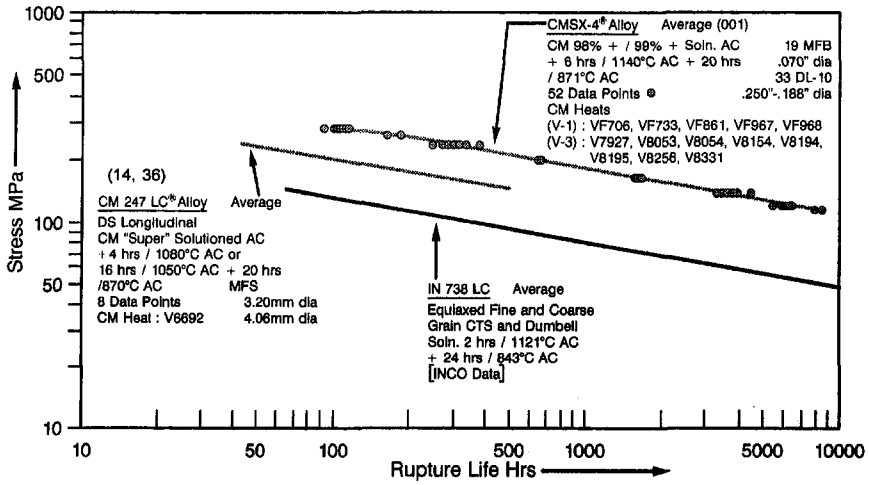

Fig. 5 Stress rupture 982°C (1800°F)

levels, to ensure the essential absence of topologically close-packed (TCP) phases following extended high-temperature, stressed exposure in turbine airfoil applications. It is known that Re partitions mainly to the γ matrix, reduces rates of diffusion, and thus retards coarsening of the γ' strengthening phase, and increases γ/γ' misfit [30]. Atom-probe micro-analyses of Re containing modifications of PWA 1480 and CMSX-2 alloys reveal the occurrence of short range order in the γ matrix [31, 32]. Small Re clusters (approximately 1.0 nm in size) are detected in the alloys. The Re clusters act as efficient obstacles to dislocation movement in the γ matrix channels compared to isolated solute atoms in solid solution and thereby play a significant role in improving alloy strength. The benefits of Re to mechanical properties are seen in situations where dislocation movement within the γ phase matrix channels is controlling. Where dislocations pass readily through both γ and γ' phases, the strength advantage of CMSX-4 is smaller. Dislocations travel mainly within the γ matrix channels at higher temperatures $\geq$ 850°C (1562°F). A consistent benefit for CMSX-4 is therefore seen in tensile strength, creep, and stress-rupture strength over the temperature range 850–1050°C (1562–1922°F). The temperature capability advantage is at least 30°C (54°F) over SRR 99.

In long-time or high-temperature creep tests, various aspects of metallurgical stability become important. It was found that between 1050°C (1922°F) and 1150°C (2102°F), the temperature capability advantage of CMSX-4 alloy over SRR 99 in terms of creep, is increased from 30°C (54°F) to 50°C (90°F). This is due to the fact that the rafted γ' structure that develops during creep at high temperatures ($\geq$1093°C (2000°F) for CMSX-4) in all practical single-crystal alloys, is stable to 1163°C (2125°F) in CMSX-4, but only to 1100°C (2012°F) in SRR 99. This benefit probably arises from two factors; the low γ/γ' mismatch (29) and low diffusion rates due to Re in CMSX-4 alloy.

The long-time phase stability of CMSX-4, in terms of its resistance to TCP phase formation, was a major aspect in all stages of the development of the alloy. Specifically the Cr content was fixed at a level and the overall chemistry balanced, to give phase stability with the presence of 3 percent Re and 6.4 percent W and also to give acceptable hot corrosion (sulfidation) resistance. TCP phase stability of CMSX-4 alloy has been proven by creep-rupture testing out to 8810 h life at 114 MPa/982°C (16.5 ksi/1800°F) and 5613 h life at 100 MPa/1038°C (14.5 ksi/1900°F), where there are no fall-offs in log-stress to log-life linear property plots at the longer lives due to undesirable microstructural changes (Figs. 5 and 6), such as the significant occurrence of TCP phases. Also, following stress-rupture testing between 1100°C (2012°F) and 1150°C (2102°F), no TCP phases were detected following 700 h at 1100°C (2012°F) and just a small amount of TCP needle phase was observed within the dendrite cores after 850 h at 1120°C (2048°F) and 1750 h at 1121°C (2050°F). The TCP phase has been analyzed on the SEM and TEM to be W + Re + Cr rich. TCP phases are potentially damaging for two reasons: They tie up γ and γ' strengthening elements in non-useful form, thus reducing creep strength. They also can act as crack initiators because of their brittle nature and reduce impact and fatigue strength. CMSX-4 has excellent long-term creep-rupture strength at 1121°C (2050°F) (the "knee" of the stressed TTT curve for TCP phase). To investigate the other aspects, a set of fully heat-treated single-crystal test bars were furnace soaked for 930 h at 1050°C (1922°F) before being machined to plain impact and low cycle fatigue (LCF) test pieces. Impact strength was improved and LCF strength at 950°C (1742°F) was only reduced by 10 percent due to coarsening of the γ' particles beyond their optimum size. The high-temperature phase stability of the alloy is considered good for all Rolls-Royce turbine engine airfoil applications.

The final mechanical property to be reviewed is fatigue strength, both low cycle (LCF) and high cycle (HCF). Single crystals show two modes of fatigue failure: a time-dependent mode with fracture perpendicular to the stress axis, which occurs under low frequency/high temperature/mean tensile stress conditions where a creep component is important, and cycle-dependent mode with crystallographic failure on {111} planes. This mode is promoted by the opposite conditions, i.e., high frequency/low temperature/zero mean stress. To take one example, at 950°C (1742°F) the time-dependent mode occurred at 0.25 $H_z/R = 0$ and at 100 $H_z/R = 0$, but at 100 $H_z/R = -1$, the failure mode changed to crystallographic.

CMSX-4 shows a benefit over non-Re-containing alloys when the time-dependent mode is in operation where dislocation activity and crack growth are mainly confined to the γ matrix phase. If the LCF data are plotted as stress for a given cyclic life versus temperature, the temperature advantage of CMSX-4 over SRR 99 is about 45°C (81°F), which is similar to the creep strength advantage at high temperatures.

Under cycle-dependent conditions, where dislocations and cracks slice through γ and γ' phases alike, the improvement for CMSX-4 is less. However, if an improved fatigue performance is required in this regime, there is a solution: HIP'ing. In both plain specimens and notched specimens (K_T = 2.2), fatigue failures initiate at single-crystal casting microporosity and the fatigue life at a given cyclic stress and temperature can be related to the size and shape of the micropores (one 100 μm interdendritic micropore is more damaging than hundreds of 30

Downloaded 02 Jun 2010 to 171.66.16.104. Redistribution subject to ASME license or copyright; see http://www.asme.org/terms/Terms_Use.cfm

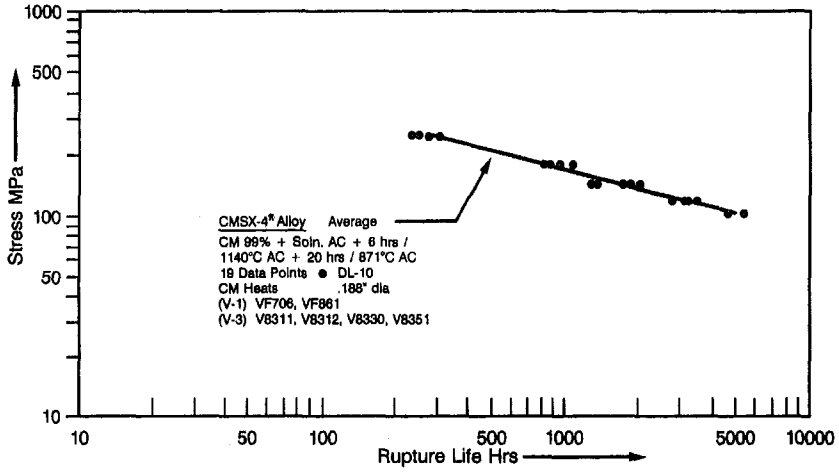

Fig. 6 Stress rupture 1038°C (1900°F)

μm spherical pores at their normal uniform spacing in single-crystal castings).

By using an appropriate solution treatment + HIP cycle, it is possible to remove all the casting microporosity aside from those micropores that are surface linked, without occurrence of internal recrystallization problems. The HIP process provides a dramatic increase in HCF strength, particularly in the lower temperature range of 500–750°C (932–1382°F). For instance, in plain specimen rotating bend HCF testing at 550°C (1022°F), the 10^7 cycle strength is increased by 95 percent; in notched ($K_T = 2.2$) axial HCF testing at 750°C (1382°F), it is increased by 60 percent. It is true that the scope for fatigue improvement using HIP is much greater at lower temperatures. At 950°C (1742°F)/$R = 0/K_T = 1$, the ratio of 10^7 cycle HCF strength to 0.2 percent proof strength in non-HIP CMSX-4 single-crystal test pieces is 0.82, at 750°C (1382°F) it is only 0.55. HIP'ing increases the fatigue strength at 750°C (1382°F) so that the ratio is now 0.79, similar to the 950°C (1742°F) ratio. HIP'ing is therefore not so beneficial at $\geq$ 950°C (1742°F) because the scope for improvement is less and oxidation commences to produce surface initiation nuclei for cracks at either pits or cracks in the adherent oxide scale.

Since HIP'ing makes fatigue crack initiation more difficult, but probably has a much smaller influence on fatigue crack propagation, the benefit of HIP will diminish as notch severity increases to the point where crack nucleation occurs at the root of the notch. This transition has not yet been precisely defined for HIP CMSX-4, but it is between $K_T = 2.2$ and $K_T = 4$.

Turning to the resistance of CMSX-4 to environmental attack (oxidation and sulphidation), there was concern in the alloy development phase that bare hot corrosion (sulfidation) resistance might be marginal at the 6.5 percent Cr content in the alloy. However, burner rig testing has shown the resistance to both bare oxidation and hot corrosion has been good [23, 24]. Cylindrical single-crystal test bars have been tested in the hot gas stream (Mach 1) from a Rolls-Royce Dart engine combustor using aviation kerosene, under two conditions:

- 1100°C (2012°F) peak temperature, cyclic (15 min cycle), 0.25 ppm salt injected into the combustor.
- 950°C (1742°F) peak temperature with a range down to a 700°C (1292°F) minimum, isothermal, 2 ppm salt injected into the combustor.

The test samples were sectioned through the region of maximum attack and assessed in terms of "loss of useful metal" by measuring the diameter not from the oxide surface or the oxide/metal interface, but from the base of the γ' depleted zone. Graphs showing the loss of useful metal versus cycles (1100°C (2012°F) oxidation test) or hours (950°C (1742°F)–700°C (1292°F) sulfidation test) are presented in Figs. 7 and 8. It is apparent that CMSX-4 compares very well with earlier directionally solidified, columnar grain (DS) superalloys. The burner rig test results with CMSX-4 have been borne out by engine testing on advanced military demonstrator programs. The trailing edges of the CMSX-4 blades, which had been machined back and were therefore bare rather than coated, showed very little oxidation, whereas blades in the same engine test in a first generation, non-Re-containing single-crystal alloy showed much more oxidation attack.

Microprobe examination of the burner rig tested samples did not show any significant Re content in the oxide scale, but Re did tend to concentrate in the γ' depleted zone beneath the

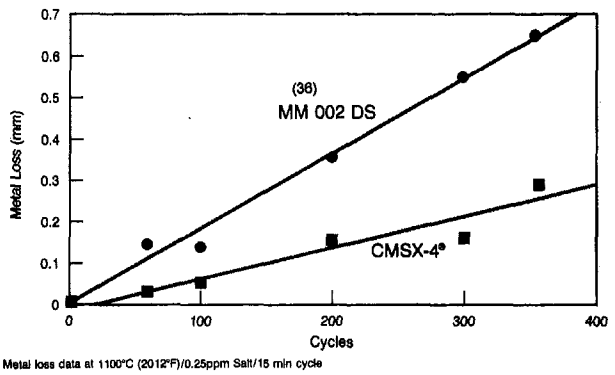

Fig. 7 Burner rig (Mach 1) bare alloy oxidation data

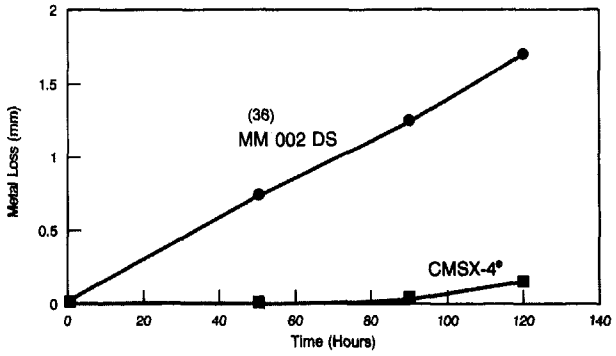

Fig. 8 Burner rig (Mach 1) bare alloy hot corrosion data: 950°C (1742°F), 2 ppm salt, isothermal

Downloaded 02 Jun 2010 to 171.66.16.104. Redistribution subject to ASME license or copyright; see http://www.asme.org/terms/Terms_Use.cfm

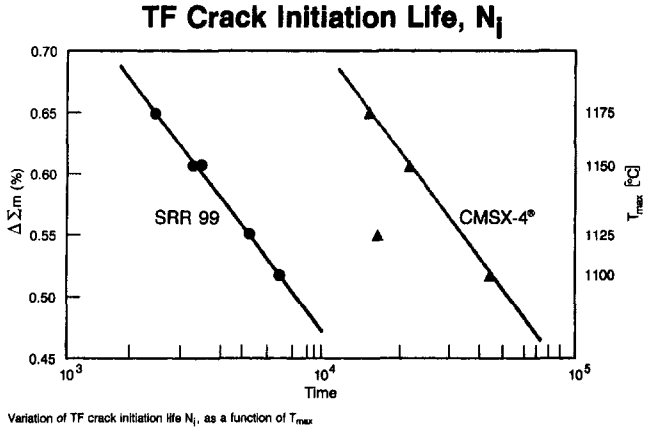

Fig. 9 *TF* crack initiation life, N_i [33]

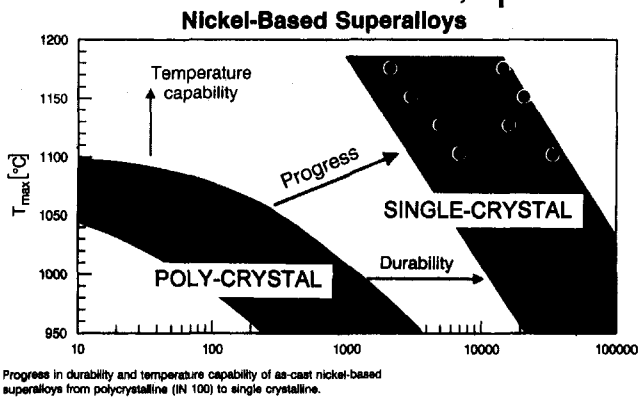

Fig. 10 *TF* crack initiation life, N_i; nickel-based superalloys [33]

oxide scale. It is possible therefore that Re reduces oxidation rates by slowing down the diffusion of reactive elements into the oxide scale.

CMSX-4 alloy has proved to be compatible with both diffusion and overlay coatings. Aluminide and platinum–aluminide coatings were applied to the cylindrical Dart burner rig samples and tested in cyclic, dynamic burner rig oxidation at 1050°C (1922°F). The life to coating failure (defined as a pit 0.75 mm (0.030″) wide, which penetrates the coating) was 60–90 percent better than for the same coatings on SRR 99. Overlay coatings are less influenced by the substrate since their initial compositions are independent of the substrate composition. However, the 1100°C (2012°F) cyclic, dynamic oxidation life of an advanced overlay coating on CMSX-4 was 10–15 percent greater than the same coating (composition and thickness) on DS Mar M 002 [36].

The thermal fatigue behavior of bare single-crystal SRR 99 and CMSX-4 has been investigated and reported in [33]. For the single-crystal alloys studied, the thermal fatigue crack initiation life (TFCIL) constitutes about 70–90 percent of the total thermal fatigue (TF) life (defined as the number of thermal cycles required to form a principal crack of 1 mm (0.040 in) in length). For polycrystalline nickel and cobalt-base superalloys, the TFCIL is normally less than 50 percent of the total life. The higher TFCIL of CMSX-4 shown in Fig. 9 [33] can be explained by the higher resistance of its oxide-scale to spalling combined with higher strength in the corresponding γ' depleted zone, probably due to increased γ' stability within this zone. In bare CMSX-4, cracks initiate from the micropores (NON-HIP). In bare SRR 99, crater-like regions are formed by a mechanism of successive oxide-scale spalling and re-oxidation of the base metal during TF. These regions are prone to crack initiation. The first generation (non-Re-containing) and Re-containing single-crystal superalloys provide significant progress in TF durability and temperature capability in comparison to conventionally cast polycrystalline superalloys Fig. 10 [33]. Additionally single-crystal superalloys provide a lower thermal fatigue crack growth rate as compared to polycrystalline alloys [33].

To summarize, CMSX-4 offers an improvement over first-generation non-Re-containing single-crystal alloys across virtually the whole range of properties that are relevant to turbine blade and vane engine applications. CMSX-4 is also compatible with advanced coating systems. Its fatigue properties can be improved by HIP if the application, blade design, and life cycle cost make this worthwhile.

Pegasus Engine Test Results

The initial production standard for the HP 1 and HP 2 cored turbine blades for the Pegasus 11-61 (F 402-RR-408) engine (Fig. 11) were single-crystal cast in first-generation RR 2000 alloy (6, 7, Table 1). Both stages of blades are film cooled and originally a CoCrAlY overlay coating was used. More recently an additional aluminide coating has been applied on top of the CoCrAlY for additional oxidation protection.

One of the specification requirements for certification of Pegasus-408 engine (to demonstrate a 1000 h time between hot section repair) was to satisfactorily complete an Accelerated Simulated Mission Endurance Test (ASMET). This test was identical to that carried out on the earlier Pegasus 406 engine and was derived from analysis of various Harrier II (AV-8B) aircraft missions, aimed at producing a 530 h engine test that realistically simulates 1000 h of service usage in ISA + 5°C ambient conditions.

The ASMET for specification compliance was carried out at the Rolls-Royce (Bristol) test facilities using Pegasus bench engine #964 build 3 with standard RR 2000 alloy single-crystal blades. After a total run time of 580 h, including 454 h under endurance conditions, at a maximum first stage HP vane outlet gas temperature (SOT) of 1585 K [1312°C (2395°F)], oxidation/sulfidation resulting in base alloy attack was seen on the HP 1 and HP 2 blades.

A program was subsequently initiated to validate improved blade cooling and coating options. Additionally a material change to the second-generation single-crystal alloy CMSX-4 was to be engine tested and validated. Eight CMSX-4 single crystal HP 1 blades were successfully cast in the CRDF using the existing wax and core tooling and machined to the existing cooling configuration. No airfoil overlay coatings were applied to the CMSX-4 blades.

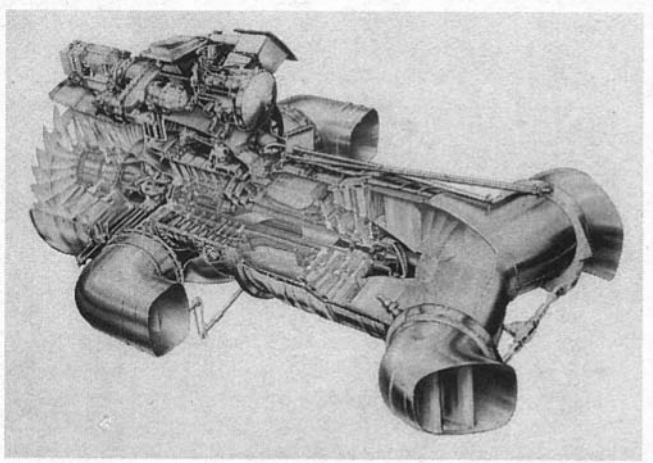

Fig. 11 Pegasus 11-61 (F402-RR-408) vectored-thrust turbofan

Downloaded 02 Jun 2010 to 171.66.16.104. Redistribution subject to ASME license or copyright; see http://www.asme.org/terms/Terms_Use.cfm

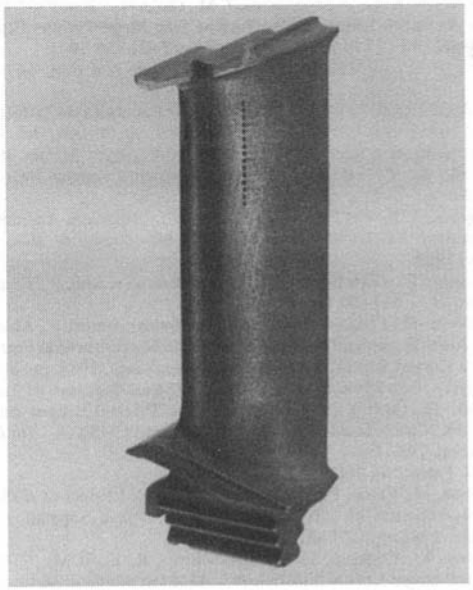

Fig. 12 Pegasus-408 HP1 single-crystal coated blade—CMSX-4® Alloy—following ASMET engine testing

All of the improved standards to HP 1 and HP 2 turbine blades were fitted to Pegasus bench engine #964 build 4 for a condensed ASMET. A total run time of 265 h (200 h endurance) and 2850 major lift cycles was completed, with turbine temperatures simulating both ISA + 5°C and ISA + 35°C ambient conditions (maximum SOT of 1640 K [1367°C (2492°F)]). Engine strip examination showed the uncoated CMSX-4 HP 1 blades to be in visually good condition. Radial (blade longitudinal) creep growths measured following the engine test were half that seen on the other HP 1 RR 2000 blades. Laboratory cut-up examination of the uncoated CMSX-4 blades showed slight evidence of oxidation and sulfidation in the airfoil, up to a depth of 0.08 mm (0.0032 in.). Metallographic examination of the post-engine test γ' structure in the airfoils indicated that metal temperatures in the range 1050–1100°C (1922–2012°F) had been experienced.

Full design and manufacturing activity was initiated in mid-1991 to introduce single crystal HP 1 and HP 2 turbine blades in CMSX-4 alloy for the Pegasus-408 engine, with a 2000 h service life, incorporating sand tolerant film cooling features. Concurrent engineering between the Pegasus design team, the PCF, machining and coating groups was initiated from the outset of this phase of the program to ensure maximum single-crystal castability, casting yield, blade quality, and minimized overall cost. The HP 1 blade utilizes the existing ceramic core with three longitudinal airfoil cooling passages. The HP 2 is a new design moving from a solid single-crystal casting to a ceramic cored casting with two longitudinal airfoil cooling passages. A new advanced overlay coating is planned to be used. This new coating has a good match to CMSX-4 base material thermal expansion properties and has demonstrated a 10:1 life advantage over platinum-aluminide diffusion coatings during cyclic, high-temperature burner rig oxidation testing.

In the meantime, a further half set of HP 1 single-crystal blades in CMSX-4 were manufactured incorporating the sand tolerant film cooling features and the CoCrAlY + aluminide coating. These blades were fitted to Pegasus bench engine #964 build 5 for further ASMET testing. This commenced in late 1992 and completed a total run time of 200 h (160 h endurance) and 1220 major lift cycles up to a SOT of 1615 K [1342°C (2448°F)]. Examination of the CMSX-4 blades after the engine test showed them to be visually in very good condition (Fig. 12), with creep growth half that seen on the RR 2000 blades. Cut-up laboratory metallographic examination showed there to be no signs of coating deterioration.

Manufacture of the production standard CMSX-4 HP 1 and HP 2 blades for the main Pegasus engine validation program (4 engine sets) is complete as of Dec. 1993. No problems have been encountered, with good single-crystal casting yields of over 75 percent achieved on both blades. The validation program has begun (Oct. 1993) and includes a successfully completed blade thermal paint engine test, two endurance tests; a 530 h ASMET (50 h completed as of early December) and a 150 h. Durability Proof Test (DPT), together with spool strain gaging and rig testing (fatigue, torsion, impact, and spin). Completion of production standardization is due in Spring 1994 with production single-crystal CMSX-4 HP 1 and HP 2 blades being available for engine build at the same time.

Conclusions

The high level of balanced properties determined by extensive laboratory evaluation has been confirmed during engine testing the Rolls-Royce Pegasus vectored thrust turbofan, particularly during multicycle, high-temperature lift conditions and accelerated endurance running. Post-engine test examination of the CMSX-4 blades (HP 1) including cut-up metallographic examination, demonstrate the durability features including high-temperature impact properties, resistance to over-temperature excursion, creep and oxidation resistance, and coating performance.

Acknowledgments

The authors wish to acknowledge the significant contributions to this work from the following colleagues:

Rolls-Royce:	Colin P. Beesley, David A. Ford, Tony D. Hill, Tony Denton, Hamish C. Low, Mike J. Goulette, and David A. Hopkins.
Cannon-Muskegon:	John M. Eridon, Tom A. Versalle, Gary DeWind, and Jack DeHorn

CMSX-2®, CMSX-3®, CMSX-4®, and CMSX-6® are registered trademarks of the Cannon-Muskegon Corp. Lamilloy® and CastCool® are registered trademarks of Allison Engine Co.

References

1 Pickering, F. E., (GE), "Advances in Turbomachinery," Cliff Garrett Award Lecture, *Aerosp. Eng.*, Jan. 1986, pp. 30–35.

2 Gell, M., Duhl, D. N., Giamei, A. F., (PWA), "The Development of Single Crystal Superalloy Turbine Blades," 4th Int. Symp.,[2] Sept. 1980, pp. 205–214.

3 Wukusick, C. S., [GE (AE)], "Directional Solidification Alloy Development," NAVAIR Contr. N62269-78-C-0315, Final Report, 25 Aug. 1980.

4 Holmes, J. W., et al. (MIT), O'Hara, K. S. [GE (AE)], "Thermal Fatigue Testing of Coated Monocrystallize Superalloys," ASTM STP 942, Phil., 1988, pp. 672–691.

5 Strangmen, T. E., et al. (Garrett), "Development of Exothermically Cast Single Crystal MAR M 247 and Derivative Alloys," 4th Int. Symp. Sept. 1980, pp. 215–224.

6 Goulette, M. J., Spilling, P. D., Arthey, R. P., (RR), "Cost Effective Single Crystals," 5th Int. Symp.,[2] Oct. 1984, pp. 167–176.

7 Ford, D. A., Arthey, R. P., (RR), "Development of Single Crystal Alloys for Specific Engine Applications," 5th Int. Symp.,[2] Oct. 1984, pp. 115–124.

8 Doner, M., Heckler, J. A., (Allison), "Effects of Section Thickness and Orientation on the Creep-Rupture Properties of Two Advanced Single Crystal Alloys," Aerospace Tech. Conf., Long Beach, CA, Oct. 1985.

9 Bachelet, E., and Lamanthe, G., (Snecma), Nat. Symp.—Single Crystal Superalloys, Viallard-de-Lans (France), 26–28 Feb. 1986.

10 Yamazaki, M., et al. (NRIM), "Alloy Design for High Strength Nickel-Base Single Crystal Alloys," 5th Int. Symp.,[2] Oct. 1984, pp. 157–166.

11 Petrov, D. A., and Tumanov, A. T., "The Use of Single Crystal Blades," *Aircraft Engineering*, No. 9, 1973.

12 Harris, K., Erickson, G. L., and Schwer, R. E., (CM), "Development of the Single Crystal Alloys CMSX-2 and CMSX-3 for Advanced Technology Turbines," ASME Paper No. 83-GT-244.

13 Harris, K., Erickson, G. L., and Schwer, R. E., (CM), Verbal Presentation, TMS Mtg, Phil., PA, 3 Oct. 1983.

Downloaded 02 Jun 2010 to 171.66.16.104. Redistribution subject to ASME license or copyright; see http://www.asme.org/terms/Terms_Use.cfm

14 Harris, K., Erickson, G. L., Schwer, R. E., (CM), "MAR M 247 Derivations—CM 247 LC DS Alloy, CMSX® Single Crystal Alloys, Properties and Performance," 5th Int. Symp.,[2] Oct. 1984, pp. 221–230.

15 Harris, K., Erickson, G. L., Schwer, R. E., (CM), "CMSX® Single Crystal, CM DS and Integral Wheel Alloys—Properties and Performance," *Proc. Cost 50/501 Conf. Liège,* Oct. 6–9, 1986, pp. 709–728.

16 Wortmann, J., Wege, R., (MTU), Harris, K., Erickson, G. L., Schwer, R. E., (CM), "Low Density Single Crystal Superalloy CMSX-6®," *Proc. 7th World Conf. on Inv. Casting,* Munich, 29 June 1988.

17 Yukawa, N., et al. (Toyohashi Univ.), "High Performance Single Crystal Superalloys Developed by the d-Electrons Concept," 6th Int. Symp.,[2] Sept., 1988, pp. 225–234.

18 Cetel, A. D., and Duhl, D. N., (PWA), "Second-Generation Nickel-Base Single Crystal Superalloy," 6th Int. Symp.,[2] Sept. 1988, pp. 235–244.

19 Gell, M., Duhl, D. N., Gupta, K. K., and Sheffler, K. D., (PWA), *JOM,* July, 1987, pp. 11–15.

20 Khan, T., (Onera), Brun, M., (Turbomeca), *Symp. on Single Crystal Alloys,* MTU/SMCT, Munich, June 1989.

21 PWA Publication, "F100-PW-220, The Standard of Excellence," June 1993.

22 Wukusick, C. S., and Buchakjian, L., Jr. [GE(ARE)], "Improved Property-Balanced Nickel-Base Superalloys for Producing Single Crystal Articles," U. K. Patent Application #GB 2 235 697 A, Mar. 13, 1991.

23 Harris, K., Erickson, G. L., and Schwer, R. E., (CM), Frasier, D. J., Whetstone, J. R., (Allison), "Process and Alloy Optimization for CMSX-4 Superalloy Single Crystal Airfoils," *Proc. Cost Conf. Liège,* Sept. 24–27, 1990, Part II, pp. 1281–1300.

24 Harris, K., Erickson, G. L., Sikkenga, S. L., (CM), Brentnall, W. D., Aurrecoechea, J. M., and Kubarych, K. G., (Solar®), "Development of the Rhenium Containing Superalloys CMSX-4® and CM 186 LC® for Single Crystal Blade and Directionally Solidified Vane Applications in Advanced Turbine Engines," 7th Int. Symp.,[2] Sept. 1992, pp. 297–306.

25 Kubarych, K. G., Aurrecoechea, J. M., (Solar®), "Post Field Test Evaluation of an Advanced Industrial Gas Turbine First Stage Turbine Blade," *TMS/ASM Materials Wk '93 Proc.,* Pittsburgh, PA, 17–21 Oct 1993.

26 Pratt, D. C., and Wilkinson, D. H., (AETC), *6th Wld. Conf. on Inv. Casting,* Oct. 1984.

27 Isobe, S., et al. (Daido), "The Effects of Impurities on Defects in Single Crystals of Nasair 100," *Proc. Int. Gas Turbine Conf.,* Tokyo, Oct. 1983.

28 Harris, K., CM Report—"Status CMSX-4 Alloy," 31 Oct. 1989.

29 Harris, K., CM Report—"High Temperature Ageing Heat Treatment CMSX-4 Alloy," 14 Dec. 1989.

30 Giamei, A. F., and Anton, D. L., (UTRC), "Rhenium Additions to a Ni-Base Superalloy: Effects on Microstructure," *Met. Trans. A.* 16A, pp. 1997–2005, Nov. 1985.

31 Blavette, D., (Faculté des Sciences de Rouen), Caron, P., Khan, T., (Onera), *Scripta Met.,* Vol. 20, No. 10, Oct. 1986.

32 Blavette, D., (Faculté des Sciences de Rouen), Caron, P., Khan, T., (Onera), "An Atom-Probe Study of Some Fine Scale Microstructural Features in Ni-Base Single Crystal Superalloys," 6th Int. Symp.,[2] Sept. 1988, pp. 305–314.

33 Meyer-Olbersleben, F., Rézai-Aria, F., (Swiss Fed. Inst. of Technology), Goldschmidt, D., (MTU), "Investigation of the Thermal Fatigue Behaviour of Single Crystal Nickel-Based Superalloys SRR 99 and CMSX-4," *7th Int. Symp.,*[2] Sept. 1992, pp. 785–794.

34 U.S. Patent No. 4,935,072 (Garrett).

35 Pessah, M., Caron, P., and Khan, T., (Onera), "Effect of μ Phase on the Mechanical Properties of a Nickel-Base Single Crystal Superalloy," 7th Int. Symp.,[2] Sept. 1992, pp. 567–576.

36 Harris, K., Erickson, G. L., and Schwer, R. E., (CM), "Directionally Solidified and Single-Crystal Superalloys," *ASM International Metals Handbook, Vol. 1; Properties & Selection,* pp. 995–1006. 1989.

[2] Superalloys, Seven Spring, PA, *TMS Proc.*

Downloaded 02 Jun 2010 to 171.66.16.104. Redistribution subject to ASME license or copyright; see http://www.asme.org/terms/Terms_Use.cfm

Experimental Leakage and Rotordynamic Results for Helically Grooved Annular Gas Seals

D. W. Childs
Department of Mechanical Engineering,
Texas A&M University,
College Station, TX 77843

A. J. Gansle
Sanden International (U.S.A.), Inc.,
Wylie, TX 75098

Rotordynamic-coefficient and leakage test results are presented for three grooved seals with helix angles of 0, 15, and 30 deg against rotation. The seals are 50.8 mm long and 152.4 mm in diameter. Tests were done for two supply pressures (up to 17 bars), three speeds (5000, 12,000, and 16,000 rpm), four pressure ratios, and three inlet fluid prerotation conditions. The results showed that increasing the helix angle yields a progressive reduction in the cross-coupled stiffness coefficient k and a progressive increase in leakage. The helically grooved seals consistently yield negative cross-coupled stiffness coefficients for nonprerotated inlet flow; hence, k in these seals would oppose forward whirl of a rotor. Helically grooved seals become less effective at reducing k with increasing preswirl; hence, for optimum effectiveness they should be used with a swirl brake. Comparison between helically grooved and honeycomb-stator seals showed that helically grooved stators had reduced (negative) whirl-frequency ratios for nonprerotated flows but were no better than honeycomb-stator seals for elevated fluid prerotation. The 15 and 30 deg helix grooves leaked about 1.6 and 2.2 times, respectively, as much as the honeycomb-stator seals.

Introduction

For small motion about a centered position the reaction-force model of an annular gas seal is

$$-\begin{Bmatrix} F_X \\ F_Y \end{Bmatrix} = \begin{bmatrix} K & k \\ -k & k \end{bmatrix} \begin{Bmatrix} X \\ Y \end{Bmatrix} + \begin{bmatrix} C & c \\ -c & C \end{bmatrix} \begin{Bmatrix} \dot{X} \\ \dot{Y} \end{Bmatrix}, \quad (1)$$

where F_X and F_Y are reaction-force components acting on the rotor, X and Y define the motion of the rotor relative to the stator, and the rotordynamic coefficients K, k, C, and c are the direct stiffness, cross-coupled stiffness, direct damping, and cross-coupled damping, respectively. The whirl frequency ratio

$$f_w = \frac{k}{C\omega} \quad (2)$$

is a measure of rotordynamic stability. For a synchronously precessing rotor of orbit amplitude e, it is the ratio of the destabilizing force ke and the stabilizing force $C\omega e$.

The influence of gas annular seals on the rotordynamic characteristics of compressors and turbines is well known. Various approaches have been taken to reduce the cross-coupled-stiffness coefficients of conventional labyrinths (swirl brakes and shunt injection), and replacement of conventional labyrinths with seals using smooth rotors and honeycomb stators has proven to be effective in eliminating some rotordynamic problems (Zeidan et al., 1993). Tests show that longer honeycomb seals have low cross-coupled stiffness and high damping, yielding low values for f_w (Childs et al., 1989, 1990). Vance (1993) has recently proposed a new "damper" seal design for labyrinths, which appears to cause a major increase in direct damping plus a reduction in cross-coupled stiffness coefficients.

Contributed by the International Gas Turbine Institute and presented at the 40th International Gas Turbine and Aeroengine Congress and Exhibition, Houston, Texas, June 5–8, 1995. Manuscript received by the International Gas Turbine Institute February 13, 1995. Paper No. 95-GT-179. Associate Technical Editor: C. J. Russo.

Figure 1 illustrates a smooth-rotor, helically grooved stator annular seal, which provides an additional option for improved rotordynamic performance. The helix angle α is set to oppose fluid rotation and yield a reduction in the average circumferential fluid velocity. The angle α can vary from zero (circumferential grooving) to 90 deg (axial grooving). For *liquid* seals, Iwatsubo et al. (1990) have shown that a helically grooved stator can yield *negative* cross-coupled stiffness coefficients. Hence, for their tests, the cross-coupled stiffness coefficient actually opposes forward whirl of the rotor.

The present test program was initiated to see whether comparably favorable results could be obtained for a gas seal. Under ideal circumstances, the design of the seals would be guided by an analysis tool, and measured values would be compared to predictions. Unfortunately the authors are not aware of an appropriate code for helically grooved seals in the turbulent regime. Walowit (1992) has developed a fine-groove-based analysis for laminar spiral-grooved seals in a program sponsored by NASA Lewis; however, it is not appropriate for the highly turbulent flow experienced in the present study.

Test Apparatus and Variables. The experimental test facility used for this study was originally developed as a joint NASA-USAF funded research program. A complete description of the test facility is provided by Childs et al. (1986) with modifications provided by Pelletti and Childs (1991).

The test apparatus uses air as the working fluid. Rotordynamic coefficients, axial pressure distribution, and leakage rates of various types of annular gas seal have been measured in this facility. Figure 2 illustrates a cross section of the test rig around the test seal position. Seal flow enters from the right and proceeds through preswirl vanes before entering the test seal section. The stator of the test seal is mounted in a stator holder, which is, in turn, supported in three piezoelectric load cells. Flow exits the test seal and can either proceed axially through the back-pressure seal or the pressure-control port, which is provided between the test-seal exit and the back-pressure seal. Air can either be removed from or injected into this port to control the back pressure. Hence, the pressure ratio across the

Copyright © 1996 by ASME

Downloaded 02 Jun 2010 to 171.66.16.104. Redistribution subject to ASME license or copyright; see http://www.asme.org/terms/Terms_Use.cfm

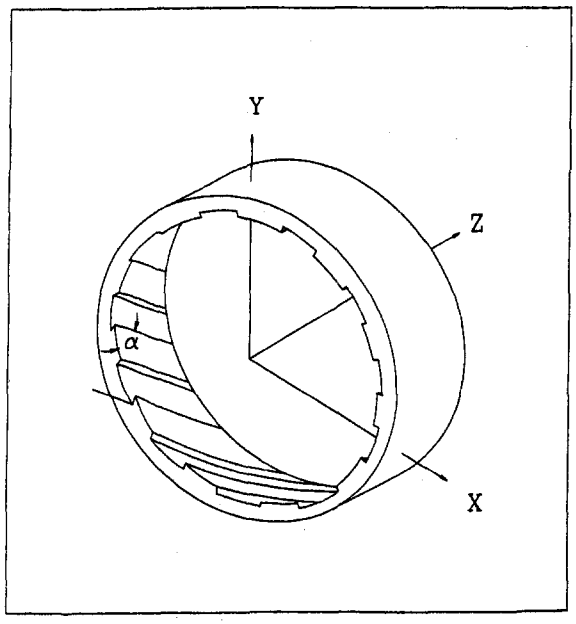

Fig. 1 Helically grooved stator

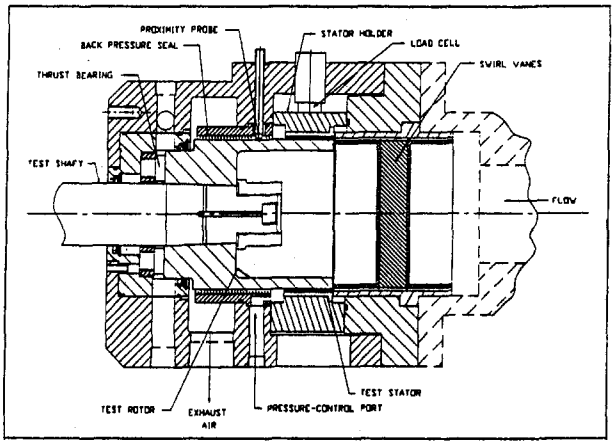

Fig. 2 Cross section of test rig

seal can be controlled independently from supply pressure. Table 1 provide the operational test point data. A scanivalve system is used to measure upstream and downstream pressures plus axial pressure gradients throughout the seal. Upstream and downstream temperatures are also measured.

The test shaft shown at the left of Fig. 2 is suspended in a pendulum fashion from an upper support shaft, which is not shown. The test shaft can be moved statically in horizontal and vertical directions to center the test-seal rotor in the stator. A hydraulic shaker is used to excite the seal in the horizontal

Table 1 Operating-points data

Rotor Speed (rpm) ω	Inlet Pressure (bar) P_r	Pressure Ratio (-) P_{ra}	Inlet Preswirl in the Direction of Rotor Rotation
1 - 5000	1 - 7.90	1 - 0.67	1 - None
2 - 12000	2 - 13.1	2 - 0.56	2-Intermediate
3 - 16000		3 - 0.50	3 - High
		4 - 0.45	

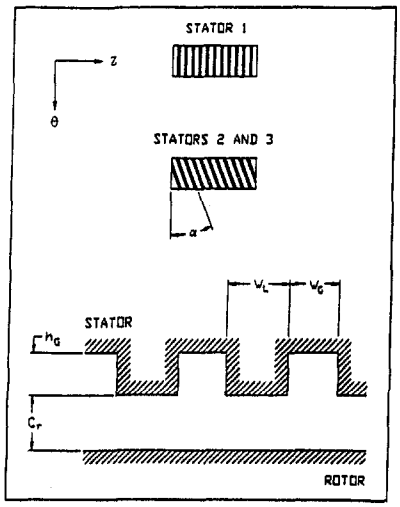

Fig. 3 Test seal dimensions

direction for rotordynamic-coefficient identification. During excitation, relative rotor motion is measured in the X and Y directions. (The Y motion is negligible due to external constraints.) Reaction forces and the stator acceleration are also measured. These measurements are used in the frequency domain to identify the rotordynamic coefficients of Eq. (1) (Pelletti and Childs, 1991).

Figure 3 and Table 2 provide the seal nominal dimensions. Three helix angles were tested with $\alpha = 0$, 15, and 30 deg. Tests were conducted at the two clearances of 0.229 mm (9 mil) and 0.305 mm (12 mil). Additional test parameters are provided in Table 1. The inlet fluid prerotation in the direction of the rotor rotation $U_0(0)$ is nondimensionalized to form the inlet-circumferential-velocity ratio $u_0(0) = U_0(0)/R\omega$, where $R\omega$ is the rotor surface velocity. Seal pressure ratio $P_{r\alpha}$ is defined as the absolute back pressure divided by the absolute inlet pressure.

Experimental Results. Experimental results are presented for the rotordynamic and leakage characteristics of groove-on-stator helically grooved annular gas seals in Figs. 4–11. All data are presented for an inlet pressure of 13.1 bar. Results are not presented for cross-coupled damping c, because the values

Nomenclature

C = direct damping, FT/L
c = cross-coupled damping, FT/L
C_r = seal radial clearance, L
e = whirl amplitude, L
f_w = whirl-frequency ratio defined in Eq. (2)
F_X, F_Y = components of seal reaction force, F
h_g = groove depth, L
K = direct stiffness, F/L
k = cross-coupled stiffness, F/L
L = seal length, L
P_b = back (sump) pressure, F/L^2
P_r = inlet (reservoir) pressure, F/L^2
P_{ra} = absolute pressure ratio, = P_b/P_r
R = radius of seal, L
$u_0(0) = U_0(0)/R\omega$ = inlet circumferential velocity ratio
W_L = land width, L
W_g = groove width, L
Z = axial coordinate, L
μ = fluid viscosity, FT/L^2
μ_0 = flow coefficient defined in Eq. (3)
ω = rotor angular velocity, T^{-1}

Downloaded 02 Jun 2010 to 171.66.16.104. Redistribution subject to ASME license or copyright; see http://www.asme.org/terms/Terms_Use.cfm

Table 2 Seal dimensions

Stator Number	α (deg.)	N_G	W_L (mm)
1	0°	10	2.45
2	15°	25	2.56
3	30°	50	2.39

C_r = .305 mm, R = 76.2 mm, L = 50.8 mm
W_G = 2.38 mm, h_G = .381 mm, N_G= number of grooves

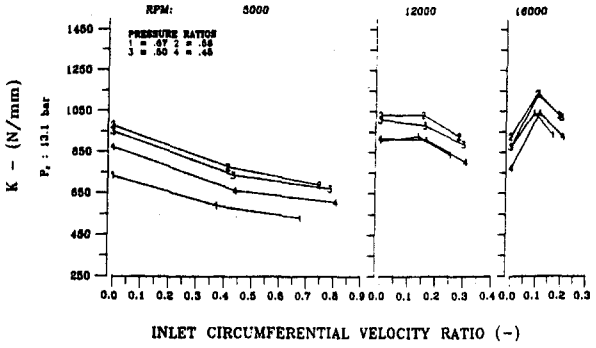

Fig. 4 Direct stiffness, K, as a function of inlet circumferential velocity ratio for α = 15 deg and C_r = 0.305 mm

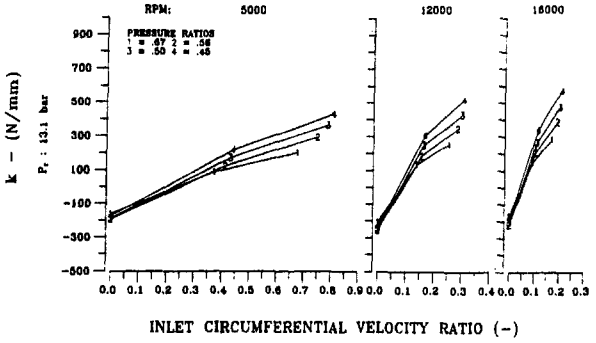

Fig. 5 Cross-coupled stiffness, k, as a function of inlet circumferential velocity ratio for α = 15 and C_r = 0.305 mm

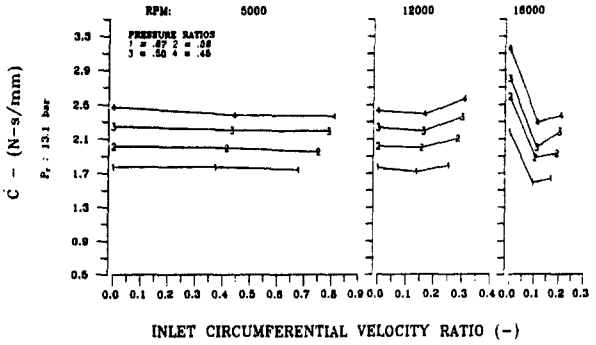

Fig. 6 Direct damping, C, as a function of inlet circumferential velocity ratio for α = 15 and C_r = 0.305 mm

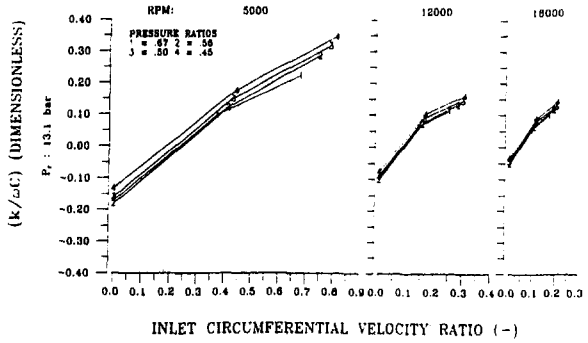

Fig. 7 Whirl frequency ratio as a function of inlet circumferential velocity ratio for α = 15 and C_r = 0.305 mm

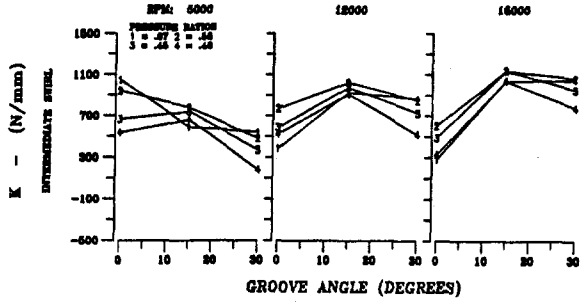

Fig. 8 Direct stiffness, K, as a function of groove angle for C_r = 0.305 mm and P_r = 13.1 bar

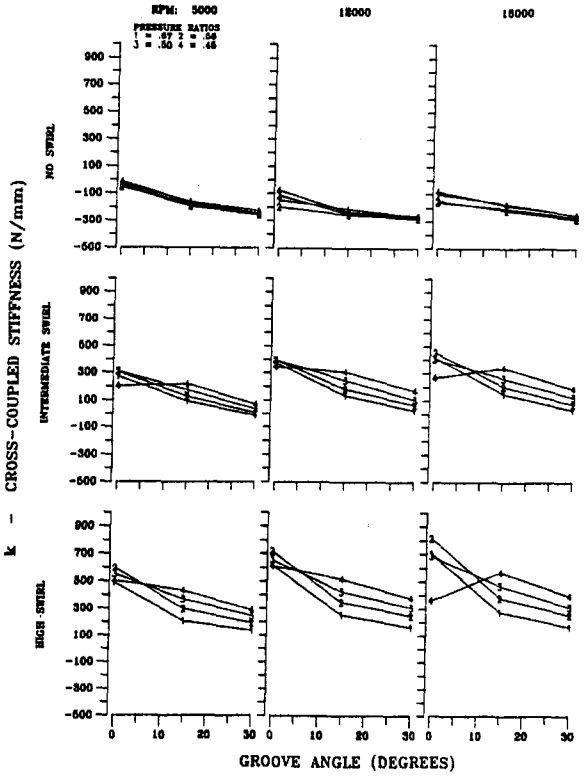

Fig. 9 Cross-coupled stiffness, k, as a function of groove angle for C_r = 0.305 mm and P_r = 13.1 bar

Downloaded 02 Jun 2010 to 171.66.16.104. Redistribution subject to ASME license or copyright; see http://www.asme.org/terms/Terms_Use.cfm

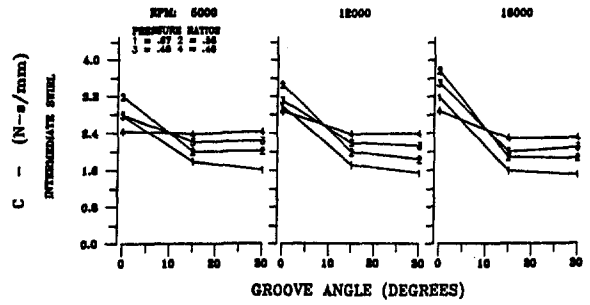

Fig. 10 Direct damping, C, as a function of groove angle for C_r = 0.305 mm and P_r = 13.1 bar

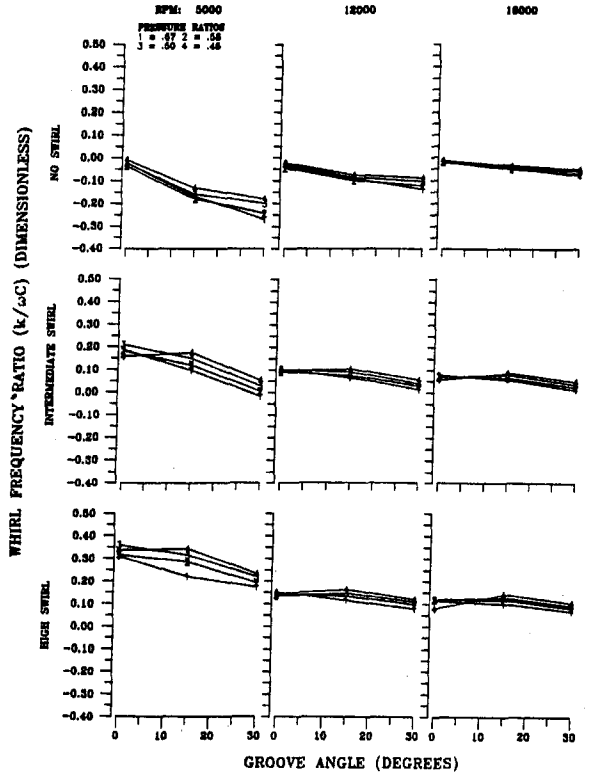

Fig. 11 Whirl frequency ratio as a function of groove angle for C_r = 0.305 mm and P_r = 13.1 bar

measured for this coefficient are generally below the resolution of the system. A complete discussion of all test parameters is provided by Gansle (1993).

Measurement Uncertainty. The uncertainty analysis in the measurement of the dynamic coefficients were determined using the method described by Holman (1989). The maximum calculated uncertainty values for K, k, and C were found to be 100. N/mm, 56.1 N/mm, and 0.13 N-s/mm, respectively.

Inlet Circumferential Velocity and Pressure Ratios. Figures 4–7 show the effect of $u_0(0)$ on the rotordynamic coefficients K, k, C, and whirl frequency ratio f_w. The data for inlet circumferential velocity ratio (preswirl) are presented for an inlet pressure of 13.1 bar, clearance of 0.305 mm, and groove angle of 15 deg. The direct stiffness K generally decreases with an increase in preswirl. K increases in moving from P_{ra} = 0.67 to P_{ra} = 0.56 and then decreases for further decreases in the pressure ratio. As expected, the cross-coupled stiffness k increases with an increase in preswirl. Note particularly that k is negative at zero inlet swirl in accordance with Iwatsubo et al. (1990) water-seal experience. For higher values of $u_0(0)$, k increases with decreasing P_{ra} (increasing ΔP). The direct damping C does not vary in a consistent manner with increasing $u_0(0)$; however, it increases with decreasing P_{ra} (increasing ΔP). The whirl-frequency ratio increases with increasing preswirl and increases slightly with decreasing P_{ra}. Very similar results were obtained for a supply pressure of 7.9 bars.

Groove Angle. Figures 8–11 show the effect of groove angle on the rotordynamic coefficients K, k, C, and whirl frequency ratio f_w. The groove angle data are presented for an inlet pressure of 13.1 bar and clearance of .305 mm. The direct stiffness K is comparatively insensitive to changes in the groove angle. The cross-coupled stiffness k decreases with an increase in groove angle, indicating improved stability as the groove angle increases. Based on the results of Iwatsubo et al. (1990), an optimum groove angle was expected but not obtained for this range of helix angles; i.e., k was expected first to decrease and then to increase for increasing groove angles. The direct damping C generally decreases with an increase in groove angle. At low speeds, the whirl frequency ratio f_w decreases with an increase in groove angle and remains unchanged at higher speeds.

The results of Fig. 11 show that helical grooving is most effective in reducing f_w for no preswirl and reduced speed. In practical terms this implies that the seals' rotordynamic performance could be significantly improved if used in conjunction with a swirl brake.

Figure 12 compares the whirl-frequency ratio for a smooth seal, a honeycomb seal, and 15 and 30 deg helix seals. In all cases, the helically grooved seal has much better performance with nonprerotated flow. Very similar results were obtained with a supply pressure of 7.9 bars.

Leakage Comparisons. Leakage through the test seal is measured using a turbine flowmeter. Temperatures and pressures are used to convert the measured value to the flow coefficient defined by

$$\mu_0 = \frac{\dot{M}/2\pi R}{C_r\sqrt{\dfrac{P_r^2 - P_b^2}{ZR_gT}}} \tag{3}$$

where $\dot{M}$ is the mass flow rate, R_g is the gas constant, T is the absolute temperature, and Z is a compressibility-correction factor. Figure 13 shows the flow coefficient as a function of inlet pressure for groove angles of 15 and 30 deg plus results for a honeycomb seal, and a smooth seal. The 15 deg helix leaks substantially less than the 30 deg helix and smooth seals but considerably more than the honeycomb.

Discussion and Conclusions

Test results for the helically grooved seals show enhanced rotordynamic stability through the development of negative

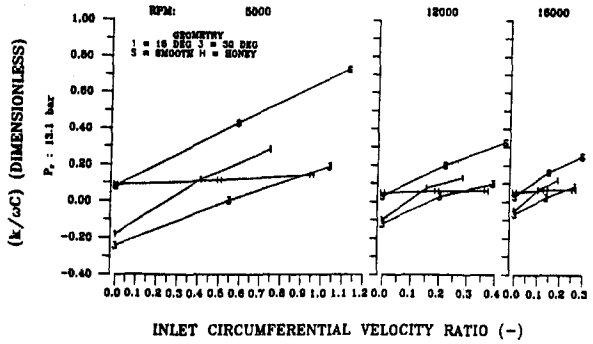

Fig. 12 Whirl frequency ratio as a function of inlet circumferential velocity ratio for α = 15 deg, α = 30 deg, smooth, and honeycomb seals for P_{ra} = 0.56 and C_r = 0.305 mm

Downloaded 02 Jun 2010 to 171.66.16.104. Redistribution subject to ASME license or copyright; see http://www.asme.org/terms/Terms_Use.cfm

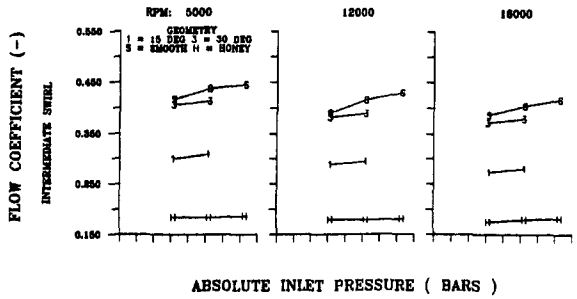

Fig. 13 Flow coefficient as a function of absolute inlet pressure for α = 15 deg, α = 30 deg, smooth, and honeycomb seals for P_{ra} = 0.56 and C_r = 0.305 mm

cross-coupled stiffness coefficients. Values for k continue to decline as the helix angle α increases from 0 to 15 deg and then from 15 to 30 deg. The reduction in k is much better with nonprerotated flow, showing that optimum rotordynamic results would be obtained by the addition of a swirl brake to the helically grooved seals. Also, the reductions in k were moderated by increasing running speed.

For nonprerotated flow the helically grooved seals yielded consistently lower whirl-frequency ratios than honeycomb or smooth seals having comparable dimensions. For prerotated flows the honeycomb-stator seals were superior.

Leakage comparisons between helically grooved seals (α = 15, 30 deg), a smooth seal, and a honeycomb-stator seal showed that the 15 deg helix seal, 30 deg helix angle, and smooth seal leaked approximately 1.66, 2.2, and 2.3 times more than the honeycomb-stator seal.

The results presented show that helically grooved seals have the potential for significantly enhanced rotordynamic performance through the development of reduced or negative cross-coupled stiffness coefficients k. There is clearly an associated leakage penalty when compared to honeycomb-stator seals, which increases with increases in the helix angle α. The seals tested in this study were manufactured without benefit of any analytical or computational developments and, accordingly, are not in any sense "optimized." The results certainly encourage the development of appropriate analysis tools for helically grooved seals including stator sections with both smooth and grooved surfaces.

References

Childs, D. W., Nelson, C. C., Scharrer, J., Elrod, D., and Hale, K., 1986, "Theory Versus Experiment for the Rotordynamic Coefficients of Annular Gas Seals: Part 1—Test Facility and Apparatus," ASME *Journal of Tribology,* Vol. 108, pp. 426–432.

Childs, D., Elrod, D., and Hale, K., 1989, "Annular Honeycomb Seals: Test Results for Leakage and Rotordynamic Coefficients; Comparisons to Labyrinth and Smooth Configurations," ASME *Journal of Tribology,* Vol. 111, pp. 293–301.

Childs, D., and Elrod, D., and Ramsey, C., 1990, "Annular Honeycomb Seals: Additional Test Results for Leakage and Rotordynamic Coefficients," in *IFToMM, Proceedings of the Third International Conference on Rotordynamics,* Lyon, France, pp. 303–312.

Gansle, A. J., 1993, "A Comparison of Theoretical and Experimental Coefficients for Helically Grooved Annular Gas Seals," M.S. Thesis, Mechanical Engineering Department, Texas A&M University.

Holman, J. P., 1989, *Experimental Methods for Engineers,* McGraw-Hill, New York, pp. 41–42.

Iwatsubo, T., Sheng, B., and Ono, M., 1990, "Experiment of Static and Dynamic Characteristics of Spiral Grooved Seals," *Rotordynamic Instability Problems in High-Performance Turbomachinery,* NASA CP No. 3122, proceedings of a workshop held at Texas A&M University, pp. 223–234.

Pelletti, J. M., and Childs, D. W., 1991, "A Comparison of Experimental Results and Theoretical Predictions for the Rotordynamic Coefficients of Short (L/D = 1/6) Labyrinth Seals," ASME *Design Technical Conference,* Sept., ASME DE-Vol. 35, pp. 69–76.

Vance, J., 1993, "A New Damper Seal for Turbomachinery," *Vibration of Rotating Systems,* ASME DE-Vol. 60, pp. 139–148.

Walowit, J. A., 1992, "Users Manual for Computer Code SPIRALG Gas Lubricated Spiral Grooved Cylindrical and Face Seals," NAS3-25644.

Zeidan, F. Y., Perez, R. X., and Stephenson, E. M., 1993, "The Use of Honeycomb Seals in Stabilizing Two Centrifugal Compressors," presented at the 22nd Turbomachinery Symposium.

Downloaded 02 Jun 2010 to 171.66.16.104. Redistribution subject to ASME license or copyright; see http://www.asme.org/terms/Terms_Use.cfm

H. R. Millwater

Y.-T. Wu

J. W. Cardinal

G. G. Chell

Materials and Structures Division,
Southwest Research Institute,
San Antonio, TX 78222

Application of Advanced Probabilistic Fracture Mechanics to Life Evaluation of Turbine Rotor Blade Attachments

This paper describes the application of an advanced probabilistic fracture mechanics computational algorithm with inspection simulation to the probabilistic life assessment of a turbine blade attachment, sometimes referred to as a steeple or fir tree. The life of the steeple is limited by high cycle fatigue. The methodology utilized combines structural finite element analysis, stochastic fatigue crack growth, and crack inspection and repair. The resulting information provides the engineer with an assessment of the probability of failure of the structure as a function of operating time and the effect of the inspection procedure. This information can form the basis of inspection planning and retirement-for-cause decisions.

Introduction

Structural failure is often caused by high cycle fatigue crack growth. An important characteristic of a structural design and operation is the cycles to failure, i.e., cycles until a critical crack size is reached, often called life. There are many parts of this process that are uncertain, for example, crack initiation time and location, the initial crack size and aspect ratio, the fatigue crack growth material parameters, structural geometry and material properties, and the loading. A probabilistic life evaluation procedure can provide the engineer with the probability of structural failure as a function of operating time given the uncertainties in the input data.

The inspection and repair procedure is an important aspect of structural maintenance. Inspecting and replacing cracked structures can significantly increase the structural life. The inspection process itself has uncertainties in that one cannot guarantee that a crack of a certain size can be detected or that a crack less than a certain size will be undetected. There is always the possibility that a crack can be detected or missed. Thus, one defines a probability of detecting cracks of different sizes. This information is contained in the Probability of Detection (POD) curve.

The inspection and repair process involves costs, thus, it would be useful to know a priori the potential effectiveness of a particular inspection method and perhaps to plan the inspection schedule to optimize inspection effectiveness while minimizing costs. The effect of the inspection procedure on the crack size distribution and the remaining life is shown below.

The capability to compute the probability of failure efficiently as a function of operating time, i.e., cycles, was presented in a recent publication (Millwater et al., 1994). The approach used was to combine an advanced probabilistic algorithm described in the paper by Wu et al. (1990), structural finite element modeling, and a fatigue crack growth algorithm. The stress intensity factor solution as a function of crack length was determined using the weight function approach with the stress along the crack path computed using a finite element model of the uncracked body.

The method is very efficient because: (*i*) an advanced probabilistic algorithm is used, which minimizes the number of fatigue crack growth solutions required. (*ii*) The crack in the structure is not explicitly modeled. The weight function method computes the stress intensity factor for any crack size from the stress along the crack front of the uncracked structural model. (*iii*) An adaptive step size solution algorithm is used to minimize the integration steps in the solution of the crack growth law.

This paper adds the inspection and repair procedure to the probabilistic fracture mechanics algorithm and demonstrates its application on a life assessment of a steeple. The developed methodology is general and can be applied straightforwardly to other structural configurations with different geometry, loading, fatigue properties, and POD.

Inspection and Repair

The inspection and repair procedure is simulated by replacing any detected cracks with a crack from the repair crack size distribution. The mathematical details can be found in the paper by Berens and Hovey (1984). Only a summary is given here.

The inspection and repair procedure modifies the pre-inspection crack size probability density function (pdf) by detecting and repairing a percentage of cracks of different sizes, thus defining a postinspection crack size pdf. The postinspection crack size pdf is defined as

$$f^+(a) = G_0 f_R(a) + (1 - \mathrm{POD}(a)) f^*(a) \qquad (1)$$

where $f^+(a)$ is the postinspection crack size pdf, $f^*(a)$ is the preinspection crack size pdf, $f_R(a)$ is the repair crack size pdf, $\mathrm{POD}(a)$ is the POD curve, and G_0 is the percentage of locations for which a positive crack indication will be given. G_0 is computed as

$$G_0 = \int_0^\infty \mathrm{POD}(a) f^*(a) da \qquad (2)$$

For example, $f^*(a)$ can be an initial crack size distribution or a distribution after a specified operating time.

Application Example

This example concerns the probabilistic life assessment of a blade attachment steeple fir tree of a low-pressure steam turbine subject to fatigue cracking. Only a summary of the structural

Contributed by the International Gas Turbine Institute and presented at the 40th International Gas Turbine and Aeroengine Congress and Exhibition, Houston, Texas, June 5–8, 1995. Manuscript received by the International Gas Turbine Institute February 27, 1995. Paper No. 95-GT-214. Associate Technical Editor: C. J. Russo.

Copyright © 1996 by ASME

Downloaded 02 Jun 2010 to 171.66.16.104. Redistribution subject to ASME license or copyright; see http://www.asme.org/terms/Terms_Use.cfm

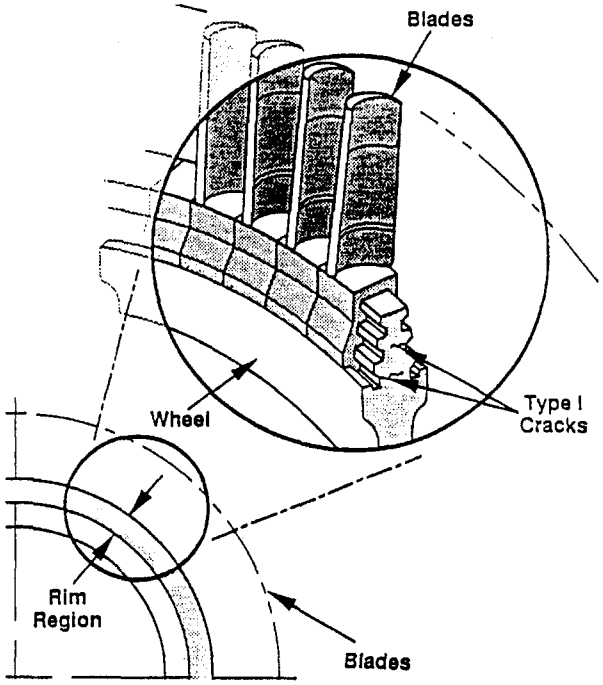

Fig. 1 Steeple configuration

and fatigue model is presented here. More detail can be found in the paper by Millwater et al. (1994). Although demonstrated on a steam turbine, the technology is general and can be applied in a straightforward manner to gas turbine structures.

A schematic of the steeple configuration is shown in Fig. 1. The life of the steeple may be limited by either stress corrosion cracking (SCC) or corrosion fatigue crack growth. This analysis addresses only the corrosion fatigue crack growth, but could be extended in a straightforward manner to also consider stress corrosion cracking. Similar structures were analyzed previously using deterministic solution methods (Lyle et al., 1991; Cardinal and Lyle, 1991).

Cracks initiate below the hook attachments of the steeple due to high stress concentration. The cracks propagate due to oscillatory loading on the steeple by the blade.

Structural Model and Loads. A finite element model of the steeple is shown in Fig. 2. The model is axisymmetric with 876 elements and 995 nodes. A crack is assumed to exist under the second hook, i.e., the initiation time is zero. The crack path chosen to be analyzed is shown in Fig. 2 and is typical of that found in service (Lyle et al., 1991).

This analysis considers only a single crack. However, cracks can initiate and propagate under all hooks. A more complete analysis would consider the probability of failure due to all cracks. This analysis would require system reliability probabilistic methods, such as in the paper by Torng et al. (1992), new weight functions for multiple cracks, and a more comprehensive finite element model of the steeple and disk to account for load redistribution.

A critical crack size of 0.4 in. is chosen based on experience. When cracks reach this length, the performance of the structure is impaired due to excessive deflection and/or vibration of the blade. A crack size of 0.4 in. is reached before the fracture toughness is exceeded; thus, the failure is due to a performance criterion, excessive deflection or vibration, rather than a fracture instability criterion. Fracture instability can also be handled by the probabilistic fracture mechanics methodology presented here as shown by Millwater et al. (1994).

The steeple is analyzed at a steady-state operating speed of 3600 rpm. The static loading consists of (1) the radial load on

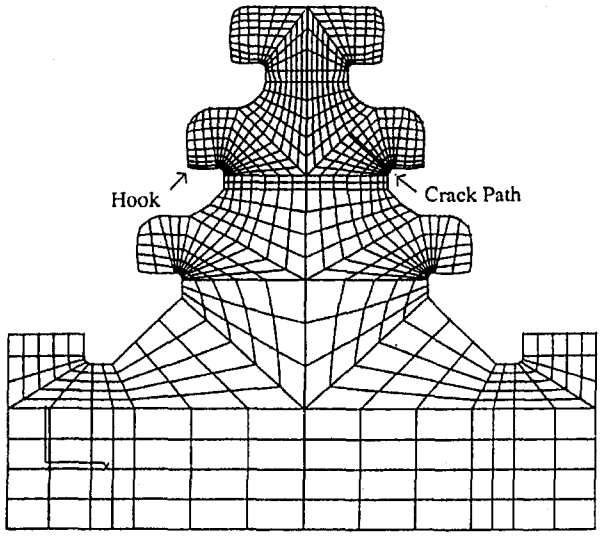

Fig. 2 Steeple finite element model

the steeple hooks due to the blade, (2) the centrifugal load on the steeple due to the rotating disk. Bending loads from the blade are not considered. The centrifugal load was applied by enforcing displacement conditions on the bottom of the steeple. The displacement values were determined from a previous analysis of a three-dimensional structure of the disk. The total radial load due to the blade is determined from

$$F = \frac{W}{g}\omega^2 r \tag{3}$$

where W is the weight of the blade, g is the gravitational constant, ω is the angular velocity in rad/s, and r is the radius to the center of mass of the blade. The load is distributed as 20, 30, 50 percent to the top, middle, and bottom hooks, respectively. The load distribution was determined from previously analyzed two-dimensional models of the mated steeple and blade (Lyle et al., 1991).

The variation of the uncracked stress field normal to the crack path is computed using a finite element analysis as a function of distance along the crack. The stress variation is fit with a sixth order polynomial, which is then used to compute the stress

Table 1 Crack growth parameters and material properties (3.5NiCrMo V)

Material Properties	
Elastic Modulus	30.0E6 psi
Poisson's Ratio	0.3
Fracture Toughness	150 ksi $\sqrt{\text{in}}$
Crack Growth Parameters	
A_1	3.543E9
A_2	3.597E8
n_1	3.713
n_2	2.247
R	0.9

Downloaded 02 Jun 2010 to 171.66.16.104. Redistribution subject to ASME license or copyright; see http://www.asme.org/terms/Terms_Use.cfm

Table 2 Random variable definitions

Random Variable	Mean	Standard Deviation	Distribution
Fluctuating Load (% of static load, lb_f)	5.0	5.0	lognormal
Hook Radius (inches)	0.0625	0.00188	normal
Initial Crack Size (inches)	0.01	0.004	lognormal
Crack Growth Parameter (A_1)	3.543E9	3.543E8	lognormal

intensity factor K_{MAX} for any crack length using the weight function approach. The alternating stress intensity factor, ΔK, is then defined as $\Delta K = K_{MAX}(1 - R)$ where R is the load ratio.

Crack Growth Model. Representative crack growth rate material properties were determined from an experimental program (Lyle et al., 1991). The data were fitted to a three-component fatigue crack growth rate model (Saxena et al., 1979; Saxena and Hudak, 1980). This crack growth model is defined as

$$\frac{1}{da/dN} = \frac{A_1}{\Delta K^{n_1}} + \frac{A_2}{\Delta K^{n_2}} - \frac{A_2}{[(1 - R)K_c]^{n_2}} \quad (4)$$

Note that this model is not asymptotic at low da/dN, i.e., it has no ΔK_{th}. The three-component law more accurately models the low ΔK, Region I, behavior than the Paris equation. It is useful in this problem because much of the crack growth occurs at low ΔK, i.e., Region I of the crack growth curve. The crack growth and material properties used for this analysis are listed in Table 1.

The three-component law can be reduced to the Paris Law in Region II as follows:

$$\frac{da}{dN} = \left(\frac{1}{A_1}\right)\Delta K^{n_1} \quad (5)$$

Random Variables. The random variables and their statistics were chosen to be representative of in-service conditions. The statistical values, however, were chosen as representative and were not obtained by detailed statistical analysis. The purpose here is to demonstrate methodology and capabilities.

The random variables are listed in Table 2. The fluctuating load is assumed to be caused by blade vibration loads. As such, it is difficult to determine and therefore has a high coefficient of variation (COV) of 100 percent. The fluctuating loads are applied in addition to the static blade loads on the finite element model. The mean of the fluctuating load is defined as 5 percent of the static blade load. The distribution of the fluctuating load to the hooks is in the same proportion as the static load.

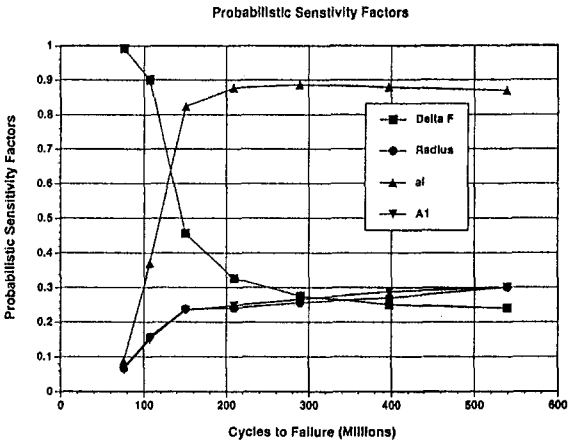

Fig. 4 Probabilistic sensitivity factors

The machined radius under the hook affects the stress concentration factor. An estimated small coefficient of variation of 3 percent is chosen for the radius since this is a machined quantity. The initial crack size COV was chosen based on destructive inspection of steeples (Lyle et al., 1991). A coefficient of variation of 40 percent is consistent with the crack length measurements. The COV of crack growth material constant A_1 was estimated from experience. The mean value was obtained from the paper by Lyle et al. (1991). The choice of distribution type was based on experience.

Results. The cumulative distribution function of the cycles to failure of the steeple was computed using the Advanced Mean Value with iterations (AMV+) and Monte Carlo simulation probabilistic algorithms in conjunction with the fatigue remaining life assessment methodology described in the paper by Millwater et al. (1994). The CDF is shown in Fig. 3. No inspection and repair of the crack distribution was used in this calculation. The results are in good agreement between Monte Carlo

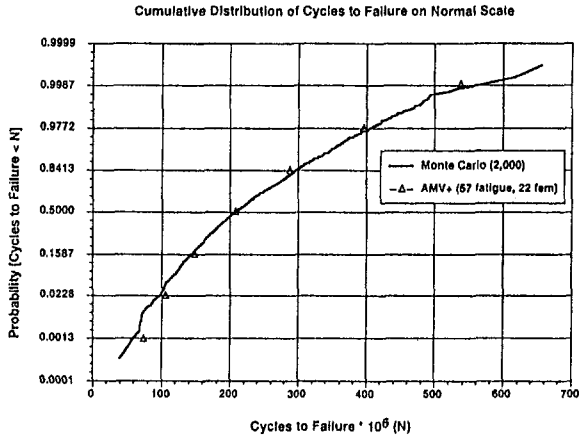

Fig. 3 Cumulative distribution function of cycles to failure on normal scale

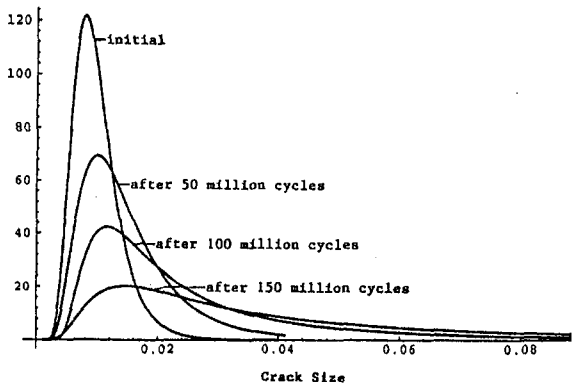

Fig. 5 Crack size pdf's

Downloaded 02 Jun 2010 to 171.66.16.104. Redistribution subject to ASME license or copyright; see http://www.asme.org/terms/Terms_Use.cfm

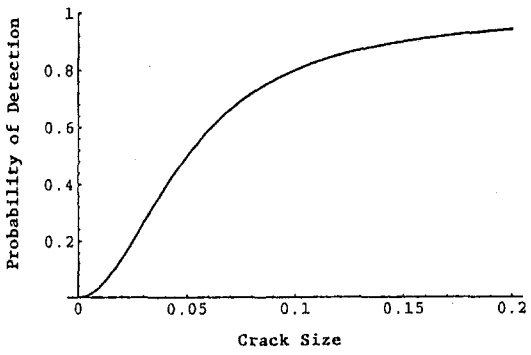

Fig. 6 Probability of detection curve

Table 3 Probability of failure in the next 50 million cycles

Current No. Cycles When/If Inspected	P_f *Without* Inspection @ Current No. Cycles + 50 Million Cycles	P_f *With* Inspection @ Current No. Cycles + 50 Million Cycles
50 million	2.15%	0.73%
100 million	13.59%	4.56%
150 million	34.13%	12.87%

simulation and AMV+. However, AMV+ required only 57 fatigue life analyses, of which 22 required finite element solutions; some finite element solutions are reused. Monte Carlo simulation using 2000 fatigue life analyses, each requiring a finite element analyses, gives comparable results to AMV+. Note, however, that approximately 300,000 Monte Carlo simulations are required to obtain a solution with less than 10 percent error with 95 percent confidence at a low probability of 0.0013.

The AMV+ method also computes probabilistic sensitivity factors (PSF's), which identify which random variables most affect the cumulative distribution of life. The PSF's are shown in Fig. 4. Given the random variable data used here, i.e., Table 2, the probabilistic sensitivity factors indicate that the cycles to failure are only marginally sensitive to the crack growth material constant and hook radius. The analysis indicates that the fluctuating load dominates for short lives, i.e., the left tail of the distribution, and the initial crack size dominates throughout the rest of the distribution.

In addition to computing remaining life, one can compute the crack size pdf's at specified times. The initial crack size pdf and the crack size pdf after 50, 100, and 150 million cycles are shown in Fig. 5.

One can apply an inspection and repair procedure, as described in Eqs. (1, 2) to modify the crack size pdf and therefore to reduce the probability of failure. For example, the POD curve shown in Fig. 6 is applied to the initial crack size pdf and the crack size pdf after 50, 100, and 150 million cycles. We assume that all detected cracks are removed. In practice, the decision to repair the cracks or replace the part would be based on many factors such as probability of failure given a detected crack, cost of failure, cost of replacement, and others.

The pre- and postinspection crack size pdf's are shown in Fig. 7. In general, the inspection removes large cracks. Figure 7 indicates that little is accomplished in inspection of the initial crack. Thus, given a POD curve and an initial crack size distribution, one can use this methodology to determine whether an initial inspection is useful. A larger effect on the crack size pdf is obtained after 150 million cycles because the crack size pdf is larger and hence more cracks are detected and removed.

The effect of the inspection process on the remaining life can be estimated by modifying the crack size pdf through inspection after a specified number of cycles and then continuing the remaining life probabilistic analysis using the postinspection crack size pdf. For this problem, we compared the probability

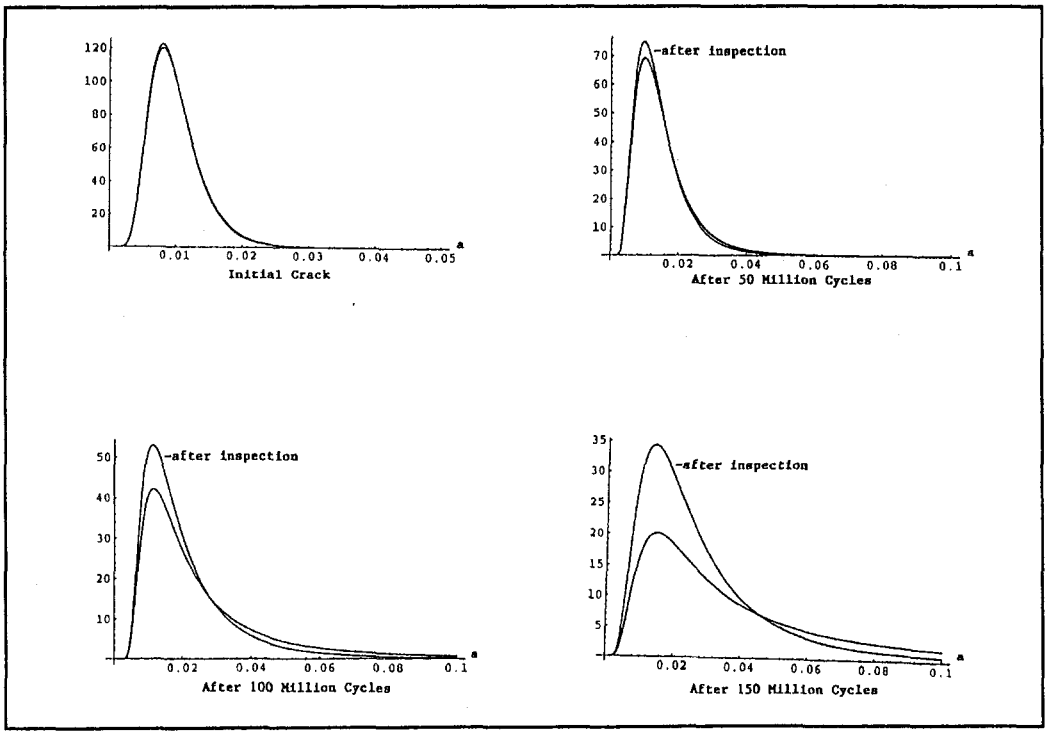

Fig. 7 Crack size pdf's before and after inspection

Downloaded 02 Jun 2010 to 171.66.16.104. Redistribution subject to ASME license or copyright; see http://www.asme.org/terms/Terms_Use.cfm

of failure without inspection to the probability with inspection and repair. The inspection and repair procedure was applied to the crack size pdf after 50, 100, and 150 million cycles. The probability of failure within the next 50 million cycles was then computed. Table 3 shows the results.

Discussion

One can see from Table 3 that the inspection and repair procedure can significantly alter the probability of failure. The probability of failure after inspecting and repairing after 50 million cycles and continuing crack growth for another 50 million cycles is decreased from 2.15 to 0.73 percent. The effectiveness of the inspection and repair procedure depends on several factors such as the critical crack size, rate of crack growth, accuracy of the inspection method, i.e., POD curve, and the sensitivity of the probability of failure to the crack size. If the critical crack size is very small, than an inspection method with a POD curve sensitive enough to detect cracks near critical size is required. The sensitivity of the probability of failure to the crack size will also determine the effectiveness of the inspection procedure. Typically, however, the crack size is an important factor on the probability of failure. The scheduling of the inspection process will depend in part on the rate of crack growth. Rapidly growing cracks will require a more frequent inspection procedure.

Summary and Conclusions

The accurate prediction of life assessment due to fatigue of complex structures is an important capability for fracture control. An approach, presented in detail in the paper by Millwater et al. (1994) and extended here to include inspection and repair, combines advanced probabilistic algorithms, finite element analysis, and fracture mechanics for an efficient, accurate solution method.

The cost of the inspection and repair procedure may be substantial. The engineer must balance the cost of the procedure with the probability of failure and the cost of failure, repair, or replacement. The inspection procedure can be applied repeatedly to reduce the probability of failure continually. At some point, more frequent inspection and repair are required to ensure a constant probability of failure, and thus, it may be more economical to replace the structure. One requirement for this decision process is an accurate evaluation of the probability of failure before and after inspection and repair of realistic structures. Computational methods presented here provide needed information on which to base decisions regarding the type of inspection procedure to use, the frequency and schedule of the inspections, and the replacement of the structure.

Acknowledgments

The authors would like to thank Mr. David Riha for his assistance with the finite element modeling and Ms. Linette McCord for the manuscript preparation.

References

Berens, A. P., and P. W. Hovey, 1984, "Flaw Detection Reliability Criteria," Vol. 1, AFWAL-TR-84-4022, Apr.

Cardinal, J. W., and Lyle, F. F., Jr., 1991, "Remaining Life Assessment Methodology for LP Disc Rim Cracking," *Proceedings of the EPRI Steam Turbine and Generator NDE, Life Assessment and Maintenance Workshop,* Charlotte, NC, July 16–19.

Lyle, F. F., Jr., et al., 1991, "Remaining Life Methodology for Disc Rim Cracking," SwRI Project No. 06-1106, Final Report, Mar.

Millwater, H. R., Wu, Y.-T., and Cardinal, J. W., 1994, "Probabilistic Structural Analysis of Fatigue and Fracture," Paper No. AIAA-94-1507.

Saxena, A., Hudak, S. J., Jr., and Jouris, G. M., 1979, "A Three Component Model for Representing Wide-Range Fatigue Crack Growth Behavior," *Engineering Fracture Mechanics,* Vol. 12.

Saxena, A., and Hudak, S. J., Jr., 1980, "Evaluation of the Three Component Model for Representing Wide Range Fatigue Crack Growth Rate Data," *Journal of Testing and Evaluation,* JTEVA, Aug. 5.

Torng, T., Wu, Y.-T., and Millwater, H. R., 1992, "Structural System Reliability Calculation Using a Probabilistic Fault Tree Analysis Method," Paper No. AIAA-92-2410.

Wu, Y.-T., Millwater, H. R., and Cruse, T. A., 1990, "An Advanced Probabilistic Structural Analysis Method for Implicit Performance Functions," *AIAA Journal,* Vol. 28, No. 9, pp. 1663–1669.

Downloaded 02 Jun 2010 to 171.66.16.104. Redistribution subject to ASME license or copyright; see http://www.asme.org/terms/Terms_Use.cfm

Fatigue Crack Growth Behavior of PWA 1484 Single Crystal Superalloy at Elevated Temperatures

J. Telesman
NASA Lewis Research Center,
Cleveland, OH 44135

L. J. Ghosn
Case Western Reserve University,
Cleveland, OH 44135

A study was done to determine the fatigue crack growth behavior of a PWA 1484 single-crystal nickel-base superalloy in a temperature range of 427°C to 871°C. Two distinctive failure modes were observed, which were a function of both temperature and frequency. At lower temperatures and higher frequencies crack growth occurred on the {111} octahedral slip planes at an oblique angle to the loading direction. Higher temperatures and decrease in frequencies favored a Mode I type failure process. The failure mode transitions were explained by invoking arguments based on environmental damage mechanisms. The fatigue crack growth rate data were analyzed using three different crack driving force parameters. The parameters investigated consisted of the Mode I stress intensity parameter corrected for the inclined crack trajectory, and two different octahedral Mode II parameters, which are based on the calculation of resolved shear stresses on the {111} slip systems. The Mode I ΔK parameter did a fair job in correlating the data but did not collapse it into a single narrow band. The two octahedral crack driving force parameters, ΔK_{RSS} and a newly proposed ΔK_{OCT}, collapsed all the data into a single narrow band. In addition to correlating the fatigue crack growth rates, the two octahedral parameters also predicted the {111} planes on which the crack growth took place.

Introduction

A life prediction methodology based on the damage tolerance approach is predicated on the ability to model the fatigue crack propagation behavior successfully for a given material. The current damage tolerance life prediction methodologies are a product of the experience gained from the structural applications of polycrystalline alloys and are based on the assumption that principal normal stresses and strains govern the fatigue life. These models have been successful in predicting service lives of polycrystalline components for which fatigue cracks grow in the direction perpendicular to the maximum applied principal stress (i.e., Mode I cracks). However, the fatigue crack growth in the single-crystal nickel-base superalloy components has been shown, under certain conditions, to occur on the {111} octahedral slip plane facets at some oblique angle to the principal stress direction. The failure on the {111} octahedral slip planes is governed by the resolved shear stresses and not the maximum principal stresses.

This phenomenon was elegantly demonstrated by Chen (1985). He tested a single-crystal superalloy specimen with the (111) plane being parallel to the starter notch but perpendicular to the loading direction. The maximum principal normal stress was much higher on this (111) plane than on any of the other slip planes; however, the *resolved shear stress on it was negligible.* The (111) plane with high principal normal stresses *remained uncracked.* The fatigue cracks grew only on the slip planes with the highest resolved shear stresses.

The octahedral failure mode is not well understood and is also not accounted for in the current state-of-the-art life prediction models. In order to include the octahedral failure mode in the life prediction models, an analytical crack driving force parameter that governs this type of failure mode has to be identified and its accuracy validated. One such promising fracture mechanics-based parameter is ΔK_{RSS}, which was initially proposed by Chen and Liu (1988). This parameter determines the crack tip resolved shear stress intensity on all 12 $\{111\}/\langle 110\rangle$ slip systems present in the nickel-base alloys. Initial evaluation of the parameter by Telesman and Ghosn (1989) showed it to be a powerful analytical tool. This parameter not only correlated the crack growth data of a PWA 1480 single crystal alloy, but also predicted on the microscopic level the active octahedral failure planes, the crack trajectory, and the influence of the state of stress.

While the ΔK_{RSS} parameter has shown considerable promise in modeling octahedral failure mode, it does have some important limitations. In a study done recently on the effect of orientation on the fatigue crack growth behavior of PWA 1480 single crystal alloy, K_{RSS} was *not* able to collapse the fatigue crack growth data for some of the single crystal orientations tested (Telesman and Ghosn, 1993). Thus, a development of a more sophisticated octahedral crack driving force parameter, which will serve as a basis for the development of life prediction methodology for single crystal components, is still required.

Another issue that needs further attention is the transition from an octahedral failure mode to a Mode I failure mode. Increase in the test temperature (Cunningham et al., 1994) and a decrease in the test frequency (Leverant and Gell, 1975) have been shown to change the failure mode in single crystal superalloys from octahedral to a noncrystallographic Mode I type failure. The micromechanisms responsible for the failure mode change are not fully understood and the methodology for predicting the limiting conditions under which the transition occurs has not been developed.

These issues were examined in the current study. The investigation consisted of fatigue crack growth testing and analysis of (001) oriented PWA 1484 single crystal alloy at temperatures

Contributed by the International Gas Turbine Institute and presented at the 40th International Gas Turbine and Aeroengine Congress and Exhibition, Houston, Texas, June 5–8, 1995. Manuscript received by the International Gas Turbine Institute April 5, 1995. Paper No. 95-GT-452. Associate Technical Editor: C. J. Russo.

Copyright © 1996 by ASME

Downloaded 02 Jun 2010 to 171.66.16.104. Redistribution subject to ASME license or copyright; see http://www.asme.org/terms/Terms_Use.cfm

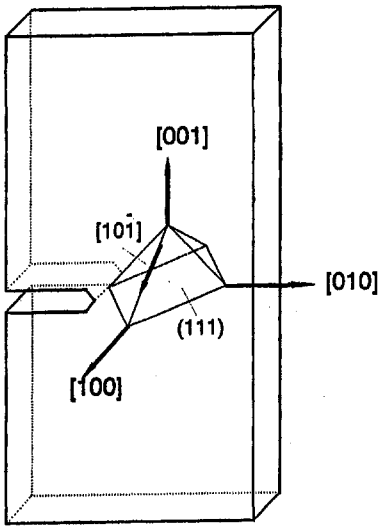

Fig. 1 Crystal orientation with respect to SEN specimen geometry

ranging from 427°C to 871°C. The testing was conducted in a specially designed high-temperature in situ loading stage mounted inside a scanning electron microscope, which allowed for real time detailed high-magnification observations of the micromechanical failure processes and the measurement of the crack opening displacement field.

Experimental Procedure

The material tested was a single-crystal nickel-base superalloy, PWA 1484, HIP'd to remove casting porosity. The details regarding the composition and processing of this alloy as well its predecessor PWA 1480 alloy are found in Cunningham et al. (1994). Seven single-edge-notch (SEN) geometry specimens were tested in the in situ loading stage mounted in the SEM. The crystallographic orientation of the specimens was obtained through x-ray diffraction. The primary loading direction was within 2 deg of the (001) direction with the secondary orientation being of the (010) type (Fig. 1).

The test matrix showing the test temperatures and R ratios is shown in Table 1. Tests were performed in a load control mode at a frequency of 15 Hz, with the exception of specimen 1484-2 for which both the test temperature and frequency were varied. The specimens were precracked at the test temperature in the SEM.

The tests were interrupted at intervals ranging from 5000 cycles in the low crack growth regions to 100 cycles in the high crack growth regions to make crack length measurements using an electronic micrometer built into the SEM. High-magnification photomicrographs were taken at various loads during the test interruptions to record the fatigue damage mechanisms and measure crack opening displacements. Due to the setup limitations, crack growth was monitored only on one side of the specimen. The tests were conducted until an a/W of approximately 0.5 was reached. After the test was finished, the specimen was removed and the crack lengths were measured on both sides using an optical microscope. All the specimens were placed back in the loading rig and loaded to failure at room temperature. The failed specimens were examined in the SEM.

Table 1 Test matrix

SPECIMEN	TEMP (°C)	R RATIO	FREQUENCY (Hz)
1484-5	427	0.5	15
1484-8	593	0.1	15
1484-4	593	0.5	15
1484-1	593	0.7	15
1484-6	760	0.5	15
1484-3	871	0.5	15
1484-2	760	0.5	1-15
	815	0.5	3-15
	871	0.5	1-15

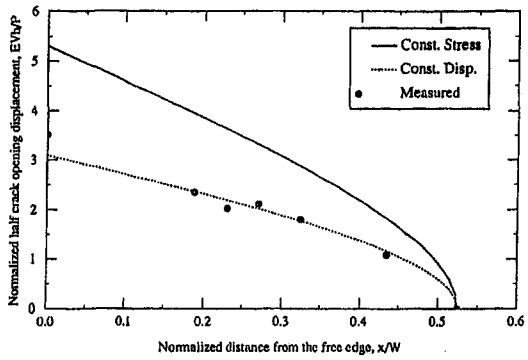

Fig. 2 Measured COD's versus predictions for constant stress and constant displacement conditions

The vacuum inside the SEM was monitored during the tests. The vacuum level was approximately 1×10^{-6} Torr for the 427°C and 593°C tests, and 1×10^{-5} Torr for the 760°C and 871°C. The decrease in vacuum level was due to an increase in outgassing as the test temperature was increased.

Stress Intensity Factor Solutions. The stress intensity solutions for a pin loaded SEN specimen are not valid when wedge loading is applied due to the differences in constraint. A boundary integral equation method was used to calculate stress intensity factor and the crack opening displacements by assuming constant displacement conditions at the wedges. The following fourth-order equation was fitted to the wedge loaded solution:

$$K = \frac{P}{b\sqrt{W}}\left[0.153 + 4.99\left(\frac{a}{W}\right) - 8.45\left(\frac{a}{W}\right)^2 + 18.83\left(\frac{a}{W}\right)^3 - 10.25\left(\frac{a}{W}\right)^4\right] \quad (1)$$

where P is the applied load, b and W are, respectively the specimen thickness and width. This equation is valid for specimen height-to-width ratio of 3.

To check whether the assumed constant displacement conditions are in effect during wedge loading in our in situ rig, the measured crack opening displacement profile for a Mode I crack with an a/w of 0.52 was compared to both constant displacement and constant stress crack opening solutions. As shown in Fig. 2, the measured crack opening profile agrees very well with the assumed constant displacement solution.

Inclined Cracks. Chan and Cruse (1986) have shown that isotropic Mode I stress intensity factor solutions are valid for anisotropic single-crystal crack growth specimens for cracks that are inclined less than 30 deg from the starter notch. However, in the present study the cracks were often inclined approximately 45 deg to the starter notch, necessitating a separate analysis to calculate the Mode I and Mode II stress intensity factors along the actual crack path. Again a boundary integral equation (BIE) technique was used to calculate the Mode I and II stress intensity factors.

Downloaded 02 Jun 2010 to 171.66.16.104. Redistribution subject to ASME license or copyright; see http://www.asme.org/terms/Terms_Use.cfm

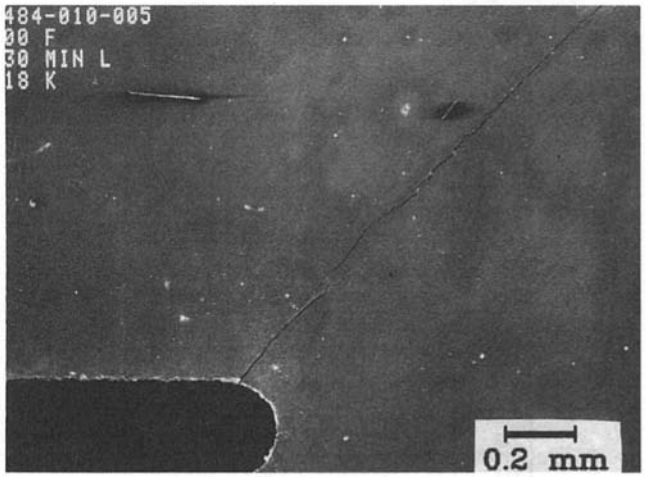

Fig. 3 Crack growing at 45 deg to the applied loading direction at 427°C

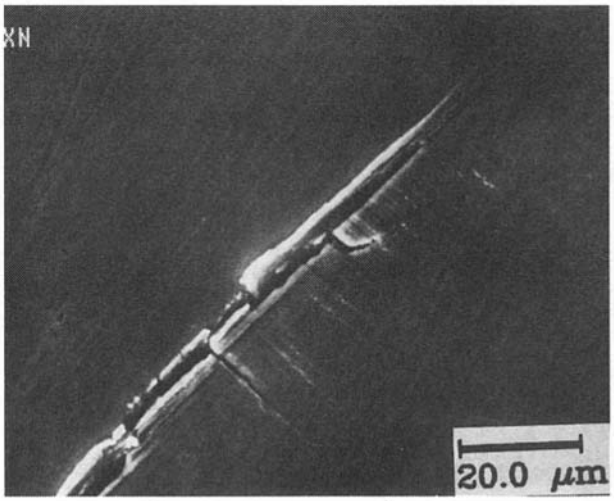

Fig. 4 Octahedral mode crack growth process at 427°C

The stress and displacement fields along the measured crack trajectory were determined for each specimen using two-dimensional multidomain BIE method. The two surfaces of the crack are modeled in separate subregions with appropriate continuity along the interface. Quadratic variations of the displacements and tractions are assumed. The stress intensity factor at the crack tip is then determined by two different methods to make sure that the analysis is correct. The stress intensity is calculated by taking the limiting value of the stress field as the distance from the crack tip, r, approaches zero, as well as through calculation of quarter point crack opening displacements near the crack tip, along the actual crack path.

Results and Discussion

In Situ Crack Growth Observations

427°C and 593°C Tests. For these two test temperatures, crack growth occurred primarily on the {111} octahedral planes. At these temperatures the crack growth, as monitored in the SEM, occurred either on a single active octahedral slip system, resulting in a fatigue crack inclined at 45 deg to the applied load axis as seen in Fig. 3 or on two different slip systems. Cunningham et al. (1994) have termed this failure mode as *macroscopic octahedral* since it creates large crystallographic {111} oriented facets on the fracture surface. Higher magnification observations revealed that the crack would meander at times slightly away from the operative slip system for few microns of growth, but would eventually return to the octahedral plane (Fig. 4).

Measurements of the crack closure loads were obtained from the in situ observations. The crack tip region was open for almost the entire loading cycle, thus indicating that at $R = 0.5$, crack closure does not have a significant effect on the crack growth rates. The crack tip remained opened over the entire loading cycle at R of 0.5 and 0.7, with closure occurring for the R of 0.1 test at load levels of 0.2 to 0.3 of P_{max}.

The observation of the crack tip remaining open over the majority of the loading cycle suggests that even for a crack growing on an octahedral slip plane, the principal normal stresses (i.e., Mode I component) may still be an important component of the crack driving force. This is an agreement with others who have suggested that while the resolved shear stresses damage the slip planes ahead of the crack tip, normal stresses still may be required to separate the damaged surfaces (Duquette et al., 1970).

760°C and 871°C Tests. The fatigue crack growth damage processes were considerably more complex for the tests conducted at these temperatures. Crack initiation occurred on the macroscopic octahedral planes but within 200 μm of growth, the crack left the octahedral plane and started growing in a direction perpendicular to the applied load (i.e., Mode I crack). This Mode I noncrystallographic failure process was active for the largest portion of the specimen life. However, in the high ΔK regime, at both temperatures, crack growth again transitioned to the {111} octahedral slip planes (Fig. 5). The octahedral failure mode remained in effect until the test was terminated.

Multitemperature and Multifrequency Test. In order to examine the variables that control the transition in the fatigue failure modes in the PWA 1484 single-crystal alloy, a test was performed in which the role of test temperature, frequency, and the crack growth rate was analyzed. The testing was done at 760°C, 815°C, and 871°C. The test frequencies ranged from 1 to 15 Hz.

It was shown that the fatigue failure mode can be controlled at these test temperatures by changing the test frequency. Examples of the failure mode transition as a function of frequency are shown in Fig. 6. Table 2 shows the summary of the observed failure modes versus test temperature, frequency, and crack growth rate (both in terms of da/dN and da/dt). From this table, as well as from previously described 760°C and 871°C tests, the transition crack growth rates in terms of da/dt were

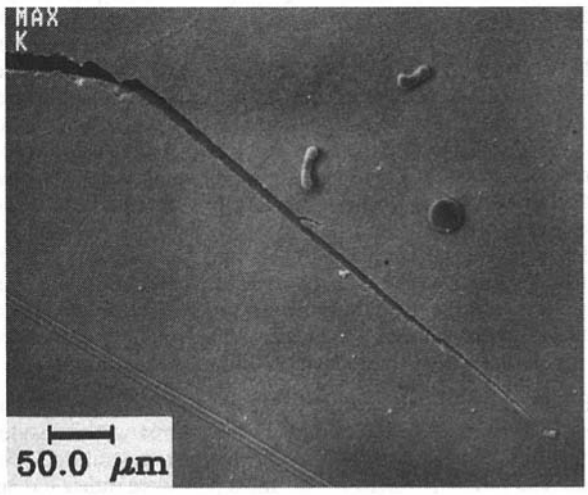

Fig. 5 At 760°C and 871°C failure mode transitioned from Mode I to octahedral at high ΔK

Downloaded 02 Jun 2010 to 171.66.16.104. Redistribution subject to ASME license or copyright; see http://www.asme.org/terms/Terms_Use.cfm

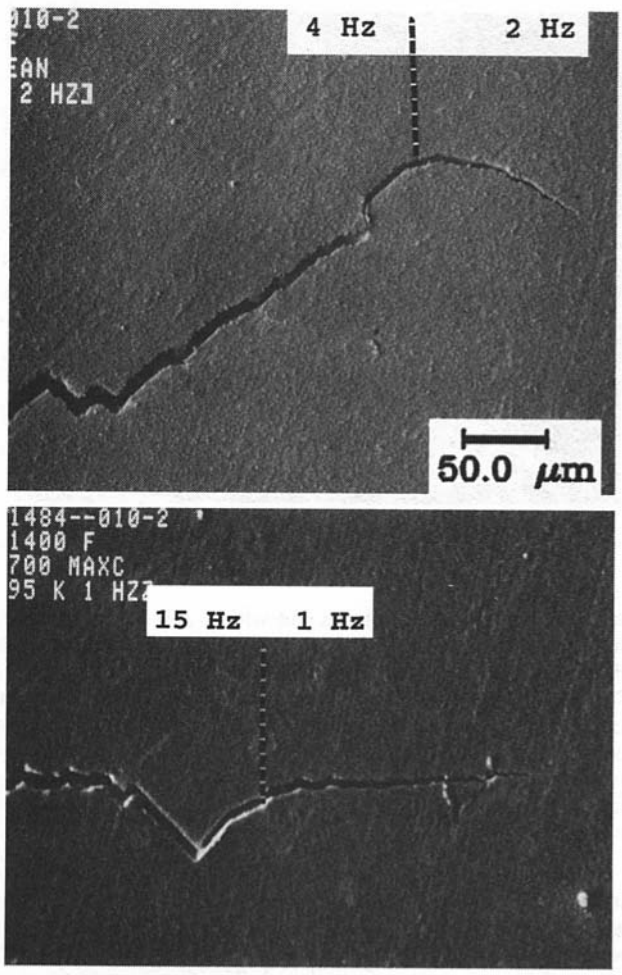

Fig. 6 Examples of the influence of frequency on the failure mode in vacuum

calculated and are plotted as a function of temperature in Fig. 7. The crack growth rate, at which the transition from noncrystallographic Mode I type to an octahedral failure mode occurs, increases with an increase in the test temperature. The postulated mechanisms that drive the failure mode transition will be discussed later.

Fractography: 427°C and 595°C Tests. The fractography of test specimens at these temperatures revealed the fatigue failure to have occurred predominantly on either one or two crystallographic facets (Fig. 8(*a*)). While the 427°C specimen failed exclusively on the octahedral facets, the 593°C specimen revealed small regions of Mode I failure. Higher magnification of the failure facets revealed a classical cleavage type failure with the associated river patterns and fracture steps (Fig. 8(*b*)). The octahedral failure resulted in a very smooth fatigue fracture surface, which might explain the very low observed crack closure levels.

The presence of cleavage-type failure features supports the earlier observation that stresses normal to the slip plane must play some role in the failure process. The formation of such features as river patterns is typically considered to be dependent on the normal stress component (Phillips et al., 1965).

Fractography: 760°C and 871°C Tests. The failure surfaces of specimens tested at these temperatures were considerably different in comparison to the lower temperature specimens. The failure surfaces for the most part were rather flat and exhibited a more typical Mode I type appearance (Fig. 9). Higher magnifications revealed an operative noncrystallographic failure mode, which consisted of homogeneously distributed fine features (Fig. 9). These features were on the order of 1–4 μm, and thus were larger than the γ' precipitates. Beach marks created by test interruptions were clearly visible; however, no evidence of striations was detected.

In the latter stages of these high-temperature crack growth tests, the active fatigue failure mode transitioned to a macroscopic octahedral type. The fractography confirmed this observation, as is evident by the large crystallographic failure facet on the failed specimens (Fig. 10). These facets originated on the outside faces of the specimens and extended further into the thickness of the specimen with continued crack growth.

Fatigue Crack Growth Results: Mode I Stress Intensity. The fatigue crack growth rate data for all seven tests are shown in Fig. 11 in terms of Mode I stress intensity factor, ΔK. The

Table 2 Failure mode transitions in the 1484-2 specimen

TEMP (°C)	FREQ (Hz)	da/dn m/cyc	da/dt m/sec	FATIGUE MODE
760	1	1.3E-8	1.3E-8	MODE I
760	3	5E-9	1.5E-8	MODE I
760	15	5E-9	7.5E-8	OCTAH
760	1	3.2E-9	3.2E-9	MODE I
760	15	2.5E-8	3.8E-7	OCTAH
760	1	5E-8	5E-8	MODE I
760	3	5E-8	1.5E-7	MODE I
760	7.5	3.6E-8	2.7E-7	OCTAH
760	15	3.6E-8	5.3E-7	OCTAH
760	15	3.6E-8	5.3E-7	OCTAH
815	15	3.8E-8	5.6E-7	MODE I
815	15	5.8E-8	8.6E-7	OCTAH
815	15	8.4E-8	1.3E-6	OCTAH
815	3	1E-7	3E-7	MODE I
815	7	1.3E-7	9.1E-7	OCTAH
871	15	2.3E-7	3.4E-6	OCTAH
871	1	1.9E-7	1.9E-7	MODE I
871	3	1.9E-7	5.6E-7	MODE I
871	6	2.8E-7	1.7E-6	OCTAH
871	4	3.8E-7	1.5E-6	OCTAH
871	2	3.8E-7	7.6E-7	MODE I

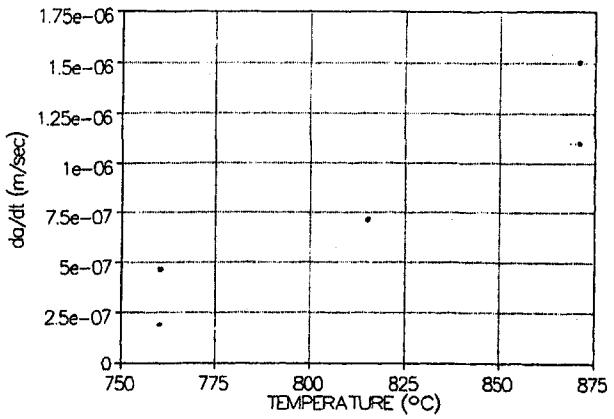

Fig. 7 The crack growth rates in terms of *da/dt* as a function of test temperature at which mode transition from Mode I to octahedral occurred

Downloaded 02 Jun 2010 to 171.66.16.104. Redistribution subject to ASME license or copyright; see http://www.asme.org/terms/Terms_Use.cfm

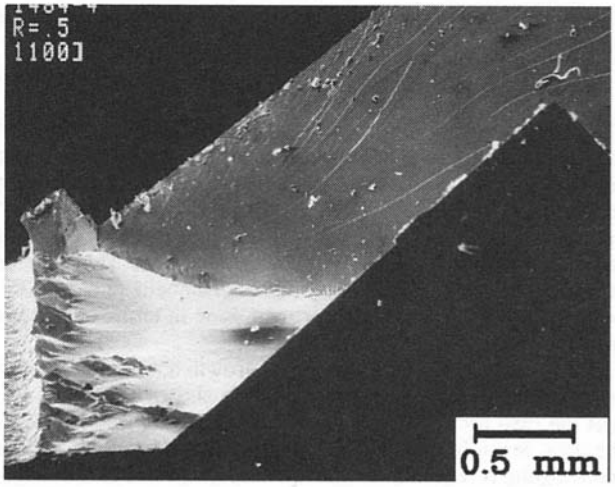

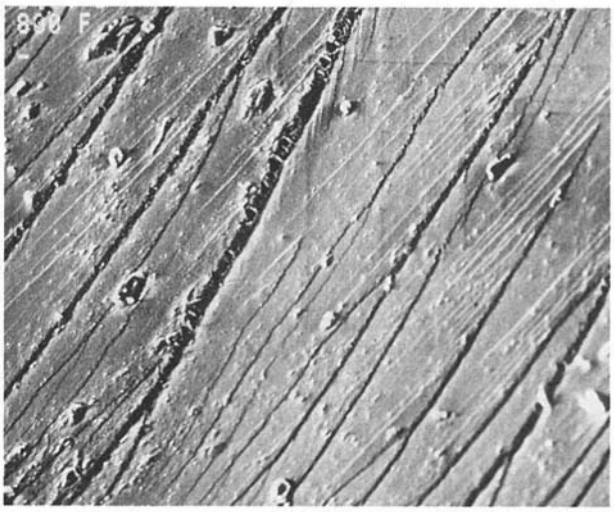

Fig. 8 Crack growth at 427°C and 593°C occurred on large {111} facets. Higher magnification shows cleavage type features on the crystallographic facets.

stress intensity solution takes into account the crack trajectory for each individual test as well as the constraint imposed by wedge loading. For comparison purposes, also shown are the room-temperature Paris region fatigue crack growth data obtained previously for a similarly oriented PWA 1480 single-crystal alloy tested at $R = 0.5$. All the PWA 1484 data fall

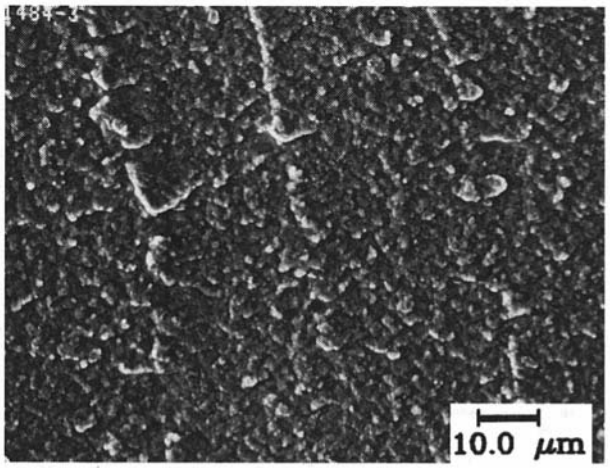

Fig. 9 Mode I failure features typically observed at 760°C and 871°C

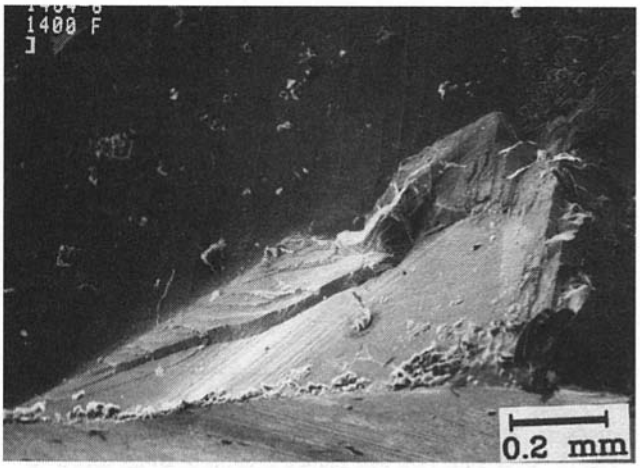

Fig. 10 760°C, the transition from Mode I to octahedral failure at high ΔK, initiated at the outside surface as seen by the presence of a large {111} facet

within a fairly narrow region; however, the PWA 1480 alloy data fall outside of this band and exhibit slower crack growth rates.

Figure 12 shows the effect of R ratio for tests conducted at 593°C. As shown, the effect of R ratio is not very significant even though at R of 0.1, the data exhibit slightly lower crack growth rates. This is not unexpected since the closure levels

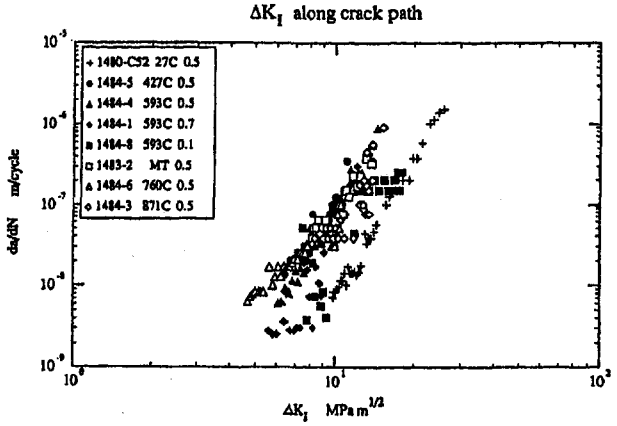

Fig. 11 FCG results for all tests in terms of trajectory corrected ΔK_I parameter

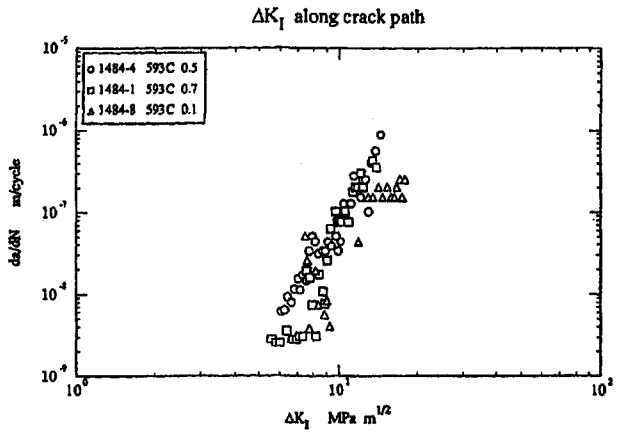

Fig. 12 The effect of R ratio at 593°C on FCG rates

Downloaded 02 Jun 2010 to 171.66.16.104. Redistribution subject to ASME license or copyright; see http://www.asme.org/terms/Terms_Use.cfm

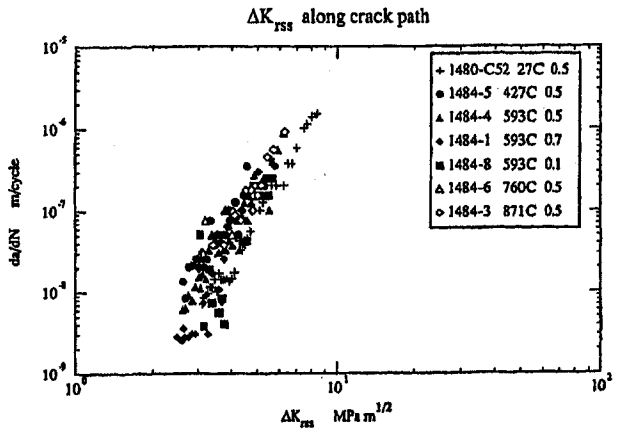

Fig. 13 Octahedral FCG data plotted in terms of ΔK_{RSS} parameter

were low for all R ratios and thus did not significantly influence the results.

Fatigue Crack Growth: Octahedral Parameters. The resolved shear stress intensity parameter, K_{RSS}, is defined following the Chen and Liu formulation, as the limiting value of the resolved shear stress, τ_{RSS}, multiplied by $\sqrt{2\pi r}$, as r approaches zero:

$$K_{RSS} = \lim_{r \to 0} \tau_{RSS}\sqrt{2\pi r} \tag{2}$$

where τ_{RSS} is defined as the projection of the stress tensor $[\sigma]$ on a plane whose outward normal is n in the direction of the Burgers vector, b.

$$\tau_{RSS} = \vec{b} \cdot [\sigma]\vec{n} \tag{3}$$

The stress field is reconstructed using the asymptotic singular solution near the crack tip. First, the stress intensity factors K_I and K_{II} are determined analytically by following the macroscopic crack path and using the two-dimensional BIE analysis. Then, the stress tensor is evaluated using the classical singular solution, for both plane strain and plane stress given by:

$$\sigma_{ij} = \frac{1}{\sqrt{2\pi r}} (K_I f_{ij}^{I}(\theta) + K_{II} f_{ij}^{II}(\Theta)) \tag{4}$$

where $f_{ij}(\Theta)$ are the angular components of the stress field. The angle Θ used in Eq. (4) is equal to the angle between the trace of a particular slip plane on the faces of the specimen and the horizontal axis. After determining the orientation of all the slip planes and slip directions, the values of K_{RSS} are determined by projecting the stresses near the crack tip on the {111} planes in a particular slip direction and taking the limit as r approaches zero. In other words, K_{RSS} can be taken to be the Mode II stress intensity factor on a particular slip plane in the direction of Burgers vector. Finally, fatigue cracking is postulated to occur along slip systems with the highest ΔK_{RSS} value.

The fatigue crack growth data were plotted as a function of the calculated ΔK_{RSS} parameter in the regimes where the octahedral failure mode was observed and is shown in Fig. 13. The figure also includes the previously described PWA 1480 data. As shown, this parameter does an excellent job in collapsing all the octahedral data, including the PWA 1480 data set, into a relatively narrow band. Further analysis showed that the cracks grew on slip planes with the highest ΔK_{RSS} values.

One of the byproducts of the BIE analysis was the calculation of the entire stress tensor on the active slip plane. Since ΔK_{RSS} parameter has been previously shown to have significant limitations, the known stress tensor was used to formulate another octahedral crack driving force parameter. This parameter termed K_{OCT} is simply a geometric mean of the K_{RSS} parameter and K_I normal to the active slip plane:

$$\Delta K_{OCT} = [(\Delta K_{RSS})^2 + (\Delta K_{I\,ON(111)})^2]^{1/2} \tag{5}$$

The rationale for the formulation of this parameter is based on the assumption that stresses normal to the slip plane act to separate the surfaces of the slip plane weakened by dislocation motion and thus contribute to the crack driving force. Our observations of the octahedral crack growth processes supported the importance of both of these stress components. This type of reasoning has been proposed by others (Duquette et al., 1970); however, their formulations were not done in terms of fracture mechanics-based parameters.

The octahedral failure mode crack growth data were replotted as a function of this parameter and are shown in Fig. 14. As was the case for the ΔK_{RSS} parameter, the ΔK_{OCT} collapsed all the data, including PWA 1480, into a narrow band. Of course, more testing is required in order to validate the use of the ΔK_{OCT} as the crack driving force parameter for octahedral failure in single crystal alloys. It should also be pointed out that only the K_{RSS} component of this new parameter can be used to predict the active slip system since slip is always governed by the resolved shear stresses.

Failure Mode Transitions. The transition of the fatigue failure mode from a Mode I type to the {111} octahedral mode, which occurred at both the 760°C and 871°C, can be explained by invoking environmental damage mechanisms. Similar failure mode transitions have been reported by Cunningham et al. (1994), but at considerably lower temperatures for tests done in air. They found that for similarly oriented PWA 1484 alloy tested in air, the failure mode was macroscopic octahedral for a specimen tested at 204°C; however, at 427°C the failure mode was already a noncrystallographic Mode I type. The main difference between these two studies is the test environment, since in both cases similar frequencies and R ratios were utilized.

Oxygen is the obvious candidate to which the environmental damage can be attributed, since the partial pressure of oxygen in the SEM chamber is 5 to 6 orders of magnitude smaller than in ambient atmosphere. The two types of oxygen embrittlement mechanism usually cited are the formation of an oxide layer ahead of the crack tip or the embrittling effect of bulk oxygen absorption ahead of the crack tip (Antolovich and Jayaraman, 1983). For both mechanisms the primary controlling parameters are temperature, time (i.e., cycling frequency), and oxygen concentration.

For either mechanism to be in effect, it is required that the environmental damage processes keep up with the rate of crack growth. McGowan and Liu (1983) suggested that for a given material at a given ΔK, there exists a corresponding fatigue

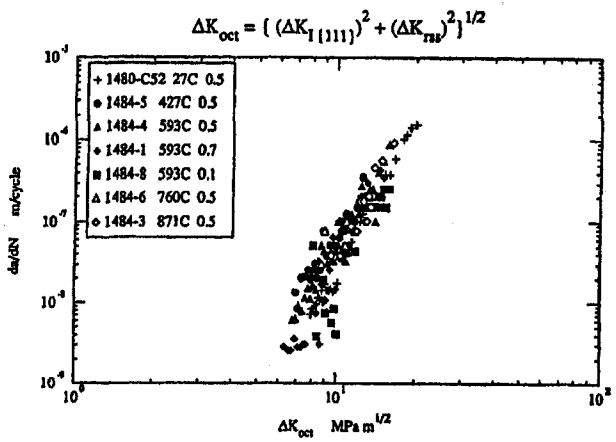

Fig. 14 The octahedral FCG data in terms of ΔK_{OCT}

Downloaded 02 Jun 2010 to 171.66.16.104. Redistribution subject to ASME license or copyright; see http://www.asme.org/terms/Terms_Use.cfm

crack increment per cycle, Δa_f, which is caused purely by the fatigue process devoid of the environmental influence. If Δa_f is substantially greater than the depth of environmental penetration per cycle, Δa_p, than the fatigue crack growth is primarily caused by the nonenvironmental fatigue process. However, if Δa_p is equal to or greater than Δa_f, then the environmental mechanisms determine the fatigue crack growth behavior.

The observed fatigue crack growth behavior closely follows the trends predicted by invoking either of the two types of oxygen damage mechanism. As shown by the failure mode observations described in Table 2, for a given temperature, a decrease in the frequency tended to drive the failure mode away from an octahedral to a noncrystallographic Mode I type by allowing more time for the oxygen penetration depth to increase (i.e., $\Delta a_p \geq \Delta a_f$).

The same type of mechanism can be used to explain the transition from the noncrystallographic to octahedral failure mode, which occurred for the isothermal 760°C and 871°C constant frequency tests. The transition can be explained by observing that the change to an octahedral failure mode occurred in the high da/dN and high ΔK regimes. It is likely that at these stress intensities the resultant fatigue crack growth rates exceeded the rates of oxygen penetration at the crack tip, thus limiting the environmental effect in agreement with the McGowan and Liu hypothesis.

The crack growth rate, in terms of da/dt, at which the transition from noncrystallographic Mode I type to an octahedral failure mode occurs, increased with an increase in the test temperature (Fig. 7). These results are consistent with the proposed role of the environment since an increase in temperature will accelerate the diffusion type mechanisms responsible for oxygen penetration. Thus the oxygen penetration depth, Δa_p, becomes larger as the temperature is increased, if the frequency remains constant. Since the failure mode transition is dependent on $\Delta a_f > \Delta a_p$, higher crack rates are required for the transition to occur as the temperature is increased. Thus an increase in the test temperature should result in the environmental effect persisting into higher crack growth rate regimes as was documented in this study.

Considerable amount of further work is required to characterize fully the environmental damage mechanisms occurring in single-crystal superalloys and to develop models that will be able to predict the conditions under which failure mode transitions take place.

Summary

A study was done to determine the fatigue crack growth behavior of a PWA 1484 single-crystal nickel-base superalloy in a temperature range of 427°C to 871°C. A unique aspect of single-crystal crack growth behavior is the extensive growth on the active slip systems. This little understood mode of crack growth is not typically taken into account in the existing life prediction methodologies of single-crystal components. The specific objectives of the study were to gain an understanding of the micromechanisms and the crack driving forces controlling octahedral crack growth in single crystal alloys. In addition, the variables that control the transition from an octahedral failure mode to noncrystallographic Mode I type were investigated.

Two distinctive failure modes were observed that were a function of temperature and frequency. The lower temperatures and higher frequencies resulted in crack growth on the {111} octahedral slip planes at an oblique angle to the loading direction. Higher temperatures and decrease in frequencies favored a Mode I type failure process with the crack growing perpendicular to the applied loading direction. The failure mode transitions were explained by invoking arguments based on environmental damage mechanisms. Higher temperatures and lower frequencies allow for oxygen embrittlement to occur ahead of the crack tip through either a formation of an oxide or bulk diffusion. The criterion for the environmental damage failure mode to be in effect is the requirement that the rate of oxygen embrittlement has to be of the same magnitude or greater than the crack growth increment per cycle. If this not achieved a crystallographic failure mode will prevail.

The fatigue crack growth rate data were analyzed using three different crack driving force parameters. The parameters investigated consisted of the Mode I stress intensity parameter, corrected for the inclined crack trajectory, and two octahedral parameters, which take into account the crystallographic orientation of the single crystal specimens. The two octahedral crack driving force parameters investigated were the ΔK_{RSS}, which is based solely on the calculation of the Mode II stress intensity on the 12 slip systems, and a newly proposed ΔK_{OCT}, which in addition to the Mode II calculations also takes into account the stresses normal to the {111} slip planes.

The Mode I parameter did a fair job in correlating the data but did not collapse them into a single narrow band. The two octahedral parameters collapsed all the data into a single narrow band. In addition to correlating the fatigue crack growth rates, the two octahedral parameters also predicted the {111} planes on which the crack growth took place.

Acknowledgments

The authors are grateful to Pratt & Whitney for supplying the test material and specimens. Discussions with Mr. Dan DeLuca, Dr. Susan Cunningham, and Mr. Konrad Haake were very helpful in the course of this study.

References

Antolovich, S. D., and Jayaraman, N., 1983, "The Effect of Microstructure on the Fatigue Behavior of Ni Base Alloys," in: *Proc. of the 27th Sagamore Army Materials Research Conference,* J. J. Burke and V. Weiss, eds., pp. 119–144.

Chan, K. S., and Cruse, T. A., 1986, "Stress Intensity Solutions for Anisotropic Compact Tension Specimen With Inclined Cracks," *Eng. Fracture Mechanics,* Vol. 23, No. 5, pp. 863–874.

Chen, O. Y., 1985, "Crystallographic Fatigue Crack Propagation in Single Crystal Superalloys," PhD Thesis, University of Connecticut, Storrs, CT.

Chen, Q., and Liu, H. W., 1988, "Resolved Shear Stress Intensity Coefficient and Fatigue Crack Growth in Large Crystals," NASA CR-182137.

Cunningham, S. E., DeLuca, D. P., and Haake, F. K., 1994, *Crack Growth and Life Prediction in Single Crystal Nickel Superalloys,* Vol. I, WL-TR-94-4089, Aug.

Duquette, D. J., Gell, M., and Piteo, J. W., 1970, "A Fractographic Study of Stage I Fatigue Cracking in Nickel-Base Superalloy Single Crystal," *Met. Trans.,* Vol. 1, pp. 3107–3115.

Leverant, G. A., and Gell, M., 1975, "The Influence of Temperature and Cyclic Frequency on the Fatigue Fracture of Cube Oriented Nickel-Base Superalloy Single Crystal," *Met. Trans A,* Vol. 6A, pp. 367–371.

McGowan, J. J., and Liu, H. W., 1983, "Kinetic Model of High Temperature Crack Growth," in: *Proc. of the 27th Sagamore Army Materials Research Conference,* J. J. Burke and V. Weiss, eds., pp. 377–390.

Phillips, A., Kerlins, V., and Whiteson, B. W., 1965, *Electron Fractography Handbook,* ML-TDR-64-416.

Telesman, J., and Ghosn, L. J., 1989, "The Unusual Near-Threshold FCG Behavior of a Single Crystal Superalloy and the Resolved Shear Stress as the Crack Driving Force," *Engineering Fracture Mechanics,* Vol. 34, No. 5/6, pp. 1183–1196.

Telesman, J., and Ghosn, L. J., 1993, "Effect of Crystal Orientation on the Fatigue Crack Growth of a Single Crystal Alloy," *Proceedings, Fatigue 93,* J. Bailon and J. I. Dickson, eds., EMAS Publishing, Vol. II, pp. 835–841.

Downloaded 02 Jun 2010 to 171.66.16.104. Redistribution subject to ASME license or copyright; see http://www.asme.org/terms/Terms_Use.cfm

Surface Integral and Finite Element Hybrid Method for Three-Dimensional Analysis of Arbitrarily Shaped Surface Cracks

W. D. Keat

D. M. Maybury

Department of Mechanical and Aeronautical Engineering, Clarkson University, Potsdam, NY 13699-5725

B. S. Annigeri

United Technologies Research Center, East Hartford, CT 06040

A three-dimensional surface integral and finite element hybrid method has been developed for modeling arbitrarily shaped surface cracks in complex structural components. Accurate stress intensity factors were obtained by decomposing the problem into a surface integral model of the fracture in a domain of infinite extent and a finite element model of the uncracked domain. Boundary conditions were enforced by applying corrective traction to the surfaces of both constituent models. Coupling between the two formulations was minimized by implementing the fundamental solution for a force multipole near a planar free surface. Surface cracks intersecting nonplanar free surfaces were modeled in a piecewise linear fashion by deploying multiple sets of these functions. The effectiveness of this approach was demonstrated for well-documented cases, including a corner crack in a thick plate and a three-dimensional edge crack. The results of these benchmark studies will be used to develop a set of heuristics for assuring suitable finite element mesh densities in the vicinity of the fracture.

Introduction

Alternative computational methods for three-dimensional fracture analysis range from finite elements, boundary elements, and weight function techniques, to line spring models and the surface integral method. It is fair to conclude that each method can be identified with its own unique set of strengths and weaknesses. The rationale for the hybrid method discussed here is that each of the methods listed above has attributes, often not duplicated by the other methods, that can contribute to an effective three-dimensional fracture analysis.

The surface integral and finite element hybrid method (SIFEH) employs the principle of superposition to combine a surface integral model of the fracture in an infinite (or semi-infinite) region with a finite element model of the uncracked finite body. The two formulations are coupled through the need to enforce boundary conditions on the external boundaries and on the fracture surface. The coupling is generally weak so that the two meshes can be set up independently. Hence, when conducting a crack propagation study, only the surface integral discretization of the fracture surface needs to be remeshed; the volume discretization associated with the finite element model remains fixed. One may note that for a linear elastic analysis, the use of boundary elements would appear to have been an equally valid choice for representing the finite body. However, the finite element method was retained here in anticipation of future modeling of material nonlinearities and thermal effects.

The generality of this hybrid method depends to a large degree on the library of fundamental solutions that are available for use with the surface integral method. The multipole solutions corresponding to a fracture event in an infinite region are well documented and have been used with the three-dimensional hybrid formulation to model embedded cracks in finite bodies of arbitrary shape (Keat et al., 1988). The same multipole solutions proved ineffective at modeling surface cracks because the strong coupling induced between the two formulations required finite element meshes so refined as to negate the advantages of a hybrid approach. The fundamental solutions for multipoles in a half-space were thus introduced to handle the problem of a surface crack intersecting a planar free surface in a finite body (Annigeri et al., 1988). This paper further generalizes the hybrid method by considering surface cracks intersecting free surfaces of arbitrary shape.

Surface Integral Formulation

The surface integral method (Cleary, 1977) represents the fracture as a distribution of force multipoles, which through Hooke's law may equivalently be expressed in terms of displacement discontinuities. The key feature of the method is that only the surface of the fracture needs to be discretized.

The traction induced at a point on the fracture can be found by summing the effects of the multipoles acting over the crack surface, S_c. If expressed in terms of components of relative displacement δ_k rather than dipole intensity, the following integral equation results:

$$t_i = \iint_{S_c} (\Gamma^S_{ijk} + \Gamma^{NS}_{ijk}) n_j \delta_k dA \qquad (1)$$

where the fundamental solution has been decomposed into singular (Γ^S) and nonsingular parts (Γ^{NS}) to facilitate the use of specialized integration procedures, n_j is the unit normal to the fracture surface, and t_i is the traction at a point on the fracture. A technique known as subtraction of the singularity was invoked to render the first part integrable. In effect, a rigid body displacement was subtracted from the singular integrand, allowing it to be integrated in a Cauchy principal-value sense:

$$t_i = \iint_{S_T} \Gamma^S_{ijk} n_j (\delta_k - \hat{\delta}_k) dA + \iint_{S_c} \Gamma^{NS}_{ijk} n_j \delta_k dA \qquad (2)$$

Contributed by the International Gas Turbine Institute and presented at the 40th International Gas Turbine and Aeroengine Congress and Exhibition, Houston, Texas, June 5–8, 1995. Manuscript received by the International Gas Turbine Institute March 23, 1995. Paper No. 95-GT-456. Associate Technical Editor: C. J. Russo.

Copyright © 1996 by ASME

Downloaded 02 Jun 2010 to 171.66.16.104. Redistribution subject to ASME license or copyright; see http://www.asme.org/terms/Terms_Use.cfm

where $\hat{\delta}_k$ is the relative displacement at the point of collocation. The domain of the first integral was redefined to be a plane of infinite extent, S_T, consistent with the integral representation of the rigid body displacement. The numerical problem of solving for the unknown crack opening/shear magnitudes may thus be formulated as a system of equations, each of the form of Eq. (2), which enforce the known traction boundary conditions at as many points on the crack surface as there are unknown parameters defining the crack opening variation.

Selection of the appropriate interpolation functions for crack opening/shear is crucial to the overall accuracy of the formulation. The variation of crack opening within each element of the fracture discretization was assumed to have the following form:

$$\delta_k = \sum_{l=1}^{L} h^l \hat{\delta}_k^l \tag{3}$$

where h^l are the interpolation functions, and $\hat{\delta}_k^l$ are nodal values of crack opening. In the present study, all crack opening nodes were assumed to be situated at collocation points located in the interior of the elements, leading to the result that opening/shear variations between elements are discontinuous. This assumption simplified some of the analytical integrations and was justified by the high accuracy that has been consistently observed in benchmark studies (Keat, 1989). The interpolation functions for crack opening assigned to the interior and perimeter crack elements are represented in Eqs. (4) and (5), respectively:

$$\delta_k = C_1 + C_2 x + C_3 y + C_4 xy \tag{4}$$

$$\delta_k = C_5 \rho^{1/2} \tag{5}$$

where the C_i are constants that depend on the crack opening/shear nodal values and their locations; ρ is the perpendicular distance from the crack front. Equation (4) corresponds to a four-noded (or linear) element. A constant element is also sometimes used in the interior and can be obtained from Eq. (4) by truncating the last three terms. The form of Eq. (5) was extracted from the asymptotic solution for a crack in a plane strain, homogeneous region.

Hybrid Formulation

The basic idea behind the hybrid formulation as originally developed by Annigeri and Cleary (1984) is to decompose the problem of a crack in a finite body into: (1) a finite element model of the finite body without the crack and (2) a surface integral model of the crack in an infinite (or semi-infinite) region. For the superposition of these models to represent a valid solution, the boundary conditions in the original problem must be satisfied. Toward this end, the finite element model is used to enforce all exterior boundary conditions while simultaneously the surface integral model is used to enforce boundary conditions on the crack surfaces. Enforcement of the boundary conditions requires the calculation of two correction vectors, here denoted as $\{T^c\}$ and $\{R^c\}$. They are needed to cancel out the nonzero tractions occurring in the two models where surfaces have not been explicitly represented.

Thus the system of equations associated with the finite element model may be stated as follows:

$$[K]\{U\} = \{R\} - \{R^c\} \tag{6}$$

where $[K]$ is the finite element stiffness matrix, $\{U\}$ is the nodal displacement vector, $\{R\}$ is the external nodal load vector. The correction load vector $\{R^c\}$ consists of nodal forces that are statically equivalent (but opposite in sign) to the tractions occurring in the surface integral model on surfaces coincident with the external boundaries. It can therefore be expressed in terms of the degrees of freedom associated with the surface integral model, i.e., the crack opening displacements $\{\delta\}$:

$$\{R^c\} = [G]\{\delta\} \tag{7}$$

The system of equations defining the surface integral model is generated using boundary collocation:

$$[C]\{\delta\} = \{T\} - \{T^c\} \tag{8}$$

where $[C]$ is the surface integral coefficient matrix, $\{T\}$ are traction boundary conditions at the collocation point positions. The correction traction vector $\{T^c\}$ is equal (but opposite in sign) to tractions occurring in the finite element model at positions coincident with the collocation point locations. It can therefore be expressed in terms of the degrees of freedom associated with the finite element model, i.e., the finite element nodal displacements $\{U\}$:

$$\{T^c\} = [S]\{U\} \tag{9}$$

Substituting Eqs. (7) and (9) into Eqs. (6) and (8), respectively, and writing the results in partitioned matrix form leads to:

$$\begin{bmatrix} K & G \\ S & C \end{bmatrix} \begin{Bmatrix} U \\ \delta \end{Bmatrix} = \begin{Bmatrix} R \\ T \end{Bmatrix} \tag{10}$$

which can be solved directly for the unknown nodal displacements and crack openings. Equation (10) can be further modified to allow for the imposition of displacement boundary conditions on the external boundaries (Annigeri and Cleary, 1984).

Accurate Modeling of Surface Flaws

The original version of the hybrid formulation, with its reliance on the multipole solutions for an infinite region, proved ineffective at modeling surface cracks, as successive finite element mesh refinements failed to lead to monotonic convergence. The coarse finite element meshes used with these early models were unable to capture the singular R^c fields produced along the line of intersection of the fracture with the free surface.

To reduce the coupling between the finite element and surface integral models, fundamental solutions for multipoles in a half-space were derived (Keat, 1989) by a process of differentiation starting from the Papkovitch functions of Rongved (1955). Use of these functions with the hybrid formulation eliminated the R^c field on the free surface explicitly represented in the half-space solution; the R^c fields were applied to the remaining faces in the usual manner.

Because of the added cost involved in using the fundamental solutions for the half-space, a criterion is needed to determine whether a given crack element lies close enough to a planar interface to warrant the use of these functions. Any valid test must take into consideration the global dimensions of the fracture. To understand this, assume that a given crack element has a small enough nondimensional depth to classify it as being a near-interface fracture event. The nonuniqueness, and thus the fallibility, of this test can be observed if the element is subdivided into smaller and smaller elements, until each subelement has a large enough nondimensional depth to overturn its original classification.

A test based on the following ratio has been proposed:

$$r(z) = \frac{\iint_{S_e} \Gamma^{NS} dA}{\iint_{S_e} \Gamma^{S} dA} \tag{11}$$

where the fundamental solution has been resolved into singular (Γ^S) and nonsingular (Γ^{NS}) components, which are integrated over the surface of the fracture. For a given crack geometry and material property set, this ratio will depend exclusively upon the location of the field point, with the perpendicular distance (z) of the field point from the interface having the primary influence. Equation (11) has been used in a Newton–

Downloaded 02 Jun 2010 to 171.66.16.104. Redistribution subject to ASME license or copyright; see http://www.asme.org/terms/Terms_Use.cfm

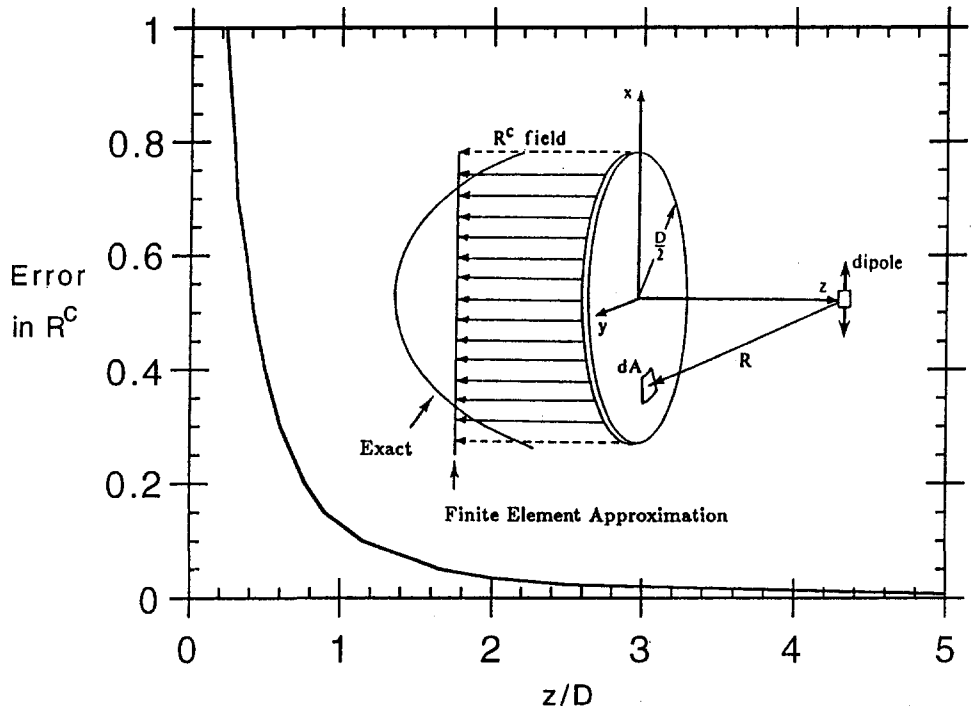

Fig. 1 Effect of dipole depth on the error induced in the finite element representation of the R^C field. Insert shows simplified geometry used to evaluate the error analytically.

Raphson algorithm to search iteratively for the critical depth at which the fundamental solution for the half-space should become active.

In a hybrid analysis, the largest value of $r(z)$ that can be tolerated, without sacrificing accuracy, will depend to a large extent on the sizing of the finite element mesh. An estimate of how well the R^e field can be represented using the finite element interpolation functions was derived analytically for the simplified geometry of Fig. 1. In the figure, an individual finite element surface, over which the R^e field is presumed to occur, has been idealized by a planar circular area. A tensile dipole is constrained to lie on a central axis perpendicular to the circular area. The dipole might represent, for example, the nearest tip of an approaching fracture. The influence function (Γ^S) associated with the dipole is assumed to have the following form:

$$\Gamma^S \propto \frac{1}{R^3} \tag{12}$$

where R is the distance from the dipole to a point on the circular area. One may note that the resulting R^e field will become increasingly singular as z is allowed to approach zero. Yet, due to the symmetry of the configuration and the low order of the finite element interpolation functions (linear with cross terms), the best that the element can do is to represent this variation as a uniform stress field of intensity:

$$\bar{\Gamma}^S = \frac{\iint_A \Gamma^S dA}{A} \tag{13}$$

which is applied to the surface of the finite element in the form of four equal nodal forces. The error measure is therefore defined as

$$\epsilon = \frac{\iint_A |\Gamma^S - \bar{\Gamma}^S| \, dA}{\bar{\Gamma}^S A} \tag{14}$$

where Eq. (14) indicates the relative error between the actual and idealized R^e fields. The error is plotted as a function of dimensionless dipole depth in Fig. 1. Note that this result does not take into account the level of mesh refinement in the z direction and thus does not address the accuracy of T^e.

Computational Strategy for Cracks Intersecting Multiple Free Surfaces

For this class of problem, the fracture is allowed to approach and/or intersect more than one planar free surface. Through cracks and corner cracks are typical examples.

The hybrid method was adapted to this class of problem by introducing modifications that allow for the use of multiple sets of fundamental solutions. Figure 2 shows the component models that would be used to model a fracture situated close to two planar free surfaces. Two surface integral models, each one modeling separate halves of the fracture, have been employed to represent the fracture. Each crack element is assigned to one of the surface integral models on the basis of which planar free surface exerts the greatest influence upon it. This influence can be assessed, for example, by evaluating the ratio in Eq. (11), or by calculating the perpendicular distances between the crack element and the free surfaces.

All three models are coupled as a result of satisfying traction and displacement boundary conditions. Each surface integral model contributes tractions in the form of an $\{R^e\}$ field to those surfaces of the finite element model that it does not explicitly model. Also, since each surface integral domain only partially models the fracture, it will receive corrective tractions from all of the other models including its surface integral complements. The corrective tractions $\{T^{c2}\}$ and $\{T^{c3}\}$ in Fig. 2 are absorbed in the surface integral coefficient matrix and thus do not alter the form of the governing matrix equations.

Convergence Studies

The convergence studies were aimed at determining appropriate meshes first for a corner crack in a thick plate and second for a three-dimensional edge crack in a thick plate (see Fig. 3). Component solutions used with the hybrid formulation to model these geometries are shown in Fig. 4.

Downloaded 02 Jun 2010 to 171.66.16.104. Redistribution subject to ASME license or copyright; see http://www.asme.org/terms/Terms_Use.cfm

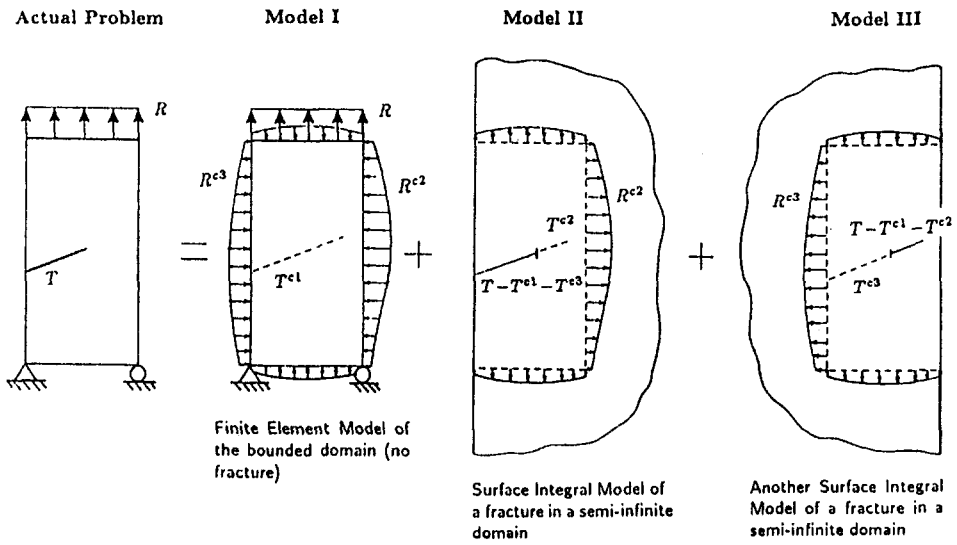

Fig. 2 Component geometries used with the hybrid method to model a fracture near multiple planar surfaces in a bounded domain

The surface integral discretizations can generally be set up without reference to the demands on the finite element model. Previous experience with embedded fractures (Keat et al., 1988) and semi-elliptical surface cracks (Annigeri et al., 1988) suggested that the meshes depicted in Fig. 5 would be more than adequate for representing the elastic behavior of the crack geometries under consideration. The discretizations were created using an automatic mesh generator specially designed for use with the surface integral models under mode I conditions. Mesh density was controlled by specifying the number of crack elements along each edge. Tip elements, defined by Eq. (5), were employed along the crack fronts; linear and constant elements were used to model the interiors of the corner and edge cracks, respectively. Also, each crack element was associated, based on proximity, with one of the half-space solutions depicted in Fig. 4.

A succession of finite element meshes (see Fig. 6) of increasing density was used to analyze both crack geometries. Uniform element spacing was used in all three coordinate directions

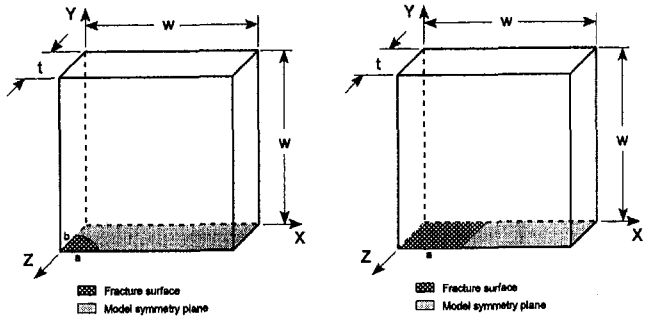

Fig. 3 Corner crack and edge crack geometries used to assess effectiveness of hybrid strategy for surface cracks. Plate dimensions are defined such that: $T/W = 0.2$.

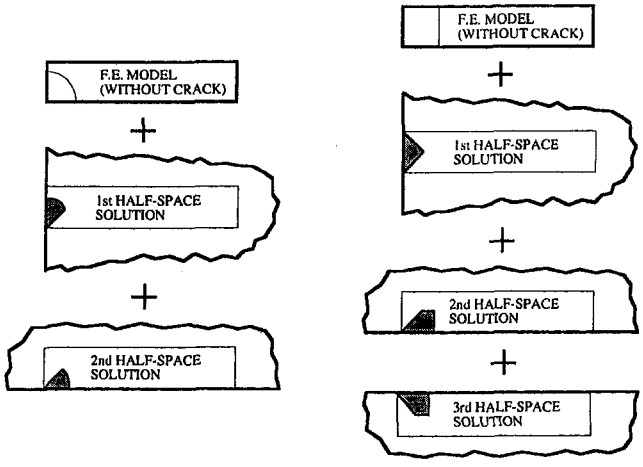

Fig. 4 Cross-sectional view of component geometries used to model corner crack (left) and edge crack (right)

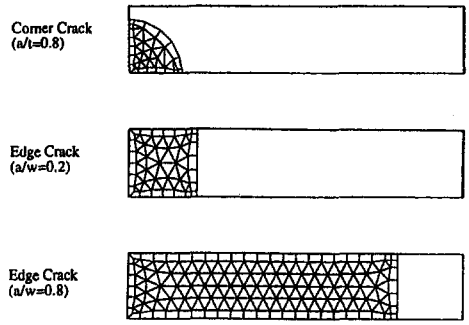

Fig. 5 Surface integral discretizations

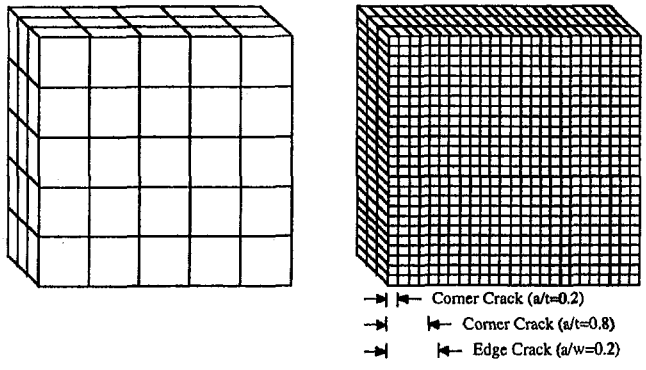

Fig. 6 Finite element discretizations corresponding to 5 × 5 × 3 and 25 × 25 × 3 mesh refinements

Downloaded 02 Jun 2010 to 171.66.16.104. Redistribution subject to ASME license or copyright; see http://www.asme.org/terms/Terms_Use.cfm

under the desired assumption that the finite element and surface integral meshes can be set up independently. Furthermore, the number of finite elements through the thickness of the plate was held fixed at three, as being typical of what a finite element modeler would employ with a plate structure of comparable dimensions. Thus five different finite element meshes were employed: $5 \times 5 \times 3$, $10 \times 10 \times 3$, $15 \times 15 \times 3$, $20 \times 20 \times 3$, $25 \times 25 \times 3$. Expected major source of error is the inability of the finite element mesh to represent exactly the R^c fields.

The results for the convergence study of the corner crack geometry are displayed in Fig. 7. Crack radius to thickness ratios (a/t) of 0.2 and 0.8 were examined. Accuracy was assessed by comparison with the finite element results of Newman and Raju (1981) using the error measures defined below:

$$\text{Avg. percent dev.} = \frac{\sum_{i=1}^{n} \left\{ W_i \left(\frac{K_{1i}^{\text{SIFEH}} - K_{1i}^{FE}}{K_{1i}^{FE}} \right) \right\}}{\sum_{i=1}^{n} W_i} \times 100$$

$$\text{Max. percent dev.} = \max_{i=1,n} \left\{ \frac{K_{1i}^{\text{SIFEH}} - K_{1i}^{FE}}{K_{1i}^{FE}} \right\} \times 100 \quad (15)$$

where K_{1i}^{SIFEH} and K_{1i}^{FE} are the hybrid and finite element results, respectively, for the mode I stress intensity factor at the ith tip element; W_i is a nondimensional weighting factor, which is proportional to the length of crack front associated with the ith tip element. Inspection of Fig. 7 indicates that convergence does occur with the average errors flattening out at about 3 percent for both a/t ratios. The persistent error at convergence is not surprising in view of the fact that the crack mesh and the number of finite elements through the thickness of the plate were both held fixed throughout the studies. Although the number of finite elements at convergence may appear excessive, in fact the hybrid method is performing well when one considers that the smaller corner crack ($a/t = 0.2$) is fully contained within a single element of the $25 \times 25 \times 3$ mesh (refer to Fig. 6). The same accuracy could have been achieved using many fewer degrees of freedom by refining the finite element mesh in the vicinity of the fracture. Thus one may conclude that reference should be made to the location and proportions of the crack when setting up the finite element model.

Results for a short three-dimensional edge crack ($a/w = 0.2$) are presented in Fig. 8. Observed rates of convergence are comparable to those for the corner crack. However, when the same studies were conducted for a long edge crack ($a/w = 0.8$), convergence could not be attained because of the severity of the R^c field.

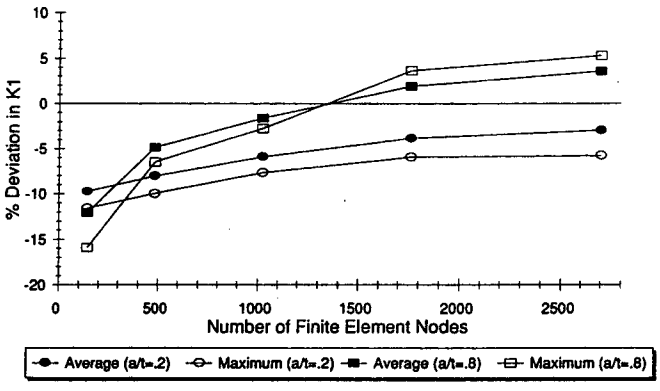

Fig. 7 Percentage deviation of hybrid results from finite element results of Raju and Newman (1981) for corner crack geometry

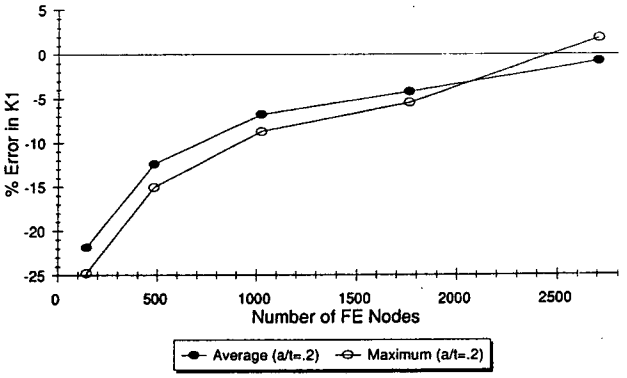

Fig. 8 Percentage deviation of hybrid results from results of Brown and Srawley (1966) for edge crack geometry

This may suggest a need to introduce fundamental solutions that explicitly represent both faces of an infinite plate.

Summary

The use of superposition provides SIFEH with the flexibility needed to model surface cracks of complex shape effectively. Though specialized influence functions had to be introduced to reduce the degree of coupling between the surface integral and finite element models, it was sufficient to employ just the half-space solution as it could be used with superposition to model a nonplanar boundary in a piecewise linear sense. Results indicate that though this strategy significantly weakens the coupling between the two discretizations, the finite element mesh may have to be refined in the vicinity of the fracture. Additional savings in CPU time can be obtained by using a method of substructuring described by Annigeri et al. (1988) to restrict the surface integral domain to a localized region containing the fracture.

The computational strategy described here is just a partial solution to the problem of modeling a surface crack of arbitrary shape. It should be carefully noted that each of the geometries considered here had two geometrical characteristics in common: (1) The boundaries intersected by the surface cracks could easily be modeled as piecewise planar, and (2) all interior angles of the crossection were less than 180 deg. It would seem on first glance that both of these conditions must be met in the vicinity of the fracture for the method to hold up. However, preliminary results (e.g., for a surface crack at a hole) indicate that there is the potential for this strategy to work effectively for a much broader range of problems.

References

Annigeri, B. S., and Cleary, M. P., 1984, "Surface Integral Finite Element Hybrid Method for Fracture Mechanics," *International Journal for Numerical Methods in Engineering,* Vol. 20, pp. 869–885.

Annigeri, B. S., Keat, W. D., and Cleary, M. P., 1988, "Fracture Mechanics Research Using the Surface Integral and Finite Element Hybrid Method," *Proceedings of First Joint Japan/U.S. Symposium on Boundary Element Methods,* Pergamon Press, University of Tokyo, pp. 191–202.

Brown, W. F., and Srawley, 1966, "Plane Strain Crack Toughness Testing of High Strength Metallic Materials," ASTM STP 410, p. 12.

Cleary, M. P., 1977, "Fundamental Solutions for a Fluid-Saturated Porous Solid," *International Journal of Solids and Structures,* Vol. 13, pp. 785–806.

Keat, W. D., Annigeri, B. S., and Cleary, M. P., 1988, "Surface Integral and Finite Element Hybrid Method for Two and Three Dimensional Fracture Mechanics Analysis," *International Journal of Fracture,* Vol. 36, pp. 35–53.

Keat, W. D., 1989, "Surface Integral and Finite Element Hybrid Method for the Analysis of Three Dimensional Fractures," Ph.D. Thesis, M.I.T., Cambridge, MA.

Newman, J. C., and Raju, J. S., 1981, "Stress Intensity Factor Equations for Cracks in Three-Dimensional Finite Bodies," NASA Technical Memorandum 83200, pp. 1–49.

Rongved, 1955, "Force Interior to One of Two Joined Semi-infinite Solids," *Proceedings of Second Midwestern Conf. on Solid Mech.,* pp. 1–13.

Downloaded 02 Jun 2010 to 171.66.16.104. Redistribution subject to ASME license or copyright; see http://www.asme.org/terms/Terms_Use.cfm

A Probabilistic Method for the Fatigue Life Assessment of Powder Metallurgy Parts of Aircraft Engines

R. Krafft

S. Mosset

SNECMA,
Département Méthodes
de conception et CAO,
Centre d'essais de Villaroche,
77550 Moissy-Cramayel—France

This paper will present a probabilistic approach developed in order to assess the fatigue life of aircraft engine parts (turbine disks) obtained by powder metallurgy technique. First of all, the main issues will be pointed out and the theoretical principles of the method will be described. Then the design implications and the experimental correlation will be emphasized. The scale effect is a major concern for the fatigue life assessment of a powder metallurgy part. It no longer allows the designer to evaluate the life of a massive part directly from experimental results based on small specimen fatigue tests as is done in the classical methodology. In order to describe this scale effect correctly, incubation sites (inhomogeneities like ceramic inclusions) must be characterized. The size of these inhomogeneities and their positions in the part appeared to be the most relevant parameters. Hence the methodology developed at SNECMA integrates the scale effect scatter through a binomial probability distribution as well as a temperature and stress-dependent life evaluation for each inhomogeneity size and position. The life calculation of a part implies an analysis of its whole volume and surface. An iterative process determines the number of cycles corresponding to a global reliability level requirement for the part. The complete methodology is then validated by comparing the calculated initiation distribution with experimental results on small specimens and test disks.

I Introduction

The use of powder metallurgy to produce nickel base super alloys allows far higher γ' precipitate ratios than conventional metallurgy. Due to the large fraction of hardening precipitates, these super alloys show, among other properties, improved static characteristics ($R_{0,2}$, R), creep strength, and low-cycle fatigue strength compared to conventional alloys. The achieved gain in mechanical properties makes this production process very attractive. As a result, the aircraft engine designer is able to reduce the weight of the parts by increasing their load and thermal level beyond the limitations of conventional alloys. However, this production process generates new phenomena that influence the design methods.

Inhomogeneities introduced during the powder atomization phase prove to be the main cause for fatigue initiation in powder metallurgy alloys. Hence, the LCF life calculation methods applied to industrial components must allow for these inhomogeneities. As a matter of fact they may induce a scale effect on life as evidenced, from a theoretical viewpoint, by the probabilistic models proposed by McCartney (1980) or Pineau (1990). Using the concepts introduced by Pineau to analyze surface initiations from inclusions, Lautridou et al. (1993) have developed a probabilistic model suited for crack initiation prediction in powder metallurgy alloys. This model associated with a temperature and stress-dependent random life distribution for each inhomogeneity size and position in the part is the base of the following life prediction methodology.

Contributed by the International Gas Turbine Institute and presented at the 40th International Gas Turbine and Aeroengine Congress and Exhibition, Houston, Texas, June 5–8, 1995. Manuscript received by the International Gas Turbine Institute February 13, 1995 Paper No. 95-GT-218. Associate Technical Editor: C. J. Russo.

II Powder Metallurgy Specificity to Low Cycle Fatigue

II (1) Overview of the Powder Metallurgy Production Process. Unlike conventional metallurgy where the molten alloy is directly cast and then forged, powder metallurgy consists in turning the molten alloy into a very fine metallic powder (grain size of some tens of micrometers) prior to being compacted, extruded, and forged. Due to the powdering phase, the γ' precipitate ratio can be controlled and significantly increased. The powder is obtained by atomization with an argon jet blowing at the outlet of the nozzle of the crucible containing the molten alloy. Despite all the precautions taken to ensure powder cleanliness, some inhomogeneities always remain. They are mainly fine inclusions that separate from the heat-resistant ceramic walls of the atomization crucible as well as small argon bubbles entrapped into the powder grains and later turning into porosities once the alloy has been extruded and forged.

II (2) Low Cycle Fatigue Initiation Sites in Powder Metallurgy Alloys. These inhomogeneities prove to have a great influence on the LCF strength of powder metallurgy alloys. In actual fact they make up the main part of initiation sites, particularly in fine grain alloys, such as N18. Probabilistic models developed for this specific problem (Pineau, 1990; McCartney, 1980) show a potential scale effect due to these inhomogeneities; the greater the volume of stressed material, the shorter the life is. Hence the conventional approach for fatigue design becomes less reliable. Because of this expected scale effect, there is not a very good confidence that the direct use of fatigue curves obtained by a statistical analysis of laboratory tests (small specimens) will correctly predict the LCF life of large industrial components.

Copyright © 1996 by ASME

Downloaded 02 Jun 2010 to 171.66.16.104. Redistribution subject to ASME license or copyright; see http://www.asme.org/terms/Terms_Use.cfm

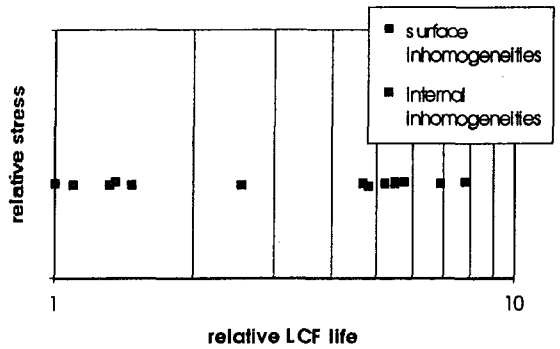

Fig. 1 Life comparison between surface and internal inhomogeneities of same size under the same loading

III Theoretical Principles of the Method

III (1) Overview of the Probabilistic Model Developed by de Bussac et al.

III (1-1) Characterization of Inhomogeneities. The inhomogeneities were characterized before modeling the scale effect they induce. The fatigue test dispersion analysis readily shows that the position of the inhomogeneity at the origin of the initiation is a major parameter. Initiation due to a surface inhomogeneity results in a much shorter life compared to an internal inhomogeneity (Fig. 1). This is why the probabilistic model was initially developed to describe initiations from surface inhomogeneities.

Similarly inhomogeneity size appears to be a significant parameter to describe the effect of inhomogeneities on life as mentioned by Domas (1992) (Fig. 2).

Lautridau et al. have selected the parameter $t = \sqrt{L \times 1}$ calculated from the greatest dimension L and from the greatest normal dimension 1 measured on the fractographies of the inhomogeneities at the origin of initiation. It is assumed that there is no preferential orientation of the inhomogeneities in the alloy.

III (1-2) Surface Initiation Probability. Initiation probability before No cycles on a surface S is defined as the initiation probability before No cycles of at least one of the inhomogeneities likely to intersect the surface. The following hypothesis is used:

There is a deterministic relationship between size t of the inhomogeneity at the origin of initiation and life N $(N = f(t))$ (1)

Considering hypothesis (1), the initiation probability before No cycles on a surface S is equal to the probability of presence on S of at least one inhomogeneity the size of which is higher than $t_o = f^{-1}$ (No). If we consider n inhomogeneities of single size t uniformly distributed over a reference volume V_r, the initiation probability of at least one inhomogeneity on a surface S included in V_r is expressed as follows:

$$P(N \leq N_0) = P(t \geq t_0) = 1 - \exp\left[-n \cdot \frac{S}{V_r} \cdot \left(t - \frac{t_0^2}{t}\right)\right] \quad (2)$$

$(S/V_r) \cdot (t - t_0^2/t)$ is the individual probability of one inhomogeneity of size t intercepting surface S and creating an inhomogeneity the size of which is equal to or greater than t_o.

Formula (2) can be extended in the cases of multiple inhomogeneity size classes and continuous inhomogeneity size distribution.

III (1-3) Volume Initiation Probability. Cases of initiations from internal inhomogeneities have been also reviewed by Lautridou et al. Initiation probability before No cycles for a volume V corresponds to initiation probability before No cycles of at least one of the inhomogeneities likely to be included in this volume.

Using hypothesis (1), if we consider n inhomogeneities of single size t uniformly distributed over a reference volume V_r, the initiation probability of at least one inhomogeneity within volume V included in V_r is expressed as follows:

if $t \geq t_o = f^{-1}$ (No)

$$P(N \leq N_0) = P(t \geq t_o) = 1 - \exp\left[-n \cdot \frac{V}{V_r}\right] \quad (3)$$

if $t < to$

$$P(N \leq N_0) = P(t \geq t_0) = 0$$

Formula (3) can be extended in the cases of multiple inhomogeneity size classes and continuous inhomogeneity size distribution.

III (2) Improvements of the Model. The main hypothesis of the model is a deterministic relationship between size t of the inhomogeneity at the origin of initiation and life N observed under the relevant loading conditions $(N = f(t))$. In other words, life scatter related to an inhomogeneity of a given size is disregarded. However, it does exist as shown in Fig. 2 where initiations from surface inhomogeneities on fatigue specimens are illustrated.

Hence, computations of the part's life using this hypothesis are questionable since an arbitrarily defined nonrandom value must be picked up in advance from the random life distribution of each inhomogeneity.

Thus it proves necessary to take into account this new random variable in the probabilistic model in order to completely solve the problem of predicting a reliable life for a part. Only the integration of this life scatter in terms of an individual initiation distribution per inhomogeneity allows these doubts to be raised.

Therefore, each inhomogeneity size t has a life $N(t)$, which is a random variable function of:

- its size t and depth x within the part,
- the loading conditions $(\Delta\sigma, R_\sigma)$ and the temperature Θ around its location in the part.

$N(t)$ is expressed by a lognormal law:

$$\log (N(t)) = N[\log (\bar{N}(t)), s(t)]$$

with average life $\bar{N}(t) = f(\Delta\sigma, R_\sigma, \Theta, t, x)$

and standard deviation $s(t) = g(\Delta\sigma, R_\sigma, \Theta, t, x)$

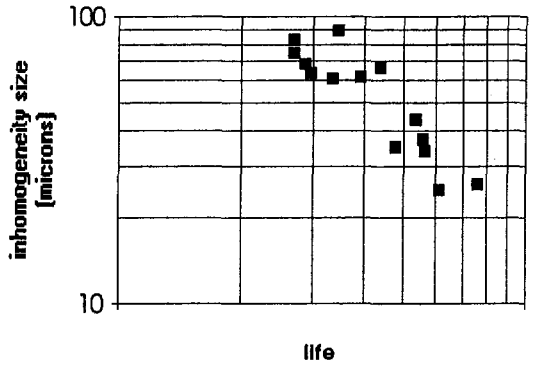

Fig. 2 Life comparison between surface inhomogeneities of different sizes under the same loading

Downloaded 02 Jun 2010 to 171.66.16.104. Redistribution subject to ASME license or copyright; see http://www.asme.org/terms/Terms_Use.cfm

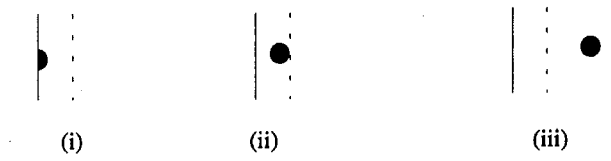

Fig. 3 (*i*) surface, (*ii*) subsurface, (*iii*) internal inhomogeneity

Parameter x of depth allows three possible cases to be taken into account (Fig. 3):

(*i*) The inhomogeneity intersects the surface.
(*ii*) The inhomogeneity does not intersect the surface; however, it is close to it and its life is influenced as a result.
(*iii*) The inhomogeneity is far away from the surface and life is no longer dependent on the distance from the surface.

As a conclusion, initiation probability calculated for a part integrates occurrence probability and life dispersion for each size of the inhomogeneities distribution in the part (Fig. 4).

IV Principles of Application to Parts

IV (1) Part Initiation Probability Calculation. Because of the scale effect, the calculation of the initiation probability for a part needs to associate with stresses and temperatures the corresponding loaded volume and surface. As a part is not uniformly stressed nor isothermal, it is very difficult to calculate its initiation probability directly. As a matter of fact, it would be necessary to consider every possible location for each inhomogeneity in the stress and temperature fields of the part. A stress and temperature partition is defined to overcome this problem. Upon every subsequently defined domain D_i (either a volume or a surface) the initiation probability for each inhomogeneity is independent of its location. The initiation probability for the part is then calculated from the initiation probabilities of its domains using the weak link theory.

Three types of domain are used to process the three cases mentioned in Para. III (2) (Fig. 5):

- surface domains for inhomogeneities intersecting the surface.
- subsurface volume domains for inhomogeneities not intersecting the surface but sufficiently close to it for their life to be affected.
- internal volume domains for inhomogeneities far away from the surface so that their life does not depend on the distance from the surface.

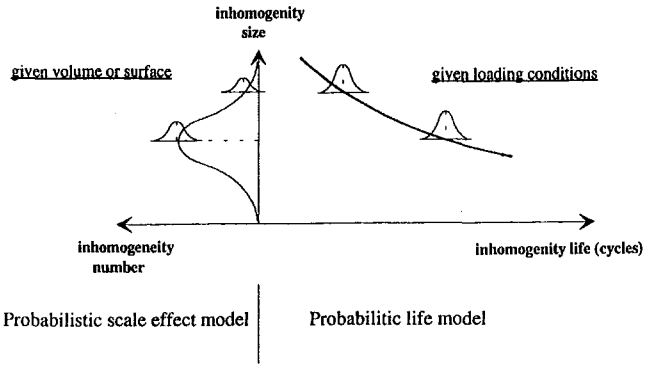

Fig. 4 Integration of the occurrence probability and life dispersion of the inhomogeneities in the initiation probability

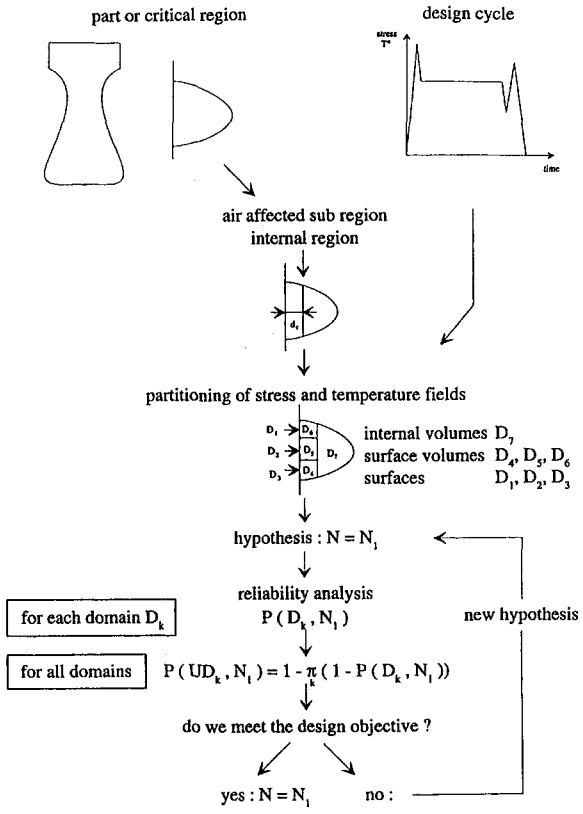

Fig. 5 Life calculation procedure for a P.M. part

In order to adapt this new approach to conventional life assessment practice, it has been decided to retain one analysis per critical location. Life calculation for each location allows improved criticality assessment thereof.

This being considered, reliable part life is the result of an initiation probability calculation, all the locations making up the part being combined. In other words, the whole volume and surface of the part are considered.

The life calculation of a part or a critical location for a targeted reliability level follows an iterative process that requires initiation probabilities to be determined for a sequence of life hypothesis (Fig. 5). In actual fact life corresponding to a given initiation probability cannot be directly calculated since the function linking the probability with the number of cycles is a complex one.

V Experimental Validation

In the method presented herein, two models are used to calculate initiation probability for a part. These models (probabilistic modeling of the scale effect and life model per inhomogeneity size) have been defined and validated separately. Then, the whole method must be validated to experience. This is all the more important since new constraints are induced by this method, compared to the conventional life assessment practice.

As a result it must be assured that life distribution predicted for a given structure in using the method is in compliance with the experimental life distribution obtained after the structure has been subjected to fatigue tests.

Since the validation of life distribution requires a great deal of tests to be meaningful, it has been done from fatigue tests carried out on laboratory specimens.

Supplementary tests have also been conducted on small-scale half-disks representative of real parts in order to verify that the methodology can predict correctly the life of an industrial component.

Downloaded 02 Jun 2010 to 171.66.16.104. Redistribution subject to ASME license or copyright; see http://www.asme.org/terms/Terms_Use.cfm

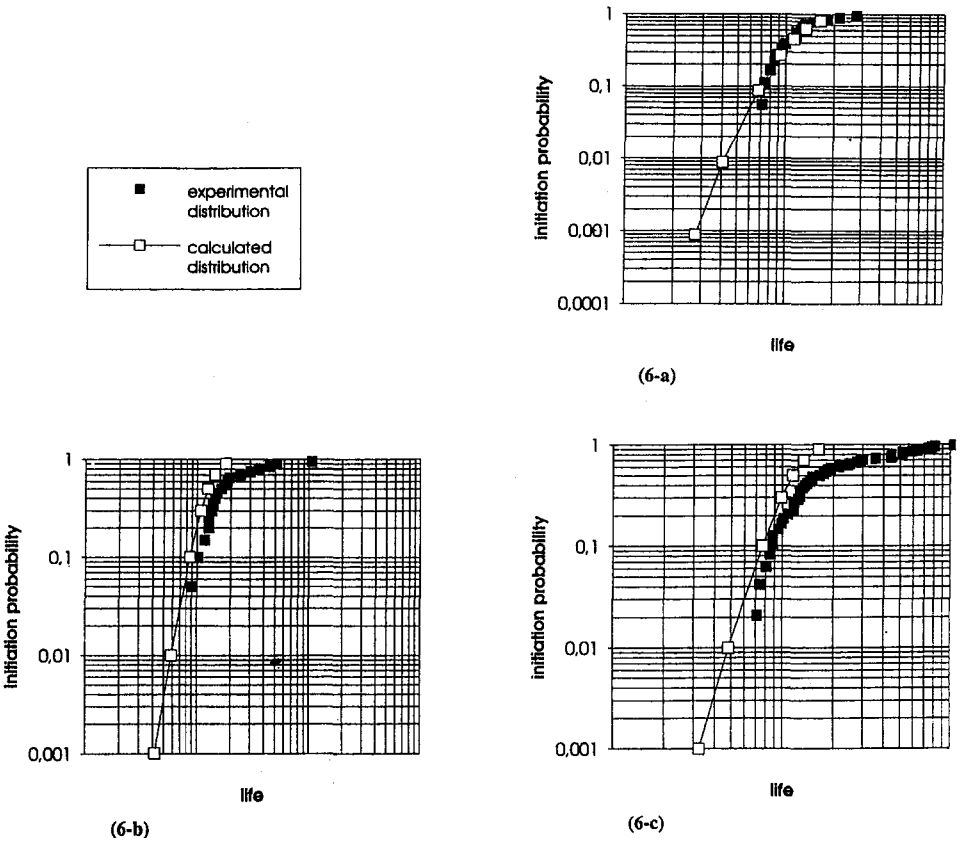

Fig. 6 Comparison of the calculated and experimental life distribution for (*a*) surface inhomogeneities, (*b*) subsurface inhomogeneities, (*c*) internal inhomogeneities

V (1) Validation of Predicted Life Distribution on the Basis of Laboratory Tests. Figures 6(*a*) to 6(*c*) show the correlation between experimental life and calculated life distributions for strain controlled fatigue tests on laboratory specimens in N18.

The specimen is modeled considering three domains:

- a surface domain for inhomogeneities intersecting the surface.
- a subsurface volume domain for inhomogeneities located in the vicinity of the surface.
- an internal volume domain for inhomogeneities located far from the surface.

Experimental results are classified into three categories corresponding to the previous three domains. The distance of the inhomogeneity from the surface is measured on the fractographies of initiation sites.

Figure 6(*a*) compares experimental life distribution with calculated life distribution for inhomogeneities intersecting the surface of the specimen. The correlation is good for all initiation probability levels.

Figure 6(*b*) compares experimental life distribution with calculated life distribution for inhomogeneities located near the surface of the specimen. The correlation is also correct.

Figure 6(*c*) compares experimental life distribution with calculated life distribution for all the inhomogeneities of the specimen. The correlation is good for low initiation probabilities. This is where the method must be validated since it will be used to determine a reliable life for which the reliability level required to cover the material scatter is typically 0.999.

In the range of high initiation probabilities (0.4 to 1) the deviation noted between prediction and experience is due to the use of a simplified model for the life of internal inhomogeneities. In actual fact, due to the higher criticality of surface initiations (Fig. 1), the surface inhomogeneities life model has been identified first and then transposed in a simple and conservative way to internal inhomogeneities, which have long lives. This conservative modeling is enough to estimate the minor contribution of these inhomogeneities to low initiation probabilities (short lives) mainly ruled by surface and subsurface inhomogeneities. Work is currently under way to define a life model specific to them.

V (2) Validation on the Basis of Small Test Disks. Several scale half-disks were tested in various conditions:

- N18 at 650°C
- N18 at 600°C
- seeded Astroloy at 600°C

Since the number of tested disks is rather small, the validation is based on the comparison of calculated median and 0.9 reliability lives with experimental lives for each condition. Figure 7

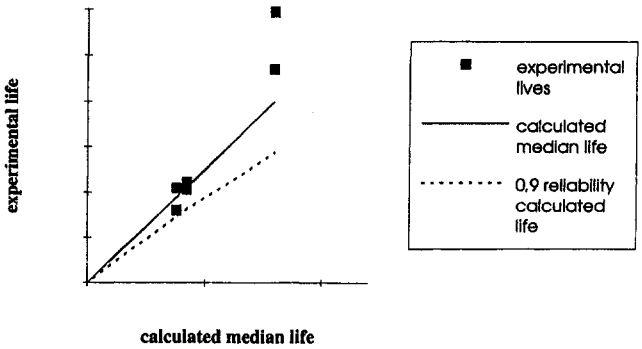

Fig. 7 Comparison of calculated median and 0.9 reliability lives with experimental lives for small test disks

Downloaded 02 Jun 2010 to 171.66.16.104. Redistribution subject to ASME license or copyright; see http://www.asme.org/terms/Terms_Use.cfm

shows these results. The predicted median life is fairly well correlated with experimental results. As a conclusion, the methodology is able to predict correctly the life of an industrial component. Further testing is under way to increase the validation level of the method on industrial components.

VI Conclusions

The proposed method has been developed to overcome the problem of predicting a reliable low cycle fatigue life for powder metallurgy parts when initiation occurs on inhomogeneities like ceramic inclusions or porosities. It is based on a probabilistic modelization of the scale effect combined with a stress and temperature-dependent probabilistic life model for each inhomogeneity size and position in the part. The application of the method requires all the volume and surface of the part to be analyzed in a partition of the stress and temperature fields. A good correlation is obtained between predicted and experimental lives on both small laboratory specimens and scale half-disks representative of aircraft turbine disks.

As the method has already been validated from a large number of laboratory fatigue specimens tested in the various loading and thermal conditions of an aircraft engine rotating component, an extensive validation program is currently under way to confirm the good prediction capability of the method for representative or real engine components tested in both military and commercial conditions.

References

Domas, P. A., 1992, "Substantiating Powder Metal Life Methodologies for Engines," AGARD Report 790, "Impact of Materials Defects on Engine Structure Integrity," pp. 11–1 to 11–8.

Lautridou, J. C., de Bussac, A., and Soniak, F., 1993, "A Probabilistic Model for Fatigue Life Prediction of P.M. Ni Base Super Alloys Containing Inclusions," *Proceedings of the 5th Int. Conf. on Fatigue and Fatigue Thresholds,* Montreal, Canada.

McCartney, L. N., 1980, "Can Safety Factors Be Reduced Safely When Designing Against Fatigue?" *Fatigue Engng. Mater. Struct. II,* pp. 387–400.

Pineau, A., 1990, "Super Alloys Discs Durability and Damage Tolerance in Relation to Inclusions," in: *High Temper. Mater. for Power Engng.,* E. Bachelet et al., eds., pp. 913–934.

Downloaded 02 Jun 2010 to 171.66.16.104. Redistribution subject to ASME license or copyright; see http://www.asme.org/terms/Terms_Use.cfm

Fatigue Cracking in Fiber-Reinforced Metal Matrix Composites Under Mechanical and Thermal Loads

G. Bao
Department of Mechanical Engineering,
The Johns Hopkins University,
Baltimore, MD 21218

R. M. McMeeking
Department of Mechanical and
Environmental Engineering,
University of California,
Santa Barbara, CA 93106

This article reviews micromechanical models developed for fatigue cracking in fiber-reinforced metal matrix composites under mechanical and thermal loads. Emphasis is placed on the formulae and design charts that can quantify the fatigue crack growth and fiber fracture. The composite is taken to be linear elastic, with unidirectional aligned fibers. Interfacial debonding is assumed to occur readily, allowing fibers to slide relative to the matrix resisted by a uniform shear stress. The fibers therefore bridge any matrix crack that develops. The crack bridging traction law includes the effect of thermal expansion mismatch between the fiber and the matrix and a temperature dependence of the frictional shear stress. Predictions are made of the crack tip stress intensities, matrix fatigue crack growth, and maximum fiber stresses under mechanical or thermomechanical loads. For composites under thermomechanical load, both in-phase and out-of-phase fatigue are modeled. The implications for life prediction for fiber-reinforced metal matrix composites are discussed.

1 Introduction

Fiber-reinforced metal matrix composites (MMC) are designed and developed for high-performance aerospace applications, including advanced gas turbine engines and supersonic airframes. Under combined thermal and mechanical loads, fatigue cracking often occurs in the composite, reducing the load carrying capacity, and sometimes leading to catastrophic failure. Prediction of fatigue crack growth in fiber-reinforced metal matrix composites under thermomechanical loading is of critical importance in the safe design of aerospace structures.

The present understanding of fatigue behavior of unidirectional fiber-reinforced MMCs is as follows. Under cyclic tensile loading in the fiber direction, matrix fatigue cracks initiate from defects such as broken fibers, notches, or holes. When the fiber/matrix interface is relatively weak, debonding and sliding occur readily along the interface, allowing the fibers to bridge the matrix crack in its wake, thus reducing the crack tip stress intensity and the fatigue crack growth rate. If the maximum applied stress is sufficiently low, the stresses in the bridging fibers are less than the fiber strength; the fibers do not break and the rate of matrix fatigue crack growth reaches a steady state. If the maximum applied stress is high, the bridging fibers will break at a critical crack length, leading to an accelerated crack growth rate and the final rapture.

In the absence of thermal loading, crack bridging models have been developed (e.g., Marshall et al., 1985; Marshall and Cox, 1987; Hutchinson and Jensen, 1990) based on the assumption that the fractional sliding shear stress τ is a constant along the interface. Corresponding mechanical fatigue crack growth analyses have been performed for metal matrix composites by McMeeking and Evans (1990) and Bao and McMeeking (1994a). Comparisons between the model predictions and experimental measurements at room temperature made by Walls et al. (1993) show good agreement. When fibers are perfectly bonded to the matrix, they must fracture simultaneously with the matrix. The composite fatigue behavior can be predicted by simply considering matrix fatigue crack growth under combined thermal and mechanical cyclic stressing.

The roles of bridging fibers may change in the presence of thermal loading. Without thermal loading, the bridging fibers exert closure forces on the crack surfaces, thus increasing the fracture resistance, leading to a much better composite fatigue behavior compared with that of the matrix. With thermal loading, the bridging fibers may act as a "jack" opening the crack; crack bridging could be detrimental rather than helpful. In addition, the bridging contributions are very different in the in-phase and in the out-of-phase thermomechanical fatigue. A systematic analysis of the interplay between crack bridging and thermomechanical loading has been carried out recently by Bao and McMeeking (1994b).

In this paper, micromechanics models developed for fatigue crack growth of metal matrix composites under mechanical and thermomechanical cyclic loadings are reviewed. Emphasis is placed on the formulae and design charts that could quantify the fatigue crack growth and fiber fracture. For composites under thermomechanical loads, different roles of fiber bridging in the in-phase TMF and the out-of-phase TMF are examined. Predictions are made of the crack tip stress intensities, matrix fatigue crack growth, and maximum fiber stresses under mechanical or thermomechanical loads. Finally, the implications of the model predictions for the life prediction and design of fiber-reinforced metal matrix composites under thermomechanical loading conditions are discussed.

2 Crack Bridging Analysis

2.1 The Crack Bridging Law. Consider a single mode I crack bridged by intact fibers as shown schematically in Fig. 1. The behavior of intact fibers in the bridging zone is represented by a cylindrical model consisting of a single fiber embedded in a matrix cylinder. Shear lag analysis following Budiansky et al. (1986), McCartney (1987), and Cox (1990) shows that under monotonic thermal and mechanical loadings, the crack opening displacement δ is related to the bridging stress t by

Contributed by the International Gas Turbine Institute and presented at the 40th International Gas Turbine and Aeroengine Congress and Exhibition, Houston, Texas, June 5–8, 1995. Manuscript received by the International Gas Turbine Institute March 18, 1995. Paper No. 95-GT-315. Associate Technical Editor: C. J. Russo.

Copyright © 1996 by ASME

Downloaded 02 Jun 2010 to 171.66.16.104. Redistribution subject to ASME license or copyright; see http://www.asme.org/terms/Terms_Use.cfm

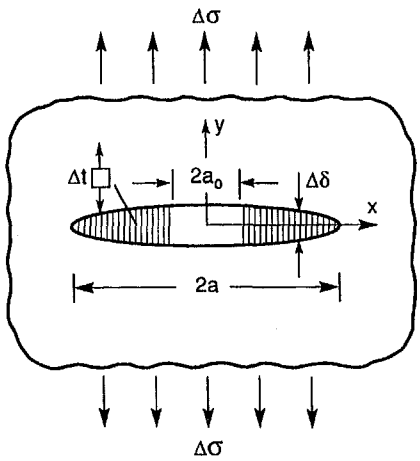

Fig. 1 A partially bridged matrix crack subject to a cyclic stress

$$\delta = \lambda[t + fE_f(\alpha_f - \alpha_m)T]^2 \tag{1}$$

where T is the temperature defined with $T = 0$ being the stress-free processing temperature, and λ is a material parameter given by

$$\lambda = \frac{D(1-f)^2E_m^2}{4f^2E^2E_f\tau} \tag{2}$$

where D is the fiber diameter, f is the volume fraction of fibers, E_m is Young's modulus for the matrix, E_f is Young's modulus for the fiber, E is the rule of mixtures axial modulus for the composite, and τ is the shear stress at the sliding interface at temperature T. It should be noted that under certain circumstances the crack will tend to close rather than open during monotonic loading. For example, if T is negative and α_f is greater than α_m, the crack will tend to close when $t = 0$. This will also be true if t is positive but small. It will be assumed that the crack can remain open and traction free on the matrix surface at all times so that matrix closure effects will not be taken into account. This will generally be true for the common situation in which $a_m > a_f$ and T is negative. Without thermal loading, the crack bridging law (2) becomes $\delta = \lambda t^2$, which has been used in previous fatigue studies (e.g., Bao and McMeeking, 1994a).

Following McMeeking and Evans (1990), the crack bridging law under cyclic loading conditions is similar to that in Eq. (1) with

$$\Delta\delta = \pm\tfrac{1}{2}\lambda[\Delta t + fE_f(\alpha_f - \alpha_m)\Delta T]^2 \tag{3}$$

where $\Delta\delta$ is the change in crack opening displacement, Δt is the change in bridging stress, ΔT is the temperature change. The sign preceding λ should be chosen according to whether $\Delta t + fE_f(\alpha_f - \alpha_m)\Delta T$ is positive or negative. The positive sign is used when this term is positive and the negative sign is used when the term is negative. The parameter λ is that given in Eq. (2) except that τ is replaced by $[\tau(T_1) + \tau(T_2)]/2$ where T_1 and T_2 are the temperatures at the extremes of the cyclic range; i.e., the relevant interface shear stress is the average of the interface shear stresses at the extremes of the cycle. This does not necessarily mean that τ is a linear function of T, as demonstrated by Bao and McMeeking (1994b).

2.2 The Bridging Stress Distribution. There are two key quantities pertaining to the thermomechanical fatigue behavior of fiber-reinforced metal matrix composites. One is the stress intensity amplitude at the crack tip, which governs the matrix cracking, and the other is the maximum stress in the bridging fibers, which dictates fiber fracture. Both can be obtained from the stress profile in the bridging zone. Typically, the fatigue specimens for matrix cracking fatigue tests are notched panels with finite widths. The calculation of bridging stress distribution in such specimens can be carried out using finite elements (e.g., Bao and McMeeking, 1994a) or by solving integral equations (Cox and Lo, 1992). To gain some insight into the role of crack bridging in thermomechanical fatigue, attention in this paper is focused on a mode I, plane strain crack in a large body, as shown schematically in Fig. 1. Specifically, a linear elastic composite infinite body contains a center crack of length $2a$ and is subjected to remote cyclic loading $\Delta\sigma$. The unbridged center section has the length $2a_0$, while the sections of length $a - a_0$ at both ends of the crack represent the segment bridged by intact fibers. Clearly a fully bridged crack is the special case $a_0 = 0$. A partially bridged crack can be created by fiber failure or by the initial presence of a notch. Thus $2a_0$ can be the initial notch size but it can also be the current unbridged length due to fiber failure.

Under cyclic loading conditions, the crack opening displacement change $\Delta\delta$ in the bridging zone is related to the change in bridging stress Δt by the crack bridging traction law Eq. (3). The elastic analysis of the body follows a standard approach as used by Marshall et al. (1985) and McCartney (1987). $\Delta\delta$ is related to the amplitude of the applied stress $\Delta\sigma$ and the amplitude of the bridging stress Δt by

$$\Delta\delta = \Delta\delta_A + \Delta\delta_B \tag{4}$$

where

$$\Delta\delta_A = \frac{4}{\bar{E}}\Delta\sigma\sqrt{a^2 - x^2} \tag{5}$$

is the crack opening change induced by the applied stress amplitude $\Delta\sigma$ and

$$\Delta\delta_B = -\frac{4}{\bar{E}}\int_{a_0}^{a}\Delta t(\xi)H(\xi, x, a)d\xi \tag{6}$$

is the contribution to $\Delta\delta$ due to the bridging fibers. In Eqs. (5) and (6), $\bar{E}$ is the effective Young's modulus considering material orthotropy (Bao and McMeeking, 1994a) and x is the position in the bridging zone measured from the center of the notch (Fig. 1). The Green's function H in Eq. (6) is given by

$$H(\xi, x, a) = \frac{1}{\pi}\log\left|\frac{\sqrt{a^2 - x^2} + \sqrt{a^2 - \xi^2}}{\sqrt{a^2 - x^2} - \sqrt{a^2 - \xi^2}}\right| \tag{7}$$

Substitution of Eqs. (3), (5), and (6) into Eq. (4) and use of suitable normalizations shows that the governing equation for Δt can be expressed as

$$\pm[\Delta\Sigma_b(\bar{x}) + \Delta\theta]^2/16 + \int_{a_0/a}^{1}\Delta\Sigma_b(\xi)H(\xi, \bar{x}, 1)d\xi = \Delta\Sigma\sqrt{1 - \bar{x}^2} \tag{8}$$

where $\bar{x} = x/a$,

$$\Delta\Sigma_b = \frac{D(1-f)^2E_m^2\bar{E}\Delta t}{2f^2E^2E_f\tau a}, \quad \Delta\Sigma = \frac{D(1-f)^2E_m^2\bar{E}\Delta\sigma}{2f^2E^2E_f\tau a} \tag{9}$$

are the nondimensional bridging stress amplitude and nondimensional applied stress amplitude, respectively, and

$$\Delta\theta = \frac{D(1-f)^2E_m^2\bar{E}(\alpha_f - \alpha_m)\Delta T}{2fE^2\tau a} \tag{10}$$

is the nondimensional thermal stress amplitude. The positive sign preceding the bracketed term should be used if the term in brackets is positive whereas the negative sign should be used if the term in brackets is negative.

Downloaded 02 Jun 2010 to 171.66.16.104. Redistribution subject to ASME license or copyright; see http://www.asme.org/terms/Terms_Use.cfm

2.3 Crack Tip Stress Intensity and Maximum Bridging Stress. The crack tip stress intensity amplitude, ΔK_{tip}, is given by

$$\Delta K_{tip} = \Delta K_A + \Delta K_B \tag{11}$$

where $\Delta K_A = \Delta\sigma\sqrt{\pi a}$ is due to the applied stress amplitude and

$$\Delta K_B = -2\sqrt{\frac{a}{\pi}}\int_{a_0}^{a}\frac{\Delta t(x)}{\sqrt{a^2 - x^2}}\,dx \tag{12}$$

is the stress intensity amplitude due to crack bridging. Using the nondimensional parameters defined in Eqs. (9) and (10), we have

$$\frac{\Delta K_{tip}}{\Delta\sigma\sqrt{\pi a}} = 1 - \frac{2}{\pi\Delta\Sigma}\int_{a_0/a}^{1}\frac{\Delta\Sigma_b(\xi)}{\sqrt{1-\xi^2}}\,d\xi \tag{13}$$

All stress intensity factors given below are computed from Eq. (13).

Critical to fiber fracture is the maximum stress in the bridging zone. As demonstrated by McMeeking and Evans (1990), such a stress can be obtained by solving Eq. (8), but with the quantities involved redefined. Specifically, $\Delta t/2$ in Eq. (9) should be replaced by the bridging stress t; $\Delta\sigma/2$ and $\Delta T/2$ in Eqs. (9) and (10) should be changed to the applied stress σ and the temperature T (measured from the stress-free state), respectively. The solution to Eq. (8) will then give the bridging stress $t(x)$ arising due to monotonic loading. Fiber failure models can be applied to the bridging stress to assess the extent of fiber fracture. The values for σ and T used in this calculation should be those occurring simultaneously that produce the largest value for $\sigma + fE_f(\alpha_f - \alpha_m)T$ during the load cycle. This will produce the highest fiber stresses in the cycle.

3 Fatigue Under Mechanical Load

For a composite subject to mechanical load only, the crack bridging analysis has been performed by Bao and McMeeking (1994a) taking $\Delta\theta = 0$ in Eq. (8). Their results for crack tip stress intensities, fatigue crack growth, and maximum bridging stresses are summarized below.

3.1 Matrix Fatigue Cracking Under Mechanical Load. The governing equation for matrix fatigue crack growth in fiber reinforced composite is assumed to be simply the Paris law (McMeeking and Evans, 1990)

$$da/dN = \beta(\Delta K_{tip}/\bar{E}_m)^n \tag{14}$$

where β and n are material parameters for the matrix material, and $\bar{E}_m = \sqrt{(1-f)\bar{E}E_m}$ is an effective modulus accounting for the reduced area of material being cracked as well as the load partitioning between the fiber and matrix. An underlying assumption here is that the fatigue crack growth rate in the matrix is governed by the crack tip stress intensity amplitude, ΔK_{tip}, in accord with the Paris law for the matrix alloy alone. Therefore, the intact fibers contribute to the composite fatigue behavior only through ΔK_{tip}.

Equation (14) can be rewritten in a nondimensional form

$$\frac{N\beta}{a_0}\left[\frac{\Delta\sigma\sqrt{\pi a_0}}{\bar{E}_m}\right]^n = \int_0^{\alpha}\frac{(1-\alpha)^{n/2-2}d\alpha}{[\Delta\kappa(\Delta\Sigma,\alpha)]^n} \tag{15}$$

where $\alpha = 1 - a_0/a$. The normalized crack tip stress intensity amplitude $\Delta\kappa(\Delta\Sigma, \alpha) \equiv \Delta K_{tip}/\Delta K_A$ for a mode I, plane strain crack in a large body (Fig. 1) can be given by

$$\Delta\kappa(\Delta\Sigma,\alpha) = \exp\{-\sin\alpha[A(\Delta\Sigma) + B(\Delta\Sigma)\alpha + C(\Delta\Sigma)\alpha^2]/\alpha^{1/4}\} \tag{16a}$$

where

$$A(\Delta\Sigma) = -0.049 + 3.0/\sqrt{\Delta\Sigma} - 0.027/\Delta\Sigma$$

$$B(\Delta\Sigma) = -0.399 + 2.504/\sqrt{\Delta\Sigma} - 3.207/\Delta\Sigma + 0.379/\Delta\Sigma^{3/2}$$

$$C(\Delta\Sigma) = 0.439 - 1.784/\sqrt{\Delta\Sigma} + 1.374/\Delta\Sigma - 0.04/\Delta\Sigma^{3/2} \tag{16b}$$

This curve-fitting formula is accurate to within a few percent of the numerical results given by Bao and McMeeking (1994a) for the range $0.1 \le \Delta\Sigma \le 12$.

For a center-notched tensile specimen having width $2w$ and crack lengths $a < 0.5w$, Eq. (16) is valid with $\Delta\kappa(\Delta\Sigma, \alpha)$ in Eq. (15) being replaced by $\Delta\kappa(\Delta\Sigma, \alpha)F(a/w)$ where $F(a/w)$ is given by

$$F(a/w) = \sqrt{\sec\frac{\pi a}{2w}}. \tag{17}$$

Fatigue crack growth curves can be predicted by inserting Eq. (16) into Eq. (15) and performing numerical integration. To illustrate, in Fig. 2, curves of normalized crack extension versus normalized load cycles are plotted for a center crack in a large body for $n = 2$ for four values of $\Delta\Sigma_0$ where $\Delta\Sigma_0 = \Delta\Sigma a/a_0$. Note that $\Delta\Sigma_0$ remains constant if $\Delta\sigma$ is held fixed during fatigue. The plot shows that without fiber failure, the matrix crack does not have to extend very far compared to the original notch length for the rate of crack extension to diminish dramatically. A comparison of the predictions with experimental data (Walls et al., 1993; Zok et al., 1994) for fatigue cracking of a fiber-reinforced titanium/SiC is given in Fig. 3. In performing the comparison, the parameters β and n in Eq. (14) were taken to be those of the matrix alloy (Walls et al., 1993). The value of the interface sliding stress τ, however, is uncertain. Consequently, several values of τ were used in making theoretically predictions and it appears that $\tau = 20$ MPa gives the best agreement with the experimental results.

3.2 Fiber Failure Under Mechanical Load. Experimental evidence (Walls et al., 1993) shows that when the applied stress is high, fibers fail along the matrix fatigue crack, accelerating the matrix crack growth and leading to a loss of load carrying capacity. Therefore, it can be suggested that the onset of fiber failure is effectively the end of the useful life for a fiber-reinforced metal matrix composite material. The onset of fiber failure depends primarily on the fiber strength, which, in practice, has a statistical distribution. However, to gain some insight into the influence of applied stress on fiber fracture, we

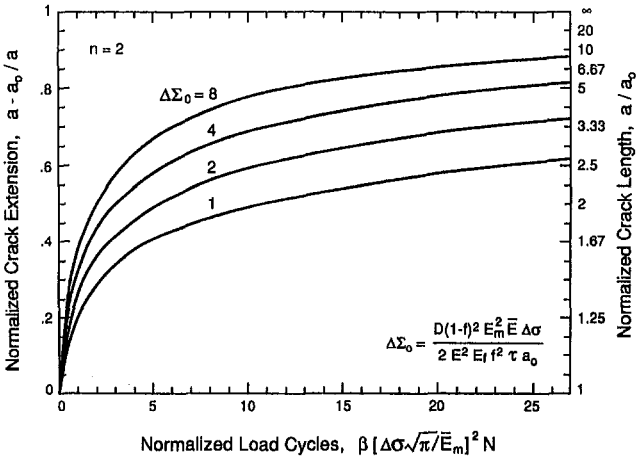

Fig. 2 Predicted fatigue crack growth curves under mechanical load when fibers do not fail

Downloaded 02 Jun 2010 to 171.66.16.104. Redistribution subject to ASME license or copyright; see http://www.asme.org/terms/Terms_Use.cfm

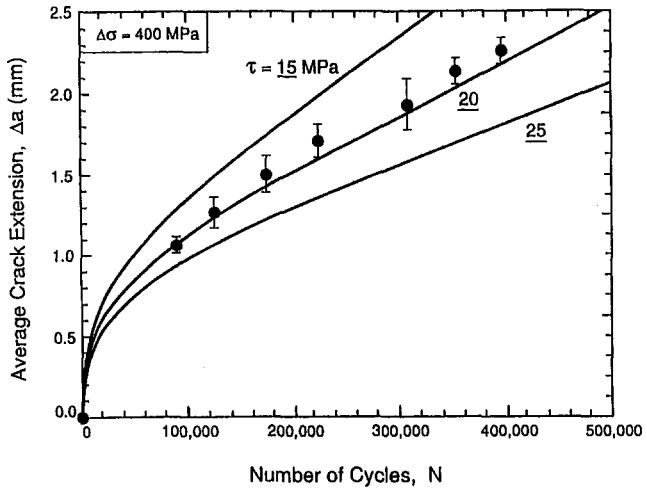

Fig. 3 Comparison of an experimental fatigue crack growth curve with model predictions

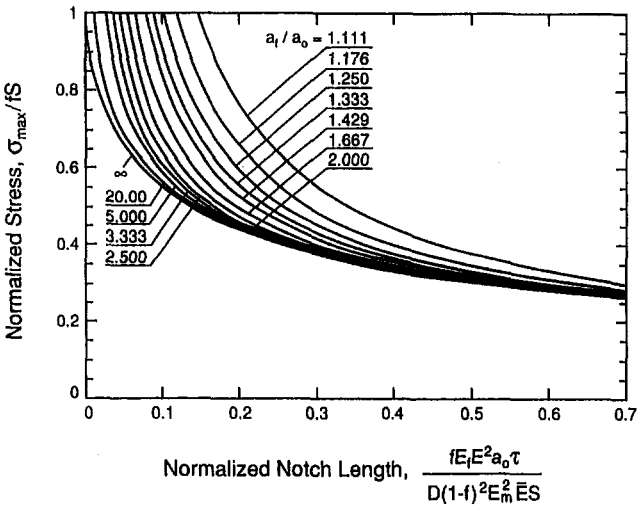

Fig. 4 Relationship between applied stress, fiber strength, and notch length for a specified extension of the matrix crack before fiber failure will occur

assume that the fibers have a unique strength S. Certain fibers have a narrow strength distribution, so that the assumption of a unique strength is a reasonable approximation to this case. Fibers with a wide strength distribution would fail more gradually than predicted below. In addition, failure of fibers with a wide distribution of strengths can occur inside the matrix rather than at the matrix crack as assumed below.

To predict the onset of fiber failure, i.e., the crack length at which fibers will break, calculations for t_{max}, the maximum stress in the bridging zone, have been carried out by Bao and McMeeking (1994a) for a center crack in a large body. The condition for fiber failure was set to be $t_{max}/f = S$. Defining a nondimensional fiber strength η

$$\eta = \frac{D(1-f)^2 E_m^2 \bar{E} S}{E^2 E_f f a_0 \tau}, \tag{18a}$$

a nondimensional maximum applied load Σ

$$\Sigma = \frac{D(1-f)^2 E_m^2 \bar{E} \sigma_{max}}{E^2 E_f f^2 a_0 \tau}, \tag{18b}$$

and a nondimensional crack bridging length $\alpha = (a - a_0)/a_0$, the numerical results of Bao and McMeeking (1994a) can be represented by the following fitting formula:

$$\eta = \phi(\Sigma) \exp\left[- \frac{(1-\alpha)^{m(\Sigma)}}{\sqrt{\alpha}\,\psi(\Sigma)} \right] \tag{19a}$$

where

$$\phi(\Sigma) = \sqrt{\Sigma^2 + (6\pi\Sigma^2)^{2/3}} \tag{19b}$$

$$\psi(\Sigma) = 13.1 - 2.3\Sigma + 0.2\Sigma^2 \tag{19c}$$

$$m(\Sigma) = 14.037 - 15.327\Sigma + 7.237\Sigma^2 - 1.5628\Sigma^3 + 0.1274\Sigma^4 \tag{19d}$$

Given fiber strength S, the maximum applied stress σ_{max}, and the initial notch size a_0, the onset of fiber failure a_f can be predicted. Shown in Fig. 4 are ratios of a_f/a_0 for various levels of loading and initial notch length taking fiber strength and volume fraction into account. For a given notch length, the contours in Fig. 4 indicate the permissible maximum stress for a given extension of the matrix crack. For example, the contour marked $a_f/a_0 = 20$ shows the maximum stress that will cause the matrix crack to reach 20 times the length of the initial notch before fiber breakage. The line with $a_f/a_0 = \infty$ is the boundary between fiber nonfailure and failure: For a maximum stress lying on or below this contour, the matrix crack can extend to infinity without fiber failure. The plot in Fig. 2 can be used to predict how many cycles of constant load amplitude will occur before the matrix crack reaches the extent at which fiber failure will commence. Thus, for large components, Figs. 2 and 4 can be combined to provide a basis for life estimation up to fiber failure for values of $\Delta\Sigma_0$ ranging from 1 to 8.

In general, the formula given in Eq. (19) is valid for the infinite body only. However, in the case of the finite strip with the matrix crack extending across the entire width so that $a = w$, we have (Bao and McMeeking, 1994a)

$$\eta^2 = \Sigma^2/(1 - a_0/w)^2 + [6\pi F^2(a_0/w)\Sigma^2]^{2/3} \tag{20a}$$

or, equivalently,

$$\left[\frac{(1-a_0/w)fS}{\sigma_{max}}\right]^{4/3} - \left[\frac{\sigma_{max}}{(1-a_0/w)fS}\right]^{2/3} = \left[\left(1 - \frac{a_0}{w}\right)^2 F^2\left(\frac{a_0}{w}\right)\frac{6\pi}{\eta}\right]^{2/3} \tag{20b}$$

where η is given by Eq. (18a) and $F^2(a_0/w) = \sec(\pi a_0/2w)$. Based on Eq. (20$b$), a map is constructed in Fig. 5 to show

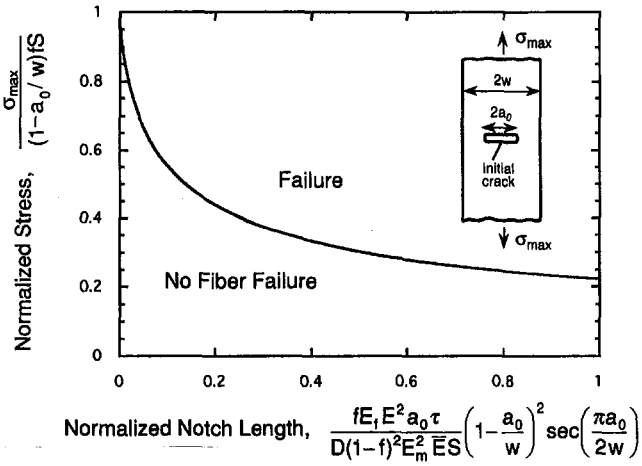

Fig. 5 Map for fiber failure and nonfailure in a finite strip with a central notch

Downloaded 02 Jun 2010 to 171.66.16.104. Redistribution subject to ASME license or copyright; see http://www.asme.org/terms/Terms_Use.cfm

when fibers will fail and when they do not. Below the line in the diagram, no fiber failure will occur no matter how much matrix fatigue crack growth occurs. However, if a component is highly stressed so that it operates above the line in the diagram, eventually fiber failure will occur during matrix fatigue crack growth. Cunningham (1993) and Walls et al. (1993) have found this diagram to be effective in distinguishing the incidence of fiber failure from nonfailure in experiments.

4 Fatigue Under Thermal and Mechanical Loads

Under thermomechanical loading conditions, the fatigue behavior of the composite is influenced by the thermal expansion mismatch between fibers and the matrix. In most of the fiber-reinforced metal matrix composites, the fibers are made of ceramics with coefficient of thermal expansion (CTE) α_f lower than that of the metal matrix α_m. Thus when cooling down, tensile stress builds up in the matrix, while compressive stress results in the fibers; the opposite is true when the composite is warming up. The thermal stresses due to CTE mismatch can be very high, possibly exceeding the applied mechanical stress range. The actual coupling of thermal stress and mechanical stress can be very complex, for both the applied load and temperature change independently with time. As in most of the thermomechanical fatigue analysis, two limiting cases are considered: The temperature change ΔT is completely in phase (IP) or completely out-of-phase (OP) with the mechanical loading amplitude $\Delta\sigma$. Accordingly, $\Delta\theta < 0$ represents in-phase TMF while $\Delta\theta > 0$ represents out-of-phase TMF.

4.1 Bridging Stress Distribution. For a partially bridged crack in a large body with an unbridged segment $2a_0$, the bridging stress distributions have been obtained by solving Eq. (8) numerically (Bao and MeMeeking, 1994b) for various values of the crack length ratio a/a_0 and the nondimensional mechanical and thermal loading $\Delta\Sigma$ and $\Delta\theta$. The results show that thermal stress alone can prop open partially bridged matrix cracks and cause a positive stress intensity factor. This will occur if T is negative and α_m exceeds α_f, as is the case typically for metal matrix composites, which are cooled down from their processing temperature. In the cyclic case, the thermal bridging stresses will cause a crack tip stress intensity factor amplitude. Thus purely thermal cycling will cause matrix fatigue crack propagation for partially bridged cracks.

Figure 6 shows the bridging stress distributions for combined mechanical and thermal cycling when $\Delta\Sigma = 0.25$ and $a_0/a = 0.5$. Results for both positive and negative $\Delta\theta$ are shown. All curves in Fig. 6 have peak stresses at the notch root indicating that fiber fracture is likely to start there. The bridging stress amplitude near the crack tip is compressive when $\Delta\theta$ is positive. This occurs because the crack opening at the tip is zero and

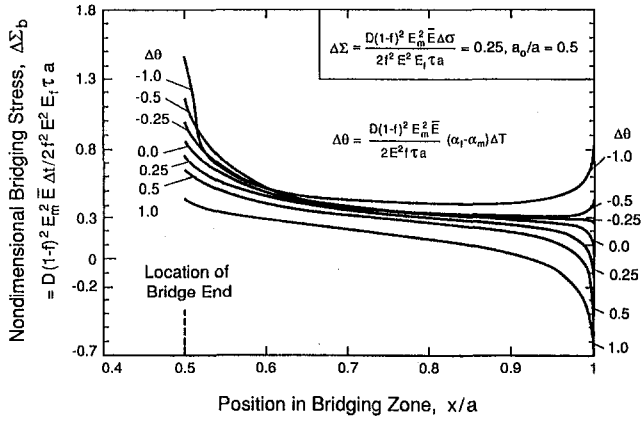

Fig. 6 Bridging stress for a partially bridged crack

Eq. (3) shows that the bridging stresses have to be compressive to sustain this when $\Delta\theta$ is positive. Similarly, when $\Delta\theta$ is negative, the bridging stress at the crack tip has to be tensile. Thus a major portion of the differences in the results shown in Fig. 6 is simply the offset caused by this effect. The apparent change in trend as $\Delta\theta$ decreases from -0.5 to -1.0 is because the first term on the left-hand side of Eq. (8) changes sign when $\Delta\Sigma_b + \Delta\theta$ becomes negative, and the solution for $\Delta\Sigma_b$ must be continuous. In fact, a similar transition appears on the $\Delta\theta = -0.5$ curve but it is hardly seen.

It is evident from Fig. 6 that, compared with the purely mechanical fatigue case ($\Delta\theta = 0$), the bridging stress is lower when $\Delta\theta$ is positive and higher when $\Delta\theta$ is negative. Consequently, the crack tip stress intensity amplitude is expected to be higher when $\Delta\theta$ is positive. However, when $\Delta\theta$ is negative, the maximum stress in the bridging zone is higher. Therefore, in the typical case in which positive $\Delta\theta$ represents out-of-phase TMF, the crack tip stress intensity amplitude is greater than in the isothermal case with the same applied stress. Similarly, in the typical case in which negative $\Delta\theta$ represents in-phase TMF, the crack tip stress intensity amplitude is lower than in the isothermal case. This ranking is the same as was found for fully bridged cracks. However, the maximum bridging stress, which will tend to induce fiber failure, is higher in in-phase TMF than in the isothermal case and is lower in out-of-phase TMF than in the isothermal case. Thus, in typical cases, in-phase TMF will cause less rapid matrix fatigue crack growth than the isothermal case at the same stress but will be more prone to fiber failure. In contrast, in typical cases, out-of-phase TMF will cause more rapid matrix fatigue crack growth than the isothermal case at the same stress but will be less prone to fiber failure.

4.2 Matrix Fatigue Cracking Under Thermomechanical Load. Figure 7 shows the stress intensity factor amplitude due to purely thermal cycling (i.e., no mechanical stress cycling) for partially bridged cracks. The results are shown for several levels of thermal stress amplitude and are shown as a function of bridge length as a fraction of total crack length. The same results apply for positive and negative ΔT, with ΔK_{tip} positive if $(\alpha_f - \alpha_m)\Delta T$ is positive and vice versa. These results show, as expected, that there is no stress intensity for unbridged cracks ($a = a_0$) and that the results converge to the fully bridged results when the unbridged segment is a negligible fraction of the matrix crack length. In between, ΔK_{tip} increases monotonically with crack length for fixed a_0. However, when shown in the form normalized by $fE_f(\alpha_f - \alpha_m)\Delta T\sqrt{\pi a}$, there is a maximum between the results for short and long bridge lengths.

Shown in Figs. 8(a) and 8(b) are normalized crack tip stress intensities $\Delta K_{tip}/\Delta K_A$ plotted against the normalized bridge length $(a - a_0)/a$ for $\Delta\Sigma_0 = 0.5$ for several values of $\Delta\theta_0$ where $\Delta K_A = \Delta\sigma\sqrt{\pi a}$, $\Delta\Sigma_0 = (a/a_0)\Delta\Sigma$, and $\Delta\theta_0 = (a/a_0)\Delta\theta$. Two features in Fig. 8 are noteworthy. The fatigue driving force ΔK_{tip} increases with increasing $\Delta\theta_0$, as is expected. Further, when $\Delta\theta_0$ is large (say, ≥ 1.0; see Fig. 8(b)), ΔK_{tip} can exceed ΔK_A, the applied stress intensity amplitude. Due to compressive thermal stresses, the development of a bridge can increase the stress intensity factor amplitude. This indicates that in certain circumstances, the fibers prop open the crack rather than providing shielding. Crack bridging, therefore, can be detrimental to the fatigue behavior of the composite. This is in contrast to the isothermal case in which crack bridging always improves the composite fatigue resistance to matrix cracking. Note also, that if $\Delta\theta_0$ is less than -0.5 (see Fig. 8(b)), ΔK_{tip} can become negative. Due to tensile thermal stresses, the development of a bridge can provide so much shielding that the sign of the stress intensity factor reverses. This means that when tensile mechanical stress is added to the applied load, the crack opening will diminish rather than opening further (since the tensile mechanical stress will cause ΔK_{tip} to be less negative), and vice versa. Thus, the crack tip cycling

Downloaded 02 Jun 2010 to 171.66.16.104. Redistribution subject to ASME license or copyright; see http://www.asme.org/terms/Terms_Use.cfm

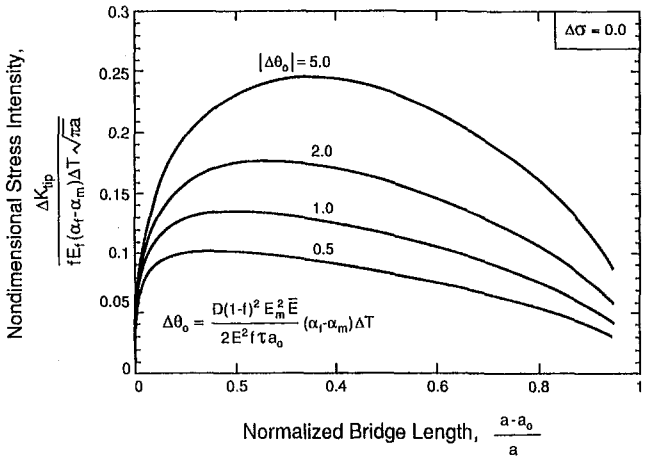

Fig. 7 Stress intensity amplitude as a function of bridge length for a partially bridged crack for temperature cycling

will be out of phase with the mechanical stress cycling. Of course, the rate of fatigue crack growth will be unaffected by this phenomenon since it will depend only on the magnitude of ΔK_{tip}. However, it can be seen in Fig. 8(b) that ΔK_{tip} can pass from positive to negative as a bridge is extended by fatigue crack growth. As a consequence, the rate of fatigue crack growth will diminish as ΔK_{tip} falls to zero and the matrix crack may become nonpropagating. However, a change in the mechanical stress amplitude or the thermal stress amplitude will cause ΔK_{tip} to become nonzero and the crack can be caused to recommence growth. Thus, the trapped state of the fatigue crack would be easily destabilized. However, if $\Delta\theta_0 = -\Delta\Sigma_0$ (i.e., if $fE_f(\alpha_f - \alpha_m)\Delta T = -\Delta\sigma$), the net fatigue driving force for extensively bridged cracks (i.e., $\Delta\sigma + fE_f(\alpha_f - \alpha_m)\Delta T$) will be zero. In this case, ΔK_{tip} will approach zero as a bridge is built by fatigue growth and therefore the matrix fatigue crack will become markedly nonpropagating.

Even if ΔK_{tip} is negative, shutting of matrix fatigue cracks is not likely to be an issue. As emphasized previously, the typical case is a metal matrix with ceramic fibers in which $\alpha_m > \alpha_f$. Such materials are processed at high temperature and used in service at temperatures below the processing level. Thus, the operating temperature is negative. Consequently $fE_f(\alpha_f - \alpha_m)T$ will be positive and could readily be a few hundred MPa. For example, when SiC fibers are used in a Ti alloy matrix with $f = 0.35$, each Celsius degree below the stress-free temperature induces a value for $fE_f(\alpha_f - \alpha_m)T$ of approximately 1 MPa. Thus, as soon as matrix fatigue crack growth occurs and a bridge is developed, a large positive K_{tip} will be induced by that bridge due to the large thermal stress. The fatigue cycling will occur around this mean value of K_{tip} but the cyclic ΔK_{tip} is unlikely to cause the total K_{tip} to go to zero. Thus crack closure is unlikely to occur.

For investigation of the effect of thermal cycling on the fatigue growth of matrix cracks, the Paris law Eq. (14) can be integrated numerically, subject to the results in Figs. 7–8 for $\Delta K_{tip}/\Delta K_A$ with ΔK_A always taken to be positive. Fibers are assumed to remain intact during crack growth. Therefore, the unbridged segment length is always the initial notch length. Figure 9 shows the resulting curves for purely thermal cycling with no mechanical load cycling when the amplitude of the thermal cycles is constant during crack growth. The Paris law exponent is taken to be 2. A small bridge of length 0.001 a_0 was assumed to exist at the beginning of the growth process to initiate fatigue cracking. In Fig. 9, it can be seen that the rate of growth is initially small. This stage corresponds to the left end of Fig. 7 where ΔK_{tip} is small. The rate of growth increases as the crack lengthens and ΔK_{tip} increases. The rate then evolves to a steady level of growth as large bridge lengths are developed. Displayed in Fig. 10 are the resulting fatigue crack growth curves under thermomechanical loads for $\Delta\Sigma_0 = 1$, $n = 2$ for various thermal stress amplitudes. These results are for TMF in which the frequency of temperature cycling is the same as

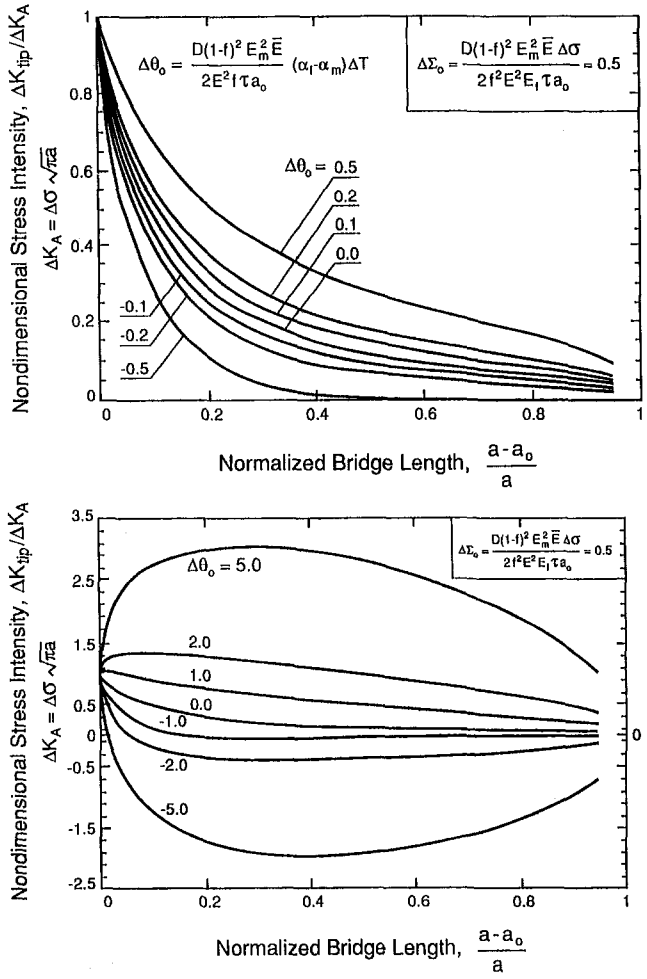

Fig. 8 Stress intensity amplitude as a function of bridge length for a partially bridged crack for thermomechanical cycling

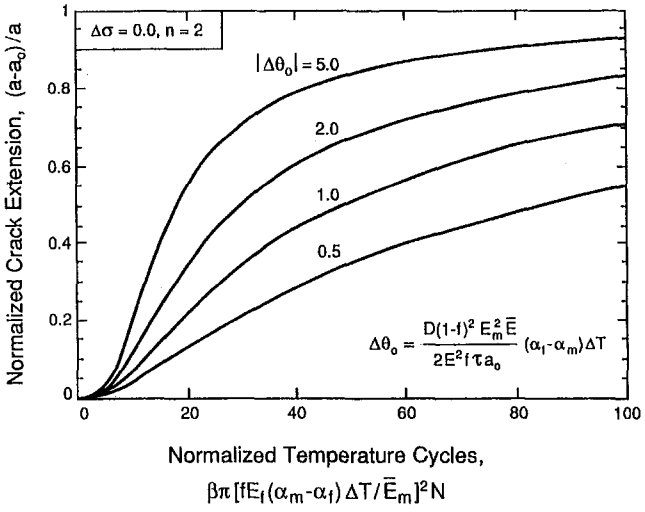

Fig. 9 Crack growth as a function of the number of temperature cycles for fatigue at constant thermal stress

Downloaded 02 Jun 2010 to 171.66.16.104. Redistribution subject to ASME license or copyright; see http://www.asme.org/terms/Terms_Use.cfm

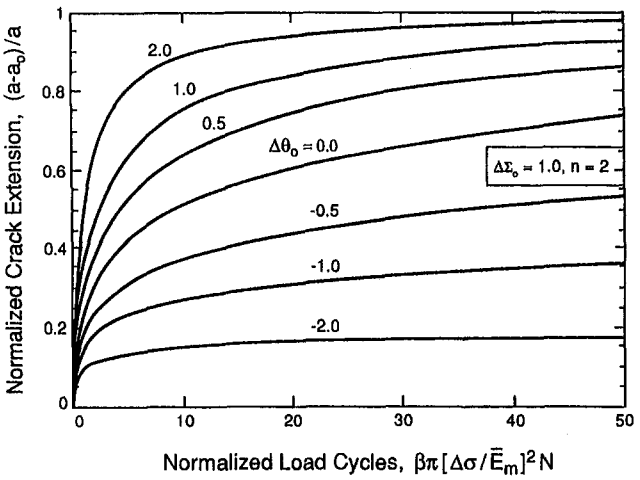

Fig. 10 Crack growth as a function of the number of load cycles for thermomechanical fatigue

that for mechanical load cycling and the two loads are either exactly in-phase or out-of-phase. Also, the amplitude of the temperature and mechanical stress cycles is constant during crack growth. It is found that when $\Delta\theta_0$ is positive, fatigue crack growth is significantly higher than that due to mechanical load alone, depending on the magnitude of the thermal stress amplitude. When $\Delta\theta_0$ is negative, the amount of fatigue growth is less than in the isothermal case.

4.3 Fiber Fracture Under Thermomechanical Load. The governing equation for the bridging stress distribution corresponding to monotonic loading σ and temperature T is essentially identical to Eq. (8). Solutions for the maximum bridging stress t_{max} have been obtained by Bao and McMeeking (1994b) corresponding to the nondimensional applied load Σ_0

$$\Sigma_0 = \frac{D(1-f)^2E_m^2\bar{E}\sigma}{E^2E_f f^2\tau a_0} \tag{21}$$

and the nondimensional thermal load θ_0

$$\theta_0 = \frac{D(1-f)^2E_m^2\bar{E}(\alpha_f-\alpha_m)T}{E^2 f\tau a_0} \tag{22}$$

The fiber strength is assumed to have a unique value S and the condition for fiber failure is set to be $t_{max}/f = S$.

For very large panels, the conditions leading to the preservation of fibers can be summarized in the form of a map as used by Bao and McMeeking (1994a). Such a map is shown in Fig. 11. The map shows combinations of maximum applied stress, temperature, and initial notch length that will lead to fiber failure and to no fiber failure as determined by the deterministic fiber strength. Dividing lines in the map are shown for various temperatures. Below the dividing line, matrix cracks will be grown from the notch, but fibers will never fail and therefore the composite will have infinite life. Above the dividing line, matrix fatigue crack growth will eventually lead to fiber failure, and therefore the composite will have a finite lifetime. It can be seen that if θ_0 is negative, fiber failure is more prone to occur. On the other hand, if θ_0 is positive, it is more likely that matrix fatigue crack growth will occur without fiber failure. For metal matrix composites, θ_0 will generally be positive, since $\alpha_f < \alpha_m$ and T, measured from the stress-free processing temperature, will be negative. Thus, when thermal effects are accounted for, a larger window exists for the preservation of fibers than is apparent from isothermal considerations.

5 Concluding Remarks

Models have been presented for matrix crack growth and fiber fracture in metal matrix composites subject to mechanical and thermal loads. Emphasis is placed on the formulae and design charts that could quantify the effects of applied load, thermal load, and notch size. For a composite under mechanical load only, predictions have been given for the relationship between the matrix crack length and the number of loading cycles of a given amplitude. In addition, the matrix crack length when fibers will begin to fail has been identified in terms of fiber strength, maximum applied stress, and initial notch size. These predictions have been compared to experimental data for fatiguing of titanium/SiC fibrous composites and the model has been shown to work well (Walls et al., 1993; Zok et al., 1994). Predictions have also been made for the matrix crack length as a function of the number of loading cycles for both out-of-phase and in-phase TMF. Maps have been constructed for fiber failure and nonfailure during crack growth for composites under mechanical load or thermomechanical load.

In making the comparison between the model and the data, empirical values have been used for fiber and matrix elastic moduli, fiber volume fraction, fiber diameter, monolithic matrix fatigue crack growth rates, and the interface shear stress τ. The value of τ for a composite is often uncertain; different τ values may be needed to model the fatigue behavior under various loading conditions. Nevertheless, it is found that without fiber failure, the model with a single value of τ obtained by fitting the fatigue crack growth curve of one experiment can predict the results of other experiments carried out with different notch lengths (Walls et al., 1993).

It has been shown that thermal strains can induce bridging stresses in partially bridged matrix cracks. These stresses can, in turn, alter the stress intensity factor at the tip of the matrix crack and therefore affect the fatigue crack growth rate for the crack. For metal matrix composites, where α_m exceeds α_f, in-phase TMF in which the temperature increases at the same time as the stress will lead to a reduced rate of fatigue crack growth compared to isothermal fatigue. Out-of-phase TMF gives rise to an increased rate of fatigue cracking. On the other hand, in-phase TMF will make it more likely that fibers will fracture and out-of-phase cycling will reduce the likelihood of fiber failure. As in the isothermal case, a low applied stress will avoid fiber failure no matter how long the matrix crack grows, while a high applied stress will cause fiber failure and therefore lead to rapid fatigue cracking since the bridging shielding effect will be destroyed. It is notable that thermal cycling by itself without applied load will induce a crack tip stress intensity factor amplitude and therefore will cause matrix fatigue cracking. However, it should be noted that no data exist for matrix fatigue cracking

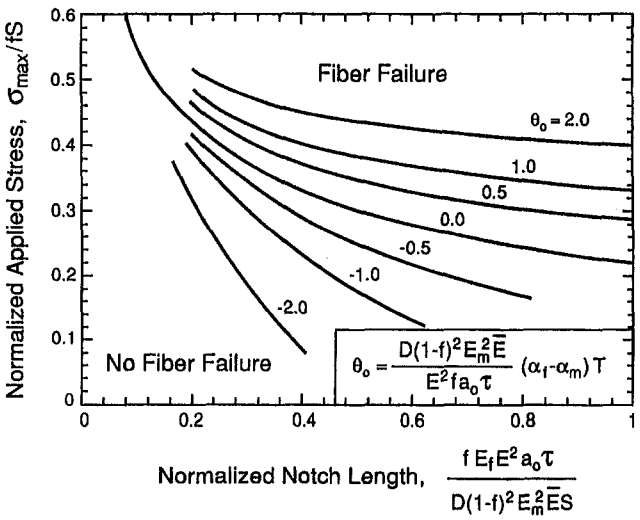

Fig. 11 Map for fiber failure during crack growth under thermomechanical load

Downloaded 02 Jun 2010 to 171.66.16.104. Redistribution subject to ASME license or copyright; see http://www.asme.org/terms/Terms_Use.cfm

by TMF. The validity of the model presented in this paper can only be confirmed by comparison with data.

Acknowledgments

The work of GB was supported in part by NSF through a Research Initiative Award MSS-9210250. The work of RMM was supported in part by the University Research Initiative at UCSB funded by the Advanced Research Projects Agency through ONR contract No. N0014-92-J-1808.

References

Bao, G., and McMeeking, R. M., 1994a, "Fatigue Crack Growth in Fiber Reinforced Metal Matrix Composites," *Acta Metall. Mater.*, Vol. 42, pp. 2415–2425.

Bao, G., and McMeeking, R. M., 1994b, "Thermomechanical Fatigue Cracking in Fiber Reinforced Metal Matrix Composites," submitted to *J. Mech. Phys. Solids.*

Budiansky, B., Hutchinson, J. W., and Evans, A. G., 1986, "Matrix Fracture in Fiber-Reinforced Ceramics," *J. Mech. Phys. Solids*, Vol. 34, pp. 167–189.

Cox, B. N., 1990, "Interfacial Sliding Near a Free Surface in a Fibrous or Layered Composite During Thermal Cycling," *Acta Metall. Mater.*, Vol. 38, pp. 2411–2424.

Cox, B. N., and Lo, C. S., 1992, "Load Ratio, Notch and Scale Effects for Bridged Cracks in Fibrous Composites," *Acta Metall. Mater.*, Vol. 40, pp. 69–80.

Cunningham, S. E., 1993, private communication.

Hutchinson, J. W., and Jensen, H. M., 1990, "Models of Fiber Debonding and Pullout in Brittle Composites With Friction," *Mech. Mater.*, Vol. 9, pp. 139–163.

Marshall, D. B., Cox, B. N., and Evans, A. G., 1985, "The Mechanics of Matrix Cracking in Brittle-Matrix Fiber Composites," *Acta Metall. Mater.*, Vol. 33, pp. 2013–2021.

Marshall, D. B., and Cox, B. N., 1987, "Tensile Fracture of Brittle Matrix Composites: Influence of Fiber Strength," *Acta Metall. Mater.*, Vol. 35, p. 2607.

McCartney, L. N., 1987, "Mechanics of Matrix Cracking in Brittle-Matrix Fiber-Reinforced Composites," *Proc. Roy Soc. Lond.*, Vol. A409, p. 329.

McMeeking, R. M., and Evans, A. G., 1990, "Matrix Fatigue Cracking in Fiber Composites," *Mech. Mater.*, Vol. 9, pp. 217–227.

Walls, D. P., Bao, G., and Zok, F. W., 1993, "Mode I Fatigue Cracking in a Fiber Reinforced Metal Matrix Composite," *Acta Metall. Mater.*, Vol. 41, pp. 2061–2071.

Zok, F. W., Connell, S. J., and Du, Z. Z., 1994, "Fatigue Maps for Titanium Matrix Composites," to be published in ASTM STP on *Life Prediction Methodology for Titanium Matrix Composites.*

Downloaded 02 Jun 2010 to 171.66.16.104. Redistribution subject to ASME license or copyright; see http://www.asme.org/terms/Terms_Use.cfm

Determination of Blade Stresses Under Constant Speed and Transient Conditions With Nonlinear Damping

J. S. Rao
Department of Mechanical Engineering,
Indian Institute of Technology,
New Delhi 110 016, India

N. S. Vyas
Department of Mechanical Engineering,
Indian Institute of Technology,
Kanpur 208 016, India

Determination of resonant stresses is an important step in the life estimation of turbomachine blades. Resonance may occur either at a steady operating speed or under transient conditions of operation when the blade passes through a critical speed. Damping plays a significant role in limiting the amplitudes of vibration and stress values. The blade damping mechanism is very complex in nature, because of interfacial slip, material hysteresis, and gas dynamic damping occurring simultaneously. In this paper, a numerical technique to compute the stress response of a turbine blade with nonlinear damping characteristics, during steady and transient operations of the rotor, is presented. Damping is defined as a function of vibratory mode, rotor speed, and strain amplitude. The technique is illustrated by computing the stress levels at resonant rotor speeds for typical operation of a turbomachine.

Introduction

Fatigue analysis of turbomachine blading and consequent life prediction essentially requires the stress loading history of the blade. The blade during its operational span undergoes various transient rotor operations like step-up, step-down, partial admission, etc., in addition to steady-state rotor operations.

It is well established that damping in a vibratory system plays a very significant role in the estimation of resonant stresses. In the case of a turbomachine blade, important sources of energy dissipation arise from Coulomb effects, material hysteresis, and steam/gas environmental dynamics. These damping mechanisms can be infinitely variable and no predictive theory presently exists to relate these mechanisms to specific blade damping properties.

Lazan (1968) gave a comprehensive coverage of material damping. Coulomb damping mechanisms in engine blades were discussed by Srinivasan and Cutts (1983). Lagnese and Jones (1983) conducted theoretical analysis and measured platform damping. Rieger and Beck (1980) developed a laboratory test rig and investigated damping in several types of turbine blades. Usmani (1986) used a finite element method to determine the free vibration response of a blade-root system with the centrifugal load simulated by axial tension. Finite element methods have also been used by Ostachowics and Szwedowic (1986) and Providakis and Beskos (1986). Rao et al. (1986a) measured blade damping in a spin rig and compared the analytical stress response with the experimental values (1986b). Friction damping in jet engines is described by Griffin and Bielak (1984). Steam damping arising out of oscillatory motion in steam environment has been discussed by Hammons (1982). Crawley (1983) measured aerodynamic damping in vacuum and transonic tunnel tests of a fan. Damping properties of steam turbines and compressor stages have been discussed by Rieger (1984).

Attempts have been made by several researchers to obtain a reasonably good mathematical model for an accurate determination of blade response under steady as well as transient excitation. Stress response of single rotating blades under steady operations was obtained by Rao et al. (1986b). Transient vibration analysis has been undertaken by Irretier (1986) and Vyas et al. (1987). Models for multiple blade models have also been developed. Some recent works include Jones and Muszynska (1983), MacBain and Whaley (1984), and Sinha and Griffin (1984).

Despite a large amount of work reported above, the estimation of damping under the overall influence of various mechanisms and the usage of such damping data in an appropriate mathematical model has been a major hurdle in determining forced response of a turbine blade.

Rao et al. (1986b) carried out theoretical and experimental investigations on the vibratory stresses for steady operations of single rotating turbine blades under the influence of periodic excitation with nozzle wakes simulated by electromagnets. Modal damping data were obtained experimentally for various rotor speeds by Rao et al. (1986a). The average damping ratio ζ_{avg} computed from a decaying modal signal (typically in Fig. 1) using

Contributed by the International Gas Turbine Institute for publication in the JOURNAL OF ENGINEERING FOR GAS TURBINES AND POWER. Manuscript received by the International Gas Turbine Institute April 30, 1992. Associate Technical Editor: L. S. Langston.

Copyright © 1996 by ASME
Downloaded 02 Jun 2010 to 171.66.16.104. Redistribution subject to ASME license or copyright; see http://www.asme.org/terms/Terms_Use.cfm

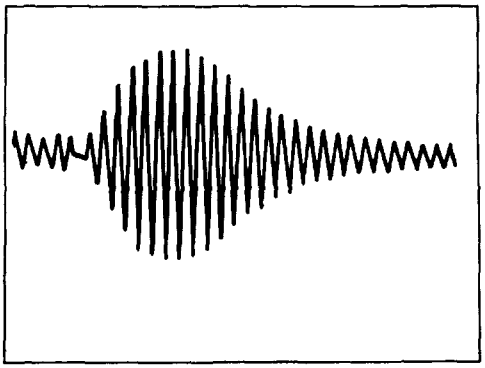

Fig. 1 Typical modal damping signal for rotor speed 700 rpm

$$\delta = \frac{2\pi\zeta_{\text{avg}}}{\sqrt{1-\zeta_{\text{avg}}^2}} = \frac{1}{n}\ln\frac{x_0}{x_n}$$

over the entire decaying range of the signal, was employed to obtain the analytical resonant stress levels. Large discrepancies between these and the corresponding experimental values were observed. This discrepancy was mainly attributed to ignoring the dependence of the damping ratio on the vibratory amplitude. A theoretical model was presented by Vyas et al. (1987) for the transient response of blade during step-up and step-down operations of a turbomachine. The instantaneous resonant stress levels were obtained using the average damping ratio ζ_{avg} as defined earlier.

In this paper, a method of determining the stress values at resonance under steady as well as accelerating conditions of operation is presented to incorporate the dependence of the damping ratio on vibratory amplitude along with its dependence on rotational speed and mode of vibration.

Blade Vibration Model

A single free-standing blade can be considered a tapered, twisted asymmetric aerofoil cross section beam mounted on a rotating disk at a stagger angle (Fig. 2*a*). The cross section of the blade at a height z, is shown in Fig. 2(*b*). The centroid of the cross section is located at G, while O is the center of flexure. The distance between the centroid and center of flexure is given by r_x and r_y as shown. A particle initially at point P with coordinates (x, y) in the Oxy axis system moves to point P_1, under the influence of angular displacement θ and further from P_1 to P_2 by $x(z, t)$ and then vertically to position P' by $y(z, t)$ under the influence of bending displacements. The kinetic energy of the blade rotating with a constant speed is [see Carnegie (1967)]:

$$T = \frac{1}{2}\rho\int_0^l A\left\{\left(\dot{x}+r_y\dot{\theta}\right)^2+\left(\dot{y}-r_x\dot{\theta}\right)^2\right\}dz + \frac{1}{2}\int_0^l I_{cg}\dot{\theta}^2dz + \frac{1}{2}\rho\omega^2\left[-\int_0^l\left\{\left(x'+r_y\theta'+r_y'\theta\right)^2 + \left(y'-r_x'\theta-r_x\theta'\right)^2\right\}(RI_1+I_2)dz + \sin^2\phi\int_0^l A\left(x+r_y\theta\right)^2dz + \cos^2\phi\int_0^l A\left(y-r_x\theta\right)^2dz - \sin 2\phi\int_0^l A\left(x+r_y\theta\right)\left(y-r_x\theta\right)dz\right] \quad (1)$$

For accurate determination of blade stress fields, Reissner's functional has been employed, which simultaneously yields good stress and displacement fields. The Reissner's functional is given by [see Dym and Shames (1973)]:

$$I_R = \iiint_v\left\{\tau_{ij}\epsilon_{ij} - U^*(\tau_{ij})\right\}dv - \iiint_v B_iu_idv - \iint_s T_iu_ids \quad (2)$$

Using beam theory and stress–strain displacement relationships, the above can be shown to be

$$I_R = \int_0^l\left\{-M_yx'' + M_xy'' + T_\theta\theta' + \frac{T_\theta^2}{2C} - \frac{M_x^2I_{y1y1}+M_y^2I_{x1x1}-2M_xM_yI_{x1y1}}{2E\left(I_{y1y1}I_{x1x1}-I_{x1y1}^2\right)}\right\}dz \quad (3)$$

The dynamic Reissner functional is set as

$$L = T - I_R \quad (4)$$

Nomenclature

A = area of cross section
$A_i \cdots F_i$ = generalized coordinates, see Eq. (5)
B_i = body force distribution, see Eq. (2)
a, b = coefficients in trigonometric series of forcing functions
C = torsional stiffness
c = see Eq. (15*b*)
D = diameter of inscribed circle
E = modulus of elasticity
F = see Eq. (15*b*)
F_x, F_y = forcing functions
f = shape function for bending deflections
$\bar{f}$ = shape function for angular deflections
G = modulus of rigidity
H_{mk} = mth harmonic response in the kth mode
h = shape function for bending and twisting moments
$I_1 = A_0(l-z) + \frac{1}{2}A_1(l^2-z^2) + \cdots + \frac{A_n}{n+1}(l^{k+1}-z^{k+1})$
$I_2 = \frac{1}{2}A_0(l^2-z^2) + \frac{1}{3}A_1(l^3-z^3) + \cdots + \frac{A_n}{n+2}(l^{n+2}-z^{n+2})$
I_{x1x1} = second moment of area about $x1x1$ axis
I_{y1y1} = second moment of area about $y1y1$ axis
I_{x1y1} = product moment of area about $x1y1$ axis
I_{cg} = moment of inertia per unit length
I_R = Reissner's functional
K = see Eq. (15*b*)
L = Reissner's dynamic functional
l = blade length
M = moment
M_xM_y = moments in x and y directions
m = harmonic number
n_s = number of nozzles
p_k = natural frequency in kth mode
Q = forcing vector
R = disk radius
r = radius of curvature of blade profile at a point

Downloaded 02 Jun 2010 to 171.66.16.104. Redistribution subject to ASME license or copyright; see http://www.asme.org/terms/Terms_Use.cfm

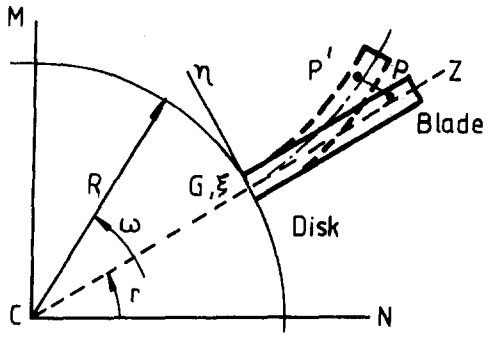

Fig. 2(a) Blade mounted on rotating disk

Using shape functions

$$x = \Sigma A_i(t) f_i(z)$$
$$y = \Sigma B_i(t) f_i(z)$$
$$\theta = \Sigma C_i(t) \tilde{f}_i(z)$$
$$M_x = \Sigma D_i(t) h_i(z)$$
$$M_y = \Sigma E_i(t) h_i(z)$$
$$T_\theta = \Sigma F_i(t) h_i(z) \tag{5}$$

where

$$f_i(Z) = \frac{(i+2)(i+3)}{6} Z^{i+1} - \frac{i(i+3)}{3} Z^{i+2} + \frac{i(i+1)}{6} Z^{i+3}$$

$$\tilde{f}_i(Z) = Z^i - \frac{i}{i+1} Z^{i+1}$$

$$h_i(Z) = \frac{(1-Z)^i}{i+1} \tag{5a}$$

which satisfy the boundary conditions of a cantilever.

The Ritz process

$$\frac{\partial L}{\partial A_i} = 0 \quad \text{etc.} \tag{6}$$

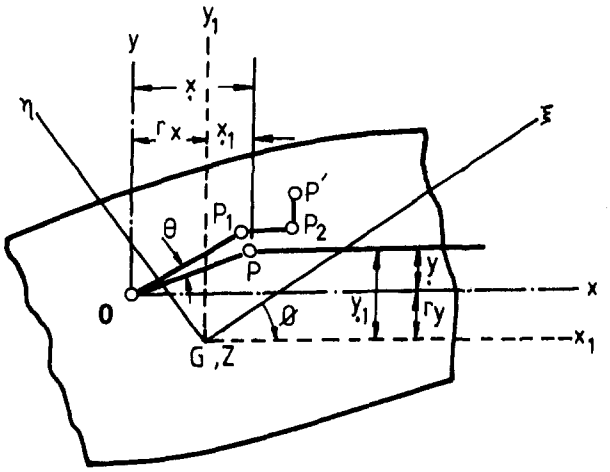

Fig. 2(b) Elemental displacement relations in a blade cross section at distance z from the root

is applied to the dynamic Reissner functional above to obtain the equations of motion

$$p^2[M]\{q\} - [K]\{q\} = 0 \tag{7}$$

where $[M]$ and $[K]$ are mass and stiffness matrices and the vector $\{q\}$ contains

$$\{q\}^T = \{A_i, \cdots, D_i \cdots\}$$

Nozzle Passing Excitation Forces

The excitation forces $F_x(z, t)$, $F_y(z, t)$, $M(z, t)$ in the x, y, and θ directions are periodic with the instantaneous nozzle passing frequency

$$\nu = n_s \omega = n_s(\omega_0 + \alpha t),$$

and can be expressed in Fourier form as,

$$F_x(z, t) = a_{0x}(z) + \sum_m a_{mx}(z)\cos(m n_s \omega t) + \sum_m b_{mx}(z)\sin(m n_s \omega t)$$

Nomenclature (cont.)

r_x, r_y = coordinates of center of flexure
s = surface area
T = kinetic energy
T_i = traction force in ith direction
T_θ = twisting moment
t = time
t_1 = blade profile thickness
U = elemental length along the camber line
U^* = complementary energy density function
u_i = displacement in ith direction
v = volume
xx, yy = coordinate axes through center of flexure
$x1x1, y1y1$ = coordinate axes through centroid
z = distance along blade length
Z = z/L
α = angular acceleration
ϵ_{ij} = strain
$\eta\eta, \xi\xi$ = coordinate axis, see Fig. 2
η = generalized coordinate
ζ = modal damping ratio
ζ_{avg} = average modal damping ratio
ν = nozzle passing frequency
ρ = mass density
$\sigma_1, \sigma_2, \sigma_3$ = principal stresses
σ_{alt} = basic alternating stress
σ_{mean} = basic mean stress due to zeroth NPF component
σ_z = bending stress
τ_{ij} = stress
$\tau_{r\theta}$ = maximum shear stress
τ_{xz}, τ_{yz} = shear stresses
ϕ = stagger angle
ϕ_t = angle through which the tangent rotates
ψ_z = pretwist angle at distance z
ω = angular frequency
ω_0 = initial angular frequency
$'$ = denotes differentiation with z
$\dot{}$ = denotes differentiation with t
$\cdot$ = denotes coordinate quantity, thus, $\dot{x}$

Downloaded 02 Jun 2010 to 171.66.16.104. Redistribution subject to ASME license or copyright; see http://www.asme.org/terms/Terms_Use.cfm

$$F_y(z,t) = a_{0y}(z) + \sum_m a_{my}(z)\cos(mn_s\omega t) + \sum_m b_{my}(z)\sin(mn_s\omega t)$$

$$M(z,t) = a_{0M}(z) + \sum_m a_{mM}(z)\cos(mn_s\omega t) + \sum_m b_{mM}(z)\sin(mn_s\omega t) \quad (8)$$

The forcing functions are obtained from an experiment, and the coefficients in the equations above are obtained by Fourier analysis and given in Table 3.

Steady-State Response—Constant Speed Operation

Blade damping is modeled as nonlinear functions of strain amplitude, speed of operation for each mode of vibration. Initially, damping can be assumed to be proportional and viscous, so that the energy dissipated is

$$W_d = \frac{C_v T}{\rho} \quad (9)$$

The process of incorporating the nonlinear model will be considered later. The equations for forced damped motion are then obtained as

$$[M]\{\ddot{q}\} + [C]\{\dot{q}\} + [K]\{q\} = \{Q_0\} + \sum_m \{Q_m\}\cos m\nu t + \sum_m \{Q_{m+6}\}\sin m\nu t \quad (10)$$

where

$$\{q\}^T = \{A_i, \ldots, D_i, \ldots\}$$

$$M_{11} = \rho\int_0^l A_i f_i f_j dz$$

$$C_{11} = \frac{C_v M_{11}}{\rho}$$

$$Q_{01} = \int_0^l \alpha_{0x} f_j dz, \text{ etc.} \quad (10a)$$

The modal analysis technique is employed to obtain decoupled equations of forced motion. Hence, using

$$\{q\} = [U]\{\eta\} \quad (11)$$

we get

$$M_k(\ddot{\eta}_k + 2\zeta_k p_k\dot{\eta}_k + p_k^2\eta_k) = Q_{0N_k} + \sum_m Q_{mN_k}\cos m\nu t + \sum_m Q_{(m+6)N_k}\sin m\nu t \quad (12)$$

The solution of the above in terms of displacement and moment vectors, due to each harmonic, is of the form

$$H_{0_k} = \frac{Q_{0N_k}/M_k}{p_k^2}$$

$$H_{m_k} = \eta_{m_k} + \eta_{(m+6)k} = \frac{\sqrt{\left(Q_{mN_k}^2 + Q_{(m+6)N_k}^2\right)}/M_k}{\sqrt{\left\{p_k^2 - (m\nu)^2\right\}^2 + 4\zeta_k^2 p_k^2 (m\nu)^2}} \times\cos(m\nu t - \psi_{m_k} - \delta_{m_k}) \quad (13)$$

where

$$\psi_{m_k} = \tan^{-1}\left[\frac{2\zeta_k p_k(m\nu)}{p_k^2 - (m\nu)^2}\right]$$

$$\delta_{m_k} = \tan^{-1}\left[\frac{Q_{(m+6)N_k}}{Q_{mN_k}}\right] \quad (14)$$

and the subscript m indicates the harmonic number.

With the help of Eqs. (13), (11), and (5), the deflections and moments of the blade for the force harmonics can be determined. For computation of bending moments, we can use the following formulae [see Carnegie (1957)]:

$$M_X = M_x\cos\psi_z - M_y\sin\psi_z$$

$$M_Y = M_y\cos\psi_z + M_x\sin\psi_z$$

The normal stress is given by [see Roark and Young (1976)]:

$$\sigma_z = \frac{M_Y x}{I_{yy}} + \frac{M_X y}{I_{xx}} \quad (15a)$$

The maximum shear stress occurs in the vicinity of one of the points, where the largest inscribed circle touches the boundary of the blade profile of the section (Roark and Young, 1976). This stress is given by

$$\tau_{r\theta} = \frac{T_\theta}{K}c \quad (15b)$$

where

$$K = \frac{1}{3}F/\left(1 + \frac{4}{3}F/AU^2\right)$$

$$F = \int_0^U t_1^3 dU$$

U is the elemental length along the camber line of the blade; t_1 is the profile thickness as a function of U. If the radius of the curvature of the boundary at the point is positive, then

$$c = \frac{16A^2D}{16A^2 + \pi^2D^4}\left[1 + 0.15\left(\frac{\pi^2D^4}{16A^2} - \frac{D}{2r}\right)\right]$$

If the radius of the curvature of the boundary at the point is negative, then

$$c = \frac{16A^2D}{16A^2 + \pi^2D^4}\left[1 + \left\{0.118\ln\left(1 - \frac{D}{2r}\right) - 0.238\frac{D}{2r}\right\}\tanh\frac{2\phi}{\pi}\right]$$

with D as the diameter of the inscribed circle, r the radius of the curvature of the profile at the point, and ϕ the angle through which a tangent to the boundary rotates in turning or traveling around the re-entrant position in radians. The shear stresses τ_{zx} and τ_{yz} can be readily computed from $\tau_{r\theta}$.

The principal stresses are

$$\sigma_1 = 0$$

$$\sigma_{2,3} = \frac{\sigma_z}{2} \pm \sqrt{\left(\frac{\sigma_z}{2}\right)^2 + \tau_{yz} + \tau_{zx}^2} \quad (16)$$

The basic mean stress (zeroth harmonic) and alternating stress components can be determined by using the corresponding principal stress by using the following formula:

$$\sigma_{\text{mean}}, \sigma_{\text{alt}} = \sqrt{\frac{I}{2}\left[\sigma_2^2 + \sigma_3^2 - 2\sigma_2\sigma_3\right]} \quad (17)$$

Downloaded 02 Jun 2010 to 171.66.16.104. Redistribution subject to ASME license or copyright; see http://www.asme.org/terms/Terms_Use.cfm

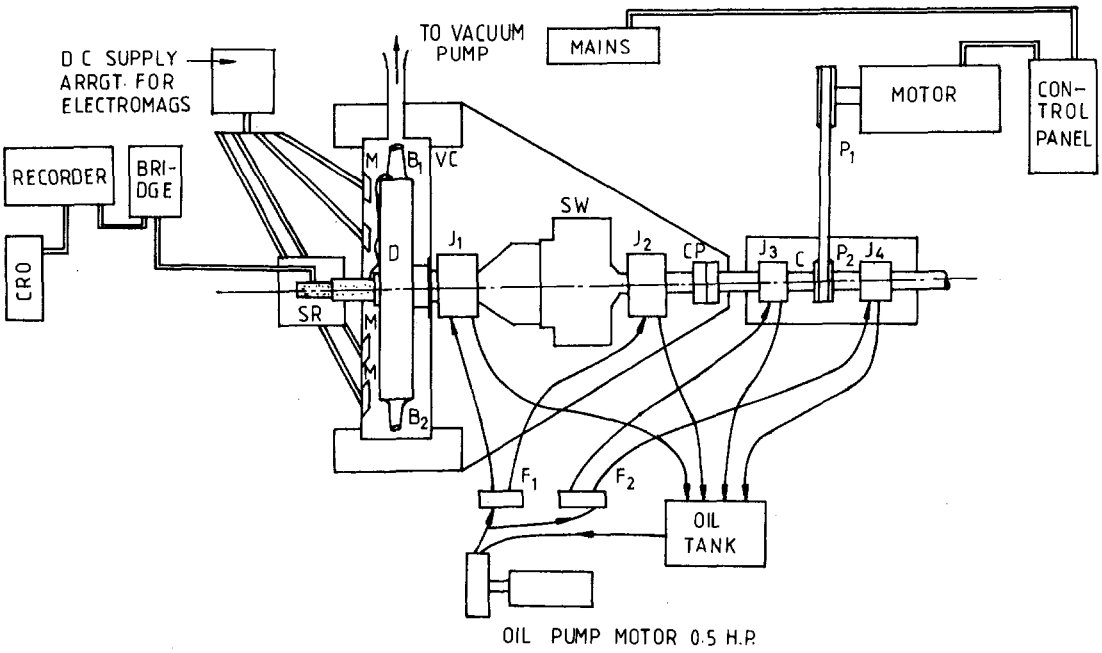

Fig. 3 Schematic layout of experimental setup (*D* = disk; *B* = blades; *M* = electromagnets; *SR* = slip ring; *SW* = shrunk-on-disk; *VC* = vacuum chamber; *F* = oil filters; *J* = journal bearings; *CP* = coupling; *C* = connecting shaft; *P* = pulleys)

Experimental Work

Investigations have been carried out on spinning blades to validate the analytical formulation given above. Experiments were conducted to obtain the damping data and blade stresses under constant-speed operation conditions.

Rig. The experimental rig consists of a disk with two blades mounted on an overhung rotor. The disk along with the blades is enclosed in a vacuum chamber. The rotor is supported on two journal bearings and run by a 30 kW thyristor controlled motor (see Fig. 3). The blades are tapered, twisted, and have an asymmetric cross section with a tee root. They are mounted diametrically opposite to each other. Multisurface noncircular journal bearings are used and oil is supplied by a 0.5 hp oil pump. A triaxial set of strain gages was fixed at an experimental point near the blade root. The connections from the gages are led to a slip ring and from there to a recorder and analyzer through an amplifying bridge.

Excitation. Nozzle excitation to the blades is simulated by electromagnets, which are mounted on the periphery of the outer plate of the vacuum chamber. The electromagnets are calibrated and the forcing functions are estimated using a separate experimental set up; see Rao et al. (1986b).

Damping. The resonant response to be determined from Eq. (12) is dependent on system parameters, the most complex among them being the modal damping ratio. Damping is a complex phenomenon by itself and for the case of turbine blades it primarily consists of friction at the mating surfaces and material hysteresis. The overall damping is known to be dependent on the rotational speed (influencing the blade-disk root friction) and strain amplitude (influencing hysteresis). The dependency above was quantitatively assessed for each mode by Rao et al. (1986a) with tests conducted in the vacuum spin rig, described above. The spinning blades were set into transient vibration by switching off electromagnetic excitation. From the filtered decay signals of each mode, equivalent modal damping ratios were obtained as function of rotational speed and strain amplitude. Typical equivalent modal damping values for *I* mode, obtained from free vibratory response (Fig. 1), are shown in Fig. 4 as a function of strain amplitude for different rotor speeds.

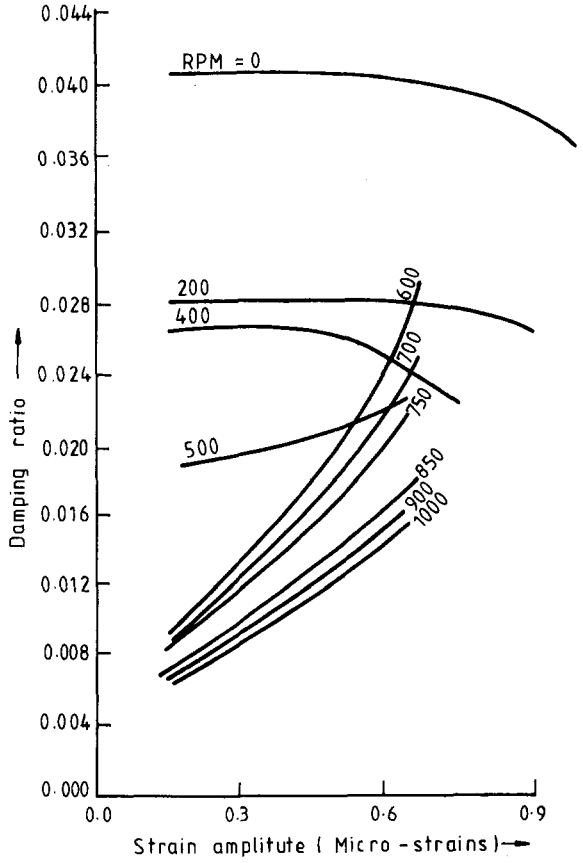

Fig. 4 *I* mode damping ratio as a function of strain amplitude for different rotor speeds

The average damping values obtained from such plots for the first four modes are depicted in Fig. 5. From Fig. 5 it is clear that there is a threshold speed in each mode, below which friction damping is predominant. In the first and

Downloaded 02 Jun 2010 to 171.66.16.104. Redistribution subject to ASME license or copyright; see http://www.asme.org/terms/Terms_Use.cfm

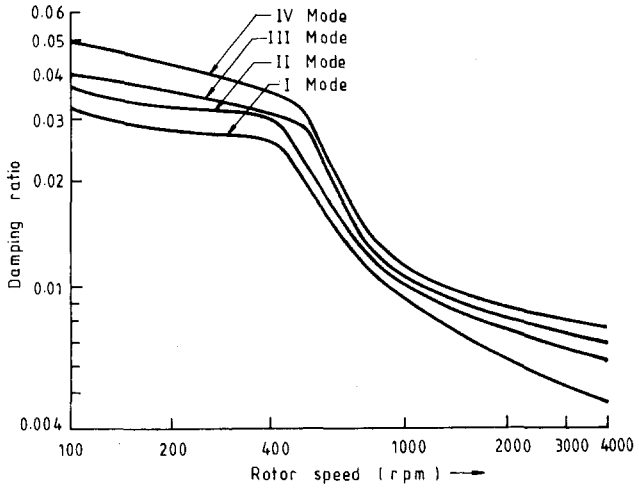

Fig. 5 Average damping ratios for the first four modes as function of rotor speed

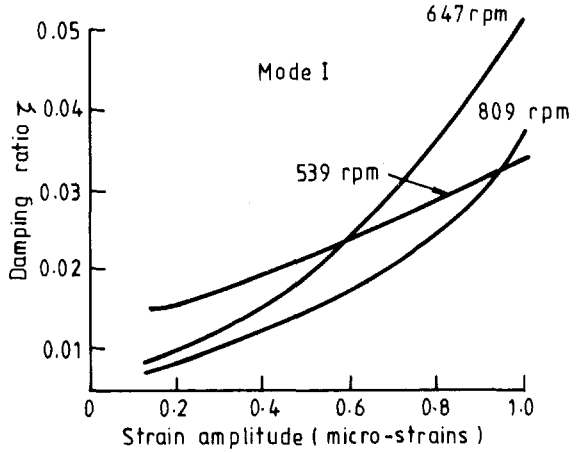

Fig. 6 Damping ratios for three rotor speeds where blade resonance occurs in *I* mode

second modes, this threshold speed is approximately 400 rpm and for the third and fourth modes, it is around 500 rpm. This threshold speed may be called the friction threshold speed, beyond which the effect of friction decreases due to the centrifugal force, causing increased interlocking between the blade root and the disk.

From Fig. 5, it can also be observed that the damping at higher speeds, say 1000 rpm and above, is predominantly due to hysteresis. In this region, the blade root gets totally interlocked with the disk and there is no relative movement between them. The speed beyond which there is only hysteresis available for energy dissipation may be called hysteresis threshold speed. In this region beyond the hysteresis threshold speed, say 1000 rpm in this case, there is no energy loss due to friction at the blade root–disk junction.

There is a transition region between the friction threshold speed, and the hysteresis threshold speed, where the energy dissipation occurs due to both friction and material hysteresis simultaneously. For the blade data considered in this paper, the fundamental natural frequency is 646.95 Hz. As the excitation is due to 12 magnets simulating the nozzles in a turbine stage, there are three critical speeds for the blade, viz., 539.125 rpm, 646.95 rpm, and 808.6875 rpm in the transition region of Fig. 5, corresponding to the sixth, fifth, and fourth harmonics, respectively. The damping data for these speeds is obtained by interpolation from the relations in Fig. 4 and shown in Fig. 6.

Table 1 α_i of Eq. (18); $0.1 \times 10^{-6} < \epsilon < 1.0 \times 10^{-6}$

	Rotor speed (rpm)		
	539.125	646.95	808.6875
α_0	0.010287	0.007240	−0.001460
α_1	0.029565	0.004731	0.057824
α_2	−0.025293	0.050749	−0.100043
α_3	0.028727	−0.027351	0.129434
α_4	−0.010978	0.008639	−0.063694
α_5	0.001923	0.007853	0.015665

Table 2 Geometric and material properties

Dist cm	A, cm^2	I_{xx}, cm^4	I_{yy}, cm^4	I_{xy}, cm^4	$C \times 10^{-3}$, Nm^2/rad	r_x, cm	r_y, cm
0.0	2.127	0.3447	0.9489	0.4705	0.9702	−0.213	0.075
2.5	1.738	0.3651	0.6717	0.4158	0.7776	−0.094	0.135
5.0	1.647	0.4927	0.5174	0.4146	0.7576	−0.082	0.073
7.5	1.263	0.5054	0.3097	0.2943	0.6113	−0.178	0.113
10.0	1.008	0.4356	0.1543	0.2243	0.4424	−0.282	0.222
11.0	0.736	0.3258	0.0858	0.1572	0.3087	−0.303	0.453

L = 11.1 cm, E = 200 GPa, R = 18 cm, G = 75 GPa, ϕ = 90 deg, ρ = 0.08 N/cm^3, n_s = 12

Table 3 Fourier component amplitudes

	F_x (N/cm)	
m	a_{mx}	b_{mx}
0	0.0622	0.0000
1	−0.0642	−0.0169
2	0.0110	0.0140
3	−0.0024	0.0005
4	−0.0027	0.0013
5	−0.0001	−0.0020
6	−0.0005	0.0028
	F_y (N/cm)	
m	a_{my}	b_{my}
0	−0.0064	0.0000
1	0.0153	−0.0392
2	−0.0063	0.0095
3	0.0024	0.0005
4	0.0012	0.0019
5	0.0007	−0.0012
6	−0.0018	0.0015
	M (N-cm/cm)	
m	a_{mM}	b_{mM}
0	0.0280	0.0000
1	−0.0269	−0.0173
2	0.0037	0.0089
3	−0.0006	0.0004
4	−0.0010	0.0011
5	0.0001	−0.0012
6	−0.0007	0.0017

The damping ratios for each mode are expressed as polynomial functions of strain amplitude at various rotor speeds, thus

$$\zeta = a_0 + a_1\epsilon + a_2\epsilon^2 + \cdots + a_5\epsilon^5 \qquad (18)$$

The constants a_i in Eq. (18) for I mode are obtained by a curve fitting routine and given in Table 1.

Computer Program and Results

A general purpose computer program is developed to obtain the free and forced vibration response of blades. The program requires inputs of

- blade profile data
- blade material properties
- nozzle excitation data, and
- damping data.

The program calculates the geometric properties of the blade at the sections where the profile data are provided and

Downloaded 02 Jun 2010 to 171.66.16.104. Redistribution subject to ASME license or copyright; see http://www.asme.org/terms/Terms_Use.cfm

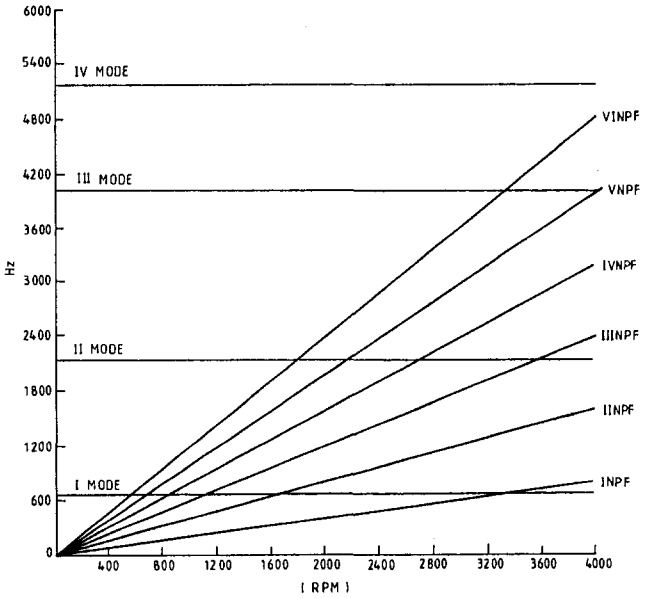

Fig. 7 Campbell diagram

Table 4 Basic vibratory stress at root (MPa)

rpm	Analytical values	Experimental (Vyas, 1986)	Percent error
539.125	0.1772	0.1034	71
646.950	0.1102	0.0661	67
808.6875	0.7620	0.1438	430

then expressed as functions of the blade length using a curve fitting routine. For the test blade, the geometric properties are given in Table 2 along with the material properties.

Using five term shape functions for deflections and moments, the mass and stiffness properties are then set up with the help of 19th degree Gaussian quadrature for integrations. The asymmetric eigen matrix is then solved to obtain the natural frequencies and mode shapes. The excitation is periodic with the nozzle passing frequency and is expressed in Fourier form with six harmonic components (Table 3). The Campbell diagram (Fig. 7) shows the first four natural frequencies of the test blade interacting with the six nozzle passing harmonics to indicate rotor speeds where blade resonance occurs.

Steady Response With Average Damping. With the average damping values given in Fig. 5, basic vibratory stress σ_{alt} obtained at the blade root are listed in Table 4, for three speeds where blade resonance occurs, viz., 539.125, 646.95, and 808.6875 rpm. Corresponding experimental results obtained by Vyas (1986) are also given.

The stresses thus computed employing average damping are very inaccurate. This is because the modal damping is predominantly dependent on the vibrational amplitude as well.

Steady Response With Nonlinear Damping. Equation (13) is obtained on the assumption that the damping is linear and viscous in nature. This is a common form of derivation of the model, since it facilitates a simpler solution. However, the damping is rarely linear in practical systems, such as the present case of blades under consideration. To keep the elegance of the linear model in obtaining solutions in a simplified manner and at the same time account for the nonlinearity in the damping, the following numerical technique involving an iteration procedure is developed. This procedure is based on the assumption that the damping can

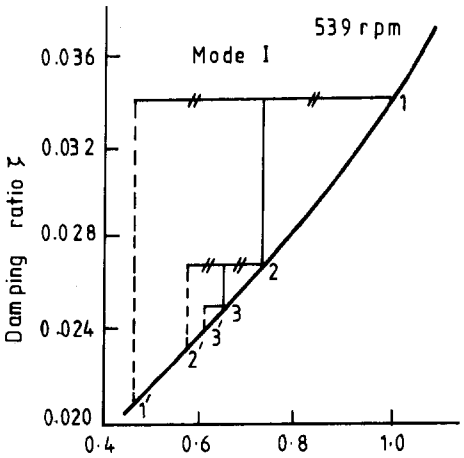

Fig. 8 Iteration procedure

Table 5 Iteration values

Starting values		Resultant values	
μ-strains	ζ	Stress MPa	μ-strains
a. 539 rpm			
1.00000	0.03400	0.09098	0.45490
0.72747	0.02679	0.11487	0.57435
0.65091	0.02499	0.12295	0.61475
0.63284	0.02458	0.12496	0.62480
0.62882	0.02449	0.12541	0.62705
0.62794	0.02447	0.12551	0.62755
b. 647 rpm			
1.00000	0.05000	0.03311	0.16555
0.58276	0.02325	0.06968	0.34840
0.46557	0.01819	0.08871	0.44355
0.45456	0.01776	0.09082	0.45410
c. 809 rpm			
1.00000	0.03700	0.17128	0.85630
0.92814	0.03271	0.19316	0.96580
0.94696	0.03386	0.18672	0.93360
0.94028	0.03345	0.18898	0.94490
0.94259	0.03359	0.18819	0.94095
0.94178	0.03354	0.18847	0.94235

be represented by an equivalent viscous model for a given amplitude of vibration, thus keeping the simplicity of the mathematical formulation and at the same time satisfying the amplitude-dependent damping phenomenon.

The computer program is made to generate modal damping surfaces in the rotor speed–strain amplitude plane, from the previously recorded experimental data, using curve-fitting subroutines with sixth-degree polynomials, see Table 1. The strain amplitude axis can be readily proportioned to stress amplitudes for all principal components of stress, using stress–strain relationships.

Starting with an assumed value of strain and corresponding modal damping ratio, point 1, Fig. 8, the principal component of stress and resultant strain is estimated, point 1′. The average of the assumed and estimated values of strain and the corresponding modal damping ratio are taken as the starting values for the next iteration. The process is repeated until two successive values of stress are obtained within a specified limit of accuracy. The iterative steps and final principal stresses obtained within an accuracy of 0.1 percent, are listed in Table 5.

A comparison between the theoretical stresses given in Table 4 obtained by the average damping method proposed above is given in Table 6 along with the experimental results.

It can be seen that incorporation of nonlinear damping has significantly reduced the gap between experimental and ana-

Downloaded 02 Jun 2010 to 171.66.16.104. Redistribution subject to ASME license or copyright; see http://www.asme.org/terms/Terms_Use.cfm

Table 6 Comparison of analytical and experimental stresses

Rotor speed (rpm)	Experimental stress (MPa)	Analytical stress (MPa) With average damping	Percent error	With nonlinear damping	Percent error
539	0.1034	0.1772	71	0.1255	21
647	0.0661	0.1102	87	0.0908	37
809	0.1438	0.7620	430	0.1885	31

lytical results, particularly for the case of 809 rpm. This reinforces the critical aspect of the dependence of modal damping not only on the speed for also on vibrational amplitude.

Transient Response—Constant Acceleration Operation. Consider now an operation of step-up or step-down operation of the engine from an initial angular velocity ω_0, with a constant acceleration α. The kinetic energy expression in Eq. (1) is modified to

$$T = \frac{1}{2}\rho\int_0^l A\left\{\left(\dot{x} + r_y\dot{\theta}\right)^2 + \left(\dot{y} - r_x\dot{\theta}\right)^2\right\}dz + \frac{1}{2}\int_0^l I_{cg}\dot{\theta}^2 dz + \frac{1}{2}\rho(\omega_0 + \alpha t)^2\left[-\int_0^l\left\{\left(x' + r_y\theta' + r_y'\theta\right)^2 + \left(y' - r_x'\theta - r_x\theta'\right)^2\right\}(RI_1 + I_2)dz + \sin^2\phi\int_0^l A\left(x + r_y\theta\right)^2 dz + \cos^2\phi\int_0^l A(y - r_x\theta)^2 dz - \sin 2\phi\int_0^l A\left(x + r_y\theta\right)(y - r_x\theta)dz\right] \quad (1a)$$

The excitation forces will be now of the form

$$F_x(z,t) = \alpha_{0x}(z) + \sum_m \alpha_{mx}(z)\cos\left\{mn_s\left(\omega_0 t + \frac{1}{2}\alpha t^2\right)\right\} + \sum_m b_{mx}(z)\sin\left\{mn_s\left(\omega_0 t + \frac{1}{2}\alpha t^2\right)\right\}$$

$$F_y(z,t) = \alpha_{0y}(z) + \sum_m \alpha_{my}(z)\cos\left\{mn_s\left(\omega_0 t + \frac{1}{2}\alpha t^2\right)\right\} + \sum_m b_{my}(z)\sin\left\{mn_s\left(\omega_0 t + \frac{1}{2}\alpha t^2\right)\right\}$$

$$M(z,t) = \alpha_{0M}(z) + \sum_m \alpha_{mM}(z)\cos\left\{mn_s\left(\omega_0 t + \frac{1}{2}\alpha t^2\right)\right\} + \sum_m b_{mM}(z)\sin\left\{mn_s\left(\omega_0 t + \frac{1}{2}\alpha t^2\right)\right\} \quad (8a)$$

Following the procedure used before for the steady operation conditions, we get

$$M_k\left(\ddot{\eta}_k + 2\zeta_k p_k\dot{\eta}_k + p_k^2\eta_k\right) = Q_{0N_k} + \sum_m Q_{mN_k}\cos\left[mn_s\left(\omega_0 t + \frac{1}{2}\alpha t^2\right)\right] + \sum_m Q_{(m+6)N_k}\sin\left[mn_s\left(\omega_0 t + \frac{1}{2}\alpha t^2\right)\right] \quad (12a)$$

The solution for Eq. (12a) for each term in the forcing function can be written using Duhamel's Integral as

$$\eta_{0k} = \int_0^t \frac{Q_{0N_k}}{p_{1k}M_k}e^{-\zeta_k p_k(t-\tau)}\sin p_k(t-\tau)d\tau$$

$$\eta_{mk} = A_c\cos(p_{1k}t + \lambda_c)$$

$$\eta_{(m+6)k} = A_s\sin(p_{1k}t + \lambda_s) \quad (19)$$

with

$$A_c = \frac{1}{2}\sqrt{(-I_{1c} + I_{2c})^2 + (I_{3c} + I_{4c})^2}$$

$$A_s = \frac{1}{2}\sqrt{(I_{1s} + I_{2s})^2 + (-I_{3s} + I_{4s})^2}$$

$$\lambda_c = \tan^{-1}\frac{I_{3c} + I_{4c}}{-I_{1c} + I_{2c}}$$

$$\lambda_s = \tan^{-1}\frac{-I_{3s} + I_{4s}}{I_{1s} + I_{2s}}$$

$$I_{1c} = \int_0^t \frac{Q_{mN_k}}{p_{1k}M_k}e^{-\zeta_k p_k(t-\tau)} \times \sin\left\{mn_s\left(\omega_0\tau + \frac{1}{2}\alpha\tau^2\right) - p_{1k}\tau\right\}d\tau$$

$$I_{2c} = \int_0^t \frac{Q_{mN_k}}{p_{1k}M_k}e^{-\zeta_k p_k(t-\tau)} \times \sin\left\{mn_s\left(\omega_0\tau + \frac{1}{2}\alpha\tau^2\right) + p_{1k}\tau\right\}d\tau$$

$$I_{3c} = \int_0^t \frac{Q_{mN_k}}{p_{1k}M_k}e^{-\zeta_k p_k(t-\tau)} \times \cos\left\{mn_s\left(\omega_0\tau + \frac{1}{2}\alpha\tau^2\right) - p_{1k}\tau\right\}d\tau$$

$$I_{4c} = \int_0^t \frac{Q_{mN_k}}{p_{1k}M_k}e^{-\zeta_k p_k(t-\tau)} \times \cos\left\{mn_s\left(\omega_0\tau + \frac{1}{2}\alpha\tau^2\right) + p_{1k}\tau\right\}d\tau$$

$$I_{1s} = \int_0^t \frac{Q_{(m+6)N_k}}{p_{1k}M_k}e^{-\zeta_k p_k(t-\tau)} \times \sin\left\{mn_s\left(\omega_0\tau + \frac{1}{2}\alpha\tau^2\right) - p_{1k}\tau\right\}d\tau$$

$$I_{2s} = \int_0^t \frac{Q_{(m+6)N_k}}{p_{1k}M_k}e^{-\zeta_k p_k(t-\tau)} \times \sin\left\{mn_s\left(\omega_0\tau + \frac{1}{2}\alpha\tau^2\right) + p_{1k}\tau\right\}d\tau$$

$$I_{3s} = \int_0^t \frac{Q_{(m+6)N_k}}{p_{1k}M_k}e^{-\zeta_k p_k(t-\tau)} \times \cos\left\{mn_s\left(\omega_0\tau + \frac{1}{2}\alpha\tau^2\right) - p_{1k}\tau\right\}d\tau$$

$$I_{4s} = \int_0^t \frac{Q_{(m+6)N_k}}{p_{1k}M_k}e^{-\zeta_k p_k(t-\tau)} \times \cos\left\{mn_s\left(\omega_0\tau + \frac{1}{2}\alpha\tau^2\right) + p_{1k}\tau\right\}d\tau$$

$$p_{1k} = p_k\sqrt{1 - \zeta_k^2} \quad (20)$$

Downloaded 02 Jun 2010 to 171.66.16.104. Redistribution subject to ASME license or copyright; see http://www.asme.org/terms/Terms_Use.cfm

Table 7 Iteration at resonant speeds

	Starting values		Resultant values	
RPM	μ-strain	ζ	Stress 10^5Pa	μ-strain
	1.00000	0.03423	0.00026	0.00013
	0.50006	0.02171	0.02266	0.01133
	0.25570	0.01663	0.13945	0.06972
539.125	0.16271	0.01454	0.29371	0.14686
	0.15478	0.01436	0.31397	0.15698
	0.15588	0.01438	0.31107	0.15553
	0.15571	0.01438	0.31153	0.15576
	1.00000	0.05170	0.00000	0.00000
	0.50000	0.01958	0.03925	0.01963
	0.25981	0.01142	0.54126	0.27063
646.95	0.26522	0.01157	0.51698	0.25849
	0.26252	0.01149	0.52903	0.26451
	0.26351	0.01152	0.52456	0.26228
	0.26302	0.01151	0.52679	0.26339
	0.26321	0.01151	0.52594	0.26297
	1.00000	0.03734	0.00058	0.00029
	0.50014	0.01504	0.74995	0.37498
	0.43756	0.01337	0.28056	0.64028
808.6875	0.46885	0.01419	0.98423	0.49212
	0.48048	0.01450	0.89065	0.44533
	0.47467	0.01435	0.93642	0.46821
	0.47144	0.01426	0.96270	0.48135
	0.47305	0.01430	0.94948	0.47475
	0.47390	0.01433	0.94263	0.47132
	0.47348	0.01431	0.94605	0.47303

Table 8 Stresses at resonant and near-resonant speeds

Rotor speed (rpm)	Stress (10^5Pa)
539.0000	0.31147
539.1000	0.28326
539.1250	0.31153
539.1500	0.28669
539.2000	0.19856
646.8000	0.52263
646.9000	0.51565
646.9500	0.52594
647.0000	0.37295
647.1000	0.33283
808.6000	0.90891
808.6800	0.83599
808.6875	0.94605
808.7000	0.81242
808.8000	0.77661

Table 9 Comparison of resonant stresses obtained using average damping and nonlinear damping

Rotor speed	Stress (10^5Pa)	
(rpm)	ζ_{avg}	ζ nonlinear
539.1250	0.03743	0.31153
646.9500	0.07244	0.52594
808.6875	0.96960	0.94605

Transient Response With Nonlinear Damping. Blade root stresses are thus computed for three instantaneous resonant rotor speeds (539.125, 646.95, and 808.6875 rpm) and near-resonant rotor speeds, with $\omega_0 = 0$ and constant acceleration $\alpha = 1600$ rpm. Table 7 gives the convergence of stress values and Table 8 gives the final stresses.

Table 9 compares the stress values at resonant speeds obtained by using averaged modal damping ratio (ζ_{avg}) and those obtained in Table 7 by using nonlinear modal damping envelopes. The influence of nonlinear damping is very clear from this table, particularly at lower resonant speeds, where Coulomb damping is predominant. At these speeds the stress values predicted with average modal damping are very low and it is necessary to use appropriate nonlinear damping dependent on mode, rotational speed, and strain amplitude.

The damping measurements made by Rao et al. (1986a) were used in the calculations above. The strains were measured near the root of the blade and the test speeds were restricted to 1000 rpm. The excitation is from electromagnets and it is much below the usual loads that can be taken by the test blade. Most of these restrictions were taken from the safety point of view of tests in the laboratory. Thus, the strain values are much smaller than those encountered in practice. The influence of friction damping is, of course, fully represented. In view of these remarks, a comprehensive redesign of the test rig is necessary to look at more practical values. Also tests are to be performed under accelerating and decelerating conditions of the rotor.

Conclusions

A procedure to determine the stress response of a turbine blade with nonlinear damping characteristics during steady and transient operation of the rotor is presented. The damping considered is a function of the mode of vibration, rotational speed, and strain amplitude of the blade. The iteration technique proposed is shown to give quick convergency for the computed stress levels. The nonlinear damping is shown to have predominant influence on the steady as well as transient blade response.

References

Carnegie, W., 1957, "Static Bending of Pre-twisted Cantilever Blading," *Proc. Instn. Mech. Engrs.*, Vol. 171, p. 873.

Carnegie, W., 1967, "The Application of the Variational Method to Derive the Equations of Motion of Vibrating Cantilever Blading Under Rotation," *BMEE*, Vol. 6, p. 29.

Crawley, E. F., 1983, "Aerodynamic Damping Measurement in a Transonic Fan," ASME JOURNAL OF ENGINEERING FOR GAS TURBINES AND POWER, Vol. 105, p. 575.

Dym, C. L., and Shames, I. H., 1973, *Solid Mechanics, A Variational Approach*, McGraw-Hill, New York.

Griffin, J. H., and Bielak, J., 1984, "Research on Friction Damping in Jet Engines at Carnegie Mellon University," *Proc. Vib. Damping Workshop*, Long Beach, AD-A152, p. M-1.

Hammons, T. J., 1982, "Electrical Damping and Its Effect on Accumulative Fatigue Life Expenditure of Turbine-Generator Shafts Following Worst Case Supply System Disturbances," University of Glasgow, United Kingdom, IEEE.

Irretier, H., 1986, "Transient Vibrations of Turbine Blades Due to Passage Through Partial Admission and Nozzle Excitation Resonances," *Proc. IFToMM Intl. Conf. Rotor Dynamics*, Tokyo, p. 301.

Jones, D. I. G., and Muszynska, A., 1983, "A Discrete Model of a Multiple Blade System With Interblade Slip," *Vibrations of Blades and Bladed Disk Assemblies*, ASME, p. 137.

Lagnese, T. J., and Jones, D. I. G., 1983, "Measurement and Analysis of Platform Damping in Advanced Turbine Blade Response," *Proc. Shock Vib. Bull.*, US Naval Res. Labs., Proc. 53, Pt. 4, p. 19.

Lazan, B. T., 1968, *Damping of Materials and Members in Structural Mechanics*, Pergamon Press, New York.

MacBain, J. C., and Whaley, P. W., 1984, "Maximum Resonant Response of Mistuned Bladed Disks," ASME *Journal of Vibration, Acoustics, Stress, and Reliability in Design*, Vol. 106, p. 218.

Ostachowics, W., and Szwedowic, D., 1986, "Vibrations of Beams With Elastic Contact," *Computers Struc.*, p. 763.

Providakis, C. P., and Beskos, D. E., 1986, "Dynamic Analysis of Beams by the Boundary Element Method," *Computers Struc.*, p. 957.

Rao, J. S., Gupta, K., and Vyas, N. S., 1986a, "Blade Damping Measurement in a Spin Rig With Nozzle Passing Excitation Simulated by Electromagnets," *Proc. Shock Vib. Bull.*, US Naval Res. Labs., Proc. 56, Pt. 2, p. 109.

Rao, J. S., Gupta, K., and Vyas, N. S., 1986b, "Analytical and Experimental Investigations on Vibratory Stresses of a Rotating Steam Turbine Blade Under NPF Excitation," *Proc. IFToMM Intl. Conf. Rotor Dynamics*, Tokyo, p. 269.

Rieger, N. F., and Beck, L. C., 1980, "Dynamic Tests on Turbine Blades," EPRI Project Report, RP-1185-2.

Rieger, N. F., 1984, "Damping Properties of Steam Turbine Blades," *Proc. Vib. Damping Workshop*, Long Beach, AD-A152, 547, p. 2-1.

Roark, R. J., and Young, W. C., 1976, "Formulas for Stress and Strain," McGraw-Hill, New York.

Downloaded 02 Jun 2010 to 171.66.16.104. Redistribution subject to ASME license or copyright; see http://www.asme.org/terms/Terms_Use.cfm

Sinha, A., and Griffin, J. H., 1984, "Effects of Static Friction on the Forced Response of Frictionally Damped Turbine Blades," ASME JOURNAL OF ENGINEERING FOR GAS TURBINES AND POWER, Vol. 106, p. 65.

Srinivasan, A. V., and Cutts, D. G., 1983, "Dry Friction Damping Mechanisms in Engine Blades," ASME JOURNAL OF ENGINEERING FOR GAS TURBINES AND POWER, Vol. 105, p. 332.

Usmani, M. A. W., 1986, "Interface Damping in Blade Attachment Region," Ph.D. Thesis, IIT, New Delhi, India.

Vyas, N. S., 1986, "Vibratory Stress Analysis and Fatigue Life Estimation of Turbine Blades," Ph.D. Thesis, IIT, New Delhi, India.

Vyas, N. S., Gupta, K., and Rao, J. S., 1987, "Transient Response of Turbine Blade," *Proc. 7th IFToMM World Congress*, Sevilla, Spain, p. 697.

Downloaded 02 Jun 2010 to 171.66.16.104. Redistribution subject to ASME license or copyright; see http://www.asme.org/terms/Terms_Use.cfm

F117-PW-100 Hybrid Ball Bearing Ceramic Technology Insertion

J. R. Miner
Pratt & Whitney,
United Technologies,
West Palm Beach, FL 33410

J. Dell
Wright Laboratory,
United States Air Force,
Dayton, OH 45433

A. T. Galbato

M. A. Ragen

MRC Bearings,
A Unit of SKF USA,
Jamestown, NY 14701

Results of an Advanced Research Projects Agency (ARPA) sponsored project to demonstrate the operational benefits of incorporating advanced structural ceramic ball elements into the F117-PW-100 aircraft gas turbine engine high rotor thrust bearings is described. This program consists of design, fabrication, and experimental evaluation of candidate hybrid ball bearing designs in Pratt & Whitney and MRC Bearings test facilities. The bearing design criteria and development test conditions utilized for the project are compatible with the requirements of the F117-PW-100 engine system application. Two hybrid bearing designs were produced by analytically varying internal geometry features such as M-50 race curvatures and contact angles to optimize for the modulus of elasticity of the ceramic balls. CERBEC grade NBD 200 silicon nitride ceramic balls ($1\frac{1}{8}$ in. size) demonstrated integrity and a quadruple rolling contact fatigue life improvement versus state-of-the-art M-50 steel balls in single ball test rigs. Thermal performance data obtained in full-scale bearing rig performance testing with 178 mm size hybrid and all-steel baseline bearings shows comparable characteristics. The hybrid bearing displayed a distinct survivability benefit in bearing liquid lubricant starvation testing. Two dozen hybrid bearings will be fabricated for full-scale bearing rig endurance tests to be conducted in 1995–1996 as a prerequisite to validation in operating F117-PW-100 engines in 1996–1997.

Background

The Advanced Research Projects Agency (ARPA) sponsored an initiative to demonstrate and insert ceramic technology into operational military systems [1]. This paper describes some of the results from one of the programs selected under that initiative funded by ARPA and managed by the Air Force, Wright Laboratory, Aero Propulsion and Power Directorate [2]. A large (178 mm) hybrid ceramic ball bearing with standard M50 steel races and silver plated AISI 4340 steel cages but utilizing 1.125 inch silicon nitride NBD200 ceramic balls is being designed, tested and evaluated for use in the number 3 position of the F117-PW-100 engine, which powers the C-17 aircraft. Accumulating experience with hybrid ceramic bearings indicates improved life and reliability over all steel bearings. Ceramic balls are inherently resistant to corrosion pitting and nick and scratch damage, which are causes for rejection of all-steel bearings during inspection. Testing is indicating improved tolerance to oil starvation and induced failure tests indicate gradual failure modes with metal particle generation periods and quantities similar to all steel bearings. One of the objectives of the current program is to estimate the expected life benefit of this hybrid design in order to determine if incorporation will be cost effective. If so, the other favorable characteristics mentioned above will be realized as side benefits.

In addition to the benefits mentioned above for current state-of-the-art gas turbine engines, the Air Force has been investigating hybrid ceramic bearings for use at extreme conditions expected in future high-performance engines being developed as a result of the Integrated High Performance Turbine Engine Technology (IHPTET) initiative.[1] Hybrid ceramic bearings are believed to be necessary for the conditions expected in those engines. Silicon nitride has 40 percent of the density of steel and thus will allow the higher required speeds by reducing the centrifugal loading of the balls on the outer race, which becomes limiting at high speeds. The maximum operating temperature capability of a bearing with M50 steel races can be increased by using ceramic balls. The bearing maximum temperature capability can be increased even further by also using steels with higher temperature capability than M50 for the races. The current insertion program is intended to benefit from the life and reliability advantage of hybrid ceramic bearings. It will also expand the experience base in advance of uses that take advantage of the high-performance possibilities.

The subject program includes bearing design and analyses, silicon nitride ball fabrication and single ball testing as well as full-scale hybrid bearing fabrication and rig testing.

Ball integrity is verified in single ball rolling contact fatigue tests. Bearing rig tests assess thermal characteristics under engine design operating conditions. Off-design testing includes oil-off survivability demonstrations and induced defect failure progression behavior. Full-scale endurance testing provides an estimate of service life potential. Sea-level engine testing is planned in related activities.

This paper covers the design efforts, silicon nitride ball integrity verifications, and full-scale bearing rig performance and oil shut-off tests. The rest of the effort is planned to be addressed in subsequent presentations.

Bearing Design

The F117 high rotor No. 3 ball bearing, which operates up to 2.1 MDN, was selected to demonstrate the operational benefits of ceramic silicon nitride rolling elements. The internal geometry of the current all M50 steel No. 3 ball bearing was analytically optimized with ceramic elements to obtain the maximum predicted B10 life while operating within current bearing experience. A 2.5× gain in analytical B10 life is predicted for hybrid design Candidate A relative to the current all steel bear-

[1] IHPTET is a joint DoD, NASA, and industry effort, started in 1988, aimed at doubling the state-of-the-art of propulsion system capability at the turn of the century.

Contributed by the International Gas Turbine Institute and presented at the 40th International Gas Turbine and Aeroengine Congress and Exhibition, Houston, Texas, June 5–8, 1995. Manuscript received by the International Gas Turbine Institute March 18, 1995. Paper No. 95-GT-390. Associate Technical Editor: C. J. Russo.

Copyright © 1996 by ASME

Downloaded 02 Jun 2010 to 171.66.16.104. Redistribution subject to ASME license or copyright; see http://www.asme.org/terms/Terms_Use.cfm

Table 1 F117 hybrid ceramic bearing design candidate configuration summary

Configuration	fo (outer race curvature)	fi (inner race curvature)	Contact angle
Bill of Material	51.5%	52%	28.5
Hybrid Candidate A	51.25%	51.75%	27
Hybrid Candidate B	51.5%	52%	27

(Curvature expressed as percentage of ball diameter)

ing. Expected life improvement for the hybrid ball bearing designs is based on earlier P&W single ball test results that demonstrated a significant relative life improvement for silicon nitride balls as compared to M50 balls. The two hybrid design candidates as listed in Table 1 have been reviewed and selected for fabrication and component testing.

The F117 No. 3 ball bearing was originally designed during the mid-1980's by P&W. As part of the study being discussed herein, a baseline analysis was performed to determine operating performance of the existing all M50 steel bearing prior to optimizing the hybrid bearing for ceramic rolling elements. A P&W owned analytical bearing optimization computer program was used for both the original design and the ceramic hybrid bearing designs. This program builds on the Lundberg–Palmgren theory and work by A. B. Jones. Operating engine performance, bearing axial and radial loads, compartment thermals, and the condensed F117 mission duty cycle, as used in the original bearing design, were used directly in the hybrid ceramic bearing design. The baseline analysis of the current all M50 steel bearing conducted at the start of this design task in 1993 successfully reproduced the operating performance as predicted originally and ensures design analysis integrity and continuity for the presented hybrid design candidates.

The analytical approach used to determine the optimum hybrid ceramic bearing configuration is typical of mainshaft bearing design analysis. A complete parametric analysis of internal geometry with ceramic elements was performed to determine the resultant operating performance. The internal geometry configuration that maximizes life while operating within P&W current experience represents the optimum configuration. Internal geometry parameters considered in the analysis include: race curvatures, contact angle, internal radial clearance, ball size and number, and shim thickness. Operating bearing performance parameters include contact stresses, operating contact angle, spin-to-roll ratio, maximum stress velocity (SV) value, upper and lower raceway path height extremes, operating internal clearance, ball excursion, gyro slip, ball-to-race and path-to-split clearance.

The F117 No. 3 ball bearing is located in the mid-bearing compartment, as shown in Fig. 1, and is mounted on the high rotor titanium shaft and steel bull gear. The No. 3 bearing is fabricated from M50 and is an outer-race oil-damped and under-race lubricated design. The cage is an inner land piloted design with round pockets and silver plate. The cage is also lubricated through radial slots in both the forward and rear inner race lands.

The F117 mission consists of altitude composite profiles, which include take-off, followed by a climb to optimum cruise altitude, flight duration, an idle, descent, landing, and a thrust reversing sequence. Nominal flight duration times for the C-17A range from 3 hours to a maximum of 14 hours.

The No. 3 ball bearing carries a maximum axial thrust load of 9050 lb. and radial loads less than 2500 lb. The majority of operation time is at cruise power, which represents over 76.5 percent of the total mission. The ten-point condensed duty cycle, as shown in Table 2, is identical to the mission used in the original design. High rotor speeds below 10,000 rpm represent idle power settings, rotor speeds below 11,000 represent cruise power settings, and speeds above 11,000 represent max climb or max continuous power settings.

The current No. 3 ball bearing internal geometry employs an outer-race curvature of 51.5 percent, an inner-race curvature of 52 percent, a 0.010-in. shim thickness, and a print contact angle of 27–30 deg. Bearing internal geometry is selected to provide adequate bearing life for the complete mission while operating within previous experience levels at each flight condition. Originally both inner and outer-race curvatures were defined as 52 percent. In order to satisfy an increase in mission B-10 life requirements from 10,000 hours to 20,000 hours, the outer-race curvature was tightened to 51.5 percent to reduce contact stress. As shown in Fig. 2,the current all M50 steel No. 3 bearing configuration exceeds the current life requirement and is bounded by operating internal clearance and SV value.

Silicon nitride rolling elements have been identified as a means to satisfy increased speed and durability requirements of the advanced and more demanding DN levels of technology engines. The lower density of silicon nitride offers significantly lower centrifugal elemental loading and is most beneficial for high-speed outer-race life limited applications. The objective of inserting silicon nitride into the F117-PW-100 is to demonstrate the benefits of ceramic rolling elements and to gain the necessary engine field experience that will be required prior to use in advanced engine programs.

The principle material differences between silicon nitride and steel include a lower density 40 percent of steel and an elastic modulus 60 percent higher than steel. Other advantages of silicon nitride include increased hardness, increased wear and corrosion resistance, and improved surface finish, typically less than 0.2 min. Ra. Reduced centrifugal loading on the outer race provides lower contact stresses and potential for increased life. Lower centrifugal load also more closely aligns the outer race contact angle with the inner race contact angle and reduces ball sliding at the inner race contacts. This results in lower SV, lower spin-to-roll ratio, and lower heat generation. Tighter race curvatures are required in hybrid designs to increase the ball-to-race contact area to offset the otherwise smaller contact footprint due to a higher elastic modulus. The thermal expansion coefficient of silicon nitride is significantly lower than that of steel and provides increased operating internal clearance at elevated temperatures due to reduced ball diametral expansion.

Shown in Fig. 3 are the results of a parametric analysis relating overall mission B-10 fatigue life, inner and outer-race curvature, and initial print contact angle. Analytical life improvement is predicted for both hybrid design candidates. Design candidate A represents the highest attainable predicted B-10 life while operating within current all M50 steel bearing experience for each individual operating condition and consists of tighter race curvatures and optimum contact angle. Design candidate B employs current race curvatures and was selected to provide additional operating internal clearance margin. Shown in Table 3 is a complete list of operating performance for the current all M50 steel bearing, hybrid candidates A & B, and simple element replacement. Both selected design candidates are predicted to result in increased life and to operate with reduced SV, lower spin-to-roll, and larger internal clearance. Simple element replacement is predicted to operate above successful spin/roll values of the current all steel M50 bearing and is not recommended. Increase in mission life is predicted for tighter race curvatures; however, an outer-race curvature of 51.25 percent was selected in order to avoid curvatures below 51 percent since manufacturing tolerances can be up to 0.25 percent. Tighter race curvature is expected to result in increased SV and increased heat generation. The highest values of spin-to-roll and ball excursion levels for the hybrid designs occur during idle speeds as opposed to cruise conditions for the current B/M bearing. Ball excursion is predicted to be slightly higher for the hybrid designs; however, no change in the current cage pockets or pocket clearances are required.

Downloaded 02 Jun 2010 to 171.66.16.104. Redistribution subject to ASME license or copyright; see http://www.asme.org/terms/Terms_Use.cfm

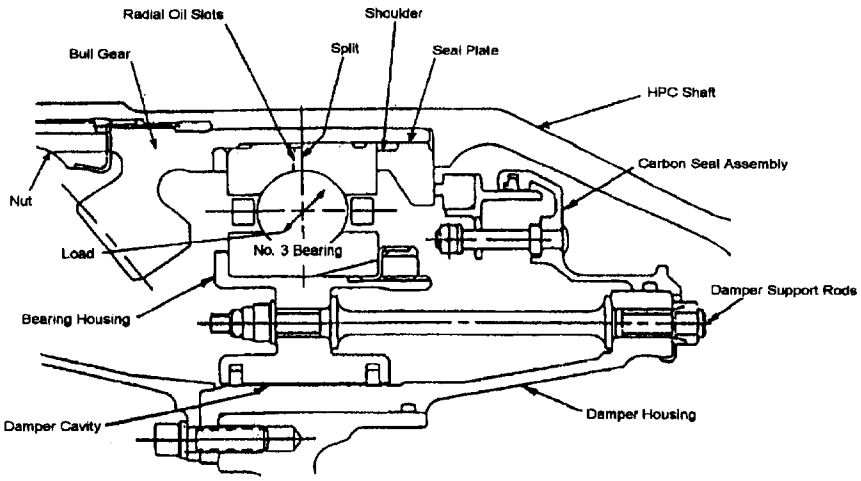

Fig. 1 F117 No. 3 bearing compartment cross section

The expected 2.5× B-10 life improvement for the optimum hybrid design candidate A includes the USAF accepted 25× material multiplier for M50 along with an additional 5× material multiplier for silicon nitride. A relative life improvement of 5× for silicon nitride over M50 has been recommended conditionally based on highly favorable silicon nitride single ball tests conducted earlier on M50 V-groove races. It should be noted that the basic Lundberg–Palmgren theory does not involve life adjustment factors. It considers only the stress intensity of the inner and outer races and not the balls for the calculation of life prediction.

However, improved bearing materials processing and in some cases even better filtration has resulted in the adoption of an overall combined life adjustment factor. This M-50 factor, e.g., 25×, has been correlated to actual field service experience in a variety of gas turbine applications.

On the other hand, such a broad data base has yet to be established for hybrid bearings. Full-scale bearing rig endurance testing and engine demonstrations for appropriate life adjustment factor substantiation are planned. In the meantime, the 5× factor is assumed in view of the single ball testing.

P&W sketch drawings for the ceramic hybrid designs were provided to SKF/MRC Bearings Inc. and component fabrication began following approval of final prints. Inner and outer races were fabricated from M50 steel (PWA 793) and NBD 200 silicon nitride ceramic elements were supplied to MRC by Cerbec, Inc.

Both hybrid design candidates are expected to result in improved performance over the current all steel M50 bearing and were accomplished by changes in race curvature and contact angle. Hybrid design candidates will use the current cage and compartment oil flow rates. Lower heat generation and improved fatigue life are expected for both hybrid design candidates. Rig testing was planned to verify the operational benefits of ceramic rolling elements and to identify the optimum candidate. Single ball and full-scale bearing testing is discussed in the next section.

Table 2 F117 condensed mission for bearing performance

Condition	Speed (rpm)	%Time	Axial Load (lbs)	Radial Load (lbs)
1	7,777	10.9	850	850
2	8,217	5.6	630	770
3	10,370	6.4	3025	2160
4	10,488	22.7	3140	2328
5	10,571	11.4	3410	2350
6	10,603	35.9	2770	2400
7	11,108	1.5	4120	2400
8	11,220	1.1	5270	2330
9	11,411	1.1	6510	2040
10	11,813	3.3	9050	1340

Ball Life Integrity

The single ball, V-groove fatigue test rig is designed to simulate the ball rolling and spinning conditions existing in a high speed ball bearing under thrust loading [3]. These machines are used to study fatigue spalling resistance as affected by material, heat treatment, surface finish, sphericity, operating temperature, loads, speeds, and lubricants.

To conduct a test, a ball specimen is placed between two 130 deg V-groove raceways and positioned horizontally by silicon–iron–bronze rods. The lower ring raceway drives the ball via a compressive load applied through a hydraulically loaded, free wheeling, upper ring raceway by means of a load cylinder located on top of the machine. The slave ring is mounted on overhung bearings, making it readily accessible. Raising the upper shaft assembly allows the test parts to be replaced. For each test, newly finished raceways, or V-grooves, are used so

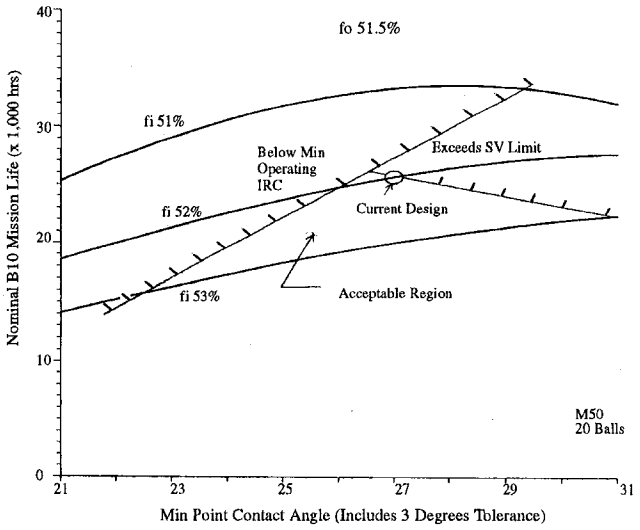

Fig. 2 Current all M50 No. 3 Ball bearing design bounded by SV and minimum operating IRC

Downloaded 02 Jun 2010 to 171.66.16.104. Redistribution subject to ASME license or copyright; see http://www.asme.org/terms/Terms_Use.cfm

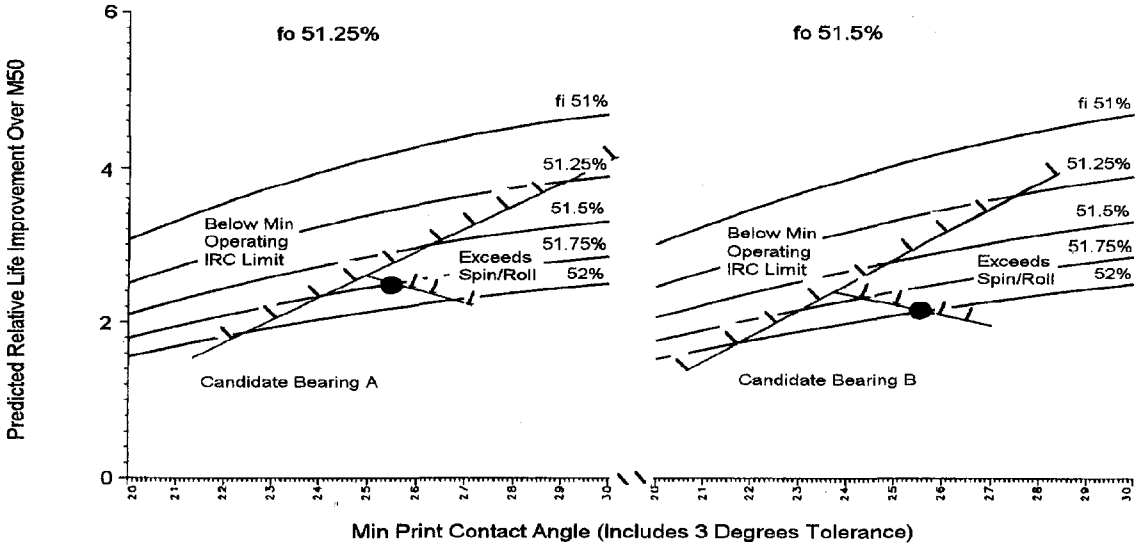

Fig. 3 Proposed F117 No. 3 Hybrid ball bearing design limited by minimum operating IRC and spin-to-roll

that virgin ball/raceway rolling/sliding contact is achieved. Ball or raceway failure is indicated by either excessive noise, drive motor amperage excursion, or increased vibration level. In this event, an indicator light goes on and the electrical circuit of the drive motor is broken. During testing, lubricant flow rate and temperature, as well as hydraulic pressure, are continuously monitored and held within specified limits. If these limits are exceeded, the test machine will automatically shut down, and the test is suspended.

Typical test conditions for 28.575 mm ($1\frac{1}{8}$ in.) diameter balls, a commonly used size in large aircraft turbine engines, are given in Table 4.

Endurance Test Results

As previously demonstrated [3] with 12.7 mm ($\frac{1}{2}$ in.) diameter balls, properly densified and accurately finished Si_3N_4 balls are significantly more fatigue resistant than high-quality VIM-VAR M50 balls. Testing of 28.575 mm ($1\frac{1}{8}$ in.) diameter NBD 200 Si_3N_4 balls confirmed the fatigue life improvement over M50. For comparison, under the test conditions given in Table 4, the median unbiased L10 life for M50 balls (based on 90 tests from 4 different ball lots) is 43.4 hours with a 90 percent confidence band of 34.9 to 51.3 hours. No legitimate spalls or failures were obtained with properly finished, surface-defect free Si_3N_4 balls with suspensions extending to 300 hours duration. Accordingly, a one-sided 90 percent confidence band calculation estimates the L_{10} life to be greater than or equal to 166 hours, thus establishing the fatigue life of NBD 200 Si_3N_4 balls to be approximately 4 times the life of M50 steel balls under the extremely high stress levels described above.

Testing of 1 $\frac{1}{8}$ in. diameter balls exhibiting known surface defects was also conducted to assess the effects of such surface

Table 3 Proposed F117 No. 3 ceramic ball bearing optimum design candidates

	Current Design	*Design Candidate A*	*Design Candidate B*	*Simple Element Replacement*
Outer Race Curvature	51.5%	51.25%	51.5%	51.5%
Inner Race Curvature	52%	51.75%	52%	52%
Print Contact Angle (deg)	27–30	25.5–28.5	25.5–28.5	27–30
Print Internal Clearance (mils)	7.5–9.0	5.3–6.9	6.5–8.4	7.5–9.4
Nominal B–10 Mission Life (hrs)	25,600	12,575	10,675	11,325
Nominal B–10 Mission Life Using 5x material factor over M50		62,875	53,375	56,625
Relative Life Improvement Using 5x material factor over M50 (hrs)		2.46	2.08	2.21
Min Ball–to–Race Clearance (in)	0.0014	0.0011	0.0015	0.0018
Max Spin/Roll Ratio	0.927	0.918	0.929	1.031
Max Ball Excursion (in)	0.303	0.308	0.315	0.366
Max Gyro Slip Coefficient	0.05	0.057	0.058	0.061
Max Inner Race Path Height	18%	17.7%	17.9%	19.6%
Max Outer Race Path Height	8%	11.6%	11%	11.4%
Max SV Value [$x10^6$ (lb/in^2) (ft/sec)]	2.17	2.03	1.98	2.05
Min Operating IRC (in)	.0014	.0019	.0032	.0041
Min Operating Contact Angle (deg)	14.6	17.75	19.04	20.98
Max Inner Race Contact Stress (ksi)	161	183	188	184
Max Outer Race Contact Stress (ksi)	160	164	170	168

Downloaded 02 Jun 2010 to 171.66.16.104. Redistribution subject to ASME license or copyright; see http://www.asme.org/terms/Terms_Use.cfm

Table 4 V-groove/ball rig test conditions for 28.575 mm (1 $\frac{1}{8}$ in.) balls

Hertzian stress	=	3800 Mpa (550 ksi)
Shaft speed	=	7800 rpm
Stress rate	=	6 X 106 cycles/hour
Lubricant flow rate	=	3.4 kg/min (7.5 lb/min)
Lubricant temperature	=	366°K (200°F)
Raceway surface finish	=	0.05–0.10 μm (2–4 μin.)

discontinuities. A percentage of balls from the above-tested lot were found to have surface defects, commonly referred to as 'C' cracks. A typical 'C' crack is shaped roughly like the letter C and occupies about one third the circumference of a circle. The most severe 'C' cracks were visible at magnifications of 10× to 20× under normal white light illumination. The least severe 'C' cracks were visible only using fluorescent dye penetrant in ultraviolet light with magnification.

A total of ten tests were run wherein 'C' cracks were intentionally located in the test ball load tracks. Seven of these tests resulted in spalling failures of the test balls with running times varying from 6.9 to 71.5 hours. The remaining three tests resulted in suspensions—ball S/N's 4 and 5 were suspended after 60 hours and ball S/N 26 was suspended after 150 hours. Based on these test results, a median unbiased L_{10} life of 5.2 hours was calculated for NBD-200 balls with 'C' cracks using the Maximum Likelihood Weibull calculation program.

In summary, the single ball testing results show that the L_{10} life of defect-free CERBEC NBD-200 balls is at least four times higher than M50 balls tested under the same conditions. However, if 'C' cracks are present on the surface of the balls, the L_{10} life of the NBD-200 balls can be as low as one-eighth that of M50 balls.

Full-Scale Bearing Testing

The test rig is driven by a 200 hp DC motor. The output shaft of the motor is connected via a flexible coupling to a speed increaser gearbox with a 11.96 to 1 ratio. A splined stub shaft is used to transmit power from the gearbox output shaft to the test head.

The two test bearings are mounted in a face-to-face arrangement within the test head and are subjected to the same thrust load via a hydraulic load piston. There is no provision in the test head for applying radial load. Each test bearing is underrace lubricated via two oil jets, which direct the lubricant underneath an oil scoop, which feeds oil slots located under the bearing inner ring. A central baffle separates the two test bearing compartments with respect to lubrication. Each test bearing compartment has three oil drain lines, which are plumbed to a common drain pipe that is connected to a scavenge pump.

The lubricant supplied to the test bearings is filtered using a 3 μm filter. The flow rate to each oil jet is controlled with a separate flow meter. A circulation heater is used to heat up the lubricant to the desired oil-in temperature. A heat exchanger provides cooling as required to keep the oil-in temperature from rising during the tests. The lubricant supply lines are plumbed such that the lubricant can be shut off to both test bearings simultaneously or to either test bearing.

Three thermocouples, mounted equally spaced around the circumference, are used to measure the outer ring temperature of each test bearing. The thermocouples are in contact with the O.D. surface of the bearing outer ring. Separate thermocouples are also used to measure the oil-in and oil-out temperatures for each test bearing. A computerized data acquisition system was used to record the data for the full-scale bearing tests. The data recorded included time, shaft rotational speed, applied thrust load, lubricant flow rate to each test bearing, and the temperatures. For the oil shutoff tests, these parameters were recorded approximately once per second. For the bearing performance tests, the parameters were recorded once every 10 seconds.

Hybrid Bearing Parametric Performance Tests

Four hybrid bearings were fabricated at MRC using defect-free 1.125 in. diameter CERBEC NBD 200 silicon nitride balls. Two each of the candidate hybrid bearing designs were fabricated, i.e., HKJ13242 and HKJ13243. Both hybrid bearing designs are very similar to the 1B6016 bearing, which is used in the PWA F117 engine No. 3 position. The primary differences in the bearing designs as fabricated are highlighted in Table 5. The HKJ13243 hybrid bearing has the same nominal raceway curvatures as the 1B6016 bearing, but a slightly lower nominal contact angle and less radial clearance. The HKJ13242 hybrid bearing has slightly tighter inner and outer raceway curvatures, the same nominal contact angle as the HKJ13243 bearing, and less radial clearance than the HKJ13243.

The performance characteristics of the two hybrid bearing designs were evaluated in rig tests. A test matrix was established that is representative of the range of operating conditions experienced by the F117 engine No. 3 bearing. This was accomplished using three different rotational speeds (7,000, 10,000, and 12,000 rpm), three different thrust loads (2500, 5000, and 10,000 pounds), and three different oil-in temperatures (150, 200, and 250°F), resulting in 27 different test points. The hybrid bearings were run for one hour at each of these 27 test points. In addition, they were run for three hours at an overload condition defined by a rotational speed of 12,300 rpm, a thrust load of 17,000 pounds, and an oil-in temperature of 180°F. For all of the test points, each test bearing received 5.6 gpm of MiL-L-23699 oil.

Two all-metal 1B2246 bearings (S/N 0290 and 0291) were run in the test rig at all 28 test points to establish a baseline for comparing the performance of the hybrid bearings. The 1B2246 bearing, which is the predecessor to the 1B6016, is dimensionally identical to the 1B6016, but has 52100 steel balls instead of M50. The stabilized temperatures were recorded at each test condition during the baseline test of the all-metal bearings and the tests of the hybrid bearings.

Figure 4 is a plot showing bearing DELTAT as a function of thrust load and speed for the 1B2246, HKJ13242, and HKJ13243 bearings with an oil-in temperature of 200°F. Similar plots were developed for oil-in temperatures of 150°F and 250°F, respectively. Based on the performance test data, there does not appear to be a significant difference with respect to bearing operating temperature or oil-out temperature for the 1B2246, HKJ13242, or HKJ13243 bearing designs.

All of the hybrid bearings were examined after the 30 hour performance tests and found to be in excellent condition with no significant signs of distress. Some discoloration of the cages around the ball pockets was noticed. The discoloration was more noticeable on the cages of the HKJ13243 bearings.

Table 5 Comparison of bearing design parameters

Bearing Design	*Current 1B6016*	*Candidate A HKJ13242*	*Candidate B HKJ13243*
Nom. inner race curvature (%)	52.00	51.75	52.00
Nom. outer race curvature (%)	51.50	51.25	51.50
Nominal contact angle (Deg.)	28.50	27.00	27.00
Nominal IRC (inches)	0.0084	0.0061	0.0074

Downloaded 02 Jun 2010 to 171.66.16.104. Redistribution subject to ASME license or copyright; see http://www.asme.org/terms/Terms_Use.cfm

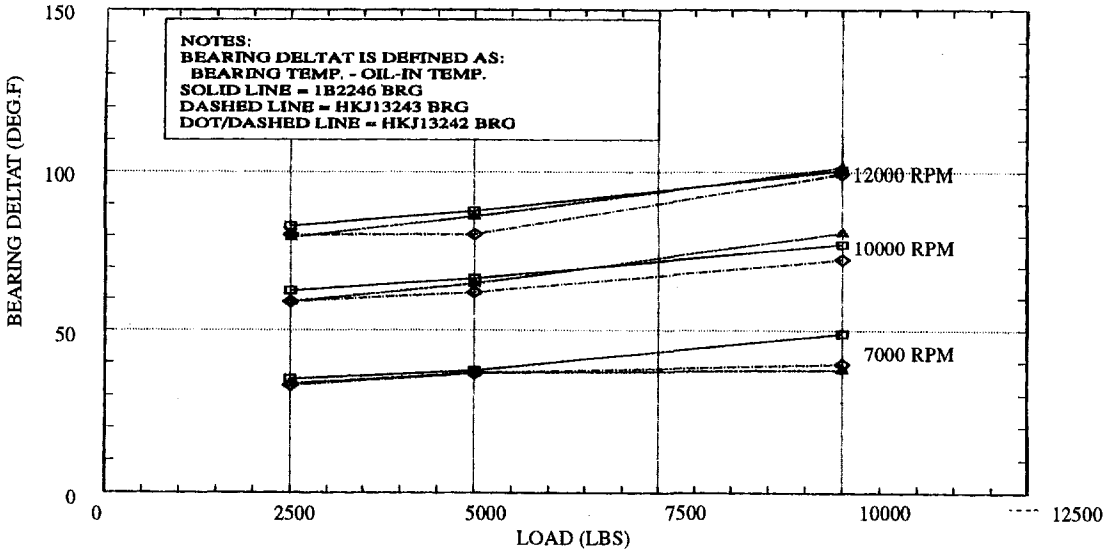

Fig. 4 Bearing delta *T* as a function of thrust load and speed for the 1B2246, HKJ13242, and HKJ13243 bearings with an oil-in temperature of 200°F

Oil Shutoff Testing

A number of tests were run to evaluate the performance of the HKJ13242 hybrid ball bearing in situations where the lubricant supply to the bearing is terminated. The oil shutoff tests provided direct comparison between the HKJ13242 hybrid bearing and the PWA F117 engine No. 3 bearing (PWA 1B6016 or 1B2246) at several engine operating conditions.

Oil Shutoff Test of 8-4-94—TAKEOFF Condition

The first oil shutoff test involving the hybrid bearing was performed at MRC on 8-4-94. The purpose of this test was to demonstrate that the hybrid bearing could run for 30 seconds at the TAKEOFF condition after oil shutoff. This is a typical requirement imposed on jet engine mainshaft bearings.

The test rig was assembled with hybrid bearing HKJ13242 S/N E001 in the front position (closest to the hydraulic load piston and gearbox). In the rear position, an all-metal bearing (1B2246 S/N 0291) was mounted. The 1B2246 bearing used in this test was technically a discrepant part. The bearing was originally rejected at inspection due to a problem with the moly-disulfide coating on the raceways. The coating was subsequently stripped and the bearing met all print geometric requirements.

The operating conditions given in Table 6 correspond to the PWA F117 engine No. 3 bearing. The test rig was run at TAKEOFF with full oil flow until the bearing temperatures stabilized. The oil flow to both bearings was shut off simultaneously by turning a ball valve in the lubricant supply line. The test rig was run for thirty seconds with the oil shut off, but almost immediately thereafter the test rig seized up, accompanied by loud squealing. Oil flow was restored to the test bearings as quickly as possible and power to the drive motor was shut off.

The temperature of both test bearings as a function of time after the oil was shut off is shown in Fig. 5. The temperature of the hybrid bearing reached 326.5°F, a temperature rise of only 26.5°F. The temperature of the all-metal bearing, on the other hand, rose dramatically after fifteen seconds. The all-metal bearing reached a maximum temperature of 456°F, a temperature rise of 149°F.

For all conditions, a flow rate of 5.6 GPM of MIL-L-23699 lubricant was supplied at 200°F to each bearing prior to oil shutoff.

Table 6 Oil shutoff test conditions

CONDITION	*THRUST LOAD (LBS)*	*SPEED (RPM)*
IDLE	915	7721
CRUISE	3582	10754
MID–CLIMB	6352	11298
TAKEOFF	10416	11821

Upon rig disassembly the all-metal bearing was found to be seriously damaged. A significant amount of material was removed from the 52100 balls in the form of large thin plates, which were dispersed throughout the bearing compartment. The inner and outer raceways exhibited smearing damage around their entire circumferences. The hybrid bearing, on the other hand, was in excellent condition with no signs of distress evident.

Oil Shutoff Tests of 11-30-94—IDLE and CRUISE Conditions

This test build was intended to provide a direct comparison of the oil shutoff capabilities of the hybrid bearing and the current all-metal bearing design. The test rig was assembled with hybrid bearing HKJ13242 S/N E001 installed in the front position. An all-metal bearing, 1B6016 S/N 0691 with M50 balls, was installed in the rear position. The 1B6016 bearing was in full compliance with all inspection requirements.

The plan for this test build was to evaluate the oil-off characteristics of both test bearings at progressively more severe operating conditions starting with IDLE and proceeding to CRUISE, MIDCLIMB, and TAKEOFF. To accomplish this, the oil was to be turned off to one test bearing at a time and then restored before damage occurred. Based on previous testing at PWA, it was believed that damage could be avoided by limiting the bearing outer ring temperature to 350°F.

Successful oil shutoff tests were run at IDLE for both the all-metal and hybrid bearings. Both test bearings were run without oil for approximately 13 minutes without problem. A tem-

Downloaded 02 Jun 2010 to 171.66.16.104. Redistribution subject to ASME license or copyright; see http://www.asme.org/terms/Terms_Use.cfm

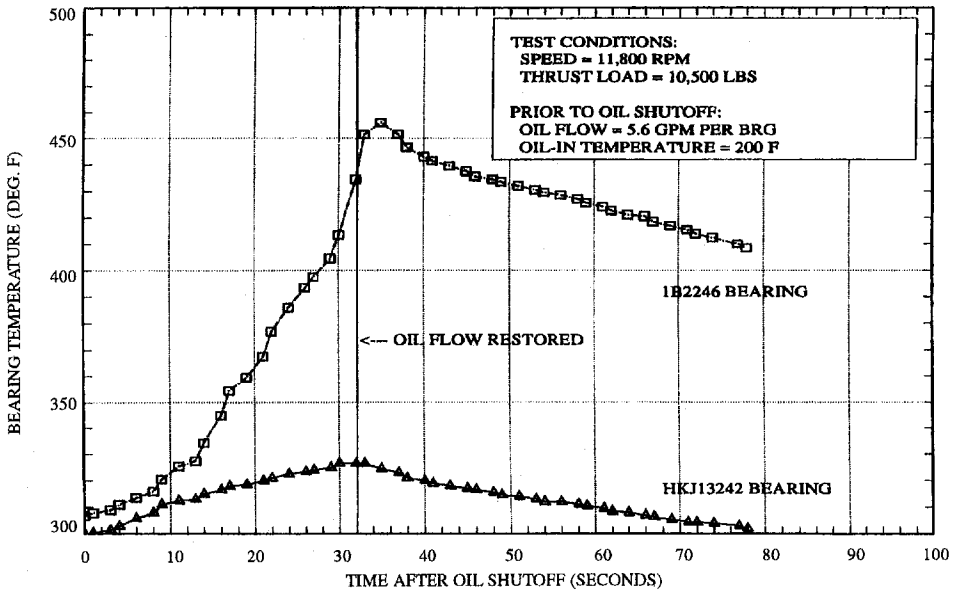

Fig. 5 Bearing temperatures versus time after oil shutoff

perature rise of 43°F was recorded for the hybrid bearing, while the temperature rise of the all-metal bearing was only 12°F.

The test rig was next run at CRUISE and the bearing temperatures were allowed to stabilize. The oil flow was then shut off to the all-metal bearing. After running with the oil off for approximately one minute, the test rig suddenly began making loud squealing noises. The oil flow was restored as quickly as possible, but not in time to prevent serious bearing damage. Figure 6 is a plot of bearing temperature versus time for this run. The bearing temperature spiked rapidly after reaching approximately 290°F. This occurred after running with the oil off for 55 seconds. It is believed that the all-metal bearing had lost all clearance at that point, even though the bearing temperature was well below the 350°F limit established prior to this test.

The test was discontinued and the rig was disassembled to examine the test bearings. The all-metal bearing sustained significant smearing damage around the full circumference of the inner and outer raceways. All of the balls exhibited wide dark bands, although it did not appear that there was any significant material removal from them. The hybrid bearing was found to be in excellent condition with no signs of distress.

Oil Shutoff Tests of 12-5-94—CRUISE, MIDCLIMB, and TAKEOFF

The test rig was assembled with hybrid bearing HKJ13242 S/N E001 in the front position and an all-metal bearing, 1B6016B S/N 0708, in the rear position. The 1B6016B bearing was in full compliance with all bearing inspection requirements.

In this test build, the performance characteristics of the hybrid bearing and all-metal bearing were determined with the oil off at the CRUISE, MIDCLIMB, and TAKEOFF conditions. Based

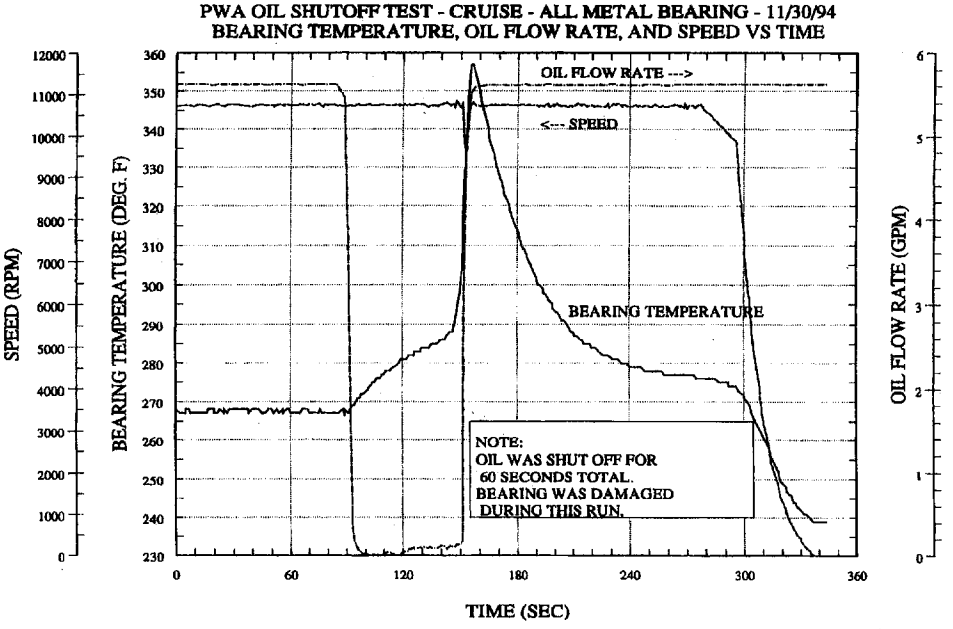

Fig. 6 Bearing temperature, oil flow rate, and speed versus time for all-metal bearing at cruise

Downloaded 02 Jun 2010 to 171.66.16.104. Redistribution subject to ASME license or copyright; see http://www.asme.org/terms/Terms_Use.cfm

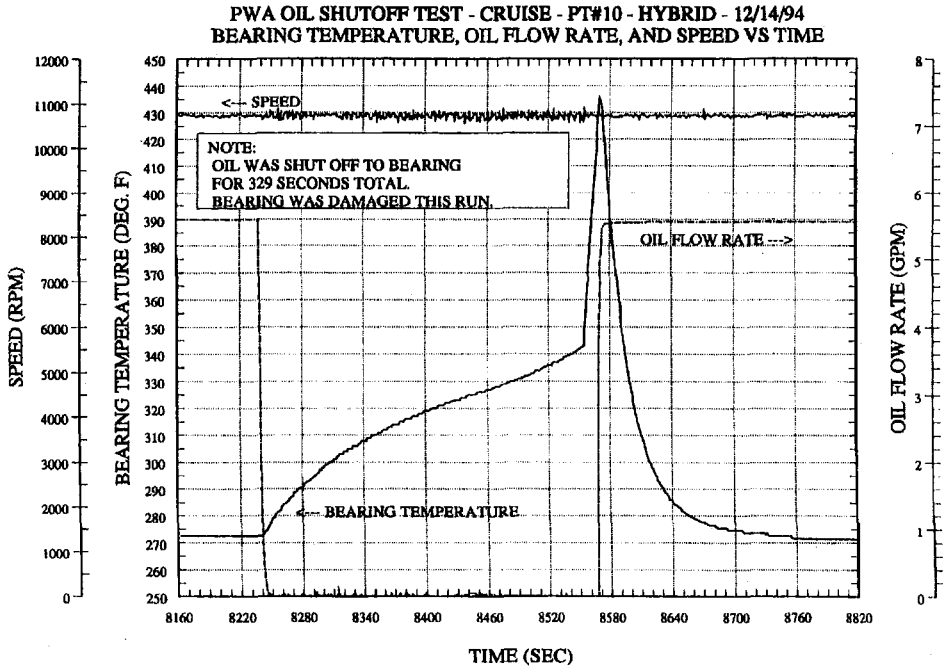

Fig. 7 Bearing temperature, oil flow rate, and speed versus time for the hybrid bearing at cruise

on the oil shutoff testing of 11-30-94, more conservative criteria were applied with respect to the restoration of oil flow to the test bearings. The temperature rise of the bearing outer ring was limited to 20°F for the all-metal bearing and 25°F for the hybrid bearing. The test bearing rate of temperature increase was monitored and not allowed to exceed 5°F/second. Finally, oil was restored to the bearing if any abnormal rig noises were observed.

Successful oil shutoff tests were run for both test bearings at CRUISE, MIDCLIMB, and TAKEOFF. For all three conditions, the hybrid bearing was run longer with the oil off than the all-metal bearing—73 seconds versus 42 seconds at CRUISE, 44 seconds versus 26 seconds at MIDCLIMB, and 25 seconds versus 16 seconds at TAKEOFF. It is believed that the all-metal bearing was very close to locking up and sustaining damage because slight rig noises were heard as the oil flow was being restored at CRUISE and TAKEOFF. The hybrid bearing, on the other hand, did not generate any abnormal rig noises during any of the test points.

The hybrid bearing was found to be in excellent condition and showed no signs of distress. The all-metal bearing did exhibit small intermittent black rub marks around the circumference of the loaded inner ring half.

Oil Shutoff Tests of 12-14-94—CRUISE, MIDCLIMB, and TAKEOFF

The objective of this test build was to better define the oil-off capabilities of the hybrid bearing at the CRUISE, MIDCLIMB, and TAKEOFF conditions. It was believed that in the previous oil shut-off tests, the hybrid bearing never reached the point of impending damage. The intent in this test series was to run the hybrid bearing for longer periods of time with the oil off at each of these three conditions, and ultimately to establish the time-to-failure at the CRUISE condition.

The test was assembled with the all-metal bearing, 1B6016B S/N 0708, in the front position and the hybrid bearing, HKJ13242 S/N E001, in the rear position. Oil shutoff tests of the hybrid bearing were performed at CRUISE, MIDCLIMB, and TAKEOFF with the bearing outer ring temperature rise limited to 30°F. The hybrid bearing was run successfully for 148 seconds at CRUISE, 53 seconds at MIDCLIMB, and 27 seconds at TAKEOFF.

The hybrid bearing was then run at CRUISE with the oil shut off until damage occurred. Figure 7 is a plot of bearing temperature versus time for this test. As indicated, the hybrid bearing was run for approximately 5 $\frac{1}{2}$ minutes (329 seconds) with the oil off before damage occurred. The maximum bearing temperature recorded was 437°F, a temperature rise of 165°F. It appears that the hybrid bearing did not lose all clearance until the bearing outer ring temperature reached approximately 342°F (a temperature rise of 70°F).

In order to insure that the hybrid bearing sustained enough damage to highlight the failure mechanism, one more oil shutoff test was performed. The hybrid bearing was run at CRUISE with the oil off for 95 seconds, at which point the test rig was making loud noises. The chip collector was then examined and found to be covered with metallic debris. The test rig was disassembled and the hybrid bearing was examined and found to be damaged. The cage I.D. land surface experienced significant wear. The silicon nitride balls did not appear to be damaged. The loaded inner ring half sustained damage with metallic debris rolled over the edge of the split surface and wear of the cage-land surface was visible. Wear of the inner ring cage-land surface was also visible on the unloaded inner ring half. The outer ring raceway surface sustained smearing damage over its entire circumference.

Results and Conclusions

1 Hybrid ball bearings, incorporating steel rings and CERBEC NBD 200 silicon nitride balls, were successfully designed for use in the PWA F117 engine No. 3 position.
2 Single ball testing of 1.125 in. diameter NBD 200 balls resulted in a fatigue life improvement factor of at least 4× relative to M50 steel. The failure mode of Si3N4 balls is very similar to the spalling observed for M50 balls.
3 Full-scale bearing tests, which included a wide variety of operating conditions, demonstrated that the hybrid bearings performed well. Under normal lubrication, the hybrid

Downloaded 02 Jun 2010 to 171.66.16.104. Redistribution subject to ASME license or copyright; see http://www.asme.org/terms/Terms_Use.cfm

bearings displayed thermal characteristics very similar to the current all-metal bearings.

4 Oil shutoff testing demonstrated that the hybrid bearings exhibited greater tolerance to oil starvation than the all-metal bearings. Under CRUISE conditions, the hybrid bearing ran for approximately $5\frac{1}{2}$ minutes after oil shutoff before any signs of distress were observed. This duration is about five times as long as the all-metal bearing under the same conditions.

Acknowledgments

The authors wish to thank the Advanced Research Projects Agency who sponsored this work and Norton Advanced Ceramics, Inc. (CERBEC) who contributed expertise to this program. We are grateful to Dr. L. Fehrenbacher of Technology Assessment & Transfer, Inc., without whose patience and understanding this paper would not have been possible; and especially to W. Ironside and G. Kohutovic of Pratt & Whitney Large Commercial Engines for assistance with the design analysis benchmarking and development testing.

References

1 ARPA BAA91-10, "Advanced Ceramic Technology Insertion Program Solicitation," 1999.

2 Contract F33615-92-C-2200; "Ceramic Bearing Technology Insertion," 1992.

3 Cundill, R. T., Galbato, A. T., Harris, T. A., "Fatigue Life of Silicon Nitride Balls," STLE 92-AM-8A-2, 1992.

Downloaded 02 Jun 2010 to 171.66.16.104. Redistribution subject to ASME license or copyright; see http://www.asme.org/terms/Terms_Use.cfm

J. V. Poplawski
J. V. Poplawski & Assoc.,
Bethlehem, PA 18017

D. R. Atwell

M. J. Lubas

V. Odessky

General Dynamics Corporation,
Groton, CT 06340;
Avenel, NJ 07001

Predicting Steady-State Temperature, Life, Skid, and Film Thickness in a Greased Preloaded Hybrid Ball Bearing

This paper describes the use of the SHABERTH computer program supplemented with experimental temperature and skid data to quantify steady-state bearing operation. Parametric studies on ball diameter and number, contact angle, curvature, grease type, and preload are presented with their influence on contact stress, fatigue life, skid load, film thickness, and inner and outer race temperatures. These results are compared for a steel versus hybrid bearing set in a DB and DFSL mounting. The method presented can be applied to the design of other steel and hybrid ball thrust bearing systems.

Introduction

Many classes of rotating machinery utilize preloaded duplex angular contact ball bearings for support of vertical shafts. Some examples include vertically mounted pumps, motors, and fans. Furthermore, grease lubrication is desirable in applications when loads, speeds and temperatures warrant it. Using grease precludes the need for pumps, coolers, and other equipment required in a circulating oil system.

The traditional bearing arrangements used on such shafts consist of a duplex preloaded back to back or "*O*" arrangements of the two bearings in the upper bearing location. This type of mounting provides high stiffness, precise axial location, and capability to counteract thrust reversal. A typical upper bearing arrangement is shown in Fig. 1. In many applications where loads and speeds are low to moderate, the available bearing catalogue rating and selection methods provide good designs that give many years of service life. Certain applications, however, may require that several conflicting performance characteristics be satisfied. This can place the equipment designer into a realm of design compromises that must be made to assure that the bearing satisfies the intended application. This usually requires quantifying bearing performance above and beyond the capability of the method provided in catalogue selection. In addition, recent interest in hybrid ceramic bearings introduces a whole new set of issues in bearing selection. Therefore, this paper will illustrate a methodology, with use of available computer tools, to help quantify temperature, life, skid, and film thickness for hybrid bearing configurations that are grease lubricated. It will also present of experimental data that were generated to "benchmark" these analytical models.

Design Considerations. Vertical shafts of the type described can operate at several speeds and experience both upwards and downwards thrust loading. Usually, the radial load is small with respect to the preload and applied thrust loads. The challenge faced in selecting an appropriate bearing size, internal geometry, preload, and grease requires a delicate balance between the following design parameters:

1 Bearing capacity and L_{10} fatigue life—maximize
2 Heat generation and temperature—minimize
3 Operating bearing temperature gradient—minimize
4 Operating clearances and preload—control
5 Hertzian contact stress—minimize
6 Minimum thrust to prevent skid—assurance
7 Load split—control
8 Lubricant film thickness—maximize
9 Grease properties—effect heat and film thickness
10 Grease replenishment—fresh grease is desirable
11 Appropriate race and element materials
12 Which life adjustment factors to use.

These parameters will carry different weightings for different applications. This paper will show how to quantify the aforementioned parameters and leave the setting of "relative importance" to the individual design team.

The Tradeoff Dilemma. Many applications of such bearing arrangements fall below 1×10^6 DN (DN = bore (mm) $\times$ rpm) and are considered low to moderate in speed. The L_{10} fatigue life of bearings in this regime is maximized by increased bearing dynamic capacity. High dynamic capacity is achieved with large diameter balls, high contact angle, and close raceway curvatures. Ball size, contact angle, and curvatures conducive to increased capacity tend to result in increased heat generation. Higher heat generation will effect temperature level and gradient within the bearing. Increasing temperature levels and gradients will feed back to reduced lubricant film thickness, increased preload, further increase in heat generation, and possible thermal lockup of the bearing set due to the reduced clearance.

Reducing the initial design preload level can result in reduced stiffness of the set. Also, the resulting load split upon application of external thrust may cause the effective net thrust on a ball row to fall below the minimum required thrust load to prevent skidding of the balls. Attempts to enhance the operating film thickness by employing a larger grease fill of a more viscous grease may cause a significant increase in heat generation and bearing temperature.

Furthermore, in applications where the resistance to contamination damage or extreme stiffness is a significant concern, the use of a hybrid bearing design consisting of metal races and silicon nitride balls will further complicate the situation. The direct substitution of a silicon nitride ball into an identical steel bearing will result in a 14 percent higher Hertzian contact stress. The silicon nitride ball, with a higher elastic modulus than steel, gives a smaller contact area to support the ball load. The fatigue

Contributed by the International Gas Turbine Institute and presented at the 40th International Gas Turbine and Aeroengine Congress and Exhibition, Houston, Texas, June 5–8, 1995. Manuscript received by the International Gas Turbine Institute March 10, 1995. Paper No. 95-GT-392. Associate Technical Editor: C. J. Russo.

Copyright © 1996 by ASME

Downloaded 02 Jun 2010 to 171.66.16.104. Redistribution subject to ASME license or copyright; see http://www.asme.org/terms/Terms_Use.cfm

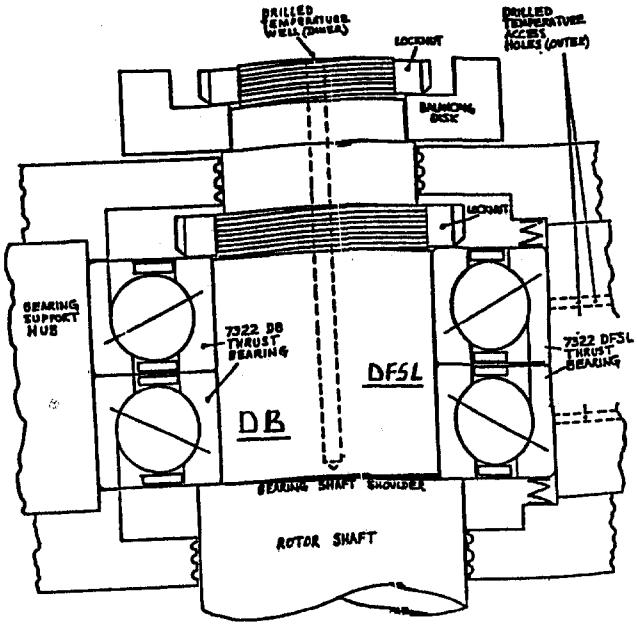

Fig. 1

life of a rolling contact is inversely proportioned to the 9th power of contact stress. Thus, direct substitution results in a bearing that has a classical L_{10} fatigue life at 30 percent of the all-steel bearing. Contact angle and raceway curvature must be altered to increase the life, but these changes will affect the thermal and dimensional characteristics of the bearing.

Trying to quantify all of these interactions with hand calculations is almost impossible. Fortunately, there are computerized analysis programs that can be used to quantify many of the bearing design-lubricant interactions that have been discussed. One such computer program is called SHABERTH.

The SHABERTH (1981) program was developed by SKF Industries under government funding. It is considered a "public domain" code and is available through COSMIC.[1] Specific details of the program can be found from SHABERTH (1991). SHABERTH can perform a thermal/dimensional analysis of a bearing system. Bearing internal geometry, load, speed, preload, lubricant properties, and initial clearances are used to estimate bearing heat generation. Heat generation is applied to a "finite difference" heat flow and temperature model of the bearing area, which had been specified as input. The resulting temperature distribution is used to calculate changes in bearing clearances and preload. These new values are used to re-estimate heat generation, a new temperature field, and updated clearances and preload. This process is automatically repeated until the changes in the temperature field and bearing clearance and preload for additional interations are small. At that point, a steady-state thermal and dimensional equilibrium state has been found. Our work incorporated the SKF film model and a Level 1 analysis mode where heat generation and film thickness are computed based upon the ball kinematics of Jones (1959).

SHABERTH Tricks and Enhancements

Preloading. The analysis reported required the development of certain methodologies and enhancements to the SHABERTH program. SHABERTH does not allow for input of bearing preload directly as a preload thrust or axial displacements of the bearing inner race. Therefore, curves of preload thrust versus negative internal diametral clearance (IDC) had to be developed for a single bearing row. Appropriate values of negative IDC were then imposed on the bearing DB set as an initial interference.

Hybrid Contact. The SHABERTH program permits different material properties for the elements versus raceway. Therefore, ceramic balls in metal raceways can be analyzed from a stress standpoint with an approximate life correction for dissimilar materials. Since the heat flow and ball to race contact temperature subroutine is hard coded for a steel ball on a steel race, alterations were made to allow a ceramic ball to steel race computation. The resulting modification was designated SHABHYB.

DFSL Mount. In a conventional DB or "solid" preload mounting of a bearing set, dimensional changes within the bearing set interact to alter the initial preload of a DB arrangement. For example, as the bearing temperature changes such that the temperature gradients from inner to outer race increase, the initial preload will increase. The preload will also increase due to ball centrigual forces acting within the bearing. Preload increase in a DB mount in these two examples is due to deflections being imposed on very stiff springs (Hertzian contact) since the raceways are mounted rigidly.

In a DFSL spring mounting (Fig. 1) changes in clearance and deflections are absorbed by axial movement of the raceway pushing against a much softer preload spring. The DFSL mount was approximated in SHABERTH and SHABHYB, by adjusting the bearing IDC and setting the thermal expansion coefficients of the shaft and bearing materials close to zero. This approach prevented temperature-induced dimensional changes from altering the bearing IDC. Comparisons of resulting per-row thrust were made with programs that model DFSL sets to show that the method was adequate over the range of loads and speeds examined.

Temperature Model. Heat generation and temperature prediction in rolling bearing systems is a difficult task. Bearing thermal equilibrium involves a marriage of the bearing, its mounting, shaft, housing, and the operational environment. Temperature models of a bearing system require "benchmarking." Temperature measurements on similar bearing configurations aided in the adjustment of heat transfer coefficients, refinement of model detail and the treatment of lubricant viscous and churning loss. These tests also showed that judging the adequacy of a temperature model based upon bearing outer race temperature can be misleading.

Skid Model. The onset of ball skidding in bearings of the type studied has been attributed to a gyroscopic slip mechanism discussed by Phillips and Dray (1982). Skid occurs when the gyroscopic moments developed on a ball exceed the traction moments provided at the ball to race contacts. In 1969 Poplawski and Mauriello published an approximate method for estimating when skidding can occur in ball thrust bearings. This tool aided the designer in setting the minimum required thrust load. For our study, the Poplawski model was resurrected and altered to include a "peak traction coefficient" acting in the ball to race contacts that counteract the gyroscopic moments. The traction coefficients must be experimentally determined as described by Sharma (1981) and will depend on the Hertzian stress level, lubricant type, and contact temperature.

The skid model iterates on a value of thrust load at which the moment balance is upset. The model includes ceramic balls. Model-calculated skid thrust loads for an all-steel 2315 bearing size and a hybrid 2315 bearing with silicon nitride balls are compared to test data presented by Phillips and Dray (1982), and Phillips (1991) in Fig. 2. As one can see, the gyroscopic skid model does a very good job at estimating skid loads for this type of bearing.

[1] NASA Computer Software Management and Information Center, The University of Georgia, Athens, GA.

Downloaded 02 Jun 2010 to 171.66.16.104. Redistribution subject to ASME license or copyright; see http://www.asme.org/terms/Terms_Use.cfm

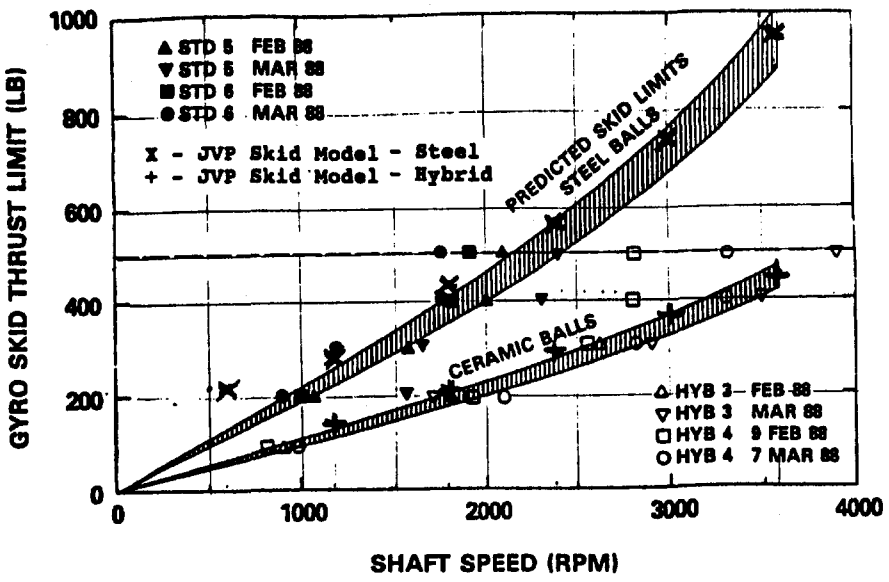

Fig. 2 Skid model correlation_steel and hybrid bearings

Steady-State Temperature Model Correlation

Figure 3 shows a schematic of the initial 7322DB (110 × 240 × 100 mm) bearing set mounted on a shaft and in the housing. The numbers are the node locations used in the SHABERTH finite difference heat flow and temperature calculation model. The dashed line represents an adiabatic surface across which no heat flow is allowed. The test bearing had thirteen 1.5 in. diameter balls and a 25 deg contact angle. The test was run at 1650 pounds downward thrust load at various speeds from 150 to 1200 rpm. The initial bearing preload was 2800 pounds. The test bearings were made from AISI 52100 steel. A light (ISO VG28) and heavy (ISO VG220) base oil viscosity grease were tested. Ambient temperature was about 20°C (70°F). Table 1 lists the results of measured steady-state outer race temperatures at four different speeds.

The data reported as Test II were used to benchmark the initial SHABERTH model. The convective cooling coefficients used in the model were adjusted such that a match between the measured and calculated outer race temperature was achieved.

The corresponding model calculated inner race temperatures gave temperature gradients that were unrealistic. The gradient varied from 19°F at 600 rpm to 56°F at 1200 rpm. Since the inner race is hotter than the outer race, the bearing would lose clearance and probably thermally preload and lock up. The model-predicted inner race temperatures were much too high.

The initial SHABERTH model was altered to add more shaft mass and additional cooling of the bearing end cap as shown in Fig. 3. Meanwhile, a second test configuration was assembled and contained a drilled hole into which a thermocouple was embedded (Fig. 1) to allow recording of the shaft center temperature along with the outer race. When the SHABERTH model-calculated shaft center temperature matches the measured value, an estimated inner race temperature is possible via the SHABERTH output.

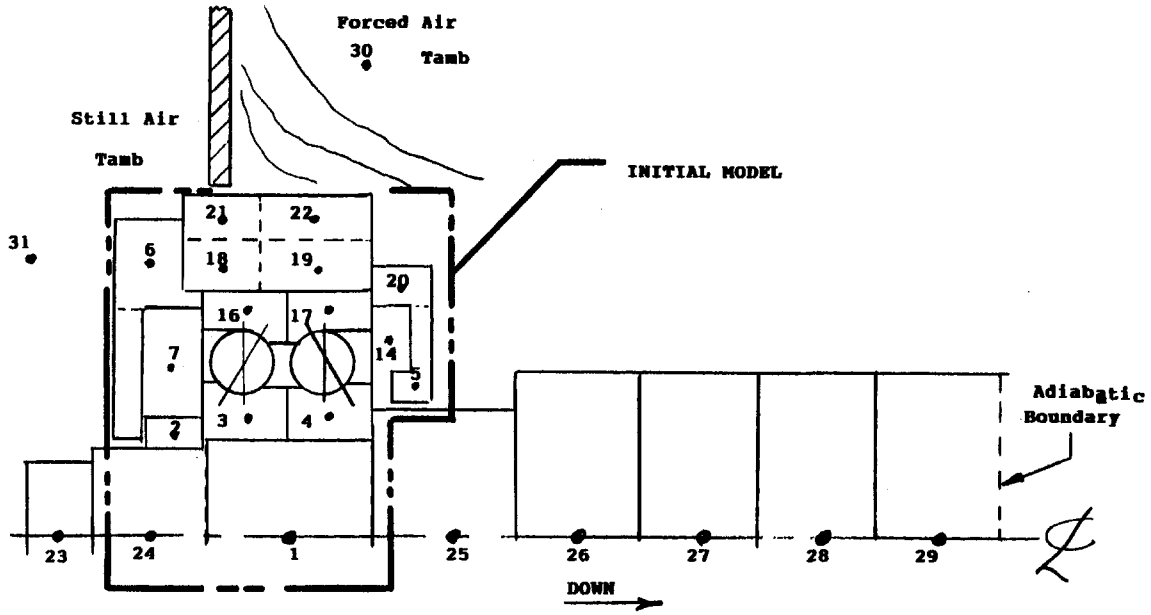

Fig. 3 SHABERTH thermal model

Downloaded 02 Jun 2010 to 171.66.16.104. Redistribution subject to ASME license or copyright; see http://www.asme.org/terms/Terms_Use.cfm

Table 1 Outer race temperature measurements on an all-steel 7322DB and DFSL set for a light and heavy viscosity base oil grease; peak and equilibrium temperature (°C) above ambient

rpm	TEST I DFSL Grease A	TEST II DB Grease A	TEST III DB Grease C	TEST IV DFSL Grease C
150 Peak	3.0	6.5	4.0	5.0
150 Equilibrium	3.0	6.5	4.0	5.0
300 Peak	4.2	6.0	8.0	14.0
300 Equilibrium	3.0	6.0	7.0	14.0
600 Peak	3.0	7.0	22.0	19.0
600 Equilibrium	3.0	6.5	7.5	19.0
1200 Peak	4.0	15.0	25.5	27.0
1200 Equilibrium	3.0	10.0	25.5	27.0
Ambient	20.5	20.5	22	25.5

Temperature measurements on a DFSL 7322 set operating at 1650# thrust, 1200 rpm, a spring preload of 1000 pounds with an ISO VG220 base oil grease are given in Table 2. Temperatures recorded at 150 and 1200 rpm compare very well with those estimated using the altered SHABERTH model for the DFSL mount. Note that an adjustment of the SHABERTH "cavity factor," which is used to estimate the viscous or churning loss, was required to simulate the effect of the heavier grease. The calculated outer and inner race temperatures and temperature gradient for Test II of Table 1 using the revised model (Fig. 4) are much more realistic.

Additional inspection of data in Table 1 showed the lighter ISO VG28 base oil grease had very little temperature increase over the speed range tested for both the DB and DFSL mounting (Tests I and II). Also, the more viscous ISOVG220 base oil grease in the DB arrangement had a substantial increase in outer race temperature (Test III).

These temperature studies reveal that increasing the grease viscosity in the DB set will result in a significant increase in bearing outer race temperature level (and correspondingly the inner race temperature level) due to greater heat generation, dimensional change, and preload increase. More significantly, the tests showed that the forgiving nature of the DFSL mount with its ability to absorb clearance and preload changes result in lower operating temperatures that remained fairly constant over the speed range studied.

Parametric Study

Valid parametric tradeoffs can now be examined with the benchmarked SHABERTH thermal/dimensional model of the two bearing set and the gyroscopic skid model. The following examples of a hybrid bearing with a DFSL mount illustrate the utility of this analytical approach. The goal is to design a bearing with a ball complement (diameter and number), contact angle and raceway curvatures that will give adequate L_{10} fatigue life with low operating temperatures and temperature gradients at a cubic mean thrust load of 3000 pounds and 350 rpm average speed. A second condition is to try to maintain a film thickness such that a specific film parameter Λ always exceeds 4 for the range of shaft speeds considered. Lambda values greater than 4 are conducive to achieving full separation between ball and raceway per Harris (1984). The four ball complement variables and properties of the three candidate greases that were studied appear in Table 3. The three greases span the range from light-weight to heavy with regard to their base oil viscosity and density.

Table 2 Shaft ID temperature measurements—7322 DFSL steel bearing and ISO VG 220 base oil viscosity grease at 1000# PLD, 1650# rotor wt (thrust) & 27 deg ambient; adjusted H_{21} + 30% cavity factor

	T_{OR}		T_{IR}		T_{SHAFT}		
rpm	Meas.	Calc	Meas.	Calc	Meas.	Calc	ΔT
150	34°C	32.7	—	32.7°C	35°C	32	0
1200	51°C	50.7	—	70°C	58°C	60.4	19.3°C

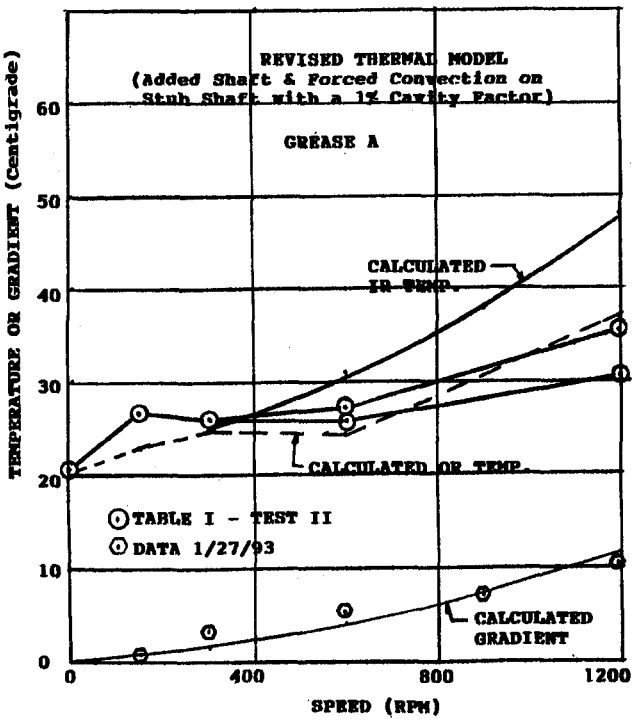

Fig. 4 Revised temperature model correlation

L_{10} Fatigue Life. The effect of contact angle and raceway curvature on L_{10} fatigue life for the four ball complements presented in Fig. 5 indicate that L_{10} fatigue life can be maximized by increasing the contact angle and using closer raceway curvatures. The ball complement $B2$ gives the near-optimum L_{10} fatigue life. However, high contact angle and close curvatures will generate more heat and increase bearing race temperature and gradients.

Bearing Operating Temperature and Gradient. The SHABERTH thermal/dimensional model was used to estimate the bearing inner and outer race temperatures for the hybrid DFSL set having a 25 deg angle, 52 percent outer and 51.5

Table 3 Parametric study variables; envelope size: 110 × 240 × 100 mm DFSL hybrid set

Code	Number	Diameter, in.	Preload
B1	13	1.50	800#
B2	17	1.125	630#
B3	25	0.75	400#
B4	36	0.50	200#

Race material: M50 VIM-VAR steel; ball material: silicone nitride; cubic mean loading: 3000# downward thrust

Greases	Code	Base oil at 40°C	Viscosity (CST) at 100°C	Density (g/cc)
ISO VG28	A	32	6.5	0.84
ISO VG100	B	101	11.3	0.89
ISO VG220	C	215	21.5	1.91

Downloaded 02 Jun 2010 to 171.66.16.104. Redistribution subject to ASME license or copyright; see http://www.asme.org/terms/Terms_Use.cfm

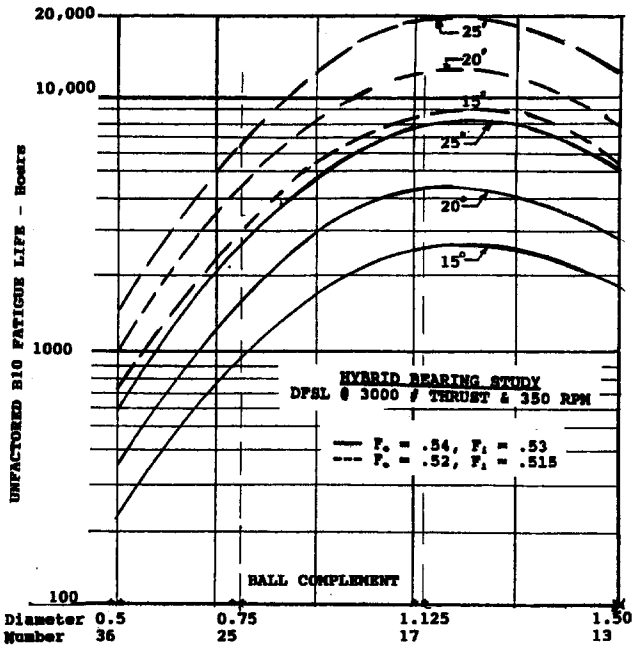

Fig. 5 Fatigue life study

percent inner curvatures. Four ball complements and three greases were evaluated at 3000 pounds thrust at speeds of 150 rpm to 1200 rpm.

The change in bearing inner and outer race temperatures with speed is shown for the four ball complements and grease *A* in Fig. 6. At 1200 rpm the estimated outer and inner race temperatures are in the range of 45°C (113°F) and 54°C (129.2°F), respectively, giving a gradient of 9°C (16.2°F) for the lightweight viscosity grease *A*. The ball complement has a small effect on the temperature as noted by the closeness of the temperature curves.

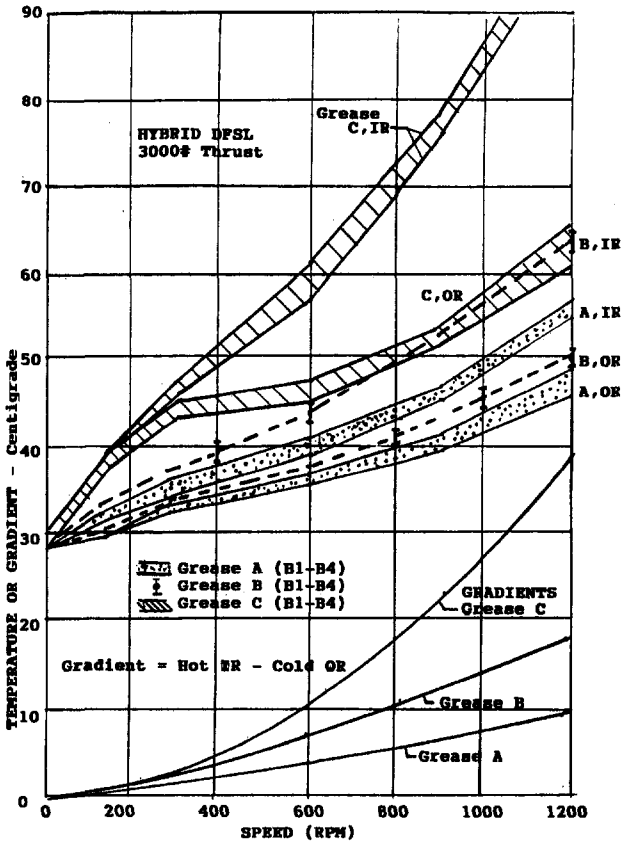

Fig. 6 Hybrid DFSL predicted temperature range for greases *A*, *B*, and *C* and *B*1–*B*4 complements

Table 4 Parametric study results summary

	At 1200 rpm – F			Λ	
Grease	T_{OR}	T_{IR}	Gradient	150 rpm	1200 rpm
A	113	129.2	16.2	2.8/3.8	7.3/9.0
B	122	149	27.0	7/12.5	12.5/16.3
C	145	217.5	72.0	20.5/30	15.6/17.2

The medium viscosity base oil grease *B* results presented in Fig. 6 show an outer and inner race temperature of about 50°C (122°F) and 65°C (149°F), respectively. The corresponding gradient would be 15°C (27°F). The higher grease viscosity generated more heat and increased bearing temperatures. Notice that the inner race temperature rose more than the outer race.

The temperature predictions for the heavy viscosity base oil grease *C* are also shown in Fig. 6. Not only is the viscosity of grease *C* about double that of *B*, its density is 1.91 g/cc versus 0.89 g/cc of grease *B*. Both the increased viscosity and density have escalated the churning heat generation effect. The result is bearing inner and outer temperatures of 63°C (145.4°F) and 103°C (217.4°F), respectively, with a gradient of 40°C (72°F). The comparison of inner and outer race temperatures of grease *A* versus *C* show the dramatic change in the thermal condition of the bearing. The change in the operating temperature gradients within the bearing show the significant change that occurs when the heavy grease *C* is used. The operating temperatures and gradients at 1200 rpm for the three greases are summarized in Table 4.

Film Thickness Specific Film Parameter. The interaction of ball complements, speed, temperature, and grease type on the operating film thickness is shown in Fig. 7. The specific film parameter Λ is defined as the ratio of the film thickness at the inner race contact to the composite surface roughness at that contact. Recall that a $\Lambda > 4$ was desired over the range of speeds studied.

The lower set of curves shows the change in specific film parameter as shaft speed increases from 150 to 1200 rpm for grease *A*. Film thickness increases with speed and viscosity. Higher speeds usually result in higher temperatures, especially with higher viscosity base stocks. This causes a reduction in film thickness. The viscosity reduction effect is present as curves *B*1–*B*4 increase, flatten, and begin to decrease. This effect is exemplified for the heavy grease *C* where a significant loss in film thickness occurs at speeds above 500 rpm. In this case, improved film thickness due to the higher speed is offset by a significant reduction in viscosity due to heat.

These results also show that the largest diameter ball (*B*1) develops the thickest film. The effect of ball diameter on film thickness is more pronounced for the heavier grease (Grease *C* versus *A*).

The specific film parameter Λ for grease *A*, at a value less than 4, does not meet one of the design requirements at the low 150 rpm speed point. Greases *B* and *C* have a specific film parameter Λ greater than 4 over the entire speed range.

Selection of the Best Bearing Design. The L_{10} fatigue life was greatest for ball complement *B*2 having seventeen 1-$\frac{1}{8}$ in. diameter balls. Therefore, the best design of the ones reviewed would have ball complement *B*2, a 25 deg contact angle, and a 52 percent outer and 51.5 percent inner race curvature. The unfactored L_{10} fatigue life would be about 20,000 hours or 2.28 years. An adjusted L_{10} fatigue life was estimated using the recently released STLE *Life Factors Guide* (1992). A material

Downloaded 02 Jun 2010 to 171.66.16.104. Redistribution subject to ASME license or copyright; see http://www.asme.org/terms/Terms_Use.cfm

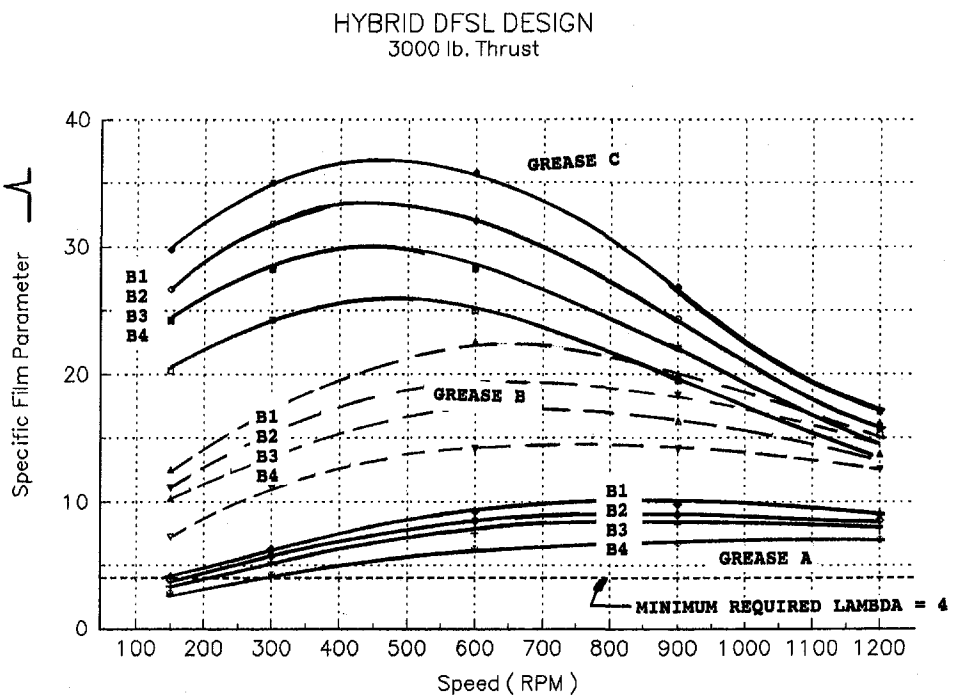

Fig. 7 Specific film parameter—greases *A*, *B*, and *C*

factor for the M50 steel was selected as 2 plus processing factor of 6 for VIM-VAR steel. This would give an adjusted L_{10} fatigue life of 240,000 hours or 27.4 years.

Grease results for the three greases suggest that grease *B* with an ISO VG 100 base oil viscosity would meet our requirements. Bearing temperatures, gradients, and specific film parameters for the three greases are summarized in Table 4.

The lighter ISO VG28 grease does not meet the requirements for $\Lambda > 4$. The heavy grease *C* would produce high bearing temperatures and gradients and would not give a significant improvement in film thickness at the 1200 rpm speed due to the excessive heat generation in the bearing. Therefore, the ISOVG 100 base oil grease *B* appears to be the best suited.

Having selected the design and grease combination, additional computer runs should be made at each point in the load/speed spectrum. A tabulation of important bearing parameters should be reviewed to ensure that adequate performance exists. Computer runs should also be made for a bearing in a geometrically degraded state.

The bearing design would have to be checked under any overload or shock loading that may occur during operation. Check on adequate shoulder height to prevent the ball from rolling over the shoulders would be required. Also, Hertzian contact stresses should be kept below the Brinell level. Finally, the bearing should not be structurally overstressed under the application of potential high overload.

Summary

The approach outlined in this paper is meant to serve as a guide to those involved in the selection and evaluation of grease lubricated preloaded angular contact ball bearings. The sample 7322 angular contact ball bearing set was used to illustrate the steps that were required in proceeding from a statement of design requirements to a final selection of a bearing and grease combination. Details and discussion were presented regarding the selection of analytical tools, the development of models for temperature and skid load estimation, benchmarking the models, and use of the correlated models to do parametric studies.

These efforts have produced a modified SHABERTH program ball to race heat flow and contact temperature subroutine that now include a ceramic ball and an approximate way for simulating a spring loaded DFSL set.

The availability and use of programs such as SHABERTH combined with some bearing knowledge and experimental data can significantly enhance the chances for a trouble-free design. Every dollar spent during the design phase on critical or difficult applications can save thousands of dollars in the field should a problematic situation be inherent in that design.

References

Harris, T. A., 1984, *Rolling Bearing Analysis,* 2nd ed., Wiley, New York, p. 508.

Jones, A. B., 1959, "Ball Motion and Friction in Ball Bearings," ASME *Journal of Basic Engineering,* Vol. 81, pp. 1–12.

Phillips, J. G., and Dray, J. F., 1982, "A Tribological Study of Ball Skidding in Angular Contact Ball Bearings," *Proceedings of the National Conference on Power Transmission,* Vol. IX, pp. 169–176.

Phillips, J. G., 1991, "Hybrid Bearings," *DARPA Ceramic Bearing Technology Program Conference Proceedings.*

Poplawski, J. V., and Mauriello, J. A., 1969, "Skidding in Lightly Loaded High Speed Ball Thrust Bearings," ASME Paper No. 69-LUBES-20.

SHABERTH, 1981, "Steady State and Transient Thermal Analysis of a Shaft Bearing System—A Users Manual," SKF Industries, King of Prussia, PA.

Sharma, S. K., 1981, "Traction Behavior of Some Lubricants and Hydraulic Fluids," ASME *Journal of Lubrication Technology,* Vol. 103, pp. 372–3.

STLE, 1992, *Life Factors for Rolling Bearings,* E. V. Zaretsky, ed., STLE, SP-34, Park Ridge, IL.

Downloaded 02 Jun 2010 to 171.66.16.104. Redistribution subject to ASME license or copyright; see http://www.asme.org/terms/Terms_Use.cfm

Hybrid Ceramic Bearings for Difficult Applications

M. M. Dezzani

P. K. Pearson

The Torrington Company,
Torrington, CT 06790

The Torrington Company, under contract from the Advanced Research Projects Agency (ARPA), has developed a hybrid bearing with improved properties for difficult applications. M50 and M50 NiL steel rings were nitrided to produce rolling contact raceway surfaces with hardnesses near Rockwell C 70. Rings were assembled with NBD-200 silicon nitride balls. Full-scale bearing tests were run under conditions that included 150°C temperature, surface flaws created by hard particle contamination, partial EHD lubrication, and the sliding action of balls running under thrust loading. The hybrid bearings had longer life than all steel bearings and demonstrated resistance to the surface peeling mode of failure initiation. Higher strength of the rolling contact surfaces, high residual compressive stresses in the nitrided layers, and a more favorable action in ceramic to steel rolling contact are discussed as the reasons for improved performance of the hybrid over all-steel bearings.

Introduction

This paper describes the manufacturing and testing of a hybrid bearing development for use in difficult applications. Silicon nitride has a long history of demonstrating good properties for rolling contact fatigue. It also has very high hardness and resistance to high temperature and corrosion damage that make it suitable for extreme application conditions. In theory all-ceramic bearings would be desirable, but their use has been limited by problems of ring manufacturing as well as application problems arising from differences in thermal expansion properties. The most common use for ceramics today is in hybrid bearings using silicon nitride rolling elements and steel rings. These perform well in applications such as machine tool spindles where conditions are predictable, clean, and controlled, but their use in more demanding applications is limited by the properties of the steel rings. An improved hybrid bearing is needed to withstand conditions of higher temperatures, poor lubrication, contamination, and poor rolling with sliding. These are the conditions that cause failures in service and make surface-initiated fatigue the most frequent mode of failure in bearings today.

Hybrid Bearing Development

The hybrid bearings for this development used Norton Advanced Ceramics NBD-200 hot isostatically pressed silicon nitride balls. The balls were finished to Grade 5 tolerances. Rings were manufactured from both M50 (4.0 Cr, 4.2 Mo, 1.0 V, 0.8 C) and M50 NiL (4.0 Cr, 4.2 Mo, 1.3 V, 3.5 Ni, 0.13 C) steels. Nitriding was chosen to improve the surface and near-surface zones of the steel rings. Nitriding increases the hardness to be closer to that of the silicon nitride. Nitriding is a diffusion process that becomes part of the microstructure and, therefore, not subject to delamination as hard coatings might be. Nitrided zones are thicker than applied coatings. Nitriding temperatures are close to the tempering temperatures for M50 and M50 NiL steels. Therefore, the high bearing hardness below the nitrided layer is not changed significantly.

The nitriding process used for the bearing rings was ferritic nitrocarburizing; that is, a hydrocarbon gas was added to the nitriding atmosphere. Rings were nitrided in a fluidized bed furnace for 32 hours at 525°C (975°F) using an atmosphere flow of 600 cubic feet per hour ammonia, 300 cfh nitrogen, and 200 cfh propane. The sequence of manufacturing operations for the rings was soft machining, carburizing (M50 NiL only), hardening, tempering, rough grinding of all surfaces, nitriding, finish grinding, and polishing of raceways. The raceway finish of the inner rings was 0.08 μm, the outers 0.12 to 0.16 μm Ra. The compound or white layer on nitrided surfaces causes poor rolling contact fatigue life, and all of this was removed from the raceway surfaces by finish grinding. The hardnesses and residual stresses at and below the raceway surfaces are shown in Figs. 1 and 2, respectively.

Bearing Test Procedures

The bearing test procedures were designed to simulate conditions found in aircraft turbine main shaft bearings; however, features of this test address the conditions that cause failures in many types of bearings and applications. Temperature of operation is high. Contamination creates surface flaws. Thin films provide only partial elastohydrodynamic (EHD) lubrication. Thrust operation causes ball spin, which creates sliding in the rolling contact zones.

Tests were carried out using 40 mm bore angular contact thrust bearings with nine 0.5-in. balls and bronze retainers. Tests were run at 10,000 rpm with oil corresponding to MIL-L-7808J at 150°C (300°F). The calculated EHD film thickness was 0.076 μm (3 μin.). The thrust load of the hybrid bearings was 7500 N (1700 lb), and the maximum compressive contact stress was 2.62 GPa (380 ksi). The test results were compared to previous tests of all steel bearings run at equivalent contact stress and also at equivalent load. For the 2.62 GPa contact stress condition, all-steel bearings were run under 11,800 N (2700 lb) load. At equivalent loading of 7500 N, all-steel bearings develop a lower contact stress of 2.28 GPa (330 ksi).

The bearings were first run for 15 minutes in oil that had been contaminated with 2.5 ppm of 20 μm aluminum oxide. The bearings were disassembled and washed, and the rings were examined for surface damage. The bearings were then reassembled and run in different rigs with clean oil. Details of this test and previous test results were reported by Averbach et al. [1–3].

Test Results

The bearing life results are listed in Tables 1–4. Three types of all-steel bearing used M50 steel balls in M50 steel rings, in

Contributed by the International Gas Turbine Institute and presented at the 40th International Gas Turbine and Aeroengine Congress and Exhibition, Houston, Texas, June 5–8, 1995. Manuscript received by the International Gas Turbine Institute March 18, 1995. Paper No. 95-GT-391. Associate Technical Editor: C. J. Russo.

Copyright © 1996 by ASME

Downloaded 02 Jun 2010 to 171.66.16.104. Redistribution subject to ASME license or copyright; see http://www.asme.org/terms/Terms_Use.cfm

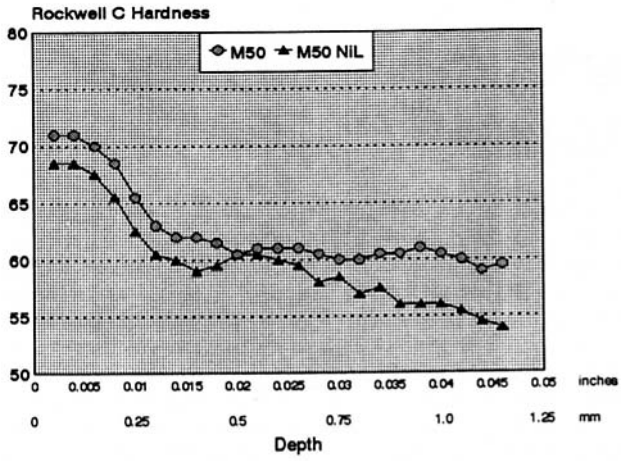

Fig. 1 Hardness profiles, M50 and M50 NiL steel bearing rings

M50 NiL steel rings, and in M50 NiL steel rings with TDC coating. TDC is a thin dense chromium coating with hardness near Rockwell C 70, applied so as to have compressive residual stresses for good rolling contact performance.

The hybrid bearings showed superior performance at the equivalent contact stress condition. They were also superior at equivalent loading, a condition under which the all-steel bearings were running at a lower contact stress. None of the ten nitrided M50 hybrids failed within the 2000 hour suspension time for the test. The nitrided M50 NiL hybrid bearings had three failures, but the L10 life of this hybrid combination was longer than the life of any of the all-steel bearings, even though the best of the all-steel bearings had the very hard TDC surface on M50 NiL rings. The absence of nitrided M50 hybrid failures prevented the calculation of an L10 life for this group. Tables 2 and 4 show statistical calculations of 90 percent lower confidence limits, assuming a Weibull slope of 1.5 for the nitrided M50.

Differences in surface behavior accompanied the differences in life, and these observations support the conclusions to be drawn from the life results. The all-steel bearing failures began with a process of peeling. Peeling is the growth of shallow areas of surface distress less than 100 μm (0.004 in.) deep. The failure process begins when the already thin lubrication film becomes even thinner as it spreads out at the surface flaws caused by the contamination. Partial EHD conditions allow metal-to-metal

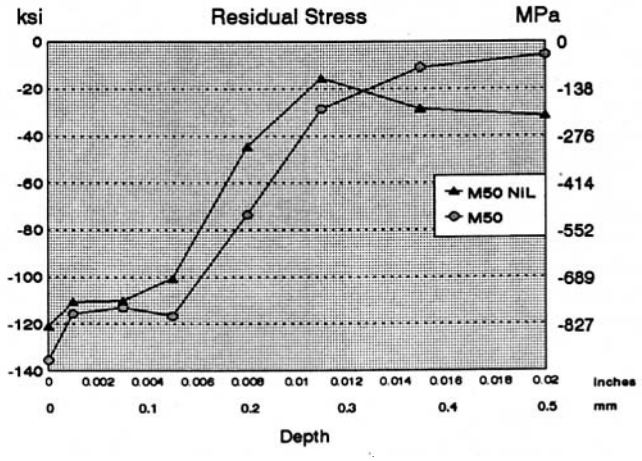

Fig. 2 Residual stress, nitrided M50 and M50 NiL steel bearing rings

Table 1 Summary of results for 208 bearing tests, hours; maximum contact stress 380 ksi; (FI) failed inner ring, (FB) failed ball, (S) suspended

Hybrid Nitrided M50	Hybrid Nitrided M50 NiL	M50	M50 NiL With TDC
2034 (S)	797 (FI)	68 (FI)	434 (FI)
2034 (S)	1299 (FI)	147 (FI)	486 (FI)
2038 (S)	1882 (FI)	310 (FI)	722 (FI)
2038 (S)	2001 (S)	316 (FI)	695 (FB)
2020 (S)	2016 (S)	334 (FI)	1100 (FB)
2020 (S)	2022 (S)	746 (FI)	1504 (S)
2006 (S)	2032 (S)	1127 (FI)	1535 (S)
2038 (S)	2032 (S)	1500 (S)	1535 (S)
2004 (S)	2001 (S)	1500 (S)	1544 (S)
2004 (S)	2174 (S)	1500 (S)	1587 (S)
			1684 (S)

contact at the edges of the flaws. The coefficient of friction rises to increase stress at the surfaces. The failure process ends when peeling creates a larger area of surface distress from which a macro spall develops. An example of this from an M50 all-steel bearing is shown in Fig. 3. The TDC-coated raceways followed the same failure process, with the difference being that the harder TDC surface made the initial contamination flaws smaller and the rate of peeling slower, leading to the longer life of the TDC-coated raceways. The nitrided raceways with silicon nitride balls were free of peeling damage. They had many flaws because the aluminum oxide contamination was harder than the nitrided surfaces, but none of these developed into peeled areas. Nitrided raceways are shown in Fig. 4.

Discussion

At least three conditions may account for the better performance of the nitrided M50 and M50 NiL hybrid bearings. These are harder, dent-resistant surfaces, very high residual compressive stresses to resist crack initiation and propagation, and more favorable action at the ceramic to steel rolling contact interface.

Analytical studies have explained how conditions of roughness, traction, contamination, and flaws cause stresses at the surfaces to be greater than the subsurface stresses of Hertzian contact. Olver et al. have shown that contacting surfaces of normal roughness can result in stress on the order of twice that of the subsurface maximum shear [4]. Chiu has calculated the high tensile stresses that develop in the presence of individual surface flaws [5]. Fatigue begins when behavior ceases to be perfectly elastic and microyielding takes place. Harder sur-

Table 2 Summary of Weibull analysis for 208 bearing tests; maximum contact stress 380 ksi

Bearing Material	L_{10}, hours	90% Lower Confidence L_{10}, hours	Weibull Slope
Hybrid Nitrided M50	-*	1187	1.5 (estimated)
Hybrid Nitrided M50 NiL	998	444	1.72
M50 NiL & TDC Rings	478	254	2.47
M50	93	25	1.02

* No Failures, therefore an L_{10} life could not be determined

Table 3 Summary of results for 208 bearing tests, hours; approximately 1700 pounds thrust load; (FI) failed inner ring, (FB) failed ball, (S) suspended

Hybrid Nitrided M50	Hybrid Nitrided M50 NiL	M50	M50 NiL	M50 NiL With TDC
2034 (S)	797 (FI)	429 (FI)	270 (FI)	374 (FI)
2034 (S)	1299 (FI)	445 (FI)	317 (FI)	901 (FI)
2038 (S)	1882 (FI)	502 (FI)	326 (FI)	1082 (FI)
2038 (S)	2001 (S)	635 (FI)	677 (FI)	2213 (S)
2020 (S)	2016 (S)	666 (FI)	779 (FI)	2213 (S)
2020 (S)	2022 (S)	1390 (FI)	998 (FI)	2278 (S)
2006 (S)	2032 (S)	1916 (FI)	1372 (FI)	2278 (S)
2038 (S)	2032 (S)	2010 (FI)	1500 (FI)	2395 (S)
2004 (S)	2001 (S)	2095 (S)	2715 (S)	3571 (S)
2004 (S)	2174 (S)	2095 (S)	2890 (S)	3571 (S)

Downloaded 02 Jun 2010 to 171.66.16.104. Redistribution subject to ASME license or copyright; see http://www.asme.org/terms/Terms_Use.cfm

Table 4 Summary of Weibull analysis for 208 bearing tests, approximately 1700 pounds thrust load

Table 4: Summary of Weibull Analysis for 208 Bearing Tests, Approx. 1700 Pounds Thrust Load

Bearing Material	L_{10}, hours	90% Lower Confidence L_{10}, hours	Weibull Slope
Hybrid Nitrided M50	*	1187	1.5 (estimate)
Hybrid Nitrided M50 NiL	998	444	1.72
M50	368	172	1.73
M50 NiL	232	112	1.53
M50 NiL & TDC Rings	533	152	1.33

* No Failures, therefore an L_{10} life could not be determined

faces have higher yield properties to resist this onset of fatigue. This explains the excellent rolling contact performance of the silicon nitride itself in addition to the improved life of the nitrided steel surfaces and, to a lesser extent, the TDC coating.

The high residual compressive stresses in the nitrided layer are also expected to contribute to longer life. The residual stresses in the outermost zone within 0.025 μm (0.001 in.) of the surface are the product of grinding and finishing and tend to be similar for all steels. It is just below this depth, the zone into which cracks must propagate for peeling as well as macro spalling, that the compressive stresses from nitriding will resist crack growth. The rolling contact action of ceramic to steel must also be considered. Rhoads et al. demonstrated that hybrid bearings are capable of sustained operation at reduced oil flow in high-speed turbine engine bearings [6]. Insufficient lubrication film is at the beginning of the failure process in many applications. Ceramic hybrid bearings operate at lower temperatures and prevent any possibility of metal to metal contact, both beneficial features when lubrication films are thin and partial EHD conditions exist.

The difference between the nitrided M50 and nitrided M50 NiL hybrid bearings in these tests may be statistical or, if real, show a benefit from the greater carbide content and harder M50 surface in resisting the microscuffing that takes place in partial EHD conditions.

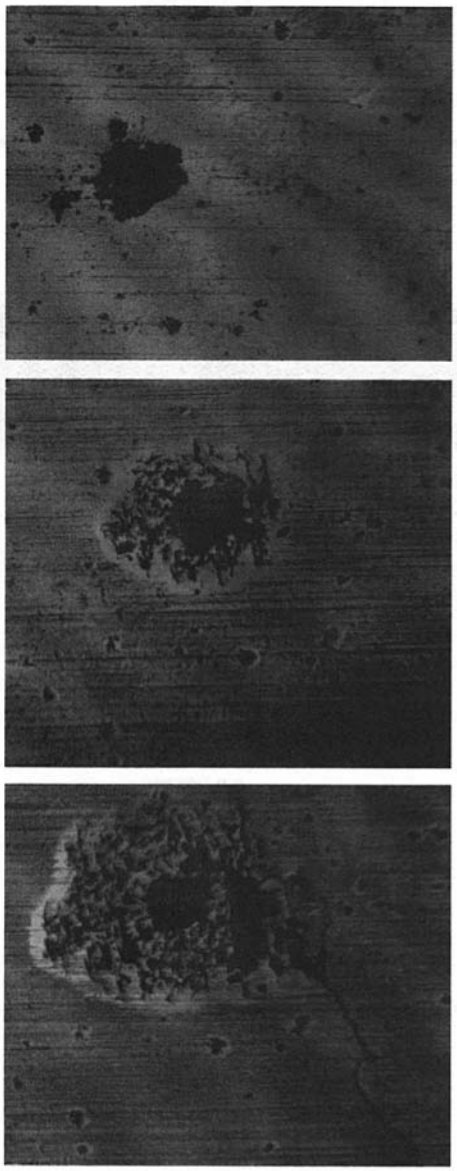

Fig. 3 Progression of damage in M50 raceway, all-steel bearing. Upper, initial 15 minute damage. Middle, after running 22 hours. Lower, macro spall developing at 68 hours. Mag. ×80.

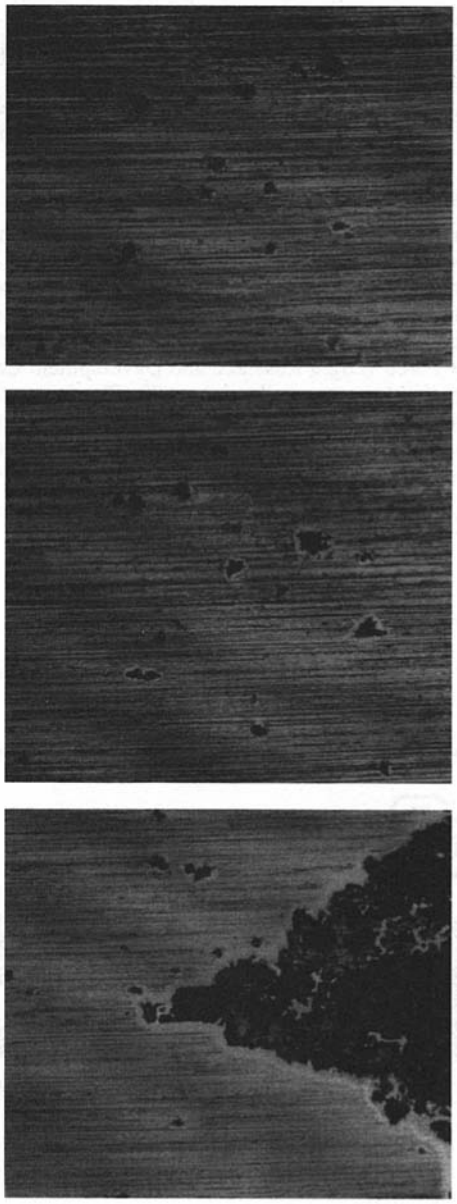

Fig. 4 Nitrided raceways in hybrid bearings. Upper, M50 after initial 15 minute damage. Middle, M50 after running 208 hours. Lower, M50 NiL spall after 797 hours. Mag. ×80.

Downloaded 02 Jun 2010 to 171.66.16.104. Redistribution subject to ASME license or copyright; see http://www.asme.org/terms/Terms_Use.cfm

Conclusion

Hybrid bearings using silicon nitride balls and nitrided M50 and M50 NiL raceways perform better than all-steel bearings in conditions of contamination, surface flaws, marginal lubrication, and traction that are the cause of many failures in service.

Acknowledgments

The authors wish to thank the Advanced Research Projects Agency who sponsored the Improved Hybrid Bearing development and the many others who contributed to this work. The bearing test procedure and baseline all-steel data were developed in collaboration with GE Aircraft Engines under contract to the Air Force Wright Research and Development Center. We are also grateful to many colleagues at The Torrington Company who were part of this effort, especially Mr. Henry Daverio for the bearing life testing, Mr. Donald Church for the laboratory work, and Dr. Jack Woodilla, Director of the Advanced Technology Center, for support and encouragement of this materials development program.

References

1 Averbach, B. L., and Bamberger, E. N., "Analysis of Bearing Incidents in Aircraft Gas Turbine Mainshaft Bearings," *Tribology Transactions,* Vol. 34, No. 2, 1991, pp. 241–247.

2 Averbach, B. L., Van Pelt, S. G., Pearson, P. K., and Bamberger, E. N., "Surface Initiated Spalling Fatigue in M50 and M50 NiL Bearings," *Lubrication Engineering,* Vol. 47, No. 10, 1991, pp. 837–843.

3 Averbach, B. L., Van Pelt, S. G., and Pearson, P. K., "Initiation of Spalling in Aircraft Gas Turbine Bearings," AIAA Paper No. 90-2291, 1990.

4 Olver, A. V., Cole, S. J., and Sayles, R. S., "Contact Stresses in Nitrided Steels," *19th Leeds Lyon Symposium on Tribology,* Sep. 1992; published Elsevier, 1993.

5 Chiu, Y. P., "The Role of Residual (Internal) Stresses on Microspalling Rolling Contact," *Rolling Element Bearing Symposium '91,* Orlando, FL, 1991.

6 Rhoads, M. A., Bashyam, M., and Crecelius, W. J., "Large Engine Hybrid Ceramic Bearings," ASME Paper No. 94-GT-262, 1994.

Downloaded 02 Jun 2010 to 171.66.16.104. Redistribution subject to ASME license or copyright; see http://www.asme.org/terms/Terms_Use.cfm

Thermodynamic Analysis of New Combination of Supercharged Boiler Cycle and Heat Recovery Cycle for Power Generation

M. Akiba

E. A. Thani

Department of Mechanical Engineering,
Yokohama National University,
Yokohama 240, Japan

The aim of this paper is to study the performance of a new combination of supercharged boiler–gas turbine cycle, which is expected to reduce the cooling air in the combustor and heat recovery cycle, from a thermodynamic point of view. Two designs of this cycle were adopted and the influences of various operating parameters, such as compressor pressure ratio, ambient temperature, inlet gas temperature of gas turbine, percentage of excess air, and number of feedwater heaters, were studied. Three techniques were applied to increase the overall cycle efficiency: first, increasing the mean temperature of heat supplied by increasing the inlet gas temperature of the gas turbine; second, decreasing the mean temperature of heat rejected through a heat recovery cycle; and third, reducing the percentage of excess air in the supercharged boiler. A performance comparison between the adopted cycles and a conventional heat recovery cycle was made. The results show that there is an improvement in overall cycle efficiency of about 8.5–9.5 percent with the first design of the adopted cycle over the conventional heat recovery cycle, while an improvement of overall cycle efficiency of about 1.0–5.5 percent is obtained for the second design.

Introduction

Recently, in an attempt to conserve energy, special attention is being paid to combined cycle power plants, such as those composed of Brayton–Rankine cycles, which have higher efficiencies than conventional thermal power plants. One of the applicable methods of saving energy and increasing the thermal efficiency, in addition to reducing steam generator size, is to supercharge the steam generator by using a gas turbine-driven compressor to furnish combustion air [1–4]. If the gas turbine output power is sufficient only for driving the compressor, we have the well-known Velox cycle introduced by Brown Boveri in the early 1930s [1]. If, on the other hand, the inlet gas temperature to the gas turbine is much higher, the gas turbine can furnish sufficient excess power to drive an alternator and generate more electrical power. This cycle is called the supercharged boiler combined cycle. Developments in materials science (metallurgy) and pressure vessel technology make it possible to build such a steam generator. The reduction in size and heat transfer surface of a supercharged boiler are due to two reasons. First, as the operating gas-side pressure is increased, the emissivity of the nonluminous radiating gases increases markedly [1, 3]. Second, the higher gas density and available pressure drop permit much higher gas mass flow rates (compared with the conventional steam generator) to be used in the convection section, with higher accompanying convection heat transfer coefficients [1–3].

This paper will concentrate on the combination of supercharged boiler cycle and the heat recovery cycle, adopting two designs of this cycle. It will also discuss the effect of variations of its operating parameters and compare its performance with a conventional heat recovery cycle.

Description of the Cycle

Figure 1 shows an example of the first design combining the supercharged boiler cycle with the heat recovery cycle. In this arrangement the compressor supplies pressurized air to the boiler. All combustion takes place in the boiler and steam can be generated at any suitable pressure and temperature.

High-temperature pressurized gas from the boiler is expanded as it flows through the gas turbine. The power so developed drives the compressor and the generator. The gas from the gas turbine exhausts into a heat recovery boiler to generate steam. In turn, the steam is used to run a steam turbine. An unfolded temperature–enthalpy diagram for the first design of this cycle is illustrated in Fig. 2. The Y axis of this diagram represents the temperature of air, flue gases, water, or steam in the cycle. The X axis represents the enthalpy of each process in the cycle as a percentage of the total input of enthalpy from 0 percent to 100 percent, while the second portion from 100 percent to 0 percent represents the distribution of the input enthalpy through the whole cycle. In this diagram the enthalpy of the air increases across the compressor due to work input (W_c). The dotted line shows the change from air to products in the combustion process as an equivalent heating process. Heat (Q_{SB}) is transferred to the supercharged boiler, while the drop in gas enthalpy is the gas turbine work (W_{gt}). Heat (Q_{HRB}) is heat transferred to the recovery boiler and there is a stack heat loss (Q_{sta}). Also shown in this figure are the processes of generating steam in the supercharged boiler and heat recovery boiler.

Figure 3 shows the second design of this combined cycle, in which the supercharged boiler provides the lower cycle with only a fraction of its requirements. The high-temperature pressurized gases heated from the supercharged boiler expand in the gas turbine. The gas turbine exhausts into a heat recovery boiler that generates steam to a reheat steam turbine. This design is easy to operate, and has lower initial costs and higher specific output power when compared to the first design. The only difference between features (A), (B), and (C) of Fig. 3 is the enthalpy of water entering the supercharged boiler. In feature (A) water enters the supercharged boiler from a high-pressure economizer; in feature (B) water enters the supercharged boiler from a low-pressure economizer, and in feature (C) water enters the condenser directly. Figure 4 shows the unfolded tempera-

Contributed by the Power Division and presented at the JSME–ASME ICOPE-93, Tokyo, Japan, September 12–16, 1993. Manuscript received at ASME Headquarters August 1, 1995. Associate Technical Editor: D. Y. S. Lou.

Copyright © 1996 by ASME

Downloaded 02 Jun 2010 to 171.66.16.104. Redistribution subject to ASME license or copyright; see http://www.asme.org/terms/Terms_Use.cfm

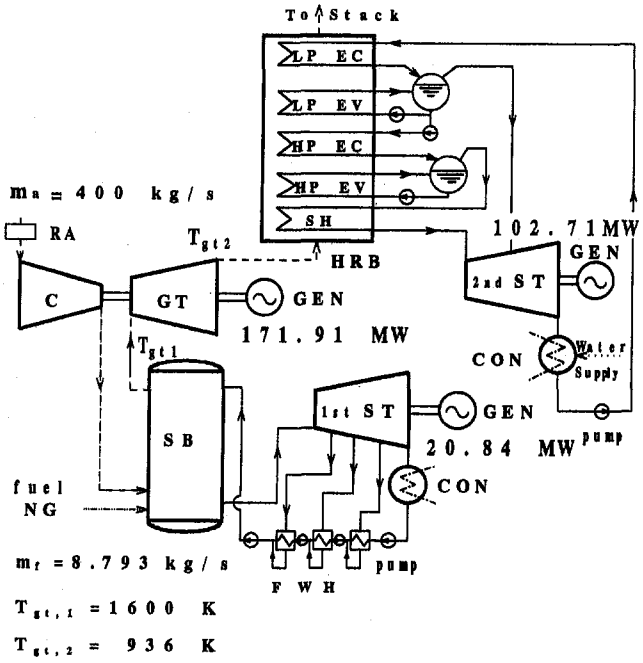

Fig. 1 Schematic diagram of the arrangement of the first design

ture–enthalpy diagram for the second design of this combined cycle. The temperature–entropy diagram of the second design (*A*) is illustrated in Fig. 5.

Analysis

The two designs described in the previous section are used to calculate the adopted cycle performance. Appropriate assumptions are made through analyzing many combined cycles [2–10]. Those assumptions are listed in Table 1.

First Design. In this cycle, thermodynamic properties of air and gases were calculated point by point by using the Gas Tables [11]. Steam Tables [12] are used to find the thermodynamic properties of water and steam.

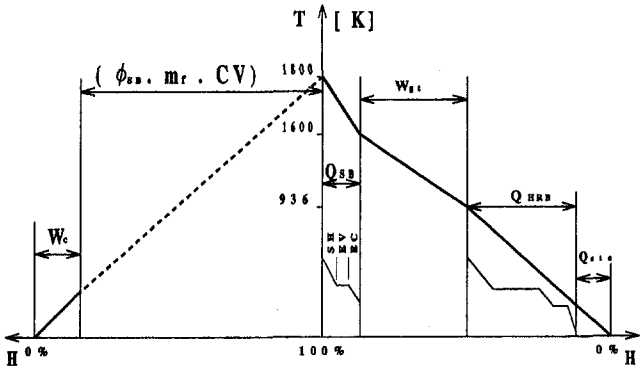

Fig. 2 Unfolded temperature–enthalpy diagram for the first design

The heat balance for the supercharged boiler can be expressed by the following equation:

$$m_a h_{c,2} + m_f CV = \frac{m_s}{\Phi_{SB}} (h_{SB,2} - h_{SB,1}) + (m_a + m_f)\, h_{gt,1} \quad (1)$$

For a defined percentage of excess air, Eq. (1) divided by m_a becomes

$$h_{c,2} + \frac{(FA\ CV)}{\Psi} = \frac{m_s}{m_a} \frac{(h_{SB,2} - h_{SB,1})}{\Phi_{SB}} + \left(1 + \frac{FA}{\Psi}\right) h_{gt,1} \quad (2)$$

Many operating parameters were used in the calculation to assess their effects on the performance of this cycle. Compressor pressure ratios of 9, 12, 16, or 20; inlet temperatures of gas turbine of 1400, 1500, or 1600 K; percentage of excess air of 10, 50, 100, 150, or 200 percent; and number of feedwater heaters of 3, 4, or 5 with temperature rises in each heater equal to 70, 50, and 40°C, respectively, were used in this study.

At a given compressor pressure ratio, inlet gas temperature to the gas turbine, and steam conditions, the mass of steam generated from a supercharged boiler per kg of air can be calculated from Eq. (2). Since the thermodynamic properties of each point in the Brayton cycle are known, the compressor power, gas turbine power, and the net power can be calculated. In

Nomenclature

CV = calorific value, kJ/kg
FA = fuel to air ratio by mass
h = specific enthalpy, kJ/kg
h_h = specific enthalpy of water outlet from high pressure economizer, kJ/kg
h_l = specific enthalpy of water outlet from low pressure economizer, kJ/kg
m = mass flow rate, kg/s
m_{1st} = mass flow rate of generated steam at low pressure in the heat recovery boiler of the second design, kg/s
Q = heat transferred, kJ/s
T = temperature, K
W = power, MW
w_{sp} = specific power output, kJ/kg of air or kW/kg/s
ΔT = temperature difference, °C
η = efficiency, percent
η_O = overall cycle efficiency, percent
π = compressor pressure ratio
ϕ = effectiveness of the boiler, percent
Ψ = equivalence ratio

Subscripts

a = air
amb = ambient
c = compressor
con = condenser
f = fuel
gt = gas turbine
hst = high pressure steam turbine
HRB = heat recovery boiler
is = isentropic
lst = low pressure steam turbine
rs = reheat steam
s = steam
SB = supercharged boiler
sc = steam entering the combustion chamber
st = steam turbine
sta = stack
1 = inlet to the component
2 = outlet from the component

Acronyms

C = compressor
CON = condenser
EC = economizer
EV = evaporator
FWH = feedwater heater
GEN = generator
GT = gas turbine
HRB = heat recovery boiler
HP = high pressure
IP = intermediate pressure
LP = low pressure
NG = natural gas [(CH_4 = 0.788, C_2H_6 = 0.140, N_2 = 0.068, CO_2 = 0.004 by volume at 1 atm and 15.6°C); (HHV = 9012 kcal/m^3)]
RA = room of absorbing air
RH = reheater
SB = supercharged boiler
SH = superheater
ST = steam turbine
WSP = water separator

Downloaded 02 Jun 2010 to 171.66.16.104. Redistribution subject to ASME license or copyright; see http://www.asme.org/terms/Terms_Use.cfm

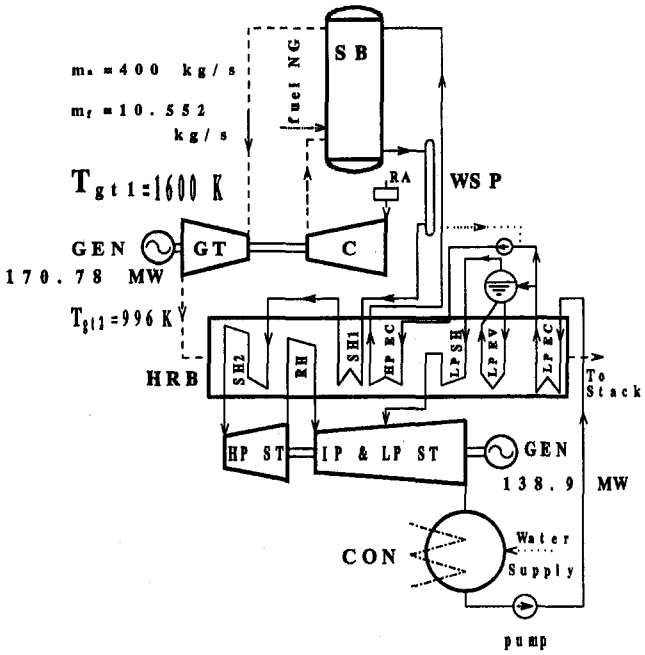

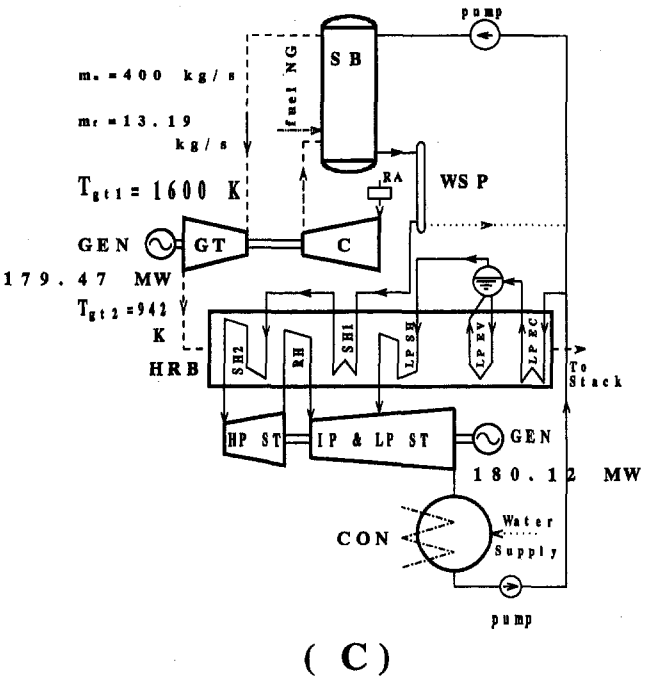

Fig. 3 Schematic diagram of the arrangement of the second design

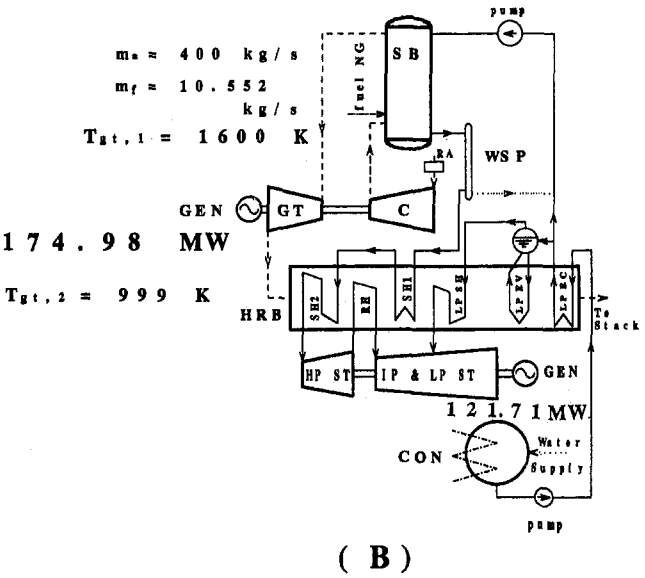

addition, the net power of the first steam cycle can be calculated, since the thermodynamic properties at all points of the regenerative cycle are known.

An accurate computer program was used to evaluate the heat recovery boiler. By using the modulated equations of state for mixed air, the generated steam and the net power of the second steam cycle can be calculated [7]. Figure 6 shows the flow chart of the program. Table 2 shows the inlet conditions used in the first and second steam turbines.

Second Design. The performance of this cycle was evaluated for inlet temperature to the gas turbine equal to 1600 K with varying compressor pressure ratio of 9, 12, 16, or 20. Equation (2) can be used to express heat balance for the supercharged boiler of the second design.

The heat balance for the heat recovery boiler can be expressed by the following equation:

$$m_s[(h_{\text{hst},1} - h_s) + (h_{rs} - -h_{\text{hst},2}) + X] + m_{\text{lst}}\,(h_{\text{lst},1} - h_{\text{con}}) = \Phi_{\text{HRB}}\,(m_a + m_f)(h_{gt,2} - h_{\text{sta}}) \quad (3)$$

Here:

$$X = (h_h - h_{\text{con}}) \quad \text{(in the second design } (A)\text{)}$$

$$X = (h_l - h_{\text{con}}) \quad \text{(in the second design } (B)\text{)}$$

$$X = 0 \quad \text{(in the second design } (C)\text{)}$$

With a given percentage of excess air, Eq. (3), divided by m_a, can be rewritten as:

$$\frac{m_s}{m_a}[(h_{\text{hst},1} - h_s) + (h_{rs} - h_{\text{hst},2}) + X] + \frac{m_{\text{lst}}}{m_a}(h_{\text{lst},1} - h_{\text{con}}) = \Phi_{\text{HRB}}\left(1 + \frac{FA}{\Psi}\right)(h_{gt,2} - h_{\text{sta}}) \quad (4)$$

From Eq. (4) the value of (m_{lst}/m_a) can be calculated. The same procedure used in the first design was followed to calculate the net power of the Brayton cycle and the Rankine cycle of the second design. Table 3 shows the steam conditions used in this cycle.

Discussion of Results

Figure 7 shows the relation between the percentage of excess air in the supercharged boiler and the overall cycle efficiency for the first design at inlet gas turbine temperature of 1600 K. At a constant compressor pressure ratio, the overall cycle efficiency increases as the percentage of excess air increases, up to 200 percent of excess air. After that the efficiency will decrease sharply because there is no steam produced from the supercharged boiler and the cycle becomes a conventional heat recovery cycle. Also, at a constant percentage of excess air and as the compressor pressure ratio increases, the overall cycle

Downloaded 02 Jun 2010 to 171.66.16.104. Redistribution subject to ASME license or copyright; see http://www.asme.org/terms/Terms_Use.cfm

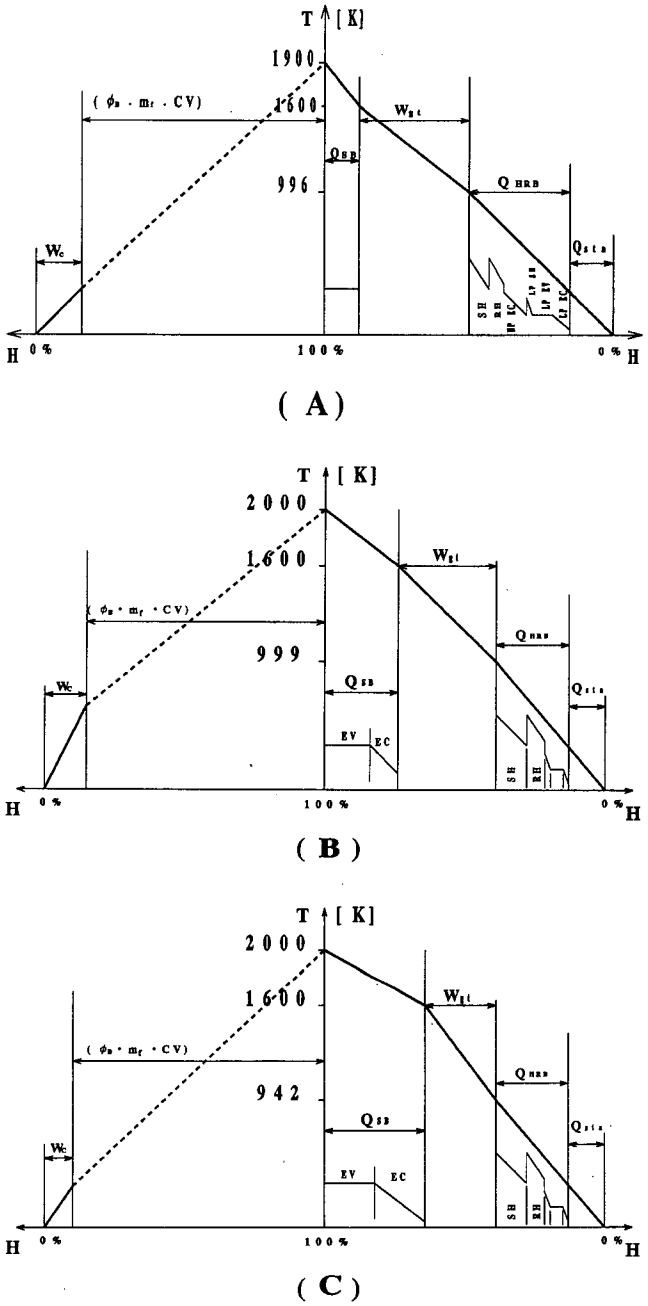

Fig. 4 Unfolded temperature–enthalpy diagram for the second design

efficiency will first increase until a certain compressor pressure ratio is reached, then decrease.

Figures 8–10 show plots of the overall cycle efficiency versus the net output power of the first design with 3, 4, and 5 feedwater heaters, respectively. These figures indicate that increasing the inlet temperature of the gas turbine increases both the net power and the overall cycle efficiency. At a constant inlet temperature of the gas turbine, the net power and the overall cycle efficiency increase as the compressor pressure ratio increases. But the overall cycle efficiency and net power will decrease with further increases in compressor pressure ratio, which means that the optimum compressor pressure ratio for each temperature can be obtained. Figures 11 and 12 show a plot of the overall cycle efficiency versus the net output power of the first and second designs at inlet gas temperature of gas turbine of 1600 K for different ambient

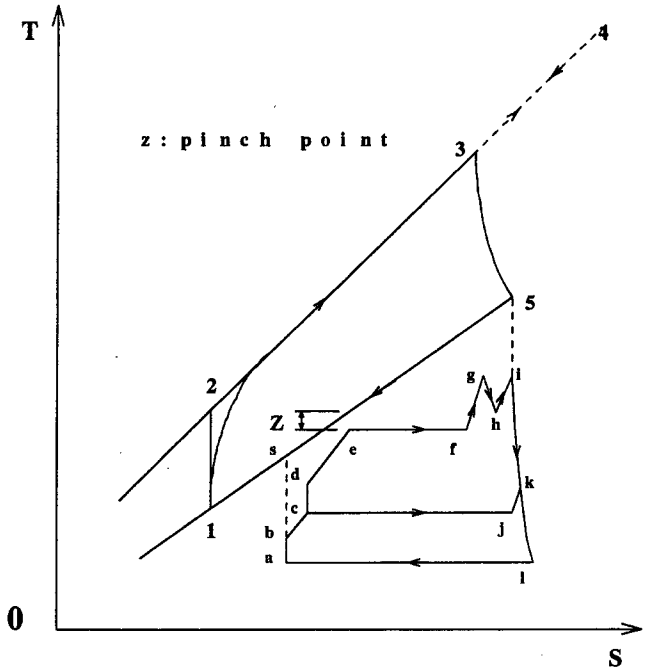

Fig. 5 Temperature–entropy diagram of the second design (*A*)

temperatures. It is clear from both figures that as the ambient temperature decreases the efficiency and net output power of the cycle increase due to a reduction in compressor power. Tables 4 and 5 show the performance and specific output comparisons between the first design, the second design, and a conventional heat recovery cycle. This comparison was performed at the same mass flow rate of air at 400 kg/s, with

Table 1 Assumptions of the cycle

Assumption	Unit	Const. used
1. Ambient temperature.	K	288.00
2. Atmospheric pressure.	bar	1.013373
3. Air leakage (internal).	%	0.50
4. Isentropic efficiency of the compressor.	%	85.00
5. Gas – side pressure loss in the SB.	%	6.00
6. Effectiveness of SB.	%	91.50*
7. Isentropic efficiency of the gas turbine.	%	90.00
8. Gas turbine exhaust gases pressure.	bar	1.10
9. ΔT of gases between SB and GT.	°C	3.00
10. ΔT of steam between SB and ST.	°C	3.00
11. Isentropic efficiency of steam turbine.	%	87.00
12. Feed-water heater loss (from outlet enthalpy).	%	1.00
13. Condenser pressure.	bar	0.05
14. ΔT of gases between GT and HRB.	°C	3.00
15. ΔT of steam between HRB and ST.	°C	3.00
16. Pinch point of HRB at HP.	°C	15.00
17. Pinch point of HRB at LP.	°C	25.00
18. Efficiency of boiler feed pump.	%	70.00
19. Effectiveness of heat recovery boiler.	%	80.00[6]
20. Mechanical efficiency.	%	99.00
21. Generator efficiency.	%	98.00

* The figure is calculated using practical data.

Downloaded 02 Jun 2010 to 171.66.16.104. Redistribution subject to ASME license or copyright; see http://www.asme.org/terms/Terms_Use.cfm

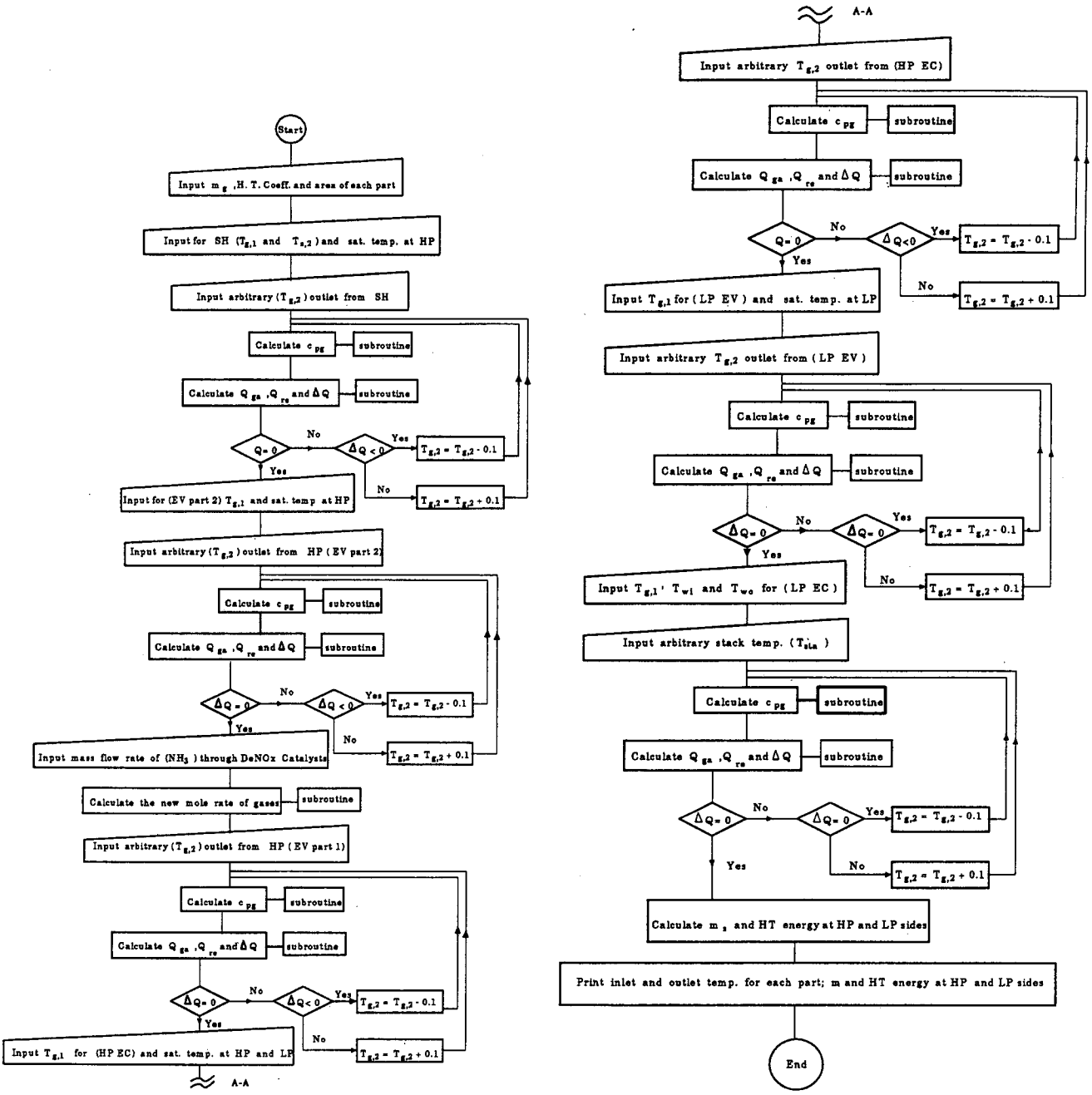

Fig. 6 Flow chart of heat recovery boiler program

Table 2 Steam conditions of the first design

Parameter	1st ST	2nd ST
Press. bar	170.00	70.00
Temp. °C	550.00	550.00

Table 3 Steam conditions of the second design

Parameter	HP ST	IP ST	LP ST
Press. bar	101.30	23.40	4.50
Temp. °C	540.00	540.00	260.00

Downloaded 02 Jun 2010 to 171.66.16.104. Redistribution subject to ASME license or copyright; see http://www.asme.org/terms/Terms_Use.cfm

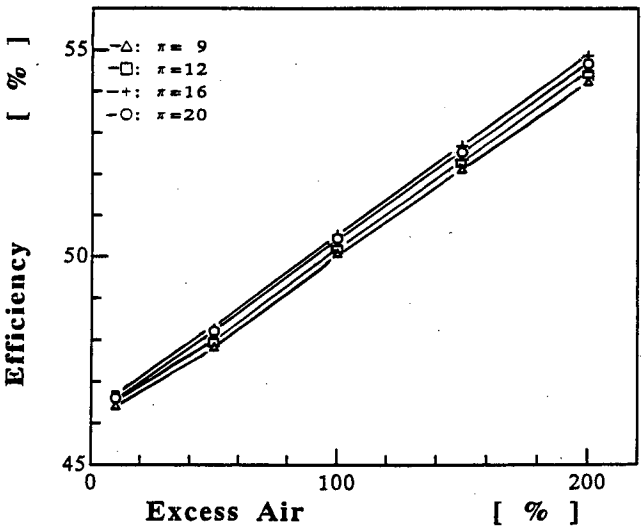

Fig. 7 Relation between the percentage of excess air and the overall cycle efficiency

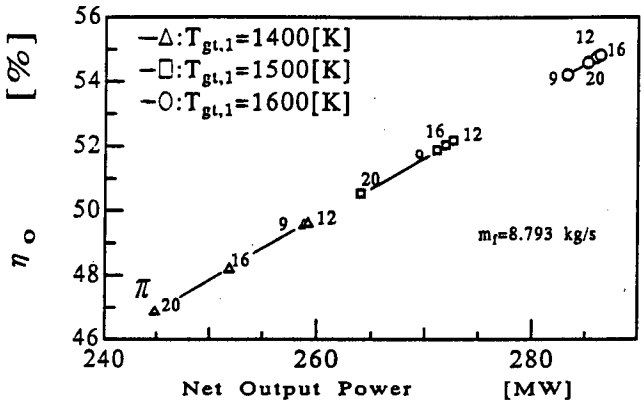

Fig. 8 Overall cycle efficiency versus net power at 3 FWH

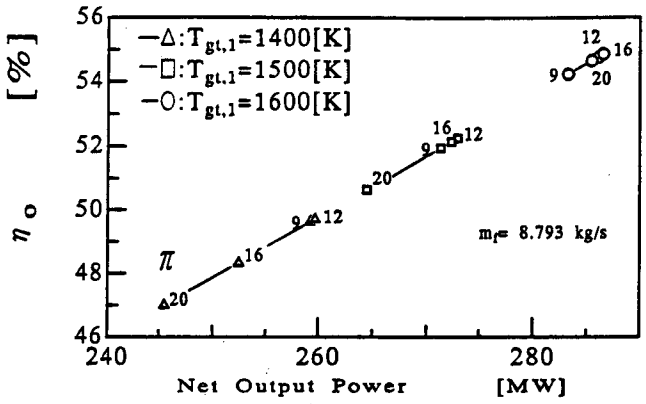

Fig. 9 Overall cycle efficiency versus net power at 4 FWH

natural gas as fuel, inlet temperature of gas turbine at 1600 K, and other assumptions as mentioned in Table 1.

In the conventional heat recovery cycle three cases of steam added to the combustion chamber were studied. In the first case, there was no steam added to the combustion chamber. In the second case, the mass flow rate of steam entering the combustion chamber was 4 kg/s (about 50 percent of fuel amount). In the third case, 8 kg/s of added steam to the combustion chamber was used (about 100 percent of fuel amount). Adding steam to the combustion chamber leads to an increase in the specific output power and reduction in NO_x emission; the steam is also used for cooling the combustion chamber.

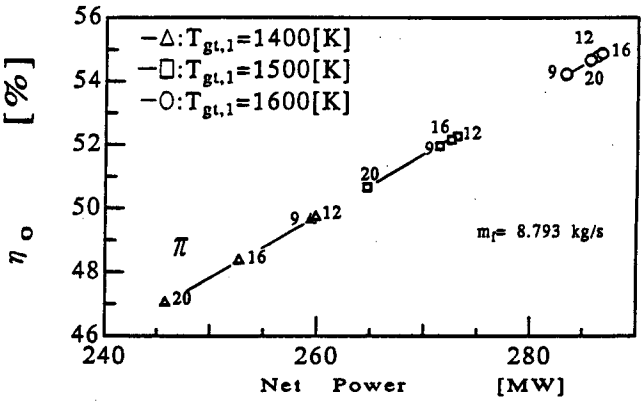

Fig. 10 Overall cycle efficiency versus net power at 5 FWH

Table 4 shows that the first design has the highest overall cycle efficiency among the cases studied at all compressor pressure ratios. Also, the efficiencies of the second design (*A*) are higher than those of the second design (*B*) and (*C*) for all cases of the conventional heat recovery cycle. Table 5 shows that all cases of the proposed cycles have higher specific output than the conventional heat recovery cycle, because of the lower percentage of excess air used in the proposed cycles. In the conventional heat recovery cycle, the temperature of the flue gases is reduced to reach the desired inlet gas turbine temperature mainly by increasing the percentage of excess air while, in the proposed cycles, lower percentage of excess air is needed because part of the heat energy of flue gases is transferred to the water wall of the supercharged boiler to generate steam. As a result, the size of the compressor will be smaller and more useful energy can be obtained.

Conclusions

Based on the assumptions made and the results obtained as illustrated in the tables and figures in this paper, the following conclusions are drawn:

1 The amount of air required to produce net output power in the conventional heat recovery cycle is higher than the amount of air required to produce the same net output power in the proposed cycles, which means that the compressor size of the proposed cycles is less than the compressor size in the conventional heat recovery cycle for the same net output power.

2 In the first design with inlet gas temperature of gas turbine at 1600 K, the net power produced by the Brayton cycle is about 55–59 percent of the total net output power of the combined cycle and the overall cycle efficiency is about 8.5–9.5 percent higher when compared to the conventional heat recovery cycle.

3 In the second design (*A*) with gas inlet temperature at 1600 K, the net output power of the Brayton cycle is about 56–68 percent of the total net output power produced by the combined cycle and the overall cycle efficiency is about 1.0–5.5 percent higher when compared to the conventional heat recovery cycle.

Downloaded 02 Jun 2010 to 171.66.16.104. Redistribution subject to ASME license or copyright; see http://www.asme.org/terms/Terms_Use.cfm

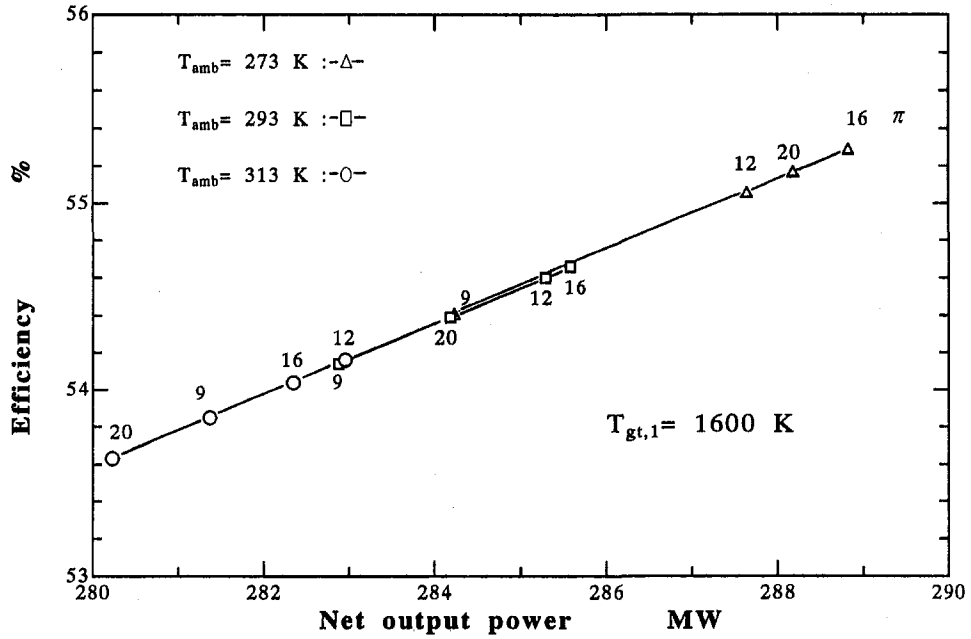

Fig. 11 Overall cycle efficiency versus net power for first design at different ambient temperature

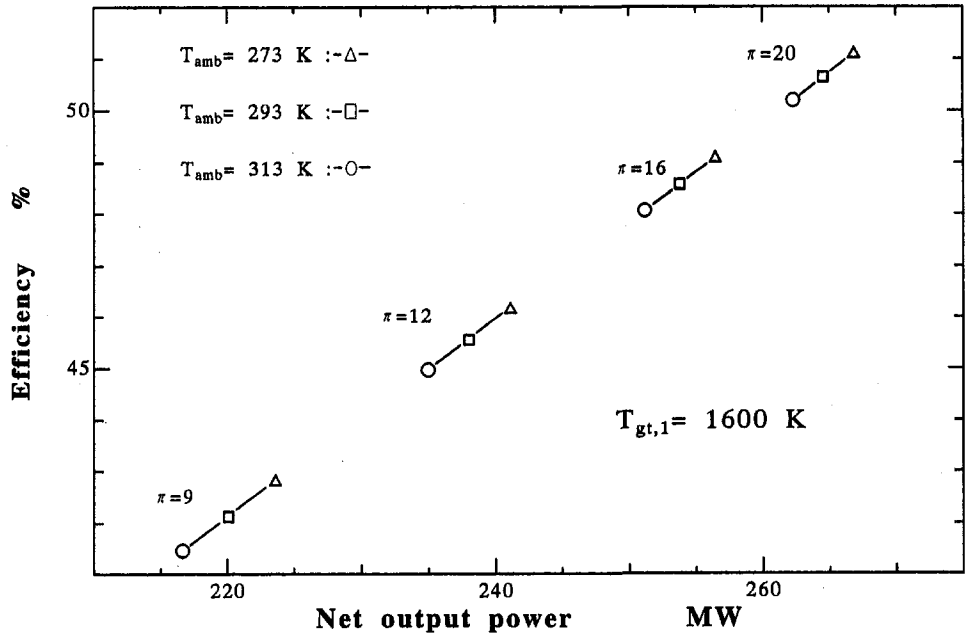

Fig. 12 Overall cycle efficiency versus net power for second design at different ambient temperature

Table 4 Performance comparison

π	First Design			Second Design			Heat Recovery Cycle		
	FWH=3	FWH=4	FWH=5	A	B	C	m_{sc}=0	m_{sc}=4	m_{sc}=8
	η_{com} %	η_{com} %	η_{com} %	η_{com} %	η_{com} %	η_{com} %	η_{com} %	η_{com} %	η_{com} %
9	54.20	54.21	54.22	46.47	44.85	43.27	44.91	45.22	45.48
12	54.74	54.76	54.77	49.39	47.99	44.59	45.41	45.74	46.08
16	54.81	54.85	54.86	48.42	47.32	45.88	45.28	45.69	46.05
20	54.59	54.64	54.66	50.50	48.44	47.01	44.15	44.59	45.01

Table 5 Specific output comparison

π	First Design			Second Design			Heat recovery Cycle		
	FWH=3	FWH=4	FWH=5	A	B	C	m_{sc}=0	m_{sc}=4	m_{sc}=8
	w_{sp} kJ/kg	w_{sp} kJ/kg	w_{sp} kJ/kg	w_{sp} kJ/kg	w_{sp} kJ/kg	w_{sp} kJ/kg	w_{sp} kJ/kg	w_{sp} kJ/kg	w_{sp} kJ/kg
9	708.1	708.2	708.2	728.5	878.8	1130.6	596.5	600.7	604.1
12	715.1	715.3	715.4	774.2	940.3	1165.0	580.5	584.7	589.0
16	716.0	716.5	716.7	632.4	741.7	899.0	554.3	559.2	563.7
20	713.0	713.7	713.9	659.6	759.3	614.0	520.5	525.5	530.5

Downloaded 02 Jun 2010 to 171.66.16.104. Redistribution subject to ASME license or copyright; see http://www.asme.org/terms/Terms_Use.cfm

References

1 Gorzengo, W. P., and Zoschak, R. J., "The Supercharged Steam Generator: Some Aspects of Design and Pressure Level Selection," ASME Paper No. 66-GT/CMC-68, 1966.

2 Silberring, L., "The Supercharged Steam Generator," *Sulzer Technical Review,* Vol. 47, No. 3, 1965, pp. 133–138.

3 Peeler, J. P. K., and Piggott, K. L., "The Combined Gas Turbine-Steam Cycle for Power Generation, Part I—A Literature Survey and Discussion," *Mech. and Chem. Engg. Trans. I. E., Aust.,* Vol. MC8, No. 2, Paper No. 3192A, 1972, pp. 125–130.

4 Smith, D. J., "Advance in Fluidized Bed Combustion and Cogeneration," *Power Engineering Journal,* Vol. 89, 1985, pp. 26–32.

5 Peeler, J. P. K., and Piggott, K. L., "The Combined Gas Turbine-Steam Cycle for Power Generation, Part II—Theoretical Study of a Coal Fired System," *Mecha. and Chem. Engg. Trans. I. E. Aust.,* Vol. MC8, No. 2, Paper No. 3192A, 1972, pp. 125–130.

6 Horlock, J. H., *Combined Power Plants Including Combined Cycle Gas Turbine (CCGT) Plants,* Pergamon Press, Oxford, 1992.

7 Akiba, M., Thani, E. A., and Tomizawa, M., "A Study of High-Accuracy Calculation of Combined Brayton–Rankine Cycles for Power Generation," *JSME International Journal,* Series B, Vol. 36, No. 1, 1993, pp. 178–183.

8 Cerri, G., and Colagé, A., "Steam Cycle Regeneration Influence on Combined Gas-Steam Power Plant Performance," ASME JOURNAL OF ENGINEERING FOR GAS TURBINES AND POWER, Vol. 107, 1985, pp. 574–581.

9 Consonni, S., Lozza, G., Macchi, E., Chiesa, P., and Bombarda, P., "Gas-Turbine-Based Advanced Cycles for Power Generation, Part A: Calculation Model," *Proceeding of the 1991 Yokohama International Gas Turbine Congress,* Vol. III, *1999,* pp. 201–210.

10 Agarwal, V. B., and Hardas, A. M., "Combined Steam and Gas Turbine Cycle of 30 MW Capacity for Low Cost Power Generation," *Energy Management Journal,* Oct.–Dec. 1985, pp. 295–300.

11 Keenan, J. H., Chao, J., and Kaye, J., *Gas Tables,* Wiley, New York, 1983.

12 Keenan, J. H., Keyes, F. G., Hill, P. G., and Moore, J. G., *Steam Tables,* Krieger Publishing Company, FL, 1992.

Downloaded 02 Jun 2010 to 171.66.16.104. Redistribution subject to ASME license or copyright; see http://www.asme.org/terms/Terms_Use.cfm